Investigation of Microbunching Instabilities in Modern Recirculating Accelerators

Cheng-Ying Tsai

Dissertation submitted to the Faculty of the
Virginia Polytechnic Institute and State University
in partial fulfillment of the requirements for the degree of

Doctor of Philosophy
in
Physics

Mark L. Pitt, Chair
Rui Li
Chenggang Tao
R. Bruce Vogelaar

March 21, 2017
Blacksburg, Virginia

Keywords: Microbunching, Collective Instability, Coherent Synchrotron Radiation, Recirculating Accelerators

Investigation of Microbunching Instabilities in Modern Recirculating Accelerators

Cheng-Ying Tsai

ABSTRACT

Particle accelerators are machines to accelerate and store charged particles, such as electrons or protons, to the energy levels for various scientific applications. A collection of charged particles usually forms a particle beam. There are three basic types of particle accelerators: linear accelerators (linac), storage-ring (or circular) accelerators, and recirculating accelerators. In a linac, particles are accelerated and pass through once along a linear or straight beamline. Storage-ring accelerators propel particles around a circular track and repetitively append the energy to the stored beam. The third type, also the most recent one in chronology, the recirculating accelerator, is designed to accelerate the particle beam in a short section of linac, circulate the beam, and then either continue to accelerate for energy boost or decelerate it for energy recovery. The beam properties of a linac machine are set at best by the initial particle sources. For storage rings, the beam equilibria are instead determined by the overall machine design. The modern recirculating machines share with linacs the advantages to both accelerate and preserve the beam with high beam quality, as well as efficiently reuse the accelerating components. The beamline design in such a machine configuration can however be much more complicated than that of linacs.

As modern accelerators push toward the high-brightness or high-intensity frontier by demanding particles in a highly charged bunch (about nano-Coulomb per bunch) to concentrate in an ever-decreasing beam phase space (transverse normalized emittance about 1 μm and relative energy spread of the order of 10^{-5} in GeV beam energy), the interaction amongst particles via their self-generated electromagnetic fields can potentially lead to coherent instabilities of the beam and thus pose significant challenges to the machine design and operation. In the past decade and a half, microbunching instability (MBI) has been one of the most challenging issues for such high-brightness or high-intensity beam transport, as it would degrade lasing performance in the fourth-generation light sources, reduce cooling efficiency in electron cooling facilities, and compromise the luminosity of colliding beams in lepton or lepton-hadron colliders.

The dissertation work will focus on the MBI in modern recirculating electron accelerators. It has been known that the collective interactions, the coherent synchrotron radiation (CSR) and the longitudinal space charge (LSC) forces, can drive MBI. The CSR effect is a collective phenomenon in which the electrons in a curved motion, e.g. a bending dipole, emit radiation at a scale comparable to the micro-bunched structure of the bunch distribution. The LSC effect stems from non-uniformity of the charge distribution, acts as plasma oscillation, and can eventually accumulate an amount of energy modulation when the beam traverses a long section of a beamline. MBI can be seeded by non-uniformity or shot noise of the beam, which originates from granularity of the elementary charge. Through the aforementioned collective effects, the modulation of the bunch sub-structure can be amplified and, once the beam-wave interaction formed a positive feedback, can result in MBI. The problem of MBI has been intensively studied for linac-based facilities and for storage-ring accelerators. However, systematic studies for recirculation machines are still very limited and form a knowledge gap. Because of the much more complicated machine configuration of the recirculating accelerators than that of linacs, the existing MBI analysis needs to be extended to accommodate the high-brightness particle beam transport in modern recirculating accelerators. This dissertation is focused on theoretical investigation of MBI in such machine configuration in the following seven themes:

(1) Development and generalization of MBI theory

The theoretical formulation has been extended so as to be applicable to a general linear beamline lattice

including horizontal and vertical transport bending elements, and beam acceleration or deceleration. These featured generalizations are required for MBI analysis in recirculation accelerators.

(2) Construction of CSR impedance models
In addition to the steady-state CSR interaction, it has been found that the exit transient effect (or CSR drift) can even result in more serious MBI in high-brightness recirculation arcs. The one-dimensional free-space CSR impedances, especially the exit transients, are derived. The steady-state CSR impedance is also extended to non-ultrarelativistic beam energy for MBI analysis of low-energy merger sections in recirculating accelerators.

(3) Numerical implementation of the derived semi-analytical formulation
This includes the development of a semi-analytical Vlasov solver for MBI analysis, and also benchmarking of the solver against massive particle tracking simulations.

(4) Exploration of multistage amplification behavior of CSR microbunching development
The CSR-induced MBI acts as an amplifier, which amplifies the sub-bunch modulation of a beam. The amplification is commonly quantified by the amplification gain. A beam transport system can be considered as a cascaded amplifier. Unlike the two-stage amplification of four-dipole bunch compressor chicanes employed in linacs, the recirculation arcs, which are usually constituted by several tens of bending magnets, show a distinguishing feature of up to six-stage microbunching amplification for our example arc lattices. That is, the maximal CSR amplification gain can be proportional to the peak bunch current up to sixth power. A method to compare lattice performance has been developed in terms of gain coefficients, which nearly depend on the lattice properties only. This method has also proven to be an effective way to quantify the current dependence of the maximal CSR gains.

(5) Control of CSR MBI in multibend transport or recirculation arcs
The existing mitigation schemes of MBI mostly aim to linac-based accelerators and may not be practical to the recirculating accelerator facilities. Thus a set of conditions for suppression of CSR MBI was proposed and examined for example lattices from low ($\sim$100 MeV) to high ($\sim$1 GeV) energies.

(6) Study of more aspects of microbunched structures in beam phase spaces
For a cascaded amplifier in circuit electronics, the total amplification gain can be estimated as the product of individual gains. In a beam transport line of an accelerator, the (scalar) gain multiplication was examined and found to under-estimate the overall microbunching amplification. The concept of gain matrix was developed, which includes the density, energy and transverse-longitudinal modulations in a beam phase space, and used to analyze MBI for a proposed recirculating machine. Throughout the gain matrix approach, it reasonably gives the upper limit of spectral MBI gain curves. This extended analysis can be employed to study multi-pass recirculation.

(7) Study of MBI for magnetized beams
Driven by a recent energy-recovery-linac based cooler design for electron cooling at Jefferson Lab Electron-Ion Collider Project, the generalized theoretical formulation for MBI to a transversely coupled beam has been developed and applied to this study. A magnetized beam in general features non-zero canonical angular momentum, thus considered to be a transversely coupled beam. A novel idea of utilizing magnetized beam transport was proposed for improvement of cooling efficiency and possible mitigation of collective effects. A concern of MBI regarding this design was studied and excluded. The large transverse beam size associated with the beam magnetization is found to help suppress MBI via the transverse-longitudinal correlation.

Part of this work is supported by Jefferson Science Associates, LLC under U.S. Department of Energy (DOE) Contract No. DE-AC05-06OR23177.

Investigation of Microbunching Instabilities in Modern Recirculating Accelerators

Cheng-Ying Tsai

GENERAL AUDIENCE ABSTRACT

Particle accelerators are machines to accelerate and store charged particle beams, such as electrons or protons, to the energy levels for various scientific applications. There are three basic types of particle accelerators: linear accelerators (linac), storage-ring (or circular) accelerators, and recirculating accelerators. The third type, also the most recent one, is designed to accelerate a particle beam in a short section of linac, circulate and then continue to accelerate it for energy boost or decelerate it for energy recovery. The modern recirculating machines possess the advantages to both accelerate and preserve the beam with high beam quality, as well as efficiently reuse the accelerating components. As modern accelerators push toward the high-brightness or high-intensity frontier by demanding particles in a highly charged bunch to concentrate in an ever-decreasing beam phase space, the interaction amongst particles via their self-generated electromagnetic fields can potentially lead to coherent instabilities of the beam and thus pose significant challenges to the machine design and operation. Microbunching instability (MBI) has been one of the most challenging issues for such high-brightness or high-intensity beam transport, as it would degrade lasing performance in the fourth-generation light sources, reduce cooling efficiency in electron cooling facilities, and eventually compromise the luminosity of colliding beams in lepton or lepton-hadron colliders.

The dissertation work will focus on the MBI in modern recirculating electron accelerators. The research attempts to develop a comprehensive theoretical formulation of MBI with aspects including among various degrees of freedoms the beam itself, the beamline lattice optics, and incorporation of all relevant collective effects that the beam encounters, for example the coherent synchrotron radiation (CSR) and the longitudinal space charge (LSC) effects. This dissertation includes the following seven themes: 1) Development and generalization of MBI theory to arbitrary linear lattices and coupled beams with constant and varying energies; 2) Construction of CSR impedance models from steady state to transient state and from high to low energy regime; 3) Numerical implementation of the developed theory as a fast and numerical-noise-free Vlasov solver and benchmarking with massive particle tracking simulation; 4) Exploration of multistage cascaded amplification mechanism of CSR microbunching development; 5) Control of CSR-induced MBI in multi-bend transport or recirculation arcs; 6) Study of more aspects of microbunched structures in beam phase spaces; and 7) Study of MBI for magnetized beams and confirming the suppression of MBI for a recent cooler design for Jefferson Lab Electron Ion Collider project.

ACKNOWLEDGMENT

It seems like it was only last month that I came to Jefferson Lab and started my second stage of graduate student life. But it was long ago and has been 45 months since I left town of Hokies. Happy times always pass by so fast! When student happy time comes to an end, I would like to express my deepest gratitude to people who help me, who work with me, who support me, whom I learn with, and whom I live with.

In the academic parts, I would like to sincerely express my gratitude to my advisor at JLab, Dr. Rui Li, who has unreservedly provided me thorough guidance, in nearly all aspects, in not only this dissertation but also the fascinating field of collective beam dynamics in accelerator physics. Her help, insights, persistence, patience, and enthusiastic encouragement have indebted me in an incalculable way. She has also been the audience and advisor (with perfect attendance) in my series presentations on many topics I am interested in. Presuming I can live my graduate life over again, without question I would still choose her as my advisor.

I would also like to voice my appreciation to my supervisor at Virginia Tech, Prof. Mark Pitt, who, almost at all costs, has taken care of both the administrative and academic parts, including my tuition situations, submitting NSF proposals, travel expenses to training courses, conferences, experimental activities and so on. As for the administrative part, Prof. Hari Areti, Audrey Barren, Christa Thomas, Betty Wilkins, and Christine Petit-Jean-Genaz must have done much silent work to prevent me from administrative chores at JLab, Virginia Tech, conference registration issues and student travel grants. Christa's hospitality and kindness are always remembered when I knocked on her door on the first day to the campus.

During these years at JLab I have had the privilege of working with, in fact been advised by, many great scientists. Drs. David Douglas and Chris Tennant have not only provided me with necessary help but directly contributed to the dissertation almost everywhere. Dr. Jie Chen had provided much help regarding cluster computing, as well as many CCPRs from JLab Computer Center. I cannot imagine how troublesome it would be if any advancement of this work can be made without those artful examples. Dr. Steve Benson has kindly provided and coordinated a stimulating environment, which results in advancements of our work.

My thanks also go to my Ph.D. committee members at Virginia Tech, Profs. Chenggang Tao and Bruce Vogelaar, for their valuable comments and suggestions regarding the dissertation draft. These may make the context of this dissertation more readable to non-accelerator physicists.

It deserves here to mention Dr. Simone Di Mitri, a colleague and a friend when we first met in Stony Brook (ERL2015) and later in Daejeon (FEL15) and Chicago (NAPAC16). His active encouragement and continuous support lead to fruitful results, including a contributed presentation at following accelerator

conferences and a published paper. I had also fruitful discussion with Dr. Irwan Setija, when we first met in ERL Workshop, during his visit to JLab in 2015, and later teleconference meetings.

As a graduate student in US, I have possessed the advantage of educational resources, particularly the US Particle Accelerator School (USPAS). I thank Dr. William Barletta, Susan Winchester, Irina Novitski, and people I may not know, for their decision to support me to attend with financial assistance. I benefit much from the instructors which offer the courses I took, from the graduate accelerator physics course by Dr. William MacKay and Prof. Todd Satogata to the most recent and relevant collective instability course by Prof. Alex Chao and Dr. Gennady Stupakov. I would also give thanks to Prof. Shyh-Yuan Lee, who always encourages young students to work as hard as they can. Although ten hours a day does not meet his expectation, it almost reaches the maximum in my schedule. Another education resource is the seminar held by Center of Accelerator Science (CAS) in Old Dominion University (ODU). I would like to acknowledge Prof. Gail Dodge for her invitation to me to attend CAS seminars at ODU.

In addition, many discussants from different periods, institutions and various situations are also greatly appreciated, including Tomonori Agoh (KEK, for CSR calculation), Michael Borland (ANL, for `elegant`), Ping-Jung Chou (NSRRC), Slava Derbenev (Rick's cafe), Paul Gueye (Hampton University), Aliaksei Halavanau (NIU, for his tree code), He Huang, Joe Grames (PEPPo), Geoff Krafft, Fanglei Lin (for `MAD-X`), Chris Mayes (CLASSE), Chad Mitchell (LBL), Vasiliy Morozov, Wei-Ping Pan (NTHU), Philippe Piot (NIU/Fermilab), Ji Qiang (LBL), Yves Roblin, Mike Spata, Riad Suleiman (PEPPo), Marco Venturini (LBL), Guohui Wei, Juhao Wu (SLAC), He Zhang, Yuhong Zhang and so on.

Last but one, my friends during my graduate studies in Blacksburg, they are Nai-Ching Wang, Tsung-Han Yang, Yian Chen, and Jr-wei Tsai; during USPAS, Yung-Chuan Chen and Yuan Hui Wu, and during my stay in Newport News, Jianxun Yan, are all acknowledged.

Last but most importantly, I would express my warmest thanks to my family members, my wife Xi Chen, for her patience to my regular "absence", and my parents, Tien-Fu Tsai, Yueh-Tao Hsu, Lei Chen, and Xiaohui Chen, for endless and unconditional support in every aspect.

CONTENTS

LIST OF TABLES

LIST OF FIGURES

CHAPTER 1
Introduction

1.1 High-brightness electron beams in accelerators and collective effects

Particle accelerators have long been used as powerful discovery tools in many scientific fields to answer fundamental questions. In these fields, the frontier of the scientific research activities extends as the capabilities of the accelerators are enhanced. The capabilities of accelerators as discovery tools, in turn, depend strongly on the possibility for the accelerators to provide high-intensity or high-brightness electron or ion beams. For example, high-energy accelerators, including lepton and hadron colliders, are used to probe the basic structure of matter and to explore mechanisms of fundamental interactions in the micro-world of the universe. Achieving high luminosity using high-intensity or high-brightness beams is the key for the success of high-energy colliders. Similarly, synchrotron radiation light sources, based on high energy electron storage rings, and free electron lasers (FEL), based on linear accelerators (linac), are used throughout the material and biological sciences for determining molecular structure and revealing dynamical processes such as chemical reactions or protein folding. Achieving high brightness of the photons generated from high-intensity or high-brightness electron beams is again the key to the success of the light sources.

As modern accelerators push toward the high-intensity or high-brightness frontier by demanding particles in a highly charged bunch to concentrate in an ever-decreasing phase space volume, the interaction amongst particles through their self-generated electromagnetic fields, which we call *collective* interaction, could cause collective instabilities of the beam and thus pose significant challenges to the machine design and operation. The collective interaction can take many different forms: space charge is the mean-field of direct Coulomb interaction amongst particles within a bunch; wakefield[1] on particles is the result of the Coulomb fields generated from a charged beam, and is scattered and diffracted by a non-uniform or resistive vacuum chamber; and the list goes on. Collective effects are the impact of these collective interactions on beams, which often involves rearrangement of the particle distribution in phase space in an undesirable way and the onset of instabilities [35].

The history of advancement in accelerator science is the history of developing new accelerator concepts and technology to accelerate and control charged particle beams and the history of observing, explaining and curing various new collective instabilities [36]. As we overcome old instabilities and push for higher beam intensity, new instabilities appear as new limiting factors for machine designs. Among them, the coherent synchrotron radiation (CSR) induced microbunching instability (MBI) is the most recently discov-

[1] In Chapter 4, we would introduce the concepts of wakefields and impedances, as are commonly used in accelerator community for study of collective beam instabilities. At the moment, we can think of wakefields as the electromagnetic fields generated by the traversing charged particle beams. In most situations the electromagnetic fields, which were generated by the leading portion of a beam and then affect the trailing part of the beam particles, are usually referred to as wake-fields (head-tail interaction). Following this convention, we still use the terminology CSR wakefield, even though CSR is tail-head interaction.

ered outstanding collective instability that takes place parasitically when a high-brightness electron bunch is transported through a curved orbit. Synchrotron radiation emitted by an accelerated electron bunch traversing in a curved orbit is usually incoherent due to the random arrangement of phases of the emitted fields from individual electrons. However, when the bunch length (or the sub-bunch structure) is sufficiently short compared to the radiation wavelength, the emitted fields are nearly in phase with each other and thus result in CSR. The radiation reaction on the beam may lead to the CSR-induced microbunching instability. In addition to CSR, the beam quality degradation can arise from the longitudinal space charge (LSC) effect. The LSC effect stems from density ripples/fluctuations of the bunch charge distribution and can accumulate an amount of energy modulation (similar to plasma oscillation) when the beam traverses a long section of a beam line. The LSC-induced microbunching can also play an important role as CSR MBI, as had been emphasized in the existing literature (see, for example, Refs. [154],[82]). Overcoming these collective effects requires accelerator physicists to first fully understand the underlying mechanism from first principles.

The investigation of collective effects on beam dynamics often involves: (1) analysis of Vlasov-Maxwell equations, where Vlasov equation describes the particle beam phase-space dynamics and Maxwell equations govern the electrodynamics; (2) large-scale computation to simulate the dynamics of several millions (or even billions) of particles[2] under collective interactions, to benchmark the theory and to simulate realistic experiments; and (3) experiments to measure the collective effects on the beam using existing accelerators or test facilities, to eventually confirm the theoretical understanding. By making the assumption of an ideal unperturbed beam phase-space distribution and simplifying the collective-interaction model, theoretical analysis can give deep insights and understanding of the mechanism of collective effects, as well as provide dependence of the collective phenomena on experimental parameters. Simulation has the capability to model beam dynamics with realistic experimental conditions and has been proved a very useful tool to obtain predictions of phenomena in actual accelerator machines. Experimental tests serve to verify the validity of both theoretical understanding and numerical modeling. Only when numerical simulations give consistent results with theoretical results for simplified cases, and meanwhile give predictions agreeing with experimental measurements, can we claim the complete understanding of the physical process and the mastery of predictive simulation tools for future machine designs to control or mitigate the collective effects.

1.2 Recirculating machine as a type of modern particle accelerators

The particle accelerators can be in general categorized into three different types of configurations in terms of revolution numbers of a beam: (1) single-pass; (2) infinite-pass; and (3) few-passes. In this subsection, we follow two excellent review articles, Refs. [97, 123], and briefly introduce typical features of each accelerator configuration. Readers are referred to Refs.[97, 123] for more details. In what follows we restrict to the case of electron accelerators.

[2]For example, in a practical situation, there are usually $\sim 10^{10}$ electrons per bunch, or ~ 1 nC of bunch charge, in linac-based short-wavelength free electron laser sources.

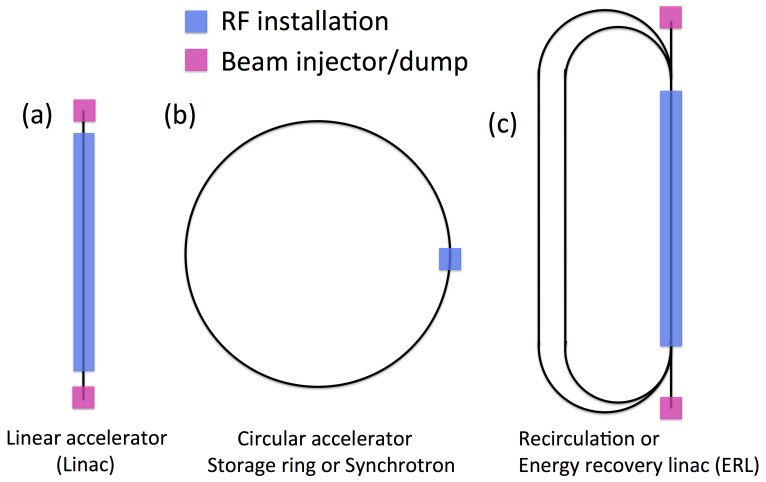

Figure 1.1: Main accelerator types. Picture reproduced from Refs. [97, 123].

The first type of accelerators, shown in Fig.1.1(a), belongs to electron linear accelerators (linacs). Some main features include:

- In such type of accelerators, the beamline has a definite beginning and an end. By linear it means the beam transport follows a nearly straight/linear line;
- There is a substantial length of radio-frequency (RF) beam-acceleration devices;
- An individual electron resides in the accelerator in a very short time, compared to relevant radiation damping times;
- If a laser-driven photocathode gun is used as the electron source, it is relatively easy to load, or program, the beam current or beam polarization delivered to users by controlling the duration and polarization of the lasers that stimulate electron production at the gun;
- The emittance of the electrons in a typical beam tends to be set by phenomena in the low-energy electron source region (or, by the initial conditions), and this emittance may be well preserved during the acceleration to high energy;
- The pulse duration, and more generally the longitudinal phase space distribution, is relatively easily manipulated by using standard beam-RF and electron beam optical techniques.

The second type is the so-called synchrotrons or storage rings, shown in Fig.1.1(b). In an electron storage ring, typical characteristics regarding this configuration consists of:

- Instead of linear, the electrons are bent on a roughly circular orbit.

- Because of centripetal force, the accelerated electrons radiate copious amounts of synchrotron radiation (SR), including incoherent and coherent. To achieve a long-term equilibrium it is necessary to supply energy to the circulating electrons. The energy loss due to SR is replenished with a single RF cavity (or a few RF cavities) and the RF only occupies a very small portion of the total machine circumference;
- The equilibrium beam qualities are determined by a competition/balance between the radiation damping, due to which the electrons are damped onto the closed orbit at the correct accelerating phase, and the quantum radiation excitation, which tends to excite both transverse and longitudinal oscillations;
- The stored electron beam, for which (if stable operation) we presume to circulate for infinite number of revolutions, gradually reaches to the equilibrium after the time interval of several tens of synchrotron oscillation periods;
- The transverse beam emittances, the equilibrium bunch length, and energy spread of a beam in an electron storage ring can be neither arbitrarily nor determined by initial conditions but by the machine optics configuration.

The third type of accelerator configuration refers to the recirculating machines, shown in Fig.1.1(c), and features:

- Similar to linacs, there is substantial RF accelerating sections. The beam has a definite beginning and ending. Unlike linac, the beam in the recirculating machine goes through the accelerating cavities more than once;
- In some situations, the first-pass beam is accelerated by the RF field, the second-pass beam may be decelerated by the same RF field provided the RF phase has reversed sign when the second-pass beam arrives; or, in other situations, the first N passes are used to accelerate the beam and the subsequent N passes to decelerate the beam. This configuration is also called the energy recovery linac (ERL) accelerator;
- There does not exist the concept of closed or equilibrium orbit, different from the storage ring case. That is, the beam properties are determined by the source region (or the initial conditions);
- Such a hybrid arrangement, by applying beam energy recovery, allows one accelerator to feature some advantages of both of the usual arrangements, i.e. Fig.1.1(a,b);
- The electron circulation time is short compared to a typical radiative emittance buildup time, i.e. no equilibrium is established, implying that the emittance delivered to the end user may be smaller than the storage ring case, as is desired. The minimum pulse length is no longer set by radiative effects but by the ability to generate and manipulate.

Table 1.1: Comparison of typical beam and machine parameters for three different configurations of accelerators. High-energy electron linac is assumed with room-temperature RF cavities.

Parameter	High-energy electron linac	Storage ring	Superconducting recirculation linac or ERL
Accelerating gradient (MV/m)	>50	N.A.	10-20
Duty factor	≤ 0.01	$\sim$1	$\sim$1
Average current (mA)	≤ 1	100-1000	10-100
Average beam power (MW)	0.5	1-500	≥ 1000
Normalized emittance (μm)	1	5	0.5-1
Bunch length	$\sim$100 fs (30 μm)	$\sim$20 ps (6 mm)	$\sim$100 fs (30 μm)

To get more feel about the three different accelerator configurations, Table 1.1 illustrates typical beam parameters for the three different types of accelerators. As can be seen, the recirculating machine can deliver beams with high-duty factor (compared with linacs) and thus high average current, and short bunch length and excellent beam emittance (compared with storage rings). Although the original idea of an ERL based on superconducting RF (SRF) technology was proposed early in 1965 [171], this particular configuration was relatively late in implementation in 1987 at Stanford University [160]. In the future, it is likely that electron recirculation will be widely applied to build recirculating machines because of their superior beam quality. Recirculating accelerators share with linacs the ability to accelerate and preserve the emittance of very-low-emittance injector beams. For the latter, in fact, it can be more challenging than in linacs and can take more efforts to preserve the beam phase space qualities because more bending elements, thus more severe CSR, are present in recirculating machines. Also, as in linacs, one can manipulate the longitudinal phase space of the electron beam to deliver very short beam pulses to the end user. Applying energy recovery has allowed one to conceive of recirculating linacs with high average currents and also to have efficiencies approaching those in storage rings.

Recirculating arcs are important and necessary components in recirculation machines or energy recovery linacs (ERL). As summarized above, ERL is a novel accelerator scheme in which the beam energy acquired from acceleration by RF structures is later recycled, by using recirculating arcs, to resend the beam back to the linac at a decelerating phase after the beam fulfills its scientific mission. This combination could significantly advance the state of the art in X-ray free-electron lasers (XFELs) that will make new discoveries possible for sciences in biology and material science. In the past decade, new ERL-based X-ray light sources are under active design (see, for example, Ref. [130]). These designs feature high electron bunch intensities with bunch charge 20-100 pC at high energy (3-10 GeV) with superior phase space quality: low transverse emittance (0.1-0.5 mm-mrad) and energy spread (10^{-5} to 10^{-4}) and ultra-short bunch length (from $\sim$100 fs to $\sim$2 ps). ERL is also employed in the design of electron-ion colliders as the future instrument for nuclear science [49, 116]. The attractive features of ERL present many new challenges [80] to the accelerator physics studies, such as transverse beam instability (e.g. beam breakup instability), beam loss and halo formation, CSR and LSC induced microbunching instability. These topics are under intense study, as already reported in many ERL workshops.

Recirculating arcs are also employed in other recent proposals of hard X-ray light sources that use recirculating linac for cost efficiency but do not involve energy recovery. These include X-ray FEL Oscillator (XFELO) designs [93], which use low-gain oscillators to provide fully coherent and stable X-ray pulses, and the X-ray FEL upgradable to 25 keV photons [215] using a recirculating linac. These machines put more stringent requirements on beam quality, such as even smaller energy spread and smaller normalized beam emittance. Another device that utilizes recirculating arcs for transporting high-brightness electron beams is the Circulator Cooler Ring (CCR) of the Jefferson Lab Electron-Ion Collider (JLEIC) [1, 2] (or former Medium-energy Electron-Ion Collider, MEIC). Electron cooling is the most crucial technology for JLEIC to achieve its design luminosity, which requires intense electron beams with small emittance and energy spread to provide electron cooling for the ion beam. To circumvent the limit of the gun technology in providing ampere level average current, CCR is designed for the electron beam to circulate the ring and cool the ion beam for several tens of times and be dumped before the electron beam quality is deteriorated by both the cooling process and the CSR and space charge effects in the cooler ring. Beam physics in CCR is unique because unlike the situation in a usual storage ring, in CCR the beam does not reach the equilibrium. Among the many new challenges put forth by these new designs, one important common issue is the preservation of high beam phase space quality and getting CSR and space charge effects under control while transporting high-brightness beams through a sequence of dipoles in recirculating arcs. This particular concern of beam dynamics in CCR, while not serving as the essential in this dissertation, indeed constitutes the initial motivation to this work.

In the next two subsections we will review recent status of experimental and theoretical studies of CSR and microbunching instabilities in modern accelerators. It deserves here to clarify the train of thoughts and the focus of the dissertation: 1) MBI (usually occurred in longitudinal phase space) is a collective instability phenomenon and has been known to be driven by CSR or LSC; 2) In addition to MBI, CSR can also result in beam phase space degradation, for example, transverse beam emittance growth; 3) Complete collective effect studies should include both beam dynamics (e.g. MBI) and electrodynamics (e.g. CSR and LSC) aspects. In the dissertation while we put more emphasis on the collective phenomenon, MBI, than electrodynamics of CSR, we also study possible ways to mitigate CSR-induced transverse beam emittance growth. It should be noted that CSR-induced emittance growth is not a collective phenomenon. However CSR and MBI are closely related to each other.

1.3 Recent status of CSR and microbunching instability experimental studies in modern electron accelerators

As modern accelerators push toward the high-intensity or high-brightness frontier, by demanding electron beams with high bunch charge concentrated in ever-decreasing phase space volume, the needs for understand-

ing and mitigating the detrimental effects of CSR and LSC on the generation and transport of high-brightness electron beams become crucial issues for accelerator designs. The CSR effect takes place when a high-intensity or high-brightness electron bunch is transported on a curved orbit. The beam phase space dilution and self-organizing phenomena, such as microbunching instability caused by CSR and LSC interaction, could prevent next generation X-ray FEL from reaching their designed high brightness at short wavelength, or prevent next generation lepton or electron-ion colliders to reach their designed luminosities at high energies. Extensive studies of CSR effects in bunch compression chicanes[3] of linac-based FEL [55] and in synchrotron-light-source storage rings [129] have been carried out in the past fifteen years. Consequently, considerable knowledge has been gained on the emittance growth and longitudinal phase space modulation or fragmentation caused by CSR interaction in bunch compressor chicanes, as well as on the onset of CSR-induced microwave instability (MWI) in storage rings[4]. In addition, the ubiquitous LSC effect can also degrade beam phase space quality. It is found that LSC-induced microbunching instabilities can also deteriorate the machine performance for a single-pass FEL when the beam bunches are transported and accelerated to high energies in a long beamline [152, 81, 193].

Here we note that CSR itself can be a double-edged sword; in view of beam dynamics, of primary interest in this dissertation, CSR can result in deleterious effects on electron beams, while, from the viewpoint of light-source users, taking advantage of coherent radiations, to produce a stable CSR for an optimized/dedicated storage ring accelerator design is their ultimate goal. There have been extensive applications and exploration of utilizing CSR to generate radiations in terahertz (THz) frequency ranges[5], e.g. Refs.[31, 90, 4, 159, 91, 210, 69, 168]. In this section we briefly review the most recent experimental status of MBI study in modern accelerators with more focus on beam dynamics aspects in single-pass and recirculation/ERL machines.

The pursuit of high-brightness beams drives the advance in diagnostics technology to measure bunch length and emittance for ultra-short bunches with high peak current and low transverse and longitudinal emittances. Recently, there are many measurements of CSR and LSC effects on electron bunches and their comparisons with simulations. On several single-pass linac based FELs, the comparison of emittance growth, between experimental measured results after the bunch being compressed by a magnetic chicane and simu-

[3] A chicane is a modular unit composed of a sequence of a few dipoles, typically four or five dipoles. Usually the purpose is to provide bunch-length manipulation via time-of-flight dependence of particles in a beam. These dipoles generate a dispersive region in the chicane. Thus particles with slightly different energies travel different paths or trajectories. Prior to the chicane, the bunch is accelerated by the radiofrequency (RF) cavity off-crest so that electrons with different bunch (internal) positions gain different energies. This is later quantified by the *chirp* parameter. In the setting of a normal chicane, assume head particles are with lower energy and tail particles with higher energy, then the higher-energy particles travel a longer trajectory than the lower-energy particles. At the exit of such a chicane, the bunch is compressed. Decompression can work in the opposite way. For low-energy space-charge dominated beams, an unconventional chicane had been recently proposed for bunch compression [78].

[4] In single-pass or recirculation machines, we usually use the term microbunching instability (MBI). In storage ring facilities, the term microwave instability (MWI) is employed. Theoretical treatments to these two different configurations may be similar but not exactly the same. In this dissertation we focus more on the single-pass treatment [79, 81, 193]. A short discussion of connecting these two configurations will be made in Sec. 3.4.

[5] Around the threshold the bunch length is found to be in the picosecond (ps) time scales.

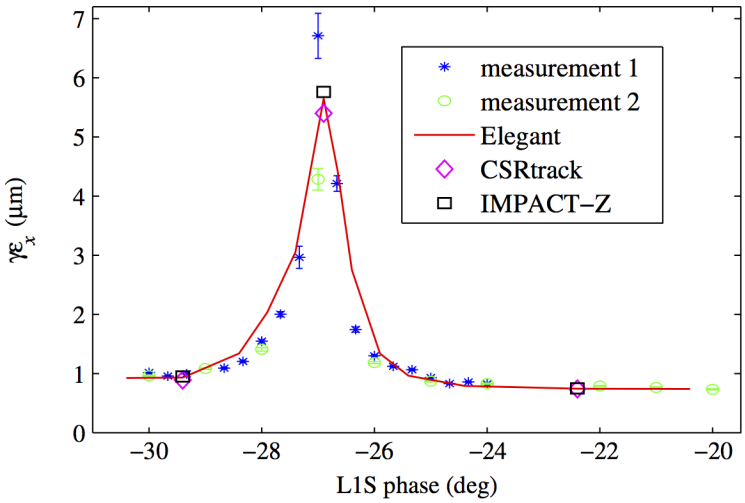

Figure 1.2: Comparison between measured and simulated horizontal emittances as a function of upstream RF phase in linac (L1S) after the first bunch compressor chicane for 250 pC bunch charge at LCLS. The horizontal emittance growth is partly due to CSR. Picture from Refs. [10].

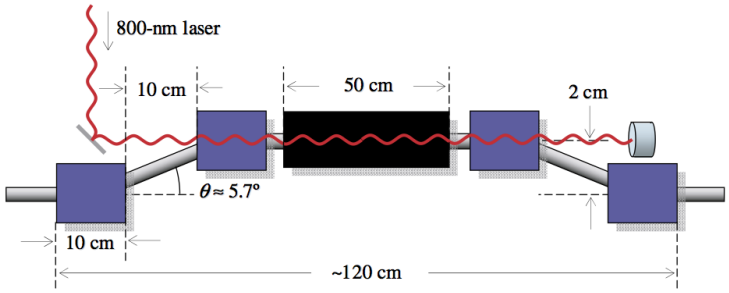

Figure 1.3: Layout of the LCLS laser heater inside a (small) magnetic chicane at 135 MeV. The laser heater, installed at upstream of the LCLS linac, is used to mitigate MBI. Picture from Ref.[82]

lated results by `elegant`[21], `CSRtrack`[56] and `IMPACT`[141], showed very good agreement, as demonstrated in Ref. [10] for the case of Linac Coherent Light Source (LCLS), shown in Fig.1.2.

The laser heater used at LCLS (see Fig.1.3), developed to provide increased (uncorrelated or sliced) energy spread for suppression of the LSC and CSR induced microbunching instability, shows expected results on the improvement of FEL performance [82]. Until recently, studies of MBI usually drew support from the signal of coherent optical transition radiation (COTR) to investigate microbunching [118]. With the X-band transverse deflecting cavity (XTCAV) [12], now it is possible to project the electron longitudinal phase space distribution at the end of the accelerator [146]. Ratner *et. al.* have used a detailed analysis of the MBI behavior to identify the dominant sources of microbunching, and confirm the shot-noise based theoretical model of MBI. The measured results are in good agreement with particle tracking simulation results using real number of electrons [140], shown in Fig.1.4 below.

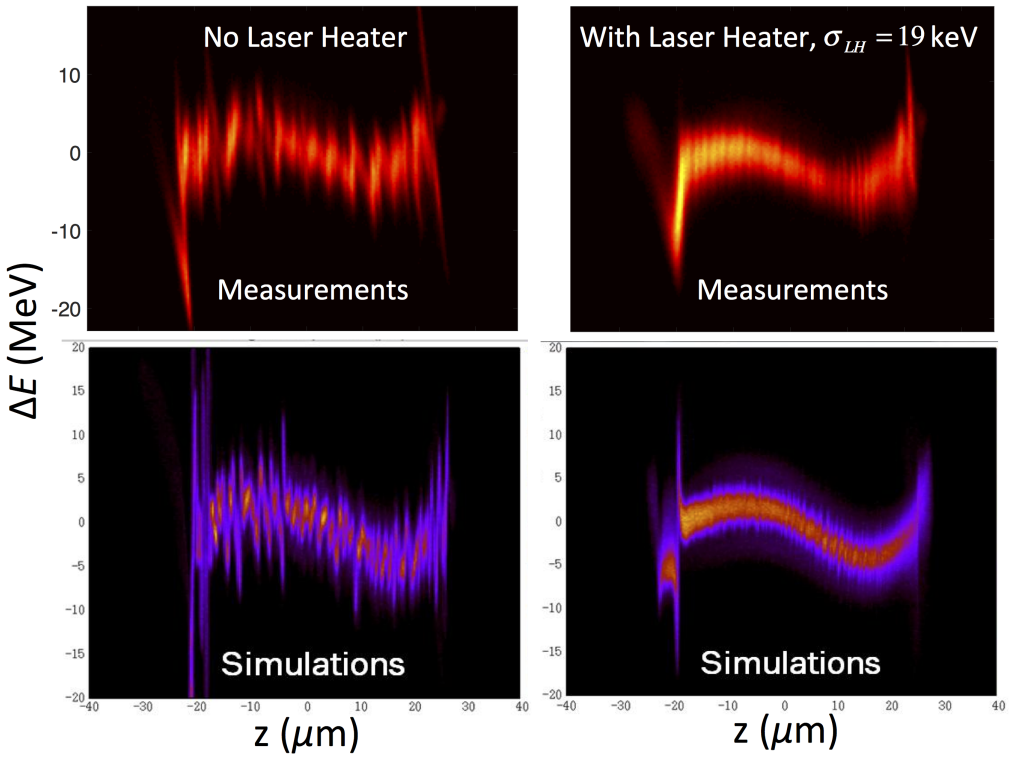

Figure 1.4: Comparison of experimental measurements (top row) and IMPACT simulation results (bottom row) of MBI. Picture from Ref.[140]

The above measurements of MBI are largely based on shot-noise model. At the Source Development Laboratory (SDL) of Brookhaven National Laboratory, a laser-induced modulation of the bunch density (rather than that with shot noise) by their developed photocathode laser system had been applied to benchmark the theoretical calculations for the microbunching instability. By comparing the pre-modulated electron beams with the un-modulated ones before and after the compression, they directly measured the microbunching gain. The results showed good quantitative agreement with theoretical predictions. See for example Figs.1.5 and 1.6.

In addition to the above mentioned single-pass linac based facilities, the prediction of a current threshold for the onset of CSR-induced microwave instability (MWI) is also confirmed by several experiments, e.g. Fig.1.7[95]. Furthermore, in a storage ring with a toroidal chamber, theory predicted [205] that CSR fields should appear in whispering gallery modes, as verified by experimental measurements at the NSLS VUV ring [34, 98] and later at Canadian Light Source [206].

In 2000, with the successful operation of a high-power FEL based on energy recovery technology at Jefferson Lab (JLab) [131], ERL has become an important transformative technology solution for many new designs of next generation light sources and colliders. With their unique advantages in producing

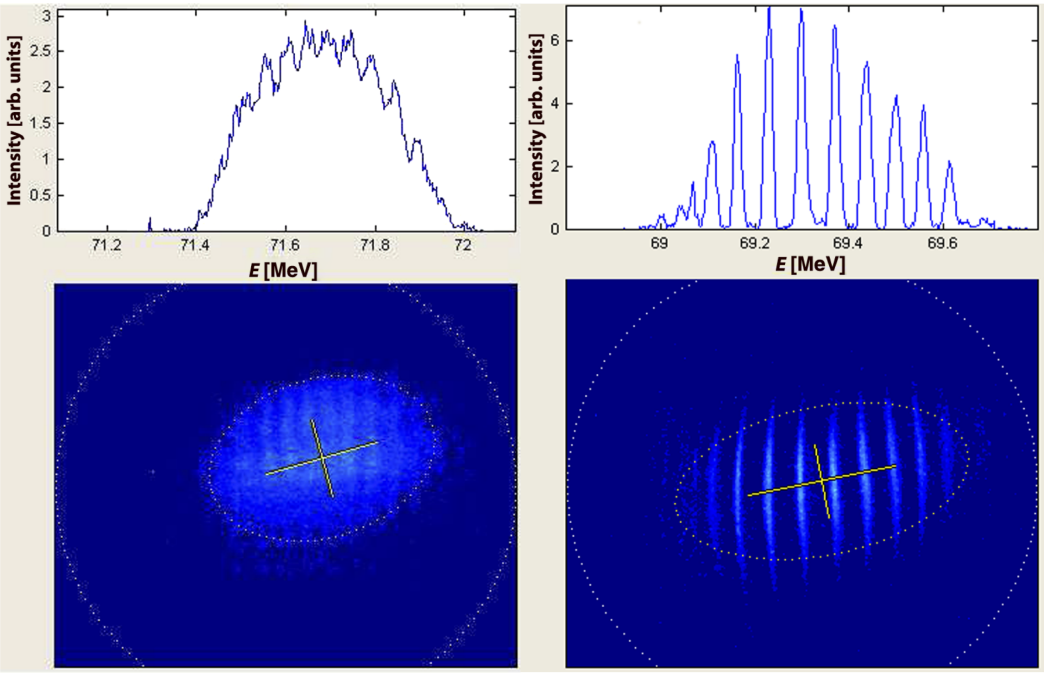

Figure 1.5: Microbunched structure observed at the Source Development Laboratory at Brookhaven National Lab before (left panel) and after (right panel) bunch compression [157]. The bunch charge is 90 pC and beam energy 70 MeV. The horizontal axes give spectrometer readings in MeV. The vertical axes shows amplitudes in arbitrary units. The initial modulation wavelength (left) is about 60 μm and final wavelength (right) is about 25 μm. The compression factor is set 2.5. Picture from Ref.[157].

high-intensity or high-brightness, high power, and short pulse beams for a wide range of energy-efficient applications, ERL designs also pose several outstanding challenges on the fundamental accelerator physics. One such major challenge is the compelling need to extend the knowledge on the development of CSR and LSC induced microbunching instability theory in bunch compression chicanes to wider regimes that include mergers at low energy, with nonrelativistic CSR and LSC effects on a curved orbit, and substantial bending regions at high energy, such as recirculating arcs where CSR-induced microbunching amplification could be enormous. Recently, an experiment conducted at JLab infrared (IR) FEL, the effects of CSR, not specific to MBI, on beam phase space quality were studied [76]. Hall *et. al.* explored the CSR effects on the beam with variation of the bunch compression in the IR beamline and examined the impact of CSR on the average energy loss as a function of bunch compression as well as that on the energy spectrum of the bunch. Simulation of beam dynamics in the machine, including the one-dimensional CSR model, shows reasonably good agreement with the measured effect of CSR on the average energy loss as a function of compression. While additional measurements for further examination of the impact of CSR or MBI on the beam should be deserved, JLab FEL, unfortunately, had been shut down due to funding issues since shortly after those measurements were taken [76]. In addition to usual ERLs [132], recirculating arcs are crucial components for many other applications, such as the circulator cooler ring (CCR) design of JLEIC [1], proposed by JLab, and

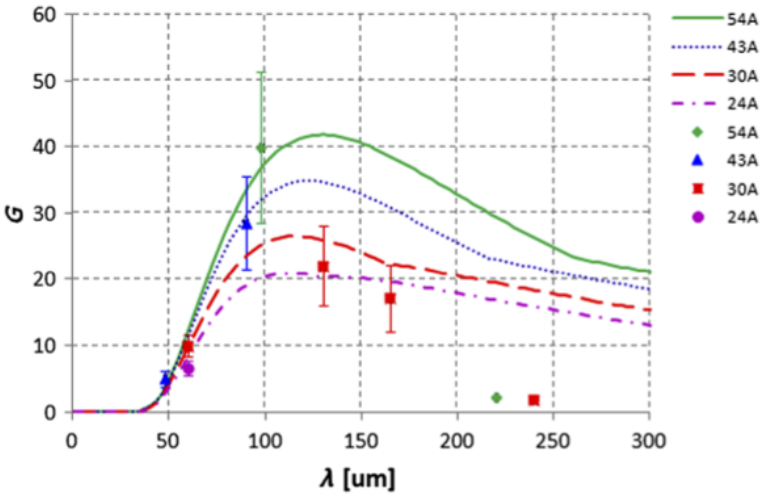

Figure 1.6: Comparison of the direct measurement of microbunching gain and the theoretical predictions. The horizontal axis shows the modulation wavelength of the uncom- pressed beam. The vertical axis shows the microbunching gain. The symbols represent the experimental data (green diamonds correspond to the 54 A current, a blue triangle shows the 43 A current, and red squares and pink circles, respectively, represent the 30 and 24 A currents). The lines depict the theoretical curves for the microbunching gain (the green solid line corresponds to the 54 A current, the blue dotted line shows the 43 A current, and the red dashed and pink dash-dotted lines, respectively, represent the 30 and 24 A currents). Picture from Ref.[157].

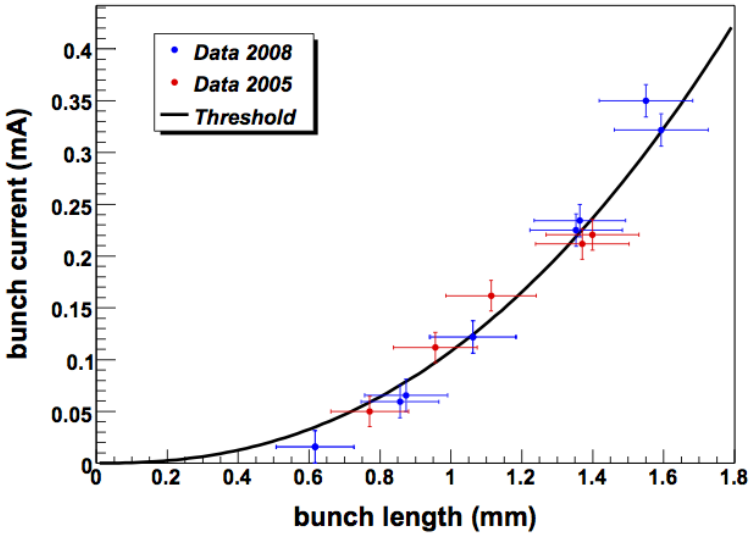

Figure 1.7: The measured threshold current as function of bunch length at ANKA storage ring. The black curve shows the fit to to the storage-ring microbunching theory. Picture from Ref.[95].

the FFAG (Fixed-Field Alternating Gradient)-arcs in the ERL-based eRHIC (electron-ion collider based on Relativistic Heavy Ion Collider), currently designed at Brookhaven National Laboratory (BNL). Extending the knowledge of CSR and LSC effects to the new regime of recirculating arcs has been an important issue for the successful designs of ERLs as well as the CCR in JLEIC.

1.4 State-of-the-art microbunching instability theory and simulation: motivation of the work

In this section, we put more emphasis on the recent advances of microbunching instability theory and simulation from two aspects: beam dynamics and electrodynamics.

From Sec. 1.3 we have already had a sense how MBI can degrade the machine performance and an impression that the results from theory and simulation are largely consistent with experimental measurements. The underlying physical mechanism of MBI can be illustrated in Fig.1.8. Assume in a high-brightness beam, an initial density modulation can be present in the beam bunch, shown in top left of Fig.1.8. This situation can be due to injector photo-cathode laser system. It can also result from unavoidable random fluctuation caused by granularity of the elementary charges[6]. The initial small density modulations can be converted into energy modulations (bottom left of Fig.1.8) due to short-ranged wakefields or high-frequency impedances[7] when the bunch traverses in a beam transport line, e.g. the space charge or CSR effects. Then, the energy modulations would be transformed back to density counterparts downstream a (longitudinal) dispersive region, or more specifically, through the momentum compaction R_{56} (bottom right of Fig.1.8)[8]. The density-energy conversion, if forming a positive feedback, can result in the enhancement of modulation amplitudes (compare top left and top right of Fig.1.8). Instability due to such mechanism is characterized by MBI.

MBI has been one of the most challenging issues associated with beamline designs such as magnetic bunch compressor chicanes for FELs or linear colliders. Moreover, it also poses difficulties in the design of transport lines for recirculation or ERL machines. Because a typical recirculation machine, e.g. Fig.1.1(c), can have a long linac or straight section and a large number of bending dipoles (forming the recirculation arcs) and thus can potentially incubate such density-energy conversion along the beamline.

[6] In SACLA (Spring-8 Angstrom Compact Free Electron Laser in Japan), a thermionic-cathode gun was used, which does not involve a drive laser in the injection system. However, COTR was still observed at the exit of third bunch compressor chicane, from which shot noise of the charge had been suspected of contributing to the cause [118].

[7] The wakefield, by its literal meaning, is the electromagnetic field induced by the passing charged particle beam. The induced electromagnetic field can have an energy kick (or force) on the motion of individual particles. Of our interest, those individual particles are within the same bunch, so we term the short-range wakefield. In another aspect, a passing charged particle beam, or a current, behaves as an electric circuit. A quantity, called the impedance, is then introduced and quantified as the ratio of induced electric/electromagnetic voltage to the circuit current. In Chapter 4, we would introduce in more detail the concepts of wakefields and impedances. Mathematically, the impedance is defined as the Fourier (or Laplace) transformation of the wakefields. In this aspect, the *short-range wakefield* would correspond to the *high-frequency impedance*.

[8] The physical meaning of the momentum compaction, or R_{56}, is the (longitudinal) path length difference due to a unit of particle energy difference. Usually such path difference occurs in an energy-dispersive region. An example is the bending dipole, where particles with (slightly) different energies will undergo (slightly) different path lengths. Such momentum compaction factor, R_{56}, is one of the most important quantities in our analysis and will be formally introduced later in Chapter 2.

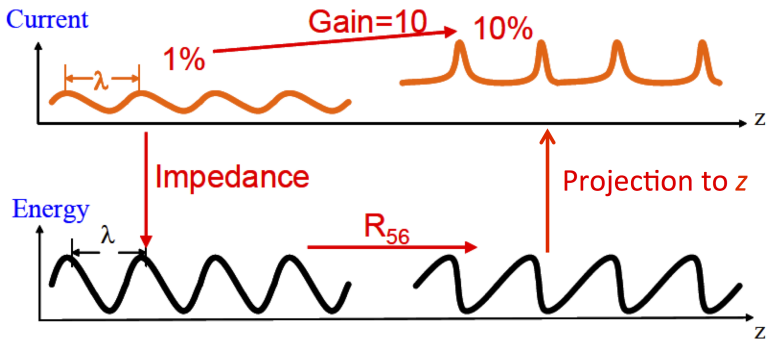

Figure 1.8: An illustration of microbunching instability in a transport line. Picture from Ref.[84].

The successive accumulation and conversion mechanism between density and energy modulations can result in serious microbunching amplification, or MBI. Any driving source of beam performance limitations in such a high-brightness electron beam transport system must be carefully examined in order to preserve the beam phase-space quality.

From the viewpoint of beam dynamics, we now have known that CSR microbunching may degrade beam phase space quality. The history can be traced back and found that the numerical particle tracking prediction was earlier than the experimental observation of MBI. At one time, it was thought that the most important effect of CSR was only to increase the projected beam emittance and energy spread [24]. However, `elegant` [19, 20] tracking simulations first predicted in 2001 that it can lead to significant microbunching instability and may have a dramatic impact on subsequent lasing performance in X-ray FEL facilities. Since then, various theoretical models have been developed to describe this instability.

In 2002, Saldin, Schneidmiller, and Yurkov (SSY) [152] first treated the problem of MBI as a klystron-like instability. This capture of similarity of MBI to the working principle of klystron gives a simple and clear picture how the structure of bunch modulation evolves. Table 1.2 briefly compares the similarity and difference of working principles between klystron and MBI. They considered the case without bunch compression and assumed high-gain approximation. The effect of finite transverse beam emittance was estimated but not yet fully incorporated in their theoretical treatment.

Then, Heifets, Stupakov and Krinsky (HSK) in 2002 [79] extended the treatment by including bunch compression as well as finite transverse beam emittance. In Ref.[79], a linearized Vlasov equation was obtained by applying the standard perturbation technique. The method of characteristics, which has been commonly used to solve first-order partial differential equation in plasma physics, was employed to further simplify the linearized Vlasov equation. Finally they derived a linear integral equation of Volterra type

Table 1.2: Comparison of beam-wave interaction between klystron and MBI

	Klystron	MBI
Initial bunching	seeded by "buncher cavity"	seeded by photocathode laser system or upstream LSC-induced plasma oscillation
Interaction mechanism	drift-space ballistic or velocity bunching	short-ranged wakefield or high-frequency impedance, with $R_{56}(s' \to s)$
Effects	final bunching is amplified; "catcher cavity" is to absorb or store energy transferred from electron beam	final bunching is amplified; beam phase space dilution or fragmentation may occur; will degrade FEL performance or cheapen luminosity of colliding beams

for the bunching factor[9]. Through the bunching factor, they can estimate the microbunching gain[10] in a physical system. HSK had applied the integral equation to estimate the effect of MBI for the second bunch compressor (BC2) of LCLS [79]. For convenience of subsequent discussion throughout the dissertation, we consider their approach of solving the problem belongs to semi-analytical method. This is to be contrast with directly solving the Vlasov equation (either linearized or the original nonlinear form) for phase space distribution function by using mesh or grid in phase space domain.

Almost at the same time, Huang and Kim (HK) [81] derived the same integral equation through an elegant but slightly different approach. By applying the method of iteration, they proceed to solve the equation and analytically obtained an explicit formula up to second-order iteration in a simplified three-dipole bunch compressor chicane[11]. The formula is then used to estimate the microbunching gain factor for BC1 and BC2 of LCLS [81]. Applications of both the semi-analytical calculation and analytical formula to LCLS BC2 give the overall CSR-induced microbunching gain smaller than 2 over a wide spectral range[12]. HK also indicated that the overall gain can be contributed mainly by a two-stage amplification for a high-gain or high-current operation (quadratic term of beam current). Here we note that the two-stage amplification, which corresponds to second-order iteration they employed, is not generally applicable to arbitrary cases. The extension to multi-stage amplification concept for general beamline transport, as part of the work in this dissertation, will be made clear later.

The above works [79, 81] are mainly theoretical advance of MBI in single-pass linac based accelerators.

[9]Note that in the original form the Vlasov equation describes the evolution of beam phase space distribution, instead of bunching factor. Here the bunching factor is quantified by the Fourier transformation of the phase space distribution function, as will be defined later in Chapter 3.

[10]The gain is defined as the ratio of bunching factors at two specified locations, see Chapter 3 for more detail.

[11]The formula is applicable to typical four-dipole chicanes, because the central two dipoles are usually closed spaced.

[12]The magnitude of the gain, as a function of modulation wavelength or frequency, may vary with the initial modulation amplitudes, but here we assume the gain is independent of modulation amplitudes, i.e. linear gain. There are at least three indications here: (1) The gain factor only reflects the amplification ratio, instead of absolute modulation value; (2) By specifying different locations, the modulation amplitudes in general are different; (3) The gain factor can be due to one or some particular collective effects, e.g. only CSR gain is considered in Refs.[79, 81]. From (2), care must be taken of at which initial and final locations when the gain is evaluated.

In subsequent discussion, we briefly investigate the recent development regarding the study of MBI in numerical simulation aspects. Numerical treatments of MBI can be divided into two categories: time-domain and frequency-domain methods. One of the time-domain treatments, or the most common and intuitive approach, is based on particle tracking. Particle tracking simulation (see, for example, Refs.[21, 141]) with inclusion of relevant collective effects can be valuable for beam dynamics studies. It allows general beamline lattice, yet requires careful treatment of various numerical parameters to ensure numerical convergence before the reliable results are obtained [22, 173]. Another dedicated time-domain approach is based on Monte-Carlo Particle method, as implemented in Ref.[11]. The time-domain treatment turns out to be considerably challenging when MBI becomes severe[13]. To compare with the linear theory at the onset of MBI, the initially imposed density modulation needs to be small enough to remain in the linear regime while such modulation requires to be large enough to rise above the numerical noises originated from the limited number of simulation particles. This implies that large number of simulation particles and long computation time are required for reaching convergent results of microbunching gain, and strenuous efforts are needed to do parametric studies for machine design or optimization in order to minimize microbunching effects. Direct solution of the (nonlinear) Vlasov equation for the two-dimensional (2-D) longitudinal phase-space distribution[14], based on semi-Lagrangian approach, was studied by Venturini *et al.*[192, 193, 196]. The issue of numerical noise is greatly reduced with this approach, but the transverse effects of beam intrinsic spread are only approximately counted. Venturini *et al.* [192, 193, 196] also applied the same approach to an only longitudinal beam dynamics in a storage ring using 1-D CSR impedance based on the rigid-bunch model. The simulation revealed bursting of CSR radiation and microbunching/microwave instability in storage rings, and gave an instability threshold in good agreement with the analytical prediction. The formulation extended to full 4-D or 6-D becomes further intricate and application to machine design would become prohibitively expensive[15]. Reaching a compromise becomes an issue for the moment, among: (1) obtaining reasonable accuracy of numerical simulation results; (2) tolerable computational time and load; and (3) determination of physical scope in a particular problem.

In reviewing the theoretical developments (including analytical and numerical) of MBI, we also find that the scope of their application primarily covers linac-based accelerator systems. As the advance of source technology in the past two decades made the sub-millimeter (or down to tens of micrometer) electron bunch available, CSR effects came into play and attracted increasing attention for their detrimental impact

[13]This is mainly because the number of (macro-)particles employed in the numerical simulation ($\sim 10^6 - 10^7$) is much less than the realistic number of particles ($\sim 10^{10}$) in a beam bunch. For the case of MBI, which involves (physical) shot noise of the beam, additional efforts must be made for particle tracking simulation in order to obtain correct or converged results (see Chapter 5 for more detailed discussion).

[14]Throughout the dissertation, if otherwise specified, 2-D denotes a position coordinate and its corresponding conjugate momentum coordinate. In the most general situation, the phase space coordinate is specified by a six-tuple or 6-D vector, i.e. $(x, x', y, y', z, \delta \equiv \Delta E/E)$, where x and y are transverse horizontal/radial and vertical positions, x' and y' are the corresponding angular divergences, with s the global longitudinal coordinate, and z and δ are the (local) longitudinal coordinate and energy deviation (assuming $z > 0$ for the bunch head). All these quantities are measured with respect to the reference particle and are a function of the (global) longitudinal path coordinate s.

[15]To the knowledge of the author, the development of full 4-D (or 6-D) nonlinear Vlasov solver based on semi-Lagrangian approach, which can be free from numerical noise and thus suitable for MBI study, might have been attempted but not yet fully implemented.

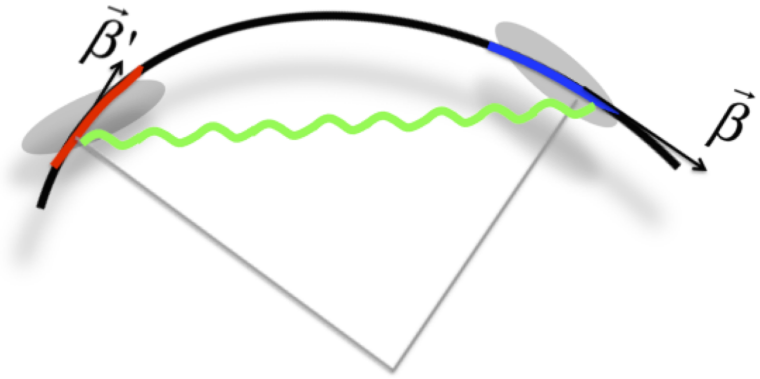

Figure 1.9: Bunch tail-to-head interaction on a curved orbit via CSR.

on beam quality during the transport and compression of high-peak-current electron bunches. In the past decade, CSR effects were well studied for a *single-pass* device and for *storage rings*, mostly based upon a 1-D longitudinal CSR model for free-space interactions. However, there are still many important remaining questions, as manifested by the series of microbunching workshops where cutting edge studies of the effects of CSR and LSC interactions on microbunching instability are reported and intensely discussed. In particular, CSR effect in *recirculating* or *ERL* arcs is far from fully explored.

The CSR effect takes place when a high-intensity or high-brightness electron bunch is transported on a curved orbit. As a short electron bunch with high peak current moves along a curved orbit, the particles interact with each other via Lienard-Wiechert fields [87]. As shown in Fig.1.9, the fields generated from the tail of a bunch at retarded time travel on a straight path, overtaking the bunch motion on the curved orbit, and, if retardation condition met, interact with particles at the head of the bunch by applying Lorentz force on the leading particles. Such an interaction can cause trailing particles to lose energy and leading particles to gain energy, thus causing phase space re-arrangement in an *undesirable* way since the particles' transverse motion on a curved orbit becomes strongly correlated to the energy of the particles because of the dispersive nature of a bending system. These are called CSR effects on beams. Possible consequences for a bulk of bunch are emittance dilution and increase of beam energy spread. They can be explained as follows: the energy change (and redistribution, resulting in increase of energy spread) due to CSR can be correlated to the transverse coordinates (e.g. x or x') through the dispersion function R_{16} or its derivative R_{26} (which we will define in Sec. 2.3). Since the energy change varies for different longitudinal slices of particles, such energy variation within a beam bunch can potentially dilute the projected transverse emittance. In addition to the energy redistribution, overall the bunch loses energy throughout the interaction process in the form of CSR, as the synchrotron radiation fields, emitted by individual electrons at wavelength longer than the characteristic length of the beam bunch, superimpose with each other constructively to form a strong coherent radiation wave.

Some distinctive features of the CSR interaction make it more harmful to the transport of high-brightness electron beams than many other collective interactions. First, the CSR interaction is very sensitive to variation or modulation in the bunch longitudinal charge distribution. In particular, perturbation of the longitudinal charge distribution at shorter wavelength causes larger amplitude of CSR overtaking field strength[16], which can further amplify the perturbation. Such a process, in combination with LSC interaction, tends to cause microbunching or sometimes fragmentation of the beam longitudinal phase space distribution as observed in many experiments, e.g. Ref. [146]. Second, unlike the usual space charge force from Coulomb interaction amongst particles moving on a straight path, which has diminishing effect at high energy due to the relativistic cancellation of the **E** and **B** fields in the Lorentz force[17], for motion on a curved orbit, this relativistic cancellation no longer holds. So the CSR force continues to be prominent even at high energy. Thus, the detrimental effects of CSR on beam dynamics need to be carefully assessed or circumvented for all the designs of modern electron accelerators.

The study of CSR effects on high brightness beams presents significant challenges to accelerator physics. This is the result of the very nature of CSR interaction, since for fully self-consistent analysis or simulation of the beam-wave dynamical process one needs to take accurate account of retardation by retrieving the history of particle motion and identifying the source particles (which emitted radiation) through the intersection of the past light cone of the test particles with the world lines of source particles. Throughout this dissertation only 1-D CSR model based on longitudinally rigid bunch is studied. For 2-D or 3-D[18] CSR interaction, there is also a subtle interplay of the longitudinal non-inertial space charge force with the transverse centrifugal space charge force that is not straightforwardly manifested from direct solutions of Maxwell equations [105]. This interplay can be easily misrepresented if the dynamics is treated non-self-consistently or with approximations. Furthermore, the sensitivity of the CSR force on the perturbation of the bunch distribution demands extreme care for the numerical simulations to differentiate numerical noise from actual physical signal coming from shot noise in the bunch.

In the past two decades, as the community has pushed for accelerators with higher-brightness beams with shorter bunches, intense efforts have been made around the globe to reach a deeper understanding of the CSR effects. Vast progress has been made in all fronts of analysis, simulation and experiments.

On the analysis front, the analysis of steady-state and transient CSR forces for a rigid bunch (so called 1-D model) on a circular orbit in free space were developed [42, 128, 153], and CSR impedance for a rigid bunch on a circular orbit with shielding by parallel plates or toroidal walls were obtained [128, 204, 7]. Sensitivity of CSR interaction with bunch longitudinal distribution was discussed as the potential source of the observed bunch fragmentation [106]. The CSR impedance from a 1-D rigid bunch model was further

[16] In Chapter 4, we would see for steady-state CSR, $Z_{\rm CSR}^{\rm s.s.} \propto k^{1/3} \propto \lambda^{-1/3}$.

[17] In Chapter 4, we would see in general, $Z_{\rm LSC}^{\parallel} \propto \gamma^{-1}$.

[18] To be clear, here 2-D means (x, s) plane and 3-D denotes (x, y, s) space. See Fig.2.1 in Chapter 2.

applied to the analysis of the Vlasov equation in the study of CSR-induced microbunching instability in both scenarios of storage rings [79] and single-pass devices such as bunch compression chicanes [152, 79, 81], as outlined above. The analysis of CSR impedance shielded by a toroidal boundary for a circular orbit was extended to the case of a short circular path by approximating the Maxwell equations using a parabolic equation [163, 7, 8]. Moreover, the longitudinal space charge force (LSC) on a beam traveling on a straight path followed by a bunch compression chicane was shown to cause more severe microbunching instability than that from the CSR force alone [154, 155, 82]. More refined analysis of the 3-D effect of LSC on MBI has been recently presented [147]. The analysis of the 2-D CSR effect demonstrated cancellation between the centrifugal space charge force in the transverse Lorentz force and the non-inertial space charge force in the longitudinal Lorentz force in their joint effect on particle transverse dynamics [107, 108], and showed that after the cancellation is taken into account, the particle dynamics is mainly influenced by the effective longitudinal CSR force. Further analysis of the behavior of the effective longitudinal CSR force shows a *delayed* response of CSR force to the bunch length variation as a result of retardation [105]. Recently, more analyses were developed on extending the transient CSR behavior to the low energy regime [121] and on 2-D CSR effects [85].

On the simulation front, early numerical simulations of CSR effects include *one* model which uses unperturbed source beamlets to generate CSR force and uses test beamlets to feel the CSR field as a perturbation [57], and *another* self-consistent model which uses 2-D[19] Gaussian macroparticles to generate CSR force that meanwhile influences the dynamics of the macroparticles [109, 110]. These simulations are good at simulating *bulk* CSR effects; however, due to the use of macroparticles or beamlets, they are limited by the achievable resolution of density modulation during the microbunching process. As mentioned previously, CSR-induced microbunching instability was first discovered through numerical simulation by the code `elegant` [19], which uses an analytical formulation of CSR force based on a 1-D longitudinal rigid-line bunch model. As outlined above, this code gives simulation results in excellent agreement with experimental observations [10] (see also Fig.1.2) for the parameter regimes used in modern accelerators. The sensitive dependence of CSR force on bunch distribution underscores the importance of modeling the bunch from start to end (S2E). For an FEL facility, S2E means simulating the particle dynamics from the birth of a bunch at the cathode all the way to the undulator for the generation of radiation. In an S2E simulation, all possible collective interactions encountered by the beam along the orbit, such as space charge on a straight path, linac wakefield, and CSR in bends, are modeled by one simulation [143, 144] or consecutive simulations (see, for example, Ref.[20]). Such simulations have demonstrated to be extremely useful for the explanation of experimental results and for the design of future machines.

While CSR simulation with a 1-D CSR model achieves many big successes, many researchers continue with their endeavors to extend the simulation to 2-D and 3-D CSR modeling. A self-consistent 2-D[20]

[19] Here 2-D means (x, s) or within the bending plane.

[20] Here 2-D means (x, s) of the geometry, while beam dynamics is considered in 4-D (x, x', z, δ) phase space.

Vlasov-Maxwell solver was developed [11] assuming a linear optics transport. The particle-in-cell (PIC) version of the fully self-consistent CSR code, as an extension of the pioneering 2-D code [110] based on the macroparticle model [110], is also currently under development [170]. Recently, a code modeling the 3-D CSR based on direct Lienard-Wiechert interaction was developed [151].

1.5 Outline of our approaches and results

To accurately and efficiently quantify the direct consequence of MBI at the onset, characterized by the microbunching amplification factor or the microbunching gain, we have recently developed a semi-analytical linear Vlasov solver [177] based on the frequency-domain treatment. This semi-analytical approach transforms the linearized Vlasov equation to an integral equation and solves for the bunching factor, and allows the proper inclusion of the transverse effects of beam intrinsic spread. The involvement of transverse beam emittances, causing Landau damping or phase mixing, was confirmed [152, 79, 81] to be an effective stabilizing mechanism for MBI. Our work extended the existing theoretical formulation of HSK and HK [79, 81] and included more relevant collective effects, such as LSC, CSR and linac geometric effects, using analytical impedance expressions. Since we do not directly solve phase-space distribution function using mesh, the numerical noise issue is not a limiting factor and the numerical computation is much faster than the aforementioned treatments. To validate the Vlasov results, particle tracking simulation, an extremely valuable *numerical machine* for beam dynamics studies, always serves as an excellent benchmarking tool of our developed Vlasov solver. The main reason of using particle tracking is that it employs entirely different methodology (time-domain treatment) from our frequency-domain treatment. `elegant`[21] [21] is chosen as our main tool for this task.

In this dissertation, to systematically study the microbunchig dynamics in recirculating machines, we have extended the existing theoretical formulation [79, 81] and incorporated more relevant physical models by:

(i) including both transverse horizontal and vertical bending, in which the horizontal bends for recirculation arcs and vertical bends for spreaders and recombiners;

(ii) allowing beam acceleration or deceleration for energy boosting or recovery;

(iii) improving and incorporating more relevant collective effects in addition to the steady-state free-space CSR that was considered in Refs.[79, 81, 193].

Here we distinguish in three viewpoints our work in this dissertation from the existing work done in the early days. First, although there have been extensive studies on microbunching dynamics, e.g. phase space

[21] Choosing `elegant` in our studies is based on the following two considerations. First, `elegant`, as the first particle tracking code to predict MBI, has been programmed to carefully tailor the numerical noises but still retain the physical one [22] and was extensively used and benchmarked in some specific lattices. Second, by taking advantage of standardized format used in `elegant`, our Vlasov solver since its development relies on and benefits from many capabilities of `elegant`.

fragmentation (see, for example, Ref.[84] and references therein), they mostly focus on bunch compressors in a linac-based free-electron laser (FEL) driver. There are still very limited works reported on quantitative microbunching gain studies in transport arcs or recirculation machines. To our knowledge, Borland first [23] did some preliminary studies of microbunching gains on Advanced Photon Source (APS) upgrade ERL machine using `elegant` tracking with several collective effects included. Further understanding of the underlying physics would require more detailed study of contribution of each individual physical mechanism as well as careful benchmarking of particle tracking results with theory. Thus, more focused studies of the longitudinal microbunching gain with numerical benchmarking also serve as a purpose of our work. Second, as will be detailed later, the intuitive argument of quantifying microbunching in a beamline as the product of scalar gains in each individual sections is in general incomplete and the gain is found to be underestimated [175]. Our Vlasov solver, incorporated with `elegant`, adopts a general linear beamline lattice and all relevant beam and lattice parameters to treat the microbunching analysis in a more self-consistent way. This also allows us to systematically study the impact of lattice optics on MBI. Third, by virtue of the general purpose of `elegant`, our Vlasov solver allows us to perform parametric design studies and machine optimization if MBI would be a concern in the beamline design.

This solver is certainly not almighty. While our newly-developed semi-analytical Vlasov solver can be much more efficient and accurate in calculating microbunching gain than using particle tracking simulation, we emphasize the limitations of the formalism upon which our solver bases. First, only the effects of linear beamline elements can be accounted for. For an ERL or specialized beamline design with sextupole or higher-order magnetic elements, their effects are overlooked in our consideration. Second, the when the modulation wavelength is comparable to overall bunch length, our theoretical model will be invalid. Third, for the case of large gain, the linear Vlasov solver can neither be applied to the nonlinear nor saturation regimes. Fourth, since the theoretical formulation (and thus the Vlasov solver) is based on integral equations governing the bunching factor and phase space modulations, it cannot provide as much information as particle tracking code does, e.g. the detailed structures of phase space distribution. Fifth, in the presence of beam acceleration (or deceleration), the method we adopted assumes the rate of energy gain (or loss) is adiabatic. This may not be valid for rapid acceleration at very low beam energy. Sixth, the impedance models adopted in the solver is idealized and does neither account for bunch centroid offset nor transverse dependence along bunch slides.

The main contributions in this dissertation can be categorized in the following several themes:

(1) Development of MBI theory and extension to new application regimes;

(2) Construction of CSR wakefield and impedance models, in particular for low-energy regimes and transient effects;

(3) Numerical implementation of the derived semi-analytical formulation, together with careful benchmarking against massive particle tracking simulations;

(4) Investigation of the underlying physics of microbunching development in recirculation arcs, including the multistage amplification behavior of CSR microbunching;

(5) Proposal of several ways and a set of sufficient conditions based on optics control of MBI in transport or recirculation arcs;

(6) Exploration and formulation of many more aspects of microbunched structures in beam phase space dimensions; and

(7) Theory and formulation of MBI for magnetized beams.

1.6 Organization of the Dissertation

This dissertation is organized as follows. In Chapter 2, we introduce the fundamentals of charged beam dynamics, starting from single-particle and then multi-particle dynamics. The Hamiltonian mechanics, as a natural fit to the theoretical formulation, and its consequences are outlined, including the symplecticity, the concept of phase space, and Liouville theorem with the reduced form, i.e. the Vlasov equation. We will begin the discussion of single-particle dynamics from construction of the accelerator Hamiltonian and then study the linearization of Hamilton's equations of motion, as has been done in typical accelerator textbooks. The linear equations of motion, formulated by linear algebra, describe the linear beam optics in a particle transport system, which provides basic knowledge for subsequent studies in the dissertation. For multiple particle dynamics in an electromagnetic environment, the set of Vlasov-Maxwell equations is generally employed. We will discuss the basic concepts of the system and then make two important approximations, which are applicable to the problems of our interest. The (explicitly coupled) Vlasov-Maxwell equations can then be formulated using Vlasov equation and the language of wakefields or impedances.

In Chapter 3, we would begin with the qualitative description of microbunching instability (MBI), including its driving sources, mechanisms, and effects. The seeding sources can originate from either modulation of photocathode lasers in electron gun injector system or the longitudinal space charge (LSC) induced plasma oscillation upstream the beamline. The main mechanism are found to be driven by CSR, LSC and linac geometric effects. These consequences, usually undesired, can degrade the downstream lasing performance for FELs or beam luminosities for colliders. To proceed with quantitative treatment, we employ Vlasov equation and the standard perturbation techniques. The governing equations for phase space modulations will be derived in the single-pass accelerator configuration. A brief discussion is made to relate the derived formulation with that for storage-ring accelerator configuration. An important natural damping mechanism, called Landau damping or phase space smearing, is then introduced. After introducing necessary background for beam dynamics, we illustrate the CSR microbunching instability occurred in the second bunch compressor chicane of Linac Coherent Light Source (LCLS) as our first example.

In Chapter 4, in contrast to the previous chapter mainly dealing with beam dynamics, we focus on electrodynamics by starting from introducing the basic concepts of wakefields and impedances and basic

properties of (coherent and incoherent) synchrotron radiation. Then we derive the CSR, LSC, and linac geometric wakefields and impedances in many scenarios. Throughout the dissertation the Vlasov analysis is performed in frequency domain, in which the impedance is applied. Though, the time-domain wakefields may provide a more intuitive picture regarding the underlying physics. Therefore an effort has been spent to illustrate the behavior of wakefileds, particularly the CSR wakes.

In Chapter 5, having introduced the theoretical formulation in both beam dynamics and electrodynamics, we would numerically implement the developed theories to application of microbunching analysis in practical beamline designs. A semi-analytical Vlasov solver has then been developed. Because the beamline of our interest is assumed to be part (or the whole) of a recirculating or energy-recovery-linac (ERL) machine, it can be much more complicated and hardly allow analytical formulas for analysis, unlike the case in a bunch compressor chicane with few-dipole configuration. The existing theoretical treatments of microbunching analysis, which usually aim to estimate the impact of microbunching in a very specific portion of a linac-based machine, would now be extended to a general beamline lattice. The Vlasov solver, which primarily focuses on microbunching gain calculation, adopts inputs and outputs from a well-known beamline design and particle tracking code `elegant`. This option makes the solver useful for beamline designers to evaluate impact of microbunching for any given lattice design and might help improve or iterate their design strategies once this instability becomes a concern.

In the subsequent four chapters, we would explore the applications and capabilities of the solver to many aspects. In Chapter 6, we would develop a method to characterize multistage CSR microbunching development in terms of stage orders. The stage orders enable a quantitative comparison of the impact of lattice optics on the CSR microbunching gain for different lattices under similar initial beam parameters. We find that the microbunching instability in the multi-bend arcs considered in this study has a distinguishing feature: the multistage amplification. The fact that CSR microbunching gain grows as (up to) six-stage amplification is quantified for our example recirculation arcs with a total of 24 dipoles, while two-stage amplification was previously concluded for a typical four-dipole bunch compressor chicane. Attempts to relate a lattice optics pattern with the obtained stage gain functions through a physical interpretation are also made.

In Chapter 7, as a practical application of our developed Vlasov solver, we explore the optics conditions for mitigation of CSR induced microbunching instability. It has been known that CSR effect can result in possible beam emittance growth in the transverse dimension and lead to microbunching instability in the longitudinal phase space. Although many schemes have been proposed to suppress the CSR induced emittance growth for transport lines, only a few scenarios have been introduced to suppress CSR induced microbunching instability, especially for recirculation arcs. The conditions for control or suppression of microbunching gains along multi-bend transport or recirculation arcs are proposed, examined and confirmed. Examples are presented, including low-energy, medium-energy, and high-energy recirculation arcs.

In Chapter 8, as part of advanced studies of MBI related phenomena, the concept of microbunching would be extended to more aspects of phase space modulations. Microbunching structures residing in transverse-longitudinal cross planes were observed in particle tracking simulation. The governing equations would be derived and then implemented in our Vlasov analysis. This analysis shall be a crucial step to systematically characterize MBI for a beamline complex and for multi-pass beam recirculation.

In Chapter 9, a generalized formulation capable of treating transport of transversely coupled beams (or magnetized beam, in particular) will be developed. The work in this chapter is mainly driven by an early design of Circulator Cooler Ring (CCR) for the Jefferson Lab Electron Ion Collider (JLEIC) [1, 2, 46], as it revealed significant MBI. It is envisioned that the MBI could be substantially suppressed by using a magnetized beam. Our new formulation developed in this dissertation is then employed to confirm prediction of microbunching suppression for a magnetized beam transport in the recirculation arc of a recent JLEIC ERL based cooler design for electron cooling. The smearing effect in the transverse and longitudinal beam phase space, found to effectively suppress MBI, is also discussed.

In Chapter 10, the findings or remarks from preceding chapters would be generally concluded and a proposal for potential further extension of the work in this dissertation as advanced studies of microbunching instability related phenomena would be briefly described.

Finally throughout the dissertation, the CGS units would be used unless otherwise stated or especially specified.

CHAPTER 2
Theory of Single-Particle Beam Dynamics and Vlasov-Maxwell System

In this Chapter we will begin to introduce the fundamentals of charged particle beam dynamics, starting from single-particle and then multi-particle dynamics. In Sec. 2.1 the Hamiltonian mechanics, as a natural fit to the theoretical formulation, and its consequences are outlined, including the symplecticity, the concept of phase space, and a reduced form of Liouville theorem, i.e. the Vlasov equation. In Sec. 2.2 the discussion of single-particle dynamics starts from constructing the accelerator Hamiltonian and then study the linearization of Hamilton's equations of motion, as has been done in typical accelerator textbooks. In Sec. 2.3 we use the linear equations of motion, formulated by linear algebra, to describe the linear beam optics in a single-particle transport system, which provides basic knowledge for subsequent studies in the dissertation. For multiple particle dynamics, the set of Vlasov-Maxwell equations in an electromagnetic environment is generally employed. We will discuss in Sec. 2.4 the basic concepts of the system and then make two important approximations, which are largely applicable to the problems of our interest. Then the explicitly coupled Vlasov-Maxwell system equations can be separately formulated using Vlasov equation and the language of wakefields or impedances.

2.1 Symplecticity, Phase space, Liouville theorem, and Vlasov equation

Hamiltonian mechanics is a theory developed as a formulation of classical mechanics, in which a classical physical system is described by a set of canonical coordinates $(\mathbf{q}, \mathbf{p})$, where each component of the coordinate, q_k or p_k, is indexed to the frame of reference of the system. The motions of any Hamiltonian system, governed by the so-called Hamilton's equations of motion, obey a constraint called *symplecticity* [149, 73]. Symplecticity has important consequences for charged particle beam physics. The most commonly cited is the conservation of the density of system points in phase space (which would be introduced soon) – Liouville theorem. Our discussion would begin from this.

Given a system Hamiltonian $\mathcal{H}(\mathbf{q}, \mathbf{p})$, the Hamilton's equations of motion can be written as

$$\begin{aligned} q_k' &= \frac{\partial \mathcal{H}}{\partial p_k} \\ p_k' &= -\frac{\partial \mathcal{H}}{\partial q_k}, k = 1, 2, ..., N \end{aligned} \tag{2.1}$$

where N is the degree of freedom[22], the primes denote total differentiation with respect to the independent variable of the system. Of our interest, the independent variable, s, is assigned as the global longitudinal

[22]Later we will be interested in the case with $N = 3$, where $q_{1,2,3} = x, y, z$ and $p_{1,2,3}$ are their corresponding conjugate momenta, but here we retain the most general case with N.

coordinate (shown in Fig.2.1 later). To cast these equations in matrix form, we define

$$\mathbf{x} = \begin{bmatrix} q_1 \\ p_1 \\ q_2 \\ p_2 \\ \vdots \\ q_N \\ p_N \end{bmatrix} \tag{2.2}$$

as the phase space coordinate of a system point[23]. We also define

$$\mathbf{s} = \begin{pmatrix} 0 & 1 \\ -1 & 0 \end{pmatrix} \tag{2.3}$$

called the unit symplectic matrix, and

$$\mathbf{S} = \begin{pmatrix} \mathbf{s} & 0 & \cdots & 0 \\ 0 & \mathbf{s} & \cdots & 0 \\ \vdots & \vdots & \ddots & 0 \\ 0 & 0 & 0 & \mathbf{s} \end{pmatrix} \tag{2.4}$$

as the $2N$-by-$2N$ symplectic matrix.

The arrangement of this matrix has been chosen to accord with the convention typically used in accelerator community[24].

As a note, the matrix $\mathbf{S}$ has the following properties

$$\begin{aligned} \mathbf{S}^{-1} &= \mathbf{S}^T = -\mathbf{S} \\ \mathbf{S}^2 &= -\mathbf{I} \\ |\mathbf{S}| &= \det(\mathbf{S}) = 1 \end{aligned} \tag{2.5}$$

where T is the transpose operator, $\|$ or det() indicates the determinant of a matrix. Having defined the above notations, the Hamilton's equations of motion of the system, Eq. (2.1), can be expressed in the compact

[23]Later this concept of a system point would transit to an individual point particle.

[24]Note this convention is different from Goldstein's arrangement [73], which uses $\mathbf{J} = \begin{pmatrix} 0 & \mathbf{I} \\ -\mathbf{I} & 1 \end{pmatrix}$, instead of $\mathbf{S}$. Here $\mathbf{I}$ is the unit matrix. For such arrangement, the corresponding phase space coordinate is, for example, $\mathbf{x} = [q_1, q_2, p_1, p_2]^T$, where T is the transpose operator.

form

$$\mathbf{x}' = \mathbf{S}\frac{\partial \mathcal{H}}{\partial \mathbf{x}} \tag{2.6}$$

Before reaching the symplectic condition, let us consider a general canonical transformation. Such a transformation is a change of canonical coordinates that preserves the form of Hamilton's equations. Assume the canonical transformation transforms the coordinate from $\mathbf{x}$ to $\mathbf{X}$ (and their corresponding Hamiltonian from $\mathcal{H}(\mathbf{x})$ to $K(\mathbf{X})$),

$$\mathbf{X} = \mathbf{X}(\mathbf{x}, s), \text{ and } \mathbf{x} = \mathbf{x}(\mathbf{X}, s) \tag{2.7}$$

Since $\mathbf{x}$ and $\mathbf{X}$ are two sets of canonical coordinates, we have

$$\mathbf{x}' = \mathbf{S}\frac{\partial \mathcal{H}}{\partial \mathbf{x}} \tag{2.8}$$

and

$$\mathbf{X}' = \mathbf{S}\frac{\partial K}{\partial \mathbf{X}} \tag{2.9}$$

The canonical transformation also results in $K = \mathcal{H}$ if there is no explicit s-dependence. However in an accelerator system the Hamiltonian has time (s) dependence, in which

$$\frac{\partial K}{\partial \mathbf{X}} = \mathbf{S}^T \left(\frac{\partial \mathbf{X}}{\partial s} + \mathbf{M}\mathbf{S}\frac{\partial \mathcal{H}}{\partial \mathbf{x}} \right) \tag{2.10}$$

This above results can lead to the symplectic condition[25]

$$\mathbf{M}^T\mathbf{S}\mathbf{M} = \mathbf{S} \tag{2.11}$$

where $\mathbf{M}$ is the Jacobian matrix, defined as $\mathbf{M} \equiv \partial\mathbf{X}/\partial\mathbf{x}$, or transport matrix, the term that is commonly cited in accelerator physics. Sometimes, the extended condition $\mathbf{M}^T\mathbf{S}\mathbf{M} = \lambda\mathbf{S}$ is employed. For the scalar $\lambda \neq 1$, it is called extended symplectic condition [73]. Equation (2.11) can be abstract; here we provide an intuitive picture regarding the nature of symplecticity in Hamiltonian mechanics. The requirement of symplectification can be considered as follows: assume there are N particles in three-dimensional space and the interaction among the N particles is given as a system Hamiltonian H. To describe the dynamics of the N-particle system, the $6N$ phase space coordinate system, or Gibb's phase space with $3N$ position coordinates and $3N$ momenta, can be employed, in which every point (in the $6N$ phase space) specifies a *state* of

[25] Here $\mathbf{X}$ and $\mathbf{x}$ can be related by $\mathbf{X}' = \frac{\partial \mathbf{X}}{\partial s} + \frac{\partial \mathbf{X}}{\partial \mathbf{x}}\mathbf{x}' = \frac{\partial \mathbf{X}}{\partial s} + \mathbf{M}\mathbf{S}\frac{\partial \mathcal{H}}{\partial \mathbf{x}}$. Compared with Eq.(2.9), we have $\mathbf{S}\frac{\partial K}{\partial \mathbf{X}} = \frac{\partial \mathbf{X}}{\partial s} + \mathbf{M}\mathbf{S}\frac{\partial \mathcal{H}}{\partial \mathbf{x}}$ or $\frac{\partial K}{\partial \mathbf{X}} = \mathbf{S}^T\left(\frac{\partial \mathbf{X}}{\partial s} + \mathbf{M}\mathbf{S}\frac{\partial \mathcal{H}}{\partial \mathbf{x}}\right)$. Using the relation of $\partial K/\partial \mathbf{x} = (\partial \mathbf{X}/\partial \mathbf{x})^T (\partial K/\partial \mathbf{X}) = \mathbf{M}^T (\partial K/\partial \mathbf{X})$, we have $\partial K/\partial \mathbf{x} = \mathbf{M}^T\mathbf{S}\mathbf{M}\mathbf{S}^T (\partial \mathcal{H}/\partial \mathbf{x}) + \mathbf{M}^T\mathbf{S}^T (\partial \mathbf{X}/\partial s)$. Assuming $\partial^2 K/\partial x_i \partial x_j = \partial^2 K/\partial x_j \partial x_i$, this gives the condition/constraint for $\mathbf{M}$, which turns out to be the symplectic condition Eq.(2.11).

the system. It can be expected that the evolution of the system states, or dynamics of the system, can have some structural constraints, e.g. requirement of all state points lying on a hyper-surface. While the detailed descriptions of dynamics rely on the system Hamiltonian H, we try to find out if there is any constraint generally applicable to any Hamiltonian system. Symplecticity is then one of the most fundamental conditions. From the above discussion we also realize that a canonical transformation itself preserves the symplecticity of a system.

The above discussion can lead us to an important fact that is frequently used in study of accelerator beam physics: when a beam particle is described by a set of canonical coordinates, the particle transport (*itself*) can be considered as a type of canonical transformation. To see this, assume a beam particle with $\mathbf{x}$ propagates from s_0 to $s_0 + \delta s$ (with infinitesimal δs), its new coordinate $\mathbf{X}$ (at $s_0 + \delta s$) can be expressed as

$$\mathbf{X} = \mathbf{x} + \frac{d\mathbf{x}}{ds}\delta s = \mathbf{x} + \mathbf{S}\frac{\partial \mathcal{H}}{\partial \mathbf{x}}\delta s \tag{2.12}$$

The transport matrix

$$\mathbf{M} \equiv \frac{\partial \mathbf{X}}{\partial \mathbf{x}} = \mathbf{I} + \mathbf{S}\frac{\partial^2 \mathcal{H}}{\partial \mathbf{x}\partial \mathbf{x}}\delta s \tag{2.13}$$

can be readily proven to satisfy the symplecticity condition[26]. By adding up the infinitesimal transformations, we conclude that the evolution of the solutions with s is itself a canonical transformation. Although the above derivation uses matrix language, which lies on the linear transformation, we note that the symplecticity condition also applies to nonlinear beam transport.

In an effort to obtain the symplecticity condition, a following consequence, which may be the most commonly cited, is the Liouville theorem. Liouville theorem states that in any system governed by a Hamiltonian, the density of *system points* surrounding a particular system point in phase space must remain *constant* as the independent variable s evolves. As the system evolves, the "particular system point" moves through phase space, so the theorem refers to the density in a chunk of volume moving through phase space. The proof of the theorem relies on the symplecticity of the beam transport.

Before showing the mathematical form of Liouville theorem, we should comment a bit more about the *system point* meant here. The originally applied situation of the system point is referred to as the so-called Gibb's phase space, which represents a collection of possible states of the total system. Thus a system of 10^{10} particles[27] is described by a single point in a phase space of 6×10^{10} dimensions[28], and each distinct

[26] From Eq. (2.11),

$$\mathbf{M}^T\mathbf{S}\mathbf{M} = \left(\mathbf{I} - \mathbf{S}\frac{\partial^2 \mathcal{H}}{\partial \mathbf{x}\partial \mathbf{x}}\delta s\right)\mathbf{S}\left(\mathbf{I} + \mathbf{S}\frac{\partial^2 \mathcal{H}}{\partial \mathbf{x}\partial \mathbf{x}}\delta s\right) = \mathbf{S} + \mathrm{O}(\delta s^2) \tag{2.14}$$

where the properties of $\mathbf{S}$ in Eq. (2.5) are used. This means that the infinitesimal transport from s_0 to $s_0 + \delta s$ is symplectic.

[27] This number is typical in the modern high-brightness particle beams with bunch charge level of several nano-Coulombs.

[28] Here, three of them represent particle position coordinates and the remaining three for the corresponding conjugate mo-

point specifies a distinct dynamical state or "phase" of the system. The Hamiltonian of the system involves the coordinates and momenta of *all* the particles, and it dictates the motion of that single system point in the phase space. It may include terms that account for interactions between the particles of the system, e.g. binary collision in a beam. Thus such Hamiltonian is far more general than what we are interested in the dissertation. Of our interest is the simplified situation when a particle interacts more strongly with the *collective* fields of (or generated from) the other particles than its nearest neighbors [35]. This way we can treat the collective fields on the same footing as the external fields. This simplification thus greatly reduces the dimensionality from $6N$ to 6. Therefore in a phase space of 6 dimensions (instead of 6×10^{10}) in which each of *non-interacting* particles of a beam is now represented by a point. Each particle then obeys a Hamiltonian of *the same* form expressed in terms of the six canonical variables of *that* particle. To emphasize, each of these particles moves in accordance with Hamilton's equations of motion derived from the same Hamiltonian.

Now it is time to prove the Liouville theorem. Assume a bunch of beam particles (or a collection of system points), transported through a map $\mathbf{M}$, has initial and final canonical phase-space coordinates $\mathbf{x}$ and $\mathbf{X}$. The volume elements of the occupied phase space in the two locations, dv and dV, are[29]

$$dv = \prod_{i=1}^{6} dx_i \tag{2.15}$$

and

$$dV = \prod_{i=1}^{6} dX_i = |\det \mathbf{M}| \prod_{i=1}^{6} dx_i \tag{2.16}$$

From Eq. (2.14), one can find that $|\det \mathbf{M}| = 1$. This means that the volume of any given region in phase space is conserved under a canonical/symplectic transformation. The density of particles (or system points) in phase space is simply equal to the number of particles (or system points) in a given region divided by the volume of the region. Since both the number of particles (or the number of system points) and the volume occupied by them are conserved when the system obeys Hamilton's equations, we can see immediately that the density of particles (or system points) in phase space is conserved in a system obeying Hamilton's equations. Mathematically, the Liouville theorem can be expressed as

$$\frac{df}{ds} = 0 \tag{2.17}$$

where f is, in its most general form, the phase-space probability density function in $6N$ dimensional phase space.

In what follows we narrow a general discussion down to the special case of collective beam dynamics in an accelerator system. When reduced from $6N$-dimensional to 6-dimensional phase space, and written in a

menta.

[29]For simplicity, we assume the elements are shaped in n-dimensional Cartesian/orthogonal coordinate system.

more explicit form, the Liouville theorem Eq. (2.17) reads

$$\frac{\partial f}{\partial s} + \frac{\partial \mathcal{H}}{\partial \mathbf{p}}\frac{\partial f}{\partial \mathbf{q}} - \frac{\partial \mathcal{H}}{\partial \mathbf{q}}\frac{\partial f}{\partial \mathbf{p}} = 0 \tag{2.18}$$

where $\mathbf{q} \equiv (x, y, z)^T$, $\mathbf{p} \equiv (p_x, p_y, p_z)^T$, and $\mathcal{H}$ is the Hamiltonian describing the 6-dimensional system. For the subsequent discussion, we define $\mathbf{X} \equiv (x, p_x, y, p_y, z, p_z)^T$ and $f = f(\mathbf{X}; s)$ is now interpreted as the beam phase-space (probability) distribution function. Looking at *time* s in an infinitesimal six dimensional phase space element $\mathbf{X} \to \mathbf{X} + d\mathbf{X}$, the probable number of particles can be evaluated as

$$f(\mathbf{X}; s)d\mathbf{X} \tag{2.19}$$

and the normalization gives

$$\int_{-\infty}^{\infty} f(\mathbf{X}; s)d\mathbf{X} = N \tag{2.20}$$

where N is the total number of particles in a beam bunch. Equation (2.18) is also well-known as the Vlasov equation [202] or collisionless Boltzmann equation.

To end this section, we comment that the method of employing Vlasov equation, together with the collective-field approach, is in fact an approximate treatment[30], because collisions among near-neighbor particles have been excluded[31]. For the case that beam particles emit radiation, the complete description should require that the Hamiltonian have canonical variables representing the degrees of freedom of the electromagnetic field, and the corresponding symplectic condition involves the field variables as well as those of particles'. However, if the reaction of the radiation field back to the beam phase space is not sufficiently strong, we can still retain and employ the six-dimensional phase space coordinates only. This is usually the case when the accelerator beam dynamics is treated using classical electrodynamics. As for the validity of employing Vlasov equation, we remind that it is sufficient to describe the beam dynamics in a single-pass accelerator system, e.g. linac, or few-passes machines, e.g. recirculating or ERL accelerators. This is because the effects of radiation reaction, e.g. radiation damping and quantum excitation, can be negligible in the situation when the time scale is much shorter than the synchrotron oscillation period. In an electron storage ring, where the beam particles revolve for a (presumed) infinitely long time, radiation damping and quantum excitation must then be taken into account. In this case, damping and diffusion can be added to the right-hand side (RHS) of Vlasov equation, forming the Vlasov-Fokker-Plank (VFP) equation. The VFP equation is in general a nonlinear integro-partial differential equation and can be more complicated than Vlasov equation.

[30] In some situations this method is termed mean-field treatment.

[31] For example [37], the effects of intrabeam scattering (IBS) and Touschek scattering are excluded from the Vlasov treatment. Roughly speaking, IBS originates from multiple small-angle collision of near-neighbor particles and can lead to emittance growth of the beam. Touschek scattering is due to single large-angle collision of near-neighbor particles and may result in reduction of beam lifetime.

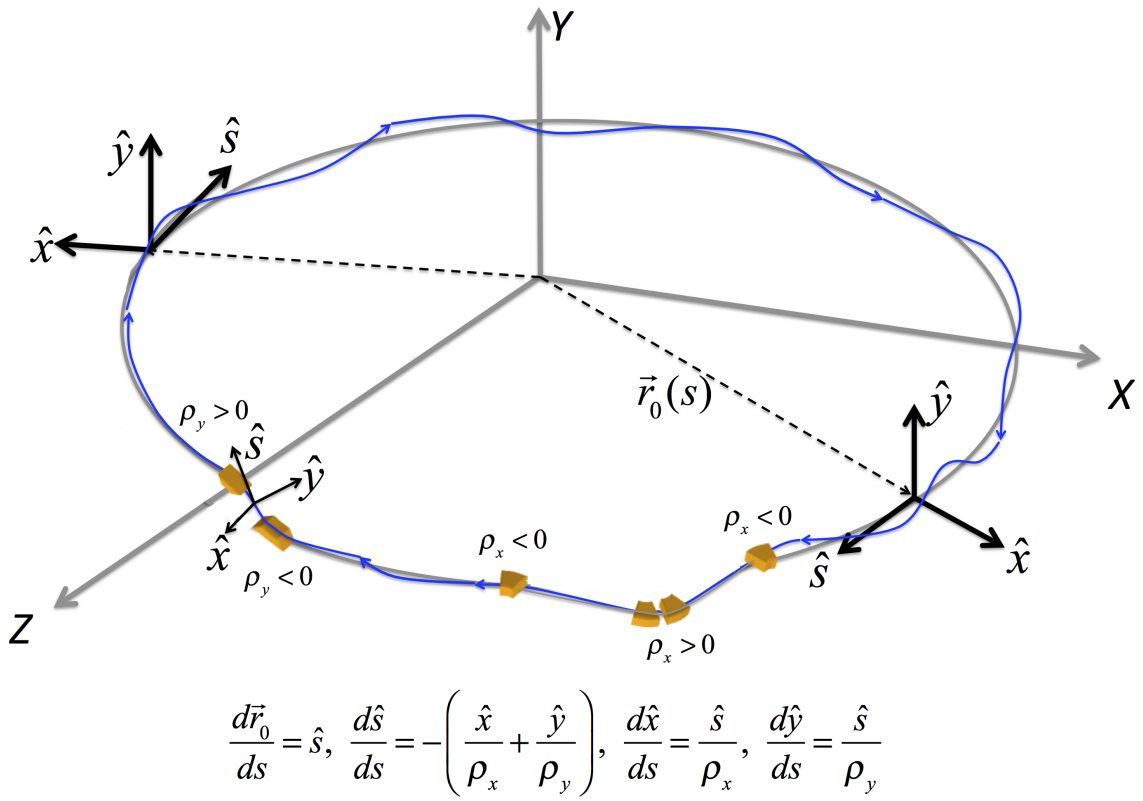

Figure 2.1: Curvilinear (Frenet-Serret) coordinate system. The gray trajectory refers to the reference orbit. The blue one is illustrated as the orbit with betatron oscillation.

2.2 Accelerator Hamiltonian

In the previous section we have discussed general features of Hamiltonian mechanics, symplecticity, Liouville theorem, and derived a reduced form, the Vlasov equation. However we did not derive any specific form of the system Hamiltonian. In this section we would derive the accelerator Hamiltonian, in which the independent variable is not chosen as t but s, because it is more convenient and in most situations the design/reference particle moves without backtracking. The most commonly cited accelerator Hamiltonian employs small amplitude approximations, where the transverse momenta are much smaller compared with the total momentum of the particle, i.e. the total particle momentum is mainly longitudinal. That is to say, particles usually move at a small angle to the nominal/reference orbit. For the notations used in the formulation, one can see Fig. 2.1. In case an accelerating cavity is present[32], the Hamiltonian would be time-dependent.

We start from the Hamiltonian for a charged particle in an electromagnetic wave [162, 208],

$$H = \sqrt{(mc^2)^2 + c^2(\pi - e\mathbf{A})^2} + e\varphi \tag{2.21}$$

[32]It can be used to accelerate, decelerate, deflect, or chirp a beam bunch.

where m and e are the rest mass and charge[33] unit of the electron, c is the speed of light, π is the canonical conjugate momentum, φ and $\mathbf{A}$ are respectively the scalar and vector potentials of the external electromagnetic fields. Assume $\varphi = 0$ below for simplicity. Note that π and A can have time dependence.

Equation (2.21) is expressed in Cartesian coordinate system. Now, we want to rewrite it in the Frenet-Serret coordinate system [102, 162] (see Fig. 2.1). To do this, we would use a generating function of the third type [162, 73],

$$F_3(\pi, x, y; s) = -\pi \cdot (r_0(s) + x\hat{x}(s) + y\hat{y}(s)) \tag{2.22}$$

The new canonical momenta can be obtained as

$$\begin{aligned}
\Pi_x &= -\frac{\partial F_3}{\partial x} = \pi \cdot \hat{x} = \pi_x \\
\Pi_y &= -\frac{\partial F_3}{\partial y} = \pi \cdot \hat{y} = \pi_y \\
\Pi_s &= -\frac{\partial F_3}{\partial s} = \pi \cdot \left(\frac{dr_0}{ds} + x\frac{d\hat{x}}{ds} + y\frac{d\hat{y}}{ds} \right) = \pi \cdot \left(\hat{s} + \frac{x}{\rho_x}\hat{s} + \frac{y}{\rho_y}\hat{s} \right) = \pi_s \left(1 + \frac{x}{\rho_x} + \frac{y}{\rho_y} \right)
\end{aligned} \tag{2.23}$$

where $\rho(x)$ and $\rho(y)$ are the bending radii of the horizontal and vertical dipoles. The new Hamiltonian now becomes

$$H = c\left[m^2c^2 + (\Pi_x - eA_x)^2 + (\Pi_y - eA_y)^2 + \left(\frac{\Pi_s}{1 + \frac{x}{\rho_x} + \frac{y}{\rho_y}} - eA_s \right)^2 \right]^{1/2} \tag{2.24}$$

we have used the notations $A_x = \mathbf{A} \cdot \hat{x}, A_y = \mathbf{A} \cdot \hat{y}, A_s = \mathbf{A} \cdot \hat{s}$. Thus far, all the variables are as a function of time, i.e. $x = x(t), y = y(t)$, and $s = s(t)$. As mentioned above, we tend to change the independent variable from t to s. Since the particle is assumed to move without backtracking, the inverse of $s(t)$ can be written as $t(s)$. Thus, $x(s) = x(t(s))$ and $y(s) = y(t(s))$, and similarly to the conjugate momenta. Let

$$h = H\left(x, \Pi_x, y, \Pi_y, s, \Pi_s; t\right) \tag{2.25}$$

where H is given by Eq.(2.24). Now, we can solve Eq. (2.25) for Π_s,

$$\Pi_s = \Pi_s\left(x, \Pi_x, y, \Pi_y, t, -h; s\right) \tag{2.26}$$

Here h is the value of the Hamiltonian. Now we introduce the new Hamiltonian as

$$K\left(x, \Pi_x, y, \Pi_y, t, -h; s\right) = -\Pi_s\left(x, \Pi_x, y, \Pi_y, t, -h; s\right) \tag{2.27}$$

where the time t is now understood as a third coordinate (in addition to x and y) and the energy h is the

[33] For electron, e is negative.

third momentum. Then we have the relation

$$\frac{dh}{ds} = -\frac{\partial K}{\partial t} \tag{2.28}$$

The explicit expression of the new Hamiltonian K can be found by solving Eq. (2.24) for $-\Pi_s$,

$$K = -\left(1 + \frac{x}{\rho_x} + \frac{y}{\rho_y}\right)\left[\frac{h^2}{c^2} - (\Pi_x - eA_x)^2 - (\Pi_y - eA_y)^2 - m^2c^2\right]^{1/2} - eA_s\left(1 + \frac{x}{\rho_x} + \frac{y}{\rho_y}\right) \tag{2.29}$$

When a short accelerating cavity with voltage V is installed in an accelerator, the effect of RF electromagnetic field at the location s_0 can be added in Eq. (2.29),

$$\begin{aligned} K = &-\left(1 + \frac{x}{\rho_x} + \frac{y}{\rho_y}\right)\left[\frac{h^2}{c^2} - (\Pi_x - eA_x)^2 - (\Pi_y - eA_y)^2 - m^2c^2\right]^{1/2} \\ &-eA_s\left(1 + \frac{x}{\rho_x} + \frac{y}{\rho_y}\right) - \frac{eV}{p_0\omega_{\mathrm{RF}}}\delta(s - s_0)\cos(\omega_{\mathrm{RF}}z/c + \phi) \end{aligned} \tag{2.30}$$

where the last term corresponds to particle acceleration/deceleration by RF electromagnetic field in a beam transport system. $\delta(...)$ is the Kronecker delta function, assuming the cavity is localized with cavity length much shorter than the other elements in the beamline. ω_{RF} and ϕ are the angular frequency and the phase of the RF cavity, assuming the field is sinusoidal.

In many cases of interest, A_s is sufficient to describe the various magnetic fields in an accelerator, so we can set $A_x = A_y = 0$ in Eq. (2.30)[34]. For example,

$$\begin{aligned} A_s = &-B_y(s)x\left(1 - \frac{x}{2\rho_x}\right) - B_x(s)y\left(1 - \frac{y}{2\rho_y}\right) + \frac{G_n(s)}{2}\left(y^2 - x^2\right) + G_s(s)xy \\ &+S(s)\left(\frac{1}{2}xy^2 - \frac{1}{6}x^3\right) \end{aligned} \tag{2.31}$$

where the first two terms represent the action of dipole components, the third and fourth terms for normal and skew quadrupole components with G_n and G_s are respectively the quadrupole gradient strengths, and the last term acts as sextupole components with S as the sextupole strength[35]. In this case, Π_x and Π_y are equal to the kinetic momenta, i.e. $\Pi_x = p_x = m\gamma v_x$ and $\Pi_y = p_y = m\gamma v_y$, and we can use p_x and p_y to replace Π_x and Π_y,

$$\begin{aligned} K = &-\left(1 + \frac{x}{\rho_x} + \frac{y}{\rho_y}\right)\left(\frac{h^2}{c^2} - p_x^2 - p_y^2 - m^2c^2\right)^{1/2} - eA_s\left(1 + \frac{x}{\rho_x} + \frac{y}{\rho_y}\right) \\ &-\frac{eV}{p_0\omega_{\mathrm{RF}}}\delta(s - s_0)\cos(\omega_{\mathrm{RF}}z/c + \phi) \end{aligned} \tag{2.32}$$

We will consider these momenta p_x and p_y as small quantities (compared with the total momentum of the

[34] When there is solenoid in an accelerator, A_x and A_y would be added.
[35] Not to be confused by the symplectic matrix $\mathbf{S}$.

particle p_0), because particles usually move at a small angle to the nominal orbit. Then we Taylor expand Eq. (2.32) in p_x and p_y and we have

$$\begin{aligned} K \approx -p\left(1+\frac{x}{\rho_x}+\frac{y}{\rho_y}\right)\left(1-\frac{p_x^2}{2p^2}-\frac{p_y^2}{2p^2}\right)-eA_s\left(1+\frac{x}{\rho_x}+\frac{y}{\rho_y}\right) \\ -\frac{eV}{p_0\omega_{\mathrm{RF}}}\delta(s-s_0)\cos(\omega_{\mathrm{RF}}z/c+\phi) \end{aligned} \tag{2.33}$$

For convenience, sometimes we use the dimensionless variables x' and y', defined as $x' \equiv dx/ds = p_x/p_s \approx p_x/p_0$, with similar expression for y' not shown here[36]. Furthermore, when the energy and the total momentum of the particle can only slightly deviate from the nominal one, then we have

$$\frac{p}{p_0} = 1+\delta+... \tag{2.34}$$

with $\delta \equiv (p-p_0)/p_0 \ll 1$. Then

$$\begin{aligned} \mathcal{H} = -(1+\delta)\left(1+\frac{x}{\rho_x}+\frac{y}{\rho_y}\right)\left(1-\frac{x'^2}{2}-\frac{y'^2}{2}\right)-\frac{eA_s}{p_0}\left(1+\frac{x}{\rho_x}+\frac{y}{\rho_y}\right) \\ -\frac{eV_{\mathrm{RF}}}{p_0^2\omega_{\mathrm{RF}}}\delta(s-s_0)\cos\left(\omega_{RF}z/c+\phi\right) \end{aligned} \tag{2.35}$$

For the case of constant beam energy, the last term in Eq. (2.35) vanishes. Substituting Eq. (2.31) into Eq. (2.35) and neglecting the constant and linear terms[37] give

$$\mathcal{H} = \mathcal{H}_{\mathrm{linear}} + \mathcal{H}_{\mathrm{nonlinear}} \tag{2.36}$$

The linear part is

$$\mathcal{H}_{\mathrm{linear}} = \frac{1}{2}\left(K_x x^2 + x'^2 + K_y y^2 + y'^2 + 2G_s xy - 2\frac{x\delta}{\rho_x} - 2\frac{y\delta}{\rho_y}\right) \tag{2.37}$$

where K_x and K_y represent the effective focusing[38], and the remaining belongs to nonlinear part,

$$\mathcal{H}_{\mathrm{nonlinear}} = -\frac{S}{B_y\rho_x}\left(\frac{1}{2}xy^2 - \frac{1}{6}x^3\right)+\cdots \tag{2.38}$$

The single-particle equations of motion for $\mathcal{H}_{\mathrm{linear}}$ can be obtained by Hamilton's equation of motion,

$$\frac{d\mathbf{X}}{ds} = \mathbf{S}\frac{\partial \mathcal{H}_{\mathrm{linear}}}{\partial \mathbf{X}} \tag{2.39}$$

[36]The coordinate transformation from p_x to x' (and p_y to y') is not canonical but extended canonical with $\lambda = 1/p_0$.

[37]The constant term in Hamiltonian is only responsible for static offset of the scale of $\mathcal{H}$. This offset is not of our current interest. The linear term, e.g. δ, only produces an offset on particle coordinate. When all the coordinates of a particle are measured with respect to a reference particle, this offset can be gone.

[38]For separate dipole and (horizontal focusing) quadrupole, $K_x = \rho_x^{-2} + G_n$ and $K_y = \rho_y^{-2} - G_n$. Note that the above formulation can be applicable to the cases with focusing in combined-function dipoles and with tilt of quadrupoles.

Written in an explicit form,

$$\begin{aligned}
\frac{dx}{ds} &= x' \\
\frac{dx'}{ds} &= -K_x(s)x + \frac{\delta}{\rho_x(s)} \\
\frac{dy}{ds} &= y' \\
\frac{dy'}{ds} &= -K_y(s)y + \frac{\delta}{\rho_y(s)} \\
\frac{dz}{ds} &= -\left(\frac{x}{\rho_x(s)} + \frac{y}{\rho_y(s)}\right) \\
\frac{d\delta}{ds} &= 0
\end{aligned} \tag{2.40}$$

The two first-order differential equations for x and x' can be combined in one second-order differential equation, resulting in the well-known Hill's equation,

$$x'' + K_x(s)x = \frac{\delta}{\rho_x(s)} \tag{2.41}$$

When the particle is accelerated, an additional friction term can be added in Hill's equation,

$$x'' + r(s)x' + K_x(s)x = \frac{\delta}{\rho_x(s)} \tag{2.42}$$

where $r(s) = E_r^{-1} dE_r(s)/ds$ is the rate of acceleration, $E_r(s)$ is the reference energy at s, and $E_0 = E_r(s=0)$ is the initial energy[39]. Here we assume $r(s)$ is adiabatically varying so that $r'(s) \ll 1$ can be neglected. If we want to retain the Hamiltonian form for varying beam energy as close to Eq. (2.37) as possible, we can make the following change of dynamic variables [193],

$$\begin{aligned}
\begin{bmatrix} \hat{x} \\ \hat{y} \end{bmatrix} &= \begin{bmatrix} x \\ y \end{bmatrix} \sqrt{\frac{E_r(s)}{E_0}} \\
\begin{bmatrix} \hat{x}' \\ \hat{y}' \end{bmatrix} &\simeq \begin{bmatrix} x' \\ y' \end{bmatrix} \sqrt{\frac{E_r(s)}{E_0}} \\
\hat{z} &= z \\
\hat{\delta} &= \delta + 1 - \frac{E_r(s)}{E_0}
\end{aligned} \tag{2.43}$$

[39] To extend the constant-energy formula to varying energy case, we usually make the substitutions $x'' = \frac{d}{ds}x' \to \frac{1}{\gamma(s)}\frac{d}{ds}\gamma(s)x'$ and $\delta = \frac{E-E_0}{E_0} \to \frac{E-E_r(s)}{E_0(s)}$. An alternative way to derive the equations of motion can use Eq. (2.45).

After the change of variables, Eq. (2.40) becomes

$$\begin{aligned}
\frac{d\hat{x}}{ds} &= \hat{x}' \\
\frac{d\hat{x}'}{ds} &= -\hat{K}_x(s)\hat{x} + \sqrt{\frac{E_0}{E_r(s)}}\frac{\hat{\delta}}{\rho_x(s)} \\
\frac{d\hat{y}}{ds} &= \hat{y}' \\
\frac{d\hat{y}'}{ds} &= -\hat{K}_y(s)\hat{y} + \sqrt{\frac{E_0}{E_r(s)}}\frac{\hat{\delta}}{\rho_y(s)} \\
\frac{d\hat{z}}{ds} &= -\sqrt{\frac{E_0}{E_r(s)}}\left(\frac{\hat{x}}{\rho_x(s)} + \frac{\hat{y}}{\rho_y(s)}\right) \\
\frac{d\hat{\delta}}{ds} &= -\kappa(s)\hat{z}
\end{aligned} \tag{2.44}$$

where $\kappa \equiv \frac{\Delta E_{\rm cav}\omega_{\rm RF}}{E_0 L_{\rm cav} c}\cos\phi_s$ with $\Delta E_{\rm cav}$, ϕ_s, $\omega_{\rm RF}$ and $L_{\rm cav}$ are, respectively, the energy gain, synchronous phase, the angular RF frequency and the length of the accelerating cavity. Equation (2.37) now has the form,

$$\bar{H}_{\rm linear} = \tfrac{1}{2}\left(K_x\hat{x}^2 + \hat{x}'^2 + K_y\hat{y}^2 + \hat{y}'^2 + \kappa\hat{z}^2 - 2\sqrt{\tfrac{E_0}{E_r}}\tfrac{\hat{x}\hat{\delta}}{\rho_x} - 2\sqrt{\tfrac{E_0}{E_r}}\tfrac{\hat{y}\hat{\delta}}{\rho_y}\right) \tag{2.45}$$

Here we use the overline on top of a quantity to emphasize that it is an unperturbed quantity by the beam self-fields. Now we have already obtained the system Hamiltonian, Eq. (2.45), for a beam particle transport through an accelerator system. This Hamiltonian, considered as pure-optics Hamiltonian[40], includes both transverse horizontal and vertical (separate) bends, focusing or defocusing quadrupoles, and/or the linear combined-function dipoles, and presence of RF accelerating cavities. Notice that only the effects of linear magnetic beamline elements are accounted for in the Hamiltonian. For an ERL or specialized beamline design with sextupole or higher-order magnetic elements, the nonlinear effects would be overlooked in the subsequent discussion[41].

2.3 Linear optics in a beam transport system

When a bunch of particles traverse through a beam transport system, the evolution of the beam can be determined separately by the so-called single-particle optics and collective (multi-particle) dynamics. For the single-particle optics, or the single-particle motion, prescribed by the accelerator design, it is solely defined by the external electric and magnetic fields of the various accelerator components specified in the design. Although, given these fields, intricate effects of linear and nonlinear single-particle dynamics can be studied in detail [35], we restrict ourselves to the *linear* part of the single-particle beam dynamics (or, linear optics)

[40] This is to be contrast with the Hamiltonian with inclusion of collective interaction.

[41] Our particle tracking simulation shows that effect of sextupoles on microbunching instability can lead to slightly reduced gain.

for simplicity.

We begin by defining the six-dimensional phase space coordinate as

$$\hat{\mathbf{X}}(s) = \left(\hat{x}, \hat{x}', \hat{y}, \hat{y}', \hat{z}, \hat{\delta}; s\right)^T \tag{2.46}$$

where $\hat{x}$ and $\hat{y}$, defined in Eq. (2.43), are transverse horizontal/radial and vertical positions, $\hat{x}'$ and $\hat{y}'$ are the corresponding angular divergences, $(') \equiv d/ds$, and $\hat{z}$ and $\hat{\delta} \equiv (E - E_r)/E_0$ are the (local) longitudinal coordinate and energy deviation (assuming $\hat{z} > 0$ for the bunch head). All these quantities are measured with respect to the reference particle and are a function of the (global) longitudinal path coordinate, s. When the beam energy is a constant, all quantities with hat are reduced to the normal ones (without hat). [see Eq. (2.43)] The superscript T indicates the transpose operator. For the convenience of subsequent discussion, we also define two subsets of $\mathbf{X}$ as

$$\hat{\mathbf{X}}_{2D}(s) = (\hat{x}, \hat{x}'; s)^T \tag{2.47}$$

and

$$\hat{\mathbf{X}}_{4D}(s) = (\hat{x}, \hat{x}', \hat{y}, \hat{y}'; s)^T \tag{2.48}$$

The linear beam optics is based on the following approximations, which are met by most modern accelerators[42][149]:

1. The position variables of a particle are small in comparison to some scale distance characteristic of the physical dimensions of a magnet or an accelerating cavity. In a quadrupole magnet, for example, the (longitudinal) scale distance is determined by the degree to which the field dependence on transverse coordinates departs from the desired linear dependence, e.g. good field region. It depends on the quality of the quadrupole. In good quadrupoles, the distance is typically many meters. In accelerating cavities, the scale distance of the electric and magnetic fields is of the order of the free-space wavelength corresponding to the operating frequency, e.g. ∼1 cm in 3 GHz.

2. The ratio of the horizontal coordinate to the bending radius is very small compared to unity, or $x, y/\rho_{x,y} \ll 1$.

3. The derivatives x' and y' are very small compared to unity, which is typical for relativistic beams. This is assured by the nature of high-brightness (thus small-emittance) particle beams, in which the transverse velocities are much smaller than the longitudinal ones.

4. The energy of a particle deviates only slightly from the energy of the reference particle.

[42] An exception can be the IOTA (Intregable Optics Test Accelerator at Fermilab) ring, which intentionally employs nonlinearity in the accelerator machine.

We comment here that there are several ways of *linearizing* the beam optics in a particle transport system:

(a) Starting from the exact Hamiltonian, e.g. Eq. (2.35), we linearize the Hamiltonian itself, i.e., expand it in a Taylor series in the six canonical variables and truncate the series appropriately, e.g. Eq. (2.37) or Eq. (2.45); or

(b) Starting from the exact Hamiltonian, we might first apply Hamilton's equations of motion to the exact Hamiltonian and then linearize the resulting differential equations; or,

(c) We might solve the exact solutions of Hamilton's equations of motion for the exact Hamiltonian, and then linearize the solutions.

It can be shown that the above three approaches can lead to the same result [149].

Our approach, formulated in Sec. 2.2, is in fact consistent with the case (a). From Eq. (2.45), the Taylor expanded Hamiltonian can be in general expressed

$$\bar{H}_{\text{linear}}\left(\mathbf{X}; s\right) = \sum_{k=1}^{6}\left(h_k\hat{x}_k + \frac{1}{2}\sum_{j=1}^{6} h_{kj}\hat{x}_k\hat{x}_j\right) \tag{2.49}$$

where $h_k \equiv \partial\bar{H}_{\text{linear}}/\partial\hat{x}_k$ and $h_{kj} = h_{jk} \equiv \partial^2\bar{H}_{\text{linear}}/\partial\hat{x}_k\partial\hat{x}_j$. Applying the Hamilton's equations of motion, we have

$$\begin{aligned}
\hat{x}_1' &= \frac{\partial\bar{H}_{\text{linear}}}{\partial\hat{x}_2} = h_2 + \sum_{j=1}^{6} h_{2j}\hat{x}_j \\
\hat{x}_2' &= -\frac{\partial\bar{H}_{\text{linear}}}{\partial\hat{x}_1} = -h_1 - \sum_{j=1}^{6} h_{1j}\hat{x}_j
\end{aligned} \tag{2.50}$$

and so forth. In the above expressions, we have set $h_1 = h_2 = 0$ because these phase space coordinates are referred to the reference particle. If we write the above differential equations in a matrix form, we have

$$\hat{\mathbf{X}}' = \mathbf{V}\hat{\mathbf{X}} \tag{2.51}$$

where

$$\mathbf{V} = \begin{pmatrix} h_{21} & h_{22} & \cdots \\ -h_{11} & -h_{12} & \cdots \\ \cdots & \cdots & \cdots \end{pmatrix} \tag{2.52}$$

The general matrix differential equation can be solved by Magnus expansion [119] and the solution for Eq.

(2.51) has the following form

$$\hat{\mathbf{X}} = \hat{\mathbf{R}}\hat{\mathbf{X}}_0 \tag{2.53}$$

where $\hat{\mathbf{X}}_0 = \hat{\mathbf{X}}(s=0) = \mathbf{X}_0$ represents the initial phase space coordinate of a particle. If the Hamiltonian contains nonlinear terms, e.g. Eq. (2.35), a more general expression can be formulated as

$$\hat{\mathbf{X}} = \hat{\mathcal{R}} \circ \hat{\mathbf{X}}_0 \tag{2.54}$$

where $\hat{\mathcal{R}}$ is map and $\circ$ represents the composition operator[43]. To first order, i.e. linear transport, $\hat{\mathcal{R}}$ can be expressed by an ordinary matrix $\mathbf{R}$, and Eq. (2.54) is reduced to Eq. (2.53). The transport matrix is in fact that introduced in Sec. 2.2, $\mathbf{M}$ for six-dimensional case, since

$$\hat{\mathbf{R}} = \frac{\partial \hat{\mathbf{X}}}{\partial \hat{\mathbf{X}}_0} \tag{2.55}$$

is a Jacobian matrix and it satisfies symplectic condition[44].

Let us write the $\hat{\mathbf{R}}$ matrix explicitly for some typical accelerator elements because it would be mentioned frequently in the subsequent discussion. In most general situations, the matrix $\hat{\mathbf{R}}$ has the following form,

$$\hat{\mathbf{R}} = \begin{pmatrix} \hat{R}_{11} & \hat{R}_{12} & \hat{R}_{13} & \hat{R}_{14} & 0 & \hat{R}_{16} \\ \hat{R}_{21} & \hat{R}_{22} & \hat{R}_{23} & \hat{R}_{24} & 0 & \hat{R}_{26} \\ \hat{R}_{31} & \hat{R}_{32} & \hat{R}_{33} & \hat{R}_{34} & 0 & \hat{R}_{36} \\ \hat{R}_{41} & \hat{R}_{42} & \hat{R}_{43} & \hat{R}_{44} & 0 & \hat{R}_{46} \\ \hat{R}_{51} & \hat{R}_{52} & \hat{R}_{53} & \hat{R}_{54} & \hat{R}_{55} & \hat{R}_{56} \\ 0 & 0 & 0 & 0 & \hat{R}_{65} & \hat{R}_{66} \end{pmatrix} \tag{2.56}$$

Several typical beamline elements in an aceelerator system include bending dipoles, focusing or defocusing quadrupoles, drift or free space elements. For simplicity, in what follows where there is no confusion, we presume the beam energy is constant, i.e. $\hat{\mathbf{R}} = \mathbf{R}$, and the coordinates are now without hat. The simplest

[43] In nonlinear optics, $\hat{\mathcal{R}}$ depends on $\hat{\mathbf{X}}_0$, i.e. $\hat{\mathcal{R}}$ has functional dependence of $\hat{\mathbf{X}}_0$, $\hat{\mathcal{R}} = f(\hat{\mathbf{X}}_0)$. To retain the formalism, we denote by $\hat{\mathcal{R}} \circ \hat{\mathbf{X}}_0$. If reduced to linear optics (or linear algebra), $\hat{\mathcal{R}}$ is independent of $\hat{\mathbf{X}}_0$ and the composition operator becomes ordinary matrix multiplication.

[44] Note that there also exists the symplectic condition for nonlinear beam transport $\hat{\mathcal{R}}$, although in Sec. 2.2 we only discussed linear transport.

element can be a drift space of length L, for which

$$\mathbf{R}^{\text{drift}} = \begin{bmatrix} 1 & L & 0 & 0 & 0 & 0 \\ 0 & 1 & 0 & 0 & 0 & 0 \\ 0 & 0 & 1 & L & 0 & 0 \\ 0 & 0 & 0 & 1 & 0 & 0 \\ 0 & 0 & 0 & 0 & 1 & \frac{L}{\gamma^2} \\ 0 & 0 & 0 & 0 & 0 & 1 \end{bmatrix} \tag{2.57}$$

For a horizontal sector dipole with bending radius ρ_x and angle θ_x (with $\rho_x\theta_x = L$),

$$\mathbf{R}^{\text{dipole}} = \begin{bmatrix} \cos\theta_x & \rho_x \sin\theta_x & 0 & 0 & 0 & \rho_x\left(1-\cos\theta_x\right) \\ -\frac{1}{\rho_x}\sin\theta_x & \cos\theta_x & 0 & 0 & 0 & \sin\theta_x \\ 0 & 0 & 1 & L & 0 & 0 \\ 0 & 0 & 0 & 1 & 0 & 0 \\ -\sin\theta_x & -\rho_x\left(1-\cos\theta_x\right) & 0 & 0 & 1 & -\rho_x\left(\theta_x-\sin\theta_x\right)+\frac{L}{\gamma^2} \\ 0 & 0 & 0 & 0 & 0 & 1 \end{bmatrix} \tag{2.58}$$

Similar expression for vertical bending dipole can be easily obtained and not shown here. It is obvious that the thin-lens approximation of a dipole becomes a drift in the bending plane. For wedge bending dipole, there is a net focusing or defocusing in the bending plane.

For the strong focusing in a quadrupole, if the focusing occurs in the horizontal (vertical) direction, it de-focuses the beam in the vertical (horizontal) direction. The matrix expression is

$$\mathbf{R}^{\text{quad}} = \begin{bmatrix} \cos\sqrt{K_x}L & \frac{\sin\sqrt{K_x}L}{\sqrt{K_x}} & 0 & 0 & 0 & 0 \\ -\sqrt{K_x}\sin\sqrt{K_x}L & \cos\sqrt{K_x}L & 0 & 0 & 0 & 0 \\ 0 & 0 & \cos\sqrt{K_y}L & \frac{\sin\sqrt{K_y}L}{\sqrt{K_y}} & 0 & 0 \\ 0 & 0 & -\sqrt{K_y}\sin\sqrt{K_y}L & \cos\sqrt{K_y}L & 0 & 0 \\ 0 & 0 & 0 & 0 & 1 & \frac{L}{\gamma^2} \\ 0 & 0 & 0 & 0 & 0 & 1 \end{bmatrix} \tag{2.59}$$

where L and $K_{x,y}$ are the quadrupole length and horizontal/vertical focusing/defocusing strengths. K_x has the opposite sign to that of K_y [45]. In an electron machine, $K_x > 0$ usually refers to horizontal focusing. For a combined-function dipole, in which a beam is not only bent but focused/defocused in the bending plane, the transport matrix can be more complicated.

If a beamline is composed of repetitive modulus, or periodic cells, for each identical cell, the general six-by-six transport matrix can be parameterized by the so-called Twiss [191] or Courant-Snyder [41] parameters. The

[45] For $K_x = -K_y > 0$, $\sqrt{K_y}L = i\sqrt{K_x}L$, $\cos\sqrt{K_y}L = \cos\left(i\sqrt{K_x}L\right) = \cosh\sqrt{K_x}L$ and $\sin\sqrt{K_y}L = \sin\left(i\sqrt{K_x}L\right) = i\sinh\sqrt{K_x}L$.

matrix expression with unit module is

$$\mathbf{R}^{\text{total}} = \begin{pmatrix} \sqrt{\frac{\beta_{2x}}{\beta_{1x}}}\left(\cos\psi_{21,x} + \alpha_{1x}\sin\psi_{21,x}\right) & \sqrt{\beta_{2x}\beta_{1x}}\sin\psi_{21,x} & & \\ -\frac{1+\alpha_{2x}\alpha_{1x}}{\sqrt{\beta_{2x}\beta_{1x}}}\sin\psi_{21,x} + \frac{\alpha_{1x}-\alpha_{2x}}{\sqrt{\beta_{2x}\beta_{1x}}}\cos\psi_{21,x} & \sqrt{\frac{\beta_{1x}}{\beta_{2x}}}\left(\cos\psi_{21,x} - \alpha_{2x}\sin\psi_{21,x}\right) & & \\ 0 & 0 & & \\ 0 & 0 & & \\ R_{51} & R_{52} & & \\ 0 & 0 & & \end{pmatrix} \begin{pmatrix} 0 & 0 & R_{16} \\ 0 & 0 & R_{26} \\ \sqrt{\frac{\beta_{2y}}{\beta_{1y}}}\left(\cos\psi_{21,y} + \alpha_{1y}\sin\psi_{21,y}\right) & \sqrt{\beta_{2y}\beta_{1y}}\sin\psi_{21,y} & R_{36} \\ -\frac{1+\alpha_{2y}\alpha_{1y}}{\sqrt{\beta_{2y}\beta_{1y}}}\sin\psi_{21,y} + \frac{\alpha_{1y}-\alpha_{2y}}{\sqrt{\beta_{2y}\beta_{1y}}}\cos\psi_{21,y} & \sqrt{\frac{\beta_{1y}}{\beta_{2y}}}\left(\cos\psi_{21,y} - \alpha_{2y}\sin\psi_{21,y}\right) & R_{46} \\ R_{53} & R_{54} & R_{56} \\ 0 & 0 & 1 \end{pmatrix} \begin{matrix} 0 & R_{16} \\ 0 & R_{26} \\ 0 & R_{36} \\ 0 & R_{46} \\ 1 & R_{56} \\ 0 & 1 \end{matrix} \tag{2.60}$$

where the subscripts 1 and 2 specify the initial and final locations of the unit module (see Fig. 2.2), and the subscripts x and y indicate the horizontal and vertical directions. In the x direction, $\beta_{1,2}$ and $\alpha_{1,2} \equiv -\beta'_{1,2}/2$ are the Twiss (or Courant-Snyder) parameters, and $\psi_{21} \equiv \int_1^2 ds/\beta$ is the betatron phase difference between 1 and 2[46].

If the general expression of Eq. (2.60) satisfies the symplecticity condition, Eq. (2.11), this requirement

[46]In the literature, the Twiss or Courant-Snyder parameters are denoted as β, α and γ, where $\gamma \equiv (1+\alpha^2)/\beta$ in either x or y or z dimension. Not to be confused with relativistic Lorentz factors. Notice that these β, α (and γ) functions refer to both beam and beamline lattice. It is obvious that Eq. (2.60) refers to lattice Twiss functions. Physically, the evolution of β-function, $\beta(s)$, describes evolution of the amplitudes of beam sizes. More specifically, $x \propto \sqrt{\epsilon_x\beta_x}\cos\psi_x$. The phase is characterized by ψ and can have s-dependence. The way to parameterize a transport matrix is not unique [39], but Twiss or Courant-Snyder parameterization is currently the most common treatment in the accelerator community. When solving Hill's equation, Eq. (2.41), we perform Floquet transformation using $x(s) = w(s)e^{-i\psi(s)}$ and obtain the nonlinear envelope and phase equations below

$$w'' + K_x(s)w - 1/w^3 = 0$$

$$\psi' = 1/w^2$$

In the equations, we define $w^2 = \beta$ and $\alpha = -ww' = -\beta'/2$. It can be seen that β-function is proportional to the square of the oscillation amplitude. α-function is related to the slope of the betatron amplitude function. The Twiss or Courant-Snyder parameters can be also related to the geometric characteristics of beam phase space ellipse [102]. Here the Twiss functions or parameters refer to beam's. See Fig. 2.3. The phase space ellipse is recorded at a certain location and its shape would stretch in drifts or thin dipoles and shear/rotate in quadrupoles. The phase space area is however conserved because of Liouville theorem (see Sec. 2.1). The maximum amplitude of the betatron motion at the location is $\sqrt{\beta\epsilon}$. The maximum divergence is $\sqrt{\gamma\epsilon}$, An important quantity ϵ, called the beam emittance, is used to characterize the phase space area occupied by the beam particles. When the Twiss parameters of a beam match those of a beamline lattice, we term the beam is matched. A beamline design is usually assumed the transported beam is a matched beam.

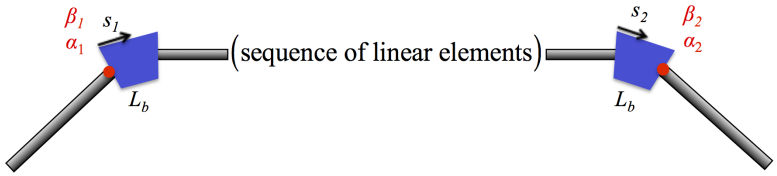

Figure 2.2: A section of beam transport line. The in-between section can consist of drift, dipole, and/or quadrupole elements.

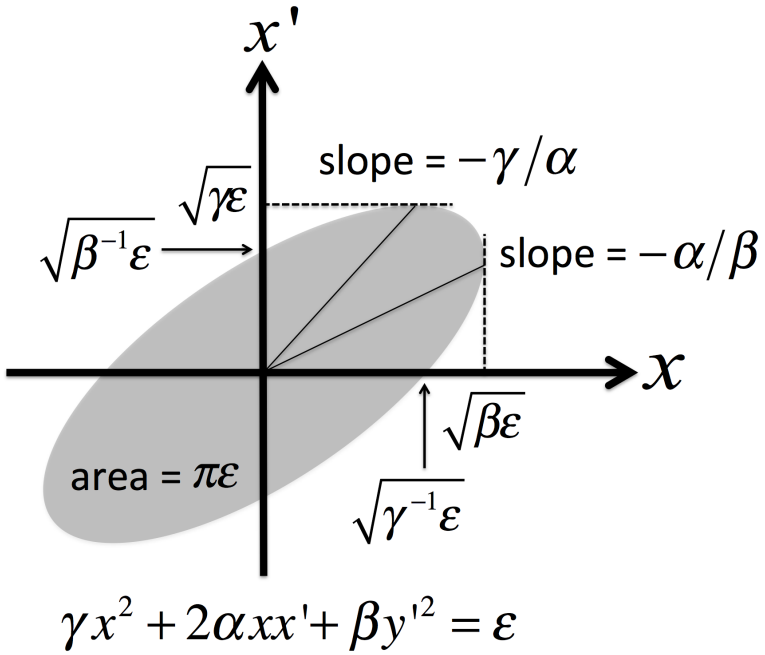

Figure 2.3: The Twiss or Courant-Snyder invariant phase space ellipse.

gives further constraints as follows

$$R_{51} = R_{16}R_{21} - R_{26}R_{11} \tag{2.61}$$

$$R_{52} = R_{16}R_{22} - R_{26}R_{12} \tag{2.62}$$

$$R_{53} = R_{36}R_{43} - R_{46}R_{33} \tag{2.63}$$

$$R_{54} = R_{36}R_{44} - R_{46}R_{34} \tag{2.64}$$

It can be seen that R_{56}, the momentum compaction factor, does not have direct constraint from the symplecticity condition and can be considered as a free parameter. From Eqs. (2.57) to (2.60), one can find that the off-diagonal block matrices, e.g. R_{13}, R_{14}, R_{23}, R_{24} and R_{31}, R_{32}, R_{41}, R_{42}, are all zero. This means that the presented transport elements are uncoupled elements. An element with any non-zero off-diagonal block matrix is said to be x-y coupled elements, e.g. solenoid, skew-quadrupole and so on. A beamline with such coupled elements is said to be coupled beamline.

So far we have formulated the single-particle optics in a beam transport line. For a realistic beam, which is composed of particles confined in the beam phase space, in addition to using Twiss or Courant-Snyder parameters (see Fig. 2.3), we can also characterize the beam distribution by some statistical quantities associated with the phase space probability density function, Eq. (2.20). Here we use its first and second moments. Define the first moment of the beam as [102, 124],

$$\langle \mathbf{X}_i \rangle = \langle x_i \rangle \equiv \frac{\int x_i f\left(\mathbf{X}\right) d\mathbf{X}}{\int f\left(\mathbf{X}\right) d\mathbf{X}} \tag{2.65}$$

where $\langle ... \rangle$ takes the average over the beam, and the second moment

$$\Sigma_{ij} \equiv \langle \left(x_i - \langle x_i \rangle\right) \left(x_j - \langle x_j \rangle\right) \rangle \tag{2.66}$$

for $i = 1, 2, ...6$. For example,

$$\begin{aligned} \bar{x} = \langle x \rangle &= \frac{1}{N} \int_{-\infty}^{\infty} x f(\mathbf{X}) d\mathbf{X} \\ \sigma_x^2 = \Sigma_{11} = \langle \left(x - \langle x \rangle\right) \left(x - \langle x \rangle\right) \rangle &= \frac{1}{N} \int_{-\infty}^{\infty} \left(x - \langle x \rangle\right)^2 f(\mathbf{X}) d\mathbf{X} \\ \sigma_{xx'} = \Sigma_{12} = \langle \left(x - \langle x \rangle\right) \left(x' - \langle x' \rangle\right) \rangle &= \frac{1}{N} \int_{-\infty}^{\infty} \left(x - \langle x \rangle\right) \left(x' - \langle x' \rangle\right) f(\mathbf{X}) d\mathbf{X} \end{aligned} \tag{2.67}$$

where the normalization, Eq. (2.20), has been imposed. It is obvious that the first moment tells us the centroid of the beam and the second moment reveals the deviation from the beam centroid.

In Eq. (2.19), we have used the six-dimensional phase-space distribution function $f\left(\mathbf{X}; s\right)$ to represent a beam. In many cases, the beam phase space distribution function is assumed to depend on the phase space coordinates through some quadratic form [65], e.g. a Gaussian distribution in one dimension $f(x) = N\left(\sqrt{2\pi}\sigma_x\right)^{-1} e^{-x^2/2\sigma_x^2}$. Disregarding the static offset of the beam core, or defining the coordinate with respect to this offset, we have $\langle \mathbf{X}(s) \rangle = \mathbf{0}$. Thus we can characterize a beam using the sigma matrix, defined as

$$\Sigma \equiv \left\langle \mathbf{X}\mathbf{X}^T \right\rangle = \begin{pmatrix} \langle xx \rangle & \langle xx' \rangle & \langle xy \rangle & \langle xy' \rangle & \langle xz \rangle & \langle x\delta \rangle \\ \langle x'x \rangle & \langle x'x' \rangle & \langle x'y \rangle & \langle x'y' \rangle & \langle x'z \rangle & \langle x'\delta \rangle \\ \langle yx \rangle & \langle yx' \rangle & \langle yy \rangle & \langle yy' \rangle & \langle yz \rangle & \langle y\delta \rangle \\ \langle y'x \rangle & \langle y'x' \rangle & \langle y'y \rangle & \langle y'y' \rangle & \langle y'z \rangle & \langle y'\delta \rangle \\ \langle zx \rangle & \langle zx' \rangle & \langle zy \rangle & \langle zy' \rangle & \langle zz \rangle & \langle z\delta \rangle \\ \langle \delta x \rangle & \langle \delta x' \rangle & \langle \delta y \rangle & \langle \delta y' \rangle & \langle \delta z \rangle & \langle \delta\delta \rangle \end{pmatrix} \tag{2.68}$$

where $\langle xx \rangle \equiv \Sigma_{11} = \sigma_x^2$. While we will apply the beam sigma matrix to a specific beam distribution, e.g. Gaussian, we note that Eq. (2.68) is generally applicable to any type of beam distribution function[47]. Below we would use the notations $\Sigma_{2D} = \left\langle \mathbf{X}_{2D}\mathbf{X}_{2D}^T \right\rangle$ and $\Sigma_{4D} = \left\langle \mathbf{X}_{4D}\mathbf{X}_{4D}^T \right\rangle$ to specify respectively the transverse two-by-two and four-by-four subsets of the sigma matrix [see also Eqs. (2.47) and (2.48)].

The (rms) geometric beam emittance can be determined by $\epsilon_{6D} = \sqrt[6]{\det \Sigma}$ for six-dimension case and $\epsilon_{4D} = \sqrt[4]{\det \Sigma_{4D}}$ and $\epsilon_{2D} = \sqrt{\det \Sigma_{2D}}$ for four- and two-dimension projection, respectively. Note that the 6-D emittance is invariant when there is no collective effects and when there is no dissipation force, e.g. beam acceleration or (incoherent) synchrotron radiation. In the situation when a beam is uncoupled in 4-D or 2-D subset, i.e. the corresponding off-diagonal block matrices in Eq. (2.68) vanish, the quantities ϵ_{4D} and/or ϵ_{2D} are conserved. Using the fact that $\mathbf{X}^T(0)\Sigma^{-1}(0)\mathbf{X}(0)$ is invariant[48] and Eq. (2.53), the transport of beam sigma matrix can be formulated as

$$\Sigma(s) = \mathbf{R}\Sigma(0)\mathbf{R}^T \tag{2.69}$$

To end this section, we comment on the coupling of a beam and the coupling of a beamline. For a coupled beam, the off-diagonal elements in the beam sigma matrix, Eq. (2.68), have non-vanishing values. For example, if a beam is characteristic of angular momentum (in $x - y$ plane), the R_{14} and R_{23} are not zero. For a coupled beamline lattice, the off-diagonal elements in the transport matrix, Eq. (2.56), have non-vanishing values. Typical elements are, for example, a solenoid, which correlates the transverse x and y motions of a beam, and a skew quadrupole, which rotates the normal quadrupole by 45 degrees. Unlike the normal quadrupole, for the latter, a beam experiences no more net focusing in one plane and defocusing in the other. When an uncoupled beam traverses a uncoupled beamline, the beam remains uncoupled. For the remaining situations, the beam in general results in an coupled beam.

2.4 Vlasov-Maxwell system and the kinetic description

Many modern accelerator systems, including linac, storage ring, and recirculation machines, often require beams of medium or high intensities. As the beam intensity increases, the electromagnetic fields self-generated by the beam would generate stronger perturbation to the external prescribed fields (which are generated by pure optics, e.g. dipoles or quadrupoles). When the perturbation is appreciable, the beam is gradually out of control and can become unstable. To describe the aspect of *collective* beam dynamics, the single-particle picture does not suffice and multi-particle self-consistent treatment would be needed. Note that all the electromagnetic fields generated by the beam must satisfy Maxwell equations. To study such a

[47] For beam phase space distribution with peculiar distortion, e.g. S-shape or a nonlinear curvature, higher order moments are required to capture the features.

[48] For a uncoupled beam, the invariant in x direction is $\gamma_x x^2 + 2\alpha_x xx' + \beta_x x'2$, which corresponds to the area of the (x, x') phase space ellipse. That quantity can be written as $\gamma_x x^2 + 2\alpha_x xx' + \beta_x x'2 = (x\ x') \begin{pmatrix} \gamma_x & \alpha_x \\ \alpha_x & \beta_x \end{pmatrix} \begin{pmatrix} x \\ x' \end{pmatrix} \propto \mathbf{X}_{2D}^T \Sigma_{2D}^{-1} \mathbf{X}_{2D}$. For 6-D case, $\mathbf{X}_{6D}^T \Sigma_{6D}^{-1} \mathbf{X}_{6D}$ is an invariant, following from the fact of the conservation of the area corresponding to the hyper-elliptical shape. The explicit expressions of beam sigma matrix will be introduced later in Chapter 9.

problem, one would require setting up and solving the Vlasov-Maxwell equations, in which the electromagnetic fields appear in the Vlasov equation as the driving force terms and the perturbed beam charge density appears in the Maxwell equations as the source terms.

Below we write the Vlasov-Maxwell equations to illustrate the general beam-wave interaction. However, in the dissertation, we will not really numerically solve the *full* Vlasov-Maxwell equations. Instead, we invoke the wakefield-impedance approach via two approximations outlined in this section to simplify the formalism. The Maxwell equations, that govern electrodynamics, read

$$\begin{aligned}
\nabla \cdot \mathbf{B} &= 0 \\
\nabla \cdot \mathbf{E} &= 4\pi\rho \\
\nabla \times \mathbf{E} &= -\frac{1}{c}\frac{\partial}{\partial t}\mathbf{B} \\
\nabla \times \mathbf{B} &= \frac{1}{c}\frac{\partial}{\partial t}\mathbf{E} + \frac{4\pi}{c}\mathbf{J}
\end{aligned} \tag{2.70}$$

where ρ and J determine $\mathbf{E}$ and $\mathbf{B}$ through f by

$$\begin{aligned}
\rho &= -e\int d\mathbf{p} f(\mathbf{q},\mathbf{p};t) \\
\mathbf{J} &= -ec\int d\mathbf{p}\beta f(\mathbf{q},\mathbf{p};t)
\end{aligned} \tag{2.71}$$

where $\mathbf{E}$ is the electric field, $\mathbf{B}$ is the magnetic induction[49], ρ is the bunch charge density, and $\mathbf{J}$ is the bunch current density.

In the aspect of beam dynamics, we have already known that the phase space distribution function $f(\mathbf{q},\mathbf{p};s)$ satisfies the Vlasov equation,

$$\frac{\partial f}{\partial s} + \frac{\partial H}{\partial \mathbf{p}}\frac{\partial f}{\partial \mathbf{q}} - \frac{\partial H}{\partial \mathbf{q}}\frac{\partial f}{\partial \mathbf{p}} = 0 \tag{2.72}$$

where $\mathbf{E}$ and $\mathbf{B}$ enter into H through Lorentz force equation $\mathbf{F} = e\left(\mathbf{E} + \frac{\mathbf{v}}{c}\times\mathbf{B}\right)$ (in particular, $\frac{\partial H}{\partial \mathbf{q}}$) and influence f, and $\mathbf{q}$ and $\mathbf{p}$ are the position and momentum vectors.

It should be noted that the Vlasov-Maxwell equations are nonlinear in nature because the time-dependent behavior of f will be modified by its self-generated fields, which in turn evolve as the distribution function f updates. The above Vlasov-Maxwell treatment is known as the kinetic description in plasma physics [86].

The above Vlasov-Maxwell system can be applied to study general beam-wave interaction problems,

[49]Here we do not distinguish the term magnetic induction with the term magnetic field, because the environment we are interested is in the free space.

e.g. plasma physics or accelerator physics. From beam dynamics viewpoint, to a large degree, both realms are quite similar. In general, they can involve nonlinear (single-particle) and collective (multi-particle) effects. However, there is an important difference between them: in plasma physics, the beam self-fields are usually larger than the external applied fields, while in accelerator physics, the beam self-fields are usually much smaller than the external applied fields. This major difference implies that perturbation techniques are applicable to accelerator physics realm with the individual particle *unperturbed* motion being prescribed by external fields (e.g. bending, steering magnets, RF cavities and etc) and the collectively *perturbed* motion being determined by the self-fields [35].

Solving the beam-wave interaction is in general a difficult and challenging problem. There might exist rarely analytical solvable models for a few particular problems. Numerically, a classic approach based on Particle In Cell (PIC) can be employed. It is however reasonable only for small devices or small portion of an accelerator chain such as electron guns, a few RF cavities or klystrons, but it becomes impractical or impossible for accelerators with much larger scales. Another numerical treatment is based on particle tracking simulation. The individual particle equations of motion are advanced once per time step and a simplified form of energy kick due to collective beam-wave interaction is applied. Depending on different physical problems (or, more specifically, different scales of wakefields), this treatment features different convergence requirements to obtain the physically reasonable results. The requirements usually include number of simulation particles, because the number of particles (called macro-particles) used in numerical simulation is usually (much) less[50] than the realistic number of particles in real life. This particle tracking approach is suitable for larger devices or large-scale of accelerator systems in virtue of modern computing technology. In addition, there is an intermediate treatment under certain additional approximations (than PIC or particle tracking), or semi-analytical treatment, to solve problems of this sort, with accurate and efficient quantification. The price to pay is usually the limited information that can be extracted from the semi-analytical treatment. This semi-analytical treatment, relying on the validity of perturbation techniques, can proceed with utilizing wakefield or impedance language. The concept of wakefields or impedances is based on the validity of the perturbation techniques, as would be further clarified by the following two important approximations [35, 36, 133].

Rigid beam approximation At medium or high energies, beam motion is affected little during its passage of an environment. This means that one can calculate the wakefields assuming the beam distribution is rigid or fixed and its motion is ultrarelativistic (i.e. $\beta = (v/c) \to 1, \gamma = \left(1\Big/\sqrt{1-\beta^2}\right) \to \infty$) during the passage[51]. In fact, we only need to calculate the wakefields generated by a "rigid unit of the beam." Wakefield or impedance contributed by a general distribution of a beam can be obtained by superposition of wakefields due to the rigid units. This approximation aims to apply for *source* particles, which generate

[50] Recently with advance of computing technology, it has been possible to perform particle tracking simulation using realistic number of simulation particles in a large-scale accelerator system. See Ref. [144] for example.

[51] In Chapter 3 we would derive a steady-state CSR impedance that is valid at lower energies (while relativistic, i.e. $\beta \to 1, \gamma < \infty$.). However, relaxing this constraint can much more complicate the problem.

the wakefields.

Impulse approximation It deserves to mention here that we do not really care the *instantaneous* electromagnetic (EM) fields self-generated by the beam. What we really care is the *integrated* impulse experienced by the test particle. This approximation states that a wakefield that is only taken care is the wake integrated over a finite distance, e.g. the length of a structure or an element. This approximation is valid for steady-state situation and aims to apply for *test* particles, which receive the impulse (or energy kick) from the source particles. Here we note that in later chapters when discussing transient CSR interaction, the impulse approximation will not be valid.

More detailed introduction of wakefield and impedance will be discussed in Chapter 4.

2.5 Summary

In this chapter we have reviewed several basic ingredients for our subsequent investigation, including the direct consequence of canonical transformation in Hamiltonian mechanics, the symplecticity condition [Eq. (2.11)]. The Liouville theorem is then obtained; it states that in any system governed by a Hamiltonian, the density or the phase-space area surrounding a particular system point must remain *constant*. Originally applied to $6N$-dimensional phase space, the concept of Liouville theorem can be reduced to the situation in which 6-dimensional phase space is sufficient to us, after the binary collision among particles can be negligible. Vlasov equation is then the mathematical formulation in the six-dimensional phase space.

In Sec. 2.2, we derived the accelerator Hamiltonian that will be used in the subsequent discussion. The Hamiltonian takes into account typical linear beamline lattice elements, including drifts, dipoles, quadrupoles and (linearized) RF cavities. Then in Sec. 2.3 we illustrate the single-particle linear optics in a beam transport system and introduced the concept of beam sigma matrix. The latter would be later employed in Chapter 9 when we deal with the transport of magnetized beams.

Section 2.4 discussed two important approximations, rigid beam and impulse approximations, which can greatly simply the general Vlasov-Maxwell system. With the two approximations, the perturbation techniques are applicable to study collective beam dynamics in particle accelerators. Within the regime of applicability of the two approximations, we can simplify the original full Vlasov-Maxwell treatment to Vlasov-wakefield or Vlasov-impedance treatment. The latter should give consistent results to, but is much more efficient than, those by directly solving the full Vlasov-Maxwell system equations. In fact, in the study of collective instabilities in accelerator physics, a first-order perturbation often suffices [35], or at least the perturbation technique is valid at the *onset* of an instability. Here we take a step further, while we will detail the concepts of wakefield and impedance later in Chapter 4: having transitioned from setting up the full Vlasov-Maxwell equations to arguing the validity of the Vlasov-wakefield or Vlasov-impedance system, we now can *separately* study beam dynamics and electrodynamics for the collective instability problem. The

beam dynamics (Chapter 3) study usually focuses on solving the Vlasov equation, provided the wakefield or impedance of a system is given. The electrodynamics part (Chapter 4) involves in solving the Maxwell equations for the EM fields generated by a rigid unit of the beam.

CHAPTER 3
Theoretical Formulation of Microbunching Instability in a Single-Pass System

In this Chapter, we would begin with the qualitative description of microbunching instability (MBI), including its driving sources, mechanisms, and effects. The seeding sources can be from either modulation of photocathode lasers in electron gun injector system or the longitudinal space charge (LSC) induced plasma oscillation upstream the beamline. The main mechanism is found to be driven by coherent synchrotron radiation (CSR), LSC and linac geometric effects, as would be elaborated in Sec. 3.1. The resultant situation of MBI can lead to fine structures developed in the longitudinal beam phase space. These consequences, usually undesired, can degrade the downstream lasing performance for FELs or beam luminosities for colliders (indirectly through poor electron cooling efficiency).

In the same section (Sec. 3.1), we would briefly outline the model assumptions made in the existing theoretical formulations and compare those with our generalized formulation. We note that some of the model assumptions are considered *essential* (or fundamental) when we apply linearization of Vlasov equation, and others are *extendable* once a further understanding or theoretical or computational effort has been made. In this dissertation, we extend some of the existing model assumptions while keeping others but we shall discuss their effects and importance in our consideration. In Sec. 3.2, serving as a building block for subsequent theoretical derivation, we start from the general (nonlinear) form of Vlasov equation, apply the standard perturbation techniques to linearize the equation, and derive the integral equations that govern the microbunching phenomena. In this section, we would also discuss the validity of linearized Vlasov equation, illustrate the microbunching in nonlinear regime, mention briefly the quasi-linear extension for this problem, and finally comment on other approaches, based on eigenvalue equation or dispersion relation, which are often employed to treat microwave instability (MWI) in a storage-ring system. In Sec. 3.3, we write down the explicit equations, in the form of Volterra integral equation, for various types of modulations. Previous results obtained in the existing formulations become special cases of our derived formulations. This section is the first one of the theoretical parts of the main contributions in this dissertation. In Sec. 3.4, we discuss the connection between the developed integral-equation formalism for single-pass (or few-passes) transport systems and dispersion-relation formalism for storage ring systems. A natural damping mechanism, called Landau damping or phase space smearing, would be briefly discussed in Sec. 3.5. Having presented the theoretical formulation, we take a classic case in Sec. 3.6 as the first example, based on the second bunch compressor (BC2) of Linac Coherent Light Source (LCLS) at SLAC, to illustrate typical microbunching gain functions, gain spectra, validity of the linear amplification regime, Landau damping (or phase space smearing), and argument of the coasting-beam approximation. To end this Chapter, we summarize by a table to compare our generalized formulation with the existing theory in Sec. 3.7.

3.1 Introduction and model assumptions

As mentioned in Sec. 1.4, microbunching instability is a single-bunch instability, driven by short-ranged wakefields or high-frequency impedances. The driving sources, or seeds, can stem from initial small density modulations, one of which is usually present in the ripples of photocathode laser electron gun system or can be considered as upstream existing microbunched structure, and then convert to energy modulations due to the short-ranged wakefields or high-frequency impedances[52]. Then, the energy modulations would be transformed back to density counterparts downstream a dispersive region through the momentum compaction R_{56} [see Eq. (2.56)]. The density-energy conversion, if forming a positive feedback, can result in the enhancement of modulation amplitudes. The concept, shown in Fig. 1.8 in Chapter 1, is now illustrated in more detail in Fig. 3.1 (a-g) below.

[52]Before we formally define the wakefield and impedance, at the moment the fact that energy change (or modulation) is related to density modulation can be deducted using dimensional analysis, i.e. $d\mathcal{E}/ds \propto (E_s \cdot dL)/ds \propto v \cdot E_s \propto I_b^{ac} \cdot Z_0^{\parallel}$, where the last relation is based on Ohm's law. The time-dependent (or, ac) component of the beam current is responsible to density modulation.

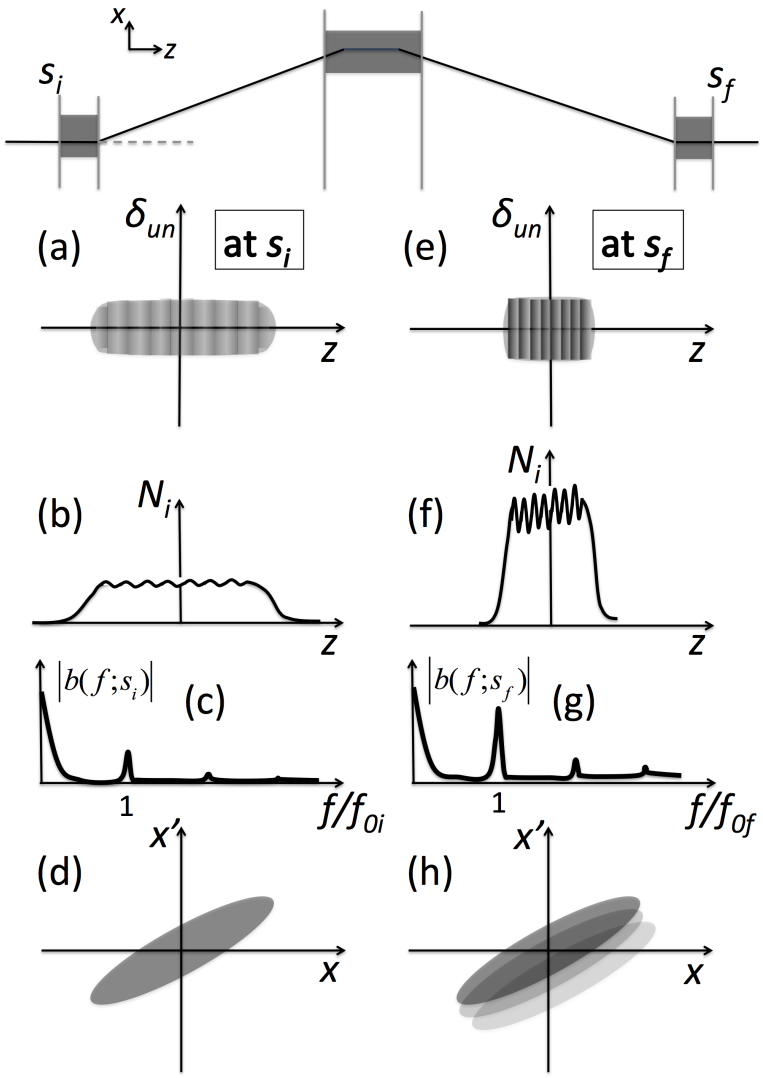

Figure 3.1: Illustration of a typical four-dipole bunch compressor chicane and the associated beam phase space characteristics before (left column) and after (right column) the bunch compression. (a,e) the longitudinal phase space distribution of the coasting beam (correlation between δ and z has been removed); (b,f) the bunch z histogram or current density distribution; (c,g) the Fourier representation of the bunch current distribution, i.e. bunch spectra; (d,h) the transverse phase space distribution of the beam. Collective effect such as CSR can result in microbunching growth, see (b,f) or (c,g), where growth in the modulation structures or spectra can be seen. CSR can also lead to transverse phase space dilution, see (d,h), where different z-slice transverse beam phase space distributions are represented by different gray colors. The mechanism of (b,f) has been illustrated in Fig. 1.8 and will be detailed in this chapter. The mechanism that causes (d,h) is not due to microbunching but will be also introduced later in Chapter 7 (Sec. 7.1.1).

The main driving sources were found to be CSR, LSC and linac geometric effects. CSR, as one of the driving sources, can be generated from electron coherent radiation emission inside a bending dipole at a wavelength range comparable to the bunch length scale or to the order of the ripple density fluctuations atop. In a single chicane, the CSR-induced MBI may not be a serious issue [79, 81]. However in a recirculation arc with many more dipoles, usually several tens, it can be a concern. In addition to CSR, the microbunching instability can also be driven by the LSC field [154]. The LSC effect stems from upstream ripples on top of the longitudinal charge density and can accumulate an amount of energy modulation when the beam traverses a long section of a beamline. It has been shown that this LSC-induced microbunching can lead to a very large overall microbunching gain of a two-stage bunch compressor system such as in LCLS [82] or even larger gain in a transport or recirculation arc with many more dipoles [169, 180]. If a beam experiences acceleration, deceleration or chirping along a section of linac with RF cavities, the periodic structure, in general, features the geometric impedance. The effect of the linac geometric wakefield on microbunching in the downstream accelerator has been also estimated [83] in LCLS.

It deserves here to mention that some distinctive features of the CSR interaction make it more harmful to the transport of high brightness electron beams than other collective interactions. First, the CSR interaction is very sensitive to variation in the bunch longitudinal charge distribution[53]. In particular, perturbation of the longitudinal charge distribution at shorter wavelength causes larger amplitude of CSR overtaking field strength, which can further amplify the perturbation. Second, unlike the usual space charge force from Coulomb interaction amongst particles moving on a straight path, which has diminishing effect at high energy due to the relativistic cancellation of the $\mathbf{E}$ and $\mathbf{B}$ fields in the Lorentz force, for motion on a curved orbit this relativistic cancellation no longer holds. So the CSR force continues to be prominent even at higher energies. Thus, the detrimental effects of CSR and LSC on beam dynamics need to be carefully assessed or circumvented for all the designs of modern electron accelerators. Figure 3.2 shows the comparison of CSR and LSC impedances in a typical spectral range. For shorter wavelengths, the impedances are more prominent. Although LSC impedance has smaller magnitude than that of CSR impedance, LSC-induced MBI can still be more serious, because along a beamline LSC can be ubiquitous and CSR usually occurs within (or near downstream of) dipoles.

In addition, both CSR and LSC can have effects on transverse plane(s). In a transverse plane, because of the dispersive nature of a bending system, the energy change/redistribution due to CSR can be correlated to the transverse coordinates (x or x') through the dispersion functions R_{16} or R_{26}. Since the energy redistribution varies for different slices of particles, such energy variation within a beam bunch can potentially dilute the transverse emittance [see Fig. 3.1 (d) and (h)].

The theoretical formulations of MBI [152, 79, 81, 193] evolve from very simplified to now more com-

[53] In Chapter 4, we can see that (steady-state) CSR wakefield expression is proportional to the derivative of bunch charge distribution, see, e.g. Eq. (4.79).

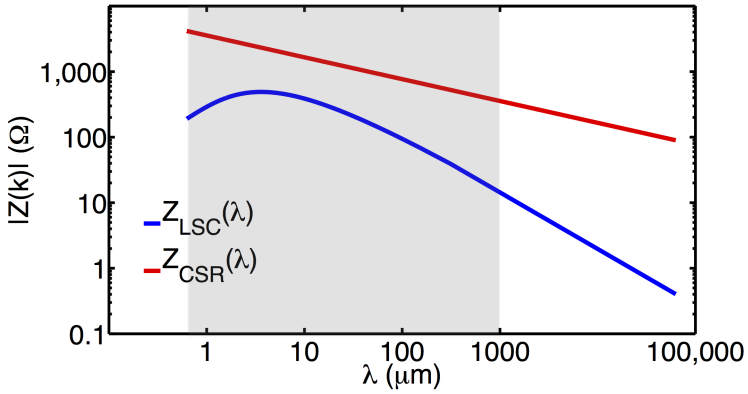

Figure 3.2: Comparison of steady-state CSR and LSC impedances. Here the reference energy $E_0 = 250$MeV and bending radius $\rho = 5$ m is assumed. The analytical expressions we used are Eqs. (4.113) and (4.166). The shaded region, which covers from $\sim 1\mu$m to ~ 1 mm is of our interest. According to Eqs. (4.113) and (4.166), when the beam energy goes higher, the blue curve should decrease while the red curve remains there.

plete models, because there are more and more beam dynamics effects included in the formulations. That is to say, more and more model assumptions are relieved. Among them, we try to divide the model assumptions into two categories; one is considered to be *essential* and the other is *extended*. The first essential assumption is that we have ignored the issue of the maximum attainable microbunching gain during MBI. We note that this is a fundamental limit due to purely relativistic effects [117]. Neglect of this fact can be partially attributed to the formulation of linearized Vlasov equation we employ throughout the analysis and the fact that the wakefield-impedance approach is not fully self-consistent[54]. Another essential model assumption is that the effect of incoherent synchrotron radiation (ISR) is excluded. ISR is not important here because it is considered a relatively slow process in both linac or recirculation machines. This can be also deduced from the accelerator Hamiltonian we constructed in Chapter 2. When the particle emits appreciable radiation, the Hamiltonian must include the dynamic variables representing electromagnetic fields and the corresponding change of symplecticity requirement.

For the extended assumptions, the first one is the coasting beam approximation, which assumes that the density or energy modulations on top of beam (longitudinal) phase space distribution is small compared with the overall unperturbed phase space distribution. This assumption can also be explained as single-frequency approximation and it has greatly simplified the numerical calculation. As the second extendable assumption, when it comes to the onset of MBI, we employ the linearization of Vlasov equation and the MBI amplification gain is linear. The validity of the linear amplification model can be visualized in Fig. 3.3 for an example of LCLS bunch compressor chicane which we will demonstrate in Sec. 3.6. The third assumption

[54]In Ref. [117], without derivation here, we directly quote Eq. (24) of that paper, original derived from a simple chicane model, $g_{\max} \leq \sqrt{1+\gamma^2\theta^2} \sim \gamma\theta$ where γ is the relativistic factor and θ is the bending of a central dipole in the chicane model. We find for the case of LCLS BC2, $\gamma \approx 8884.5$ ($E = 4.54$ GeV), $\theta \approx 1.878°$, and $g_{\max} \approx 290$. Other simulation results show that the gain of LCLS BC2 is much smaller than this number.

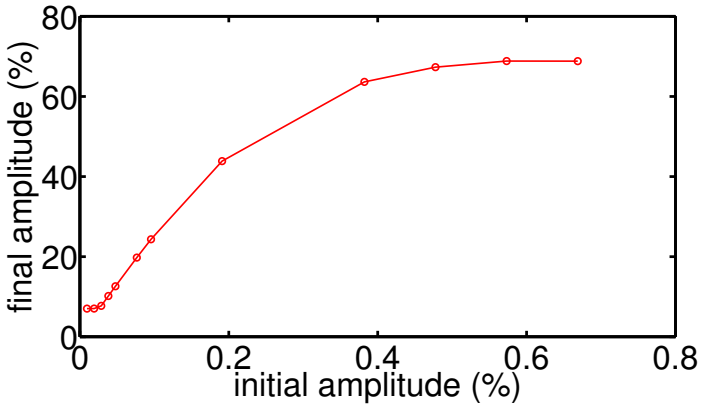

Figure 3.3: Illustration of dependence of MBI on initial modulation amplitudes. The linear amplification regime is valid when the initial amplitude is larger than 0.04% and smaller than 0.2% in this particular case.

is linear transport of a beamline. This assumption has its physical significance because what people mostly care is the core of the beam, in which trajectories of the core particles usually follow a linear relationship in the beam transport system[55]. The fourth assumption, which was assumed in the previous work [79, 81, 193], is transversely uncoupled beam. This natural assumption can arise from the fact that the uncoupled beam, in which the (even) residual coupling between transverse horizontal and vertical coupling is undesired, has long been widely used. Recently in the Jefferson Lab Electron Ion Collider project (JLEIC) at JLab, the circulating cooler ring (CCR) for the electron cooling design has been proposed using magnetized electron beam [46], in order to deliver the ion beam for achieving higher luminosities [1, 2]. The magnetized beam is a special case of a (full) transversely coupled beam. In Chapter 9, we will extend the assumption of originally transverse uncoupled beam to a general case, which allows coupling between transverse degrees of freedom.

Saldin, Schneidmiller, and Yurkov (SSY) [152] first treated the problem of MBI as a klystron-like instability [see Table 1.2 of Chapter 1] and considered the case without bunch compression and assumed high-gain approximation. We consider SSY treatment as 2-D formalism, in which only longitudinal dynamics (z, δ) is properly accounted for[56]. Then, Heifets, Stupakov, and Krinsky (HSK) [79] formally formulated the problem based on Vlasov equation and extended the treatment to include bunch compression as well as finite transverse beam emittance. Applying the standard perturbation techniques to linearize the Vlasov equation and utilizing the method of characteristics, they derived a linear Volterra integral equation for the bunching factor. Through the bunching factor, they can estimate the microbunching gain in a physical system. Almost at the same time, Huang and Kim (HK) [81], by applying the iterative method, analytically obtained an explicit formula that can also be used to estimate the microbunching gain factor. Here we emphasize that both HSK and HK's treatments are considered to be 4-D formalism, since both transverse horizontal and

[55] In recirculation or ERL machines or some specialized beamline designs, sextupole or higher-order magnetic elements are routinely used for beam phase space manipulation, where the nonlinear (curvature) effects are overlooked here.

[56] In Sec. 4-4 of Ref. [152], SSY had discussed the effect of finite transverse beam emittance.

longitudinal dynamics (x, x', z, δ) are properly included. Their applications of both the semi-analytical simulation and analytical formula to LCLS second bunch compressor (BC2) give the overall gain ≤ 2 over a wide spectral range. HK further indicated that the overall gain is contributed mainly by two-stage amplification (or quadratic term of beam current) for high-gain or high-current operation.

Among them, the integral equations derived by HSK and HK were mostly applied to bunch compressor chicanes with only steady-state free-space CSR effect included. In addition, all the above work was assumed constant energy along a beamline. Later, Venturini *et al.* [192] developed a 2-D Vlasov solver, which directly solves the Vlasov equation for only longitudinal phase space distribution function $f(z, \delta; s)$ in a more general nonlinear framework and allows the beam acceleration along a beamline.

In this dissertation, to systematically study the (linear) microbunchig dynamics in a general beamline, we have extended both the theoretical formulation [79, 81] and some relevant physical models to:

(i) include both transverse horizontal and vertical bending;

(ii) allow beam acceleration or deceleration;

(iii) add more relevant collective effects in addition to the steady-state free-space CSR that was considered in Ref. [79, 81, 193], as would be detailed in Chapter 4.

(iv) take into account more aspects of phase space microbunched structures by extending the microbunching gain factor, as a scalar, to microbunching gain matrix;

(v) accommodate the transverse coupling of a beam and/or of a transport line.

To end this section, Table 3.1 and 3.2 summarizes the model assumptions and available impedance models for use in the existing literature and in the dissertation. Explicit expressions of impedance models will be introduced in Chapter 4.

3.2 Linearized Vlasov equation

In this section, we present the general theoretical formulation of the linearized Vlasov analysis of microbunching instability, extended from the work by HSK [79] and HK [81]. Here the notations we used follow more closely the latter[57]. To quantify microbunching in a general beam transport line, we estimate various types of bunching factors (which characterize different modulations in subsets of the 6-D phase space) along the beamline, as would be defined below. Of particular interest can be the density modulation amplitude, or loosely named as bunching factor. The bunching factors at a certain location s are defined as the Fourier transform of the weighted perturbed phase-space distribution function and are complex quantities in general.

[57] In HSK [79], the normalized transverse phase space coordinates are employed. In HK [81], the standard phase space coordinates are used.

Table 3.1: Comparison of the scope of our developed semi-analytical Vlasov solver with the existing ones

	Our Vlasov solver	Heifets *et al.*	Huang and Kim
linear or nonlinear Vlasov model	linear, semi-analytical		linear, analytical
coasting or bunched beam model	coasting beam		
inclusion of transverse emittance effect	yes	yes	yes
inclusion of bending plane	horizontal & vertical	horizontal	horizontal
inclusion of beam acceleration	yes	no	no
inclusion of energy modulation	yes	no	yes, approximate expression
inclusion of transverse-longitudinal modulation (x,z) or ($x\prime$,z)	yes	no	no

Table 3.2: Comparison of collective effects included in the analysis with others

		Our Vlasov solver	Heifets *et al.*/Huang and Kim
1-D CSR	steady-state free-space	yes NUR & UR	yes only UR
	entrance transient free-space	yes UR	no
	exit transient free-space	yes NUR & UR	no
	steady-state with shielding	yes	no
LSC		yes	no
linac geometric effect		yes	no

Note: NUR: Non-UltraRelativistic, UR: UltraRelativistic

Based on the kinetic description, Sec. 2.4, and the standard perturbation techniques, the linearized Vlasov equation can be formulated and rewritten in an integral form in terms of bunching factors. To facilitate simulating recirculation or ERL-based lattices, which usually consist of spreaders and recombiners (in either $x-s$ or $y-s$ plane), we have extended the existing formulation to include both transverse horizontal and vertical bending. Furthermore, the presence of any linac section in a beamline can be taken into account. For the sake of convenience, some equations that were derived in Chapter 2 may repeat here.

We begin by defining the six-dimensional phase-space coordinate as $\hat{\mathbf{X}}(s) = \left(\hat{x}, \hat{x}', \hat{y}, \hat{y}', \hat{z}, \hat{\delta}; s\right)^T$, in which the prime denotes the derivative with respect to s, $\hat{x}$ and $\hat{y}$ are transverse position coordinates with respect to the reference particle under Frenet-Serret coordinate system, $\hat{x}'$ and $\hat{y}'$ are transverse angular divergence, $\hat{z}$ is the local longitudinal particle coordinate relative to the bunch centroid, and $\hat{\delta} = (E - E_r(s))/E_0$ is the energy deviation, where $E_r(s)$ is the beam instantaneous reference energy and $E_0 = E_r(s=0)$. Of our interest, we consider a general case that beam energy can vary along a beamline. The corresponding

Hamiltonian for pure optics linear transport can be expressed as [see Eq. (2.45)]

$$\bar{H}_{\text{linear}}(\hat{\mathbf{X}}) = \frac{1}{2}\left(K_x(s)\hat{x}^2 + \hat{x}'^2 + K_y(s)\hat{y}^2 + \hat{y}'^2 + \kappa(s)\hat{z}^2 - 2\sqrt{\frac{E_0}{E_r(s)}}\frac{\hat{x}\hat{\delta}}{\rho_x(s)} - 2\sqrt{\frac{E_0}{E_r(s)}}\frac{\hat{y}\hat{\delta}}{\rho_y(s)} \right) \tag{3.1}$$

where K_x and K_y are horizontal and vertical focusing functions, respectively. $E_r(s)$ is the reference energy at s, and $E_0 = E_r(s=0)$ is the initial energy. $\rho_x(s)$ and $\rho_y(s)$ are the bending radii of the horizontal and vertical dipoles. $\kappa = \frac{\Delta E_{\text{cav}}\omega_{\text{RF}}}{E_0 L_{\text{cav}} c}\cos\phi_s$ with ΔE_{cav}, ϕ_s, ω_{RF} and L_{cav}, respectively, the energy gain, synchronous phase, the angular RF frequency and the length of the accelerating cavity.

The corresponding single-particle equations of motion are [Eq. (2.44)]

$$\begin{aligned}
\frac{d\hat{x}}{ds} &= \hat{x}' \\
\frac{d\hat{x}'}{ds} &= -K_x(s)\hat{x} + \sqrt{\frac{E_0}{E_r(s)}}\frac{\hat{\delta}}{\rho_x(s)} \\
\frac{d\hat{y}}{ds} &= \hat{y}' \\
\frac{d\hat{y}'}{ds} &= -K_y(s)\hat{y} + \sqrt{\frac{E_0}{E_r(s)}}\frac{\hat{\delta}}{\rho_y(s)} \\
\frac{d\hat{z}}{ds} &= -\sqrt{\frac{E_0}{E_r(s)}}\left(\frac{\hat{x}}{\rho_x(s)} + \frac{\hat{y}}{\rho_y(s)}\right) \\
\frac{d\hat{\delta}}{ds} &= -\kappa(s)\hat{z}
\end{aligned} \tag{3.2}$$

We note that the above equations of motion assume the rate of energy gain or loss is slow, $E_r^{-1}dE_r/ds \ll 1$, i.e. adiabatic acceleration (or, deceleration)[58].

The general solution to Eq. (3.2) can be expressed in terms of six-by-six transport matrix as

$$\hat{\mathbf{X}}(s) = \hat{\mathbf{R}}(\tau \to s)\hat{\mathbf{X}}(\tau) = \hat{\mathbf{R}}(s)\hat{\mathbf{X}}(0) \tag{3.3}$$

where $\hat{\mathbf{R}}(0 \to s) \equiv \hat{\mathbf{R}}(s)$. Here only linear elements are taken into account; effects of nonlinear elements such as sextupoles are excluded from the current analysis. When a beam transport system is nonlinear, i.e. contain higher order terms, Eq. (3.3) should be expressed in a more general form,

$$\hat{\mathbf{X}}(s) = \hat{\mathcal{M}}(\tau \to s) \circ \hat{\mathbf{X}}(\tau) = \hat{\mathcal{M}}(s) \circ \hat{\mathbf{X}}(0) \tag{3.4}$$

[58] in general, the constraint of adiabatic acceleration can be discarded if we use p_x and p_y instead of x' and y' in our formulation. The reasons we retain x' and y' here are: (1) the primed coordinates are more compatible to the "TRANSPORT variables" [149, 29], in which `elegant` follows, and our Vlasov solver relies on the inputs/outputs from `elegant`; (2) so far the formulation works well with particle tracking simulation results, e.g. see Fig. 5.18.

where $\hat{\mathcal{M}}$ is a general map and $\circ$ represents the composition operator [16].

We have summarized the single-particle dynamics, the pure optics part, in the above. Below we will include collective effects into the analysis. As outlined in the previous chapter, the collective effect analysis involves multi-particle beam dynamics and electrodynamics parts. In the remaining of this chapter we focus on beam dynamics part and leave the detailed description of electrodynamics (i.e. wakefields and impedances) in the next chapter.

For a collection of particles, the phase-space distribution function $f\left(\hat{\mathbf{X}}; s\right)$ is often employed to describe the beam behavior. If the binary collision between particles is ignored, the evolution can be formulated by Vlasov equation in six-dimensional phase space coordinate system [see also Eq. (2.18)],

$$\frac{\partial f}{\partial s} + \left(\frac{\partial f}{\partial \hat{\mathbf{X}}}\right)^T \mathbf{S} \frac{\partial H}{\partial \hat{\mathbf{X}}} = 0 \tag{3.5}$$

where we have rewritten Eq. (2.18) in a more compact form and $\mathbf{S}$ is the unit symplectic matrix defined in Eq. (2.4) with $N = 3$. The (total) system Hamiltonian is generally written as $H = \bar{H} + H_1$ where the unperturbed Hamiltonian $\bar{H}$ is the pure-optics part (i.e. in the absence of beam self-fields). Without loss of generality, $\bar{H}$ can be attributed to the linear optics and the remaining nonlinear part, i.e. $\bar{H} = \bar{H}_{\text{linear}} + \bar{H}_{\text{nonlinear}}$. H_1 accounts for the collective interactions in the beam.

For pure optics case ($H_1 = 0$), the unperturbed or equilibrium solution $f(\mathbf{X}; s)$ can be totally determined by its initial condition via Eq. (3.4), i.e.

$$f\left(\hat{\mathbf{X}}(s); s\right) = \bar{f}\left(\hat{\mathbf{X}}(s); s\right) = \bar{f}\left(\hat{\mathcal{M}}^{-1} \circ \hat{\mathbf{X}}(s); 0\right) = \bar{f}\left(\hat{\mathbf{X}}(0); 0\right) \equiv \bar{f}_0(\hat{\mathbf{X}}_0) \tag{3.6}$$

in which for the special case of only linear beam transport $\bar{H} = \bar{H}_{\text{linear}}$, from Eq. (3.3),

$$\bar{f}\left(\hat{\mathcal{M}}^{-1} \circ \hat{\mathbf{X}}(s); 0\right) = \bar{f}\left(\hat{\mathbf{R}}^{-1}(s)\hat{\mathbf{X}}(s); 0\right) \tag{3.7}$$

This approach to solving this first-order partial differential equation is known as the method of characteristics [9].

To proceed, if we are interested in the onset of beam instability, we can assume, to first order, $f = \bar{f} + f_1$, where $f_1 \ll \bar{f}$. The perturbative part f_1 can look like Fig. 3.1(a) or (e) when it is projected onto the longitudinal phase space. Further projection on z will result in Fig. 3.1(b) or (f), i.e. the bunch current density or z histogram. For such microbunched or fine structure, it is natural to quantify by Fourier

transforming the bunch density distribution. To be more specific, we define

$$b(k_z;s)=\frac{1}{N}\int d\hat{\mathbf{X}}e^{-ik_z\hat{z}_s}f_1(\hat{\mathbf{X}};s) \tag{3.8}$$

as the density modulation, or bunching factor [59], where $k_z=2\pi/\lambda$ is the modulation wavenumber and λ the corresponding wavelength. The subscript s of $\hat{z}_s$ is used to denote the coordinate measured at s.

Then we substitute $f=\bar{f}+f_1$ into Eq. (3.5) and retain the terms up to first order. We have the equations for zeroth order,

$$\frac{\partial\bar{f}}{\partial s}+\left(\frac{\partial\bar{f}}{\partial\hat{\mathbf{X}}}\right)^T\mathbf{S}\frac{\partial\bar{H}}{\partial\hat{\mathbf{X}}}=0 \tag{3.9}$$

and, for the first order, i.e. the linearized Vlasov equation,

$$\frac{\partial f_1}{\partial s}+\left(\frac{\partial f_1}{\partial\hat{\mathbf{X}}}\right)^T\mathbf{S}\frac{\partial\bar{H}}{\partial\hat{\mathbf{X}}}+\left(\frac{\partial\bar{f}}{\partial\hat{\mathbf{X}}}\right)^T\mathbf{S}\frac{\partial H_1}{\partial\hat{\mathbf{X}}}=0 \tag{3.10}$$

In Eq. (3.10) the term $\partial H_1\Big/\partial\hat{\mathbf{X}}$ is of first order and consists of f_1 [see below Eqs. (3.11) to (3.8)]. The term $\left(\frac{\partial f_1}{\partial\hat{\mathbf{X}}}\right)^T\mathbf{S}\frac{\partial H_1}{\partial\hat{\mathbf{X}}}$, considered to be second order, has been neglected[60]. From Hamilton's equation of motion, for pure optics part, we have $\partial\bar{H}\Big/\partial\hat{\mathbf{X}}=-\mathbf{S}\Big(d\hat{\mathbf{X}}\Big/ds\Big)_0$ where $\Big(d\hat{\mathbf{X}}\Big/ds\Big)_0$ has be obtained from Eq. (3.2) and for the perturbed part (by collective effects), we have

$$\frac{\partial H_1}{\partial\hat{\mathbf{X}}}=-\mathbf{S}\left(\frac{d\hat{\mathbf{X}}}{ds}\right)_1 \tag{3.11}$$

More explicit expressions of $\Big(d\hat{\mathbf{X}}\Big/ds\Big)_1$ can be written as follows[61]

$$\left(\frac{d\hat{\mathbf{X}}}{ds}\right)_1=\frac{d}{ds}\begin{bmatrix}\hat{x}\\ \hat{x}'\\ \hat{z}\\ \hat{\delta}\end{bmatrix}_1=\frac{-Nr_e}{\gamma}\int_{-\infty}^{\infty}d\hat{z}'\lambda(\hat{z}')\begin{bmatrix}0\\ \hat{x}W_1^{\perp}(\hat{z}-\hat{z}')\\ 0\\ W_0^{\parallel}(\hat{z}-\hat{z}')\end{bmatrix}=\frac{-Nr_e}{\gamma}\int_{-\infty}^{\infty}\frac{dk_1}{2\pi}\begin{bmatrix}0\\ \hat{x}Z_1^{\perp}(k_1)\\ 0\\ Z_0^{\parallel}(k_1)\end{bmatrix}b(k_1;s)e^{ik_1\hat{z}} \tag{3.12}$$

[59] This definition assumes smooth phase space distribution, i.e. absence of granularity out of elementary charge. If shot noise is to be taken into account, the expression $b(k_z;s)=N^{-1}\sum_{j=1}^{N}e^{-ik_z\hat{z}_{s,j}}$ should be employed.

[60] This term can become important when long-term evolution is considered [207]. Here we are interested in single-pass or few-passes beam transport and small phase-space perturbation, so the contribution of this term should be negligibly small and the linearized (or first-order) Vlasov equation, i.e. Eq. (3.10), can suffice.

[61] For the moment we have in mind that the definitions of wakefields ($W_0^{\parallel}$ and $W_1^{\perp}$) and impedances ($Z_0^{\parallel}$ and $Z_1^{\perp}$) will be introduced later in Chapter 4. They are Fourier transform pairs, see Eqs. (4.9) and (4.10).

where the equations for y and y' are similar to x and x' and not shown here. In Eq. (3.12), r_e is the classical electron radius, N is the total number of particles in a beam bunch, $\gamma \equiv E/m_e c^2$ is the electron relativistic factor, λ is the line density, $b(k)$ is the bunching factor, defined in Eq. (3.8), as the Fourier transform of the perturbed phase space distribution function, $W_0^{\parallel}, W_1^{\perp}$ and $Z_0^{\parallel}, Z_1^{\perp}$ are the longitudinal and transverse wakefields and impedances along a beamline. The explicit expressions of $W_0^{\parallel}, W_1^{\perp}$ and $Z_0^{\parallel}, Z_1^{\perp}$ will be given, albeit they will be introduced later in Chapter 4.

Of our interest, we restrict the case to the collective energy kick only in the longitudinal direction. From Eqs. (3.11) and (3.12), $\partial H_1/\partial \hat{z} = -d\hat{\delta}\Big/ds$. The energy kick due to collective force at $s = \tau$ can be explicitly expressed as

$$\frac{\partial H_1}{\partial \hat{z}} = \frac{d\hat{\delta}}{d\tau} = -\frac{Nr_e}{\gamma}\int \frac{d\kappa}{2\pi} Z_0^{\parallel}(\kappa;\tau) b(\kappa;\tau) e^{i\kappa\hat{z}_\tau} \tag{3.13}$$

Equation (3.10) becomes

$$\frac{\partial f_1}{\partial s} + \left(\frac{\partial f_1}{\partial \hat{\mathbf{X}}}\right)^T \mathbf{S}\frac{\partial \bar{H}}{\partial \hat{\mathbf{X}}} - \frac{\partial H_1}{\partial z}\frac{\partial \bar{f}}{\partial \delta} = 0 \tag{3.14}$$

It deserves the discussion here regarding an assumption made behind Eq. (3.8). In this expression the coasting beam approximation has been implicitly made, i.e. we have presumed $\int d\hat{\mathbf{X}} e^{-ik_z z_s}\bar{f}(\hat{\mathbf{X}};s) = 0$ for non-vanishing k_z. In many situations, where the microbunched structure atop the unperturbed distribution is small compared with the full bunch duration, Eq. (3.8) can properly characterize the microbunching. The coasting beam approximation here is to be compared with the bunched-beam model. In that case when a microbunched structure is comparable to the overall bunch duration, the spectra of the bulk- and micro-bunches are no longer well separated and can interfere. We illustrate the situation in Fig. 3.4. Then coupling between different spatial frequencies k_z via the finite-bunch length comes into play. When it comes to critical bunch compression or parasitic compression [105], the bunched-beam model has to be considered.

Having integrated Eq. (3.14) over s along the unperturbed (pure-optics) phase space trajectory and taking advantage of the total derivative, $\partial f_1/\partial s + \left(\partial f_1\Big/\partial \hat{\mathbf{X}}\right)^T \mathbf{S}\left(\partial \bar{H}\Big/\partial \hat{\mathbf{X}}\right) = df_1/ds$, we have the perturbed phase space distribution function *after* the energy kick,

$$f_1(\hat{\mathbf{X}}_s) \simeq f_1^{(0)}(\hat{\mathbf{X}}_0) - \int_0^s d\tau \frac{\partial \bar{f}(\hat{\mathbf{X}}_\tau)}{\partial \hat{\delta}}\frac{d\hat{\delta}}{d\tau} \tag{3.15}$$

where $f_1^{(0)}(\hat{\mathbf{X}}_0)$, being the small perturbed phase space distribution function, is evaluated *before* the energy kick. This expression, considered as a form of the linearized Vlasov equation [81], would be used below and referred as one of the fundamental relations.

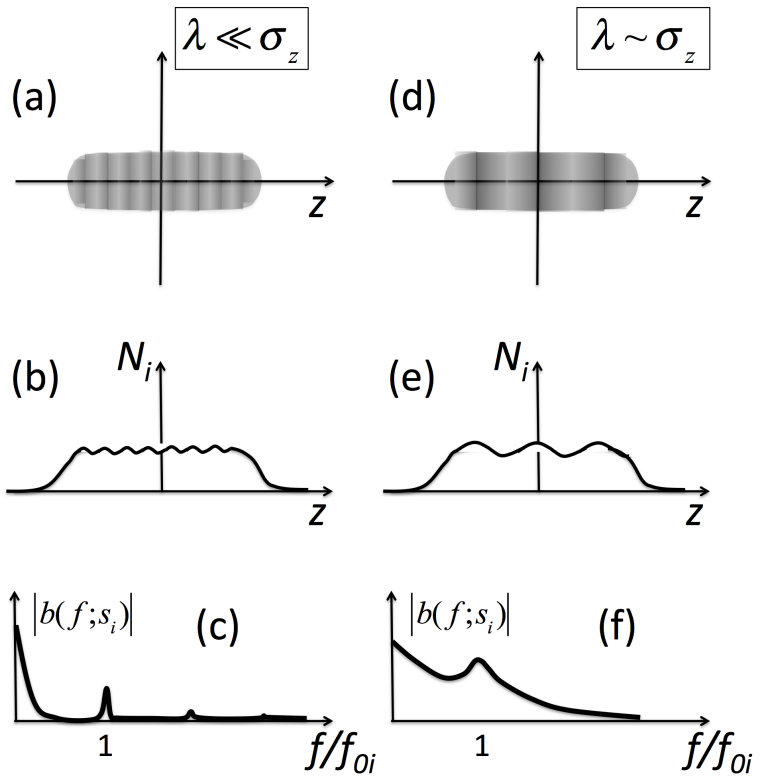

Figure 3.4: Illustration of differences of density modulations between coasting beam (left column) and bunched beam (right column) models. (a,d) the longitudinal phase space distribution; (b,e) the bunch z histogram or current density distribution; (c,f) the Fourier representation of the bunch current distribution, i.e. bunch spectrum.

To proceed to integrate the second term on the right-hand side (RHS) of Eq. (3.15), we first need to specify the initial unperturbed electron phase space distribution. We assume the Gaussian distribution in the six-dimensional phase space coordinate, i.e.

$$\bar{f}_0(\hat{\mathbf{X}}_0) = \bar{f}_0(\mathbf{X}_0) = \frac{N}{(2\pi)^3\sqrt{\det\Sigma_0}}\exp\left\{\frac{-1}{2}\mathbf{X}_0^T\Sigma_0^{-1}\mathbf{X}_0\right\} \tag{3.16}$$

where we remind that the overline atop f_0 is used to denote the unperturbed distribution, the subscript "0" stands for the quantity evaluated at $s = 0$. For an uncoupled beam, the beam distribution can be parameterized by Twiss (or Courant-Snyder) parameters, as illustrated in Fig. 2.3 [see also Eq. (2.68)]. The invariant for (x, x') is

$$\mathbf{X}_{2D,0}^T\Sigma_{2D}^{-1}\mathbf{X}_{2D,0} = \frac{x_0^2 + (\beta_{x0}x_0{}' + \alpha_{x0}x_0)^2}{\epsilon_{x0}\beta_{x0}} \tag{3.17}$$

with $\det(\Sigma_{2D}) = \epsilon_{x0}^2$. Again we remind that the emittance ϵ_{x0} is an invariant and represents the phase space area in x dimension. Note that $\hat{\mathbf{X}}(0) = \mathbf{X}(0)$. The invariant for (y, y') is similar and thus not shown here.

Using Eq. (2.68) with $\langle zz\rangle = \sigma_z^2, \langle\delta\delta\rangle = \sigma_\delta^2$, Eq. (3.16) becomes

$$\bar{f}_0(\mathbf{X}_0) = \frac{N}{(2\pi)^3\epsilon_{x0}\epsilon_{y0}\sigma_{z0}\sigma_{\delta 0}} e^{-\frac{x_0^2+(\beta_{x0}x_0'+\alpha_{x0}x_0)^2}{2\epsilon_{x0}\beta_{x0}} - \frac{\hat{y}_0^2+(\beta_{y0}y_0'+\alpha_{y0}y_0)^2}{2\epsilon_{y0}\beta_{y0}} - \frac{z_0^2}{2\sigma_{z0}^2} - \frac{\left(\delta_0^2-2hz_0\delta_0\right)}{2\sigma_{\delta 0}^2}} \tag{3.18}$$

Here ϵ_{x0} and ϵ_{y0} are the rms horizontal and vertical geometric emittances, respectively. α_{x0}, α_{y0}, β_{x0} and β_{y0} are the initial beam Twiss (or Courant-Snyder) parameters, σ_{z0} for the rms bunch length, $\sigma_{\delta 0}$ for the rms uncorrelated (or, slice) relative energy spread, and $h = \langle z\delta\rangle/\sigma_{z0}^2$ for the linear chirp parameter.

When the coasting beam approximation is made, Eq. (3.18) becomes

$$\bar{f}_0(\mathbf{X}_0) \simeq \frac{n_0}{(2\pi)^3\epsilon_{x0}\epsilon_{y0}\sigma_{\delta 0}} e^{-\frac{x_0^2+(\beta_{x0}x_0'+\alpha_{x0}x_0)^2}{2\epsilon_{x0}\beta_{x0}} - \frac{y_0^2+(\beta_{y0}y_0'+\alpha_{y0}y_0)^2}{2\epsilon_{y0}\beta_{y0}} - \frac{(\delta_0-hz_0)^2}{2\sigma_{\delta 0}^2}} \tag{3.19}$$

where $n_0 \simeq N/\sigma_{z0}$ is the particle number density of the bunch.

MBI is a phenomenon characterizing fine structure in the (longitudinal) phase space. Thus, naturally microbunching can be quantified by the Fourier transformation (of z coordinate) of the perturbed phase space distribution function as the density modulation (or, bunching factor), i.e. Eq. (3.8). As we have already derived, the evolution of the phase space distribution is governed by Eq. (3.15) to the first order. The ultimate goal in this and next sections is to derive the resultant equations in terms of the density modulation (and, moreover, other various modulations).

In this section, we have already formulated the initial beam phase space distribution starting from beam sigma matrix in general to utilizing Twiss (or Courant-Snyder) parameterization for transversely uncoupled beams in particular. We also have obtained the linearized Vlasov equation, Eqs. (3.14) and/or (3.15), and written down the explicit expression of (energy) kick due to collective effects, where they can be either transverse or longitudinal, Eq. (3.12). Notice that we still left the explicit expressions of wakefields and impedances not determined, which would be discussed in Chapter 4. The method of characteristics relies on the connection of $\hat{\mathbf{X}}(s)$ or $\hat{\mathbf{X}}(\tau)$ to its initial values, as formulated in Eq. (3.3) for linear beam transport and Eq. (3.4) for a general nonlinear transport. In the next section, we would apply these fundamental relations to derive a set of integral equations in terms of various types of modulations to characterize the evolution of microbunching along a beamline.

3.3 Volterra integral equations

In this section, we would first quantify *three* different types of initial modulations, including the density modulation [in z], the energy modulation [in (z,δ)], and the transverse-longitudinal modulation [in (x,z),

(x', z), (y, z), and (y', z)], respectively

$$b_0(k_0; 0) \equiv \frac{n_0}{N} \int dz_0 \left(\frac{\Delta n(z_0)}{n_0} \right) e^{-ik_0 z_0} \tag{3.20}$$

where n_0 is the line density,

$$p_0(k_0; 0) \equiv \frac{n_0}{N} \int dz_0 \ \Delta\delta(z_0) e^{-ik_0 z_0} \tag{3.21}$$

with $\delta = (E - E_0)/E_0$, and

$$a_{x0}(k_0; 0) \equiv \frac{n_0}{N} \int dz_0 \ \Delta x_0(z_0) e^{-ik_0 z_0} \tag{3.22}$$

$$a_{x'0}(k_0; 0) \equiv \frac{n_0}{N} \int dz_0 \ \Delta x'_0(z_0) e^{-ik_0 z_0} \tag{3.23}$$

$$a_{y0}(k_0; 0) \equiv \frac{n_0}{N} \int dz_0 \ \Delta y_0(z_0) e^{-ik_0 z_0} \tag{3.24}$$

$$a_{y'0}(k_0; 0) \equiv \frac{n_0}{N} \int dz_0 \ \Delta y'_0(z_0) e^{-ik_0 z_0} \tag{3.25}$$

It can be seen that Eqs. (3.20) to (3.25) are all quantities in Fourier-transformed (frequency- or k-) domain. Physically they characterize the modulation in some subsets of six-dimensional phase space. Figure 3.5 below illustrates these types of modulations, where Fig. 3.5(a) is the bunching factor typically referred in the literature.

Then, we would apply the fundamental relations derived in Sec. 3.2, Eq. (3.15), to formulate the equations of motion (i.e. evolutions) for these modulations. Note that in the existing formulation [81, 193], only the case with initial density modulation was considered. In Ref. [81], HK, in addition to density modulation, outlined the importance of microbunching due to initial energy modulation. There are two reasons that motivate us for extension of the previous work.

First, including all the three types of modulations are found to result in more serious microbunching[62] along a beamline or at the end of a beamline [175, 185] than only taking density modulation into account. This can be expected because different/additional phase space modulations can come into play and result in more serious microbunching. In most (previous) literature the microbunching analysis usually takes density modulation into consideration. From an integrated viewpoint, the resultant microbunching may be overlooked because of neglecting other possible contributing sources. When treating a subset of a beamline, to quantify microbunching we find the existing theoretical formulation [79, 81] can be sufficient and we intend to generalize the concept of microbunching, following similar spirits, to include other phase

[62] One may restrict the concept of microbunching to the density modulation in z, or, here we consider the modulations in (z, δ), (x, z) and (x', z) as another aspects of microbunching. In the following discussions, we would specify the type of modulation in a superscript notation once there is a need to distinguish them. When there is no confusion, in which only density modulation is considered, we ignore the superscript.

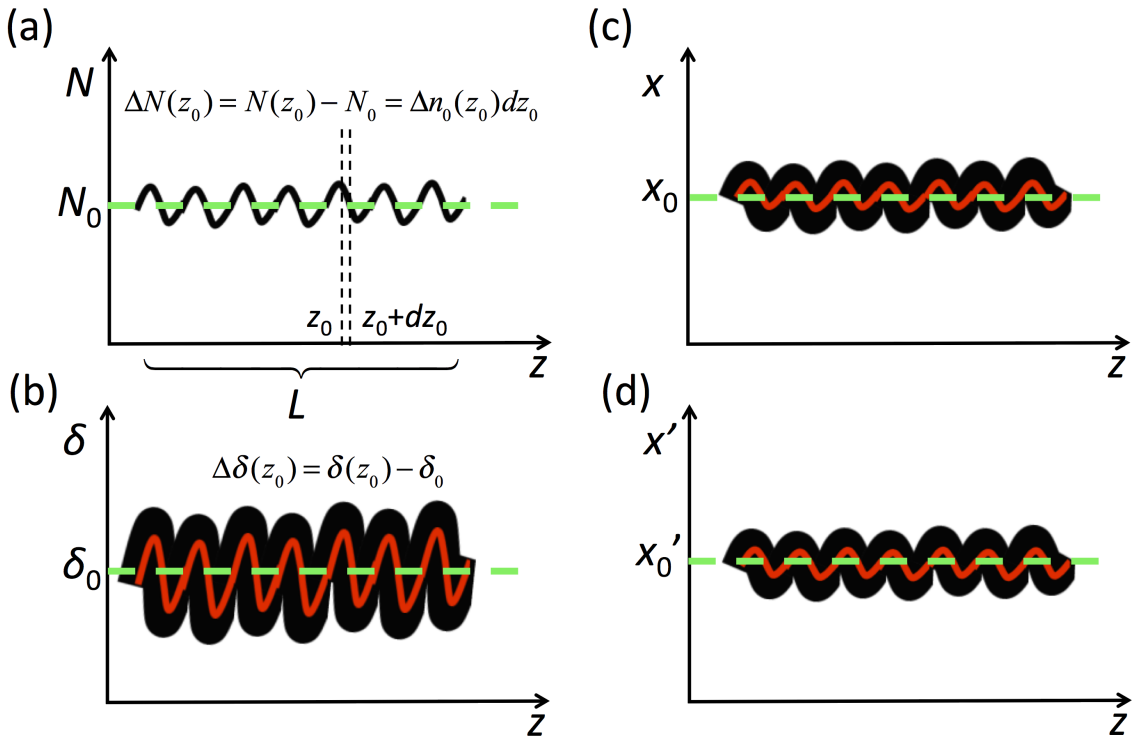

Figure 3.5: Illustration of various microbunched modulations. (a) density modulation; (b) energy modulation; (c) transverse-longitudinal (x, z) modulation, and (d) transverse-longitudinal (x', z) modulation. The green dashed line represents the (averaged) constant offset and the red solid line indicates the (averaged) sinusoidal modulation.

space modulations of the beam in broader aspects[63].

Second, for multi-pass recirculation or a long beamline, people usually estimate the overall microbunching along a beamline based on the intuitive argument: one first estimates the effect of (only density) microbunching in separate (sub-)beamline sections, and then multiplies those contributions, i.e.

$$G_{\text{total}} = \prod_{q=1}^{N} G_q = G_1 G_2 G_3 ... G_N \tag{3.26}$$

where the microbunching gain factor $G_q = |b_{q,f}/b_{q,i}|$, $b_{q,i}$ is the initial density modulation [defined in Eq. (3.20)] in q-th sub-beamline section and $b_{q,f}$ is the final density modulation evaluated by Eq. (3.8) at the exit of q-th section. The concept is illustrated in top row of Fig. 3.6. Equation (3.26) is typically applied in circuit electronics for cascaded amplifiers. The successive multiplication gives the resultant/total microbunching gain $G_{\text{total}} = |b_{N,f}/b_{1,i}|$. There is however a subtle assumption here: this quantification is true when there is only density modulation come into play. If there are other contributing sources, the expression may no

[63] In other words, if one still considers the analysis from the very beginning of a beamline, the start-to-end situation, *and*, there is *only* density modulation present in the beam, the original theoretical formulation should suffice. We note that when a beamline is long, start-to-end analysis or simulation takes much more computation time and effort.

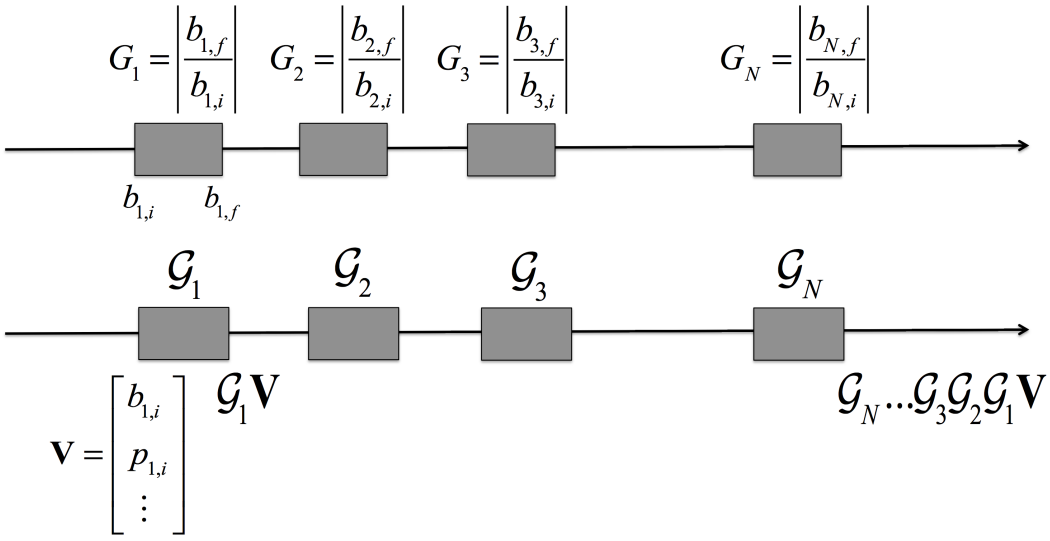

Figure 3.6: Illustration of concepts of scalar gain multiplication (top) and gain matrix (bottom).

longer be valid.

In Ref. [175], we found the intuitive argument of quantifying microbunching, by successive scalar multiplication of microbunching gains of sub-beamline sections, may result in *underestimate* of the overall effect. A natural idea is to extend the scalar (microbunching) gain to include combinations of various aspects of modulations, as defined in Eqs. (3.20) to (3.25). More thorough analyses based on concatenation of *gain matrices* (see bottom row of Fig. 3.6) which aimed to combine both density and energy modulations for a general beamline was presented [175]. Yet, quantification only focused on characterizing longitudinal phase space is still found to be far from complete; microbunching structures residing in (x, z) and (x', z) [and/or (y, z) and (y', z)] was observed in particle tracking simulation [175]. Inclusion of such cross-plane transverse-longitudinal microbunching structures in the Vlasov analysis shall be a crucial step to systematically characterize microbunching for a beamline in view of concatenating individual beamline segments. In this chapter we can only touch a bit the analysis of more aspects of microbunching than density modulation. More complete investigation will be discussed in Chapter 8.

To proceed, we quote the formal definition of density modulation, given in Eq. (3.8)

$$b(k_z; s) = \frac{1}{N} \int d\hat{\mathbf{X}} e^{-ik_z z_s} f_1(\hat{\mathbf{X}}; s) \tag{3.27}$$

In addition, microbunching can arise from or result in energy modulation, which is quantified by the Fourier transformation of the energy-modulated phase space distribution,

$$p(k_z; s) = \frac{1}{N} \int d\hat{\mathbf{X}} e^{-ik_z \hat{z}_s} \left(\hat{\delta}_s - h\hat{z}_s\right) f_1(\hat{\mathbf{X}}; s) \tag{3.28}$$

Similarly, in the transverse-longitudinal cross plane, there are

$$a_x(k_z;s) = \frac{1}{N}\int d\hat{\mathbf{X}}\ \ (\hat{x}_s)\, f_1(\hat{\mathbf{X}};s)e^{-ik_z(s)\hat{z}_s} \tag{3.29}$$

$$a_{x'}(k_z;s) = \frac{1}{N}\int d\hat{\mathbf{X}}\ \ (\hat{x}'_s)\, f_1(\hat{\mathbf{X}};s)e^{-ik_z(s)\hat{z}_s} \tag{3.30}$$

$$a_y(k_z;s) = \frac{1}{N}\int d\hat{\mathbf{X}}\ \ (\hat{y}_s)\, f_1(\hat{\mathbf{X}};s)e^{-ik_z(s)\hat{z}_s} \tag{3.31}$$

$$a_{y'}(k_z;s) = \frac{1}{N}\int d\hat{\mathbf{X}}\ \ (\hat{y}'_s)\, f_1(\hat{\mathbf{X}};s)e^{-ik_z(s)\hat{z}_s} \tag{3.32}$$

Note that, in Eqs. (3.27) to (3.32), the phase space variables are evaluated at s, which we denote in the subscript. The phase space microbunched modulation structures are illustrated in Fig. 3.5.

Up to now we have prepared all the necessary information. Our goal is to derive the governing equations for $b(k_z;s)$, $p(k_z;s)$, and the remaining quantities in Eqs. (3.27) to (3.32). By multiplying on both sides of Eq. (3.15) with $N^{-1}\exp(-ik_z(s)\hat{z}_s)$, and integrating over the six-dimensional phase space $\mathbf{X}$, we have

$$\frac{1}{N}\int d\hat{\mathbf{X}}_s f_1(\hat{\mathbf{X}};s)e^{-ik_z(s)\hat{z}_s(\hat{\mathbf{X}}_s)} = \frac{1}{N}\int d\hat{\mathbf{X}}_0 f_1^{(0)}(\hat{\mathbf{X}}_0)e^{-ik_z(s)\hat{z}_s(\hat{\mathbf{X}}_0)} - \frac{1}{N}\int_0^s d\tau\int d\hat{\mathbf{X}}_\tau \frac{\partial \bar{f}(\hat{\mathbf{X}}_\tau)}{\partial\hat{\delta}_\tau}\frac{d\hat{\delta}_\tau}{d\tau}e^{-ik_z(s)\hat{z}_s(\hat{\mathbf{X}}_\tau)} \tag{3.33}$$

Integrating $\hat{\delta}_\tau$ by parts and inserting Eq. (3.13) into the above expression, we have

$$\begin{aligned} b(k_z;s) = {} & \frac{1}{N}\int d\hat{\mathbf{X}}_0 f_1^{(0)}(\hat{\mathbf{X}}_0)e^{-ik_z(s)\hat{z}_s(\hat{\mathbf{X}}_0)} \\ & + \frac{1}{N}\int_0^s d\tau ik_z(s)\frac{I_b(\tau)}{I_A}\hat{R}_{56}(\tau\to s)\int\frac{d\kappa}{2\pi}Z_0^{\parallel}(\kappa;\tau)b(\kappa;\tau)\int d\hat{\mathbf{X}}_\tau\frac{1}{\gamma_\tau}\bar{f}(\hat{\mathbf{X}}_\tau)e^{-ik_z\hat{z}_s(\hat{\mathbf{X}}_\tau)+i\kappa\hat{z}_\tau} \end{aligned} \tag{3.34}$$

where $I_b(\tau) = ecn_0/C(\tau)$ is the instantaneous bunch current at $s=\tau$ with $C(\tau) = \left[\hat{R}_{55}(\tau) - h\hat{R}_{56}(\tau)\right]^{-1}$ the bunch compression factor, and $I_A \equiv mc^3/e \approx 17045$ A is the Alfven current[64]. $\hat{R}_{56}(\tau\to s) = \left[\hat{\mathbf{R}}(s)\hat{\mathbf{R}}^{-1}(\tau)\right]_{56}$ is the relative momentum compaction function from τ to s. The first term on the right side (RHS) of Eq. (3.34) is evaluated by Eq. (3.27) using $f_1^{(0)}(\hat{\mathbf{X}}_0)$ [explicit forms of $f_1^{(0)}(\hat{\mathbf{X}}_0)$ would be specified later in Eqs. (3.45) to (3.50)]. This term corresponds to the bunching evolution in the absence of collective effects. This implies that microbunching can vary/evolve even in the pure-optics transport. Specifically, there is no amplification of the pure-optics bunching evolution, i.e. the first term in Eq. (3.34) will not grow. If there is absence of any smearing effect, the bunching factor remains the same; if there exists a dispersive region in a transport line, the bunching factor may decrease but never disappear. We want to work out

[64] It is interesting to say a word about physical picture of Alfven current [6]. Imagine a stream of electrons, in which they are made of hard spheres (with radius r_e), is closely packed, e.g. exactly touched each by each, and is traveling with speed of light. After a time t at some location s, the electron stream passes through with a total charge of $Q \sim ect/r_e = tI_A$, then $I_A = mc^3/e$. The classical electron radius $r_e = e^2/m_e c^2$.

the first and second terms on RHS of Eq. (3.35). First, for the second term, it can be done by tracing the relevant phase space coordinates at $s = \tau$ back to the initial location ($s = 0$) with the help of Eqs. (3.3) and (3.7). z_s in the exponent of the second term on RHS of Eq. (3.34) can be expressed as

$$\hat{z}_s = \sum_{j=1}^{6} \hat{R}_{5j}(\tau \to s)\hat{\mathbf{X}}_\tau^j = \sum_{j=1}^{6} \hat{R}_{5j}(s)\mathbf{X}_0^j \tag{3.35}$$

where the superscript j indicates the j-th component of the phase space coordinate vector $\mathbf{X}$. Similarly, for z_τ, we have

$$\hat{z}_\tau = \sum_{j=1}^{6} \hat{R}_{5j}(\tau)\mathbf{X}_0^j \tag{3.36}$$

Up to now, we are left with the integral $\int d\hat{\mathbf{X}}_\tau \bar{f}(\hat{\mathbf{X}}_\tau) e^{-ik_z\hat{z}_s(\hat{\mathbf{X}}_\tau)+i\kappa\hat{z}_\tau}$. To proceed, we make change of variables from $\hat{\mathbf{X}}_\tau$ to $\hat{\mathbf{X}}_0$ (also γ_τ to γ_0) using Eq. (3.7). Then

$$\int d\hat{\mathbf{X}}_\tau \bar{f}(\hat{\mathbf{X}}_\tau) e^{-ik_z\hat{z}_s(\hat{\mathbf{X}}_\tau)+i\kappa\hat{z}_\tau} = \int d\mathbf{X}_0 \bar{f}(\mathbf{X}_0) e^{-ik_z\hat{z}_s(\mathbf{X}_0)+i\kappa\hat{z}_\tau(\mathbf{X}_0)} \tag{3.37}$$

Note that in the last equality the fact $\hat{\mathbf{X}}_0 = \mathbf{X}_0$ is used. Note also that the expression of $\bar{f}(\mathbf{X}_0)$ is given in Eq. (3.16) or (3.19). Substituting Eqs. (3.35) and (3.36) for $\hat{z}_s$ and $\hat{z}_\tau$, Eq. (3.19) for $\bar{f}(\mathbf{X}_0)$, and direct integration gives

$$\int d\mathbf{X}_0 \bar{f}(\mathbf{X}_0) e^{-ik_z\hat{z}_s(\mathbf{X}_0)+i\kappa\hat{z}_\tau(\mathbf{X}_0)} = 2\pi\delta\left(\frac{k_z(s)}{C(s)} - \frac{\kappa(\tau)}{C(\tau)}\right)\{L.D.; s, \tau\} \tag{3.38}$$

The Dirac delta function can be readily integrated in Eq. (3.34), which selects $\kappa(\tau) = k_z(s)C(\tau)/C(s)$ because

$$\int \frac{d\kappa}{2\pi} \int dz_0 \exp\left\{-i\left[k_z(s)/C(s) - \kappa(\tau)/C(\tau)\right] z_0\right\} = 1 \tag{3.39}$$

In Eq. (3.38), the Landau damping term reads

$$\{L.D.; s, \tau\} = \exp\left\{\frac{-1}{2}\begin{bmatrix} \epsilon_{x0}\beta_{x0}\left(\hat{\Re}_{51}(s,\tau) - \dfrac{\alpha_{x0}}{\beta_{x0}}\hat{\Re}_{52}(s,\tau)\right)^2 + \dfrac{\epsilon_{x0}}{\beta_{x0}}\hat{\Re}_{52}^2(s,\tau) + \\ \epsilon_{y0}\beta_{y0}\left(\hat{\Re}_{53}(s,\tau) - \dfrac{\alpha_{y0}}{\beta_{y0}}\hat{\Re}_{54}(s,\tau)\right)^2 + \dfrac{\epsilon_{y0}}{\beta_{y0}}\hat{\Re}_{54}^2(s,\tau) + \\ \sigma_{\delta 0}^2\hat{\Re}_{56}^2(s,\tau) \end{bmatrix}\right\} \tag{3.40}$$

where

$$\hat{\Re}_{5j}(s,\tau) = k_z(s)\hat{R}_{5j}(s) - k_z(\tau)\hat{R}_{5j}(\tau) = k_0\left[C(s)\hat{R}_{5j}(s) - C(\tau)\hat{R}_{5j}(\tau)\right], j = 1,2,3,4,6 \tag{3.41}$$

Before proceeding, we summarize the formula using compact notations for the second term on RHS of Eq. (3.34),

$$\begin{aligned}&\frac{1}{N}\int_0^s d\tau ik_z(s)\frac{I_b(\tau)}{\gamma_0 I_A}\hat{R}_{56}(\tau\to s)\int\frac{d\kappa}{2\pi}Z_0^{\parallel}(\kappa;\tau)b(\kappa;\tau)\int d\hat{\mathbf{X}}_\tau\bar{f}(\hat{\mathbf{X}}_\tau)e^{-ik_z\hat{z}_s(\hat{\mathbf{X}}_\tau)+i\kappa\hat{z}_\tau}\\&\equiv\int_0^s d\tau K(\tau,s)b(k_z;\tau)\end{aligned}\tag{3.42}$$

with

$$K(\tau,s)=ik_z(s)\frac{I_b(\tau)}{\gamma_0 I_A}\hat{R}_{56}(\tau\to s)Z_0^{\parallel}(k_z;\tau)\left\{L.D.;s,\tau\right\}\tag{3.43}$$

It is worth mentioning the general physical meaning of the kernel function, Eq. (3.42): a density perturbation at τ induces an energy modulation through the impedance $Z_0^{\parallel}(k_z;\tau)$ and is subsequently converted into density modulation at s through the momentum compaction function $\hat{R}_{56}(\tau\to s)$. See also Fig. 1.8.

Now the second term on RHS of Eq. (3.34) has been done. Let us come back to the first term of that equation. This term, without $Z_0^{\parallel}$, corresponds to pure optics case. For the initially small perturbed phase space distribution function, according to Eqs. (3.20) to (3.25), we specify as follows,

$$\begin{aligned}f_1^{(0)}(\mathbf{X}_0)=&\frac{n_0+\Delta n_0(z_0)}{(2\pi)^2\epsilon_{x0}\epsilon_{y0}\sqrt{2\pi}\sigma_\delta}\\&\times\exp\left\{-\frac{\left(x_0+\Delta x_0(z_0)\right)^2+\left(\beta_{x0}\left(x_0{}'+\Delta x_0'(z_0)\right)+\alpha_{x0}\left(x_0+\Delta x_0(z_0)\right)\right)^2}{2\epsilon_{x0}\beta_{x0}}\right\}\\&\times\exp\left\{-\frac{\left(y_0+\Delta y_0(z_0)\right)^2+\left(\beta_{y0}\left(y_0{}'+\Delta y_0'(z_0)\right)+\alpha_{y0}\left(y_0+\Delta y_0(z_0)\right)\right)^2}{2\epsilon_{y0}\beta_{y0}}\right\}\\&\times\exp\left\{-\frac{\left(\delta_0-hz_0+\Delta\delta(z_0)\right)^2}{2\sigma_{\delta0}^2}\right\}\end{aligned}\tag{3.44}$$

where those perturbation terms, Δn_0, Δx_0, $\Delta x_0{}'$, and etc, are assumed to be small. In what follows, to avoid redundancy of notations, we keep in mind that we will treat evolution of initially perturbed phase space distribution along a beamline but in the absence of collective effects. Then we can discard the superscript (0) and use (z), (δ,z), (x,z), (x',z) and etc to indicate a particular type of modulation. Having Taylor expanded Eq. (3.44), we obtain

$$f_1^{(z)}(\mathbf{X}_0)=\left(\frac{\Delta n(z_0)}{n_0}\right)\bar{f}_0(\mathbf{X}_0)\tag{3.45}$$

for initial modulation of the type shown in Fig. 3.5(a) or Eq. (3.20);

$$f_1^{(\delta,z)}(\mathbf{X}_0) \approx \Delta\delta \cdot \left.\frac{\partial f_0}{\partial \Delta\delta}\right|_{\Delta\delta=0} = \left(\frac{(\delta_0 - hz_0)\Delta\delta(z_0)}{\sigma_{\delta 0}^2}\right) \bar{f}_0(\mathbf{X}_0) \tag{3.46}$$

which is corresponding to Fig. 3.5(b);

$$f_1^{(x,z)}(\mathbf{X}_0) \approx \Delta x_0 \cdot \left.\frac{\partial f_0}{\partial \Delta x_0}\right|_{\Delta x_0=0} = \left(\frac{\gamma_{x0}x_0 + \alpha_{x0}x_0'}{\epsilon_{x0}}\Delta x_0\right) \bar{f}_0(\mathbf{X}_0) \tag{3.47}$$

for Fig. 3.5(c), and

$$f_1^{(x',z)}(\mathbf{X}_0)\Delta x_0' \cdot \left.\frac{\partial f_0}{\partial \Delta x_0'}\right|_{\Delta x_0'=0} = \left(\frac{\beta_{x0}x_0' + \alpha_{x0}x_0}{\epsilon_{x0}}\Delta x_0'\right) \bar{f}_0(\mathbf{X}_0) \tag{3.48}$$

for Fig. 3.5(d). Similarly, for (y, z) and (y', z), we have

$$f_1^{(y,z)}(\mathbf{X}_0) \approx \Delta y_0 \cdot \left.\frac{\partial f_0}{\partial \Delta y_0}\right|_{\Delta y_0=0} = \left(\frac{\gamma_{y0}y_0 + \alpha_{y0}y_0'}{\epsilon_{y0}}\Delta y_0\right) \bar{f}_0(\mathbf{X}_0) \tag{3.49}$$

$$f_1^{(y',z)}(\mathbf{X}_0) \approx \Delta y_0' \cdot \left.\frac{\partial f_0}{\partial \Delta y_0'}\right|_{\Delta y_0'=0} = \left(\frac{\beta_{y0}y_0' + \alpha_{y0}y_0}{\epsilon_{y0}}\Delta y_0'\right) \bar{f}_0(\mathbf{X}_0) \tag{3.50}$$

with $\gamma_{x0,y0} = \left(1 + \alpha_{x0,y0}^2\right)/\beta_{x0,y0}$.

In derivation of Eq. (3.34), we only restrict to the situation of density modulations, so Eq. (3.45) is the appropriate expression to replace $f_1^{(0)}$ in Eq. (3.15). The integration can be easily done and the result is

$$\frac{1}{N}\int d\mathbf{X}_0 f_1^{(z)}(\mathbf{X}_0) e^{-ik_z(s)\hat{z}_s(\mathbf{X}_0)} = b_0^{(z)}(k_0;0)\,\{L.D.;s,0\} \equiv b_0^{(z)}(k_z;s) \tag{3.51}$$

where $b_0^{(z)}(k_0;0)$ is quantified according to Eq. (3.20) and $\{L.D.;s,0\}$ is a special case of Eq. (3.40) for $\tau = 0$[65].

Now we have completed Eq. (3.34), which can be cast into the compact form of integral equation

$$b^{(z)}(k_z;s) = b_0^{(z)}(k_z;s) + \int_0^s d\tau K(\tau,s) b^{(z)}(k_z(\tau);\tau) \tag{3.52}$$

We emphasize that Eq. (3.45) is not the only situation that can result in density modulation along a beamline; the remaining cases in Eqs. (3.46) to (3.50) may also lead to density modulations. When we

[65]Note that $C(0) = 1$ and $\hat{R}_{5j}(0) = 0$ for $j = 1, 2, 3, 4, 6$.

combine Eqs. (3.27) to (3.32) and Eqs. (3.45) to (3.50), we should have a total of 36 integrals[66], which represent phase space modulations, i.e.

$$\int d\mathbf{X}_0 \begin{Bmatrix} 1 \\ \delta_s \\ x_s \\ x'_s \\ y_s \\ y'_s \end{Bmatrix} \times \begin{Bmatrix} f_1^{(z)} \\ f_1^{(\delta,z)} \\ f_1^{(x,z)} \\ f_1^{(x',z)} \\ f_1^{(y,z)} \\ f_1^{(y',z)} \end{Bmatrix} e^{-ik_z(s)z_s(\mathbf{X}_0)} = \begin{Bmatrix} b_0^{(z)}, p_0^{(z)}, a_{x0}^{(z)}, a_{x'0}^{(z)}, a_{y0}^{(z)}, a_{y'0}^{(z)} \\ b_0^{(\delta,z)}, p_0^{(\delta,z)}, a_{x0}^{(\delta,z)}, a_{x'0}^{(\delta,z)}, a_{y0}^{(\delta,z)}, a_{y'0}^{(\delta,z)} \\ b_0^{(x,z)}, p_0^{(x,z)}, a_{x0}^{(x,z)}, a_{x'0}^{(x,z)}, a_{y0}^{(x,z)}, a_{y'0}^{(x,z)} \\ b_0^{(x',z)}, p_0^{(x',z)}, a_{x0}^{(x',z)}, a_{x'0}^{(x',z)}, a_{y0}^{(x',z)}, a_{y'0}^{(x',z)} \\ b_0^{(y,z)}, p_0^{(y,z)}, a_{x0}^{(y,z)}, a_{x'0}^{(y,z)}, a_{y0}^{(y,z)}, a_{y'0}^{(y,z)} \\ b_0^{(y',z)}, p_0^{(y',z)}, a_{x0}^{(y',z)}, a_{x'0}^{(y',z)}, a_{y0}^{(y',z)}, a_{y'0}^{(y',z)} \end{Bmatrix} \tag{3.53}$$

To proceed, let us examine Eq. (3.33) and find that it is a special case of Eq. (3.15) with unity weight function. As outlined above, other types of phase space modulations involve with their corresponding different weight functions, as formulated in Eq. (3.53). Following the same procedures as we derive Eq. (3.33), we skip them and only present the final results below. For energy modulations, the governing equation has the form of

$$p(k_z;s) = p_0(k_z;s) + \int_0^s d\tau M(\tau,s) b(k_z(\tau);\tau) - \int_0^s d\tau L(\tau,s) b(k_z(\tau);\tau) \tag{3.54}$$

$$a_x(k_z;s) = a_{x0}(k_z;s) + \int_0^s d\tau A(\tau,s) b(k_z(\tau);\tau) \tag{3.55}$$

$$a_{x'}(k_z;s) = a_{x'0}(k_z;s) + \int_0^s d\tau B(\tau,s) b(k_z(\tau);\tau) \tag{3.56}$$

$$a_y(k_z;s) = a_{y0}(k_z;s) + \int_0^s d\tau C(\tau,s) b(k_z(\tau);\tau) \tag{3.57}$$

$$a_{y'}(k_z;s) = a_{y'0}(k_z;s) + \int_0^s d\tau D(\tau,s) b(k_z(\tau);\tau) \tag{3.58}$$

with the kernel functions

$$L(\tau,s) = \frac{I_b(\tau)}{\gamma_0 I_A} Z_0^{\parallel}(k_z;\tau) \tag{3.59}$$

which represents the direct conversion of density modulation to energy modulation through collective interaction,

$$M(\tau,s) = ik_z(s) \frac{I_b(\tau)}{\gamma_0 I_A} \sigma_{\delta 0}^2 \hat{R}_{56}(\tau \to s) \hat{\Re}_{56}(s,\tau) Z_0^{\parallel}(k_z;\tau) \tag{3.60}$$

[66] Explicit expressions for each integrations can be found in Appendix A.

$$A(\tau,s)=\frac{I_b(\tau)}{\gamma_0 I_A}Z_0^{\parallel}(k_z(\tau);\tau)$$
$$\times\left\{\begin{array}{l} i\hat{R}_{16}(\tau\to s)-k_z^2(s)\hat{R}_{56}(\tau\to s)\times \\ \left[\begin{array}{ll} & \left[\begin{array}{l}\hat{R}_{11}(\tau)\epsilon_{x0}\left(W\alpha_{x0}-V\beta_{x0}\right)+\\ \hat{R}_{12}(\tau)\epsilon_{x0}\left(W\gamma_{x0}-V\alpha_{x0}\right)-\\ \hat{R}_{16}(\tau)\sigma_{\delta 0}^2U\end{array}\right]+ \\ \hat{R}_{11}(\tau\to s) & \\ & \left[\begin{array}{l}\hat{R}_{21}(\tau)\epsilon_{x0}\left(W\alpha_{x0}-V\beta_{x0}\right)+\\ \hat{R}_{22}(\tau)\epsilon_{x0}\left(W\gamma_{x0}-V\alpha_{x0}\right)-\\ \hat{R}_{26}(\tau)\sigma_{\delta 0}^2U\end{array}\right]-\hat{R}_{16}(\tau\to s)\sigma_{\delta 0}^2U \\ \hat{R}_{12}(\tau\to s) & \end{array}\right] \end{array}\right\}\{L.D.;s,\tau\} \qquad (3.61)$$

$$B(\tau,s)=\frac{I_b(\tau)}{\gamma_0 I_A}Z_0^{\parallel}(k_z(\tau);\tau)$$
$$\times\left\{\begin{array}{l} i\hat{R}_{26}(\tau\to s)-k_z^2(s)\hat{R}_{56}(\tau\to s)\times \\ \left[\begin{array}{ll} & \left[\begin{array}{l}\hat{R}_{11}(\tau)\epsilon_{x0}\left(W\alpha_{x0}-V\beta_{x0}\right)+\\ \hat{R}_{12}(\tau)\epsilon_{x0}\left(W\gamma_{x0}-V\alpha_{x0}\right)-\\ \hat{R}_{16}(\tau)\sigma_{\delta 0}^2U\end{array}\right]+ \\ \hat{R}_{21}(\tau\to s) & \\ & \left[\begin{array}{l}\hat{R}_{21}(\tau)\epsilon_{x0}\left(W\alpha_{x0}-V\beta_{x0}\right)+\\ \hat{R}_{22}(\tau)\epsilon_{x0}\left(W\gamma_{x0}-V\alpha_{x0}\right)-\\ \hat{R}_{26}(\tau)\sigma_{\delta 0}^2U\end{array}\right]-\hat{R}_{26}(\tau\to s)\sigma_{\delta 0}^2U \\ \hat{R}_{22}(\tau\to s) & \end{array}\right] \end{array}\right\}\{L.D.;s,\tau\} \qquad (3.62)$$

$$C(\tau,s)=\frac{I_b(\tau)}{\gamma_0 I_A}Z_0^{\parallel}(k_z(\tau);\tau)$$
$$\times\left\{\begin{array}{l} i\hat{R}_{36}(\tau\to s)-k_z^2(s)\hat{R}_{56}(\tau\to s)\times \\ \left[\begin{array}{ll} & \left[\begin{array}{l}\hat{R}_{33}(\tau)\epsilon_{y0}\left(T\alpha_{y0}-S\beta_{y0}\right)+\\ \hat{R}_{34}(\tau)\epsilon_{y0}\left(T\gamma_{y0}-S\alpha_{y0}\right)-\\ \hat{R}_{36}(\tau)\sigma_{\delta 0}^2U\end{array}\right]+ \\ \hat{R}_{33}(\tau\to s) & \\ & \left[\begin{array}{l}\hat{R}_{43}(\tau)\epsilon_{y0}\left(T\alpha_{y0}-S\beta_{y0}\right)+\\ \hat{R}_{44}(\tau)\epsilon_{y0}\left(T\gamma_{y0}-S\alpha_{y0}\right)-\\ \hat{R}_{46}(\tau)\sigma_{\delta 0}^2U\end{array}\right]-\hat{R}_{36}(\tau\to s)\sigma_{\delta 0}^2U \\ \hat{R}_{34}(\tau\to s) & \end{array}\right] \end{array}\right\}\{L.D.;s,\tau\} \qquad (3.63)$$

$$
\begin{aligned}
D(\tau,s) = & \frac{I_b(\tau)}{\gamma_0 I_A} Z_0^{\parallel}(k_z(\tau);\tau) \\
& \times \left\{ \begin{array}{l} i\hat{R}_{46}(\tau\to s) - k_z^2(s)\hat{R}_{56}(\tau\to s)\times \\ \left[\begin{array}{ll} & \left[\begin{array}{l} \hat{R}_{33}(\tau)\epsilon_{y0}\left(T\alpha_{y0} - S\beta_{y0}\right) + \\ \hat{R}_{34}(\tau)\epsilon_{y0}\left(T\gamma_{y0} - S\alpha_{y0}\right) - \\ \hat{R}_{36}(\tau)\sigma_{\delta 0}^2 U \end{array} \right] \\ \hat{R}_{43}(\tau\to s) & + \\ & \left[\begin{array}{l} \hat{R}_{43}(\tau)\epsilon_{y0}\left(T\alpha_{y0} - S\beta_{y0}\right) + \\ \hat{R}_{44}(\tau)\epsilon_{y0}\left(T\gamma_{y0} - S\alpha_{y0}\right) - \\ \hat{R}_{46}(\tau)\sigma_{\delta 0}^2 U \end{array} \right] \\ \hat{R}_{44}(\tau\to s) & - \hat{R}_{46}(\tau\to s)\sigma_{\delta 0}^2 U \end{array} \right] \end{array} \right\} \{L.D.;s,\tau\}
\end{aligned} \tag{3.64}
$$

where

$$
\begin{aligned}
V(s,\tau) &\equiv C(s)\hat{R}_{51}(s) - C(\tau)\hat{R}_{51}(\tau) \\
W(s,\tau) &\equiv C(s)\hat{R}_{52}(s) - C(\tau)\hat{R}_{52}(\tau) \\
S(s,\tau) &\equiv C(s)\hat{R}_{53}(s) - C(\tau)\hat{R}_{53}(\tau) \\
T(s,\tau) &\equiv C(s)\hat{R}_{54}(s) - C(\tau)\hat{R}_{54}(\tau) \\
U(s,\tau) &\equiv C(s)\hat{R}_{56}(s) - C(\tau)\hat{R}_{56}(\tau)
\end{aligned} \tag{3.65}
$$

In Eqs. (3.59) to (3.64) the relative transport matrix elements $\mathbf{R}(\tau\to s)$ can be evaluated by the matrix multiplication, i.e. $\mathbf{R}(\tau\to s) = \mathbf{R}(s)\mathbf{R}^{-1}(\tau)$. The explicit expressions can be found in Appendix A (Sec. A.3). At the moment we have derived governing equations for various phase space modulations, Eq. (3.52) and Eqs. (3.54) to (3.58). The corresponding kernel functions are given in Eq. (3.43) and Eqs. (3.59) to (3.64). The pure-optics evolutions, not obtained yet, are grouped in Eq. (3.53). These semi-analytical equations, Eq. (3.52) and Eqs. (3.54) to (3.58), give us an indication that an initial density modulation can evolve along a beamline into different types of modulations. From this point of view, the concept of *gain matrix* becomes more clearer now. In Fig. 3.6, if we study the microbunching dynamics from a certain location (at an otherwise very beginning location), we should record as much information of phase space modulation as possible. With taking only density modulation into account, as illustrated in top row of Fig. 3.6, it is likely that the overall effect of MBI can be underestimated. It is expected that the extended formulations developed in this section should provide more complete picture about microbunching in a broader view of phase space modulations. Further investigation will be discussed in Chapter 8, where a specific example lattice will be illustrated as well.

Of the most particular interest is a quantity called the microbunching *gain*, as a function of the longitudinal coordinate s and the initial modulation wavelength λ (or, the initial wave number $k = 2\pi/\lambda$),

and is defined as

$$G(s, k = 2\pi/\lambda) \equiv \left| \frac{b(k_z; s)}{b_0(k_0; 0)} \right| \tag{3.66}$$

Hereafter, we call $G(s)$, which is a function of s for a given modulation wavenumber, the *gain function* and refer to $G_f(\lambda)$ as the *gain spectrum*, a function of modulation wavelength at the exit location of a lattice (the subscript "'f' indicates the exit of a beamline). A brief introduction of numerical procedures to solve Eq. (3.52), and thus Eqs. (3.54) to (3.58) in a similar way, would be highlighted later in Chapter 5, together with benchmarking against particle tracking simulations.

Before ending this section, we comment the following four extended assumptions made in our derivation:

(1) Coasting beam approximation: From Eq. (3.18) to Eq. (3.19), we made this assumption and the subsequent definition of bunching factors. This assumption is no longer valid when a bunch is experiencing a *critical* compression or during *roll-over* compression[67]. At critical compression, $R_{56}(s) \approx 1/h$ and $C(s) \to \infty$, in which the bunch length becomes vanishingly small[68]. In the situation, the bunching factor can be contributed from both $\bar{f}$ and f_1. The static part is similar to that due to potential well distortion (PWD) in a storage ring system, which can be solved by Haissinski equation [35]. Now $\bar{f}$ should satisfy

$$\frac{\partial \bar{f}}{\partial s} + \left(\frac{\partial \bar{f}}{\partial \hat{\mathbf{X}}}\right)^T \mathbf{S} \frac{\partial \bar{H}}{\partial \hat{\mathbf{X}}} + \left(\frac{\partial \bar{f}}{\partial \hat{\mathbf{X}}}\right)^T \mathbf{S} \frac{\partial H_1}{\partial \hat{\mathbf{X}}} = 0 \tag{3.67}$$

where H_1, reflecting the effect of collective energy kick, now contains $\bar{f}$. The situation can be further clarified by illustrating a specific case, e.g. CSR-induced microbunching. We will show in Chapter 4 that the collective energy kick due to CSR can be related (proportional) to the slope of bunch charge density distribution, i.e. $W^{\text{s.s.}}_{\text{CSR}} \propto \int_{z-\rho\phi^3/24}^{z} d\zeta \frac{1}{(z-\zeta)^{1/3}} \frac{\partial \lambda(\zeta)}{\partial \zeta}$. For static part $\bar{f}$, the uniform flat-top portion of the beam does not contribute while the Gaussian beam can lead to energy redistribution and result in a net distortion of the bulk-bunch shape. Figure 3.7 shows the difference.

Presuming we have obtained the PWD-induced unperturbed bunch distribution, we superimpose a small density modulation atop, integrate Eq. (3.15) to obtain an integral equation, which should be similar to Eq. (3.38) but without Dirac delta function there. Instead, a factor $\exp\left(-[k_z(s) - \kappa(\tau)]^2 \sigma_{z0}^2 \Big/ 2\right)$ should show up, e.g. for Gaussian $z-$distribution. It turns out that when the modulation wavelength is much smaller compared with the overall bunch duration, i.e. $k_z^{-1} \ll \sigma_{z0}$, the factor approaches to unity.

[67] This is also named parasitic compression, by D. Douglas.

[68] This statement is true only when a line bunch is considered. When a bunch has a non-zero transverse beam size, from Eq. (3.36), the longitudinal bunch length is not only determined by R_{56} (via energy spread) but also by R_{51} through σ_x or R_{52} through $\sigma_{x'}$.

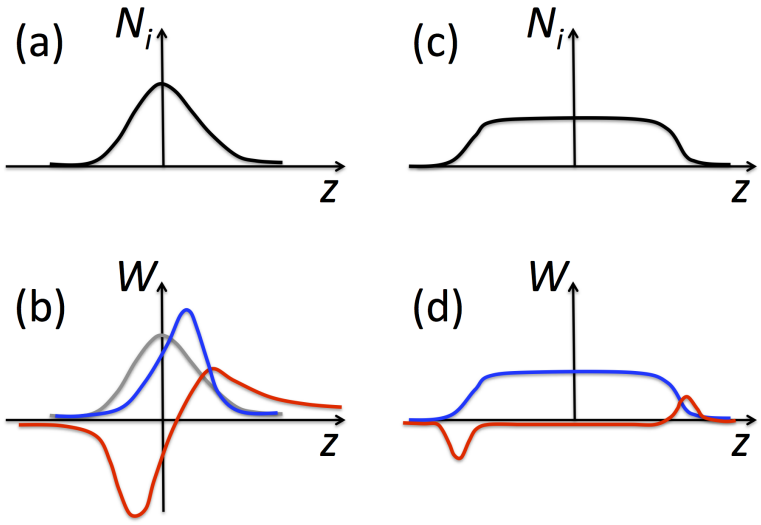

Figure 3.7: Illustration of the longitudinal bunch current density distributions before (top) and after (bottom) CSR wakefield effect for Gaussian (a,b) and quasi-coasting uniform-flattop (c,d) distributions. The red curves represent the CSR induced (bulk) wakefield, with positive values meaning energy gain. $z > 0$ for bunch head. Note that the edge effect due to finite bunch length in the coasting beam model would be neglected in our Vlasov analysis.

(2) Nonlinearity in the longitudinal beam phase space: There are two nonlinear terms that might show up in the longitudinal beam phase space in a practical situation. The first nonlinearity stems from the beam itself. The other may originate from the optics of a beamline design.

(a) For the former, when a beam is accelerated in an RF cavity, the curvature of the sinusoidal waveform features a nonlinear effect, particularly evident for a long bunch, shown in Fig. 3.8(a).

(b) For the latter, even when a beam is perfectly linearized prior to entrance in a beamline with (even only) residual nonlinearity, e.g. T_{566}[69], the longitudinal phase space distribution of the beam can still be *bent*, as illustrated in Fig. 3.8(b). Such nonlinearity or curvature becomes a limit to the minimum achievable compressed bunch length and is usually undesired. Furthermore, since the projected bunch line/charge density features a high peak local current, which may enhance CSR. Studies [111] show that this enhancement due to local charge concentration should be given serious consideration in designs of modern high-brightness accelerators. In a recirculating or ERL machine, these nonlinearities are usually undesired and a beamline design sometimes takes advantage of T_{566} to correct or cancel (by bending in opposite manner) the curvature induced by RF cavities. For linac, the third-harmonic RF cavity may be used to counteract the undesired curvature. Although these nonlinear effects are not included in the above formulation, in Chapter 6 we will discuss the effects by comparing particle tracking simulations with our semi-analytical Vlasov results and identify its physical mechanism.

(3) Transversely coupled beam: In most situations, accelerator beamline design intends to avoid or dodge

[69]The second order transport matrix, similar to Eq. (2.55), is usually assigned as a matrix $\mathbf{T}$ [29]. Here T_{566} relates z and δ^2.

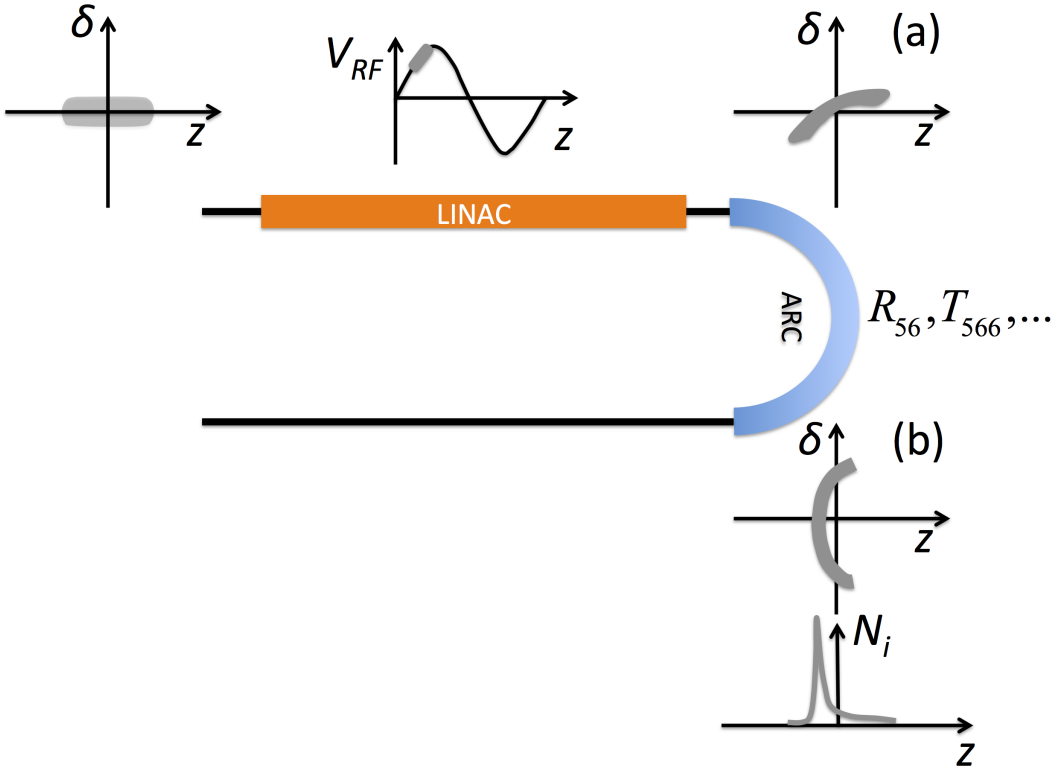

Figure 3.8: Evolution of beam longitudinal phase space distributions in a recirculation machine. Fig. (a) illustrates the nonlinear distortion of the longitudinal phase space distribution due to RF curvature in the upstream linac section. Fig. (b) shows possible consequence of such nonlinearity, which may lead to local concentration of bunch charges and cause enhancement of CSR effect.

the coupling between transverse degrees of freedom. This *convenience* leads to the simple and useful expression of Eq. (3.18) [or (3.19)] in the formulation. However, recently many novel beam manipulation schemes have been proposed and experimentally tested for applications in the light source facilities and colliders. Particularly, in the Jefferson Lab Electron Ion Collider project (JLEIC) at JLab, the circulating cooler ring (CCR) based on the electron cooling technique has been proposed using magnetized electron beam [46], in order to enhance the cooling efficiency and thus deliver the ion beam with higher luminosities [1, 2]. The magnetized beam is in general a transversely coupled beam. The motivation for our study to extend the assumption of originally transverse uncoupled beam to a general case indeed stems from this idea. The generalization will be introduced in Chapter 9, in which the resultant formulation allows coupling between transverse degrees of freedom.

(4) Absence of harmonic generation: Throughout the analysis in this chapter, we do neither consider the harmonic generation nor higher-order phase space perturbations. That is, we always assume a single frequency in the analysis and no interaction with other frequencies. Shown in Fig. 3.1(c), it can be seen that the absence of harmonic generation can be a good approximation if only the fundamental modulation frequency is dominant. Such harmonic interaction is in general a higher order interac-

tion. However, such higher-order corrections can also be important if the spectrum of modulation is broadband [200], e.g. when a beam is transport with initial shot noise. The effect of shot noise, the fluctuation in the beam density, comes from granularity of the elementary charge. Venturini had found that the microbunching amplification due to shot noise can be a few times *larger* than predicted by the analysis developed above. To illustrate this concept, consider two modulation frequencies, k_1 and k_2. From Eq. (3.40), suppression due to Landau damping of finite energy spread is proportional to $\exp\left[-k_{1,2}^2(s)R_{56}^2(s)\sigma_{\delta 0}^2\right]$ for k_1 and k_2. Suppose k_1 and k_2 are high frequency components, our theory predicts that strong exponential attenuation and no microbunching growth shall occur. However, if harmonic generation is considered, say, second-order correction, the coupling frequencies $(k_1 + k_2)$ and $(k_1 - k_2)$ will be present. It is likely that the spectral content of $(k_1 - k_2)$ will escape exponential attenuation and can appear in the modulation spectrum downstream the beamline with nonzero R_{56} [200]. Throughout the dissertation the shot-noise based analysis is beyond our scope and excluded.

3.4 Dispersion relation - connection to the storage-ring system

At present, the microbunching analysis for single-pass systems, e.g. a linac-based or recirculating accelerator, solves initial value problem for 4-D or 6-D phase space transport, and the Landau damping from emittance and uncorrelated energy spread depends on details of local optics. In storage-ring systems, however, most microbunching (or microwave) instability solves dispersion relations or eigenvalue problems for 2-D longitudinal phase space transport [see, for example Ref. [35, 32, 192]], and the Landau damping depends *only* on energy spread and *global/averaged* optics of a ring[70]. In storage rings, the energy spread is much larger than that for a single-pass device and causes the dominant Landau damping effects. Thus 2-D analysis in the longitudinal phase space would suffice. The storage ring formulation, which usually involves dispersion relation or eigenvalue problem, would give a clear threshold, above which the microbunching modulation will exponentially grow. Different situations occur for recirculating or ERL accelerators. Preliminary comparisons of the microbunching amplification process in a recirculation arc, i.e. CCR, with that in a single-pass few-dipole system, e.g. bunch compressor chicane, already show that the former is characteristic of multistage (for CCR, it is up to six stages, see Chapter 6 for detailed discussion) amplification, which differs from the two-stage amplification in a bunch compression chicane. Such multistage amplification behaves polynomially. To compare with the storage ring theory, for a storage ring lattice, we need to analyze microbunching evolution using single-pass analysis and examine if we get microbunching gains for a stable case under instability *threshold*[71], and see how the dependence on the emittance for a single-pass system is transformed to the dependence on transverse emittance in a storage ring. Below we will follow HSK [79] on how to extend the above analysis for single-pass (or recirculating) machines to storage rings to bridge the understanding of the above two scenarios by deriving the dispersion relation from Eq. (3.52) for 4-D case and comparing with 2-D expression in Ref. [164].

[70] Usually the smooth approximation, Eq. (3.68), is employed.

[71] More precisely, the relation between evolution/growth of microbunching gains and the growth rate calculated from storage-ring theory shall be connected.

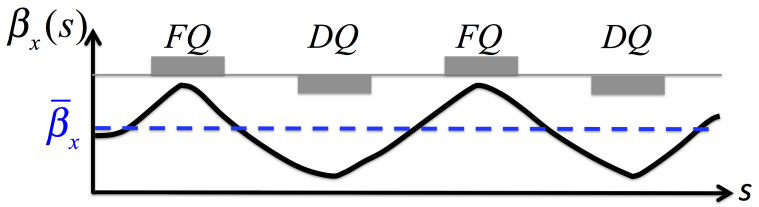

Figure 3.9: Evolution of Twiss β function along a focusing-drift-defocusing-drift (FODO) section. DQ: defocusing quadrupole and FQ: focusing quadrupole. Here $\bar{\beta}_x$ represents the average β function along the beamline (i.e. smooth approximation).

For a storage ring, we assume the bunch length is constant, so $h = 0$ and thus bunch compression factor $C \equiv 1$. We also assume the energy is constant. In a storage ring, the smooth approximation is always employed, for which we have $2\pi\nu_x \equiv \int_s^{s+L} \beta_x^{-1}(\zeta)d\zeta \approx L/\bar{\beta}_x$, where $\bar{\beta}_x$ is the smoothed betatron function (see Fig. 3.9) and the circumference of a storage ring is assumed isomagnetic or $L = 2\pi\rho_x$. Thus the betatron tune is $\nu_x = \rho_x/\bar{\beta}_x$.

The next step is to simplify the quantities in Eqs. (3.40) and (3.43) to accommodate the storage-ring situation under smooth betatron approximation. Equation (3.68) summarizes the relevant quantities for Twiss and transport matrix elements.

$$
\begin{aligned}
\bar{\beta}_x &= \frac{\rho_x}{\nu_x} \\
\bar{\alpha}_x &= -\bar{\beta}_x'/2 = 0 \\
\psi_x &= 2\pi\nu_x \frac{s}{L} = \nu_x \frac{s}{\rho_x} \\
\epsilon_{x0} &= \frac{\sigma_{x0}^2}{\bar{\beta}_x} \\
R_{16} &= \frac{\rho_x}{\nu_x^2} \\
R_{26} &= 0 \\
R_{51}(s) &= R_{16}R_{21} - R_{26}R_{11} = \frac{-1}{\nu_x} \sin\frac{\nu_x s}{\rho_x} \\
R_{52}(s) &= R_{16}R_{22} - R_{26}R_{12} = \frac{\rho_x}{\nu_x^2} \cos\frac{\nu_x s}{\rho_x} \\
R_{56}(s) &= \int \frac{R_{16}}{\rho_x} ds = \frac{s}{\nu_x^2} \\
R_{56}(\tau \to s) &= R_{56}(s) - R_{56}(\tau) + R_{51}(\tau)R_{52}(s) - R_{51}(s)R_{52}(\tau) = \frac{s-\tau}{\nu_x^2} + \frac{\rho_x}{\nu_x^3} \sin\frac{\nu_x(s-\tau)}{\rho_x} \\
\eta &= \alpha_c - \frac{1}{\gamma_0^2} = \frac{1}{L} \oint ds \frac{R_{16}}{\rho_x} \approx \frac{1}{\nu_x^2}
\end{aligned}
\tag{3.68}
$$

where the last quantity, called phase slippage factor, is usually used in the storage-ring formulation.

Substituting Eq. (3.68) into Eq. (3.40), we have the exponential term

$$\{L.D.; s, \tau\} = \{L.D.; s-\tau\} = \exp\left\{-k_z^2\left[\frac{\sigma_{x0}^2}{\nu_x^2}\left(1-\cos\frac{\nu_x(s-\tau)}{\rho_x}\right)+\frac{\sigma_{\delta 0}^2}{2\nu_x^4}(s-\tau)^2\right]\right\} \tag{3.69}$$

Now, Eq. (3.43) becomes

$$K(\tau, s) = K_1(s-\tau) = \frac{ik_z(s)I_0}{\gamma_0 I_A}\left[\frac{s-\tau}{\nu_x^2}+\frac{\rho_x}{\nu_x^3}\sin\frac{\nu_x(s-\tau)}{\rho_x}\right] Z_0^{\parallel}(k_z;\tau)\{L.D.; s-\tau\} \tag{3.70}$$

The resultant integral equation now has the form of

$$b(k_z; s) = b_0(k_z; s) + \int_0^s d\tau K(s-\tau) b(k_z(\tau);\tau) \tag{3.71}$$

The dispersion relation relates the modulation frequency k_z (or wavelength λ, with respect to z) to the spatially growing amplitude with respect to s. To derive the relation, we perform Laplace transformation on the relevant quantities,

$$\begin{Bmatrix} \hat{b}(k_z;\mu) \\ \hat{b}_0(k_z;\mu) \\ \hat{K}_1(\mu) \end{Bmatrix} \equiv \mathcal{L}\begin{Bmatrix} b(k_z;s) \\ b_0(k_z;s) \\ K_1(s) \end{Bmatrix} = \int_0^\infty ds \begin{Bmatrix} b(k_z;s) \\ b_0(k_z;s) \\ K_1(s) \end{Bmatrix} e^{-\mu s} \tag{3.72}$$

With the above transformations, Eq. (3.71) becomes

$$\hat{b}(k_z;\mu) = \hat{b}_0(k_z;\mu) + \hat{K}_1(\mu)\hat{b}(k_z;\mu) \tag{3.73}$$

or

$$\hat{b}(k_z;\mu) = \left[1-\hat{K}_1(\mu)\right]^{-1}\hat{b}_0(k_z;\mu) \tag{3.74}$$

where the convolution theorem has been applied

$$\mathcal{L}\left\{\int_0^s d\tau K(s-\tau) b(k_z(\tau);\tau)\right\} = \mathcal{L}\{K_1 * b(k_z(\tau);\tau)\} = \hat{K}_1(\mu)\hat{b}(k_z;\mu) \tag{3.75}$$

The dispersion relation is defined by the zeros in the denominator of Eq. (3.74), i.e.

$$1-\hat{K}_1(\mu) = 0 \tag{3.76}$$

In general, the solution for Eq. (3.76) is a (complex) function of k_z, say $\mu(k_z) = \mu_R + i\mu_I$. The stability is determined by $\mu_R \le 0$ for all k_z. The instability growth rate may be estimated as the largest positive μ_R,

i.e. $\tau^{-1} \approx \max\{\mu_R(k_z)\}$.

Now we consider a reduced case with 2-D (only longitudinal) dynamics, in which the kernel function, Eq. (3.70) can be simplified by presuming $\sigma_{x0} \to 0$ and neglecting the transverse-longitudinal correlations such R_{51} as and R_{52}. The 1-D kernel function can be written as

$$K(\tau, s) = K_1(s-\tau) = \frac{ik_z(s)I_0\eta}{\gamma_0 I_A}(s-\tau)\, Z_0^{\parallel}(k_z;\tau)\exp\left\{-\frac{k_z^2\sigma_{\delta 0}^2\eta^2}{2}(s-\tau)^2\right\} \tag{3.77}$$

where the phase slippage factor has been used.

Following the same procedures as outlined above, the Laplace-transformed equation can be obtained. The dispersion relation is constituted in the form of Eq. (3.76), where[72]

$$\hat{K}_1(\mu) = \frac{ik_z I_b\eta}{\gamma I_A} Z_0^{\parallel}(k_z)\int_0^{\infty} ds e^{-\mu s}(s) e^{-\frac{k_z^2\sigma_{\delta 0}^2\eta^2}{2}(s)^2} \tag{3.78}$$

Using the identity

$$\int_0^{\infty} dt(t) e^{-t^2/2 - i\Omega t} = \int_{-\infty}^{\infty} dp \frac{p e^{-p^2/2}}{p+\Omega}$$

and letting $t = k_z\sigma_{\delta 0}\eta s$ and $\Omega = -i\mu/k_z\sigma_{\delta 0}\eta$, we obtain the dispersion relation

$$\hat{K}_1(\mu) = \frac{iI_b Z_0^{\parallel}(k)}{\sqrt{2\pi}\gamma I_A k_z\sigma_{\delta 0}^2\eta}\int_{-\infty}^{\infty} dp \frac{p e^{-p^2/2}}{p+\Omega} = 1 \tag{3.79}$$

which gives the same result as that in Ref. [164] for the 1-D case in a storage ring system.

To end this section, we note that Eq. (3.79) serves in a theoretical aspect the connection between the single-pass and storage ring theories. In storage rings, Eq. (3.79) works well because, as mentioned above, in storage rings the energy spread is much larger than that for a single-pass device due to quantum excitation and causes the dominant Landau damping effects. However, this is not generally true for situations in recirculating or ERL machines. Comparison between the two scenarios is worthwhile and it is interesting to see how dependence of beam emittance plays a role at transition stage. We also remind that a fair comparison between the single-pass theory and storage-ring theory should be made when the instability occurs fast enough than one synchrotron period because the theories based on Vlasov treatment have excluded such effects. That is, when instability growth time shorter than the synchrotron period, the synchrotron radiation damping, a much slower process, should not be important. When radiation damping needs to be considered, more dedicated studies should resort to Vlasov-Fokker-Plank equation, in which radiation damping and quantum fluctuations due incoherent synchrotron radiation are included.

[72] Assume in steady state $Z_0^{\parallel}(k_z;\tau) = Z_0^{\parallel}(k_z)$.

3.5 Landau damping

In Eq. (3.40) of Sec. 3.3, the damping factor $\{L.D.; s, \tau\}$ plays a role against the remaining terms of Eq. (3.43), in which $kI_b Z_0^{\parallel}(k)\Big/\gamma I_A$ usually amplifies and $\{L.D.; s, \tau\}$ suppresses the modulation. In this section, we try to clarify the physical mechanism involving this damping factor. In some literature $\{L.D.; s, \tau\}$ is named as Landau damping. The mathematical theory of Landau damping is somewhat involved and its physical interpretations may vary from field to field. For example, in favor of plasma physics, Landau damping is often explained in the way of energy transfer from wave-particle interactions. In our particular case, we intend to illustrate this damping effect as smearing in phase space. This may provide an easier way of understanding the underlying damping mechanism.

To illustrate, we first rewrite Eq. (3.40) in a clearer form by expressing it in terms of transverse and longitudinal beam sizes. As introduced in Chapter 2, Eq. (2.68) and the discussion, we usually use beam sigma matrix to characterize a beam. For 2-D (x, x') case, the beam sigma matrix can be parameterized by Twiss (or Courant-Snyder) parameters as

$$\Sigma_{2D} \equiv \left\langle \mathbf{X}_{2D}\mathbf{X}_{2D}^T \right\rangle = \begin{pmatrix} \langle xx \rangle & \langle xx' \rangle \\ \langle x'x \rangle & \langle x'x' \rangle \end{pmatrix} = \epsilon_x \begin{pmatrix} \gamma_x & \alpha_x \\ \alpha_x & \beta_x \end{pmatrix} \tag{3.80}$$

The transverse (rms) beam size can be expressed as $\sigma_x = \sqrt{\langle xx \rangle} = \sqrt{\epsilon_x \beta_x}$ (assuming in the dispersion-free region), the transverse (rms) beam divergence $\sigma_{x'} = \sqrt{\epsilon_x \gamma_x}$, with $\gamma_x = (1 + \alpha_x^2)\big/\beta_x$, and $\sigma_{xx'} = -\epsilon_x \alpha_x$. Equation (3.40) then has the form of

$$\{L.D.; s, 0\} = \exp\left\{ \frac{-k_z^2}{2} \left[R_{51}^2(s)\sigma_{x0}^2 + R_{52}^2(s)\sigma_{x'0}^2 + 2R_{51}(s)R_{52}(s)\sigma_{x0x'0} + R_{56}^2(s)\sigma_{\delta 0}^2 \right] \right\} \tag{3.81}$$

where, for simplicity, we assume $\tau = 0$, constant-energy, and the beamline lies within (x, s) plane. The first term in Eq. (3.81) describes modulation damping due to the transverse-longitudinal correlation from finite transverse beam size, the second factor depicts damping still due to the transverse-longitudinal but from the transverse divergence, and the third term is correlation of the first two terms. The last term in Eq. (3.81) corresponds to the damping effect arising from finite beam energy spread. In storage rings, as discussed in the previous section, usually the last term in Eq. (3.81) dominates the damping mechanism because of much larger energy spread.

Below we quantify two length scales, one is z-slippage and the other is λ characteristic of the modu-

lation wavelength, so that the Landau damping shall become effective when

$$R_{51}(s)\sigma_x(s) > \lambda(s) \tag{3.82}$$

$$R_{52}(s)\sigma_{x'}(s) > \lambda(s), \text{ or} \tag{3.83}$$

$$R_{56}(s)\sigma_\delta(s) > \lambda(s) \tag{3.84}$$

where the z-slippage length can be due to R_{51}, R_{52} and/or R_{56}.

Consider a particle was initially located at the longitudinal coordinate $z_{0,i}$ (where i denotes the particle index, $i = 1, 2, ..., N$), after transport in a certain distance, at s, the new longitudinal coordinate can have a drift distance as

$$z_i(s) - z_{0,i} = R_{51}(s)x_{0,i} + R_{52}(s)x'_{0,i} + R_{56}(s)\delta_{0,i} \tag{3.85}$$

For a collection of particles, it is obvious that effective smearing (damping) should occur when particles within a bunch largely traverses for a drift length longer than the modulation wavelength, i.e. $\left\langle (z_i(s) - z_{0,i})^2 \right\rangle > \lambda^2$, or roughly $\sqrt{(R_{51}\sigma_{x0})^2 + (R_{52}\sigma_{x'0})^2 + (R_{56}\sigma_{\delta 0})^2} > \lambda$. Usually a beam with intrinsically larger spread, either σ_{x0}, $\sigma_{x'0}$, or $\sigma_{\delta 0}$, would help avoid microbunching; however, these properties contradict the pursuit of a high-brightness beam. Therefore a way to provide effective damping goes to a dedicated design which provides, e.g. larger R_{51}, R_{52}, or R_{56}[73]. However, a beamline design usually has itself constraints from other issues; this way may not provide much flexibility to directly adjust R_{51}, R_{52}, or R_{56}. In Chapter 7, we demonstrate several example lattices that finds another path which also provides effective suppression (or control) of microbunching throughout a beamline.

3.6 First example: LCLS BC2

In the previous sections we have outlined the microbunching mechanism, presented the theoretical formulations, derived integral equations for bunching evolution, and clarified the damping effect due to phase space smearing. In this section we take a classic case as the first example, based on LCLS second bunch compressor (BC2), to demonstrate typical microbunching gain functions, gain spectra, and confirm validity of the linear amplification regime, Landau damping (or phase space smearing), and argument of the coasting-beam approximation. Table 3.3 summarizes the initial beam parameters for use in the following simulations and Fig. 3.10 shows the schematic layout of LCLS BC2. A chicane is a modular unit composed of a sequence of a few dipoles, typically 4 or 5 dipoles. Usually the purpose is to provide longitudinal bunch-length manipulation via time-of-flight dependence of particles in a beam. These dipoles generate a dispersive region in the chicane, see Fig, 3.11. Thus particles with slightly different energies travel different paths or trajectories. Prior to the chicane, the bunch is accelerated (also chirped) by the RF cavity off-crest so that

[73] An example of utilizing this approach is referred to [142].

electrons with different bunch (internal) positions gain different energies. In the setting of a normal chicane for bunch compression, head particles are assumed with lower energy and tail particles with higher energy. The higher-energy particles travel a longer trajectory than the lower-energy particles[74]. At the exit of such a chicane, the bunch is compressed, see also Fig. 3.10.

We would apply the theory developed above to the analysis in the design of LCLS BC2 [100]. We will also use `elegant` tracking to study MBI in this system, and benchmark our analysis. The bunch compressor consists of four dipole magnets (shown in Fig. 3.10) of each dipole length 0.4 m with a bending radius ρ_x of 12.2 m. BC2 is located after the second linac (L2-linac, not shown here) where the beam energy is assumed 4.54 GeV, and compresses the (rms) bunch length from 195 μm down to 23 μm. Other relevant parameters of the bunch compressor are summarized in Table 3.3. The number of electrons in the bunch is about 6.5×10^9 ($\sim$1 nC). However, in our particle tracking simulation (using `elegant`), we use 50-million simulation particles, still far below the realistic number although the simulation has taken several hours for a multi-core desktop computer. Because of the limited number of simulation particles, numerical noises, mixed with the physical noise, can be eventually amplified and mess up the final results. Therefore efforts for several numerical treatments to smoothen the particle phase space distribution since its preparation and tracking (transport) were made [22]. This would be highlighted in Chapter 5. The initial beam distribution in six-dimensional phase space is assumed Gaussian in (x, x', δ), and quasi-coasting beam with uniform flattop in z (see also Fig. 3.7). To be consistent with our theory, we superimpose a sinusoidal modulation on top of z to mimic the initial perturbation (or, seed) for subsequent tracking simulation. The density modulation (or bunching factor), defined in Eq. (3.27), can be extracted from particle tracking simulation with dedicated data postprocessing. We will introduce the detailed procedures in Chapter 5 (Sec. 5.3.3).

We will also calculate the microbunching gain in the bunch compressor by semi-analytically solving Eq. (3.52) with the kernel function given by Eqs. (3.43) and (3.40). The calculated dispersion function R_{16}, the transverse-longitudinal correlation R_{51}, R_{52}, and the momentum compaction R_{56} as a function of s are shown in Fig. 3.11. They will be used to determine the kernel function. Numerical methods are used to discretize the Volterra integral equation on a mesh and then to perform the inversion of the kernel function utilizing the power of `MATLAB`[120]. Here we note that the semi-analytical Vlasov solver is much faster and cleaner than the aforementioned numerical particle tracking simulation. It is faster in microbunching gain calculation because the solver does not really track individual particles. It is free from numerical noise because the phase space distribution is assumed a continuum[75]. In Chapter 5 the detailed numerical procedures would be introduced.

In addition to the particle tracking simulation and our semi-analytical calculation, we also benchmark our results with analytical formulas derived by Huang and Kim (HK) [81]. Below we quote without derivation

[74] In our theoretical formulation, we assume $z > 0$ for bunch head and $R_{56} > 0$ for normal bunch compression. Note that `elegant` uses a different convention; see later for more discussion.

[75] Note that numerical error can occur in the numerical integration of Eq. (3.52). Thus a sufficient number of Δs steps must be ensured to obtain converged result. This numerical requirement is much more alleviated than that imposed for particle tracking simulation.

Table 3.3: Initial parameters for study of LCLS BC2.

Name	Value	Unit
Beam energy	4.54	GeV
Beam (peak) current [before, after compression]	480, 4000	A
Initial beta function (β_{x0}, β_{y0})	105, 22	m
Initial alpha function $(\alpha_{x0}, \alpha_{y0})$	5, 0	
Chirp (magnitude)	39.83	m^{-1}
Rectangular dipole radius ρ_x	12.2	m
Total length of the compressor	22.1	m
Uncorrelated (rms) energy spread	3×10^{-6}	
Transverse normalized emittance	1	μm
Compression factor	8.32	

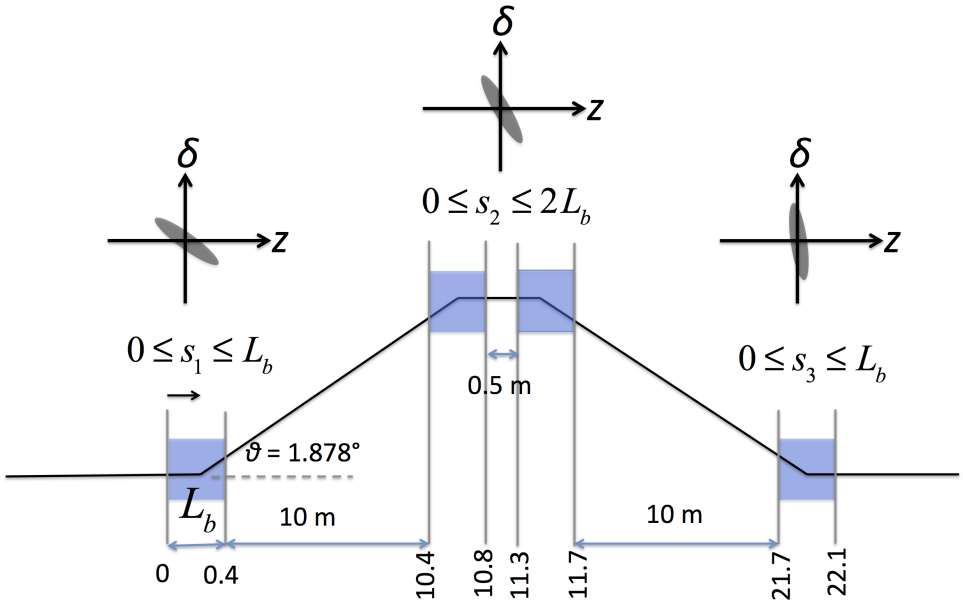

Figure 3.10: Schematic layout of a four-dipole bunch compressor chicane. The numbers indicating the path length coordinate are in unit of meter. The beam longitudinal phase space distributions evolve within the chicane.

the analytical formulas of CSR microbunching gain at the exit of the chicane, derived in Ref. [81]. The explicit expression of 1-D steady-state (ss) ultrarelativistic (UR) free space steady-state CSR impedance is

$$Z_{\mathrm{CSR}}^{\mathrm{ss,UR}}(k_z; s) = -\frac{iAk_z^{1/3}(s)}{|\rho_x(s)|^{2/3}}, A \approx -0.94 + 1.63i \tag{3.86}$$

which will be derived in Chapter 4. HK [81] solved Eq. (3.52) by method of iteration. This approach is

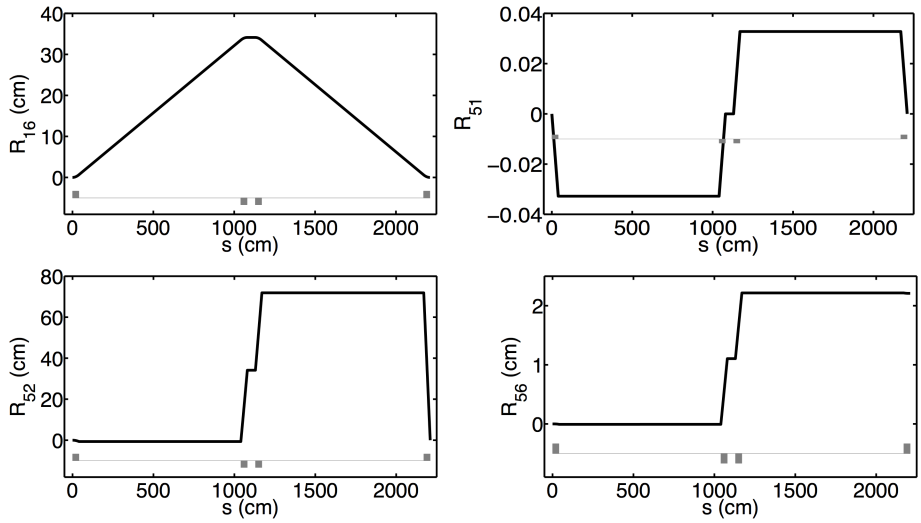

Figure 3.11: Transport functions of LCLS BC2.

suitable for the few-dipole configuration[76]. For the zeroth-order solution,

$$b_{[0]}^{(z)}(k_z;s) = b_0^{(z)}(k_z;s) \tag{3.87}$$

For the first-order solution,

$$b_{[1]}^{(z)}(k_z;s) = b_0^{(z)}(k_z;s) + \int_0^s d\tau K(\tau,s) b_{[0]}^{(z)}(k_z(\tau);\tau) \tag{3.88}$$

and the second-order solution,

$$b_{[2]}^{(z)}(k_z;s) = b_0^{(z)}(k_z;s) + \int_0^s d\tau K(\tau,s) b_{[1]}^{(z)}(k_z(\tau);\tau) \tag{3.89}$$

which can be expanded by Eq. (3.88),

$$\begin{aligned} b_{[2]}^{(z)}(k_z;s) = & \, b_0^{(z)}(k_z;s) \\ & + \int_0^s d\tau K(\tau,s) b_{[0]}^{(z)}(k_z(\tau);\tau) \\ & + \int_0^s d\tau K(\tau,s) \left\{ \int_0^\tau dt K(t,s) b_{[0]}^{(z)}(k_z(t);t) \right\} \end{aligned} \tag{3.90}$$

If only steady-state CSR effect is considered, the kernel function only exists within dipoles. Equation (3.90)

[76]In fact, in HK's derivation, they assumed three-dipole chicane, where the central two dipoles in Fig. 3.10 are assumed closely enough so that they play the role as that of three-dipole configuration.

can be further approximated as

$$\begin{aligned} b_{[2]}^{(z)}(k_z;s_f) &= b_0^{(z)}(k_z;s_f) \\ &+ \int_0^{L_b} ds_1 K(s_1,s_f) b_{[0]}^{(z)}(k_z(s_1);s_1) + \int_0^{2L_b} ds_2 K(s_2,s_f) b_{[0]}^{(z)}(k_z(s_2);s_2) \\ &+ \int_0^{2L_b} ds_2 K(s_2,s_f) \left\{ \int_0^{L_b} ds_1 K(s_1,s_2) b_{[0]}^{(z)}(k_z(s_1);s_1) \right\} \end{aligned} \tag{3.91}$$

Because of the simplicity of a chicane configuration shown in Fig. 3.10 (and the corresponding transport functions in Fig. 3.11), which is composed of only dipoles and drifts in between, the approximate transport functions can be analytically obtained by Eqs. (2.57) and (2.58). Substituting the resultant expressions for transport functions, $R_{51}(s)$, $R_{52}(s)$, $R_{56}(s)$, and $R_{56}(\tau \to s)$, into Eqs. (3.40) and (3.43), and integrating stage by stage in Eq. (3.91), we finally obtained the CSR microbunching gain as $G_f \equiv \left| b_{[2]}^{(z)}(k_z;s_f) \Big/ b_0^{(z)}(k_z;0) \right|$ with

$$G_f(\lambda = 2\pi/k_z) \approx \left| \tilde{G}_0 + \tilde{G}_1 I_{b,f} + \tilde{G}_2 I_{b,f}^2 \right| \tag{3.92}$$

where $I_{b,f}$ is the (peak) current at the exist of the chicane,

$$\tilde{G}_0 = \exp\left[-\frac{\bar{\sigma}_\delta^2}{2(1-hR_{56})^2} \right] \tag{3.93}$$

with $\bar{\sigma}_\delta = k_0 R_{56} \sigma_\delta$, $k_0 = k_z(s=0)$ is the initial modulation wavenumber

$$\tilde{G}_1 = \frac{A k_0^{4/3} R_{56} L_b}{\gamma_0 I_A \rho_x^{2/3}} \left[\left(F_0(\bar{\sigma}_x) + \frac{1 - e^{-\bar{\sigma}_x^2}}{2\bar{\sigma}_x^2} \right) e^{-\bar{\sigma}_\delta^2 / 2(1-hR_{56})^2} + F_1(hR_{56}, \bar{\sigma}_x, \alpha_{x0}, \phi, \bar{\sigma}_\delta) \right] \tag{3.94}$$

where $\bar{\sigma}_x = k_0 L_b \sqrt{\epsilon_{x0} \beta_{x0}} \big/ \rho_{x0}$ and $\phi = -\rho_x^2 R_{56} \big/ \beta_{x0} L_b^2$, and

$$\tilde{G}_2 = \left(\frac{A k_0^{4/3} R_{56} L_b}{\gamma_0 I_A \rho_x^{2/3}} \right)^2 F_0(\bar{\sigma}_x) F_2(hR_{56}, \bar{\sigma}_x, \alpha_{x0}, \phi, \bar{\sigma}_\delta) \tag{3.95}$$

$$F_0 = \frac{e^{-\bar{\sigma}_x^2} + \bar{\sigma}_x \sqrt{\pi} \mathrm{erf}(\bar{\sigma}_x) - 1}{2\bar{\sigma}_x^2} \tag{3.96}$$

with the error function

$$\mathrm{erf}(\zeta) \equiv \frac{2}{\sqrt{\pi}} \int_0^{\zeta} dt e^{-t^2} \tag{3.97}$$

$$F_1 = 2 \int_0^1 dt \frac{(1-t)H(t)}{(1-hR_{56}t)^{4/3}} \tag{3.98}$$

$$F_2 = 2 \int_0^1 dt \frac{(1-t)t(1-hR_{56})H(t)}{(1-hR_{56}t)^{7/3}} \tag{3.99}$$

$$H(t) = \exp\left\{ -\bar{\sigma}_x^2 \frac{(1-2t+\alpha_{x0}\phi t)^2 + \phi^2 t^2}{(1-hR_{56}t)^2} - \frac{\bar{\sigma}_\delta^2}{2(1-hR_{56}t)^2} \left[t^2 + \frac{(1-t)^2}{(1-hR_{56}t)^2} \right] \right\} \tag{3.100}$$

Note that Eq. (3.92) is expressed as a function of modulation wavelength at the exit of a chicane. In view of this, it can only provide the gain spectrum at a specific location. However, for particle tracking and our semi-analytical calculation, the gain function along a beamline (as a function of s) can be obtained in a given modulation wavelength [see Eq. (3.66)]. Thus we first illustrate the comparison between `elegant` tracking and our semi-analytical calculation. Both results present the evolution of bunching factors along a beamline. Figure 3.12 shows the dynamics of density bunching modulation or its ratio, the microbunching gain, along the chicane. The initial modulation wavelength is assumed 20 μm. As the beam enters the first dipole of the chicane, the bunching factor quickly drops first; this means that the density modulation is washed out a bit within the first dipole. This can be expected from the fact that R_{51} in Fig. 3.11 suddenly changes and the resultant longitudinal smearing $\Delta z \sim R_{51}\sigma_{x0}$. This gain drop is not toward zero, because $R_{51}\sigma_{x0} \approx 0.035 \times 100\ \mu\mathrm{m} = 3.5\ \mu\mathrm{m} < \lambda = 20\ \mu\mathrm{m}$ in the first dipole. When the beam goes into the second and third dipoles, the bunching factor is recovered a bit because R_{51}, R_{52}, and R_{56} increase a bit (see Fig. 3.12) and intend to *pull* the electrons back to the original position. Our reasoning so far is only based on knowledge of pure optics. When the beam reaches the last dipole, even though some transport functions (R_{51} and R_{52}, but not R_{56}) vanishes, the final bunching factor increases almost by a factor of 2. This is because the density and energy modulations convert by R_{56} and get amplified by CSR. Further, the density-energy conversion has been known as two-stage amplification. The multistage amplification will be introduced in Chapter 6. Figure 3.12 shows a comparison of the gain function $G(s)$ along the chicane lattice in the specific case of $\lambda = 20\ \mu$m. It can be seen that both `elegant` tracking and our semi-analytical Vlasov calculation match very well, even within the central two dipoles.

Figures 3.13 to 3.16 below demonstrate the intermediate results from `elegant` tracking at the exits of each dipole. The top left figures of Figs. 3.13 to 3.16 show the longitudinal phase space distribution, the top right subfigures demonstrate the longitudinal current density distribution, or z histogram, the bottom left sub-figures are the zoom-in of the central bins of z histogram, and the bottom right sub-figures the Fourier transformation of the histogram z population.

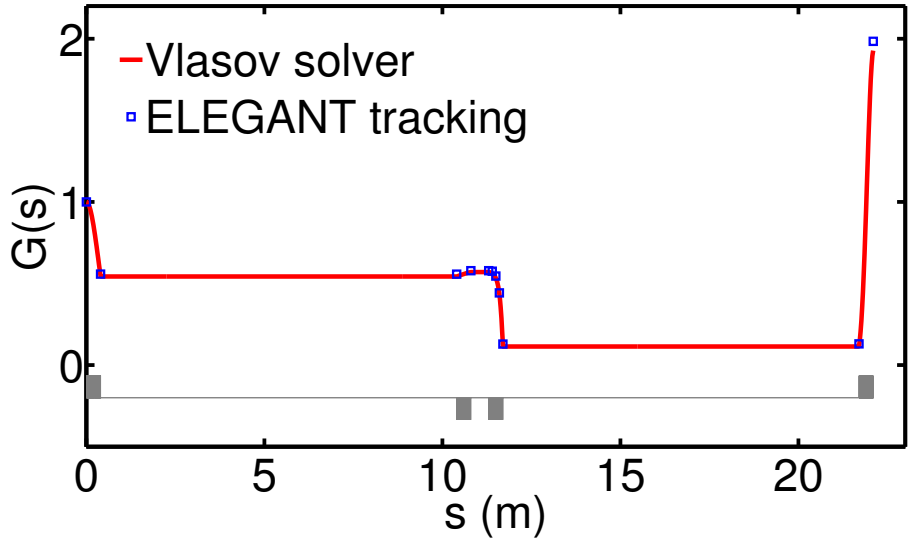

Figure 3.12: Steady-state CSR microbunching gain function $G(s)$. In this figure the modulation wavelength is 20 μm and initial modulation amplitude is assume 2.0% in `elegant` tracking. Other beam parameters are listed in Table 3.3.

From the Fig. 3.13 (at the exit of the first dipole), we can see that the (upper left) longitudinal phase space distribution features a chirp and reveals the sign convention used in `elegant`. The (upper right) current density figure demonstrates the flattop distribution where we prescribe ∼90 modulation wavelengths on the flattop and ∼150 on the full bunch duration for $\lambda = 20$ μm. The corresponding FFT spectrum is characteristic of this modulation: the peak frequency is at 14.99863 THz (or 19.988 μm), close to the desired modulation wavelength. Such clear spectral pick also reflects on the zoom-in figure of (lower right) current density distribution; the initial density modulation shows an excellent sinusoidal modulation, which matches the theoretical single-frequency model assumption.

It can be seen that from Figs. 3.14 and 3.15 (at the exit of the second and third dipole, respectively) the current density distributions (lower right) show a bit noisy. This can be expected due to the dispersive and low gain region here (see also Fig. 3.12). The FFT spectra appear to be noisy at higher frequencies but the dominant peak can be still clearly identified[77]. As the beam traverses at the last dipole, the CSR effects become significant as discussed above. Thus we see the dominant FFT spectral component becomes much larger than that at the second or third dipole. Also the current density distribution (lower right) features again a nice and clear modulation.

So far we have demonstrated results from `elegant` tracking and the semi-analytical Vlasov results. In

[77] In Fig. 3.14 we can see a second harmonic small peak present. If a beamline is with high gain, e.g. 100, this initial small peak may be eventually amplified.

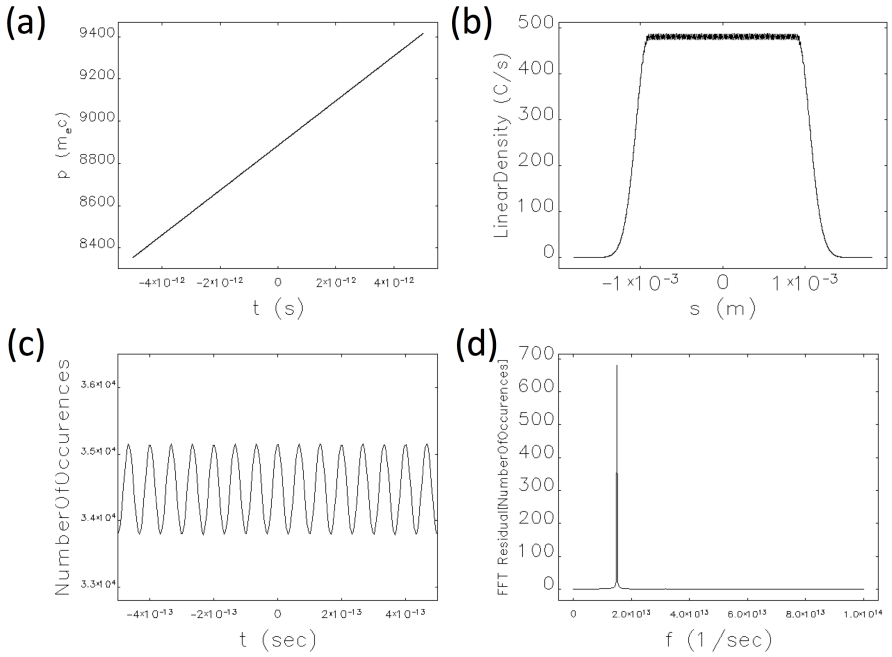

Figure 3.13: (a) Longitudinal phase space, (b) current density distribution (initial 2.0% modulation), (c) zoom-in current density distribution, and (d) FFT spectrum at the end of the first dipole, i.e. $z = 0.4$ m.

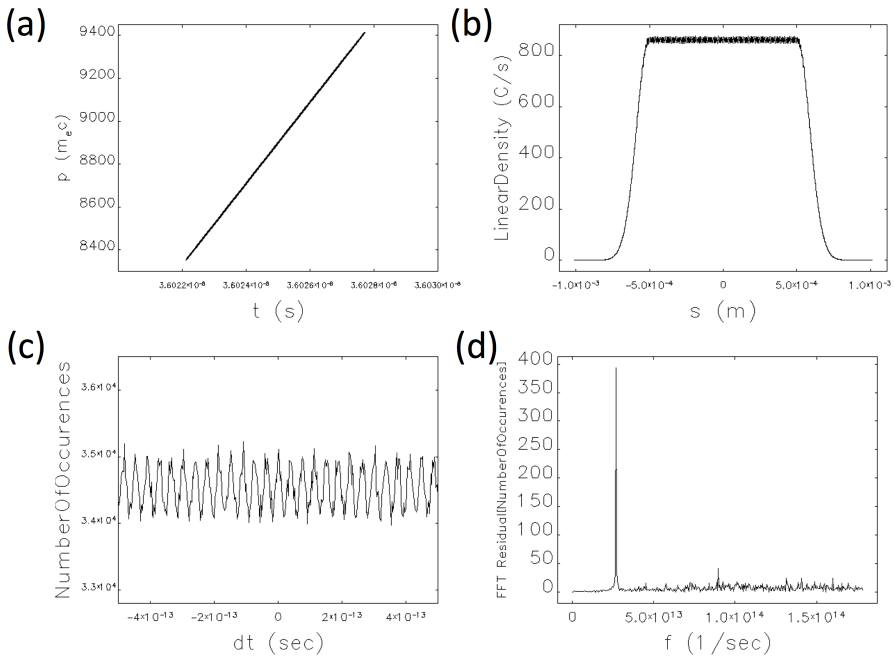

Figure 3.14: (a) Longitudinal phase space, (b) current density distribution (initial 2.0% modulation), (c) zoom-in current density distribution, and (d) FFT spectrum at the end of the second dipole, i.e. $z = 10.4$ m.

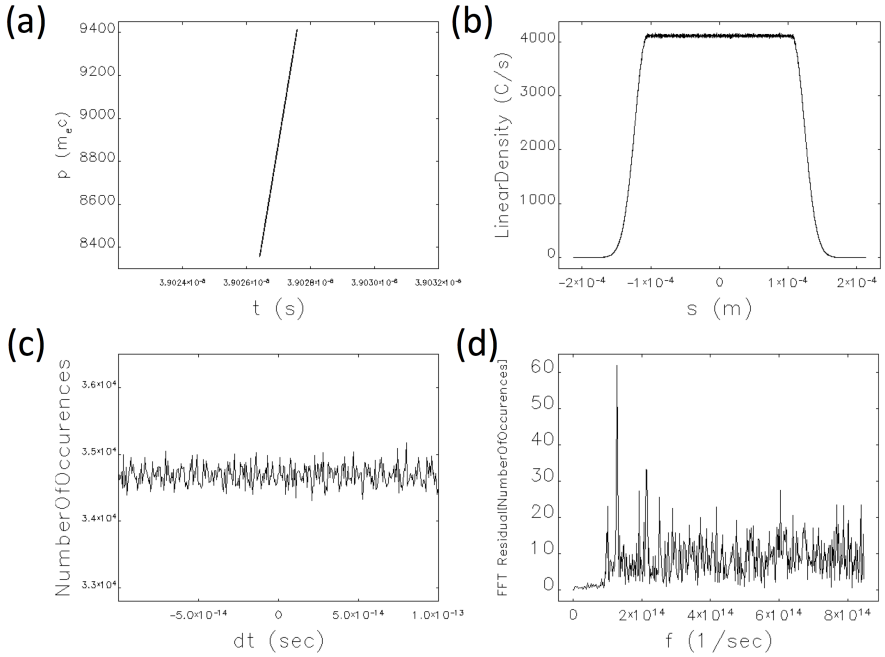

Figure 3.15: (a) Longitudinal phase space, (b) current density distribution (initial 2.0% modulation), (c) zoom-in current density distribution, and (d) FFT spectrum at the end of the third dipole, i.e. $z = 11.7$ m.

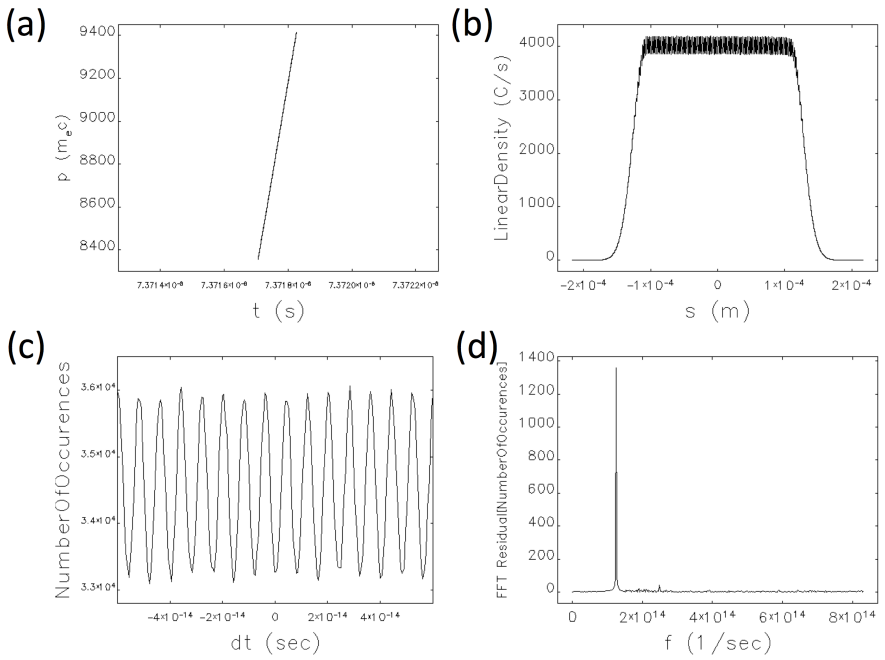

Figure 3.16: (a) Longitudinal phase space, (b) current density distribution (initial 2.0% modulation), (c) zoom-in current density distribution, and (d) FFT spectrum at the end of the last dipole, i.e. $z = 22.1$ m.

`elegant` those results are not based on arbitrarily chosen simulation parameters but extracted from careful convergence tests on various simulation parameters, including macroparticle number, number of integration kicks, CSR and histogram bins. The numerical setting of macroparticle number aims to reduce numerical noise due to very limited number of simulation particles employed in the tracking simulation. The setting of number of integration kicks ensures the convergence of numerical error due to finite/discrete mesh. The numerical noise can also arise from fluctuation due to size of binning when making a histogram. In addition, since the phase space modulation is quantified in frequency domain, i.e. Fourier transformation of the bunch current density, band-pass filtering may need to use to ensure the suppression of undesired (or unphysical) signal. We omit the details here but leave them in Chapter 5 and more detailed information in Ref. [173]. It is appropriate here that we summarize the simulation parameters from convergence tests and then begin to do production runs for a series of different initial modulation amplitudes to confirm that our simulated gain is indeed obtained in a linear amplification regime, as assumed by the theory.

In the following production runs, we would set:

- Number of macroparticles: 50×10^6 (or, R = 2500, number of particles in each CSR bin)
- Number of CSR bins: 20000 (or, F = 20, number of CSR bins for each modulation wavelength)
- Number of kicks: 400 (for tracking integration to a dipole)
- Number of histogram bins: 2000 (for data postprocessing)
- Number of clipped bins aside: 600 (to eliminate the end effects)
- Filter cutoff: 0.1 (to filter out the high harmonic frequencies)

Figure 3.17 demonstrates the results for scanning various initial modulation amplitudes. From the top left figure, we see that, within the scanned amplitude range (from 0.05 % to 2 %) of the initial modulatiom amplitudes, the amplification follows a linear relation. The top right figure can serve as double check whether the final dominant modulation wavelength is retained or drifted.

In Fig. 3.18 below we obtain the final gain spectrum by repeatedly scanning a series of modulation wavelengths λ from 2 to 70 μm. To particularly resolve the "dip" structure in the range from 5 to 10 μm, we additionally run the simulations at 1.0 % initial modulation amplitudes on finer wavelengths (5, 7, 8, and 9 μm). It can be seen from Fig. 3.18 that our Vlasov solver correctly produced the gain spectrum, compared with Fig. 3 of Ref. [79] and Fig. 1 of Ref. [81], particularly for the "dip" structure.

To end this section, we remind that a typical presentation of microbunching analysis is to plot the gain functions and spectra. The former provides a picture regarding spatial evolution of bunching factors, while the latter gives more complete information about the spectral response of a beamline to specific physical

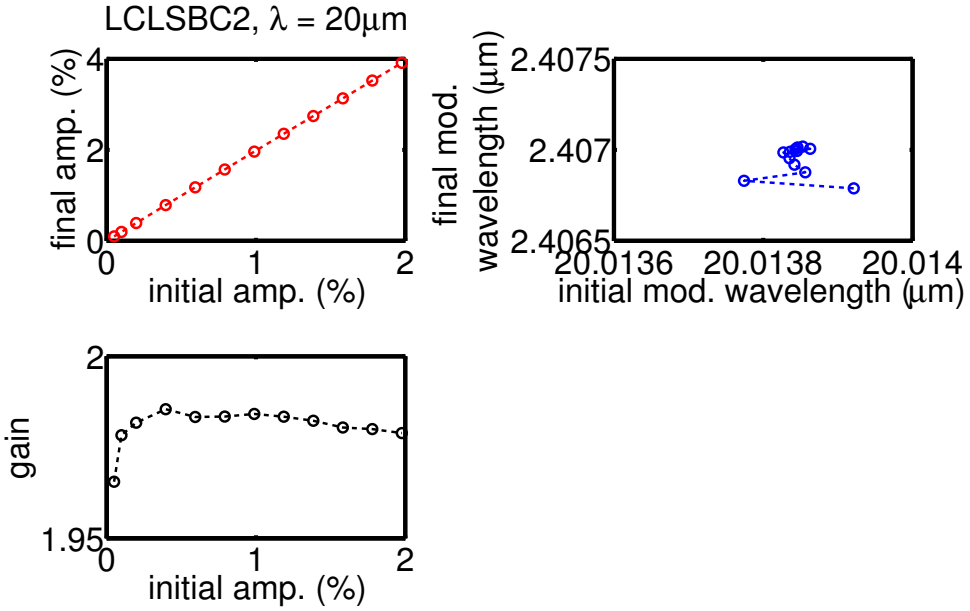

Figure 3.17: Amplitude dependence of CSR microbunching gain. In this figure the modulation wavelength is assume 20 μm. Due to the small gain, the amplification is linear in broad range of modulation amplitudes.

effects. A way to simultaneously demonstrate the spatial-spectral response is shown in Fig. 3.19 below.

3.7 Summary

As a summary in this chapter, here we distinguish in three viewpoints our work of the theoretical formulation from the existing work done in the early days. First, although there have been extensive studies on microbunching dynamics (see, for example, [84] and references therein), they mostly focus on bunch compressors in a linac-based free-electron laser (FEL) driver, as our first example demonstrates. There are still very limited works reported on quantitative microbunching gain studies in transport arcs or recirculation machines. To our knowledge, Borland first [23] did some preliminary studies of microbunching gains on Advanced Photon Source (APS) upgrade ERL machine using `elegant` tracking with several collective effects included. Further understanding of the underlying physics would require more detailed study of contribution of each individual physical mechanism as well as careful benchmarking of particle tracking results with theory. Thus, more focused analytical or semi-analytical studies of the longitudinal microbunching gain with numerical benchmarking serves as a purpose of our work. Second, the intuitive argument of quantifying microbunching in a beamline as the product of partial gains in each concatenated section is in general not self-consistent and the gain is found to be underestimated [175, 185]. Our semi-analytical Vlasov solver has implemented the extended theoretical formulations, which have been developed in Sec. 3.3. By incorporating with `elegant`, a widely used simulation package for particle tracking and beamline design, the semi-analytical Vlasov solver can adopt a general linear beamline lattice and all relevant beam and lattice parameters to

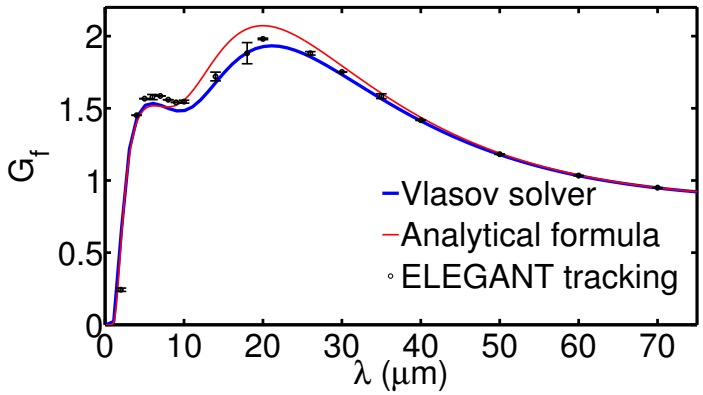

Figure 3.18: Gain spectrum $G_f(\lambda)$. The dot is given by the average of gains within the scanned modulation amplitude range (0.05% to 0.2%) while excluding those small amplitudes which produce wrong frequencies. The error bar length is quantified as two times of the standard deviations of the gains obtained for each different modulation amplitudes.

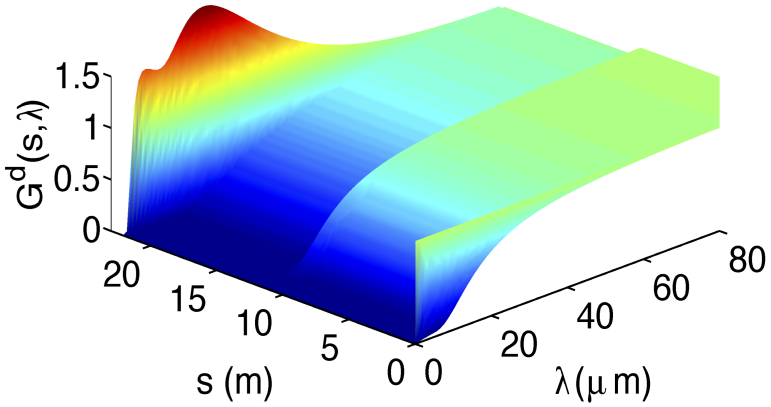

Figure 3.19: 3-D illustration of the spectral and temporal behavior of the CSR microbunching gain.

treat the microbunching analysis in a more convenient way. This also allows us to systematically study the impact of lattice design on MBI. Further studies are in Chapter 7. Third, by virtue of the general purpose of `elegant`, our Vlasov solver can serve as an option for machine optimization if MBI would be a concern in the beamline design.

CHAPTER 4
Collective Effects

We have outlined in Sec. 2.4 that to fully treat the beam-wave interaction in an electrodynamic system, one needs to solve the Vlasov-Maxwell equations, in which Vlasov equation describes the evolution of beam phase space distribution (beam dynamics), and Maxwell equations govern that of the electromagnetic waves (electrodynamics). Solving this beam-wave interaction system is a difficult problem in general, needless to say in large-scale particle accelerators. Fortunately, we can simplify the problem for our particular situation while maintaining sufficiently accurate results. The two approximations introduced in Sec. 2.4, the rigid beam approximation and impulse approximation, can achieve the goal and will lead to the concepts of wakefields and impedances. We can expect that, with these two approximations, the involvement of beam-wave interaction can now be separately analyzed as the problems of beam dynamics and electrodynamics. Note that this simplification is in methodology and does not mean that beam and wave are decoupled.

In this Chapter we start from introducing the basic concepts of wakefields and impedances in Sec. 4.1. Usually the concepts of wakefields and impedances are introduced to characterize the electromagnetic fields induced by a passing charged particle beam subject to vacuum pipe boundary conditions[78]. However in the dissertation the electromagnetic interactions of our particular interest are coherent synchrotron radiation (CSR) and longitudinal space charge (LSC) effects. Having remained to use the classical terminology of wakefield and impedances, we can still describe the collective interaction of CSR by extending the concept of vacuum pipe condition to the retardation condition. In order to calculate synchrotron radiation (SR) fields, we usually resort to two approaches: (i) the scalar and vector potentials for a charge-density distribution, and (ii) Lienard-Wiechard field for a two-particle interaction. The two approaches are in fact equivalent but in some situation one can be more convenient to formulate the problem than the other. To study the particular problem of CSR, the basic properties of SR pulse formation, including critical frequency, characteristic pulse width, and transverse and longitudinal formation lengths, will be introduced in Sec. 4.2.1 before we delve into our prime mission. Following Saldin et al. treatment using Lienerd-Wiechard field, the two-particle CSR kernels are derived in Sec. 4.2.2, which would serve as our building blocks in the subsequent derivation of various CSR impedance models. Although the frequency-domain treatment is our focus in this dissertation, the time-domain wakefields may provide a more intuitive picture regarding the underlying physics. Therefore CSR wakes for a Gaussian bunch is illustrated in Sec. 4.2.3. Having prepared all necessary information, in Sec. 4.2.3 to 4.2.5 we derive the CSR impedances including stationary, entrance and exit transient states. All the results are obtained assuming field propagation in free space. In some situations when the shielding effect dominates, e.g. the pipe is very close to the circulating beam, a modified CSR impedance should be employed and the formula is quoted [204, 7] in Sec. 4.2.6. Section 4.2.7 briefly summarizes the CSR impedance models, which have been implemented in our semi-analytical Vlasov solver. In addition to CSR,

[78]The conditions can be either finite conductivity (or resistivity) or the structure discontinuity of the beam pipe.

LSC in short-range or high-frequency regimes can play a role. In Sec. 4.3, we derive the free-space case and, similar to Sec. 4.2.7, summarizes the LSC impedance models for the case with boundary conditions. As introduced in Sec. 4.4, the third collective driving force can be the linac geometric effect, which can play an important role in recirculating or ERL accelerators.

Part of the work in this Chapter, especially Sec. 4.2.4 and 4.2.5 mainly contributed by R. Li, has been published with the title *CSR Impedance for Non-ultrarelativistic Beams*, in Proceedings of IPAC2015, Richmond, VA, USA (MOPMN004). The newly derived impedance expressions for non-ultrarelativistic and exit transient cases have been implemented in our Vlasov solver.

4.1 Basic theories

4.1.1 Wakefields and impedances

In our specific case of constructing wakefields and impedances such as CSR (Sec. 4.2), the rigid beam approximation can imply that the radiation reaction (or, CSR-induced reaction) right on the emitting particle itself (at retarded time) is neglected. Note that this approximation applies to source particles[79]. As for the wakefields due to a periodic array of geometric cavity structures in a section of linac, i.e. linac-geometric effect (Sec. 4.4), the energetic beams are usually affected little during the passage of such a structure, from which the rigid beam approximation can be valid. In the above two cases, the wakefields and impedances are solely determined by the properties of the environment, i.e. independent of beam properties[80]. For space charge force, e.g. LSC (Sec. 4.3), the nature of it, depending on the beam properties, is supposed to be excluded from the wakefield-impedance treatment. It turns out, however, that the space charge forces can almost fit into the wakefield-impedance framework, and when that is done (an illegitimate step), their wake functions will depend on beam properties such as the transverse beam size $\sigma_{x,y}$ and the beam energy γ [35]. The impulse approximation states that what is really important to collective beam dynamics is the impulse (an integrated quantity of force over a distance or time duration), instead of the instantaneous force. This approximation[81], applying to test particles, greatly simplifies the analysis, because we do neither need to know the detailed $\mathbf{E}(\mathbf{r},t)$ and $\mathbf{B}(\mathbf{r},t)$ nor the instantaneous Lorentz force.

To introduce the wakefields and impedances, we begin from formulating the Lorentz force on a test particle (see Fig. 4.1) [92],

$$\mathbf{F}(\mathbf{r}_1,s_1,\mathbf{r}_2,s_2;t)=q_2\left(\mathbf{E}(\mathbf{r}_1,s_1,\mathbf{r}_2,s_2;t)+\frac{\mathbf{v}_2}{c}\times\mathbf{B}(\mathbf{r}_1,s_1,\mathbf{r}_2,s_2;t)\right) \tag{4.1}$$

[79] Note that we are interested in 1-D CSR, for which the rigid beam/line approximation works fine.

[80] In many situations, the studies of wakefields and impedances are based on ultrarelativistic approximation, i.e. $\gamma\to\infty$. The energy dependence of the beam thus becomes implicit. When we consider the non-ultrarelativistic case of $\gamma<\infty$ (still $\beta\to 1$), the statement is no longer valid and the situation becomes much more involved (Sec. 4.2.4).

[81] The impulse approximation in fact does not apply to transient CSR. This also explains why in our subsequent analysis we intend to quantify CSR wakefield or impedance per unit length.

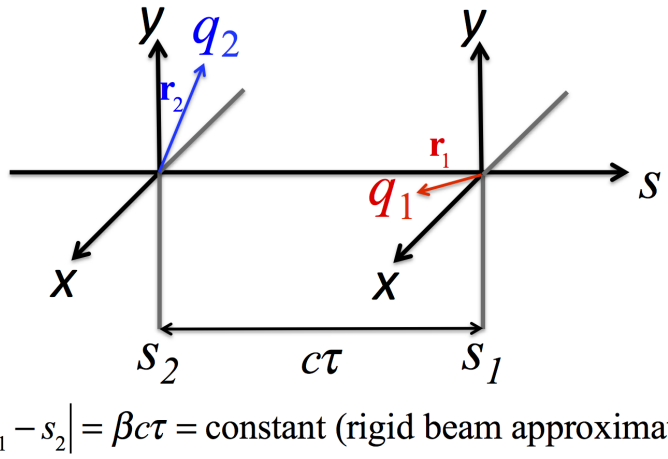

Figure 4.1: Definition of source (q_1) and test (q_2) particle coordinates, $\mathbf{r}_1$ and $\mathbf{r}_2$, respectively.

where the test particle is denoted with a subscript 2, and the source particle with 1. **E** and **B** are electric and magnetic fields produced by the source particle, **v** is the velocity vector, **r** is the transverse coordinate vector, s is the longitudinal coordinate and t the time. The rigid beam approximation sets up the following condition,

$$|s_2 - s_1| = \beta c\tau = \text{constant} \tag{4.2}$$

Now the wakefield can be defined as the force integrated over a distance per unit charges (impulse approximation),

$$\vec{\bar{W}}(\mathbf{r}_1, \mathbf{r}_2, \tau) \equiv -\frac{\beta c}{q_1 q_2} \int dt \mathbf{F}(\mathbf{r}_1, \mathbf{r}_2, \tau; t) \tag{4.3}$$

Here we use overline to indicate that it is an integrated quantity. Written in terms of longitudinal ($\|$) and transverse ($\perp$) components, we have

$$\bar{W}^{\|}(\mathbf{r}_1, \mathbf{r}_2, \tau) = -\frac{\beta c}{q_1 q_2} \int dt F^{\|}(\mathbf{r}_1, \mathbf{r}_2, \tau; t) = -\frac{c}{q_1} \int dt \beta \cdot \mathbf{E}(\mathbf{r}_1, \mathbf{r}_2, \tau; t) \tag{4.4}$$

and

$$\bar{W}^{\perp}(\mathbf{r}_1, \mathbf{r}_2, \tau) = -\frac{\beta c}{q_1 q_2} \int dt \vec{F}^{\perp}(\mathbf{r}_1, \mathbf{r}_2, \tau; t) \tag{4.5}$$

The last equality of Eq. (4.4) assumes the contribution from $\mathbf{v}_{2,\perp} \times \mathbf{B}_{\perp}$ is negligible. The definition of wakefield can be presented in a more general way by first decomposing the transverse beam distribution into orthogonal moments, e.g. the $\cos m\theta$-ring beam in polar coordinates [35],

$$\int \beta c dt \vec{F} = -\nabla V, \text{ with } V = q_2 I_m \bar{W}_m(z) r^m \cos m\theta \tag{4.6}$$

where I_m is the m-th moment of the source particle beam, $I_0 = q_1$ and $I_m = q_1 a^m$ for offset point charge where a is the transverse offset. In our case, we are interested in the collective effects per unit length[82] and on axis (i.e. $\mathbf{r}_1 = \mathbf{r}_2 = 0$). The wakefield can be redefined by further dividing $\int \beta c dt$ in the above equations. Having done so, we have

$$\bar{W}^{\parallel} \to W^{\parallel}(\tau) = -\frac{1}{q_1 q_2} F^{\parallel}(\mathbf{r}_1, \mathbf{r}_2, \tau; t) = -\frac{1}{q_1} E_s(\mathbf{r}_1, \mathbf{r}_2, \tau; t) \tag{4.7}$$

$$\bar{W}^{\perp} \to W^{\perp}(\tau) = -\frac{1}{q_1 q_2} \vec{F}^{\perp}(\mathbf{r}_1, \mathbf{r}_2, \tau; t) \tag{4.8}$$

Note that the overline has been removed. In what follows when mentioning wakefields or impedances, we have assumed those quantities are expressed in unit of length. Note that Eqs. (4.4) and (4.5) are defined in time domain. Another useful and equivalent concept, quantified in frequency domain, is called impedances. The impedance is defined by Fourier transformation[83] of wakefields. The longitudinal and transverse impedances are defined as

$$Z_m^{\parallel}(k) = \int_{-\infty}^{\infty} \frac{dz}{c} W_m^{\parallel}(z) e^{-ikz} \tag{4.9}$$

$$Z_m^{\perp}(k) = i \int_{-\infty}^{\infty} \frac{dz}{c} W_m^{\perp}(z) e^{-ikz} \tag{4.10}$$

where the imaginary unit i ahead of Eq. (4.10) is added by convention[84] [85]. Below our analysis will be on longitudinal collective effect. When the collective beam-wave interaction occurs in a short range, e.g. within the same bunch, we term short-range wakefield or high-frequency impedance for the induced electromagnetic fields. This is of our primary interest. For the opposite case when the collective interaction happens in a long range, e.g. in a bunch train, we call long-range wakefield or low-frequency impedance.

Even though the wakefields, defined in time domain, can be intuitive, the impedance concept in some situations will be more natural in analysis since it can be related by Ohm's law. Assume a (coasting) beam travels with current I_0 and with the longitudinal single spatial frequency k,

$$I_0(z, t) = \hat{I}_0 e^{ikz} \tag{4.11}$$

[82] For steady-state case, this does not make a difference. For transient state, it does.

[83] To be more precise, we can define the impedance as the Laplace transformation of the walefields. When causality is imposed, the two definitions are equivalent.

[84] The corresponding transverse force thus becomes $\vec{F}_{\perp} = iq_2 J_m(s,t) m r^{m-1} (\hat{r} \cos m\theta - \hat{\theta} \sin m\theta) Z_m^{\perp}(k)$ [35].

[85] For reference, the inverse Fourier transformations are defined as

$$W_m^{\parallel}(z) = \frac{1}{2\pi} \int_{-\infty}^{\infty} dk Z_m^{\parallel}(k) e^{ikz}$$

$$W_m^{\perp}(z) = \frac{-i}{2\pi} \int_{-\infty}^{\infty} dk Z_m^{\perp}(k) e^{ikz}$$

.

The electric field, which the beam left behind or radiated ahead, can be expressed by superposition

$$\begin{aligned} E_s(z,t) &= -\frac{1}{c}\int_{-\infty}^{\infty} d\zeta I_0(\zeta,t) W_0^{\parallel}(z-\zeta) \\ &= \frac{1}{c}\int_{-\infty}^{\infty} d\xi I_0(z-\xi,t) W_0^{\parallel}(\xi), \text{ with } \xi = z-\zeta \\ &= \frac{1}{c} I_0(z,t)\int_{-\infty}^{\infty} d\xi e^{-ik\xi} W_0^{\parallel}(\xi) \\ &= I_0(z,t) Z_0^{\parallel}(k) \end{aligned} \tag{4.12}$$

where Eq. (4.9) has been used at the last step. This is analogous to Ohm's law[86]. Here the physical meaning of impedance can be interpreted as the induced electric field (in frequency domain, a complex quantity in general) when a beam went through with unity current ($|I_0(z,t)| = \hat{I}_0 = 1$).

Assume the electromagnetic field generated by a source particle (or a particle distribution) has been obtained. A way to derive the expression of a wakefield is to first calculate the energy loss rate (of test particle), i.e. $d\mathcal{E}/cdt = e\vec{\beta}\cdot\mathbf{E}$, and then relate the energy loss to Eq. (4.4) or (4.7). The corresponding impedance can be obtained in (at least) two ways. One is to take Fourier transformation of the obtained wakefield expression, i.e. Eq. (4.9) or (4.10). The other is to apply the aforementioned interpretation of physical meaning of impedance: substitute an unity sinusoidal modulation source into Eq. (4.12) and derive the induced electric field (or wakefield). This quantity in frequency domain is the corresponding impedance expression.

So far we have briefly introduced the wakefields, Eqs. (4.7) and (4.8), and impedances, Eqs. (4.9) and (4.10). Although the wakefields or impedances of higher orders can be important in some situations, we only focus on the case of $m = 0$ and longitudinal effects. Throughout the dissertation, we use CGS unit, unless otherwise specified. Table 4.1 and 4.2 summarize the units of wakefields and impedances in CGS and MKS system. Conversion between the two systems can be done by using the relation

$$\frac{Z_0 c}{4\pi} = 1 \tag{4.13}$$

where $Z_0 = \sqrt{\mu_0/\epsilon_0} \approx 120\pi\ \Omega$ and the speed of light in vacuum $c = 1/\sqrt{\epsilon_0\mu_0}$.

4.1.2 Retarded potentials

Before proceeding to the next section, for completeness basic formulas are given without further derivation. These expressions have been introduced in classical electrodynamics course [87]. Equations (4.14) amd (4.15)

[86] The common expression of Ohm's law in circuit electronics can be $V = IZ$. A difference of length dimension is because the impedance in our case is measured per unit length.

Table 4.1: Unit conversion of wakefields between CSG and MKS.

	$\bar{W}_0^{\parallel}$	$\bar{W}_1^{\perp}$
CGS	cm^{-1}	cm^{-2}
MKS	Volt/Coulomb	Volt/Coulomb/m

Table 4.2: Unit conversion of impedances between CSG and MKS.

	$\bar{Z}_0^{\parallel}$	$\bar{Z}_1^{\perp}$
CGS	sec-cm^{-1}	sec-cm^{-2}
MKS	Ohm	Ohm/m

are representations of $\mathbf{E}$ and $\mathbf{B}$ in terms of scalar ϕ and vector $\mathbf{A}$ potentials. Equation (4.15) is equivalent to Gauss' law for magnetostatics and Eq. (4.14) results from Faraday's law.

$$\mathbf{E} = -\nabla\phi - \frac{\partial \mathbf{A}}{c\partial t} \tag{4.14}$$

$$\mathbf{B} = \nabla \times \mathbf{A} \tag{4.15}$$

For an ensemble of charged particles, we can treat them as a continuous time-dependent current and charge distributions. The electromagnetic fields generated by the charged particles can be obtained through superposition of individual contributions and can be expressed in terms of scalar and vector potentials (see also Fig. 4.2 below)

$$\phi(s,t) = \int_{-\infty}^{\infty} ds' \frac{\rho(s',t')}{|\mathbf{r}(s) - \mathbf{r}(s')|} \tag{4.16}$$

$$\mathbf{A}(s,t) = \int_{-\infty}^{\infty} ds' \frac{\vec{\beta}(t')\rho(s',t')}{|\mathbf{r}(s) - \mathbf{r}(s')|} \tag{4.17}$$

where prime ($\prime$) denotes the source charges. In Eqs. (4.16) and (4.17), the denominator can be determined by the retardation conditions, which can be expressed as

$$t' = t - |\mathbf{r}(s) - \mathbf{r}(s')|/c \tag{4.18}$$

For a single point source charge, using Eqs. (4.14) to (4.18) and $\rho(s,t) = q\delta(\mathbf{r} - \mathbf{r}_0(t))$, we can obtain the so-called Lienard-Wiecherd field generated from a source particle,

$$\mathbf{E}(\mathbf{r},t) = e\left[\frac{\hat{n} - \vec{\beta}}{\gamma^2(1 - \vec{\beta}\cdot\hat{n})^3 L^3}\right]_{\mathrm{ret}} + \frac{e}{c}\left[\frac{\hat{n} \times \left\{(\hat{n} - \vec{\beta}) \times \dot{\vec{\beta}}\right\}}{\gamma^2(1 - \vec{\beta}\cdot\hat{n})^3 L^3}\right]_{\mathrm{ret}} \tag{4.19}$$

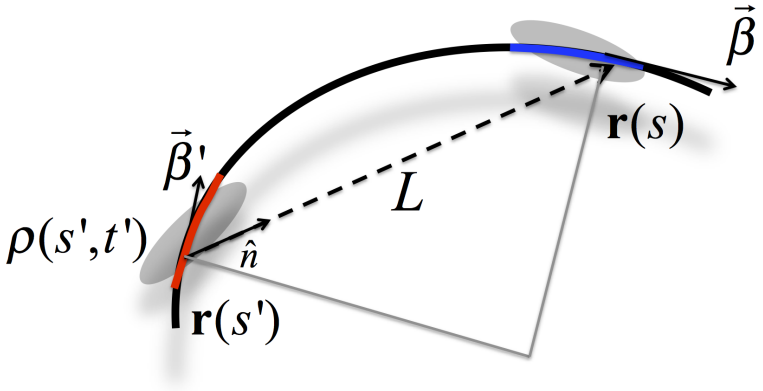

Figure 4.2: Illustration of the geometrical tail-head electromagnetic interaction. The primed quantities denote those evaluated at retarded time. See the explanation in the context.

$$\mathbf{B} = [\hat{n} \times \mathbf{E}]_{\text{ret}} \tag{4.20}$$

where, with no confusion, we omitted the superscript primes ($\prime$). The subscript [ret] is used to denote that the quantities are evaluated at retarded time. $\hat{n}$ is the unit vector directed from source particle to test particle (or, observation point). $\vec{\beta} = \mathbf{v}/c$ and γ are Lorentz relativistic factors (of source particle) and $\dot{\vec{\beta}} = d\beta \Big/ dt$. See Fig. 4.2 for the aforementioned notations.

4.2 Coherent synchrotron radiation (CSR)

4.2.1 Basic properties of synchrotron radiation (SR)

The following discussion, which we largely follow Stupakov's USPAS lecture [162], of some properties of SR is based on the situation drawn in Fig. 4.3. An observer is located at O in the plane of the particle trajectory far away from the emission site. The observer will see a periodic sequence of pulses of electromagnetic radiation with the period equal to the revolution period of the particles, say, around a storage ring. Each pulse is emitted from the region $x \approx z \approx 0$. It can be imagined that it takes some time and space for a moving charge particle to generate radiation. In this section we try to estimate what fraction of the lengths of the particle trajectory are involved into the formation of the synchrotron pulse. We first estimate the longitudinal and transverse sizes for the synchrotron radiation pulse and then relate them to the requirements of obtaining a steady-state/stationary radiation and the radiation shielding effect. The discussion is based on single-particle analysis. We then analyze the radiation of a bunch of particles.

Using the fact that $R \approx r - \rho_x \sin \omega_r \tau$ and defining the dimensionless variable $\xi = c\tau/\rho = \omega_r \tau$, the vertical magnetic field B_y at O can be obtained by Eqs. (4.15) and (4.17) [or Eq. (4.20)] and approximately

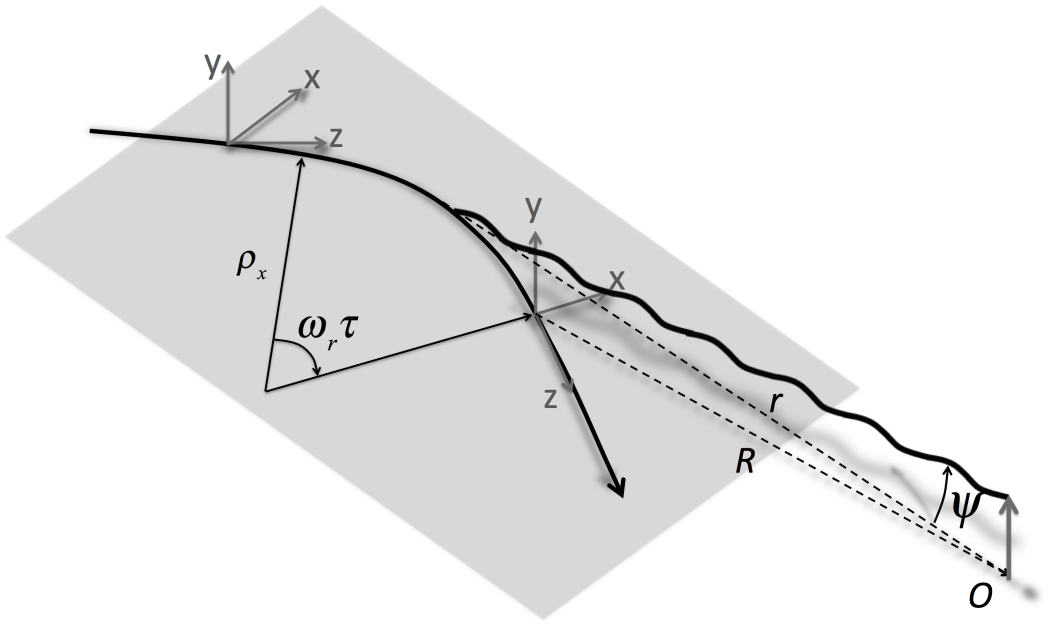

Figure 4.3: Schematic drawing of a particle trajectory, its radiation, and the location of the observation. When the observer at O receives the radiation, the source (emitting) particle had traveled an angle of $\xi = \omega_r \tau$.

expressed as

$$B_y(t) \approx \frac{4q}{cr\rho} \frac{1/\gamma^2 - \xi^2}{\left(\xi^2 + 1/\gamma^2\right)^3} \tag{4.21}$$

with the retardation condition $t = r/c + \rho/c\left(\xi/2\gamma^2 + \xi^3/6\right)$, and $\rho = \rho_x$ is the bending radius.

To proceed, let us define the dimensionless t variable as follows,

$$\hat{t} \equiv (t - r/c)\, c\gamma^3/\rho \tag{4.22}$$

and the normalized field

$$\hat{B} \equiv B_y\left(cr\rho/4q\gamma^4\right) \tag{4.23}$$

Then Eq. (4.21) can be rewritten as

$$\hat{B}(\hat{t}) \equiv \frac{1-\zeta^2}{(\zeta^2+1)^3}, \text{ with } \hat{t} = \frac{1}{2}\zeta + \frac{1}{6}\zeta^3 \text{ and } \zeta = \gamma\xi \tag{4.24}$$

Now $\hat{B}$ has a simpler form than B_y, and ζ implicitly depends on $\hat{t}$. If we plot $\hat{B}(\hat{t})$, we find in Fig. 4.4 below

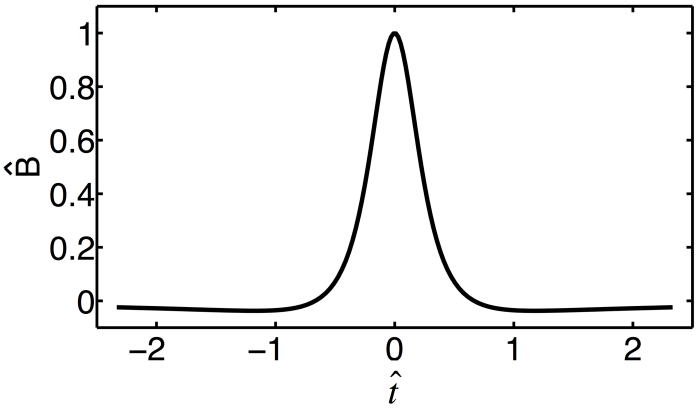

Figure 4.4: Plot of $\hat{B}$ vs. $\hat{t}$. See Eq. (4.24).

that[87]

$$\Delta\hat{t} \sim 1 \tag{4.25}$$

which means

$$\Delta t \sim \rho/c\gamma^3 \tag{4.26}$$

If we take Fourier-transform on Eq. (4.24), i.e. $\hat{B}(\hat{t}) \overset{F.T.}{\leftrightarrow} \tilde{B}(\hat{\omega})$[88], the characteristic spectral width is of $\Delta\hat{t}^{-1}$,

$$\Delta\hat{\omega} \sim 1 \tag{4.27}$$

or

$$\Delta\omega \sim c\gamma^3/\rho \tag{4.28}$$

Equations (4.25) to (4.28), the characteristic widths of temporal and spectral pulses, are our first result of SR properties. In addition, the spectrum of a synchrotron radiation pulse is also characterized by the so-called critical frequency ω_c, defined as

$$\omega_c = 3c\gamma^3/2\rho \tag{4.29}$$

Next, we discuss the formation lengths, including longitudinal and transverse formation lengths. By the longitudinal formation length, $\ell_\parallel$, we mean the length scale a radiating particle should take to generate

[87] If we plot $\hat{B}(\zeta)$, the characteristic width is similar, i.e. $\Delta\zeta \sim 1$. This means that $\Delta\xi \sim \gamma^{-1}$.

[88] In what follows, if we intend to skip the detailed derivation in Fourier transforming a quantity, we use this shorthand notation.

a radiation pulse as Fig. 4.4 shows. From Fig. 4.4, we have also known

$$\Delta\xi \sim 1/\gamma \tag{4.30}$$

which means the radiating particle travels for the time

$$\tau \sim \rho/c\gamma \tag{4.31}$$

The corresponding length as the longitudinal formation length is

$$\ell_{\parallel} \sim c\tau \sim \rho/\gamma \tag{4.32}$$

The practical importance of this formation length is that one has to have the length of the bending magnet several times longer than $\ell_{\parallel}$ in order to generate the full spectrum of SR, more precisely, to cover SR spectrum around ω_c. Radiation from a magnet that is shorter than $\ell_{\parallel}$ would have very different properties. The radiation pulse will not be like Fig. 4.4 but the two ends would be cut somewhere. In fact this sudden change or discontinuity at both ends corresponds to the so-called edge radiation [26].

Note that the above derived formation length characterizes the spectral width around ω_c. Of our particular interest, we want to find out the formation length, which covers low-frequency range, i.e. $\omega \ll \omega_c$, or with the wavelength comparable to bunch length. To do so, we need to know the radiation field in frequency domain. This can be done by Fourier transforming Eq. (4.21), i.e

$$B_y(\tau) \leftrightarrow \tilde{B}_y(\omega) \tag{4.33}$$

Presuming $\tilde{B}_y(\omega)$ has been obtained from Eq. (4.15), we have the equivalent expression in frequency domain ($\omega = ck$),

$$\tilde{B}_y(\omega) = \frac{i\omega}{c}\tilde{A}_x(\omega) \tag{4.34}$$

It turns out that the vector potential can be analytically obtained and is written as

$$\tilde{A}_x(\omega) = -\frac{q\rho}{c^2 r}e^{i\omega r/c}\int_{-\infty}^{\infty} d\xi\ \xi e^{i\left(1/\gamma^2+\xi^2/3\right)\omega\rho\xi/2c} = -\frac{iq\rho}{c^2 r\gamma^2}e^{i\omega r/c}F\left(\frac{3\omega}{4\omega_c}\right) \tag{4.35}$$

with

$$F(x) = \frac{2}{\sqrt{3}}K_{2/3}\left(\frac{2x}{3}\right) \tag{4.36}$$

where K is the Bessel function of the second kind.

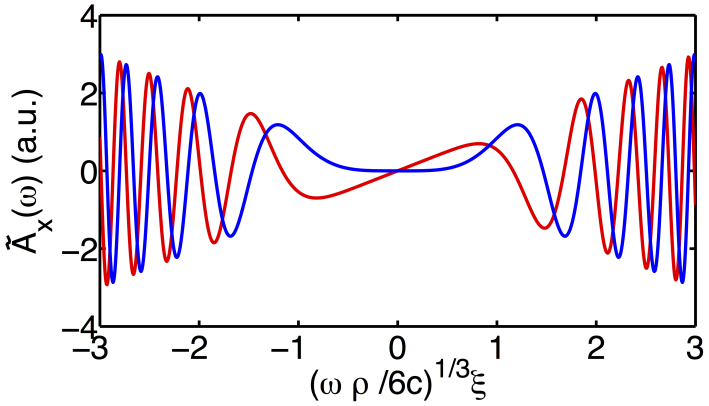

Figure 4.5: Plot of $\tilde{A}_x(\omega)$ vs ξ . The red curve represents the real part and the blue for the imaginary part.

The integrand of Eq. (4.35) is shown in Fig. 4.5 below as a function ξ. One can see that the most contributed region to the integration is within the central portion[89]. That is,

$$\Delta\xi \sim \left(\frac{c}{\rho\omega}\right)^{1/3} \tag{4.37}$$

We have known $\xi = c\tau/\rho$, thus

$$\ell_{\parallel} \sim \rho\Delta\xi \sim \rho^{2/3}\lambda\!\!\!^{-1/3} \tag{4.38}$$

where $\lambda\!\!\!^{-} \equiv \lambda/2\pi = k^{-1}$.

Equation (4.38) is the longitudinal formation length for the low-frequency regime of radiation spectrum. This will be used as the condition to determine if the CSR from a beam entering a bending dipole reaches steady/stationary state.

We have already estimated the longitudinal formation length. Before introducing the transverse formation length, we discuss a bit the energy spectrum. The energy spectrum is defined as the energy radiated per unit frequency interval per unit solid angle and can be expressed as

$$\frac{d^2\mathcal{W}}{d\omega d\Omega} = \frac{c^3 r^2}{4\pi^2}\left|\tilde{B}_y(\omega)\right| \tag{4.39}$$

If the observation lies on the plane of particle orbit (see Fig. 4.3), substituting Eq. (4.35) into Eq. (4.34) and inserting in Eq. (4.39) can give the resultant expression. For more general case of $\psi \neq 0$, the energy

[89] An idea behind evaluating this integral is the steepest descent method.

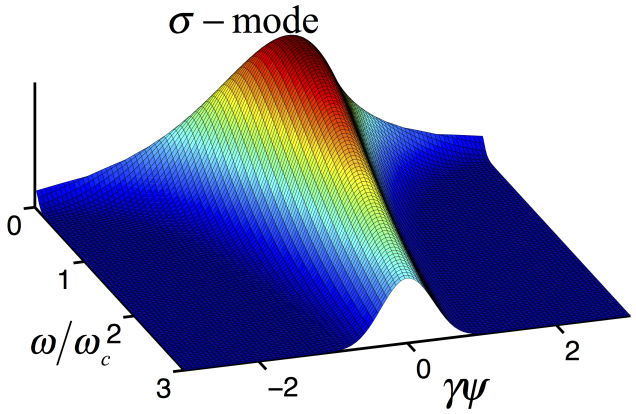

Figure 4.6: Intensity of σ-mode synchrotron radiation spectrum. See Eq. (4.40).

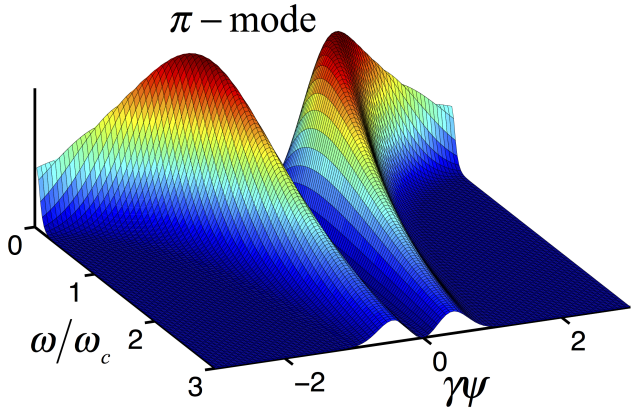

Figure 4.7: Intensity of π-mode synchrotron radiation spectrum. See Eq. (4.40).

spectrum is written as [87],

$$\begin{aligned}\frac{d^2\mathcal{W}}{d\omega d\Omega} &= \frac{q^2}{3\pi^2 c}\frac{9\gamma^2}{4}\left(\frac{\omega}{\omega_c}\right)^2\left(1+\gamma^2\psi^2\right)^2\left[K_{2/3}^2(\zeta)+\frac{\gamma^2\psi^2}{1+\gamma^2\psi^2}K_{1/3}^2(\zeta)\right] \\ &= [\sigma-\text{mode}]+[\pi-\text{mode}]\end{aligned} \tag{4.40}$$

where

$$\zeta = \frac{\omega\rho}{3c}\left(\frac{1}{\gamma^2}+\psi^2\right)^{3/2} = \frac{\omega}{2\omega_c}\left(1+\gamma^2\psi^2\right)^{3/2} \tag{4.41}$$

The first term on RHS of Eq. (4.40) is the so-called σ-mode, in which the radiation polarization is in the plane of particle trajectory. The second term is π-mode, in which the radiation polarization is perpendicular to the orbit plane.

We are particularly interested in the formation length at $\omega \ll \omega_c$. Now we want to estimate the

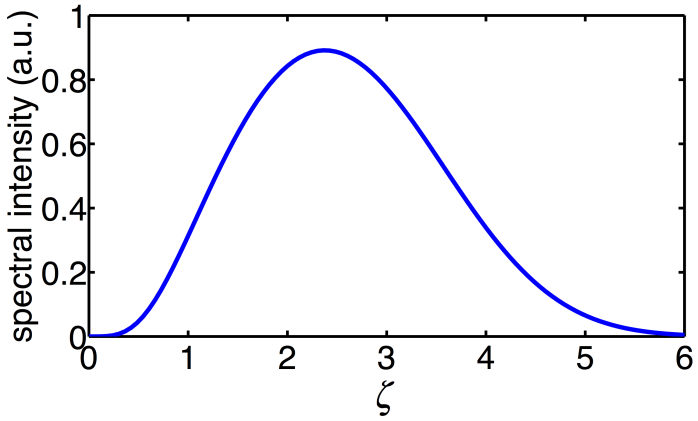

Figure 4.8: Angular dependence of synchrotron radiation spectral intensity at $\omega \ll \omega_c$.

transverse angular spread $\Delta\psi$ in this regime. Equation (4.42) is the approximate expression of Eq. (4.40)

$$\left.\frac{d^2\mathcal{W}}{d\omega d\Omega}\right|_{\omega\ll\omega_c} \sim \left(\frac{\omega\rho}{c}\right)^{2/3}\gamma^2\zeta^{4/3}\left[K_{2/3}^2(\zeta)+K_{1/3}^2(\zeta)\right] \tag{4.42}$$

and Fig. 4.8 plots the dependence on ζ, from which the characteristic width can be estimated as

$$\Delta\zeta \approx 3 \tag{4.43}$$

From Eq. (4.41), $\zeta \approx \frac{\omega}{2\omega_c}\gamma^3\psi^3$, we have

$$\Delta\psi \sim \left(\frac{c}{\omega\rho}\right)^{1/3} = \left(\frac{\lambda\!\!\!^{-}}{\rho}\right)^{1/3} \tag{4.44}$$

The transverse divergence of the radiation pulse is around $k_\perp \approx k\Delta\psi$. At low frequency range,

$$\ell_\perp \sim k_\perp^{-1} \sim \frac{\lambda\!\!\!^{-}}{\Delta\psi} \sim \rho^{1/3}\lambda\!\!\!^{-2/3} \tag{4.45}$$

This transverse formation length corresponds to the (minimal) transverse size needed for formation of radiation and is also called the transverse coherent length. The practical importance of the transverse formation length is that the radiation can be suppressed by the surrounding pipe walls, if they are put close to the beam. More specifically, if the beam propagates through a dipole magnet in a metal pipe of radius a, then the radiation with corresponding wavelength such that $\ell_\perp \geq a$ will be suppressed. That is,

$$\lambda\!\!\!^{-} \geq \sqrt{\frac{a^3}{\rho}} \tag{4.46}$$

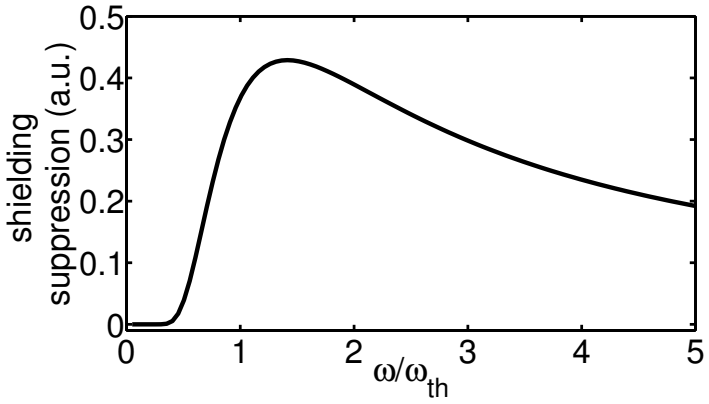

Figure 4.9: Dependence of (parallel-plate) radiation shielding on the wavelength. See also Eq. (4.142).

or

$$\omega \leq c\sqrt{\frac{\rho}{a^3}} \tag{4.47}$$

This is called the shielding effect and it is important for suppression of undesirable coherent radiation of short bunches. In the next section, we would define a shielding threshold at which

$$\omega_{\rm th} \equiv c\sqrt{\frac{2\pi^3\rho}{3a^3}} \tag{4.48}$$

for more quantitative estimation if the shielding effect becomes present. Figure 4.9 below illustrates the shielding suppression of CSR due to the presence of surrounding beam pipe. Later in Sec. 4.2 we will find that the radiation field is proportional to $\omega^{-1}\exp\left(-\omega_{\rm th}^2/\omega^2\right)$, from which the frequencies with $\omega \leq \omega_{\rm th}$ cannot propagate in the presence of boundary pipes.

The above discussion is based on single-particle analysis. Now we would like to consider the radiation fields generated by multiple particles in a bunch. Usually the number of particles in a high-brightness electron bunch can be of order of 10^{10}. Define the radiation field, which can be electric or magnetic, of a single particle is $B\left(t - t_j(\mathbf{r}_j)\right)$, with j the particle index. The resultant radiation fields generated by this bunch of particles can be superimposed

$$\mathcal{B}(t, \mathbf{n}) = \sum_{j=1}^{N} B\left(t - t_j(\mathbf{r}_j)\right) \tag{4.49}$$

where $\mathbf{n}$ is the unit vector pointing to an observer.

By taking the Fourier transformation of the single- and multiple particle fields, we have

$$B(t,\mathbf{n}) \leftrightarrow \hat{B}(\omega,\mathbf{n})$$
$$\mathcal{B}(t,\mathbf{n}) \leftrightarrow \hat{\mathcal{B}}(\omega,\mathbf{n}) \tag{4.50}$$

The radiation (power) spectrum by a bunch of particles can be obtained in Eq. (4.51)

$$\left|\hat{\mathcal{B}}(\omega,\mathbf{n})\right|^2 = \left|\left(\sum_{j=1}^{N}\hat{B}\left(\omega,\mathbf{n}\right)e^{\frac{i\omega\mathbf{n}\cdot\mathbf{r}_j}{c}}\right)\left(\sum_{k=1}^{N}\hat{B}^*\left(\omega,\mathbf{n}\right)e^{-\frac{i\omega\mathbf{n}\cdot\mathbf{r}_k}{c}}\right)\right| \tag{4.51}$$

or

$$\left|\hat{\mathcal{B}}(\omega,\mathbf{n})\right|^2 = \left|\hat{B}(\omega,\mathbf{n})\right|^2\left(N+\sum_{j,k=1(j\neq k)}^{N}e^{\frac{i\omega\mathbf{n}\cdot(\mathbf{r}_j-\mathbf{r}_k)}{c}}\right) \tag{4.52}$$

or

$$\begin{aligned}\left|\hat{\mathcal{B}}(\omega,\mathbf{n})\right|^2 &= \left|\hat{B}(\omega,\mathbf{n})\right|^2\left(N+2\sum_{j<k}^{N}\cos\left(\frac{\omega\mathbf{n}\cdot(\mathbf{r}_j-\mathbf{r}_k)}{c}\right)\right)\\ &\approx N\left|\hat{B}(\omega,\mathbf{n})\right|^2+N^2\left|\hat{B}(\omega,\mathbf{n})\right|^2F(\omega,\mathbf{n})\end{aligned} \tag{4.53}$$

where the form factor is represented as

$$F(\omega,\mathbf{n}) = \left|\int_{-\infty}^{\infty}d\mathbf{r}\rho(\mathbf{r})e^{\frac{i\omega\mathbf{n}\cdot\mathbf{r}}{c}}\right|^2 \tag{4.54}$$

From the above analysis we readily have three findings:

(i) the radiation spectrum depends on the detailed particle distribution, i.e. $F(\omega,\mathbf{n})$;

(ii) for the wavelengths longer than the bunch length, Eq. (4.52) contributes. That is,

$$\lambda \geq \sigma_z \text{ or } \omega \leq c/\sigma_z \tag{4.55}$$

The radiation power, or so-called CSR power, thus scales as the square of the number of particles. Note that N is a huge number, and

(iii) for the transverse size of the beam distribution, $\sigma_{\mathbf{r}\perp}$, the coherence can be retained only if $\sigma_{\mathbf{r}\perp}$ is smaller than the transverse characteristic width of the radiation, i.e.

$$\lambda \geq \sigma_{\mathbf{r}\perp}\psi \tag{4.56}$$

To end this section, we summarize some important characteristics of SR (and CSR) in Table 4.3. Some

Table 4.3: Summary of radiation formation and coherence conditions.

	Longitudinal	Transverse
Requirement of radiation formation	at $\omega \sim \omega_c$, $\ell_\parallel \sim \rho, /\gamma$ where $\omega_c = 3c\gamma^3/2\rho$. at $\omega, \ll \omega_c$, $\ell_\parallel \sim \rho^{2/3}\lambda\!\!\!^{-1/3}$	$\ell_\perp \sim \rho^{1/3}\lambda\!\!\!^{-2/3}$
Coherence condition	$\lambda \geq \sigma_z$	$\lambda \geq \sigma_{\mathbf{r}\perp\psi}$

of the results derived here would be applied to determine the validity of (later) developed CSR impedance models.

4.2.2 Two-particle model

Having introduced general properties of SR and CSR, we want to focus more on beam dynamics side. To study CSR effect on beam particles, we need to know the interaction between particles within a bunch when this bunch traverses a bend. We begin by considering two-particle (head and tail particle) interaction and define the rate of energy change due (of the head particle) to CSR (emitted by tail particle) as [see also Fig. 4.10]

$$\left.\frac{d\mathcal{E}}{cdt}\right|_{\text{CSR}} \equiv e\beta\cdot\mathbf{E} - \frac{e^2}{\gamma^2(s-s')^2}\begin{cases} >0, \text{ energy gain} \\ <0, \text{ energy loss}\end{cases} \tag{4.57}$$

where the second term on RHS represents the Coulombic interaction, β and γ are the Lorentz relativistic factors. The positive value is assigned as energy gain (of the head particle). The CSR wakefield is defined as [see Eq. (4.7), $q_1 = q_2 = e$ (negative value)]

$$w_{\text{CSR}} = -\frac{1}{e^2}\left.\frac{d\mathcal{E}}{cdt}\right|_{\text{CSR}} \tag{4.58}$$

.

In Eq. (4.57), by subtracting the Coulomb field, there is an advantage of removing the singularity at $s = s'$ [153]. We follow Saldin, Schneidmiller, and Yurkov's treatment (SSY) and apply their results to derive the corresponding CSR impedances. To proceed, we define the following normalized variables[90],

$$\begin{aligned}\left[\hat{\phi},\hat{u},\hat{\psi}\right] &\equiv \gamma\left[\phi,u,\psi\right] \\ [\hat{x},\hat{y}] &\equiv \gamma\,[x,y]/\rho \\ \hat{z} &\equiv \gamma^3 z/\rho\end{aligned} \tag{4.59}$$

When a beam enters a bending magnet, there are a total of four different configurations, shown in

[90]Note here that x, y, and z have different meanings from those defined in Chapter 2. Figures 2.1 and 4.10 tell the differences.

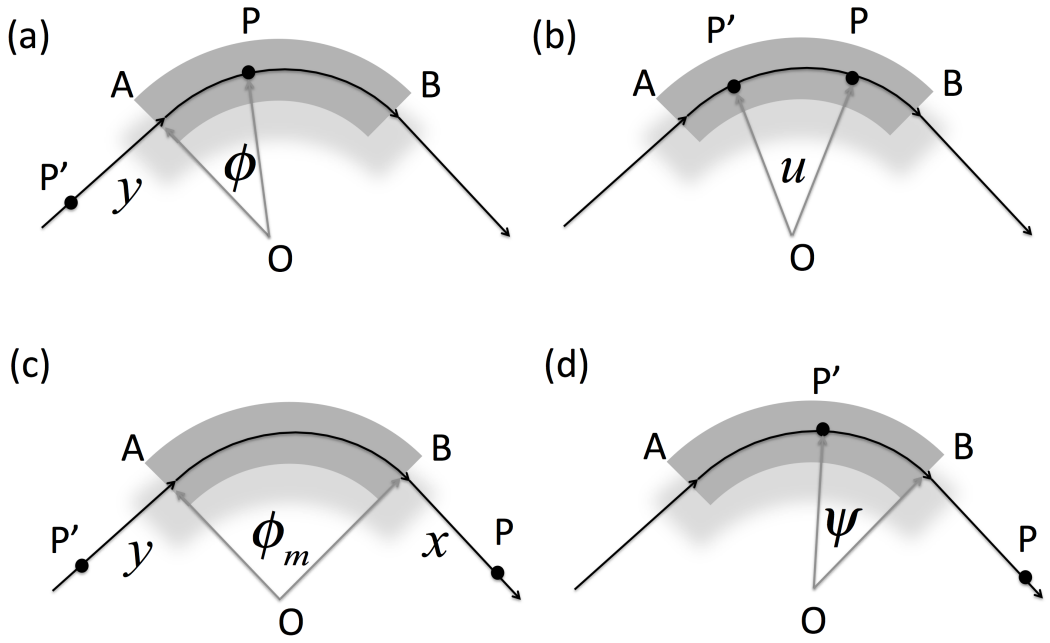

Figure 4.10: Four different geometrical configurations for a beam traversing a finite-length bending magnet. Figs. (a) to (d) are represented as Case A to D respectively.

Fig. 4.10, depending on the location of the source/tail particle P' (at retarded time) and the head/test particle P (at present time) with respect to the dipole. The electric field $\mathbf{E}$ in Eq. (4.57) can be explicitly expressed by using Lienard-Wiechert formula, Eq. (4.19). The key part is to relate the chord distance L [in the denominator of Eq. (4.19)] to arc distance $(s - s')$. The four situations have four different geometric constraints for tail and head particles.

For Case A [Fig. 4.10(a)], the resultant expression of Eq. (4.57) can be written as

$$\left(\frac{d\mathcal{E}}{cdt}\right)_A = \frac{4e^2\gamma^4}{\rho^2}\left(\hat{\phi}+\hat{y}\right)^2 \left\{ \frac{\left(\hat{\phi}+\hat{y}\right)^2 + \hat{\phi}^3\left(\frac{3\hat{\phi}}{4}+\hat{y}\right)}{\left[\left(\hat{\phi}+\hat{y}\right)^2 + \frac{\hat{\phi}^4}{4}\right]^3} - \frac{1}{\left[\left(\hat{\phi}+\hat{y}\right)^2 + \frac{\hat{\phi}^3}{12}\left(\hat{\phi}+4\hat{y}\right)\right]^2} \right\} \tag{4.60}$$

where ϕ is the angle the head particle (at s, at present time) travels within the dipole and y is the distance (of tail particle at s', at retarded time) behind the dipole entrance. ϕ and y can be related by

$$(\hat{s} - \hat{s}')_A = \frac{\hat{\phi}+\hat{y}}{2} + \frac{\hat{\phi}^3}{24}\frac{\hat{\phi}+4\hat{y}}{\hat{\phi}+\hat{y}} \tag{4.61}$$

In general we usually know the arc length $(s - s')$ and ϕ, and we want to solve Eq. (4.61) for $\hat{y}$. By substituting $\hat{\phi}$ and $\hat{y}$ into Eq. (4.60), the rate of energy change or wakefield for Case A can be obtained.

After ultrarelativistic approximation ($\gamma \to \infty$), the two-particle kernel, Eq. (4.58), can be written as [67]

$$w_{\mathrm{CSR},A} \approx -\frac{4}{\rho\phi}\delta\left(\frac{z-z'}{R} - \frac{\phi^3}{6}\right) \tag{4.62}$$

and the longitudinal wakefield for a line bunch distribution $\lambda(z)$ can be obtained by convolution,

$$W_{\mathrm{CSR},A}(z) = \int d\zeta\ \lambda(\zeta) w_{\mathrm{CSR,A}}(z-\zeta) = -\frac{4}{\rho\phi}\lambda\left(\frac{z}{\rho} - \frac{\rho\phi^3}{6}\right) \tag{4.63}$$

For convenience we have recovered the physical variables instead of normalized ones.

Similarly, for Case B [Fig. 4-4.10(b)], the two particles, the leading one at s at present time and the trailing one at s' at retarded time, both locate within a dipole, and Eq. (4.57) becomes

$$\left(\frac{d\mathcal{E}}{cdt}\right)_B = \frac{4e^2\gamma^4}{\rho^2}\left\{\frac{\frac{\hat{u}^2}{4}-1}{2\left(\frac{\hat{u}^2}{2}\right)^3} + \frac{1}{\hat{u}^2}\left[\frac{1+\frac{3\hat{u}^2}{4}}{\left(1+\frac{\hat{u}^2}{4}\right)^3} - \frac{1}{\left(1+\frac{\hat{u}^2}{12}\right)^2}\right]\right\} \tag{4.64}$$

where $\hat{u} = \hat{\phi} - \hat{\phi}'$, and it can be related to the arc length by

$$(\hat{s} - \hat{s}')_B = \frac{\hat{u}}{2} + \frac{\hat{u}^3}{24} \tag{4.65}$$

Under ultrarelativistic approximation, the two-particle kernel becomes

$$w_{\mathrm{CSR},B} \approx \frac{32e^2\gamma^4}{\rho^2\hat{u}^4} = \frac{2e^2}{3^{4/3}\rho^{2/3}(z-z')^{4/3}} = -\frac{2e^2}{(3\rho^2)^{1/3}}\frac{\partial}{\partial z'}\left(\frac{1}{z-z'}\right)^{1/3} \tag{4.66}$$

where an approximated expression for Eq. (4.65)

$$\hat{s} - \hat{s}' \approx \frac{\hat{u}^3}{24} \Rightarrow u = \left(\frac{24}{\rho}(z-z')\right)^{1/3} \tag{4.67}$$

has been used. The corresponding wakefield for a general line bunch distribution can be obtained in terms of two-particle kernel as a convolution integral

$$\begin{aligned} W_{\mathrm{CSR},B}(z) &= \int_{z-R\phi^3/24}^{z} d\zeta\ \lambda(\zeta) w_{\mathrm{CSR,B}}(z-\zeta) \\ &= \frac{4}{\rho\phi}\lambda\left(z - \frac{\rho\phi^3}{24}\right) + \frac{2}{(3\rho^2)^{1/3}}\int_{z-R\phi^3/24}^{z} \frac{1}{(z-\zeta)^{1/3}}\frac{\partial\lambda(\zeta)}{\partial\zeta}d\zeta \end{aligned} \tag{4.68}$$

Here we note that when we refer CSR to be in steady or stationary state, the first term on RHS of Eq. (4.68) vanishes and only the second term is present.

For Case C [Fig. 4.10(c)], the leading particle (at x, measured from dipole exit) is downstream outside

the dipole and the trailing particle (at y, measured from dipole entrance, at retarded time) was also upstream outside the dipole. In this case, Eq. (4.57) can written as

$$\left(\frac{d\mathcal{E}}{cdt}\right)_C = \frac{4e^2\gamma^4}{\rho^2}\left(\hat{\phi}_m+\hat{x}+\hat{y}\right)^2 \times\left\{\begin{array}{l}\dfrac{\left(\hat{\phi}_m+\hat{x}+\hat{y}\right)^2+\hat{\phi}_m^2\left(\frac{3\hat{\phi}_m^2}{4}+\hat{x}^2+2\hat{\phi}_m\hat{x}+\hat{\phi}_m\hat{y}+2\hat{x}\hat{y}\right)}{\left[\left(\hat{\phi}_m+\hat{x}+\hat{y}\right)^2+\frac{\hat{\phi}_m^2}{4}\left(\hat{\phi}_m+2\hat{x}\right)^2\right]^3}- \\ \dfrac{1}{\left[\left(\hat{\phi}_m+\hat{x}+\hat{y}\right)^2+\frac{\hat{\phi}_m^2}{12}\left(\hat{\phi}_m^2+4\hat{\phi}_m\hat{x}+4\hat{\phi}_m\hat{y}+12\hat{x}\hat{y}\right)\right]^2}\end{array}\right\} \tag{4.69}$$

where $\hat{\phi}_m$ is the normalized bending angle of the dipole. $\hat{x}$ and $\hat{y}$ are related by

$$(\hat{s}-\hat{s}')_C = \frac{\hat{\phi}_m+\hat{x}+\hat{y}}{2}+\frac{\hat{\phi}_m^3}{24}\frac{\hat{\phi}_m^2+4\hat{\phi}_m(\hat{x}+\hat{y})+12\hat{x}\hat{y}}{\hat{\phi}_m+\hat{x}+\hat{y}} \tag{4.70}$$

Under ultrarelativistic approximation, the two-particle kernel becomes [67]

$$w_{\mathrm{CSR},C} \approx -\frac{4}{\rho^2\left(\phi_m+\frac{2x}{\rho}\right)}\delta\left(\frac{z-z'}{\rho}-\frac{\phi_m^2}{6}\left(\phi_m+\frac{3x}{\rho}\right)\right) \tag{4.71}$$

and the wakefield expression has

$$W_{\mathrm{CSR},C}(z) = \int d\zeta\ \lambda(\zeta)w_{\mathrm{CSR},C}(z-\zeta) = -\frac{4}{\rho\left(\phi_m+\frac{2x}{\rho}\right)}\lambda\left(z-\frac{\rho\phi_m^2}{6}\left(\phi_m+\frac{3x}{\rho}\right)\right) \tag{4.72}$$

For Case D [Fig. 4.10(d)], which has been found to contribute significantly to beam dynamics, the head particle has already left the dipole while the tail particle was still located within the dipole. The energy loss rate can be expressed as

$$\left(\frac{d\mathcal{E}}{cdt}\right)_D = \frac{4e^2\gamma^4}{\rho^2}\left(\hat{\psi}+\hat{x}\right)^2 \times\left\{\begin{array}{l}\dfrac{\hat{\psi}^2\left[\frac{\hat{\psi}^2}{4}\left(\hat{\psi}+2\hat{x}\right)^2-\left(\hat{\psi}+\hat{x}\right)^2\right]}{2\left[\frac{\hat{\psi}^2}{4}\left(\hat{\psi}+2\hat{x}\right)^2+\left(\hat{\psi}+\hat{x}\right)^2\right]^3}+ \\ \dfrac{\left(\hat{\psi}+\hat{x}\right)^2+\hat{\psi}^2\left(\frac{3\hat{\psi}^2}{4}+\hat{x}^2+2\hat{x}\hat{\psi}\right)}{\left[\frac{\hat{\psi}^2}{4}\left(\hat{\psi}+2\hat{x}\right)^2+\left(\hat{\psi}+\hat{x}\right)^2\right]^3}- \\ \dfrac{1}{\left[\left(\hat{\psi}+\hat{x}\right)^2+\frac{\hat{\psi}^3}{12}\left(\hat{\psi}+4\hat{x}\right)\right]^2}\end{array}\right\} \tag{4.73}$$

where, for head particle, $\hat{x}$ is measured from the exit of a dipole, and $\hat{\psi}$ is the angle coordinate of the tail

particle also measured from the dipole exit. They can be related by

$$(\hat{s}-\hat{s}')_D = \frac{\hat{\psi}+\hat{x}}{2} + \frac{\hat{\psi}^3}{24}\frac{\hat{\psi}+4\hat{x}}{\hat{\psi}+\hat{x}} \tag{4.74}$$

After ultrarelativistic approximation, Eq. (4.73) can be simplified and we have

$$w_{\mathrm{CSR},D} \approx -\frac{32}{\rho^2}\frac{\left(\psi+\frac{x}{\rho}\right)^2}{\psi^2\left(\psi+\frac{2x}{\rho}\right)^4} = -\frac{4}{\rho}\frac{\partial}{\partial z'}\left(\frac{1}{\psi+\frac{2x}{\rho}}\right) \tag{4.75}$$

with the corresponding wakefield expression

$$W_{\mathrm{CSR},D}(z) = \int_{z-\Delta z_{\max}}^{z} d\zeta\ \lambda(\zeta) w_{\mathrm{CSR},D}(z-\zeta) = \frac{4}{\rho}\left[\frac{\lambda(z-\Delta z_{\max})}{\phi_m+\frac{2x}{\rho}} + \int_{z-\Delta z_{\max}}^{z} d\zeta \frac{1}{\psi+\frac{2x}{\rho}}\frac{\partial\lambda(\zeta)}{\partial\zeta}\right] \tag{4.76}$$

where

$$\Delta z_{\max} = \frac{\rho\phi_m^3}{24}\frac{\phi_m+\frac{4x}{\rho}}{\phi_m+\frac{x}{\rho}} \tag{4.77}$$

with ϕ_m the bending angle of the dipole.

Following SSY [153] and further extensions by Stupakov and Emma [67], we have now obtained the ultrarelativistic CSR wakefield expressions for Case (A-D), which cover all possible configurations for a beam traversing a finite-length bending dipole. Before proceeding to derive their impedance expressions, in the following section we try to illustrate the bulk effect of CSR on the beam itself.

4.2.3 CSR wakes for Gaussian beams

In this subsection we consider a Gaussian (line) bunch distribution to illustrate the behavior of CSR wakefields for Case A to D,

$$\lambda(z) = \frac{1}{\sqrt{2\pi}\sigma_z} e^{-\frac{z^2}{2\sigma_z^2}} \tag{4.78}$$

where σ_z is the rms bunch length of the beam. In what follows we consider first the steady-state case and then the transient cases.

For the steady-state case, first of all, the rate of energy loss at a bunch slice z can be analytically

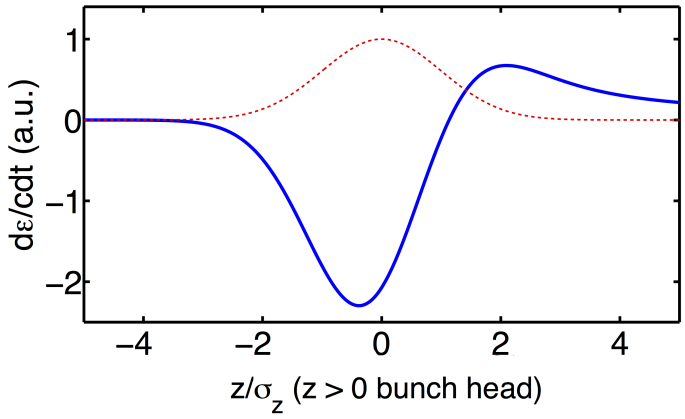

Figure 4.11: Illustration of CSR wakefield for a Gaussian bunch. The red dashed curve represents the unperturbed Gaussian bunch.

evaluated by the second term of Eq. (4.68) [42],

$$\left.\frac{d\mathcal{E}(z)}{cdt}\right|_{\mathrm{CSR},ss} = -\frac{2Ne^2}{(3\rho^2)^{1/3}}\int_{-\infty}^{z}\frac{1}{(z-\zeta)^{1/3}}\frac{\partial\lambda(\zeta)}{\partial\zeta}d\zeta = -\frac{2Ne^2}{\sqrt{2\pi}3^{1/3}\rho^{2/3}\sigma_z^{4/3}}F_0\left(\frac{z}{\sigma_z}\right) \tag{4.79}$$

where the shape function is

$$F_0(x) = \int_{-\infty}^{x} d\chi \frac{1}{(x-\chi)^{1/3}}\frac{\partial}{\partial\chi}e^{-\frac{\chi^2}{2}} \tag{4.80}$$

Figure 4.11 shows an example of Eq. (4.79) for a Gaussian bunch, where we can see that about the first third of the bunch gains some energy while the remaining portion of the bunch loses energy. The overall energy is lost because of the coherent radiation.

From Fig. 4.11, we have already seen the effect CSR can re-distribute the particle energy distribution within a bunch. Then, let us estimate to what extent this energy redistribution results in growth of energy spread. For the Gaussian bunch distribution, the rms energy spread due to CSR can be obtained by integrating Eq. (4.79) over the whole bunch,

$$\begin{aligned}\sigma_{\Delta E,\mathrm{CSR}} &= \frac{2Ne^2L_d}{\sqrt{2\pi}3^{1/3}\rho^{2/3}\sigma_z^{4/3}}\sqrt{\langle F_0^2\rangle - \langle F_0\rangle^2} \\ &\approx 0.23\frac{Ne^2L_d}{\rho^{2/3}\sigma_z^{4/3}}\end{aligned} \tag{4.81}$$

where the bracket denotes $\langle ...\rangle \equiv \int_{-\infty}^{\infty} d\chi(...)$. The average values are numerically estimated to be $\langle F_0\rangle \approx 0.15$ and $\langle F_0^2\rangle \approx 0.45$.

Finally, we estimate the CSR-induced average energy loss/offset per electron per unit length, which

Table 4.4: Numerical parameters for illustration of CSR wakes of Gaussian line bunch.

Name	Value	Unit
Bunch line distribution	Gaussian	
RMS bunch length, σ_z	50	μm
Bunch charge, q	1	nC
Dipole length, L_d	50 (long)/10 (short)	cm
Dipole radius, ρ	1.5	m
Overtaking length, L_0	14	cm

can be obtained by

$$\langle \Delta E \rangle = \int_{-\infty}^{\infty} d\zeta \lambda(\zeta) \left. \frac{d\mathcal{E}(\zeta)}{cdt} \right|_{\mathrm{CSR},ss} = \frac{2Ne^2}{\sqrt{2\pi}3^{1/3}\rho^{2/3}\sigma_z^{4/3}} \int_{-\infty}^{\infty} d\zeta F_0\left(\frac{\zeta}{\sigma_z}\right) \frac{e^{-\zeta^2/2\sigma_z^2}}{\sqrt{2\pi}\sigma_z}$$
$$\approx -0.35 \frac{Ne^2}{\rho^{2/3}\sigma_z^{4/3}} \tag{4.82}$$

where

$$\int_{-\infty}^{\infty} dx (2\pi)^{-1/2} F_0(x) e^{-x^2/2} \approx -0.6335$$

Note so far the discussion restricts the case of steady-state CSR effect only. Prior to reaching the steady state, the beam entering a bend from a straight section would experience the so-called entrance transient state, for which Eq. (4.63) depicts. Besides, there are exit transient CSR effects when a beam exits from a dipole, including one case [Case C] with the fields generated from an upstream electron (at retarded time, traveling along the upstream straight section) propagating across the dipole to downstream straight section, for which Eq. (4.72) defines, and the other [Case D] where fields generated from an electron (at retarded time) within a dipole propagating downstream the straight section, as formulated in Eq. (4.76).

Below in Figs. 4.12 to 4.16 we demonstrate the dynamics of CSR wakefields and characteristic beam parameters [91]. Table 4.4 summarizes a set of beam and lattice parameters for use in the demonstration. Note that the beam is assumed ultrarelativistic.

Let us consider the first case with 50-cm "long" bending magnet, by which we mean the dipole length is long enough for CSR field to reach the steady state. Using Eqs. (4.63) and (4.68) with given line bunch distribution Eq. (4.78), we can calculate the CSR wakefield at different locations within a dipole. Figure 4.12 shows the evolution of the CSR wakefields (in unit of MV/m) along the bunch when the beam traverses the 50-cm long dipole. In the figure, the variable s is defined as the distance the beam passed the bending magnet. It can be seen that the CSR wakefield progresses through a transient regime at bend entrance and eventually achieves a steady-state situation (black curve). It can be found from Eq. (4.67) that the steady state can be achieved after the distance $L_0 \approx \left(24\sigma_z\rho^2\right)^{1/3}$, about 14 cm for the case. Note that, for $s = 18$ cm (magenta curve), the peak is moving toward right and has little effect to the beam bunch.

[91] The two examples presented here are largely based on Stupakov and Emma [67].

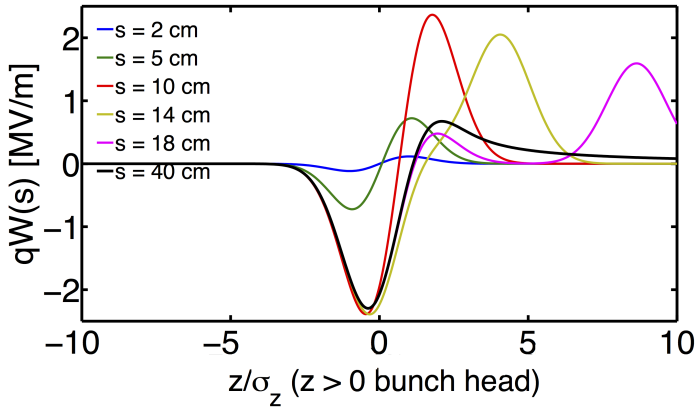

Figure 4.12: Evolution of CSR wakefields when the 1-D Gaussian bunch enters a 50-cm long dipole.

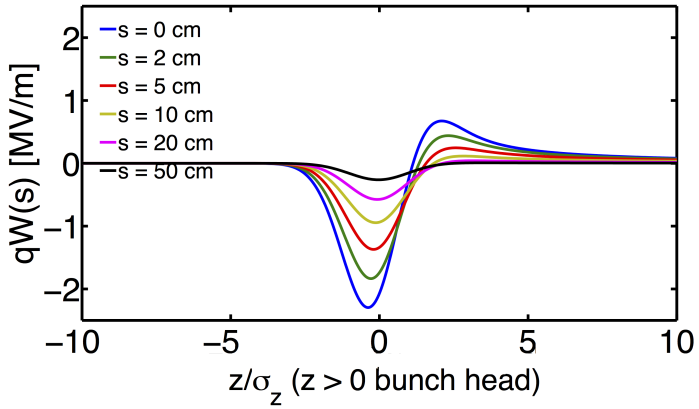

Figure 4.13: Evolution of CSR wakefields when the 1-D Gaussian bunch leaves the 50-cm long dipole. Note that the blue curve at $s = 0$ is basically same as the black curve in Fig. 4.12.

For the same magnet, Fig. 4.13 below shows the continued evolution of the CSR wakefield beyond the dipole exit, through a drift section, depicting Case C and D. The wakefields are calculated by Eqs. (4.72) and (4.76), where can be solved via Eq. (4.74). Here s is the distance measured from the dipole exit. The $s = 0$ cm case corresponds to the steady-state case depicted in Fig. 4.12 (black curve). We can see that CSR exit wakefields retain their shape but the amplitude drops off as the bunch propagates further past the exit of the dipole.

The second example considers the 10-cm "short" bending magnet, by which we mean the steady-state CSR wakefield is never reached until the beam exits the dipole. Because the beam does not know in advance whether the dipole is long or short, it can be expected that until $s = 10$ cm (red curve in Fig. 4.12) the CSR wakefields are the same as those demonstrated in Fig. 4.12. Upon the exit of the beam, the evolutionary behavior of CSR wakefields starts to deviate. Shown in Fig. 4.14, the field begins to develop at $s = 0$ cm,

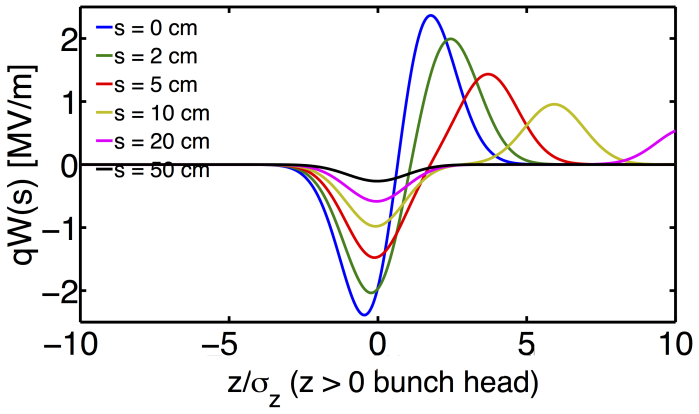

Figure 4.14: Evolution of CSR wakefields when the 1-D Gaussian bunch enters and leaves a 10-cm short dipole.

i.e. the dipole exit, which is identical to that of red curve in Fig. 4.12. Then the CSR wakefields no longer maintain their shape but the amplitude appears to taper off at similar rates.

Having demonstrated the evolution of CSR wakefields along long and short dipoles. Let us now take a look at how the average energy loss, $\langle \Delta E \rangle$, and the rms energy spread, $\sigma_{\Delta E,\mathrm{CSR}}$, change when the beam traverses the dipoles. Figure 4.15 shows the case for the 50-cm long bending magnet. In this figure we can see, after $s \approx L_0$, both the average energy loss and rms energy spread increases linearly, indicating that CSR approaches the steady state. Using the parameters listed in Table 4.4, $N = 6.25 \times 10^9$, and we can estimate the average energy loss using Eq. (4.82) as $L_d \langle \Delta E \rangle \approx -0.35 \frac{Ne^2 L_d}{\rho^{2/3}\sigma_z^{4/3}} = -0.35 \frac{N r_e mc^2 L_d}{\rho^{2/3}\sigma_z^{4/3}} \approx -0.65$ MeV, and rms energy spread Eq. (4.81) as $\sigma_{\Delta E,\mathrm{CSR}} \approx 0.23 \frac{Ne^2 L_d}{\rho^{2/3}\sigma_z^{4/3}} \approx 0.43$ MeV. Indeed the estimations are consistent with the simulation results. Slight overestimation from Eqs. (4.81) and (4.82) is due to neglect of transient CSR effects. From the figure we also observe that after the dipole the beam continuously loses its energy and increases the energy spread at a however lower rate, contributed from Case C and D. For completeness, Fig. 4.16 illustrates the average energy loss and rms energy spread for 10-cm short bending magnet.

In this subsection we have demonstrated the CSR-induced energy redistribution with asymmetric shape [Fig. 4.12 to 4.14] where, roughly speaking, the first one third usually gains some energy while the remaining parts of the bunch lose their energy. Then we estimated two quantities of general interest: the increase of rms energy spread, Eq. (4.81), and the average energy loss of a Gaussian bunch, Eq. (4.82). Finally we demonstrated the behavior of CSR wakefields for a beam traversing long and short bending magnets.

4.2.4 Free-space steady-state CSR impedance

In this and next subsections, we would derive the CSR impedances for Cases A-D presented in Sec. 4.2.2. We first derive the *steady-state* CSR impedance and then the entrance and exit/drift *transient* states. In general

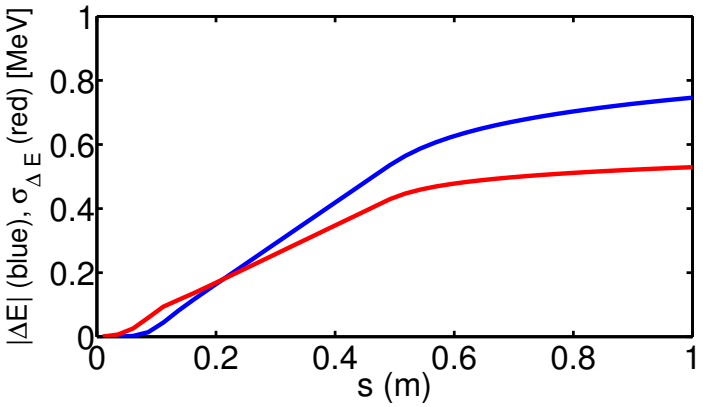

Figure 4.15: The average energy loss (blue) and rms energy spread (red) of a traversing Gaussian bunch induced by CSR along the 50-cm long dipole.

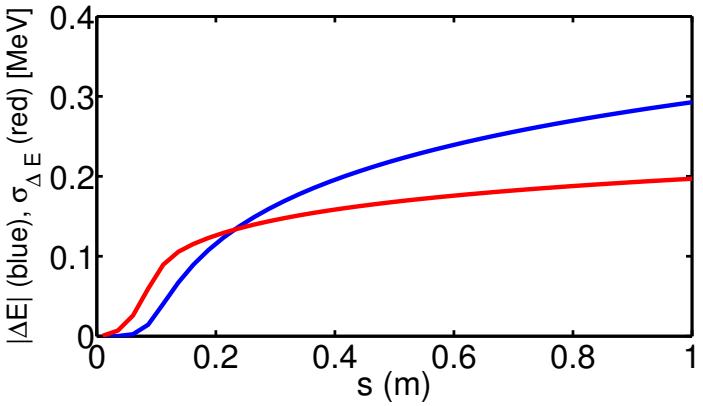

Figure 4.16: The average energy loss (blue) and rms energy spread (red) of a traversing Gaussian bunch induced by CSR along the 10-cm short dipole.

the most contributed CSR effects have been known as the steady-state and exit/drift [Case D] transient states. Therefore when we derive the steady-state CSR impedance, we start from very beginning and retain the beam energy dependence in our derivation. Although this leads to complexity, the resultant expression is valid for low energy beams, which, e.g. in the designs of low-energy mergers in ERLs, pose new challenges for the understanding of the CSR and longitudinal space charge (LSC) interactions.

Assume the current density distribution is one-dimensional (longitudinal), i.e.

$$I_0(z,t) = e\beta c\lambda(z,t) \tag{4.83}$$

with $\lambda(z,t)$ as the line distribution.

In what follows, we consider a rigid line bunch, with longitudinal line distribution λ moving at velocity $v = \beta c$ on a circular orbit with radius ρ. We will find the longitudinal wakefield on the bunch as a result

of steady-state CSR interaction in free space, and obtain the impedance from the Fourier transform of the CSR wakefield.

First, the electric field on a particle at (s,t), due to CSR interaction from all other particles in the bunch, can be expressed in terms of the retarded potentials, i.e. Eqs. (4.16) and (4.17), where the retardation condition would be formulated by Eq. (4.18). The energy loss rate for the particle per unit path length is [103]

$$\frac{d\mathcal{E}}{cdt} = e\vec{\beta}\cdot\mathbf{E} = -e\frac{d\phi}{cdt} + e\left(\frac{\partial\phi}{c\partial t} - \vec{\beta}\cdot\frac{\partial\mathbf{A}}{c\partial t}\right) \tag{4.84}$$

For steady-state CSR interaction, the condition must be satisfied,

$$\frac{d\phi}{dt} = 0 \tag{4.85}$$

The longitudinal wakefield on the particle is subsequently

$$E_s = -\left(\frac{\partial\phi}{\partial z} - \vec{\beta}\cdot\frac{\partial\mathbf{A}}{\partial z}\right) \tag{4.86}$$

in which,

$$\beta(t)\cdot\beta(t') = \beta^2\cos\left(\frac{s-s'}{\rho}\right) \tag{4.87}$$

and

$$\phi - \vec{\beta}\cdot\mathbf{A} = e\int_{-\infty}^{\infty} ds'\frac{(1-\beta^2)+\beta^2\left[1-\cos\left(\frac{s-s'}{\rho}\right)\right]}{|\mathbf{r}(s)-\mathbf{r}(s')|}\lambda(z') \tag{4.88}$$

with

$$z' = z - (s-s') + \beta\,|\mathbf{r}(s)-\mathbf{r}(s')| \tag{4.89}$$

and

$$|\mathbf{r}(s)-\mathbf{r}(s')| = 2\rho\sin\left(\frac{s-s'}{2\rho}\right) \tag{4.90}$$

Assuming

$$\lambda(z) = \tilde{\lambda}(k)e^{ikz} \tag{4.91}$$

and

$$E_s(z) = -ecZ_0^{\parallel}(k)\tilde{\lambda}(k)e^{ikz} \tag{4.92}$$

Substituting Eqs. (4.87) to (4.90) into Eq. (4.86) and comparing with Eq. (4.92), the intermediate expression of the longitudinal impedance per unit length can be written as [103]

$$Z_0^{\parallel}(k) = ik \int_{-\infty}^{\infty} ds' g(s,s')\ e^{-ik\left[(s-s')-\beta\left|2\rho\sin\left(\frac{s-s'}{\rho}\right)\right|\right]} \tag{4.93}$$

where

$$g(s,s') = \frac{\frac{1}{\gamma^2} + \beta^2\left[1-\cos\left(\frac{s-s'}{\rho}\right)\right]}{\left|2\rho\sin\left(\frac{s-s'}{\rho}\right)\right|} \tag{4.94}$$

Now we perform a change of variables by

$$\Delta s = \begin{cases} s-s' \text{ for } s' < s \\ s'-s \text{ for } s' > s \end{cases} \tag{4.95}$$

Equation (4.93) can be re-written as

$$Z_0^{\parallel}(k) = ik \int_0^{\infty} d(\Delta s) g(\Delta s)\left(e^{-ik\left[\Delta s-\beta 2\rho\sin\left(\frac{\Delta s}{2\rho}\right)\right]} + e^{-ik\left[-\Delta s-\beta 2\rho\sin\left(\frac{\Delta s}{2\rho}\right)\right]}\right) \tag{4.96}$$

Here the first exponential term represents contribution of the tail-head ($s' < s$) interaction, while the second one accounts for the head-tail ($s' > s$) interaction. We remark that the impedance in Eq. (4.96) consists of contributions from both the CSR wakefield and the longitudinal space charge wakefield (within the bend). The net power loss of the particles corresponds to the real part of the CSR impedance, while the longitudinal space charge interaction is reactive and is associated with only the imaginary part of the impedance [35].

For $\Delta s \ll \rho$, we get from Eq. (4.96) the expression for the real part of CSR impedance as

$$\mathrm{Re}\left[Z_0^{\parallel}(k)\right] = k\int_0^{\infty} d\Delta s \frac{\frac{1}{\gamma^2} + \frac{(\Delta s)^2}{2\rho^2}}{\Delta s}\left\{\sin\left[k\left(\frac{\Delta s}{2\gamma^2} + \frac{(\Delta s)^3}{24\rho^2}\right)\right] - \sin(2k\Delta s)\right\} \tag{4.97}$$

This integration can be done by taking advantage of Schwinger's formula by comparing with the incoherent

synchrotron radiation power given by Eq. (II.5) of Ref. [156] for

$$P(\omega) = \frac{e^2}{\pi}\frac{\omega}{c}\int_0^\infty \left(\frac{1}{\gamma^2} + \frac{1}{2}\frac{c^2\tau^2}{\rho^2}\right)\left\{\sin\left((\omega(1-\beta)\,\tau + \frac{\omega c^2}{24\rho^2}\tau^3\right)\frac{d\tau}{\tau} - \sin\left(2\omega\tau\right)\frac{d\tau}{\tau}\right\}$$
$$= \frac{e^2}{\pi}\frac{k}{\gamma^2\sqrt{3}}\int_{\omega/\omega_c}^\infty K_{5/3}\left(\eta\right)d\eta \tag{4.98}$$

with ω_c defined in Eq. (4.29).

Note that the synchrotron radiation power can be related to the real part of the impedance by

$$P(\omega) = \frac{1}{2\pi}e^2\left\{2\,\mathrm{Re}\left[Z_0^{\parallel}(k)\right]\right\} \tag{4.99}$$

We then have

$$\mathrm{Re}\left[Z_0^{\parallel}(k)\right] = \frac{k}{\gamma^2\sqrt{3}}\int_{\omega/\omega_c}^\infty K_{5/3}(x)dx \tag{4.100}$$

Using the identities for modified Bessel functions

$$\int_x^\infty K_{5/3}\left(\eta\right)d\eta = 2K_3(x) + \int_0^x K_{1/3}(\eta)d\eta - \frac{\pi}{\sqrt{3}} \tag{4.101}$$

and the relations to Airy functions

$$K_{2/3}(x) = -\pi\frac{\sqrt{3}}{\zeta}\mathrm{Ai}'(\zeta) \tag{4.102}$$

and

$$K_{1/3}(x) = \pi\sqrt{\frac{3}{\zeta}}\mathrm{Ai}(\zeta) \tag{4.103}$$

for $\zeta = (3x/2)^{2/3}$.

The real part of the impedance is then reduced to

$$\mathrm{Re}\left[Z_0^{\parallel}(k)\right] = \frac{k^{1/3}}{\rho^{2/3}}(-2\pi)\mathrm{Ai}'\left(\mu\right) + \frac{k\pi}{\gamma^2}\left(\int_0^\mu \mathrm{Ai}(\zeta)\mathrm{d}\zeta - \frac{1}{3}\right) \tag{4.104}$$

with $\mu = \gamma^{-2}(k\rho)^{2/3}$.

Similarly, the imaginary part of the impedance can be obtained from Eq. (4.96)

$$\mathrm{Im}\left[Z_0^{\parallel}(k)\right] = k\int_0^{\infty} d\Delta s \frac{\frac{1}{\gamma^2}+\frac{(\Delta s)^2}{2\rho^2}}{\Delta s}\left(\cos\left[k\left(\frac{\Delta s}{2\gamma^2}+\frac{(\Delta s)^3}{24\rho^2}\right)\right]+\cos(2k\Delta s)\right) \tag{4.105}$$

Note that unlike the real part of impedance, for which the integrand in Eq. (4.97) does not have singularity, here the imaginary impedance contains terms with singular integrand, i.e. $1/\gamma^2\Delta s$. It is understood that the singularity reflects local space-charge interaction. However, since on a curved orbit pairwise particle interaction involves retardation, so the LSC force here will behave differently from that on a straight section. Just as the analysis of LSC on a straight path, the physically meaningful results for LSC on a curved orbit requires us to take into account the 3-D bunch distribution, which is beyond the scope of this analysis. Therefore, our focus is only on the CSR impedance and thus we only take into account the non-singular part of the imaginary impedance

$$\mathrm{Im}\left[Z_0^{\parallel}(k)\right] = k\int_0^{\infty} d\Delta s \frac{\Delta s}{2\rho^2}\left(\cos\left[k\left(\frac{\Delta s}{2\gamma^2}+\frac{(\Delta s)^3}{24\rho^2}\right)\right]+\cos(2k\Delta s)\right) \tag{4.106}$$

To evaluate the integration, let

$$\Delta s = 2t\left(\rho^2/k\right)^{1/3} \tag{4.107}$$

and

$$x = \gamma^{-2}(k\rho)^{2/3} \tag{4.108}$$

With the use of the integral formula [5],

$$\int_0^{\infty} t\cos\left(\frac{t^3}{3}+xt\right)dt = \frac{\pi}{3}\mathrm{Bi}'(x)+\pi\int_0^{x}\left[\mathrm{Ai}'(x)\mathrm{Bi}(t)-\mathrm{Ai}(t)\mathrm{Bi}'(x)\right]dt \tag{4.109}$$

Equation (4.107) now becomes

$$\mathrm{Im}\left[Z_0^{\parallel}(k)\right] \simeq \frac{k^{1/3}}{\rho^{2/3}}\left\{\frac{2\pi}{3}\mathrm{Bi}'(x)+2\pi\int_0^{x}\left[\mathrm{Ai}'(x)\mathrm{Bi}(t)-A\mathrm{i}(t)\mathrm{Bi}'(x)\right]dt\right\} \tag{4.110}$$

The derived expressions for non-ultrarelativistic CSR impedance, Eqs. (4.104) and (4.110), can be reduced to the ultrarelativistic ones when $\gamma\to\infty$,

$$\mathrm{Re}\left[Z_0^{\parallel}(k)\right] \xrightarrow{v=c} \frac{k^{1/3}}{\rho^{2/3}}(-2\pi)\mathrm{Ai}'(0) \tag{4.111}$$

and

$$\mathrm{Im}\left[Z_0^{\parallel}(k)\right] \xrightarrow{v=c} \frac{k^{1/3}}{\rho^{2/3}}\frac{2\pi}{3}\mathrm{Bi}\,(0) \tag{4.112}$$

which is exactly the well-known steady-state CSR impedance formula quoted in Ref. [79, 81]:

$$Z_{\mathrm{CSR}}^{\mathrm{s.s.UR}}\,(k(s);s) = \frac{-ik(s)^{1/3}A}{|\rho(s)|^{2/3}},\ A = -2\pi\left[\mathrm{Bi}'(0)/3 + i\mathrm{Ai}'(0)\right] \tag{4.113}$$

To summarize, here we quote the main results derived in this subsection. For a non-ultrarelativistic (NUR) electron beam ($\beta \to 1$, but $\gamma < \infty$) traversing a bending dipole, the free-space steady-state CSR impedance per unit length can be expressed as [103]:

$$\mathrm{Re}\left[Z_{\mathrm{CSR}}^{\mathrm{s.s.NUR}}(k(s);s)\right] = \frac{-2\pi k(s)^{1/3}}{|\rho(s)|^{2/3}}\mathrm{Ai}'\,(x) + \frac{k(s)\pi}{\gamma^2}\left(\int_0^x \mathrm{Ai}(\varsigma)\mathrm{d}\varsigma - \frac{1}{3}\right) \tag{4.114}$$

$$\mathrm{Im}[Z_{\mathrm{CSR}}^{\mathrm{s.s.NUR}}(k(s);s)] \simeq \frac{2\pi k(s)^{1/3}}{|\rho(s)|^{2/3}}\left\{\frac{1}{3}\mathrm{Bi}'(x) + \int_0^x \left[\mathrm{Ai}'(x)\mathrm{Bi}(t) - \mathrm{Ai}(t)\mathrm{Bi}'(x)\right]\,dt\right\} \tag{4.115}$$

where $x = \left(k(s)\,|\rho(s)|\right)^{2/3}\Big/\gamma^2$, $k = 2\pi/\lambda$ is the modulation wave number, $\rho(s)$ is the bending radius, and Ai and Bi are Airy functions. Under ultrarelativistic approximation (UR, $\gamma \to \infty$), Eq. (4.115) is reduced to the well-known expression:

$$Z_{\mathrm{CSR}}^{\mathrm{s.s.UR}}\,(k(s);s) = \frac{-ik(s)^{1/3}A}{|\rho(s)|^{2/3}},\ A = -2\pi\left[\mathrm{Bi}'(0)/3 + i\mathrm{Ai}'(0)\right] \approx -0.94 + 1.63i \tag{4.116}$$

In the reminder of this subsection, we would first illustrate the dependence of the non-ultrarelativistic CSR impedance in Eqs. (4.114) and (4.115) on beam energy for a bunch with given frequency, and compare the results with that of the ultrarelativistic case [Eq. (4.116)]. Then, we plot the impedance spectrum for a beam at a given low energy. Finally, we calculate the wakefield for a 1-D Gaussian bunch, Eq. (4.78), using the impedance for non-ultrarelativistic beam, and demonstrate that our results agree well with the existing results, which had been obtained directly from time-domain analysis, as shown in Fig. 4.19.

In Fig. 4.17 we show the energy dependence of CSR impedances for non-ultrarelativistic beams. It can be clearly seen that at low beam energy, e.g. 10 MeV ($\gamma \sim 20$), both the real and imaginary parts of the CSR impedance deviate considerably from those of ultrarelativistic case. In the specific case with $\lambda \sim 200\mu$m, it can be observed that the ultra-relativistic expression is valid only when $\gamma > 200$ (or, equivalently, $k\rho/\gamma^3 \ll 1$). Furthermore, the shorter the modulation wavelength (or, the larger the wave number) is, the higher the beam energy is required for keeping the validity of Eq. (4.116) in ultrarelativistic regime.

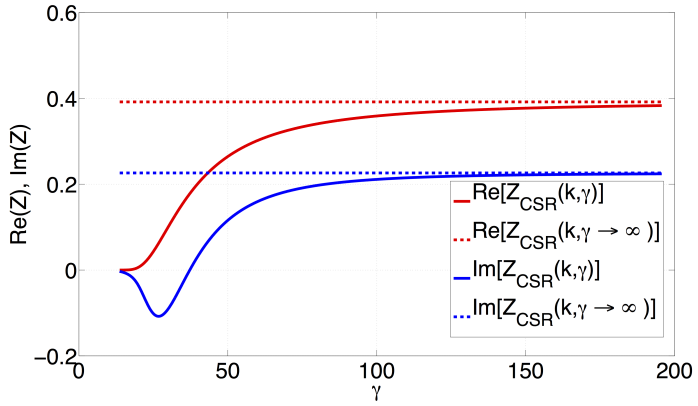

Figure 4.17: Energy dependence of the CSR impedance [Eqs. (4.114) and (4.115)]. Here we assume $k \approx 314\text{cm}^{-1}$ (or, $\lambda \approx 200\mu\text{m}$) and $\rho = 1.5$ m.

For the example with $E = 10$MeV and $\rho = 1.5$ m, Fig. 4.18 illustrates the spectral dependence of real and imaginary parts of the CSR impedances. It can be seen that the nonultrarelativistic results agree with the ultrarelativistic ones only when $k/k_c \ll 1$.

In Fig. 4.19 we show the corresponding wakefield calculated by the inverse Fourier transformation of the impedance, Eq. (4.92), for a Gaussian bunch distribution. It can be seen that for a low energy beam of $E = 10$ MeV, the CSR wake could deviate considerably from that of the ultrarelativistic case, with the latter being an overestimation of the former one. Here the behavior of wakefields for various beam energies agree well with that presented in Fig. 4(d) of Ref. [96].

4.2.5 Free-space transient CSR impedance

The CSR transient states include the entrance and exit transients. Prior to reaching the steady state, the beam entering a bending magnet from a straight section would experience the so-called entrance transient state, where the impedance per unit length can be obtained as follows. First, assume the electron beam has a sinusoidal modulation on top of line bunch distribution,

$$\lambda(z) = \tilde{\lambda}(k)e^{ikz} \tag{4.117}$$

Then the impedance can be obtained by substituting the above expression into the corresponding wakefield expression. Dividing the derived expression by $\lambda(z)$, $Z_0^{\parallel}(k) = -W_0^{\parallel} \Big/ \tilde{\lambda}(k)e^{ikz}$, will give the corresponding impedance expression.

For entrance transients, we substitute Eq. (4.117) into the wakefield expression from Case A, Eq.

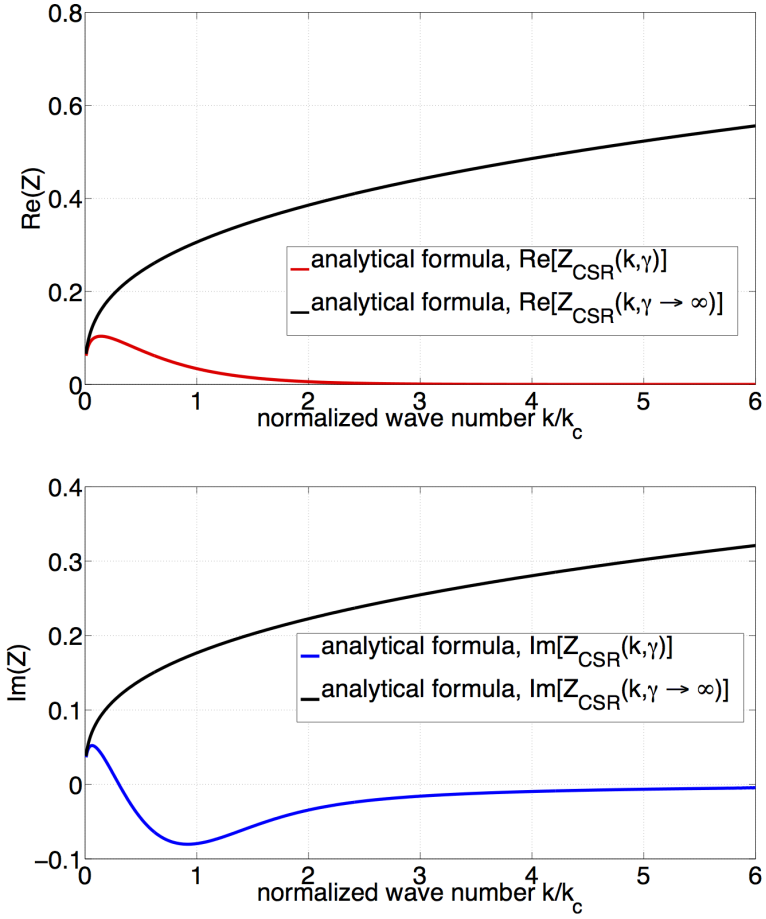

Figure 4.18: Real and imaginary parts of CSR impedance [Eqs. (4.114) and (4.115)]. Here $E = 10$ MeV and $\rho = 1.5$ m.

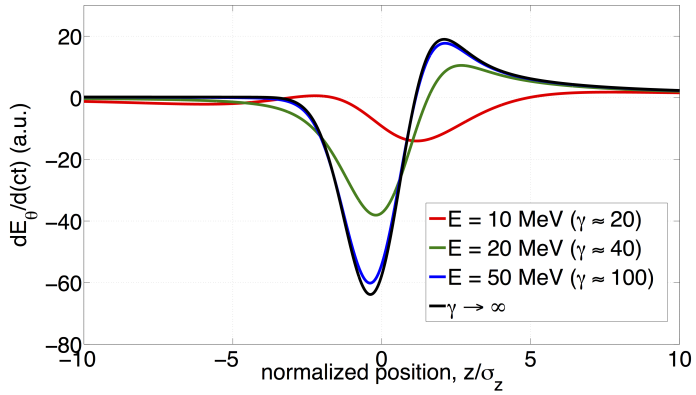

Figure 4.19: Comparison of CSR wakefields, calculated from Eq. (4.79), for $\gamma \to \infty$, and Eqs. (4.114, 4.115) via Eq. (4.92) for finite γ.

(4.63), [see Fig. 4.10(a)]

$$W_{\mathrm{CSR},A}(z) = -\frac{4}{\rho\phi}\lambda\left(\frac{z}{\rho} - \frac{\rho\phi^3}{6}\right) = -\frac{4}{s^*}\tilde{\lambda}(k)e^{ikz}e^{-4ikz_L} \tag{4.118}$$

where $s^* = \rho\phi$ and $z_L = \rho\phi^3/24$. Then the corresponding impedance expression

$$Z_{\mathrm{CSR},A}(k) = \frac{4}{s^*}e^{-4ikz_L} \tag{4.119}$$

where s^* is the longitudinal coordinate measured from the dipole entrance.

Another contribution may come from Case B [see Fig. 4.10(b)]. Having substituting Eq. (4.117) into Eq. (4.68), we have

$$\begin{aligned} W_{\mathrm{CSR},B}(z) &= \frac{4}{\rho\phi}\lambda\left(z - \frac{\rho\phi^3}{24}\right) + \frac{2}{(3\rho^2)^{1/3}}\int_{z-\rho\phi^3/24}^{z}\frac{1}{(z-\zeta)^{1/3}}\frac{\partial\lambda(\zeta)}{\partial\zeta}d\zeta \\ &= \frac{4}{s^*}\tilde{\lambda}(k)e^{ikz}e^{-ikz_L} + (ikz_L)^{1/3}\tilde{\lambda}(k)e^{ikz}\left[\Gamma(\tfrac{2}{3}) - \Gamma(\tfrac{2}{3}, ikz_L)\right] \end{aligned} \tag{4.120}$$

where $\Gamma(a)$ is the (complete) Gamma function and $\Gamma(a,z)$ the incomplete Gamma function. The corresponding impedance is then

$$Z_{\mathrm{CSR},B}(k) = -\frac{4}{s^*}e^{-i\mu} - \frac{4}{s^*}(i\mu)^{1/3}\left[\Gamma(\tfrac{2}{3}) - \Gamma(\tfrac{2}{3}, i\mu)\right] \tag{4.121}$$

where $\mu(s) = k(s)z_L(s)$ and $z_L = (s^*)^3\Big/24\rho(s)^2$.

The overall contribution of Case A and B is [125]

$$\begin{aligned} Z_{\mathrm{CSR},A+B}(k) &= \frac{4}{s^*}e^{-4ikz_L} - \frac{4}{s^*}e^{-i\mu} - \frac{4}{s^*}(i\mu)^{1/3}\left[\Gamma(\tfrac{2}{3}) - \Gamma(\tfrac{2}{3}, i\mu)\right] \\ &= \frac{4}{s^*}e^{-4ikz_L} - \frac{4}{s^*}(i\mu)^{1/3}\left[\Gamma(\tfrac{2}{3}) + \frac{1}{3}\Gamma(-\tfrac{1}{3}, i\mu)\right] \end{aligned} \tag{4.122}$$

where the following identity of the incomplete Gamma function is used

$$\Gamma(\tfrac{2}{3}, i\mu) = -\frac{1}{3}\Gamma(-\tfrac{1}{3}, i\mu) + e^{-i\mu}(i\mu)^{-1/3} \tag{4.123}$$

The first term in the square bracket on RHS of Eq. (4.122), with $\Gamma(\frac{2}{3})$, corresponds to the steady-state CSR impedance. Therefore the remaining part belongs to entrance transient CSR impedance, thus expressed as

$$Z_{\mathrm{CSR}}^{\mathrm{ent}}(k(s); s) = \frac{-4}{s^*}e^{-4i\mu(s)} + \frac{4}{3s^*}(i\mu(s))^{1/3}\Gamma\left(\frac{-1}{3}, i\mu(s)\right) \tag{4.124}$$

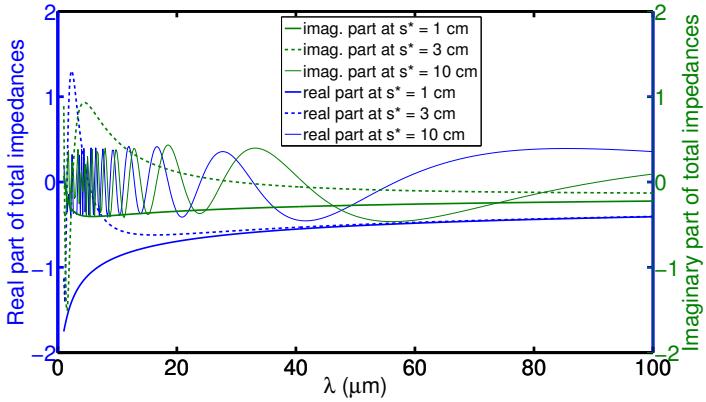

Figure 4.20: Illustration of entrance transient CSR impedance at several different entrance locations and their comparison with steady-state case. Here $L_b = 50$ cm and $\rho = 2$ m.

where $\mu(s) = k(s)z_L(s)$ and $z_L = (s^*)^3 \Big/ 24\rho(s)^2$.

Figure 4.20 below compares the entrance transient impedance with steady-state ultrarelativistic (UR) CSR case for three different locations at the dipole entrance. Here one can see that, at the location very near dipole entrance, both the real and imaginary parts of the entrance transient impedance are in general smaller than the steady-state UR-CSR. When the beam goes further within the dipole, the real and imaginary parts of the impedance oscillates rapidly and the net transient contribution becomes negligible. Note that in Sec. 4.2.1 (or Table 4.3) we have introduced the formation length. In our semi-analytical Vlasov solver, when employing the CSR entrance transient effect, we use the condition, Eq. (4.38), to determine when the transient state is included $[s^* \leq \left(24\lambda\rho^2\right)^{1/3}]$ or excluded $[s^* > \left(24\lambda\rho^2\right)^{1/3}]$.

In addition to the entrance transient state, there are also CSR exit transient effects when a beam exits from a dipole. For the Case C [Fig. 4.10(c)] with CSR fields generated from an upstream electron (at retarded time, traveling along the upstream straight section) propagating across the dipole to downstream straight section, the corresponding impedance per unit length can be obtained in a similar way. We substitute Eq. (4.117) into Eq. (4.72) and readily obtain

$$W_{\mathrm{CSR},C}(z) = -\frac{4}{\rho(\phi_m + 2x)}\lambda\left(z - \frac{\rho\phi_m^2}{6}(\phi_m + 3x)\right) = -\frac{4\tilde{\lambda}(k)e^{ikz}}{L_b + 2s^*}e^{-ik\left(\frac{L_b^2(L_b+3s^*)}{6\rho^2}\right)} \tag{4.125}$$

where s^* is the longitudinal coordinate measured from the dipole exit, $\phi_m = L_b/\rho$ is the dipole angle, and L_b is the dipole length. The correspond impedance for Case C is then

$$Z_{\mathrm{CSR},C}\left(k(s);s\right) = \frac{-4}{L_b + 2s^*}e^{\frac{-ik(s)L_b^2}{6|\rho(s)|^2}(L_b+3s^*)} \tag{4.126}$$

Figure 4.21 below shows the impedance from Eq. (4.126), where we can see the net contribution can be negligible.

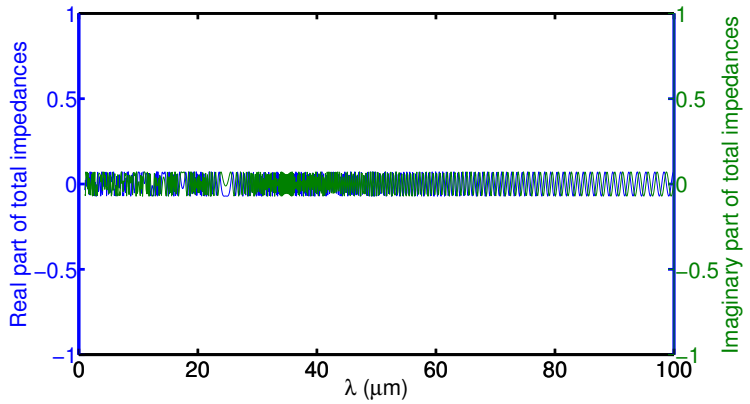

Figure 4.21: Illustration of Case-C CSR impedance at $s^* = 3$ cm. Here $L_b = 50$ cm and $\rho = 2$ m.

In addition to the steady-state CSR impedance, the most contributed CSR exit transient impedance is indeed from Case D [Fig. 4.10(d)][92]. For the impedance expression of this case where CSR fields generated from an electron (at retarded time) within a dipole propagating downstream the straight section, substituting Eq. (4.117) into Eq. (4.76) gives the first term

$$\frac{\lambda(z-\Delta z_{\max})}{\phi_m + 2x} = \frac{\tilde{\lambda}(k)e^{ikz}e^{-ik\Delta z_{\max}}}{\frac{L_b}{\rho} + 2\frac{s^*}{\rho}} \tag{4.127}$$

and the second term

$$\begin{aligned}\int_{z-\Delta z_{\max}}^{z} d\zeta \frac{1}{\psi + 2x}\frac{\partial\lambda(\zeta)}{\partial\zeta} &= \int_{z-\Delta z_{\max}}^{z} d\zeta \frac{ik\tilde{\lambda}(k)e^{ikz}e^{-ik\Delta z_{\max}}}{\psi + 2x} \\ &= -ik\tilde{\lambda}(k)e^{ikz}\int_0^{\phi_m} d\vartheta \frac{\rho\vartheta^2(\vartheta+2x)}{8(\vartheta+x)^2} e^{-ik\frac{\rho\vartheta^3}{24}\frac{4s^*+\rho\vartheta}{s^*+\rho\vartheta}}\end{aligned} \tag{4.128}$$

where

$$\Delta z_{\max} = \frac{\rho\phi_m^3}{24}\frac{\phi_m + 4x}{\phi_m + x} \tag{4.129}$$

and

$$\frac{d\zeta}{d\vartheta} = -\frac{\rho\vartheta^2(\vartheta+2x)^2}{8(\vartheta+x)^2} \tag{4.130}$$

[92]The CSR wakefield or impedance due to Case D is sometimes called CSR drift.

with $x = s^*/\rho$. Adding Eqs. (4.127) with (4.128) and divided by $\tilde{\lambda}(k)e^{ikz}$ leads to

$$Z_{\mathrm{CSR},D}(k) = \frac{4e^{-ik\Delta z_{\max}}}{L_b + 2s^*} - 4ik\rho \int_0^{\phi_m} d\vartheta \frac{\vartheta^2(\rho\vartheta + 2s^*)}{8(\rho\vartheta + s^*)^2} e^{-ik\frac{\rho\vartheta^3}{24}\frac{4s^*+\rho\vartheta}{s^*+\rho\vartheta}} \tag{4.131}$$

We remind that the transient CSR impedances derived in this subsection, Eqs. (4.124), (4.126), and (4.131), are based on ultrarelativistic beam energy. Due to practical interest of Case D in low energy regime, we adopt the following more general expressions for the CSR drift impedance by R. Li [104]. The derivation becomes more complicated but still follows similar procedures as outlined above.

$$Z_{\mathrm{CSR}}^{\mathrm{drif}}[k_z(s); s] = \frac{4}{\rho} \int_0^{\theta_m} d\vartheta \frac{df(s^*, \vartheta)}{d\vartheta} e^{-ik_z(s)\Delta z(s^*,\vartheta)} \tag{4.132}$$

where

$$f(s^*, \vartheta) = \frac{\frac{2}{\gamma^2}\left(\frac{s^*}{\rho} + \vartheta\right) + \vartheta^2\left(\frac{2s^*}{\rho} + \vartheta\right)}{\frac{4}{\gamma^2}\left(\frac{s^*}{\rho} + \vartheta\right)^2 + \vartheta^2\left(\frac{2s^*}{\rho} + \vartheta\right)^2} \tag{4.133}$$

and

$$\Delta z(s^*, \vartheta) = \frac{s^* + \rho\vartheta}{2\gamma^2} + \beta\frac{\rho\vartheta^3}{24}\frac{4s^* + \rho\vartheta}{s^* + \rho\vartheta} \tag{4.134}$$

where s^* is again the longitudinal coordinate measured from the exit of the dipole and θ_m is the angle of a bending dipole with radius ρ. β and γ are relativistic Lorentz factors. Here we remind that in our semi-analytical Vlasov calculation we only include the exit transient effects, Eqs. (4.126) and (4.132), at a nearby upstream bend.

Figure 4.22 illustrates the impedance spectrum from CSR drift, Eq. (4.132), which depends on both the wavenumber and the distance away from the dipole. From the figure we can see that the most contributing regime occurs near dipole exit (or, at shorter distances) and longer wavelengths (or small k).

4.2.6 Shielded CSR impedance (steady-state, parallel plate)

The simplified formula we adopted in our Vlasov analysis was obtained by Agoh [7, 8], who followed the theory by Warnock [204] for the shielded coherent radiation by a pair of infinite parallel plates. In this subsection we would not repeat the derivation but only highlight some important results and the underlying physics.

Assume a bunch is rigid with a rectangular transverse profile with δh in the vertical direction and vanishingly small horizontal extent. Now consider the bunch enters a isomagnetic storage ring with constant

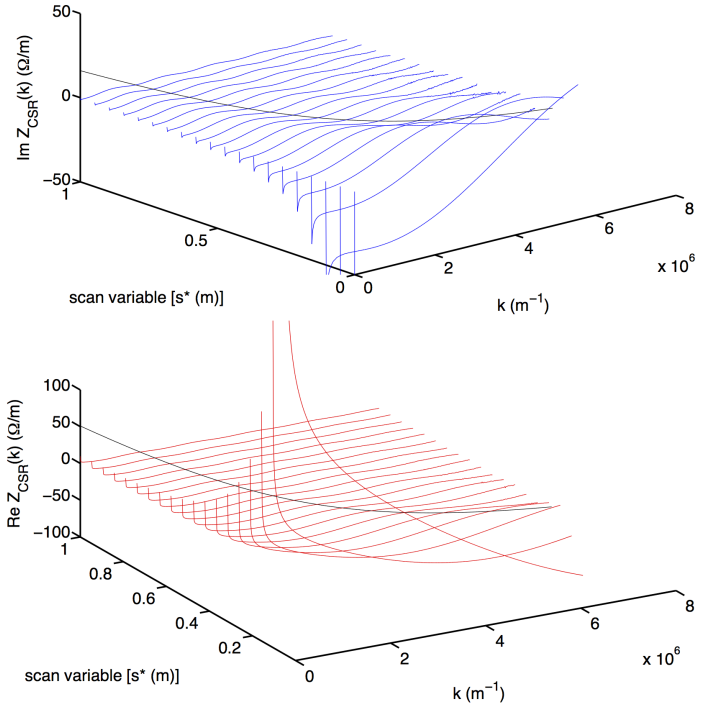

Figure 4.22: Real (top) and imaginary (bottom) parts of CSR drift impedance behavior evaluated by Eq. (4.132). Here $E_0 = 161$ MeV, $L_b = 40$ cm, and $\rho = 1.5$ m. The solid black curve is used to distinguish the slow and fast (larger k, longer s^*) oscillation.

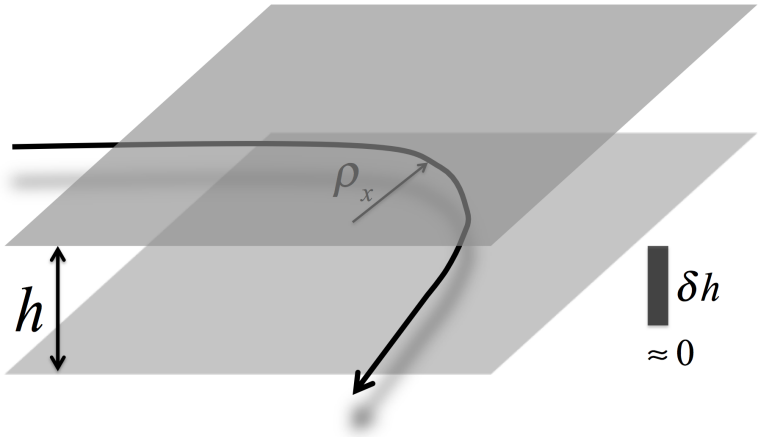

Figure 4.23: Illustration of a beam traversing a parallel plate with perfect conduction. The full height of the parallel plate is h. The vertical bunch dimension is δh with vanishingly small horizontal extension.

radius ρ_x and $v = \beta c$ between a set of parallel plates with full height h, Warnock had derived the steady-state impedance as

$$\frac{\bar{Z}(n,\omega)}{n} = \frac{8\pi^3\rho}{\beta h}\sum_{p=0}^{\infty}\Lambda_p\left[\frac{\beta\omega\rho}{nc}J_n'(\gamma_p\rho)H_n^{'(1)}(\gamma_p\rho) + \frac{\alpha_p^2}{\gamma_p^2}J_n(\gamma_p\rho)H_n^{(1)}(\gamma_p\rho)\right] \tag{4.135}$$

where $n = \omega/\omega_0 = 2\pi\rho/\lambda = k\rho$ is the harmonic number, β is the Lorentz factor, J_n and $H_n^{(1)}$ are respectively the Bessel function (of the first kind) and Hankel function (of the first kind), and the remaining notations are defined as

$$\begin{aligned}
\gamma_p &= \sqrt{\frac{\omega^2}{c^2} - \alpha_p^2} \\
\alpha_p &= \frac{\pi}{h}(2p+1) \\
\Lambda_p &= \frac{\sin^2 x}{x^2} \\
x &= \frac{\pi(\delta h)}{2h}(2p+1)
\end{aligned} \tag{4.136}$$

Usually the modulation wavelength of our interest is much more shorter than the bending radius, we discard the constraint of n being an integer number. Further assuming in the ultrarelativistic approximation ($\gamma \to \infty$ and $\beta = 1$) and $\delta h \to 0$, we divide Eq. (4.135) by the circumference of the ring $2\pi\rho$,

$$Z(k) = \frac{4\pi^2\rho k}{h}\sum_{p=0}^{\infty}\left[J_n'(r)H_n^{'(1)}(r) - (1-\frac{n^2}{r^2})J_n(r)H_n^{(1)}(r)\right] \tag{4.137}$$

where $r = n\sqrt{1-(\frac{c\alpha_p}{\omega})^2}$. Using the asymptotic expansions of the Bessel and Hankel functions, we eventually obtain a simplified expression for Eq. (4.137) with the real part

$$\mathrm{Re}\, Z_{\mathrm{CSR}}^{\mathrm{pp}}(k) = \frac{8\pi^2}{h}\left(\frac{2}{\rho k}\right)^{1/3}\sum_{p=0}^{\infty}\left[\left\{\mathrm{Ai}'(\beta_p^2)\right\}^2 + \beta_p^2\left\{\mathrm{Ai}(\beta_p^2)\right\}^2\right] \tag{4.138}$$

and the imaginary part

$$\mathrm{Im}\, Z_{\mathrm{CSR}}^{\mathrm{pp}}(k) \approx -\frac{8\pi^2}{h}\left(\frac{2}{\rho k}\right)^{1/3}\sum_{p=0}^{\infty}\left[\mathrm{Ai}'(\beta_p^2)\mathrm{Bi}'(\beta_p^2) + \beta_p^2\mathrm{Ai}(\beta_p^2)\mathrm{Bi}(\beta_p^2)\right] \tag{4.139}$$

with

$$\beta_p = (2p+1)\frac{\pi}{h}\left(\frac{\rho}{2k^2}\right)^{1/3} = (2p+1)\left[\frac{3}{4}\left(\frac{k_{\mathrm{th}}}{k}\right)^2\right]^{1/3} \tag{4.140}$$

where

$$k_{\rm th} = \sqrt{\frac{2\rho}{3}\left(\frac{\pi}{h}\right)^3} \tag{4.141}$$

is the threshold wavenumber introduced in Eq. (4.48). For the wavelength longer than the threshold $\lambda \gg 2\pi/k_{\rm th}$, only $p = 0$ contributes in Eq. (4.138). Equation (4.138) becomes

$$\mathrm{Re}\, Z_{\rm CSR}^{\rm pp}(k \ll k_{\rm th}) = \frac{4\pi^2}{h^2 k} e^{-k_{\rm th}^2/k^2} \tag{4.142}$$

which means the radiation with longer wavelength than $\lambda_{\rm th}$ would be exponentially suppressed in the presence of parallel plates. The threshold condition is determined by the full pipe width and the bending radius.

At high frequencies, Eqs. (4.138) and (4.139) reduce to free-space CSR impedance,

$$\mathrm{Re}\, Z_{\rm CSR}^{\rm pp}(k \gg k_{\rm th}) \approx 4\pi\left(\frac{k}{2\rho^2}\right)^{1/3} \int_0^\infty \frac{du}{\sqrt{u}} \left[\left\{\mathrm{Ai}'(u)\right\}^2 + u\{\mathrm{Ai}(u)\}^2\right] = 3^{1/6}\Gamma(\tfrac{2}{3})\left(\frac{k}{\rho^2}\right)^{1/3} \tag{4.143}$$

$$\mathrm{Im}\, Z_{\rm CSR}^{\rm pp}(k \gg k_{\rm th}) \approx -4\pi\left(\frac{k}{2\rho^2}\right)^{1/3} \int_0^\infty \frac{du}{\sqrt{u}} \left[\mathrm{Ai}'(u)\mathrm{Bi}'(u) + u\mathrm{Ai}(u)\mathrm{Bi}(u)\right] = \Gamma(\tfrac{2}{3})\left(\frac{k}{3\rho^2}\right)^{1/3} \tag{4.144}$$

Figure 4.24 below shows a numerical example of steady-state parallel-plate shielded CSR impedance with comparison of that in free-space case. It can be seen that at shorter wavelengths or with wider gaps the shielding effect is absent and close to the free-space results.

To summarize, here we quote the main results obtained in this subsection. For an ultrarelativistic (UR) electron beam traversing a bending dipole, the parallel-plate steady-state CSR impedance per unit length can be expressed as [7]

$$Z_{\rm CSR}^{\rm pp}(k) = \frac{8\pi^2}{h}\left(\frac{2}{k(s)\rho(s)}\right)^{\frac{1}{3}} \sum_{p=0}^{\infty} F_0(\beta_p) \tag{4.145}$$

where

$$F_0(\beta) = \mathrm{Ai}'\left(\beta^2\right)\left[\mathrm{Ai}'\left(\beta^2\right) - i\mathrm{Bi}'\left(\beta^2\right)\right] + \beta^2\mathrm{Ai}'\left(\beta^2\right)\left[\mathrm{Ai}\left(\beta^2\right) - i\mathrm{Bi}\left(\beta^2\right)\right] \tag{4.146}$$

with

$$\beta_p = (2p+1)\,\frac{\pi}{h}\left(\frac{\rho(s)}{2k^2(s)}\right)^{\frac{1}{3}} \tag{4.147}$$

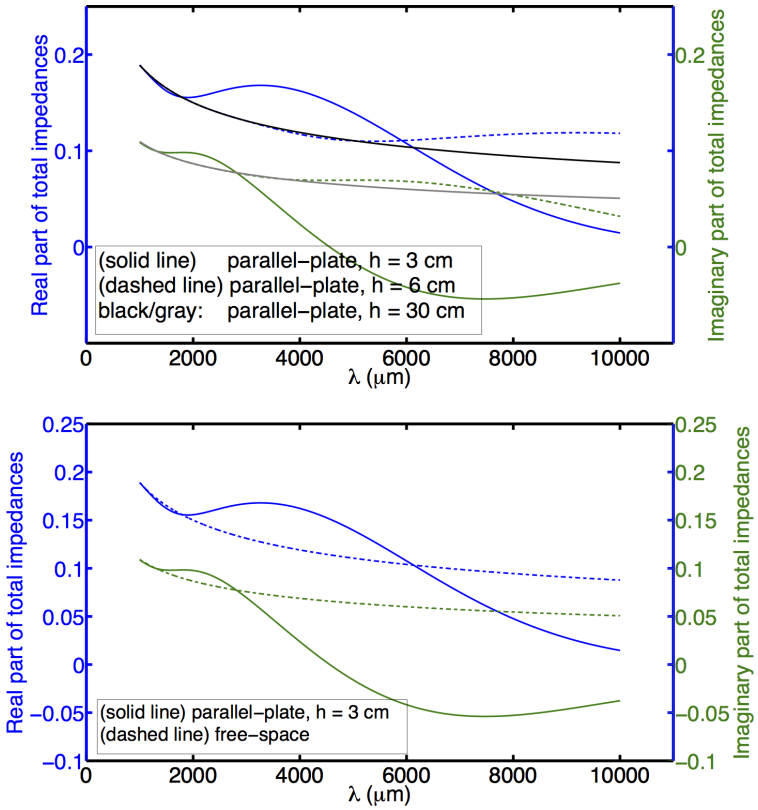

Figure 4.24: Comparison of shielded parallel-plate CSR impedance (in unit of cm^{-1}) for different beam pipe heights (left) and with free-space UR-CSR case (right). Here $\rho = 2$ m.

4.2.7 Summary Table for various CSR impedances

To end this section, we summarize the analytical impedance models used in our Vlasov solver in Table 4.5.

4.3 Longitudinal space charge force (LSC)

In Sec. 4.2 we have considered CSR effect. Effects of space charge force due to Coulomb interactions in an intense charged particle beam have long been an important issue for beam stability in beam transport systems [150]. LSC plays an essential role in microbunching dynamics. In this section, we attempt to derive LSC impedance models following similar procedures as we demonstrated in Sec. 4.2.

We start by assuming an infinitely long beam in free space with uniform transverse distribution of circular cross section. Then we calculate the longitudinal electric field generated by the beam. The impedance can be obtained by dividing the electric field by the beam current as

$$Z_0^{\parallel}(k) = \frac{\tilde{E}_z(k)}{\tilde{I}(k)} \tag{4.148}$$

Table 4.5: Summary of analytical CSR impedance models used in our semi-analytical Vlasov solver.

Free-space	Steady-state	Non-ultrarelativistic: $\mathrm{Re}\left[Z_{\mathrm{CSR}}^{\mathrm{s.s.NUR}}(k(s);s)\right] = \frac{-2\pi k(s)^{1/3}}{\lvert\rho(s)\rvert^{2/3}}\mathrm{Ai}'(x) + \frac{k(s)\pi}{\gamma^2}\left(\int_0^x \mathrm{Ai}(\varsigma)\mathrm{d}\varsigma - \frac{1}{3}\right)$ $\mathrm{Im}[Z_{\mathrm{CSR}}^{\mathrm{s.s.NUR}}(k(s);s)] \simeq \frac{2\pi k(s)^{1/3}}{\lvert\rho(s)\rvert^{2/3}}\left\{\frac{1}{3}\mathrm{Bi}'(x) + \int_0^x \left[\mathrm{Ai}'(x)\mathrm{Bi}(t) - \mathrm{Ai}(t)\mathrm{Bi}'(x)\right]\, dt\right\}$ $x = \gamma^{-2}(k\rho)^{2/3}$
		Ultrarelativistic: $Z_{\mathrm{CSR}}^{\mathrm{s.s.UR}}(k(s);s) = \frac{-ik(s)^{1/3}A}{\lvert\rho(s)\rvert^{2/3}},\ A = -2\pi\left[\mathrm{Bi}'(0)/3 + i\mathrm{Ai}'(0)\right]$
	Entrance transient	$Z_{\mathrm{CSR}}^{\mathrm{ent}}(k(s);s) = \frac{-4}{s^*}e^{-4i\mu(s)} + \frac{4}{3s^*}(i\mu(s))^{1/3}\Gamma\left(\frac{-1}{3}, i\mu(s)\right)$ $\mu(s) = k(s)z_L(s)$ $z_L = (s^*)^3 \Big/ 24\rho(s)^2$
	Exit transient	$Z_{\mathrm{CSR}}^{\mathrm{drif}}[k_z(s);s] = \frac{4}{\rho}\int_0^{\theta_m} d\vartheta \frac{df(s^*,\vartheta)}{d\vartheta}e^{-ik_z(s)\Delta z(s^*,\vartheta)}$ $f(s^*,\vartheta) = \frac{\frac{2}{\gamma^2}\left(\frac{s^*}{\rho}+\vartheta\right)+\vartheta^2\left(\frac{2s^*}{\rho}+\vartheta\right)}{\frac{4}{\gamma^2}\left(\frac{s^*}{\rho}+\vartheta\right)^2+\vartheta^2\left(\frac{2s^*}{\rho}+\vartheta\right)^2}$ $\Delta z(s^*,\vartheta) = \frac{s^*+\rho\vartheta}{2\gamma^2} + \beta\frac{\rho\vartheta^3}{24}\frac{4s^*+\rho\vartheta}{s^*+\rho\vartheta}$
With boundary condition	Parallel-plate shielding	$Z_{\mathrm{CSR}}^{\mathrm{pp}}(k) = \frac{8\pi^2}{h}\left(\frac{2}{k(s)\rho(s)}\right)^{\frac{1}{3}}\sum_{p=0}^{\infty} F_0(\beta_p)$ $F_0(\beta) = \mathrm{Ai}'\left(\beta^2\right)\left[\mathrm{Ai}'\left(\beta^2\right) - i\mathrm{Bi}'\left(\beta^2\right)\right] + \beta^2\mathrm{Ai}'\left(\beta^2\right)\left[\mathrm{Ai}\left(\beta^2\right) - i\mathrm{Bi}\left(\beta^2\right)\right]$ $\beta_p = (2p+1)\frac{\pi}{h}\left(\frac{\rho(s)}{2k^2(s)}\right)^{\frac{1}{3}}$

where $\tilde{E}_z(k)$ is the electric field (in k-domain, with transverse dependence retained here) and the current density distribution is

$$\tilde{I}(k) = e\beta c\tilde{\rho}_z(k) \tag{4.149}$$

with $\tilde{\rho}_z(k)$ the line bunch distribution.

The relation of $\tilde{\rho}_z(k)$ to $\rho_z(z)$ follows the definition of Fourier transformation

$$\tilde{\rho}_z(k) = \frac{1}{2\pi}\int_{-\infty}^{\infty} dz\rho_z(z)e^{-ikz} \tag{4.150}$$

In this section, we first consider the simplest case, the free-space LSC, and then quote the results for a more dedicated case with presence of boundary pipe. Then we discuss the effect of 3-D space charge on the beam dynamics, from which shall give us the validity of 1-D LSC models.

4.3.1 Free-space LSC

For a general three-dimensional bunch distribution,

$$\rho(x, y, z) = \rho_\perp(x, y)\rho_z(z) \tag{4.151}$$

with the normalization in transverse dimensions specified by

$$\int dxdy\rho_\perp(x, y) = 1 \tag{4.152}$$

and assume coasting beam approximation has been made

$$\int_{-L/2}^{L/2} dz\rho_z(z) = L, L \to \infty \tag{4.153}$$

The longitudinal electric field E_z generated by a single electron can be obtained as follows. First, we boost a reference frame (assume in the z direction with the velocity βc) to the rest frame of the electron, say K', in which the dynamic variables are denoted by a prime[93]. In the rest frame, this electron generates an electrostatic field, which can be readily determined by Coulomb's law.

$$\mathbf{E}'(\mathbf{x}') = -\frac{e\mathbf{x}'}{|\mathbf{x}'|^3} \tag{4.154}$$

where $\mathbf{x}' = (x', y', z')$ is the position vector of the electron with respect to a reference origin. Then, to find

[93] At the moment, the prime does not indicate the differentiation.

the electric (and/or magnetic) fields in the lab frame, we apply Lorentz transformations for the position vector and for the electromagnetic fields, which respectively follow

$$\begin{cases} x' = x \\ y' = y \\ z' = \gamma(z - \beta ct) \\ t' = \gamma(t - \beta z/c) \end{cases} \tag{4.155}$$

and

$$\begin{cases} \mathbf{E}_\perp = \gamma\left(\mathbf{E}'_\perp - \beta \times \mathbf{B}'\right) \\ E_z = E'_z \\ \mathbf{B}_\perp = \gamma\left(\mathbf{B}'_\perp + \beta \times \mathbf{E}'\right) \\ B_z = B'_z \end{cases} \tag{4.156}$$

The longitudinal electric field in the lab frame due to a relativistic electron can then be written as [87]

$$E_z(\mathbf{x}) = \frac{e\gamma(z - z')}{\left[(x - x')^2 + (y - y')^2 + \gamma^2(z - z')^2\right]^{3/2}} \tag{4.157}$$

where $\mathbf{x} = (x, y, z)$ is the position coordinate of the observation location.

For a collection of electrons, the resultant electric field can be obtained by superposition principle and expressed as

$$E_z(\mathbf{x}) = \int d\mathbf{x} G(\mathbf{x}, \mathbf{x}')e\rho(\mathbf{x}) \tag{4.158}$$

with Green function

$$G(\mathbf{x}, \mathbf{x}') = \frac{\gamma(z - z')}{\left[(x - x')^2 + (y - y')^2 + \gamma^2(z - z')^2\right]^{3/2}} = -\frac{1}{\gamma^2}\frac{\partial}{\partial z}\frac{1}{|\mathbf{x} - \mathbf{x}'|} \tag{4.159}$$

With help of Jackson Eq. (3.148) [87], Eq. (4.159) can be transformed to cylindrical coordinate system, (r, ϕ, z) [see also Fig. 4.25 below], and we have

$$G(\mathbf{x}, \mathbf{x}') = -\frac{i}{\gamma^2\pi}\sum_{m=-\infty}^{\infty} e^{im(\phi - \phi')} \int_{-\infty}^{\infty} dk e^{ik(z - z')} k I_m\left(\frac{kr_<}{\gamma}\right) K_m\left(\frac{kr_>}{\gamma}\right) \tag{4.160}$$

where I_m and K_m are modified Bessel functions of the first and second kind. In Eq. (4.160) we follow Jackson's convention by using $r_<$ ($r_>$) to denote the smaller (larger) between r and r'.

Next, we take the Fourier transformation on both sides of Eq. (4.158),

$$\begin{aligned}\tilde{E}_z(k) &= \frac{1}{2\pi}\int_{-\infty}^{\infty} dz E_z(\mathbf{x}) e^{-ikz} \\ &= -\frac{ie}{2\gamma^2\pi^2}\int_{-\infty}^{\infty} dz e^{-ikz}\int d\mathbf{x}'\rho(\mathbf{x}')\sum_{m=-\infty}^{\infty} e^{im(\phi-\phi')}\int_{-\infty}^{\infty} d\kappa e^{i\kappa(z-z')}\kappa I_m\left(\frac{\kappa r_<}{\gamma}\right)K_m\left(\frac{\kappa r_>}{\gamma}\right) \\ &= -\frac{ie}{\gamma^2\pi}\sum_{m=-\infty}^{\infty}\int d\mathbf{x}'\rho(\mathbf{x}')ke^{-ikz'}e^{im(\phi-\phi')}I_m\left(\frac{kr_<}{\gamma}\right)K_m\left(\frac{kr_>}{\gamma}\right)\end{aligned} \tag{4.161}$$

In the third equality use has been made of $\int_{-\infty}^{\infty} dz e^{i(k-k')z} = 2\pi\delta(k-k')$. Assume a transverse uniform density with circular cross section of radius r_b, i.e.

$$\rho(\mathbf{x}') = \rho_\perp(r',\phi')\rho_z(z') = \frac{\rho_z(z')}{\pi r_b^2} \tag{4.162}$$

and

$$\int dx'dy' \to \int r'dr'd\phi' \tag{4.163}$$

and we locate the observation position on axis (i.e. $r=0, x=y=0$). Then in Eq. (4.161) only $m=0$ term, $I_0(0)=1$, contributes because $I_m(0)=0$ except for $m=0$, i.e.

$$K_m\left(\frac{kr_>}{\gamma}\right) \to K_0(\xi) \tag{4.164}$$

Taking advantage of the following integration formula

$$\int_0^{\xi} dx\ xK_0(x) = 1 - \xi K_1(\xi) \tag{4.165}$$

and Eq. (4.148), the free-space LSC impedance can be obtained

$$Z_{\text{LSC}}^{\text{on-axis}}(k) = \frac{4i}{\gamma r_b}\frac{1-\xi_b K_1(\xi_b)}{\xi_b} \tag{4.166}$$

where

$$\xi_b = kr_b/\gamma \tag{4.167}$$

The geometric meaning of is illustrated in Fig. 4.25 below, which characterizes the length scale of the modulation wavelength on top of longitudinal bunch distribution. Later we would discuss the validity of the

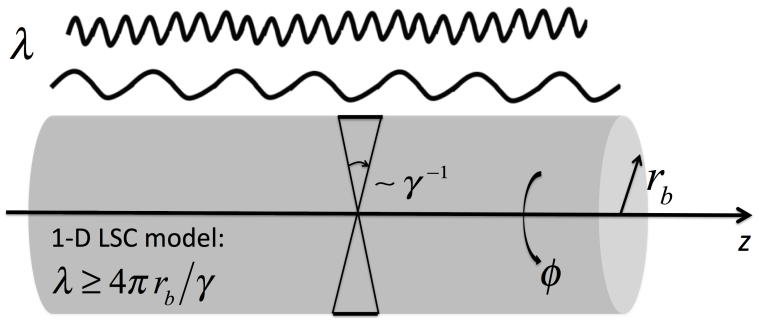

Figure 4.25: Illustration of the coasting beam model with cylindrically symmetric transverse density profile. The 1-D LSC model is valid when the modulation wavelength is longer than the characteristic length $\frac{r_b}{\gamma}$.

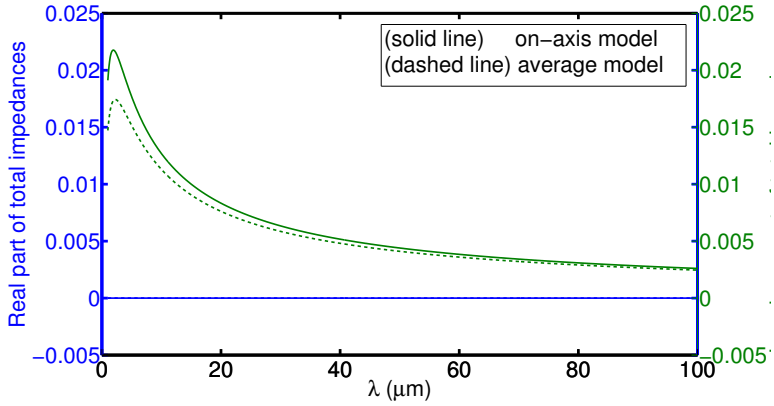

Figure 4.26: Comparison of two LSC impedances (in unit of cm^{-1}). Here the beam energy is assumed 750 MeV and $\sigma_x = \sigma_y = 0.5$ mm.

1-D LSC impedance model in Sec. 4.3.3.

Figure 4.26 below shows the spectral dependence of the 1-D LSC impedance. As already mentioned in Sec. 4.2.4, the space charge effect is reactive; the particle energy within the bunch is redistributed without energy loss.

At higher frequencies, Eq. (4.166) can have the approximate expression

$$Z_{\mathrm{LSC}}^{\text{on-axis}}(k \to \infty) = \frac{4i}{kr_b^2} \tag{4.168}$$

At extreme low frequencies, i.e. DC case, Eq. (4.166) is reduced to the familiar expression

$$Z_{\mathrm{LSC}}^{\text{on-axis}}(k \to 0) = -\frac{4ik}{\pi\gamma^2}\left(\log\frac{\xi_b^2}{4} + 2\gamma_E - 1\right) \tag{4.169}$$

The second model considers the average of the transverse beam distribution, called average model,

where it relates the first (on-axis) model by the following relation [194]

$$Z_{\rm ave} \equiv \frac{2}{r_b^2}\int_0^{r_b} rZ(k,r)dr \tag{4.170}$$

and

$$Z_{\rm LSC}^{\rm ave}(k(s);s) = \frac{4i}{\gamma r_b(s)}\frac{1-2I_1(\xi)K_1(\xi)}{\xi} \tag{4.171}$$

From Fig. 4.26 above we see the on-axis and average LSC impedance models give approximately the same results.

The third model employs an axis-symmetric beam with transverse Gaussian distribution of

$$\rho_\perp(x,y) = \frac{1}{2\pi\sigma^2}e^{-\frac{x^2+y^2}{2\sigma^2}} \tag{4.172}$$

Substituting into Eq. (4.161) and using the following integration formula

$$\int_0^\xi dx\ xK_0(x)e^{-x^2/2\xi^2} = -\frac{\xi^2}{2}e^{\xi^2/2}{\rm Ei}\left(-\frac{\xi^2}{2}\right) \tag{4.173}$$

we obtain

$$Z_{\rm LSC}^{\text{on-axis}}(k) = -\frac{i\xi_\sigma}{\sigma\gamma}e^{\xi_\sigma^2/2}{\rm Ei}\left(-\frac{\xi_\sigma^2}{2}\right) \tag{4.174}$$

with $\xi_\sigma = k\sigma/\gamma$ and ${\rm Ei}(x) \equiv -\int_{-x}^{\infty} dte^{-t}t^{-1}$ is the exponential-integral function.

At the end of this subsection, we remind that, in evaluating LSC effect using the above expressions, r_b is assigned from $\sigma_x(s)$ and $\sigma_y(s)$ (from pure-optics tracking simulation) with the weighting factor studied from the numerical fitting [209]

$$r_b \approx \frac{1.747}{2}\left(\sigma_x+\sigma_y\right) \tag{4.175}$$

4.3.2 LSC with boundary condition

In this subsection we only outline the procedures to solve the LSC field in the presence of a boundary pipe. Without further derivation, we present several analytically available LSC impedance expressions [193, 115].

Same as the first step of calculating electric field by a single electron, we solve the electrostatic problem in the rest frame of the beam by formulating the Laplace equation (or Poisson equation in the absence of source term) and solving for the electrostatic potential using separation of variables. The boundary conditions determine the coefficients of the eigenbasis. Having obtained the solution in the rest frame, we apply the Lorentz transformations to transform the coordinate vectors and fields back to the lab frame.

In our semi-analytical Vlasov solver, we employ the following expression for LSC impedance with round pipe and uniform round beam,

$$Z_{\mathrm{LSC}}^{\substack{\text{uniform-round}\\ \text{round-pipe}}}(k) = \frac{4i}{\gamma r_b}\frac{1}{\xi_b}\left[1 - \xi_b\left(K_1(\xi_b) - K_0\left(\frac{\xi_b r_p}{r_b}\right)\frac{I_1(\xi_b)}{I_0\left(\frac{\xi_b r_p}{r_b}\right)}\right)\right] \tag{4.176}$$

where the radius of the beam pipe is r_p and assumed with perfect conduction. At high-frequency limit, for $r_p/r_b > 1$, the second term in the round bracket of Eq. (4.176) decreases exponentially with $\xi_b = kr_b/\gamma$, so the expression is reduced to Eq. (4.166), as expected.

4.3.3 3-D effect of LSC and 3-D space charge effect on microbunching instability

While we use 1-D LSC model, we study 3-D effect of LSC and discuss the applicability region. The difference lies within the length scales of perturbation/fluctuation of bunch charge distribution and the transverse beam size. At the high frequency regime, we expect that the 1-D model may fail when the scaled wavelength of charge perturbation becomes comparable to or smaller than the transverse beam size (see Fig. 4.25). Because the space charge originates from the granularity of the elementary charge, it gives rise to random fluctuation of the beam current (or shot noise). To compare the 1-D and 3-D LSC models, we estimate how the field fluctuations in 1-D and 3-D cases behave by determining their statistics and correlations.

For 1-D case, assume a long beam with length L. We divide the beam longitudinally into $\mathcal{N}$ slices, with each slice $z_j \in \Delta z[j-1, j]$ with width Δz. Further assume the total number of electrons is N_b and the fluctuating (with, however, on average uniform) bunch density distribution ρ_z. For each slice, the number of electrons is randomly fluctuating and obeys the statistics

$$N_j = \langle N_j\rangle + \langle N_j\rangle^{1/2}\eta_j \tag{4.177}$$

where the average number as the expectation value

$$\langle N_j\rangle = \lambda\Delta z = N_b\Delta z/L \tag{4.178}$$

and the univariate normal random variable

$$\langle\eta_j\rangle = 0, \langle\eta_i\eta_j\rangle = \delta_{ij} \tag{4.179}$$

Then for each slice, the bunch density can be expressed as $N_j/\langle N_j\rangle$,

$$\rho_z(z_j) = 1 + \frac{\eta_j}{\langle N_j\rangle^{1/2}} \tag{4.180}$$

The correlation of 1-D bunch charge distribution is estimated as

$$\langle \rho_z(z_i)\rho_z(z_j)\rangle = 1 + \frac{\delta_{ij}}{\langle N_j\rangle^{1/2}} \tag{4.181}$$

Taking the Fourier transformations to Eqs. (4.180) and (4.181), we have

$$\langle \tilde{\rho}_z(k)\rangle = 0 \tag{4.182}$$

and

$$\langle \tilde{\rho}_z(k)\tilde{\rho}_z^*(k')\rangle = \frac{1}{(2\pi)^2}\frac{L^2}{N_b}\delta_{kk'} \tag{4.183}$$

Substituting into Eq. (4.148), the corresponding correlation of the LSC fields is estimated

$$\left\langle \tilde{E}_z(k)\tilde{E}_z^*(k)\right\rangle = \frac{4e^2N_b}{\pi^2\gamma^2r_b^2}\left(\frac{1-\xi_bK_1(\xi_b)}{\xi_b}\right)^2\delta_{kk'} \tag{4.184}$$

So far we have obtained Eq. (4.184) for 1-D case, a similar analysis follows for 3-D case. Now the beam is assumed with (on average) uniform transverse distribution with circular cross section of radius r_b. Consider an elementary volume cell with $dV = r_i dr d\phi dz$ at (r_i, ϕ_j, z_ℓ), the number of electrons lying within the volume is

$$N_{i\ell j} = \langle N_{i\ell j}\rangle + \langle N_{i\ell j}\rangle^{1/2}\eta_i\eta_\ell\eta_j \tag{4.185}$$

where the average number as the expectation value

$$\langle N_{i\ell j}\rangle = \rho_{\perp 0} r_i \Delta r \Delta\phi \Delta z \tag{4.186}$$

with the transverse bunch charge density, and

$$\langle \eta_i\rangle = \langle \eta_\ell\rangle = \langle \eta_j\rangle = 0, \langle \eta_i\eta_j\rangle = \delta_{ij} \tag{4.187}$$

Similar to Eq. (4.181), now we have the correlation of the 3-D bunch charge distribution

$$\langle \rho(r_i,\phi_\ell,z_j)\rho(r_{i'},\phi_{\ell'},z_{j'})\rangle = 1 + \frac{\delta_{ii'}\delta_{\ell\ell'}\delta_{jj'}}{\langle N_{i\ell j}\rangle^{1/2}} \tag{4.188}$$

and the corresponding correlation of LSC fields by substituting into Eq. (4.161),

$$\left\langle \tilde{E}_z(k)\tilde{E}_z^*(k)\right\rangle = \frac{4e^2N_b}{\pi^2\gamma^2r_b^2}\left(\frac{1+\xi_b^2\left[K_0^2(\xi_b)-K_1^2(\xi_b)\right]}{4}\right)\delta_{kk'} \tag{4.189}$$

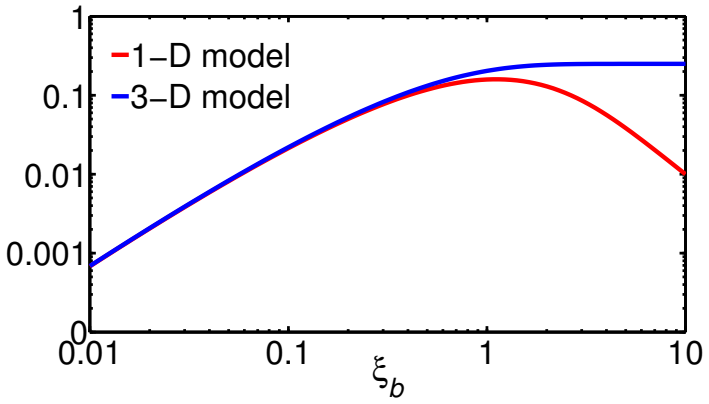

Figure 4.27: Dependence of 1-D and 3-D LSC impedance models on the characteristic dimensionless parameter ξ_b.

where use has been made of the following integration formula

$$\int_0^{\xi} dx x K_0^2(x) = \frac{\xi_b^2}{2}\left[K_0^2(\xi_b) - K_1^2(\xi_b)\right] \tag{4.190}$$

Now we want to compare Eq. (4.184) with Eq. (4.189), respectively, for 1-D and 3-D based LSC models. As shown in Fig. 4.27 below, we can see that 1-D LSC model is valid when

$$\xi_b < 0.5 \tag{4.191}$$

or

$$\lambda > 4\pi r_b/\gamma \tag{4.192}$$

Having investigated the applicability region of LSC models, let us take a look at how the (mere) LSC force and the (full) three-dimensional space charge force (instead of LSC accounting for 3-D effects) influence the microbunching dynamics. The analytical formula for 3-D space charge impedance is not available, so we study its effect by resorting to numerical simulation. For simplicity, we only take a simple drift[94] as an example. Figure 4.28 shows the evolution of microbunching density gain function along a 1.75-m drift section. Our Vlasov solver (solid lines), which adopts the impedance models derived in Sec. 4.3.1, gives consistent results with `elegant`, which also utilizes 1-D LSC model [82]. The slight difference comes from different approaches/algorithms performed in `elegant` and our Vlasov solver. It is interesting that a third particle tracking code, `TStep` [214], based on particle-in-cell (PIC) algorithm, which calculates 3-D space charge forces along a beam transport, give distinct results with those by 1-D LSC case[95].

[94]For zeroth order, a section of drift is dispersion free and the momentum compaction is zero. However to first order, the momentum compaction is nonzero and $R_{56} \approx L_d/\gamma^2$.

[95]The `TStep` result was later confirmed with another program `ELEGANT-BH` by Halavanau [75] (not shown here), which also

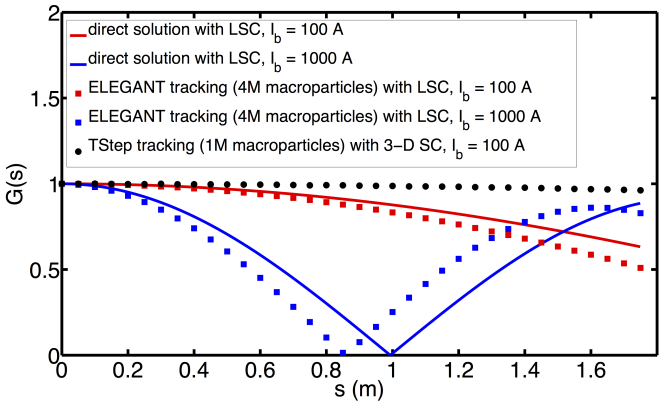

Figure 4.28: LSC gain functions for a 1.75-m drift. Note thus far we have only 1-D LSC model implemented in our code (as well as in `elegant`), `TStep` results with 3-D SC are still attached for further comparison of the $G(s)$ gain difference. A slight difference between direct solutions (red or blue dots) and `elegant` results (red or blue curves) comes from the fact of transverse beam distortion (thus rms beam sizes σ_x (Sx) and σ_y (Sy) would not properly account for the transverse beam distributions). In the simulation the initial modulation wavelength is assumed 100 μm.

4.3.4 Summary table for various LSC impedances

We end this section by summarizing the derived LSC impedance models for use in our subsequent Vlasov analysis. We remind that the validity of 1-D LSC model is for $\xi_b < 0.5$, where $\xi_b = kr_b/\gamma$ and the beam radius would be evaluated by the weighted average of transverse horizontal and vertical rms beam sizes, $r_b \approx 0.8735\,(\sigma_x + \sigma_y)$.

4.4 Linac geometric effect

In this section we consider the third category of short-ranged wakefield or high-frequency impedance induced from the geometry of a chain of RF cavities in a linac. To avoid the (nonlinear) curvature effect due to RF accelerating cavities, short bunches are accelerated in the linear accelerators. For example, in LCLS [100] the peak current is with several kA, bunch charge ∼nC, and bunch length is about 10 to 100 μm with RF frequency 2856 MHz. In the modern recirculating accelerators, e.g. JLab FEL [123], peak current ∼7.8 A, bunch charge 135 pC, bunch length ∼50 μm with RF frequency1497 MHz. For JLEIC CCR [1, 2], we have peak current 60 A, bunch charge ∼2 nC, bunch length ∼3 cm. For such high-brightness beam, in order to predict the beam quality at the downstream of the accelerator, it is essential to know how the short range wakefields or equivalently the high frequency impedances of the accelerating structure behave

takes into account 3-D space charge calculation. The purpose of presenting these results here is to demonstrate 3-D space charge force can also affect the resultant longitudinal microbunching in some parameter regimes. Indeed it will be complete to extend the thorough analysis to include both transverse and longitudinal beam dynamics and electrodynamics.

Table 4.6: Summary of analytical LSC impedance models used in our semi-analytical Vlasov solver.

Free space	Uniform circular cross section with r_b	on-axis: $Z_{\rm LSC}^{\rm on\text{-}axis}(k) = \frac{4i}{\gamma r_b}\frac{1-\xi_b K_1(\xi_b)}{\xi_b}$
		average: $Z_{\rm LSC}^{\rm ave}(k(s);s) = \frac{4i}{\gamma r_b(s)}\frac{1-2I_1(\xi)K_1(\xi)}{\xi}$
	Gaussian	on-axis: $Z_{\rm LSC}^{\rm on\text{-}axis}(k) = -\frac{i\xi_\sigma}{\sigma\gamma}e^{\xi_\sigma^2/2}{\rm Ei}\left(-\frac{\xi_\sigma^2}{2}\right)$
With boundary condition	uniform circular r_b & round pipe r_p	$Z_{\rm LSC}^{\substack{\text{uniform-round}\\ \text{round-pipe}}}(k) = \frac{4i}{\gamma r_b}\frac{1}{\xi_b}\left[1-\xi_b\left(K_1(\xi_b) - K_0\left(\frac{\xi_b r_p}{r_b}\right)\frac{I_1(\xi_b)}{I_0\left(\frac{\xi_b r_p}{r_b}\right)}\right)\right]$

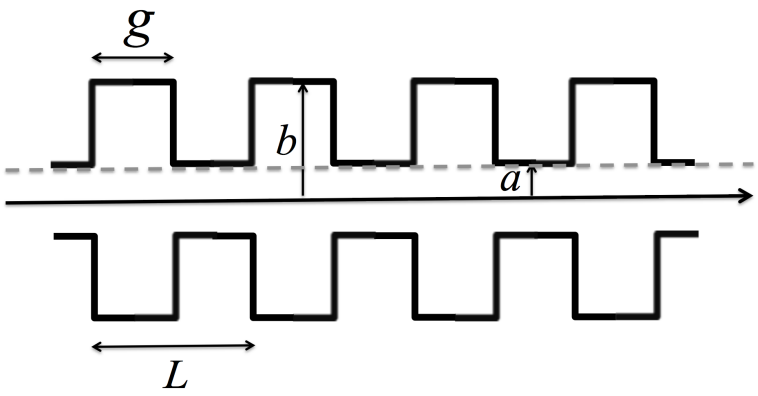

Figure 4.29: Illustration of geometric layout of an infinitely long periodic cavity structure.

and affect the beam. Gluckstern [71] had derived the longitudinal and high-frequency impedance of an infinite-long periodic structure, a solution which is valid for a structure with the small gap-to-period (g/L) ratio, shown in Fig 4.29. Later, Yokoya and Bane [212] extended his approach to derive a similar expression, which is not limited to small gaps, and applied to the linac of Next Linear Collider (NLC) [135]. In this section we briefly reproduced Yokoya and Bane's formula and later would incorporate it in our Vlasov solver.

The effects of the longitudinal geometric wakefield in the accelerator on the microbunching instability was early studied by Huang *et al.* [83]. They show that significant energy modulation can be accumulated in the linac through the geometrical wakefield and can enhance the CSR microbunching in the bunch compressors through R_{56}. In ERL or recirculation machines, the long linac section followed by an arc can potentially accumulate an amount of energy modulations by LSC or linac geometric effects. Thus we need to include this effect in the thorough analysis.

Similar to Sec. 4.2 and 4.3, we do not derive in very detail but only highlight the important steps

and summarize the resultant expression employed in the dissertation. Consider a periodic (ideally infinitely long) accelerating structure. The beam traversing the structure is assumed with $v = c$. The azimuthally symmetric cavity cell connects with the beam pipe, where the cavity region is defined within $a \leq r \leq b$ and the pipe region within $r \leq a$. Fig. 4.29 shows the geometry. The electromagnetic fields, which can be driven by arbitrary current distribution $J = J_0 e^{ikz}$, can be expanded in terms of Bessel functions in the pipe region and in terms of cavity mode eigen-functions in the cavity region. The derived fields must satisfy the boundary condition at $r = a$ by Maxwell equations. Here we assume the beam pipe is perfectly conducting. It can be expected that the field matching on the pipe-cavity boundary can give the governing equation for the fields and driving sources. Gluckstern derived the governing equation and expressed in terms of an integral equation as

$$\int_0^g dz' \left[\hat{K}_c(z, z') + \sum_{m=-\infty}^{\infty} \hat{K}_p(mL + z' - z) \right] F(z') = -i \tag{4.193}$$

where $F(z)$ is the normalized longitudinal electric field at $r = a$ within the cavity region, i.e.

$$F(z) \equiv \frac{ka^2}{4\pi J_0} e^{-ikz} E_z(a, z) \tag{4.194}$$

The longitudinal impedance per unit length is defined as

$$Z_{\text{linac}}^{\text{UR}}(k) \equiv \frac{\bar{Z}_{\text{linac}}^{\text{UR}}}{L} = \frac{\int E_z dz}{J_s L} = \frac{4\pi}{ka^2 L} \int_0^g dz F(z) \tag{4.195}$$

In Eq. (4.193) the cavity kernel is given by Eq. (3.21) of Ref. [72] for non-oscillatory part

$$\hat{K}_c(z, z') = -\frac{(1+i)\sqrt{\pi}}{a\sqrt{k(z - z')}} \Theta(z - z') \tag{4.196}$$

with Θ the step function

$$\Theta(x) \equiv \begin{cases} 1, x \geq 0 \\ 0, x < 0 \end{cases} \tag{4.197}$$

The pipe kernel $\hat{K}_p$ is

$$\hat{K}_p(z) = -\frac{2\pi i}{a} e^{ikz} \sum_{s=1}^{\infty} \frac{1}{b_s} e^{i\frac{b_s|z|}{a}} \tag{4.198}$$

with the propagation constant b_s defined as

$$b_s = \begin{cases} \sqrt{k^2a^2 - j_s^2}, ka > j_s \\ i\sqrt{j_s^2 - k^2a^2}, ka < j_s \end{cases} \tag{4.199}$$

where j_s are the zeros of the Bessel function J_0.

Gluckstern found that the high frequency behavior of the cavity kernel $\hat{K}_c$ is independent of the detailed cavity shapes. He also showed that for $m = 0$, $\hat{K}_p(z' - z) = \hat{K}_c(z, z')$; for $m > 0$, $\hat{K}_p$ oscillates rapidly at high frequency and does not contribute to the average impedance; for $m < 0$, $\hat{K}_p$ contributes to Eq. (4.193). Without derivation here, the sum over m gives the resultant expression [212]

$$\sum_{m=-\infty}^{-1} \hat{K}_p(mL + z' - z) \equiv K_s(v) = -\frac{\pi}{L}\left[1 + \sqrt{\frac{2L}{\pi ka^2}} e^{i\frac{\pi}{4}} G_0(v)\right] \tag{4.200}$$

with $v = (z' - z)/L$, and

$$G_0(v) = \frac{2}{\sqrt{\pi}} \int_0^\infty dx \left(\frac{e^{x^2 v}}{e^{x^2} - 1} - \frac{1}{x^2}\right) = \sum_{n=1}^{\infty} \left(\frac{1}{\sqrt{n - v}} - \frac{1}{\sqrt{n}}\right) + \varsigma(\frac{1}{2}) \tag{4.201}$$

where the last equality is obtained by expanding $e^{x^2 v}$ in a power series of v and collecting the expanding coefficients. Having substituted $\hat{K}_c$ and sum of $\hat{K}_p$ back into Eq. (4.193), we arrive at the integral equation [212]

$$\int_0^\gamma d\nu \bar{G}(\nu - v) F_0(\nu) = 1 \tag{4.202}$$

with

$$\bar{G}(v) = \frac{2\Theta(-v)}{\sqrt{-v}} + G_0(v) \tag{4.203}$$

and

$$F_0(\nu) = \frac{F(\nu)}{\mathcal{A}} \tag{4.204}$$

where

$$\mathcal{A} = \frac{\sqrt{\pi k L}}{1 - i}\left(\frac{a}{\pi L} + \frac{ia}{L}\int_0^\gamma d\nu F(\nu)\right) \tag{4.205}$$

The problem of solving the impedance of Eq. (4.195) now becomes solving F_0 of the integral equation Eq.

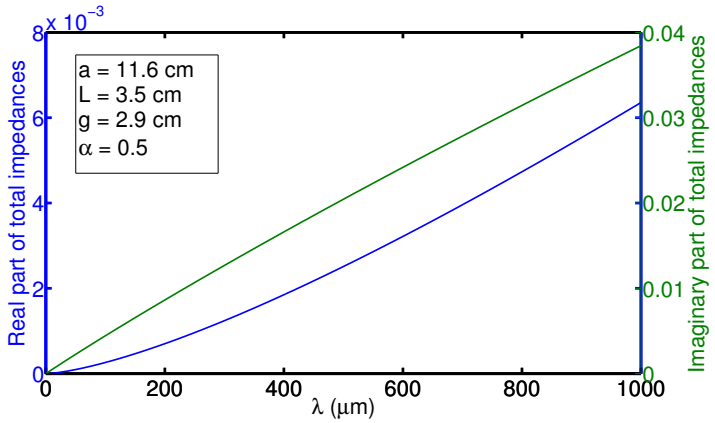

Figure 4.30: Illustration of the linac geometric impedance with parameters based on SLAC S-band traveling-wave linac.

(4.202). The resultant linac geometric impedance can then be derived from Eq. (4.195)

$$Z_{\text{linac}}^{\text{UR}}(k) = \frac{4\pi}{ka^2}\mathcal{A}\int_0^{\gamma} d\nu F_0(\nu) = \frac{4i}{ka^2}\left[1 + (1+i)\frac{\alpha(\gamma)L}{a}\sqrt{\frac{\pi}{kg}}\right]^{-1} \tag{4.206}$$

where Yokoya and Bane numerically fit the coefficient function $\alpha(\gamma)$ to the gap-to-period ratio (γ) and obtained the following fitting formula, which works well for $0 < \gamma < 1$,

$$\alpha(\gamma) \approx 1 - 0.4648\sqrt{\gamma} - 0.0704\gamma \tag{4.207}$$

with $\gamma = g/L$.

Figure 4.30 below demonstrates the linac geometric impedance spectrum, based on a typical SLAC S-band traveling-wave linac [100]. It can be seen that the real part of the impedance scales as $\lambda^{3/2}$, while the imaginary part increases with λ.

4.5 Summary

To end this chapter, we note that we have derived all the impedance models employed in our semi-analytical Vlasov analysis, including one-dimensional CSR, LSC and linac geometric effects. Until the dissertation, for CSR the available impedance models consist of free-space steady-state expressions, valid for ultrarelativistic energy regime. A contribution of this work is to extend the impedance model toward the non-ultrarelativistic beam energies or low energy regime. In addition, the entrance and exit transients of CSR wakefields and impedances are also derived. The free-space CSR exit transient impedance (Case C and D) expressions are also derived and as another contribution of the dissertation work. In the long-wavelength regime where possible shielding effect to occur, we summarized the formula from Agoh [8]. Table 4.5 for CSR impedance models are compiled in our Vlasov solver. For LSC, the free-space 1-D model is constructed, valid for

ultrarelativistic beams. The available free-space LSC models comprise those for transverse uniform round (on-axis and average models) and axisymmetric Gaussian beams. A more dedicated LSC model with coaxial uniform round beam and round pipe is also referenced based on Venturini [194] and Li [115]. Table 4.6 summarizes the available LSC impedance models implemented in our Vlasov solver. Finally for the linac-geometric impedance, we employed Gluckstern, Yokoya and Bane's semi-analytical formula with numerical fitting function for our use in Vlasov analysis.

CHAPTER 5
Numerical Implementation of Vlasov Solver and the Benchmarking Against Particle Tracking

In the preceding chapters we have introduced theoretical formulations in beam dynamics (Vlasov formalism for microbunching) and electrodynamics (construction of CSR, LSC, and linac geometric impedances). In this chapter, we would describe how to numerically implement the developed theories to application of microbunching analysis in practical beamline designs. Because the beamline is assumed to be part (or the whole) of a recirculating or energy-recovery-linac (ERL) machine, microbunching behavior can be much more complicated than a bunch compressor chicane (BC) with few-dipole configuration. The existing theoretical treatments of microbunching analysis, which usually aim to estimate the impact of microbunching in a very specific portion of a linac-based machine [152, 79, 81, 193, 209, 83], would be extended to a general beamline lattice by virtue of general-purpose particle tracking simulations. Our developed semi-analytical Vlasov solver, which primarily focuses on microbunching gain calculation, adopts inputs and optics outputs from a well-known beamline design and particle tracking code `elegant` (the acronym of ELEctron Generation ANd Tracking) [21]. This option makes our solver of convenient use for beamline designers to evaluate impact of microbunching for arbitrary lattice design and might help improve or iterate their design strategies once this instability becomes a concern. We notice that our Vlasov solver only takes the single-particle optics information from `elegant` and does not involve in tracking a large number of particles for study of MBI.

In Sec. 5.1, we first introduce in Sec. 5.1.1 how our semi-analytical Vlasov solver converts the beam optics based on particle coordinate system employed in `elegant` to ours. When the beam energy is constant, the conversion is trivial. When a beam experiences acceleration or deceleration, the conversion is required. Then we briefly introduce the numerical implementation of the derived analytical impedance models in Sec. 5.1.2 All the preparation will lead to the development of our Vlasov solver, in which a set of integral equations would be solved according to the algorithm introduced in Sec. 5.1.3.

Our developed solver would be benchmarked against an independent tool in order that the correctness of our results is validated and confirmed. While there are numerous simulation codes available in the community [11], we choose `elegant`[96]. We will describe the steps we take to prepare for microbunching instability (MBI) simulation. In Sec. 5.2, a brief introduction of preparation of initial phase space distribution with modulations is outlined in Sec. 5.2.1. Its tracking algorithm involving with CSR and LSC effects would be highlighted in Sec. 5.2.2 and 5.2.3. Section 5.2 basically addresses the numerical algorithms that `elegant` particle tracking implemented.

[96] Although we adopt the inputs and optics outputs from `elegant`, it does not mean that the algorithm of our Vlasov solver *depends on* that of `elegant`.

The outputs directly from `elegant` (raw data) basically consist of a collection of 6-D phase space coordinates of individual simulation particles. To match `elegant` setup as close to the theoretical formulations (i.e. our Vlasov solver) as possible, for different scenarios the initial phase space distribution requires additional manipulations, including the longitudinal uniform flattop distribution (Sec. 5.3.1) and the transverse magnetized beam (Sec. 5.3.2). To extract the bunching factors, while excluding undesired information, demands dedicated postprocessing, which would be described and demonstrated in Sec. 5.3.3 and 5.3.4. In Sec. 5.4 we demonstrate the microbunching analysis for a beamline with an upstream long linac followed by a 180-deg arc. To run this example requires construction of six-by-six transport matrix as a function of path length and proper incorporation of relevant collective effects along the beam transport. Finally in Sec. 5.5 we summarize and make general comments on pros and cons of particle tracking simulations and the semi-analytical Vlasov calculations.

Part of the work in this Chapter, especially implementation of the semi-analytical Vlasov solver, its benchmarking and the numerical results, has been published with the title *Linear microbunching analysis for recirculation machines*, in Physical Review Accelerator and Beams 19, 114401 (2016). They were also presented in several conferences or workshops, including 6th International Particle Accelerator Conference (IPAC), Richmond, Virginia, with the title *CSR Induced Microbunching Gain Estimation Including Transient Effects in Transport and Recirculating Arcs* (MOPMA025), and in 2015 Energy Recovery Linac (ERL) Workshop, June 7-12, Stony Brook University, New York, with the title *Linear Microbunching Gain Estimation Including CSR And LSC Impedances In Recirculation Machines* (TUICLH2034), and later in 2015 Free Electron Laser Conference, Daejeon, Korea, with the title *Linear Vlasov Solver for Microbunching Gain Estimation with inclusion of CSR, LSC, and linac geometric impedances* (MOP052).

5.1 Numerical algorithm of the Vlasov solver

This section would introduce the numerical algorithm to solve Eq. (3.52) with kernel function given by Eqs. (3.43) and (3.40). Solving Eq. (3.52) requires the complete information to construct the kernel function and numerical integration over path length s with a sufficient number of meshes. Then the discretized equation can be formulated in a vector-matrix notation. Solving an integral equation becomes now finding the inverse of its corresponding matrix.

5.1.1 Beam transport matrix

Recall that we defined the six-dimensional phase space coordinate in Eq. (2.46)

$$\hat{\mathbf{X}}(s) = \left(\hat{x}, \hat{x}', \hat{y}, \hat{y}', \hat{z}, \hat{\delta}; s\right)^T \tag{5.1}$$

where $\hat{x}$ and $\hat{y}$ are transverse horizontal/radial and vertical positions, $\hat{x}'$ and $\hat{y}'$ are the corresponding angular divergences, $(') \equiv d/ds$, $\hat{z}$ and $\hat{\delta} \equiv (E - E_r)/E_0$ are the (local) longitudinal coordinate and energy deviation

(assuming $\hat{z} > 0$ for the bunch head), $E_r = E_r(s)$ is the reference energy at s and $E_0 = E_r(s = 0)$. All these quantities are measured with respect to the reference particle and are a function of the (global) longitudinal path coordinate, s. The superscript T indicates the transpose operator. When the beam energy is a constant, all quantities with hat are reduced to the normal ones (without hat)

$$\mathbf{X}(s) = (x, x', y, y', z, \delta; s)^T \tag{5.2}$$

where, particularly, $\delta \equiv (E - E_0)/E_0$ for E_0 being the reference energy. The relation between Eqs. (5.1) and (5.2) can be connected by

$$\begin{aligned}
\begin{bmatrix} \hat{x} \\ \hat{y} \end{bmatrix} &= \begin{bmatrix} x \\ y \end{bmatrix} \sqrt{\frac{E_r(s)}{E_0}} \\
\begin{bmatrix} \hat{x}' \\ \hat{y}' \end{bmatrix} &\simeq \begin{bmatrix} x' \\ y' \end{bmatrix} \sqrt{\frac{E_r(s)}{E_0}} \\
\hat{z} &= z \\
\hat{\delta} &= \delta + 1 - \frac{E_r(s)}{E_0}
\end{aligned} \tag{5.3}$$

This subsection is intended to introduce how to retrieve the six-by-six transport matrix, defined in Eq. (2.55) as a function of s, along a beamline. In principle, this can be done by multiplication of individual transport matrices in order, the same as that for geometric ray optics. There have been numerous available tools for beamline design, so in our semi-analytical Vlasov solver (henceforth simply "solver" or "Vlasov solver") we take advantage of them instead of developing an independent package for this function[97]. For constant energy, the notation we employed in our theoretical formulation of microbunching analysis, i.e. Eq. (5.1), is reduced to that of Eq. (5.2), which `elegant` follows[98]. Therefore, we benefit much from `elegant` in our Vlasov solver for the case of constant energy. In this case, once a beamline design is given (in `elegant` format), the inputs to the solver become trivial, as have been directly provided by `elegant`[99]. In fact, the very first step of running our solver is to run `elegant` once, in order to extract the necessary information (i.e. inputs) to our solver. Note that running `elegant` at this step is for only pure optics. Instead of loading millions of simulation particles and incorporating collective effects, this initial run is only single-particle (or a few particles) tracking and takes little time. Having extracted the transport matrices (as a function of s), before proceeding to the next step, we make modification of the momentum compaction factor R_{56} from pure optics (zeroth order) to inclusion of relativistic effect[100],

$$R_{56}^{\text{solver}} = R_{56}^{\texttt{elegant}} + \frac{s}{\gamma^2(s)} \tag{5.4}$$

[97] The most commonly used format may be the one by `MAD` (Methodical Accelerator Design) developed at CERN. The simulation package on which we really rely is `elegant` [66], which basically follows the convention employed in `MAD`.

[98] Note that `elegant` has a sign difference in the longitudinal coordinate; the bunch head is assigned as $z < 0$ there.

[99] More precisely, in the namelist of `elegant` input file (∗.ele), &matrix_output must be added.

[100] Note that this modification does not violate the symplecticity for linear matrix, see Eqs. (2.61) to (2.64).

From our theoretical treatment [see, for example, Eq. (3.54)], this becomes necessary when any collective effect, e.g. LSC, is present in the drift section.

For varying energy, conversion between Eq. (5.1) and Eq. (5.2) must be done. Direct transformation from the transport matrix may be an option. The other more general way to retrieve the six-by-six transport matrix is adopted in our Vlasov solver. The idea is first to convert phase space coordinate from $\mathbf{X}(s)$, which `elegant` uses, to $\hat{\mathbf{X}}(s)$, which our solver adopts, according to Eq. (5.3). The information of $E_r(s)$ can be extracted from `elegant`. The linear transport equation has been formulated in Eq. (2.53),

$$\hat{\mathbf{X}}_f = \mathbf{R}\hat{\mathbf{X}}_i \tag{5.5}$$

where the subscripts i and f are denoted as initial and final position. Equation (5.5) can be explicitly expressed as[101]

$$\begin{bmatrix} x \\ x' \\ z \\ \delta \end{bmatrix}_f = \begin{pmatrix} R_{11}^{i\to f} & R_{12}^{i\to f} & 0 & R_{16}^{i\to f} \\ R_{21}^{i\to f} & R_{22}^{i\to f} & 0 & R_{26}^{i\to f} \\ R_{51}^{i\to f} & R_{52}^{i\to f} & R_{55}^{i\to f} & R_{56}^{i\to f} \\ 0 & 0 & 0 & R_{66}^{i\to f} \end{pmatrix} \begin{bmatrix} x \\ x' \\ z \\ \delta \end{bmatrix}_i \tag{5.6}$$

Now assuming $\hat{\mathbf{X}}_f$ and $\hat{\mathbf{X}}_i$ have been known with a few particles, we can solve the transport matrix elements, $R_{ij}^{i\to f}$, considering the set of linear equation as over-determined, i.e. the number of equations is larger than the number of unknowns. For the 4-D case, the transport matrix is 4-by-4 and has in general 16 unknowns to be determined, ignoring the symplectisity constraints for the moment. At least we need to prepare four independent simulation particles in order to solve the matrix elements. For a total of four particles with

[101] In what follows, for simplicity, the symbol caret or hat is omitted and only 4-D case is considered.

each denoted by a superscript (n) where $n = 1, 2, 3, 4$, Eq. (5.6) for the four particles can be written as

$$
\begin{bmatrix} R_{11}^{i\to f} \\ R_{12}^{i\to f} \\ R_{15}^{i\to f} \\ R_{16}^{i\to f} \\ R_{21}^{i\to f} \\ R_{22}^{i\to f} \\ R_{25}^{i\to f} \\ R_{26}^{i\to f} \\ R_{51}^{i\to f} \\ R_{52}^{i\to f} \\ R_{55}^{i\to f} \\ R_{56}^{i\to f} \\ R_{61}^{i\to f} \\ R_{62}^{i\to f} \\ R_{65}^{i\to f} \\ R_{66}^{i\to f} \end{bmatrix}
\begin{pmatrix}
x_i^{(1)} & p_{x,i}^{(1)} & z_i^{(1)} & \delta_i^{(1)} & 0 & 0 & 0 & 0 & 0 & 0 & 0 & 0 & 0 & 0 & 0 & 0 \\
0 & 0 & 0 & 0 & x_i^{(2)} & p_{x,i}^{(2)} & z_i^{(2)} & \delta_i^{(2)} & 0 & 0 & 0 & 0 & 0 & 0 & 0 & 0 \\
0 & 0 & 0 & 0 & 0 & 0 & 0 & 0 & x_i^{(3)} & p_{x,i}^{(3)} & z_i^{(3)} & \delta_i^{(3)} & 0 & 0 & 0 & 0 \\
0 & 0 & 0 & 0 & 0 & 0 & 0 & 0 & 0 & 0 & 0 & 0 & x_i^{(4)} & p_{x,i}^{(4)} & z_i^{(4)} & \delta_i^{(4)} \\
x_i^{(5)} & p_{x,i}^{(5)} & z_i^{(5)} & \delta_i^{(5)} & 0 & 0 & 0 & 0 & 0 & 0 & 0 & 0 & 0 & 0 & 0 & 0 \\
0 & 0 & 0 & 0 & x_i^{(6)} & p_{x,i}^{(6)} & z_i^{(6)} & \delta_i^{(6)} & 0 & 0 & 0 & 0 & 0 & 0 & 0 & 0 \\
0 & 0 & 0 & 0 & 0 & 0 & 0 & 0 & x_i^{(7)} & p_{x,i}^{(7)} & z_i^{(7)} & \delta_i^{(7)} & 0 & 0 & 0 & 0 \\
0 & 0 & 0 & 0 & 0 & 0 & 0 & 0 & 0 & 0 & 0 & 0 & x_i^{(8)} & p_{x,i}^{(8)} & z_i^{(8)} & \delta_i^{(8)} \\
x_i^{(9)} & p_{x,i}^{(9)} & z_i^{(9)} & \delta_i^{(9)} & 0 & 0 & 0 & 0 & 0 & 0 & 0 & 0 & 0 & 0 & 0 & 0 \\
0 & 0 & 0 & 0 & x_i^{(10)} & p_{x,i}^{(10)} & z_i^{(10)} & \delta_i^{(10)} & 0 & 0 & 0 & 0 & 0 & 0 & 0 & 0 \\
0 & 0 & 0 & 0 & 0 & 0 & 0 & 0 & x_i^{(11)} & p_{x,i}^{(11)} & z_i^{(11)} & \delta_i^{(11)} & 0 & 0 & 0 & 0 \\
0 & 0 & 0 & 0 & 0 & 0 & 0 & 0 & 0 & 0 & 0 & 0 & x_i^{(12)} & p_{x,i}^{(12)} & z_i^{(12)} & \delta_i^{(12)} \\
x_i^{(13)} & p_{x,i}^{(13)} & z_i^{(13)} & \delta_i^{(13)} & 0 & 0 & 0 & 0 & 0 & 0 & 0 & 0 & 0 & 0 & 0 & 0 \\
0 & 0 & 0 & 0 & x_i^{(14)} & p_{x,i}^{(14)} & z_i^{(14)} & \delta_i^{(14)} & 0 & 0 & 0 & 0 & 0 & 0 & 0 & 0 \\
0 & 0 & 0 & 0 & 0 & 0 & 0 & 0 & x_i^{(15)} & p_{x,i}^{(15)} & z_i^{(15)} & \delta_i^{(15)} & 0 & 0 & 0 & 0 \\
0 & 0 & 0 & 0 & 0 & 0 & 0 & 0 & 0 & 0 & 0 & 0 & x_i^{(16)} & p_{x,i}^{(16)} & z_i^{(16)} & \delta_i^{(16)}
\end{pmatrix}
\begin{bmatrix} x_f^{(1)} \\ p_{x,f}^{(2)} \\ z_f^{(3)} \\ \delta_f^{(4)} \\ x_f^{(5)} \\ p_{x,f}^{(6)} \\ z_f^{(7)} \\ \delta_f^{(8)} \\ x_f^{(9)} \\ p_{x,f}^{(10)} \\ z_f^{(11)} \\ \delta_f^{(12)} \\ x_f^{(13)} \\ p_{x,f}^{(14)} \\ z_f^{(15)} \\ \delta_f^{(16)} \end{bmatrix}
\tag{5.7}
$$

Rearranging the order of phase space coordinates,

$$
\begin{bmatrix} x_f^{(1)} \\ x_f^{(2)} \\ x_f^{(3)} \\ x_f^{(4)} \\ p_{x,f}^{(5)} \\ p_{x,f}^{(6)} \\ p_{x,f}^{(7)} \\ p_{x,f}^{(8)} \\ z_f^{(9)} \\ z_f^{(10)} \\ z_f^{(11)} \\ z_f^{(12)} \\ \delta_f^{(13)} \\ \delta_f^{(14)} \\ \delta_f^{(15)} \\ \delta_f^{(16)} \end{bmatrix}
=
\begin{bmatrix} R_{11}^{i\to f} & R_{12}^{i\to f} & R_{15}^{i\to f} & R_{16}^{i\to f} & R_{21}^{i\to f} & R_{22}^{i\to f} & R_{25}^{i\to f} & R_{26}^{i\to f} & R_{51}^{i\to f} & R_{52}^{i\to f} & R_{55}^{i\to f} & R_{56}^{i\to f} & R_{61}^{i\to f} & R_{62}^{i\to f} & R_{65}^{i\to f} & R_{66}^{i\to f} \end{bmatrix}
\begin{pmatrix}
x_i^{(1)} & p_{x,i}^{(1)} & z_i^{(1)} & \delta_i^{(1)} & 0 & 0 & 0 & 0 & 0 & 0 & 0 & 0 & 0 & 0 & 0 & 0 \\
x_i^{(2)} & p_{x,i}^{(2)} & z_i^{(2)} & \delta_i^{(2)} & 0 & 0 & 0 & 0 & 0 & 0 & 0 & 0 & 0 & 0 & 0 & 0 \\
x_i^{(3)} & p_{x,i}^{(3)} & z_i^{(3)} & \delta_i^{(3)} & 0 & 0 & 0 & 0 & 0 & 0 & 0 & 0 & 0 & 0 & 0 & 0 \\
x_i^{(4)} & p_{x,i}^{(4)} & z_i^{(4)} & \delta_i^{(4)} & 0 & 0 & 0 & 0 & 0 & 0 & 0 & 0 & 0 & 0 & 0 & 0 \\
0 & 0 & 0 & 0 & x_i^{(5)} & p_{x,i}^{(5)} & z_i^{(5)} & \delta_i^{(5)} & 0 & 0 & 0 & 0 & 0 & 0 & 0 & 0 \\
0 & 0 & 0 & 0 & x_i^{(6)} & p_{x,i}^{(6)} & z_i^{(6)} & \delta_i^{(6)} & 0 & 0 & 0 & 0 & 0 & 0 & 0 & 0 \\
0 & 0 & 0 & 0 & x_i^{(7)} & p_{x,i}^{(7)} & z_i^{(7)} & \delta_i^{(7)} & 0 & 0 & 0 & 0 & 0 & 0 & 0 & 0 \\
0 & 0 & 0 & 0 & x_i^{(8)} & p_{x,i}^{(8)} & z_i^{(8)} & \delta_i^{(8)} & 0 & 0 & 0 & 0 & 0 & 0 & 0 & 0 \\
0 & 0 & 0 & 0 & 0 & 0 & 0 & 0 & x_i^{(9)} & p_{x,i}^{(9)} & z_i^{(9)} & \delta_i^{(9)} & 0 & 0 & 0 & 0 \\
0 & 0 & 0 & 0 & 0 & 0 & 0 & 0 & x_i^{(10)} & p_{x,i}^{(10)} & z_i^{(10)} & \delta_i^{(10)} & 0 & 0 & 0 & 0 \\
0 & 0 & 0 & 0 & 0 & 0 & 0 & 0 & x_i^{(11)} & p_{x,i}^{(11)} & z_i^{(11)} & \delta_i^{(11)} & 0 & 0 & 0 & 0 \\
0 & 0 & 0 & 0 & 0 & 0 & 0 & 0 & x_i^{(12)} & p_{x,i}^{(12)} & z_i^{(12)} & \delta_i^{(12)} & 0 & 0 & 0 & 0 \\
0 & 0 & 0 & 0 & 0 & 0 & 0 & 0 & 0 & 0 & 0 & 0 & x_i^{(13)} & p_{x,i}^{(13)} & z_i^{(13)} & \delta_i^{(13)} \\
0 & 0 & 0 & 0 & 0 & 0 & 0 & 0 & 0 & 0 & 0 & 0 & x_i^{(14)} & p_{x,i}^{(14)} & z_i^{(14)} & \delta_i^{(14)} \\
0 & 0 & 0 & 0 & 0 & 0 & 0 & 0 & 0 & 0 & 0 & 0 & x_i^{(15)} & p_{x,i}^{(15)} & z_i^{(15)} & \delta_i^{(15)} \\
0 & 0 & 0 & 0 & 0 & 0 & 0 & 0 & 0 & 0 & 0 & 0 & x_i^{(16)} & p_{x,i}^{(16)} & z_i^{(16)} & \delta_i^{(16)}
\end{pmatrix}
\tag{5.8}
$$

Expressing in a compact matrix-vector notation, we have

$$Z^i_{16\times 16} R^{i\to f}_{16\times 1} = Z^f_{16\times 1} \tag{5.9}$$

In principle, $R^{i\to f}_{16\times 1}$ can be solved by finding the inverse matrix of $Z^i_{16\times 16}$. Then $R^{i\to f}_{16\times 1}$ can be rearranged to the square matrix form $R^{i\to f}_{4\times 4}$. Including vertical dimension (y, y') is trivial and not shown here. There is an issue regarding solution of Eq. (5.9) due to the preparation of the four independent simulation particles. It is found that using only four particles is not sufficient to obtain a converged result, compared with that from direct output of `elegant` for constant-energy case. This can be due to the quiet start algorithm usually employed in particle tracking simulation but undesired in our situation because of existing correlation among the particles. This issue can be resolved by turning off the special algorithm. As mentioned, the system of linear equations is over-determined. Solving the set of equation can employ least-squares method, as done in our Vlasov solver. An alternative method can use the singular value decomposition (SVD).

Figure 5.1 below shows the case of LCLS BC2, for which the energy is constant. The two approaches, one from direct output of `elegant` and the other from solution of Eq. (5.9) for tracking a few particles, show excellent agreement. Figure 5.1(d) illustrates the momentum compaction along the beamline where we can see little effect of relativistic contribution, i.e. the second term in Eq. (5.4), from Eq. (5.9) because the beam energy is high ($\gamma \approx 8845$)[102].

Let us take a look at the second example (Fig. 5.2), which would be introduced in more detail in Chapter 6. The total length of the recirculation arc beamline design is much longer than that of Fig. 5.1. Matching between the two approaches can be seen. The deviation of R_{56} due to relativistic effect is visible.

As the third example, we consider a more practical case with beam acceleration in Fig. 5.3. It can be observed that the red curves, from Eq. (5.9), now reflect the fact that the change of transport matrices during the beam acceleration with those of constant energy, particularly the dispersion function and the momentum compaction function[103].

In this subsection we have introduced how in numerical implementation we retrieve the six-by-six transport matrix for our subsequent Vlasov calculation.

[102] The blue curves presented in Figs. 5.1 to 5.3 are directly from `elegant` without modification of Eq. (5.4).

[103] This difference does not imply the correctness of either approach because they are represented based on difference phase space coordinates, Eqs. (5.1) and (5.2).

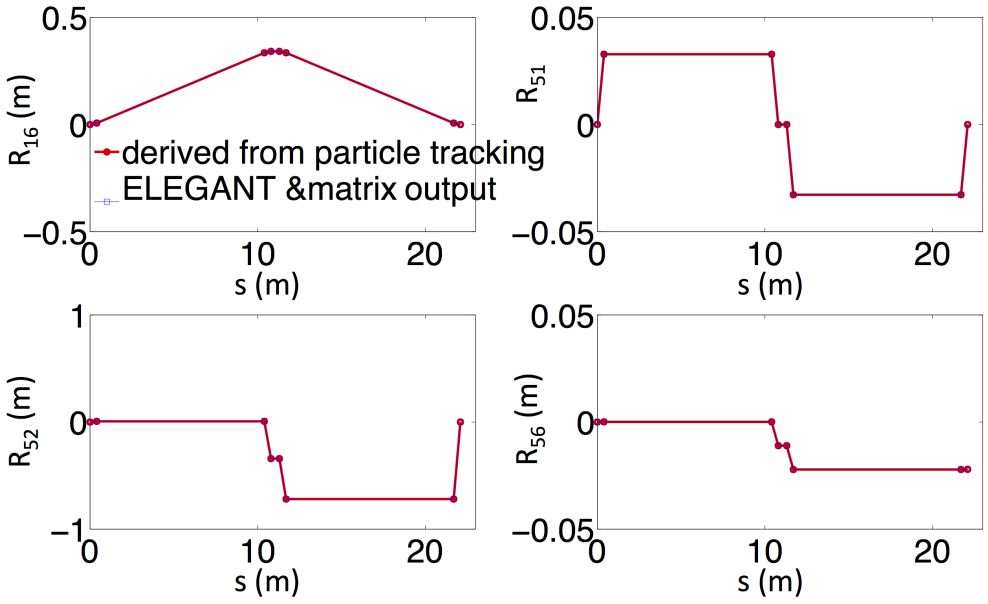

Figure 5.1: Comparison of transport functions of LCLS BC2. The red curves are obtained from that described in this section. The blue ones are directly from `elegant` output without modification of Eq. (5.4).

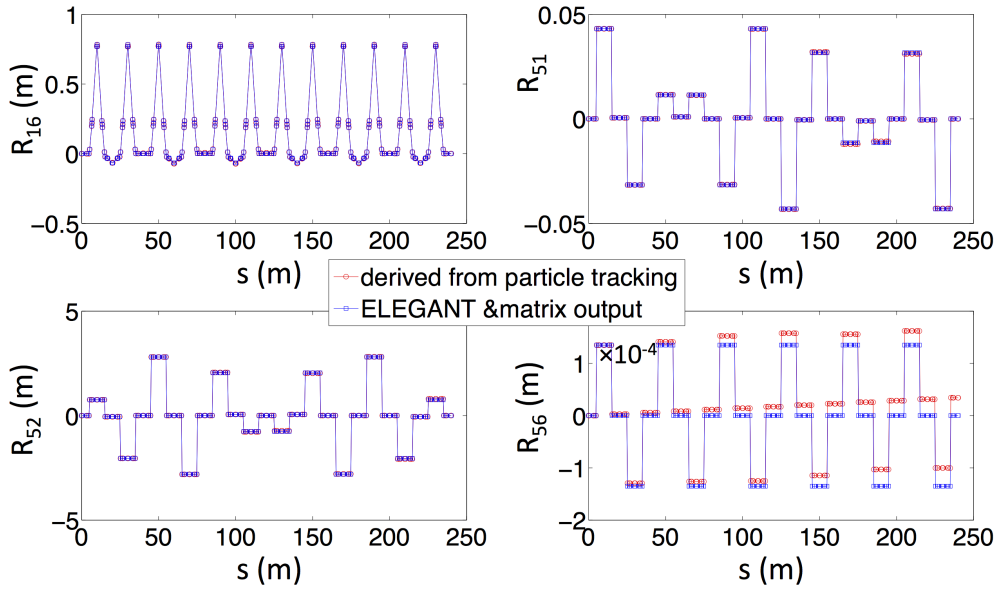

Figure 5.2: Comparison of transport functions of a high-energy recirculation arc, which will be introduced later in Chapter 7. The red curves are obtained from that described in this section. The blue ones are directly from `elegant` output without modification of Eq. (5.4). Slight deviation can be seen in the figure due to accumulation of finite γ. Note that the total length of the beamline is ten times longer than that demonstrated in Fig. 5.1.

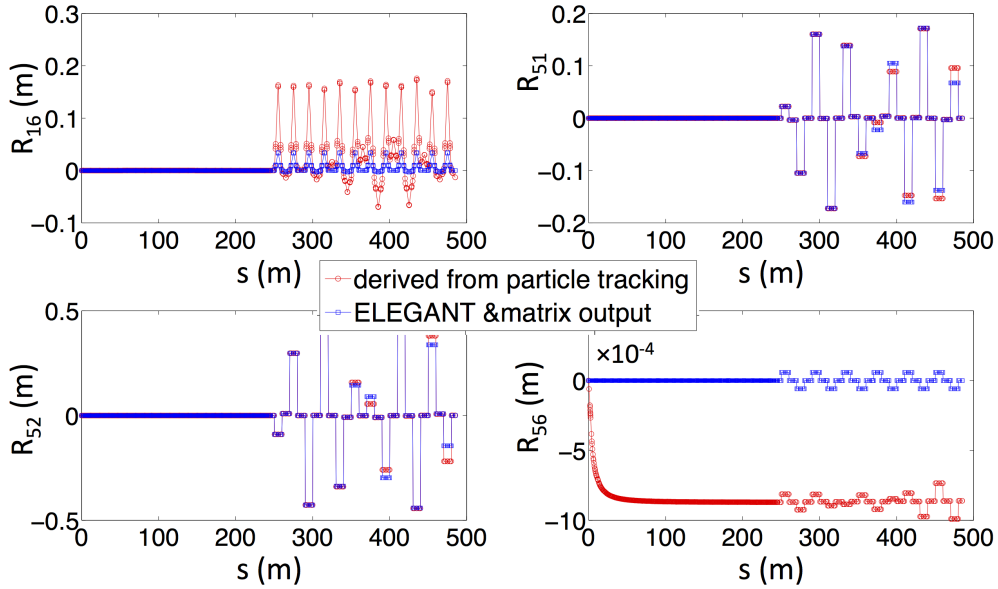

Figure 5.3: Comparison of transport functions of a linac-arc combination, which will be introduced later in Chapter 5. The red curves are obtained from that described in this section. The blue ones are directly from `elegant` output without modification of Eq. (5.4). A notable difference is observed because of the low beam energy in the upstream section of the beamline and the presence of RF cavities.

5.1.2 Implementation of collective effects in the Vlasov solver

In Sec. 4.2.7, 4.3.4 and Eq. (4.206), we have summarized relevant collective effects which would be incorporated in our Vlasov solver, including CSR, LSC and linac geometric effects. For convenience of discussion, we may repeat important expressions here and illustrate how to implement in numerical calculation.

For an electron beam traversing a finite-length dipole, CSR can have both steady-state and transient effects. In addition, when a beam goes through a long transport line, LSC can have a significant effect on accumulating energy modulations. Moreover, when a beam is accelerated, a long section of linac consisting of RF cavities is characteristic of the high-frequency geometric impedance, which can also accrue a certain amount of energy modulations. For steady-state CSR, with non-ultrarelativistic beam energy, the impedance has the form

$$\mathrm{Re}\left[Z_{\mathrm{CSR}}^{\mathrm{s.s.NUR}}(k(s);s)\right] = \frac{-2\pi k(s)^{1/3}}{|\rho(s)|^{2/3}}\mathrm{Ai}'(x) + \frac{k(s)\pi}{\gamma^2}\left(\int_0^x \mathrm{Ai}(\varsigma)\mathrm{d}\varsigma - \frac{1}{3}\right) \tag{5.10}$$

$$\mathrm{Im}[Z_{\mathrm{CSR}}^{\mathrm{s.s.NUR}}(k(s);s)] \simeq \frac{2\pi k(s)^{1/3}}{|\rho(s)|^{2/3}}\left\{\frac{1}{3}\mathrm{Bi}'(x) + \int_0^x \left[\mathrm{Ai}'(x)\mathrm{Bi}(t) - \mathrm{Ai}(t)\mathrm{Bi}'(x)\right]\, dt\right\} \tag{5.11}$$

where the wavenumber $k(s)$ is determined as $k(s) = 2\pi/\lambda(s) = k_0 C(s) = k_0\left[\hat{R}_{55}(s) - h\hat{R}_{56}(s)\right]^{-1}$, with k_0 the (given) initial wavenumber, the (given) initial chirp of the beam, and the transport matrix elements introduced in the previous section. $x = (k(s)\,|\rho(s)|)^{2/3}\Big/\gamma(s)^2$ where the bending radius has finite values within a bend and approaches infinity in a straight section. When the ultrarelativistic limit is assumed, the steady-state CSR impedance has a simplified form

$$Z_{\mathrm{CSR}}^{\mathrm{s.s.UR}}(k(s);s) = \frac{-ik(s)^{1/3}A}{|\rho(s)|^{2/3}},\ A = -2\pi\left[\mathrm{Bi}'(0)/3 + i\mathrm{Ai}'(0)\right] \tag{5.12}$$

For entrance transient CSR effect, the corresponding impedance formula is

$$Z_{\mathrm{CSR}}^{\mathrm{ent}}(k(s);s) = \frac{-4}{s^*}e^{-4i\mu(s)} + \frac{4}{3s^*}(i\mu(s))^{1/3}\Gamma\left(\frac{-1}{3}, i\mu(s)\right) \tag{5.13}$$

where $\mu(s) = k(s)z_L(s)$ and $z_L = (s^*)^3\Big/24\rho(s)^2$. Here s^* is measured from the dipole entrance. To determine if a bunch is located inside or outside a dipole, an auxiliary function $|\rho(s)|^{-1}$ is used. When a circulating locates in a dipole, this function does not vanish. To save the computing time, only s^* within the overtaking distance, $s^* \le \left(24\lambda(s)\rho(s)^2\right)^{1/3}$, the entrance transient CSR effect is considered.

For exit transient CSR effects, there are two contributions, corresponding to Case C and D in Fig. 4.10(c) and (d). For Case C,

$$Z_{\mathrm{CSR},C}(k(s);s) = \frac{-4}{L_b + 2s^*}e^{\frac{-ik(s)L_b^2}{6|\rho(s)|^2}(L_b+3s^*)} \tag{5.14}$$

where s^* is now measured from dipole exit. Again, such local path length coordinate is determined by the auxiliary function $|\rho(s)|^{-1}$. L_b is given as the length of the dipole. For Case D, which can result in significant contribution to CSR microbunching, the impedance expression has the form

$$Z_{\mathrm{CSR}}^{\mathrm{drif}}(k(s);s) = \frac{4}{\rho}\int_0^{\theta_m} d\vartheta \frac{df(s^*,\vartheta)}{d\vartheta}e^{-ik(s)\Delta z(s^*,\vartheta)} \tag{5.15}$$

with the dipole angle $\theta_m = L_b/\rho$, and

$$f(s^*,\vartheta) = \frac{\frac{2}{\gamma^2}\left(\frac{s^*}{\rho}+\vartheta\right) + \vartheta^2\left(\frac{2s^*}{\rho}+\vartheta\right)}{\frac{4}{\gamma^2}\left(\frac{s^*}{\rho}+\vartheta\right)^2 + \vartheta^2\left(\frac{2s^*}{\rho}+\vartheta\right)^2} \tag{5.16}$$

where the (total) derivative of Eq. (5.16) with respect to ϑ can be obtained (not shown here), and

$$\Delta z(s^*,\vartheta) = \frac{s^*+\rho\vartheta}{2\gamma^2} + \beta\frac{\rho\vartheta^3}{24}\frac{4s^*+\rho\vartheta}{s^*+\rho\vartheta} \tag{5.17}$$

There are two ways to implement Eq. (5.15) in a numerical calculation. One is to perform integration

by parts first and numerically evaluate the resultant integration. The other is to take differentiation first and perform numerically integration. The latter approach is suggested because of less fast oscillation at short wavelengths. Moreover, in our Vlasov calculation we usually include the exit transient effects at a nearby upstream bend.

Here we note that the above CSR impedance models are valid only when the wall shielding effect is negligible. This shielding effect becomes important when the distance from the beam orbit to the walls $h/2$ satisfies $h \leq \left(\rho(s)\lambda(s)^2\right)^{1/3}$. In this situation, one should consider to use the shielded CSR impedance in evaluating the CSR-induced microbunching gains. The corresponding impedance expression is

$$Z_{\mathrm{CSR}}^{\mathrm{pp}}(k) = \frac{8\pi^2}{h}\left(\frac{2}{k(s)\rho(s)}\right)^{\frac{1}{3}} \sum_{p=0}^{\infty} F_0(\beta_p) \tag{5.18}$$

where

$$F_0(\beta) = \mathrm{Ai}'\left(\beta^2\right)\left[\mathrm{Ai}'\left(\beta^2\right) - i\mathrm{Bi}'\left(\beta^2\right)\right] + \beta^2 \mathrm{Ai}'\left(\beta^2\right)\left[\mathrm{Ai}\left(\beta^2\right) - i\mathrm{Bi}\left(\beta^2\right)\right] \tag{5.19}$$

with

$$\beta_p = (2p+1)\,\frac{\pi}{h}\left(\frac{\rho(s)}{2k^2(s)}\right)^{\frac{1}{3}} \tag{5.20}$$

The option of including radiation shielding requires an additional parameter, h, as the full height of the parallel plate.

In the above impedance expressions, the impedance usually depends on the beamline coordinate (s or s^*) and the wavenumber $k(s)$. Further, the wavenumber depends again on the beamline coordinate, e.g. if bunch compression is involved, and the impedance is evaluated once for a fixed wavenumber. The impedances assume a beam with a constant wavenumber and a bend with constant radius at each location s.

Below we present several LSC impedance expressions implemented in our Vlasov solver. The first one is the on-axis model, which assumes a transversely uniform density with circular cross section of radius r_b[104],

$$Z_{\mathrm{LSC}}^{\text{on-axis}}(k(s);s) = \frac{4i}{\gamma r_b(s)}\,\frac{1-\xi_b K_1(\xi_b)}{\xi_b} \tag{5.21}$$

where $\xi_b(s) = k(s)r_b(s)/\gamma(s)$ has been expressed with dependence of the path-length coordinate. The

[104] Equation (5.21) is also the impedance model employed in `elegant`.

transverse beam radius is obtained by numerically fitting [209]

$$r_b \approx 0.8735\,(\sigma_x(s) + \sigma_y(s)) \tag{5.22}$$

where the transverse rms beam sizes in horizontal and vertical dimensions are available from `elegant`[105].

Here we note that the validity of 1-D LSC models is with

$$\xi_b < 0.5 \tag{5.23}$$

In the following we will use the on-axis model, in accordance with the built-in LSC impedance expression in `elegant` [66]. The second one is the average model, which integrates the radial dependence of the space charge field

$$Z_{\rm LSC}^{\rm ave}(k(s);s) = \frac{4i}{\gamma r_b(s)}\frac{1-2I_1(\xi)K_1(\xi)}{\xi} \tag{5.24}$$

The third one is for transverse axisymmetric Gaussian beam

$$Z_{\rm LSC}^{\rm on\text{-}axis}(k(s);s) = -\frac{i\xi_\sigma}{\sigma(s)\gamma(s)}e^{\xi_\sigma^2/2}{\rm Ei}\left(-\frac{\xi_\sigma^2}{2}\right) \tag{5.25}$$

with $\sigma(s) = \sigma_x(s)$ and $\xi_\sigma(s) = k(s)\sigma(s)/\gamma(s)$ are assumed.

When a beam undergoes an environment with which the effect of beam pipe can be a concern, we adopt the following impedance model for round beam with round beam pipe,

$$Z_{LSC}^{\substack{\text{uniform-round}\\ \text{round-pipe}}}(k(s);s) = \frac{4i}{\gamma(s)r_b(s)}\frac{1}{\xi_b}\left[1-\xi_b\left(K_1(\xi_b) - K_0\left(\frac{\xi_b r_p}{r_b}\right)\frac{I_1(\xi_b)}{I_0\left(\frac{\xi_b r_p}{r_b}\right)}\right)\right] \tag{5.26}$$

with $\xi_b(s) = k(s)r_b(s)/\gamma(s)$.

Note that an additional parameter, the radius of pipe r_p, should be specified if incorporating this effect.

In Eqs. (5.21) to (5.26), the longitudinal space charge field does neither take into account the offset of bunch centroid nor the transverse dependence of the field along the bunch. We note that the expressions are approximate; for the most general case of a intense or high-brightness beam a three-dimensional particle-in-cell (PIC) implementation may be an option for more accurate simulation.

To end this subsection, we remind that analytical expressions of the impedance models employed in Eqs. (5.10) to (5.26) are not limited by our Vlasov solver. Instead, general impedance data , which can be obtained from external dedicated codes, can be incorporated into the solver[106].

[105] In the namelist of input file (*.ele), it can be extracted from the output of running & run_setup.
[106] In that case, interpolation schemes may be employed.

5.1.3 Solving Volterra integral equation

In Sec. 5.1.1 and 5.1.2 we have prepared required information as our main building block of the solver. In this subsection, we want to solve the Volterra-type integral equations, i.e. Eq. (3.52) and Eqs. (3.54) to (3.58), with relevant physical effects taken into account. By dividing the beamline into grids, one can write the integral equation in its s-discretized form

$$b(s_i) = b_0(s_i) + \Delta s \left(\frac{1}{2} K(s_i, 0) b_0(0) + \sum_{j=1}^{i-1} K(s_i, u_j) b(u_j) \right) \tag{5.27}$$

for $s_i = s_0 + i\Delta s$ and $u_j = u_0 + j\Delta s$ being the grid points along the pathlength, with i and j the mesh/grid indices. Here Δs is the mesh spacing, s_0 and u_0 are the initial positions. In our case, we assume $s_0 = u_0 = 0$. We further express Eq. (5.27) in the matrix form to be,

$$\begin{bmatrix} b(s_1) \\ b(s_2) \\ b(s_3) \\ b(s_4) \\ \vdots \\ b(s_{N-1}) \\ b(s_N) \end{bmatrix} = \begin{bmatrix} b_0(s_1) \\ b_0(s_2) \\ b_0(s_3) \\ b_0(s_4) \\ \vdots \\ b_0(s_{N-1}) \\ b_0(s_N) \end{bmatrix}$$

$$+ \Delta s \begin{pmatrix} 0 & & & & & 0 \\ \frac{1}{2}K(s_2,s_1) & 0 & & & & \\ \frac{1}{2}K(s_3,s_1) & K(s_3,s_2) & 0 & & & \\ \frac{1}{2}K(s_4,s_1) & K(s_4,s_2) & K(s_4,s_3) & 0 & & \\ \vdots & \vdots & \vdots & \vdots & & \\ \frac{1}{2}K(s_{N-1},s_1) & K(s_{N-1},s_2) & K(s_{N-1},s_3) & \cdots & 0 & \\ \frac{1}{2}K(s_N,s_1) & K(s_N,s_2) & K(s_N,s_3) & \cdots & K(s_N,s_{N-1}) & 0 \end{pmatrix} \begin{bmatrix} b(s_1) \\ b(s_2) \\ b(s_3) \\ b(s_4) \\ \vdots \\ b(s_{N-1}) \\ b(s_N) \end{bmatrix} \tag{5.28}$$

or, in a shorthand notation,

$$\mathbf{b} = \mathbf{b}_0 + \mathbf{K}\mathbf{b} \tag{5.29}$$

It can be seen that the upper-right elements of the kernel matrix $\mathbf{K}$ vanish. For the remaining

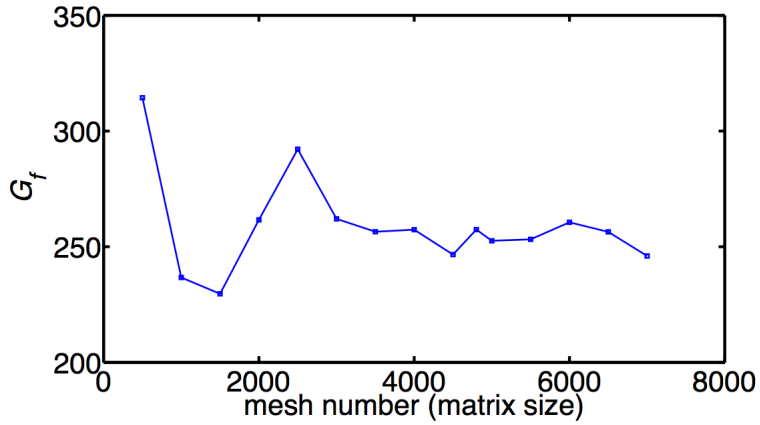

Figure 5.4: Convergence test of mesh number for the 1.3 GeV high-energy transport arc (Example 1) lattice. In this convergence test, the simulation parameters are the same as those shown in Table 6.1 and the initial modulation wavelength $\lambda = 40\mu$m. We use mesh number 4800 for the CSR gain calculation throughout the studies of the beamline.

(bottom-left) elements of $\mathbf{K}$, Eqs. (3.40), (3.41), and (3.43) are evaluated by linear interpolating the associated transport matrix functions extracted from `elegant` with proper transformations of dynamic variables, as introduced in Sec. 5.1.1. Depending upon the validity of criteria for the impedance models [Eqs. (5.10) to (5.26)] and of our interest, the overall resultant impedance at a certain location s' is evaluated by taking the sum over individual effects[107].

Numerical integration of Eq. (3.52) becomes equivalent to finding the inverse of the matrix $(\mathbf{I} - \mathbf{K})$ in Eq. (5.29) and multiplied by $\mathbf{b}_0$, i.e., $\mathbf{b} = (\mathbf{1} - \mathbf{K})^{-1}\mathbf{b}_0$. Convergence based on Eq. (3.52) or Eq. (5.29) requires that the step size of the numerical integration be small enough to resolve the fastest variation of the relevant impedance along a beamline. The convergence tests for examples presented in the dissertation have been done before the microbunching gain spectral curves are produced. An example of our about demonstrated example (in Chapter 6) is presented below in Fig. 5.4. General sawtooth behavior in Fig. 5.4 can be expected due to, for example, finite number of meshes on individual dipoles along s-integration. As the mesh number increases, such sawtooth fluctuation amplitude is reduced and the results would converge.

When constructing the kernel matrix elements, $K(s_i, s_j)$ as well as $\mathbf{b}_0$, we read the relevant initial beam and Twiss parameters and extract transport functions from `elegant` input/output files. In this way, our Vlasov solver has an advantage of treating a general linear lattice[108] and also utilizes most of the capabilities born in `elegant` [66]. Furthermore, as we have mentioned, reaching convergence of the particle tracking simulation results requires careful effort [see, for more detail, in Sec. 5.2]. Like mutual benefit, our developed Vlasov solver also makes it easier to compare/confirm results of microbunching gain obtained

[107] This statement indeed greatly enhances the power of employing frequency-domain treatments in the analysis of collective instability studies.

[108] In `elegant`, there is no restriction of linear lattice. This limit stems from our theoretical formulation, i.e. Eq. (2.52).

from the above-described semi-analytical Vlasov solver and from direct `elegant` tracking.

Finally, we note that Eq. (5.29) can be solved in an alternative way, based on iterative approach, which may provide further physical insight. More precisely, we can gradually approach the (self-consistent) solution, $\mathbf{b} = (\mathbf{1} - \mathbf{K})^{-1}\mathbf{b}_0$, by constructing a set of $\mathbf{b}'$s iteratively

$$\mathbf{b}_1 = \mathbf{b}_0 + \mathbf{K}\mathbf{b}_0 \tag{5.30}$$

and

$$\mathbf{b}_2 = \mathbf{b}_0 + \mathbf{K}\mathbf{b}_1 \tag{5.31}$$

and so on, provided the iterations converge. It was found that this iterative approach works only for finite and discretely located collective effects, e.g. CSR. Using the iterative approach, we find interesting multistage CSR microbunching amplification along a beamline, a distinct feature from that of two-stage amplification explored in few-dipole bunch compressor chicanes. These important features would be later introduced in Chapter 6. To end this subsection, we remind that Tables 3.1 and 3.2 have summarized the available capabilities in our semi-analytical Vlasov solver compared with the existing codes presented in the published literature.

5.2 Introduction of CSR and LSC models in particle tracking `elegant`

In this section we briefly outline the numerical algorithms implemented in `elegant` for CSR and LSC related tracking simulations, in particular for the study of MBI. This includes the preparation of initial modulations in six-dimensional phase space distributions and numerical algorithms for CSR and LSC. For detailed description we refer the interested readers to Refs. [21, 22, 24, 66].

5.2.1 Preparation of initial modulations in 6-D particle phase space distribution

Analysis of the microbunching gain requires that we start with a much *quieter* distribution than the usual randomly generated phase space distributions with limited number of simulation particles[109]. To resolve this issue, the level of numerical noise should be suppressed. It turns out that the mere way of randomly generated simulation particles is not enough to achieve the goal. Neither can do so to employ Halton sequence [66, 77]. For such particular purpose, in `elegant` a self-describing data sets (SDDS)-based script `smoothDist6s` is written that smoothens the six-dimensional phase space distributions of a beam. The procedures are summarized in Ref. [24], many numbers of which are obtained by trial and error, based on

[109] The noise fluctuation due to granularity of particles is proportional to $1\Big/\sqrt{N}$ where N is the number of particles. Suppose the total number of simulation particles is 10^4 times smaller than the actual number, the numerically augmented noise can be 100 times larger.

examination of the noise levels in the resulting distribution and the degree to which it reproduces features in the original distribution. We remind that the very last step of the procedures [24] sets up a potential constraint; the horizontal and vertical planes of particle phase space coordinates are assumed to be decoupled. Because of this constraint, we need a special treatment to benchmark our semi-analytical Vlasov calculation for microbunching analysis of magnetized beams. This issue would be introduced in Sec. 5.3.2.

One alternative to six-dimensional smoothing would be to perform a purely two-dimensional simulation, i.e., using only the longitudinal phase-space coordinates. This might seem reasonable given that the CSR and LSC models act directly only in the longitudinal plane. However, this is not advisable for several reasons. First, the longitudinal space charge depends on the beam size, so this would have to be artificially included if we track in the longitudinal plane only. Second, by performing six-dimensional tracking, we automatically include important gain-reducing effects from the emittance and energy spread of the beam [24].

5.2.2 Numerical algorithm for particle tracking with CSR

In `elegant`, the element of `CSRCSBEND` is employed to simulate CSR effect within dipoles, including Case A and Case B of Fig. 4.1. The equation of motion for $\delta = \Delta E/E$ is thus related to Eqs. (4.63) and (4.68). When simulating only steady-state CSR, the second term in Eq. (4.68) is used. The detailed description of CSR algorithm can be found in Ref. [25]. Below we list some important steps of its implementation. The numerical implementation relies on splitting each dipole into a user-specified number of pieces, see Fig. 5.5(a). Usually 60 pieces are adequate, though typically 100 or more are used [`N_KICKS`]. For each piece, the following steps are performed:

(1) Propagate the entire beam through the piece using a second-order or fourth-order canonical integrator [66];

(2) Compute the CSR wake through Eqs. (4.63) and (4.68);

(3) Apply the CSR energy kicks.

As noted in Ref. [25], a more accurate implementation would include the CSR energy kicks in the canonical integration. However, this would have complicated the code and is probably unnecessary in any case. Because the canonical integration through the dipole fields, (1), includes the energy dependence of the transport to all orders, the dispersive effects on the transverse coordinates of the particles are computed automatically. Computation of the CSR wake is performed as follows:

(a) Particle arrival times at the end of the dipole piece are binned, see Fig. 5.5(b);

(b) The density histogram is smoothed using Fast Fourier transform (FFT) convolution with a noise filter, called Savitzky-Golay filter [139];

(c) The same filter is used to take the derivative of the smoothed density distribution, see Fig. 5.5(c-d);

(d) Eqs. (4.63) and (4.68) are evaluated for each bin;

(e) Each particle's energy is changed by for the bin it occupies, where $(d\mathcal{E}/cdt)\,\Delta s$ is the central path length of the dipole piece, see Fig. 5.5(e).

One difficulty in these computations comes from noise in the linear density histogram due to the use of a finite number of particles and a large number of bins. This is a particular problem when taking the derivative of $\lambda(s)$, as shown in Eq. (4.68). Smoothing is used to overcome this problem, at the expense of some loss of information, e.g., real spikes in the current will be reduced. However, smoothing must be used cautiously when spikes are produced in the longitudinal distribution, which happens when employing high compression factors, with large microbunching gains, or unsmoothed input distributions. `elegant` users are always cautioned that it is necessary to vary both the number of particles and the amount of smoothing until convergence is obtained.

As for exit transient CSR effects, `elegant` provides four models [`CSRDRIFT`] for simulation of CSR in drift spaces following CSRCSBEND elements. Note that all models allow support splitting the drift into multiple `CSRDRIFT` elements. One can also have intervening elements such as quadrupoles. The CSR effects inside such intervening elements are applied in the `CSRDRIFT` downstream of the element. The most advanced model at present is based on Stupakov and Emma's formulas [67], which extends Eq. (87) of the one-dimensional treatment of Saldin *et al.* [153] to include the post-dipole region. This model includes not only the attenuation of the CSR as one proceeds along the drift, but also the change in the shape of the wakefield. Simulating exit transient CSR effects based on Stupakov and Emma's model in `CSRDRIFT` is so far the most sophisticated treatment in `elegant` and the slowest model to run. It uses the same binning and smoothing parameters as the upstream `CSRCSBEND`.

5.2.3 Numerical algorithm for particle tracking with LSC

`elegant` supplies two beamline elements that simulate longitudinal space charge (LSC) effect. One is a drift element `LSCDRIFT` and the other an RF cavity element `RFCW`. The exact form of the longitudinal space charge impedance in Eq. (4.168) is used in a kick-drift-kick (or kick-accelerate-kick) algorithm. The distance between kicks must be set properly to get a valid result. For the drift element the splitting length is automatically estimated. The acceleration element requires the user to specify the number of parts to split the cavity. For a Gaussian or a parabolic transverse beam distribution, `elegant` also employes the fitting formula as described in Eq. (4.116).

The kick-drift-kick algorithm is highlighted as follows. After the beam bunch is transported in a distance, a longitudinal histogram is made. Having computed the impedance, we next take FFT of the current histogram. This is optionally low-pass filtered to control noise. The cutoff frequency and slope of the filter are determined by the user. We then use the low-pass filter to remove high-frequency numerical

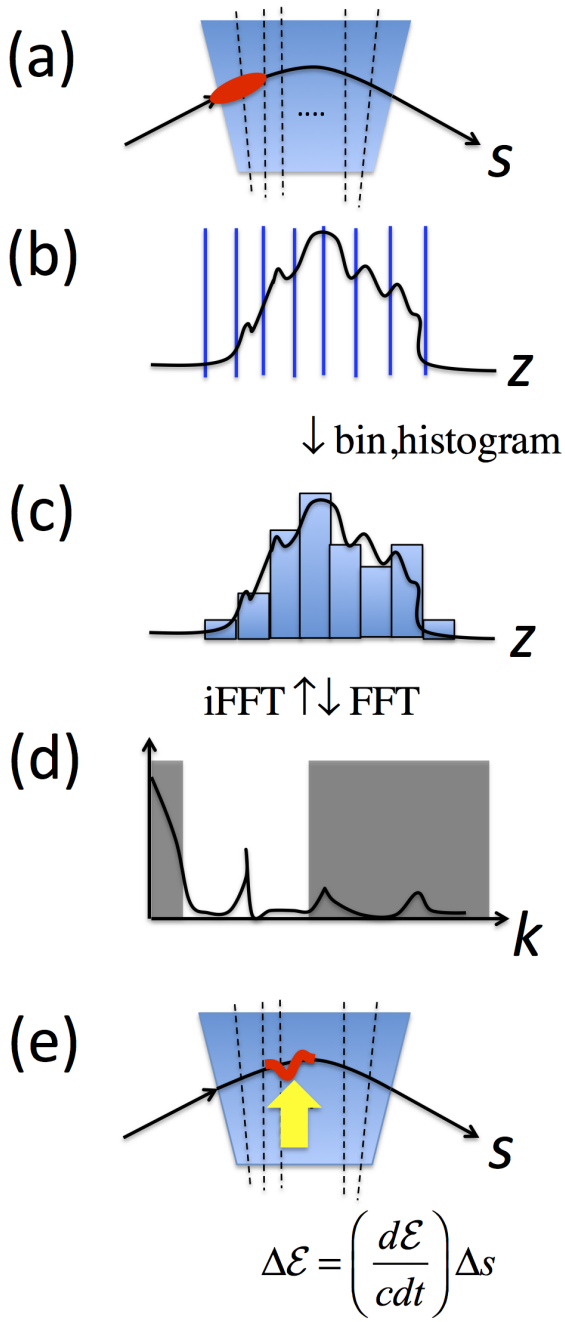

Figure 5.5: Illustration of numerical algorithm of CSR effect implemented in `elegant`.

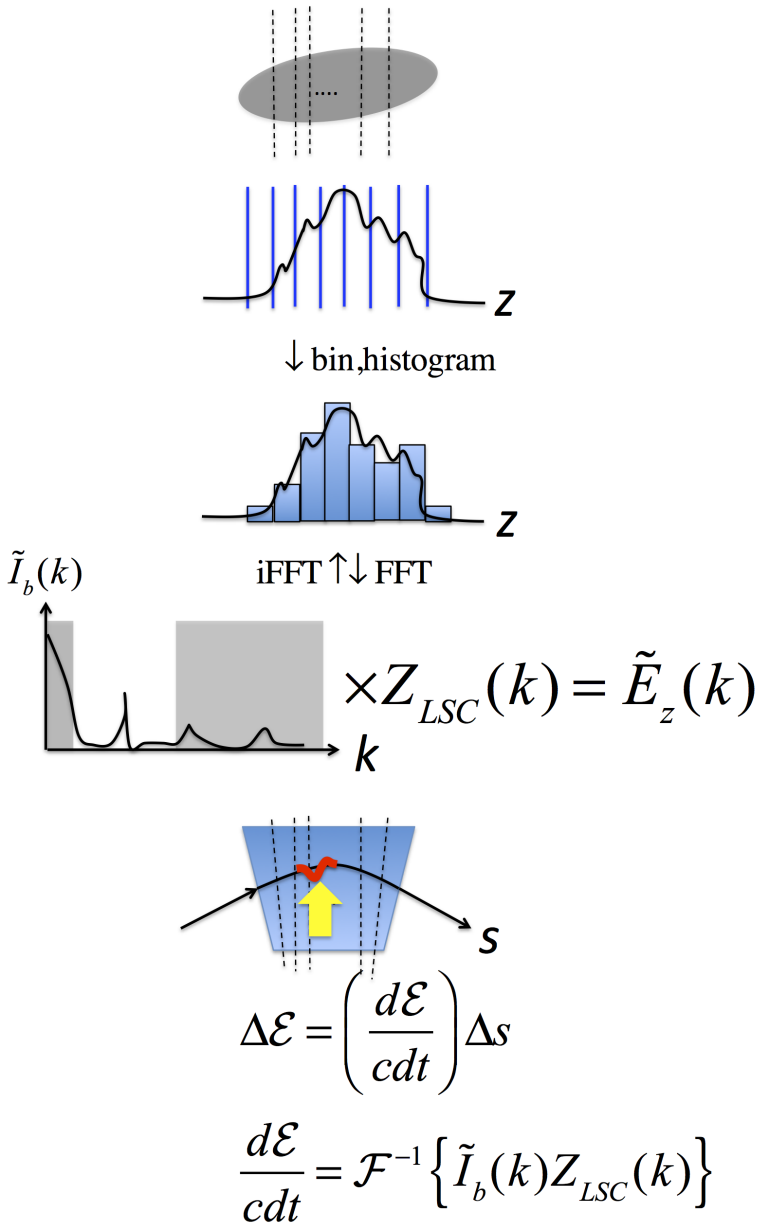

Figure 5.6: Illustration of numerical algorithm of LSC effect implemented in `elegant`.

noise. Examination of FFTs of the current histograms provides guidance in this process, which is important in obtaining meaningful results. The filtered FFT of the current is then multiplied by the impedance, and the result is inversely Fourier transformed. This gives the wake voltage as a function of bin in the original current histogram. We apply this voltage to each particle, with interpolation between bins to make a smoother result. Figure 5.6 illustrates the aforementioned steps.

5.3 Preparation and Post-processing of particle tracking simulation

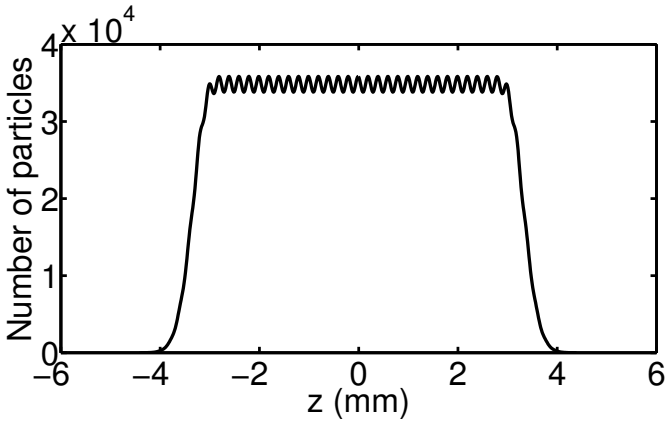

Figure 5.7: Illustration of flattop bunch density distribution. In the example, the flattop length is 6 mm, the entire bunch duration is 9 mm, with Gaussian $\sigma = 0.3$ mm to both ends, the modulation wavelength λ_m on top of the distribution is 200 μm, and the modulation amplitude/depth dm is 3%.

5.3.1 Preparation of uniform flattop bunch distribution

The quantitative measure of microbunching instability (MBI) in a single-pass accelerator system has so far relied on the theoretical formulation [152, 79, 81], upon which the coasting beam approximation is based. This approximation assumes the modulation atop the bunch current distribution or the longitudinal phase-space distribution is at a length scale small compared with the overall duration. Under this approximation, the spectral components of different modulations (i.e. different k's) are decoupled to the overall bunch spectrum [see Eq. (3.38)]. While this approximation can greatly simplify the theoretical framework and the numerical treatment of the semi-analytical Vlasov solver, it poses difficulties in numerical particle tracking simulation, in which a bunched beam is usually generated. Thus, to mimic the coasting beam in particle tracking, the flattop-density distribution is used. The flattop distribution is specially tailored so that both ends are not hard-edged but with Gaussian-softened edges. A typical bunch current distribution is shown in Fig. 5.7.

I. Initial density modulation

Following are numerical procedures to generate the uniform flattop bunch z distribution and Gaussian distributions for the remaining five coordinates (x, x', y, y', δ):

(1) The initial 4-D transverse coordinates for individual particles, (x, x', y, y'), are prepared using generic `elegant` commands. Usually the transverse phase space distribution is characterized by initial Twiss parameters (which describe the orientation of the phase space distribution) and the beam emittances (which describe the volume of the 4-D phase space). For a transversely coupled beam, or magnetized beam, we require a special manipulation, which would be detailed in Sec. 5.3.2.

(2) The 2-D longitudinal phase space distribution (z, δ) is specified by the following parameters, including beam reference energy E_0 or γ_0, rms energy spread σ_δ, linear chirp h, flattop length, modulation

wavelength λ_m, Gaussian-softened end length, the left and right ends.

(3) With the above information prepared, we first construct the flattop z-distribution and Gaussian distribution for energy coordinate. Second, we replace the longitudinal phase space distribution originally generated in (1) by that specified in (2). Detailed steps include using `sddsconvert` to cut and using `sddsprocess` to attach the (new) longitudinal phase space coordinates for individual particles in the (old) 6-D phase space distribution. If there is a chirp in the beam bunch (i.e. $z-\delta$ correlation), the sixth particle coordinate should be modified according to $\delta = \delta + hz$, where h is the chirp parameter[110].

(4) The last step is to impose a density-modulated bunch distribution. There has been a specialized SDDS tool, called `smoothDist6s`, for this particular purpose. The detailed algorithm can be found in Ref. [24] or `elegant` user manual[111]. The expression for density modulation is defined as

$$\lambda(t) = \lambda_0(1 + d_m \cos \tfrac{2\pi}{\lambda_m} z) \tag{5.32}$$

where d_m is the modulation amplitude (or depth) and λ_m is the modulation wavelength.

In Ref. [186], we have prepared a specialized script to perform the aforementioned steps (1-4) for initial density-modulated phase space distribution.

II. Initial energy modulation

The above elaborates the steps of generating a density-modulated phase-space distribution. There is another situation for MBI analysis: the case with initial energy-modulated phase-space distribution. Here the energy modulation is expressed as

$$\delta_i^{new} = \delta_i + \hat{\epsilon}_m \sin \tfrac{2\pi}{\lambda_m} z_i \tag{5.33}$$

where the index i refers to individual particles, $\hat{\epsilon}_m$ is the energy modulation amplitude, and $k_m = 2\pi/\lambda_m$ is the modulation wavenumber.

Similar to the above case for density modulation, following are numerical procedures to generate the energy-modulated phase-space distribution[112]:

(1) The initial 4-D transverse coordinates for individual particles, (x, x', y, y'), are still prepared using generic `elegant` commands, the same as the previous situation.

(2) The 2-D longitudinal phase space distribution (z, δ), is specified by the same set of parameters outlined in the previous case.

[110] Note in `elegant` a positive chirp is assigned for negative-R_{56} compression.

[111] In some situations, `smoothDist6s` may encounter a technical problem in generating small wavelength modulations. This issue can be resolved by changing occurrences in `smoothDist6` script. (See `elegant` users forum for more detail.)

[112] The longitudinal z distribution is still assumed uniform flattop.

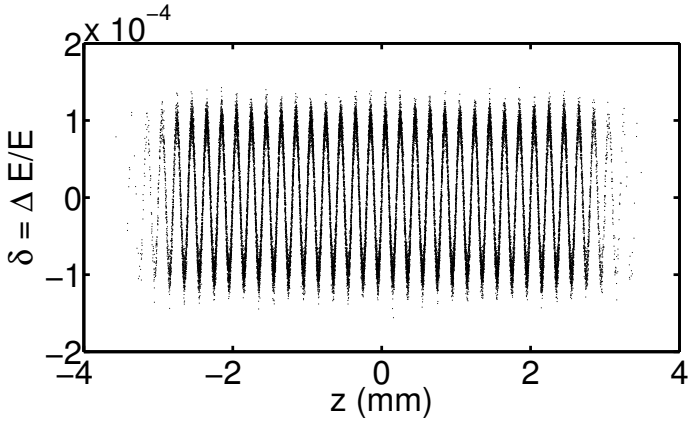

Figure 5.8: Illustration of energy-modulated phase-space distribution. In the example, the entire bunch duration is 7.2 mm, with Gaussian $\sigma = 0.3$ mm to both ends, the modulation wavelength on top of the distribution is 200 μm, and the modulation amplitude is 0.01%. Note that the z-projection (or, z-histogram), the bunch density profile, should be a constant profile.

(3) With the above information prepared, the energy-modulated phase space distribution can be constructed by Eq. (5.33): first, change of the momentum of each particle δ_i to δ_i^{new} by adding a amount of sinusoidal energy offset $\hat{\epsilon}_m \sin k_m z_i$ according to its time-like coordinate z_i. The energy-modulated phase-space distribution looks like Fig. 5.8 below.

Similarly in Ref. [186] we have prepared a specialized script to perform the steps (1-3) outlined above for initial energy-modulated phase space distribution.

5.3.2 Preparation of a magnetized beam with initial longitudinal phase space modulations

In the previous subsection we have elaborated the preparation of initial density and energy modulations for a beam phase space distribution. It is found that tailoring the initial density modulation can be more trickier than dressing the energy modulation. The algorithm implemented in `elegant` (`smoothDist6s`), as outlined above, would eventually lead to decoupling of the transverse degrees of freedom [24]. This appears not to affect if a beam was initially prepared as an uncoupled beam. Moreover, to the author's knowledge, `elegant` itself does not provide direct support to generate a transversely coupled beam.

In Chapter 9 of this dissertation, we would investigate the microbunching dynamics for transversely coupled beams[113]. This turns out to be an issue when we want to quantitatively measure the phase space modulations in order to be consistent with our theoretical formulations using `elegant`.

Having this issue in mind, we propose two questions that need to be resolved before to proceed:

(1) How to generate a transversely coupled beam in `elegant`?

[113]The idea of using magnetized beam is described in Sec. 9.1.

(2) How to add initial density and/or energy modulation atop of the magnetized beam?

After a moment of reflection, we find the initial (density) modulation, done with help of `smoothDist6s`, must be tailored before adding beam magnetization. Knowing this, the above two questions are reduced to the first one only. Douglas and Tennant [63] proposed a method to resolve the first issue. Below we try to illustrate the basic idea and the numerical procedures:

The basic idea starts from a (given) flat beam. By flat we mean one of the transverse beam emittances in two eigen-axes, e.g. ϵ_x or ϵ_y, is much smaller or larger compared with the other, i.e. $\epsilon_x \gg \epsilon_y$ or the opposite case[114]. Now consider a flat beam of (dominant) emittance ϵ is characterized by Twiss (or Courant-Snyder) parameters β, α, and $\gamma = (1+\alpha^2)/\beta$. The beam sigma matrix can be formulated using Twiss parameters similar to Eq. (3.80),

$$\Sigma(0) = \epsilon \begin{pmatrix} \beta & -\alpha & 0 & 0 \\ -\alpha & \gamma & 0 & 0 \\ 0 & 0 & 0 & 0 \\ 0 & 0 & 0 & 0 \end{pmatrix} \tag{5.34}$$

A general transverse two-by-two transport matrix can be expressed as

$$\mathbf{M}(\mu) = \begin{pmatrix} \cos\mu + \alpha\sin\mu & \beta\sin\mu \\ -\gamma\sin\mu & \cos\mu - \alpha\sin\mu \end{pmatrix} \tag{5.35}$$

Define another matrix, which rotates M by 90-deg, as

$$\mathbf{N}(\mu) = \mathbf{M}(\mu + \frac{\pi}{2}) = \begin{pmatrix} -\sin\mu + \alpha\cos\mu & \beta\cos\mu \\ -\gamma\cos\mu & -\sin\mu - \alpha\cos\mu \end{pmatrix} \tag{5.36}$$

Presume that we can construct a 4-by-4 transport matrix as follows,

$$\mathbf{T} = \frac{1}{2}\begin{pmatrix} \mathbf{M}+\mathbf{N} & \mathbf{M}-\mathbf{N} \\ \mathbf{M}-\mathbf{N} & \mathbf{M}+\mathbf{N} \end{pmatrix}_{4\times 4} = \frac{1}{2}\begin{pmatrix} m+\alpha p & \beta p & p-\alpha m & -\beta m \\ -\gamma p & m-\alpha p & \gamma m & p+\alpha m \\ p-\alpha m & -\beta m & m+\alpha p & \beta p \\ \gamma m & p+\alpha m & -\gamma p & m-\alpha p \end{pmatrix} \tag{5.37}$$

where the shorthand notations m and p are used

$$\begin{cases} m = \cos\mu - \sin\mu \\ p = \cos\mu + \sin\mu \end{cases} \tag{5.38}$$

Now we operate Eq. (5.37) on the beam. According to Eq. (2.69), we have the resultant beam sigma matrix

[114] A round beam is therefore quantified as $\epsilon_x \approx \epsilon_y$.

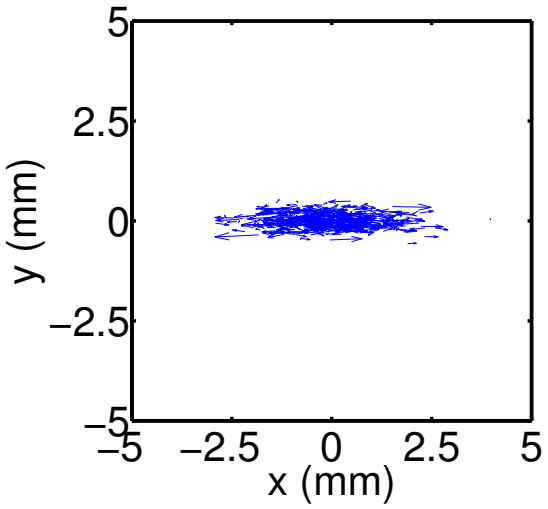

Figure 5.9: Illustration of the initial (flat) beam transverse $x-y$ distribution. The arrows indicating the angular divergences are magnified by four times of their original magnitudes. The transverse emittances are assumed $\epsilon_{\rm nx} \approx 72\ \mu{\rm m}, \epsilon_{\rm ny} \approx 2\ \mu{\rm m}$.

of the form

$$\Sigma^{\rm mag} = \mathbf{T}\Sigma(0)\mathbf{T}^T = \frac{\epsilon}{2}\begin{pmatrix} \beta & -\alpha & 0 & 1 \\ -\alpha & \gamma & -1 & 0 \\ 0 & -1 & \beta & -\alpha \\ 1 & 0 & -\alpha & \gamma \end{pmatrix} \tag{5.39}$$

Now this is a transversely coupled beam because the off-diagonal block matrices do not vanish. One might have a concern regarding the physical reality of $\mathbf{T}$ matrix. In fact, the form of Eq. (5.37) can be implemented in reality by assigning a conventional six-quadrupole telescope and the idea was early proposed [27] as an option for application to light source facilities. To numerically generate a magnetized beam can be done by reversing the procedures. We need to specify in advance the Twiss parameters for a magnetized beam and use those to construct Eq. (5.37) and prepare an initial beam phase space distribution as described in Eq. (5.34). Figure 5.9 and 5.10 below illustrate the initial flat beam and final magnetized round beam distributions in transverse configuration space and phase space.

5.3.3 Evaluation of density and energy modulations

I. Density modulation

In postprocessing of `elegant` tracking results, we determine the density modulation amplitude at a specific location by the following procedures:

(1) Make a z histogram (use `sddshist`) from 6-D phase space distribution while removing/clipping the leading and trailing part to eliminate possible edge effects;

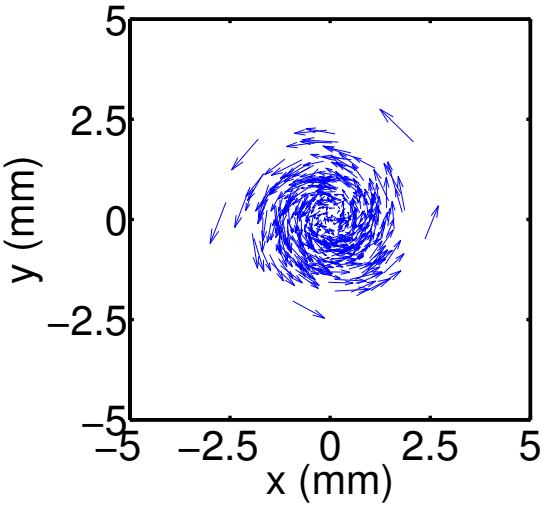

Figure 5.10: Illustration of the final (round, magnetized) beam transverse $x-y$ distribution. The arrows indicating the angular divergences are magnified by four times of their original magnitudes. The transverse emittances are now $\epsilon_{\rm nx} \approx 36\ \mu$m, $\epsilon_{\rm ny} \approx 36\ \mu$m.

(2) Fit a polynomial (use `sddspfit`, up to 7th order) to the remaining data and remove the constant offset;

(3) Take FFT (use `sddsfft`) or Numerical Analysis of Fundamental Frequencies (NAFF) (use `sddsnaff`) [99] of the fitted data and select the nominal modulation wavelength, which is supposed to be dominant over a spectral range;

(4) To extract the microbunching gain $G(s)$, a `MATLAB`[120] script is written to provide three options for choice: (a) FFT and NAFF methods; (b) Power Spectral Density (PSD) method; and (c) Method by definition. For low gain case, all the three methods should give the same results. However, for high gain case, the FFT method is usually suggested. Below we would introduce the three methods in more details.

Presuming the output files from `WATCH` points have been produced, a specialized script is written to perform the aforementioned procedures for processing the raw data from particle tracking [186].

To obtain the spectral gain curves, i.e. $G_f(\lambda)$ as a function of a series of modulation wavelengths, the above procedures (1-4) should be repeated and a series of beam distributions with different initial modulation wavelengths are prepared for production runs. While running `elegant`, we need to ensure that the final gain is not saturated in order to match our theoretical formulations. Then we can take the results of linear gain and compare them with our semi-analytical Vlasov calculations. To make sure if the above simulation parameters set up correctly, performing detailed analyses and convergence tests on the aforementioned simulation parameters is required.

Below we introduce the three methods to extract the bunching factors. For illustration, we consider

the case of density modulation.

A. Direct comparison (FFT and NAFF)

The definition of MBI gain G is the magnitude of the ratio of bunching factors at the *present* (denoted as s) to *initial* ($s = 0$, or s_0) location at some given modulation wavelength $k_z(s = 0) = 2\pi/\lambda(s = 0)$ or $k_0 = 2\pi/\lambda_0$ (and its equivalent compressed one $k_z(s) = 2\pi/\lambda(s)$, i.e.

$$G(s_f, k = 2\pi/\lambda) \equiv \left| \frac{b(k_z; s_f)}{b_0(k_0; 0)} \right| \tag{5.40}$$

where b is the bunching factor, defined in Eq. (3.27) and $k_f = k_z(s = s_f) = 2\pi/\lambda(s = s_f)$.

The output from FFT or NAFF is in fact the bunching factor. By Eq. (5.40) the microbunching gain can be readily obtained. Although this approach is straightforward for data analysis, one should always check the dominant modulation wavelength for those FFT spectra and NAFF along the beam transport line. Usually, but not always, the peaked spectral amplitude locates at the desired frequency, e.g. Figs. 3.13 to 3.16.

B. Power spectral density method (PSD)

In some situations, particularly for transport or recirculation system with multiple dipoles, the peaked FFT spectrum could be broadened after CSR interactions because of smearing effects. Then the direct comparison may not be easy to apply. In that case we may use the power spectral density (PSD) method to estimate the MBI gain. Before doing PSD, we need an additional base run with zero density modulation for the subsequent analyses.

First, we define PSD function as the squared module of the Fourier transformed function, i.e.

$$E'(s, d, \lambda) = E(s, d, \lambda) - E(s, d = 0, \lambda) \tag{5.41}$$

Then for each location, say s, with modulation depth d, and wavelength λ_0 (or frequency $f_0 = c/\lambda_0$), we integrate the PSD between $0.9f_0$ to $1.1f_0$, denoted as $E(s, d, \lambda_0)$ [see also Fig. 5.11],

$$E(s, d, \lambda) = \int_{0.9f_0}^{1.1f_0} f_{PSD} df = \int_{0.9f_0}^{1.1f_0} |FFT(f)|^2 df \tag{5.42}$$

To remove noise contribution, we subtract $E(s, d, \lambda_0)$ from $E(s, d = 0, \lambda_0)$, i.e. $E'(s, d, \lambda_0) = E(s, d, \lambda_0) - E(s, d = 0, \lambda_0)$. Finally we define the microbunching gain as

$$G(s) = \sqrt{\frac{E'(s, d, \lambda_0)}{E'(s = 0, d, \lambda_0)}} \tag{5.43}$$

Note that this approach may not be effective for the case with bunch compression because the vary-

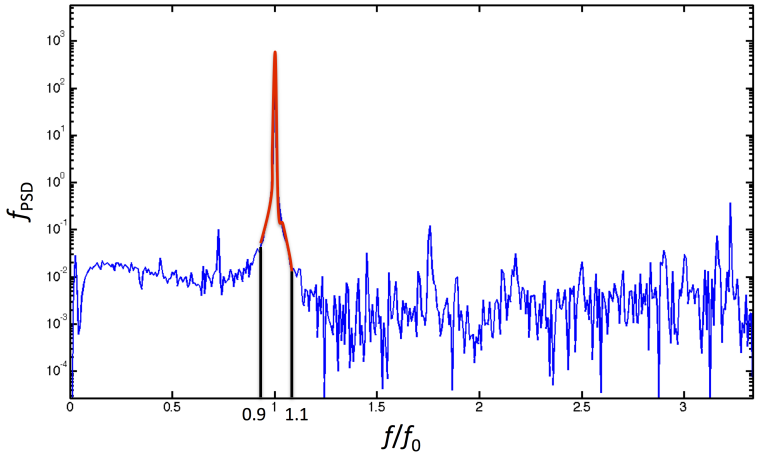

Figure 5.11: Illustration of determination of bunching factor by power spectral method (PSD). See Eq. (5.42).

ing/compressing modulation wavelengths may make the dominant wavelength or frequency difficult to identify.

C. Calculation by definition

According to the statistical definition of bunching factor within a beam bunch, we can also obtain the MBI gain by calculating $\left|\left\langle e^{ik_z z}\right\rangle\right|$ where the bracket denotes the ensemble average. The microbunching gain can be expressed as

$$G(s) = \left| \frac{\left\langle e^{ik(s)z}\right\rangle|_s}{\left\langle e^{ik_0 z}\right\rangle|_{s=0}} \right| \tag{5.44}$$

at some specific location s. Figure 5.12 demonstrates a case where the initial uncompressed modulation wavelength 20.02 μm is compressed to be 2.408 μm for LCLS BC2. The sidebands are due to the rectangular-like structure of the longitudinal bunch line distribution. Note that the bunching factor defined here is the magnitude of the complex quantity $\left|\left\langle e^{ik_z z}\right\rangle\right|$. This approach may not be effective for the case with bunch compression because of the variation of modulation wavelengths along the beam line.

II. Energy modulation

In postprocessing of energy-modulated phase-space distributions, the procedures can be slightly different from those for density modulation:

(1) As outlined in Chapter 3, the energy modulation can be considered the modulation of the longitudinal beam phase space distribution *itself* in (z, δ) plane, as shown in Fig. 5.13 below. The first step is to specify the number of slices, which needs to be larger than the number of modulation wavelengths atop the distribution. Then, for each slice, the average of particles' momenta is evaluated (as blue dots shown in Fig. 5.13);

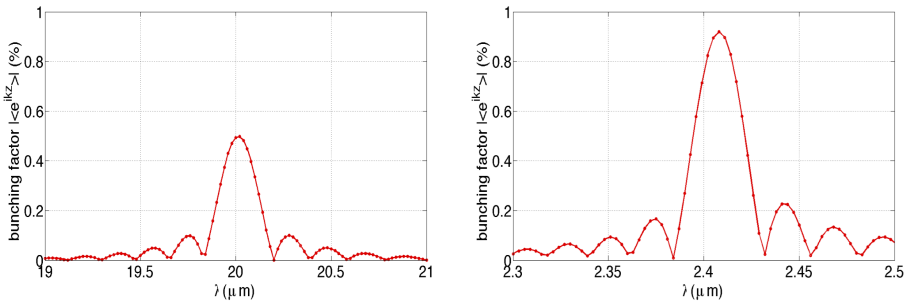

Figure 5.12: Bunching factor estimation by statistical definition Eq. (5.44); (left) at initial location $s = 0$, (right) at final location $s = s_f$. The gain by this approach is ∼1.85.

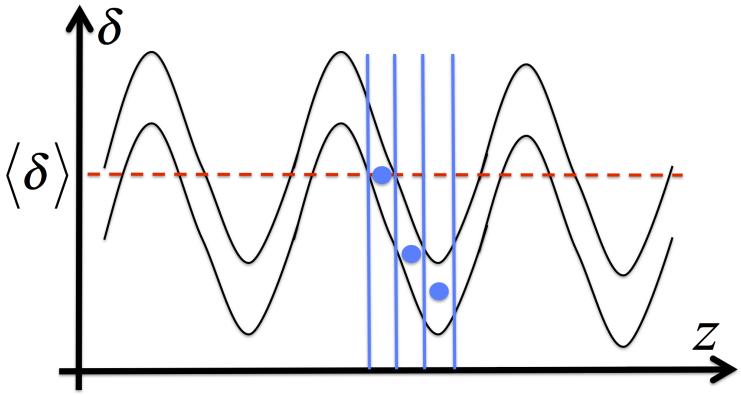

Figure 5.13: Illustration of postprocessing procedures for energy-modulated phase-space distribution. The dashed red line indicates the overall average of the particles' momenta, and the blue dots for the averages of momenta from particles within slices.

(2) All the averages of particles' momenta for individual slices form a vector, as a function of z;

(3) Take FFT for the vector, and find the maximum signal amplitude and the corresponding modulation frequency, k;

(4) In some situations, especially when the uncorrelated energy spread is larger than the energy modulation amplitude, the signal amplitude may not be clearly identified. Such induced energy modulation is sometimes considered as uncorrelated energy spread.

5.3.4 Examples

In this section, we have introduced the pre-processing (or preparation) and post-processing for particle tracking simulations. At the end of this section, we present two examples. One of them illustrated the resultant density modulations, i.e. microbunching gains, and has shown before in Fig. 3.18 for LCLS BC2. The other is shown in Fig. 5.14 below, the resultant energy modulations. In Fig. 5.14, the beamline consists of a straight section composed of focusing-drift-defocusing-drift (FODO) cells, followed by a quasi-isochronous arc [52]. The evolution of energy modulation along the beamline results from initial energy modulation, as

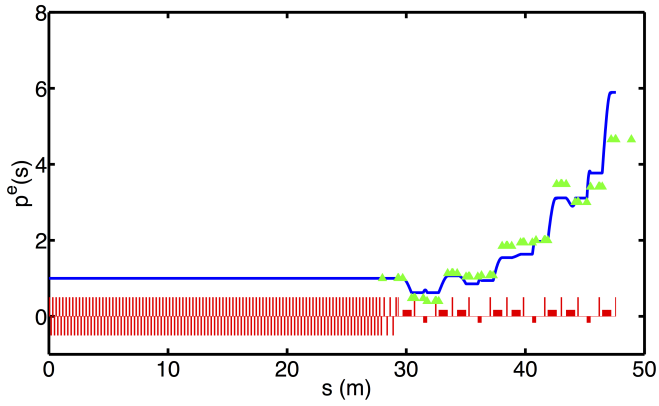

Figure 5.14: Steady-state CSR microbunching energy gain $p^e(s) \equiv \left|\frac{p(k;s)}{p(k_0;0)}\right|$ along the beamline. In the example, $\lambda_m = 100$ μm, $\hat{\epsilon}_m = 0.1\%$, and 3-million simulation particles with peak current 70 A are used. The green triangles are extracted from the developed postprocessing scripts and the red solid line from our semi-analytical Vlasov solver.

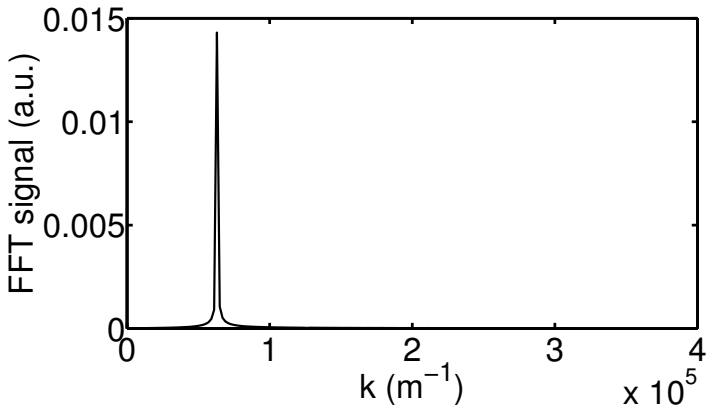

Figure 5.15: FFT spectrum of the phase-space beam distribution at the initial location $s = 0$ m.

the cartoon Fig. 5.8 shows. The corresponding FFT spectra of the energy-modulated phase-space beam distribution at two different locations are shown in Fig. 5.15 and 5.16. Compared with Fig. 5.15 (the initial FFT spectrum), Fig. 5.16 features several higher harmonic components. This indication, resulting in the gain reduction or saturation, may tell the insufficient number of simulation particles used in tracking simulation, when compared with our semi-analytical Vlasov results (blue curves in Fig. 5.14).

5.4 Example of microbunching analysis: linac-arc combination

It would be suitable in this section to demonstrate the microbunching analysis for a beamline with an upstream long linac followed by a transport arc. This combination is a typical constituent of recirculation or ERL accelerator systems. To run this example requires construction of six-by-six transport matrix as a function of path length (Sec. 5.1.1), proper incorporation of relevant collective effects along the beam

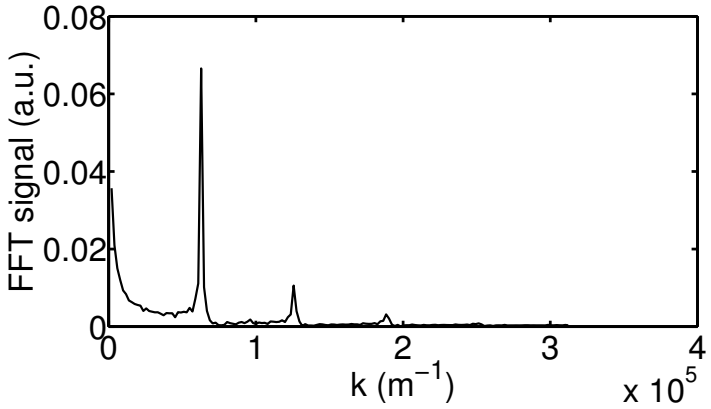

Figure 5.16: FFT spectrum of the phase-space beam distribution at the end of the first arc $s = 48.89$ m.

Table 5.1: Initial beam parameters for the linac-arc example lattice

Name	Value	Unit
Beam energy (at linac entrance)	50	MeV
Beam energy (at linac exit)	1.1	GeV
Peak bunch current	88	A
Normalized transverse emittance	0.3	μm
Initial beta function	18	m
Initial alpha function	-3.6	
Uncorrelated rms energy spread	3×10^{-4}	

transport (Sec. 5.1.2), and solution to the governing equation derived in the preceding chapters (Sec. 5.1.3). In the linac-arc combination, the linac section is followed by a 180-deg arc. The electron beam is accelerated from 50 MeV to 1.11 GeV through a 250-m long linac section which includes 200 accelerating cavities with the voltage gradient 10MV/m, RF frequency 1497 MHz and on-crest acceleration. The arc is a 180-deg arc with large momentum compaction. Moreover, it is a second-order achromat and globally isochronous with a large dispersion modulation across the entire arc. Detailed description of the arc design can be found in Chapter 7. Table 5.1 summarizes relevant beam parameters for the linac-arc combination lattice. Figure 5.17 shows the dispersion function and momentum compaction function along the entire beamline. It can be seen in Fig. 5.17 that the momentum compaction function has taken into account the non-ultrarelativistic effect.

Figures 5.18 and 5.19 show the evolution of microbunching gain functions $G(s)$ along the beamline. `elegant` tracking simulations (dots) were performed for a Gaussian beam [over transverse phase-space and energy coordinates] of 70-million macroparticles and flattop z-distribution with small density modulations on top. For consistency of comparison between our semi-analytical solutions with `elegant` results, the LSC effect is only applied within drift elements and RF cavities. LSC effect within other elements such as dipoles and quadrupoles, is neglected. In Fig. 5.19, CSR effects include both entrance transient and steady states inside individual dipoles, as well as exit transient effects in the downstream drift sections. We found in

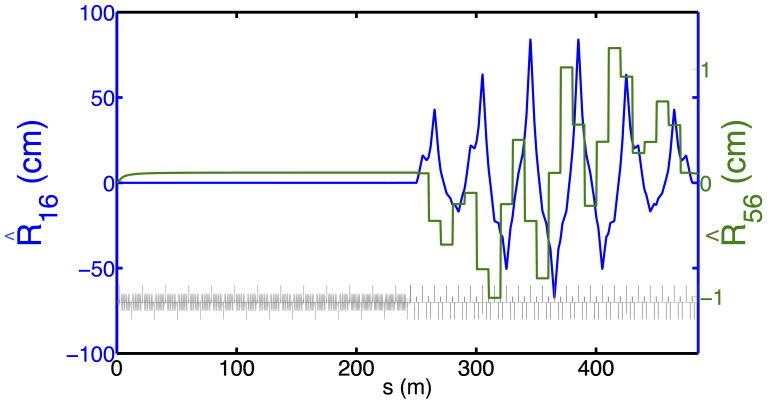

Figure 5.17: Dispersion (blue) and momentum compaction (green) functions of the example linac-arc lattice.

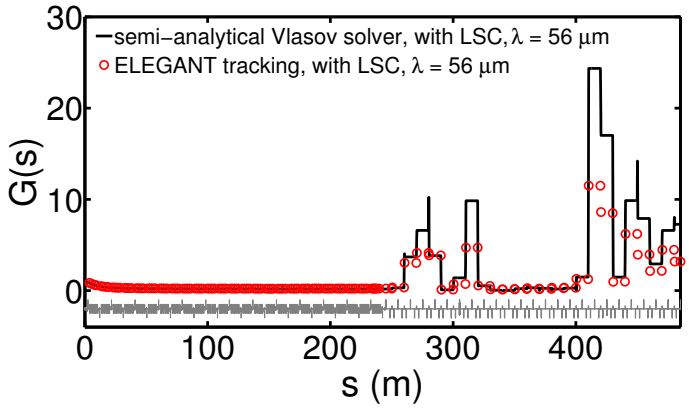

Figure 5.18: LSC-induced microbunching gain function $G(s)$ for the linac-arc lattice. Here in `elegant` tracking we assume 0.1% initial modulation amplitude.

Fig. 5.18 the microbunching gain is slightly reduced in the linac section because of LSC-induced plasma oscillation along with beam acceleration. Our semi-analytical Vlasov solutions match well with `elegant` tracking results throughout the lattice except at some particular locations (e.g., at $s = 410 - 440$ m). After carefully examining numerical parameters to ensure the convergence of `elegant` tracking results, we found the microbunching gain deviation between our semi-analytical Vlasov solutions and `elegant` results is not from numerical issues but originates from non-uniformity of the bunch profile as a result of existing (non-linear) RF curvature (see Fig. 5.20 for the longitudinal phase space distribution and projected longitudinal bunch profile). Here we assume this RF curvature from the linac is not compensated by a harmonic cavity, as usually used in linac-based FELs.

Here we would show that this bunch non-uniformity profile indeed causes the microbunching gain slightly reduced. The tracking results would be compared with our Vlasov solutions, which do exclude this effect from microbunching gain estimation. Because of the presence of RF cavity, the accelerated beam is

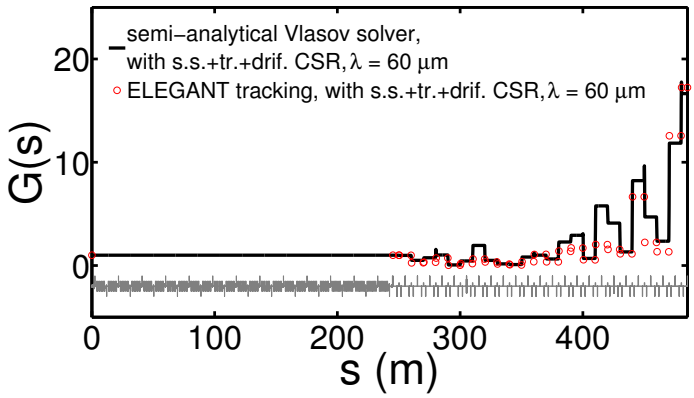

Figure 5.19: CSR-induced microbunching gain function $G(s)$ for the linac-arc lattice. Here the CSR models include both entrance and exit transients as well as steady-state effects. Here in `elegant` tracking we assume 0.6% initial modulation amplitude.

characteristic of a nonlinear RF curvature (see top figure of Fig. 5.20). In the case of on-crest acceleration, we can simply assume the particle energy deviation for each slice related to its longitudinal coordinate given by

$$\delta_i = hz_i + qz_i^2 \tag{5.45}$$

where the linear chirp h vanishes but the quadratic chirp q does exist (e.g., negative in our case). With such $(z-\delta)$ correlation, we can define an effective (local) chirp to be

$$h^{\text{eff}}(z_i) \equiv -\frac{\partial \delta_i}{\partial z_i} = -2qz_i \Rightarrow \begin{cases} < 0, \text{ for bunch tail } (z_i < 0) \\ > 0, \text{ for bunch head } (z_i > 0) \end{cases} \tag{5.46}$$

For the head of the bunch, the effective chirp is positive whereas it is negative for the tail of the bunch. The local bunch compression factor can be described as

$$C(s, z_i) = \frac{1}{\hat{R}_{55}(s) - h^{\text{eff}}(z_i)\hat{R}_{56}(s)} \Rightarrow \begin{cases} > 1, \text{ for bunch head and } \hat{R}_{56}(s) > 0 \\ < 1, \text{ for bunch tail and } \hat{R}_{56}(s) > 0 \end{cases} \tag{5.47}$$

Note that, in the positive momentum compaction region, the modulation wavelength in the head portion of the bunch is lengthened (or, decompressed) while that in the tail of the bunch is shorted (or, compressed) due to the nonzero quadratic chrip, and vice versa in the negative momentum compaction region. It is this situation that results in the non-uniformity of the bunch profile when a beam is imprinted with a nonlinear chirp.

By the above simple analysis we can explain the presence of non-uniformity of bunch profile, as shown in Fig. 5.20. Note that in the figure the bunch head is to the left. The non-uniform density-modulated

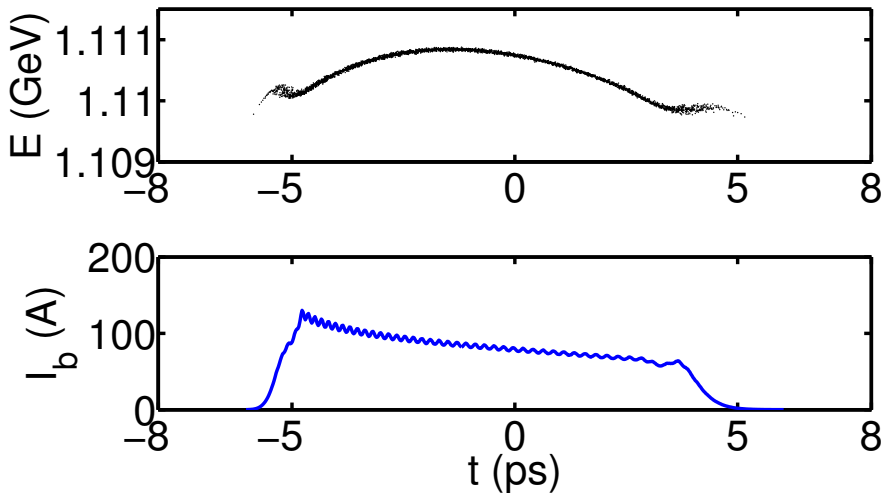

Figure 5.20: (Top) longitudinal phase space distribution at $s = 410$ m. (Bottom) bunch current density. Note here the bunch head is to the left.

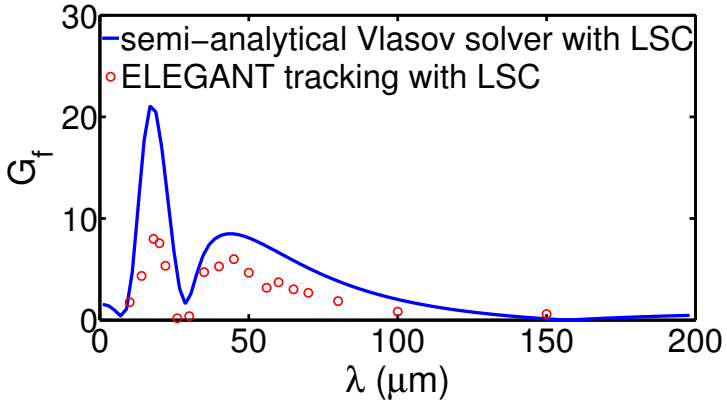

Figure 5.21: Microbunching gain spectra with LSC effects. Note here that in `elegant` simulation we vary the initial modulation amplitudes around 0.1-0.6%.

bunch profile broadens the spectral width around the nominal modulation frequency, and results in a reduced bunching factor as well as the corresponding microbunching gain.

Figures 5.21 to 5.23 show the microbunching gain spectra for cases with different collective effects involved. From Fig. 5.21, we can see the dependence of modulation wavelength on LSC-induced microbunching gain. In Fig. 5.22, both our Vlasov solver and `elegant` include all relevant CSR effects, including both transient and steady states. We believe the deviation between the two methods comes from the non-uniformity of the bunch profile.

We also notice that the gain reduction of the non-ultrarelativistic CSR (NUR, black curve) with the ultrarelativistic CSR (UR, blue curve) is negligible because CSR occurs at the high energy level. The fluc-

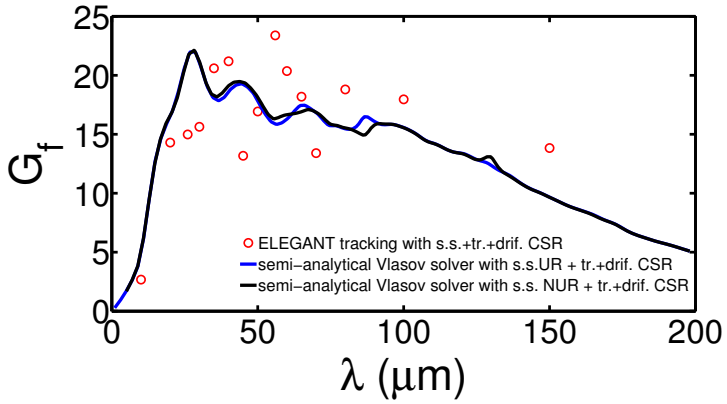

Figure 5.22: Microbunching gain spectra with all relevant CSR effects. `elegant` results include both entrance and exit transient as well as steady-state impedances. The initial modulation amplitudes are varied around 0.1-0.6% to ensure numerical convergence.

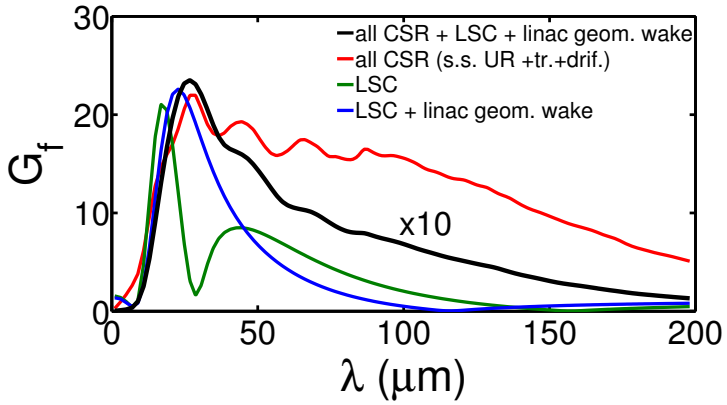

Figure 5.23: Microbunching gain spectra with various combinations of collective effects. To simulate the gain with linac geometric impedance, here we assume the linac parameters are: $a = 3.07$ cm; $L = 10.0$ cm; $g = 8.0$ cm; $\alpha = 0.528$ (see Eq. 4.206). For better illustration, the gain values with the case of all collective effects included (black curve) are presented with $\times 10$ smaller than the calculated values.

tuations shown in Fig. 5.22 are from the CSR exit transient effects, which can be observed both in our semi-analytical Vlasov solutions and `elegant` results.

In Fig. 5.23 we consider altogether the collective effects for the microbunching gain calculation. We observe that the overall microbunching gain is in fact an accumulation effect of density-energy conversion throughout the beamline. In the long section of the upstream linac, LSC and linac geometric effects have accumulated an amount of energy modulation, and subsequently such energy modulation converts to density modulation through the downstream momentum compaction. Then, the converted density modulation can be further amplified through the CSR effects downstream the arc.

To end this section, we would like to emphasize one advantage of using the developed semi-analytical Vlasov solver over particle tracking simulation (e.g., `elegant`). To the authors' knowledge, it is not trivial in time-domain particle tracking to include all relevant collective effects such as CSR, LSC and the associated geometric effects into thorough consideration for MBI analysis. However, with our Vlasov solver, it is straightforward to add these relevant impedance models into consideration. Although we do not expect the Vlasov solver, based on evaluating collective impedance expressions, to give as rich information as `elegant` tracking results do in microbunching analyses, we point out that the value of this solver lies in its speed in execution. This advantage makes the solver a powerful tool for comparative or parametric studies and for design optimization.

5.5 Summary

In this chapter we have elaborated the numerical algorithms for our semi-analytical Vlasov solver. This includes:

(i) how we retrieve the six-by-six transport matrices as a function of path length coordinate;

(ii) numerical implementation of various impedance models such as CSR, LSC and linac geometric effects, some of which require additional parameters from users' input;

(iii) the discretized form of Volterra integral equation and solution by inverse matrix approach.

Then we briefly outlined the numerical algorithms in `elegant` for particle tracking involving with CSR and LSC. To match `elegant` input conditions as close to our theoretical formulation as possible, we have paid attention to tailoring a uniform flattop current distribution with density or energy modulation atop. For a transversely coupled beam, a special treatment is made. For the output results from `elegant`, i.e. raw data, which need to be carefully extracted and exclude the undesired parts, we have described the numerical procedures to postprocess and demonstrated the results.

Having described the numerical algorithms in our semi-analytical Vlasov solver and illustrated numerical pre- and post-processing procedures in `elegant`, we have presented a practical example with a linac section followed by a transport arc, which serves as a typical constituent in a recirculation or ERL accelerator machine. The purpose is to demonstrate the microbunching analysis: the microbunching gain evolution along a general beamline with inclusion of relevant collective effects and beam acceleration and to elucidate the underlying physics behind the particle tracking results.

CHAPTER 6
Multistage CSR Microbunching Gain Development

Coherent-synchrotron-radiation-induced (CSR) microbunching instability has been one of the most challenging issues in the design of modern accelerators. We apply the developed semi-analytical Vlasov solver and applied it to investigation of the physical processes associated with microbunching gain amplification for several lattices. In this Chapter, by extending the concept of stage gain, which was proposed by Huang and Kim [81], we developed a method to characterize multistage CSR microbunching development in terms of stage orders. The stage orders enable a quantitative comparison of the impact of lattice optics on the microbunching gain for different lattices under similar initial beam parameters. We found that the microbunching instability in the multi-bend arcs considered in this study had a distinguishing feature: the multistage amplification. The fact that CSR microbunching gain grows as (up to) six-stage amplification was quantified for the presented recirculation arcs with a total of 24 dipoles, while two-stage amplification was previously reported for a typical four-dipole bunch compressor chicane. We also attempted to relate a lattice optics pattern with the obtained stage gain functions through a physical interpretation. The results from our Vlasov solver were validated by `elegant` [21] with excellent agreement. Although mathematically the iterative solution is identical to direct solution (when the solution converges), physically the approach coming from the multistage point of view can provide additional insight of the microbunching amplification process.

This Chapter is organized as follows. In Sec. 6.1 and 6.2, we introduce the direct and iterative methods for solving the governing equation for bunching factor evolution. Section 6.3 presents numerical convergence tests for the direct and iterative solutions introduced in the preceding two sections. In Sec. 6.4, we propose a method to estimate the stage gain for a general beamline and to characterize the effect of lattice optics on the effect of CSR microbunching. To demonstrate the method we discuss in Sec. 6.5 two comparative high-energy recirculation arcs as lattices and elucidate the physics underlying the method. Finally, we summarize the main results of this study in Sec. 6.6.

In this Chapter we limit ourselves to the case of mere steady-state CSR in multi-bend recirculation arcs. The objective is to study the development of microbunching gain (or the amplification factor, i.e., the ratio of the final to the initial perturbation amplitude) along a beamline and a systematic comparison between different beamline designs. We know the microbunching gain can be contributed from other driving sources, e.g. the transient CSR (especially after the bending dipoles) and the longitudinal space charge forces (LSC); here we do not aim to calculate the gain with all relevant effects included but only focus on the phenomenon of multistage amplification due to steady-state CSR.

Part of the work in this Chapter, especially Sec. 6.1 to Sec. 6.5.1, had been presented by R. Li in 2014

Free Electron Laser Conference, Basel, Switzerland, with the tile *Theoretical Investigation of Coherent Synchrotron Radiation Induced Microbunching Instability in Transport and Recirculation Arcs* (THP022), and later in 2015 Free Electron Laser Conference, Daejeon, Korea, with the tile *Multistage CSR Microbunching Gain Development in Transport or Recirculation Arcs* (MOP087).

6.1 Direct solution to Volterra integral equation

The governing equation for bunching factors or density modulations was derived in Eq. (3.52). By direct solution we refer to the self-consistent solution of Eq. (3.52); the solution is obtained as follows. After rewriting in the vector-matrix form and taking the inverse on both sides, we have

$$\mathbf{b}_k = (\mathbf{I} - \mathbf{K})^{-1}\mathbf{b}_k^{(0)} \tag{6.1}$$

where the subscript k is added to denote the spectral dependence, $\mathbf{b}_k \equiv [b_k(s_1), b_k(s_2), ..., b_k(s_M)]^T$ and $s_i (i = 1, 2, ..., M)$ represents the grid of s along a beamline ($s_1 = 0$ and $s_M = s_f$ denote the entrance and the exit of a beamline). $\mathbf{I}$ is the M-by-M identity matrix.

To quantify the microbunching instability in a single-pass system, we defined the microbunching gain as the ratio of the bunching factors at the present location s to that at the initial location $s = 0$. The gain is a function of the longitudinal coordinate s and the initial modulation wavelength λ (or $k = 2\pi/\lambda$):

$$G(s, k = 2\pi/\lambda) \equiv \left| \frac{b_k(s)}{b_k^{(0)}(0)} \right| \tag{6.2}$$

Hereafter, we call $G(s)$, which is a function of s for a given modulation wavenumber, the gain function and refer to $G_f(\lambda)$ as the gain spectrum. The gain spectrum is a function of λ at the exit of a lattice (the subscript "f" denotes the exit of a beamline). The physical meaning of Eq. (6.1), which involves the CSR effect, is as follows: a density perturbation at s' leads to energy modulation through CSR impedance within a dipole and the energy modulation is subsequently converted to density modulation at downstream s through the relative momentum compaction function $R_{56}(s' \to s)$[115].

6.2 Iterative solution to Volterra integral equation

Another method for solving Eq. (3.52) is the iterative approach, and we call the solution the iterative solution. Here we presumed the zeroth-order solution (i.e., in the absence of any collective effect, or pure

[115]For convenience of discussion, the explicit expression of $R_{56}(s' \to s)$ can be obtained by $R_{56}(s' \to s) = \left[\mathbf{R}(s)\mathbf{R}^{-1}(s')\right]_{56} = R_{56}(s) - R_{56}(s') + R_{51}(s')R_{52}(s) - R_{51}(s)R_{52}(s')$.

optics) to be

$$\mathbf{b}_k^{(0)} = \mathbf{b}_k^{(0)} \tag{6.3}$$

and we define the first-order solution as

$$\mathbf{b}_k^{(1)} = (\mathbf{I} + \mathbf{K})\, \mathbf{b}_k^{(0)} \tag{6.4}$$

The second-order solution can be obtained iteratively

$$\mathbf{b}_k^{(2)} = \mathbf{b}_k^{(0)} + \mathbf{K}\mathbf{b}_k^{(1)} = \left(\mathbf{I} + \mathbf{K} + \mathbf{K}^2\right) \mathbf{b}_k^{(0)} \tag{6.5}$$

In general, the nth order solution can be expressed as

$$\mathbf{b}_k^{(n)} = \left(\sum_{m=0}^{n} \mathbf{K}^m \right) \mathbf{b}_k^{(0)} \tag{6.6}$$

It can be seen that Eqs. (6.1) and (6.6) are equivalent when $n \to \infty$, presuming the inverse matrix of $(\mathbf{I} - \mathbf{K})^{-1}$ exists and the sum in Eq. (6.6) converges to Eq. (6.1). If a storage ring is considered instead of the single-pass system, or, if ubiquitous collective interaction (e.g., LSC) is assumed instead of localized interaction (e.g., steady-state CSR), the sum may not converge. Further, if the beam current becomes larger and larger, it takes higher orders of m to approach the solution by Eq. (6.1). As far as the authors had investigated, for achievable current scales up to kilo-ampere level, the iterative solutions can quickly approach to the corresponding direct solutions. For the case of bunch compressor chicanes of LCLS, it has been shown that the iterative solution up to $m = 2$ can sufficiently quantify the overall CSR gain (see Ref. [81] or Fig. 6.5). For the examples presented in Sec. 6.5, the convergence tests with respect to iterative order n have been demonstrated in Sec. 6.3. The convergence issue is thus not of our primary concern now. In what follows we will investigate some physically interesting properties associated with the iterative solutions, although the series convergence may not be valid from mathematical point of view for arbitrary parameter regimes. To clarify, we focus on CSR-induced microbunching development in a single-pass system (or a system with few passes) and exclude the case of a storage ring system, which is beyond the scope of our discussion. We defined the stage gain function with respect to Eq. (6.6) as follows:

$$\tilde{G}^{(n)}(s, k = 2\pi/\lambda) = \frac{\mathbf{b}_k^{(n)}(s)}{\mathbf{b}_k^{(0)}(0)}, \text{ and } G^{(n)}(s,k) = \left| \tilde{G}^{(n)}(s,k) \right| \tag{6.7}$$

where the tilde is used to denote a complex quantity.

The physical meaning of Eq. (3.52) in the presence of the effect of the CSR was highlighted in Chapter 3. Here, we provide another interpretation on the basis of Eq. (6.6): the overall CSR gain at a specific

position, for example, at the exit of a lattice, can contain multiple contributions from several stages Consider a three-dipole bunch compressor chicane lattice as an example. The zeroth-stage gain originates solely from the effect of beam optics (i.e., in the absence of any collective effect). The corresponding mathematical expression of microbunching evolution is Eq. (6.3). The first-stage gain originates from two paths. One is that the initial density modulation present at the first dipole entrance is converted to energy modulation through CSR interaction within the first dipole, and freely propagates through the optics [i.e. $R_{56}(s' \to s)$] to the final dipole with only a single iteration, which partially corresponds to the second term on the right-hand side of Eq. (6.4). The process is illustrated in Fig. 6.1(a). The other (or the remaining) contributing path is that the initial density modulation propagates by pure optics to the second dipole entrance and is converted to energy modulation via CSR. The resultant energy modulation then freely propagates toward the end of the beamline through $R_{56}(s' \to s)$. This process, depicted in Fig. 6.1(b), complements the second term of Eq. (6.4). The second-stage gain is contributed by the path that evolves from an initial density modulation, at the first dipole entrance. The initial density modulation is readily converted to energy modulation (through CSR) and subsequently transition to density modulation [through $R_{56}(s' \to s)$] up to the second dipole entrance. The same process repeats from the second dipole to the third/last dipole. This second-stage amplification corresponds to the third term of Eq. (6.5) and is conceptually illustrated in Fig. 6.1(c).

A more general statement can be made as follows: The first-stage amplification refers to CSR interaction occurring inside only *one* dipole (either the first or second dipole, in the above simple chicane), where the CSR impedance induces energy modulation because of density modulation. The microbunching structure in the beam evolves during optical propagation through the rest of the beamline. The second-stage amplification refers to CSR interaction occurring inside *two* dipoles, with the beam phase space evolving during optical propagation through the rest of the beamline.

Figure 6.1 illustrates the stage amplification processes. In this study, we will consider a multi-dipole system in a recirculation arc lattice in terms of a multistage amplification scheme. In the following section of the stage gain analysis, we shall quantify such multistage behavior of the CSR microbunching gain in a general linear lattice [e.g. Fig. 6.1(d)].

6.3 Convergence tests for direct and iterative solutions

Either finding the inverse of a kernel matrix [based on Eq. (6.1)] or evaluating the iterative solutions [based on Eq. (6.6)] to perform CSR gain calculation, the convergence tests of mesh number or order of iteration are required to obtain converged results. Here in this section, we show the convergence tests in our semi-analytical Vlasov calculation for the two example lattices. In fact Fig. 5.4 has demonstrated the convergence test of the first example based on direct solutions. The convergence test for the second example is shown below in Fig. 6.2. General sawtooth behavior can be expected due to finite number of meshes on individual dipoles along s-integration. As the mesh number increases, such sawtooth fluctuation shall be reduced and

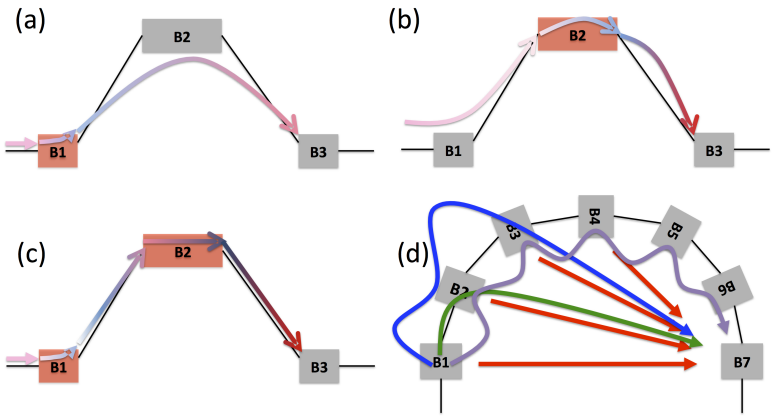

Figure 6.1: Conceptual illustration of multistage CSR microbunching gain evolution. For a typical three-dipole bunch compressor chicane (a,c), (up to) two-stage amplification can describe the microbunching gain evolution. (a) and (b) illustrate the first-stage amplification. (c) depicts the two-stage amplification. Here, for (a,c), the red-colored dipoles are where CSR effects *turn on*. Darker colors indicate further enhanced (or more intense) modulations. (d) indicates the multistage amplification for a multi-bend arc. The red lines describe the one-stage amplification, the green line for two-stage amplification, the blue line for three-stage amplification, and the purple line for higher stages.

the results would converge.

When calculating the CSR-induced microbunching gain by employing iterative approach [Eq. (6.6)], one should also check the convergence of the series sum to ensure the calculated gain approaches that by Eq. (6.1), up to which the iterative order is specified as the order of stages. Figures 6.3 to 6.5 show the convergence of the iterative solutions [or, stage gain by Eq. (6.6)] for the two example lattices. In these figures, we can see that up to six-order iteration (or, 6-stage gain) can describe the overall CSR-induced microbunching amplification. In contrast, we show an additional plot for the bunch compressor chicane, in which the CSR gain exhibits only 2-stage amplification.

6.4 Stage gain analysis

In this section, we discuss the quantification of CSR gains through the separation of the contributions of some beam parameters from that of lattice properties, and outline how we extract individual stage gains from the overall CSR gain. For thus purpose, let us Taylor expand Eq. (6.7) into a series of polynomials of the beam current Ib up to a certain order M:

$$\tilde{G}_f^{(M)} = \tilde{G}^{(M)}(s = s_f) = \tilde{G}_0 + \tilde{G}_1 I_b + ... + \tilde{G}_M I_b^M = \sum_{m=0}^{M} \tilde{G}_m I_b^m \tag{6.8}$$

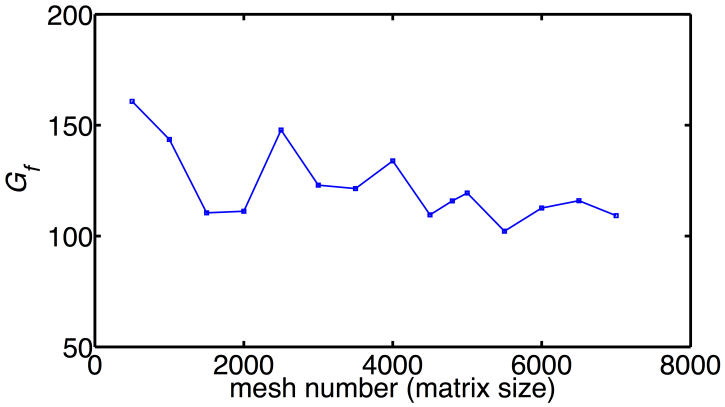

Figure 6.2: Convergence test of mesh number for the 1.3 GeV high-energy transport arc (Example 2) lattice. In this convergence test, the initial beam parameters are summarized in Table 6.1 below. To more clearly present the numeric, we set a larger beam current to 400 A and the initial modulation wavelength $\lambda = 20\mu$m. We use mesh number 4800 for the CSR gain calculation throughout the study of this example lattice.

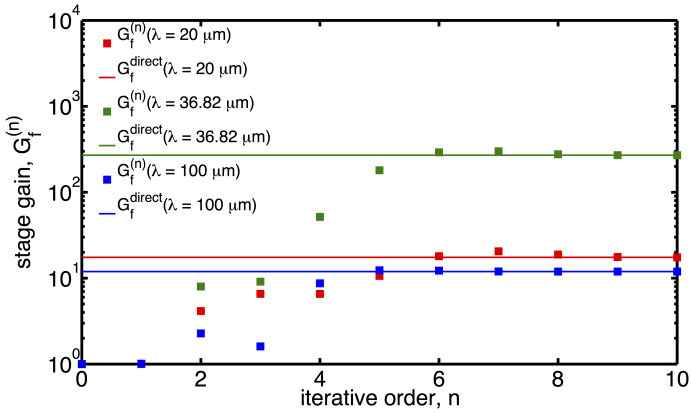

Figure 6.3: Stage gain as a function of iterative order for the 1.3 GeV high-energy transport arc (Example 1) lattice. Beam and lattice parameters are summarized in Table 6.1.

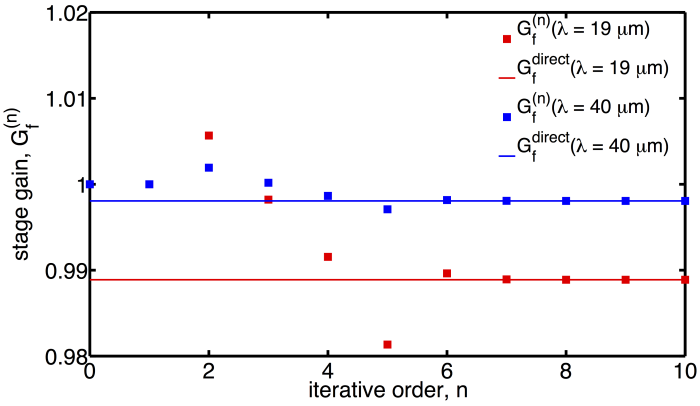

Figure 6.4: Stage gain as a function of iterative order for the 1.3 GeV high-energy transport arc (Example 2) lattice. Beam and lattice parameters are summarized in Table 6.1.

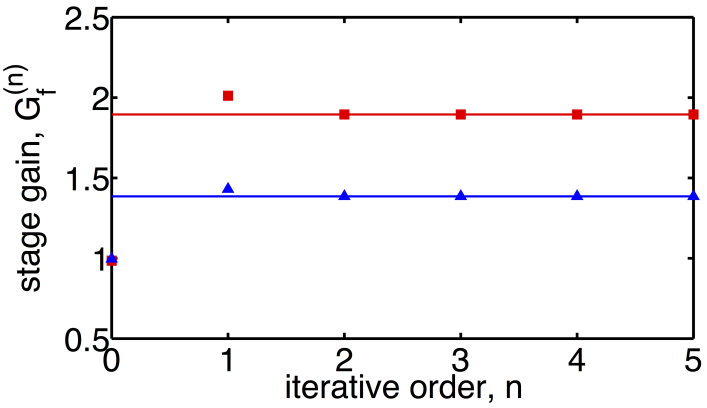

Figure 6.5: Stage gain as a function of iterative order for LCLS BC2 lattice. Beam and lattice parameters are summarized in Table 3.3.

where for simplicity we only treat isochronous arcs, i.e. $I_b = I_0$ and $C(s) = 1$. By inspection of the kernel function as derived in Eq. (3.43), Eq. (6.8) can be further formulated as

$$\tilde{G}_f^{(M)} = \sum_{m=0}^{M} A^m d_m^{(\lambda)} \left(\frac{I_b}{\gamma_0 I_A} \right)^m \tag{6.9}$$

where A is the constant in Eq. (4.116), γ_0 is a relativistic factor, and $d_m^{(\lambda)}$ is a dimensionless coefficient (given a certain modulation wavelength) that reflects the lattice optics properties at the m-th stage ($m = 0, 1, 2, ...$) and Landau damping through finite beam emittances and energy spread. As with the prime interest, in the following discussion λ is chosen to respond for the maximal CSR gain and is denoted as $\lambda_{\rm opt}$. In particular, Eq. (38) of Ref. [81] now becomes a special case of Eq. (6.9) for $M = 2$ in a typical bunch compressor chicane.

Obtaining the coefficients $d_m^{(\lambda)}$ of Eq. (6.9) can be straightforward once the information of beam and lattice optics is given. For convenience of further discussion, we define the *individual* stage gain as the modular amplitude for each term of $\tilde{G}_f^{(M)}$ as follows:

$$\mathcal{G}_f^{(m)} = \left| A^m d_m^{(\lambda)} \left(\frac{I_b}{\gamma I_A} \right)^m \right| \tag{6.10}$$

To end this section, we remind the difference between Eq. (6.7) and Eq. (6.10), the former of which evaluates the overall CSR gain while the latter only accounts for the gain from m-th stage. In the following section, we will consider two comparative examples of arc lattices to demonstrate the stage gain analysis and its connection to both direct and iterative solutions. Furthermore, the physics underlying the method will be discussed.

6.5 Example: two 1.3 GeV high-energy transport arcs

Table 6.1: Initial beam and Twiss parameters for the two arc lattices

Name	**Example 1 (large R_{56})**	**Example 2 (small R_{56})**	**Unit**
Beam energy	1.3	1.3	GeV
Bunch current	65	65	A
Normalized emittance	0.3	0.3	μm
Initial beta function	35.81	65.0	m
Initial alpha function	0	0	
Uncorrelated energy spread	1.23×10^{-5}	1.23×10^{-5}	

6.5.1 Stage gain analysis

Two 1.3 GeV high-energy recirculation arcs were considered as comparative examples (hereafter termed Example 1 and Example 2 lattices). Although both lattices have the same geometric layout, they show distinct optical behaviors upon adjusting sets of quadrupole strengths. Table 6.1 presents some initial beam parameters used in our calculations. Here, the Example 1 lattice is a 180-deg arc with large momentum compaction (R_{56}). Moreover, it is a second-order achromat and globally isochronous with a large dispersion modulation across the entire arc. By contrast, the Example 2 lattice is a 180-deg arc with small momentum compaction. This arc is also a second-order achromat but is designed to be a locally isochronous lattice with superperiods. Because of local isochronicity, the bunch length is constant at CSR emission sites with homologous phases. Although the lattice design strategy was originally aimed at CSR-induced beam emittance suppression, our studies (see Chapter 7) suggested that it is also effective in suppressing the microbunching gain. Figure 6.6 shows the Twiss functions and transport functions $R_{56}(s)$ (or the momentum compaction functions) across the arcs. Notably, $R_{56}(s)$ for Example 2 [Fig. 6.6(d)] is considerably smaller in amplitude compared with that for Example 1 [Fig. 6.6(c)] because of local isochronicity. A detailed description of the two example lattices can be found in Chapter 7.

The CSR microbunching gains for the two recirculation arcs are shown in Figs. 6.7 and 6.8. Figure 6.7 shows the gain spectra $G_f(\lambda)$ at the exits of the lattices as a function of the initial modulation wavelength. In estimating the CSR gains we have already employed three approaches, one from the direct solution [Eq. (6.2)], one from iterative method [Eq. (6.7)], and the other from particle tracking using `elegant` [21] as benchmark. A major difference between the two examples indicates that Example 1 is vulnerable to the effect of CSR microbunching, whereas the microbunching gain in Example 2 remaining around unity (i.e., there is no microbunching amplification) is little affected. Figure 6.8 presents the gain functions (i.e., the evolution of CSR microbunching gains) as a function of s for several modulation wavelengths. In Figs. 6.7 and 6.8 the shorter wavelengths enhance the Landau damping due to phase space smearing while the longer wavelengths feature negligible CSR effect. To validate our semi-analytical Vlasov solutions, we benchmark the two example lattices by using `elegant`, with which extensive convergence studies were performed [173]. Both our Vlasov solutions and `elegant` tracking results show good agreement in CSR gain estimation (see Figs. 6.7 and 6.8).

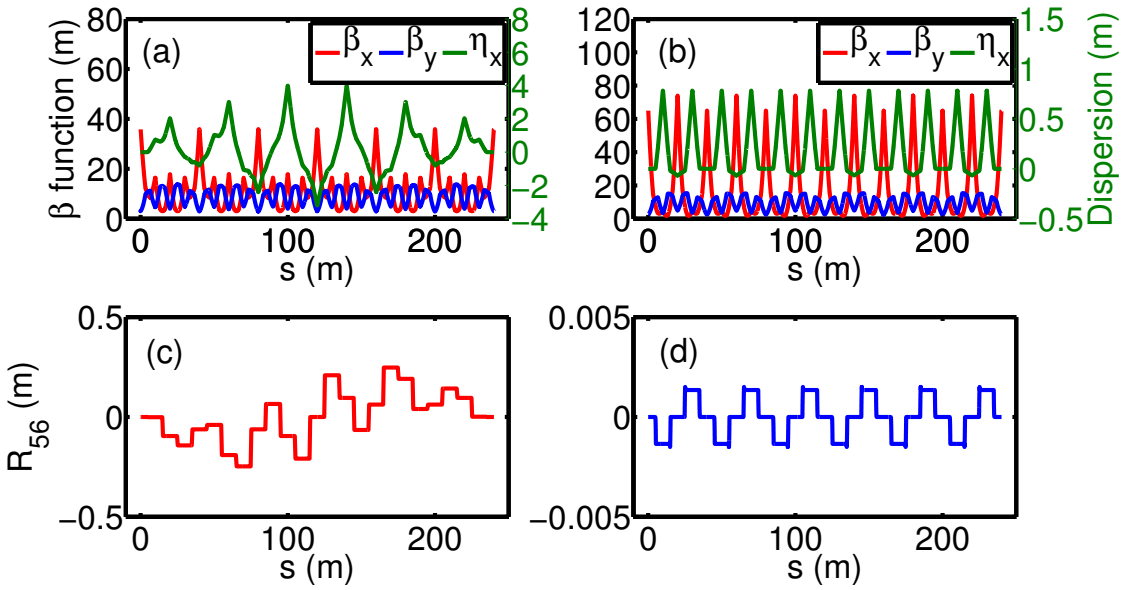

Figure 6.6: Lattice and transport functions for 1.3 GeV high-energy transport arcs with (a), (c) large momentum compaction function R_{56} (Example 1) and (b), (d) small momentum compaction function R_{56} (Example 2).

From the aforementioned numerical results (Figs. 6.7 and 6.8), we conclude that different lattice optics can yield considerably different CSR microbunching gains, despite the geometric layout of the two lattices being identical. We also observe an interesting phenomenon: these two recirculation arcs, especially Example 1, are characterized by (up to) sixth-stage gain, unlike the (up to) two-stage gain in a bunch compressor chicane [81]. This means that the overall CSR gains can be contributed by up to sixth order of the bunch peak current. We now analyze the CSR gain function in depth by asking the following two questions:

(i) how does the CSR gain function evolve along the beamline (on the basis of the stage gain concept) and can we quantify the CSR gain for each individual stage?

(ii) is there any advantage in employing the stage gain concept?

Let us consider the Example 1 and Example 2 arcs for extracting the coefficients $d_m^{(\lambda)}$ through Eq. (6.9). Using the obtained $d_m^{(\lambda)}$, we try to quantify and compare the effects of the optics on the microbunching gains resulting from CSR. From Fig. 6.7 we chose the (optimal) wavelengths as 36.82 and 19 μm for Examples 1 and 2, respectively. Figure 6.9 shows and compares the stage gain coefficients $\left|d_m^{(\lambda)}\right|$ for the two arcs. Clearly, the coefficients for Example 1 are at least three orders of magnitude larger than those for Example 2. The substantial difference in CSR gains between the two arcs can be attributed to the difference in $d_m^{(\lambda)}$. To be more specific, we want to know how the resultant CSR gain is contributed by individual stages. Using Eq. (6.10), Fig. 6.10 shows bar charts representing the individual staged gains at the exits of the two arcs $\mathcal{G}_f^{(m)}$ as a function of the beam current and stage index. Figure 6.10 shows that given a specific stage order

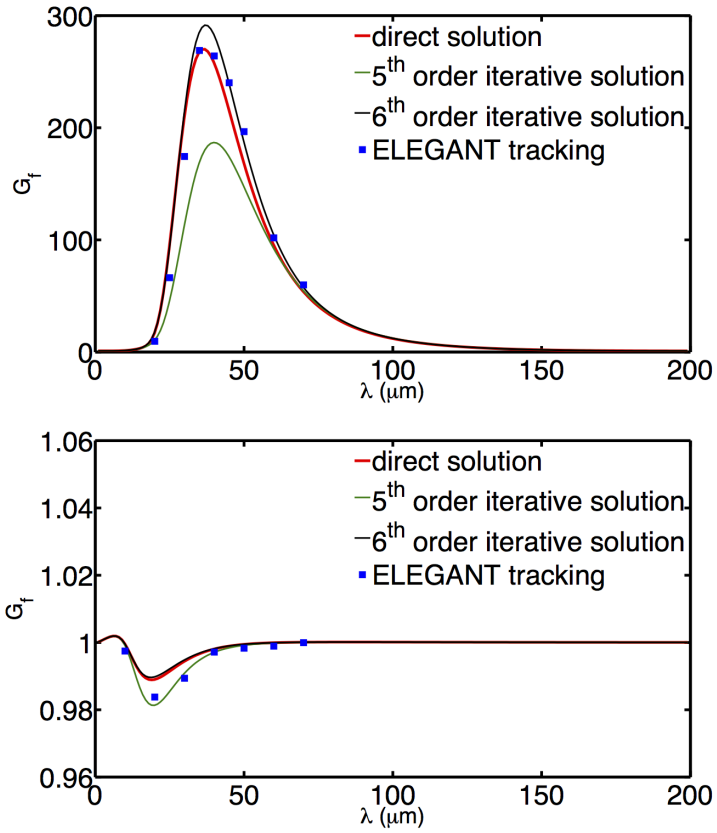

Figure 6.7: CSR gain spectra $G_f(\lambda)$ as a function of the initial modulation wavelength for the Example 1 (top) and Example 2 (bottom) lattices. The iterative solutions are obtained using Eq. (6.6). `elegant` tracking results were obtained for initial modulation amplitudes 0.05% (top) and 0.8% (bottom), and 70-million macroparticles were used in the tracking simulation.

(e.g., q), $\mathcal{G}_f^{(m)}$ increases with the beam current. For a given beam current, $\mathcal{G}_f^{(m)}$ does not necessarily increase with the stage order because the stage gain coefficient $d_m^{(\lambda)}$ depends on the properties of the lattice.

The advantage of the stage gain concept is that since $d_m^{(\lambda)}$ is independent of the beam current and beam energy, it can be used to quickly estimate the beam current dependence of the maximal CSR gain[116], provided the optimal wavelength is given. Figure 6.11 provides a comparison of the current dependence of the final overall gain, obtained from Eqs. (6.2) and (6.9), for the two lattices at a selected wavelength that is in the vicinity of the optimal wavelengths for maximal gains. In Example 1 [Fig. 6.11(a)], both direct and iterative solutions (up to the sixth order) match very well. In Example 2 [Fig. 6.11(b)], the nominal beam current (65.5 A) is well described by including up to sixth-order stage coefficients (red curve). However at higher currents (e.g., $I_b > 160$ A), higher-stage orders should be included (e.g., $M = 9$, green curve). This observation is consistent with the sixth-order iterative solutions presented in Fig. 6.7.

[116] We know the microbunching gain differs at different initial wavelengths, but here we focus on the maximal gain, which should always be of primary concern. Further, from the numerical calculations, we found that the optimal wavelength (corresponding to the maximal gain) does not deviate too much as the bunch current varies.

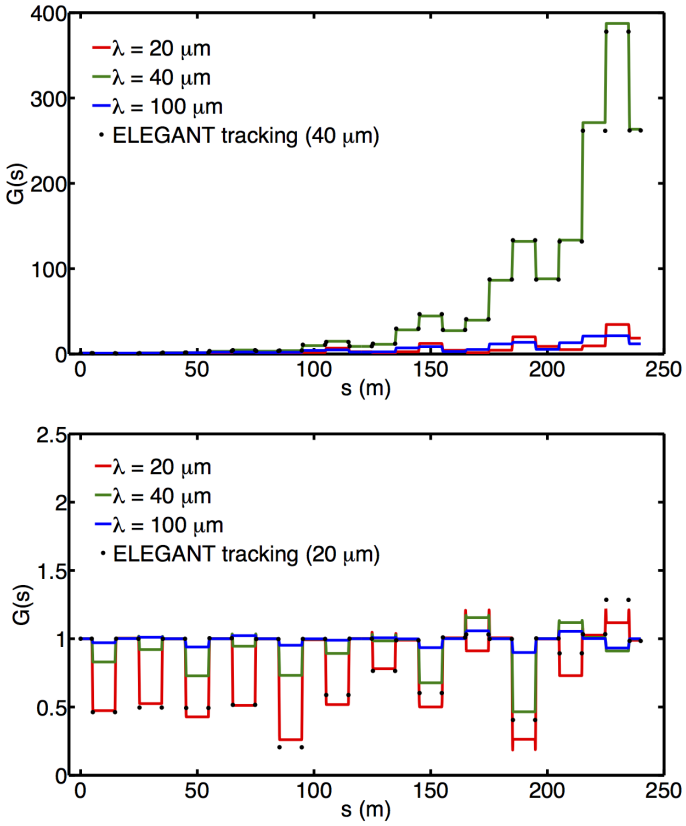

Figure 6.8: Direct solution of CSR gain functions $G(s)$ for the Example 1 and Example 2 lattices.

So far, we have discussed the quantification of individual stage gains by extracting the coefficients $d_m^{(\lambda)}$ from the kernel function. The extracted $d_m^{(\lambda)}$ can be used as quick estimate of the maximal CSR gains for a range of beam currents in a beamline. To answer our first question by using the developed stage gain concept, it would be helpful to present $R_{56}\,(s' \to s)$ for the two examples together in the analysis. Figure 6.12 shows the *quilt* pattern for the two example arcs. The upper left area in the figures vanishes because of causality. The relative momentum compaction function is indeed a continuous function, albeit Fig. 6.12 appears to feature a step-like diagram. This impression can be due to mere visualization effect. As R_{56} only varies within dipoles, it may not be easy to see the transition when the total length of a beamline is much larger than individual dipole lengths. In the two Example lattices the length of a single dipole is 4.7 cm and the total length of the beamlines is 240 m. While the momentum compaction (or the slippage) factor is often used for a storage-ring accelerator to characterize one-turn R_{56}, for a single-pass system it is usually treated as a function of path length (e.g. in linear or recirculation accelerators), as was dealt with in Fig. 1 of Ref. [79] for study of CSR microbunching in the bunch compressor chicane of LCLS. The reason is for single-pass system the detailed behavior of $R_{56}(s)$ along the beamline is required to describe bunch length variation. It deserves to comment here a connection between Figs. 6.11 and 6.12. From Eq. (6.9) it can be seen that

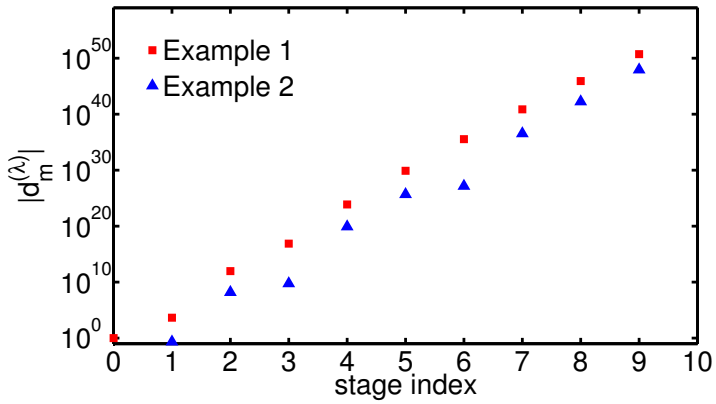

Figure 6.9: Comparison of stage gain coefficient $\left|d_m^{(\lambda)}\right|$ for the two 1.3 GeV high-energy transport arcs. The red squares and blue triangles denote Examples 1 and 2, respectively. The vertical axis represents a log scale. Note that $\left|d_m^{(\lambda)}\right|$ for Example 1 are at least three orders of magnitude larger than those for Example 2.

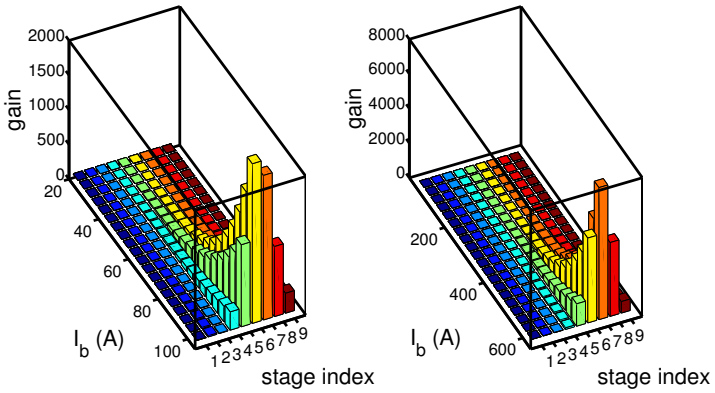

Figure 6.10: Bar chart representation of the individual staged gains [Eq. (6.10)] at the exits of the Example 1 and Example 2 lattices for several beam currents: (left) Example 1 ($\lambda = 36.82\mu$m) and (right) Example 2 ($\lambda = 19\mu$m).

$d_m^{(\lambda)} I_b^m$ always works together to determine the resultant microbunching gain. Note that the information of $R_{56}\,(s' \to s)$ is contained in $d_m^{(\lambda)}$. At larger bunch currents, higher orders of $d_m^{(\lambda)}$ will be needed to account for the resultant CSR gains because I_b^m, acting as a weighting factor, is increasing. It can also be viewed as the population of emerging deep-red blocks will increase.

In the left panel of Fig. 6.12, Example 1, the block areas with large amplitudes, particularly the bottom right deep red blocks, can potentially accumulate the CSR gain. More specifically, the energy modulation at $s' = 15$ m can cause density modulation at $s = 60$ m, and the CSR can induce further energy modulation at the same location. Such energy modulation propagates through $R_{56}(s' \to s)$ from $s' = 60$ m to $s = 100$ m, and so on. It is this situation that causes multistage CSR amplification. Of course, in

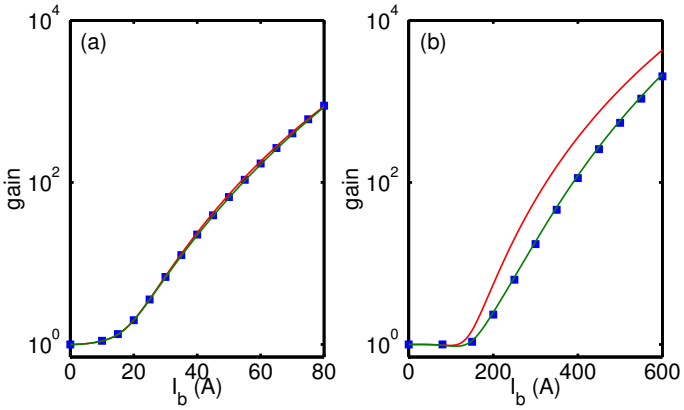

Figure 6.11: Current dependence of the maximal CSR gain for the two high-energy transport arc lattices: (a) Example 1 and (b) Example 2. The solid red curve was obtained from Eq. (6.9) with $M = 6$, the solid green curve was acquired from Eq. (6.9) with $M = 9$, and the blue square dots were obtained from from Eq. (6.2).

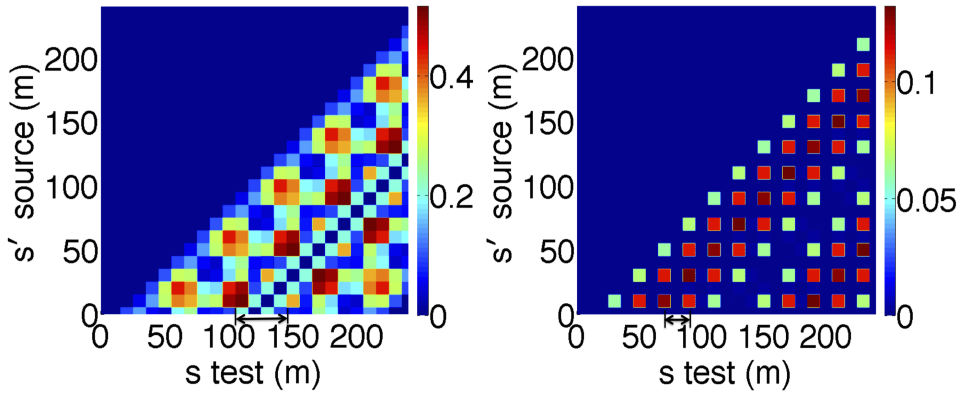

Figure 6.12: $R_{56}\,(s' \to s)$ quilt patterns for the two example lattices: Example 1 (left) and Example 2 (right).

addition to identifying the path of multistage amplification, a more comprehensive analysis should include Landau damping effect. By contrast, for Example 2 (right figure) at similar current levels, the situation is less serious because of smaller amplitudes of $R_{56}(s' \to s)$. We note that Example 2 is not immune for any level of bunch currents and it can be even further severe at much higher currents because of many more deep-red blocks in the quilt pattern.

We now have the aforementioned physical but qualitative interpretation of the multistage gain development along a beamline, and we would like to more quantitatively connect the physical picture with our developed stage gain concepts. For simplicity, we exclude the effect of Landau damping, which would make the evolution of stage gain functions more clear.

Figure 6.13 depicts a plot of the stage gain functions $G^{(n)}(s)$ [defined in Eq. (6.7)] for the Example 1

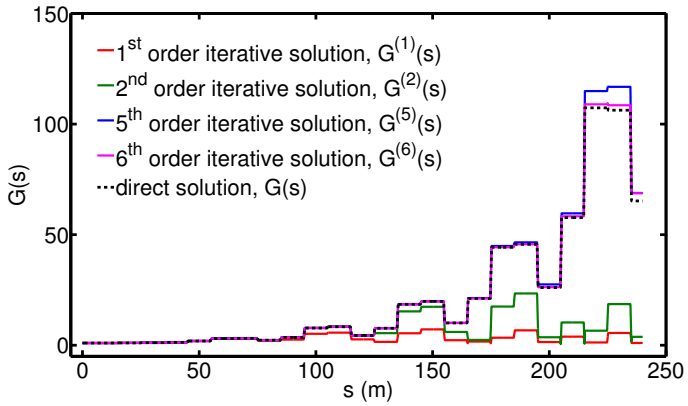

Figure 6.13: Gain functions $G^{(n)}(s)$ (solid curves) and $G(s)$ (dashed curves) for the Example 1 lattice at $\lambda = 80\mu$m in the absence of Landau damping.

lattice in the absence of the effect of Landau damping [i.e., $\epsilon_{x0} = \sigma_\delta = 0$]. The stage gain function is characteristic of a *periodic-like* oscillation for *lower*-stage amplification. In fact it closely follows the block patterns in the left panel of Fig. 6.12. A *stepwise* increasing behavior is featured for *higher*-stage amplification. This situation reflects multistage CSR microbunching amplification. For the Example 2 lattice, we have similar periodic-like pattern for lower-stage amplification. Not shown here, but it is similar to what Fig. 6.8 (bottom) shows, in which there exist many (even more) modular blocks (right panel of Fig. 6.12). However, in contrast to Example 1, the microbunching growth is of less concern for Example 2 at a comparable bunch current (65.5 A) because of the considerably smaller amplitudes of $R_{56}\,(s' \to s)$. The existence of additional modular blocks for the Example 2 reflects its higher multistage gain behavior at higher currents, as illustrated in Fig. 6.11(b). Finally we remind that application of the staged-gain description in Eq. (6.6) has limitations: it is valid only for a single-pass system (or a system with few passes) when collective interaction occurs at localized locations (e.g., CSR in dipoles).

6.5.2 Parametric dependencies and Landau damping

In this subsection, we will apply our analysis in Sec. 6.5.1 to examine the effects of finite transverse emittance and energy spread on Landau damping (or phase space smearing) for the two example lattices. The studies would give us scaling relations of Landau damping, i.e. the scaling of energy spread and emittance on maximal CSR gains $G_{f,\max}$ and the corresponding optimum wavelength $\lambda_{\rm opt}$.

For a CSR gain spectral curve, e.g. Fig. 6.7, we are most interested in the maximal gain $G_{f,\max} = \max\{G_f\,(\lambda)\}$ and the corresponding wavelength $\lambda_{\rm opt}$ (called *optimum* wavelength), where $G_{f,\max} = G_f\,(\lambda_{\rm opt})$. From the kernel function, Eq. (3.43), the overall gain is determined by several beam and lattice parameters with different functional dependencies. To systematically analyze the parametric dependencies, we consider two important beam parameters directly associated with Landau damping or phase space smearing: the

transverse beam emittances $\epsilon_{\rm nx}$, ϵ_{ny} and energy spread σ_δ. We will examine in detail the dependence of $G_{f,\rm max}$ as well as $\lambda_{\rm opt}$ on finite bunch transverse emittances with vanishing energy spread ($\sigma_\delta = 0$), and the dependence of $G_{f,\rm max}$ and $\lambda_{\rm opt}$ on finite energy spread with vanishing transverse emittance ($\epsilon_{nx,ny} = 0$). It turns out that the explored parametric dependencies also feature the multistage behaviors as was introduced in the previous subsection. At the end of this subsection, we would conclude four scaling relations for the optimum wavelengths and maximal gains for either vanishing beam emittance or energy spread cases.

For Example 1 and Example 2 lattices, we would first calculate the spectral gain curves $G_f(\lambda)$ [based on Eq. (6.2)] for various energy spreads while keep transverse beam emittances vanishing, and for various transverse beam emittances with vanishing energy spread. Then we pay attention to $G_{f,\rm max}$ and $\lambda_{\rm opt}$ and try to find some scaling relations of these two quantities to either σ_δ or ϵ_n. Figures 6.14 and 6.15 show the parametric dependencies of maximal gains $G_{f,\rm max}$ and optimum wavelengths $\lambda_{\rm opt}$ as functions of energy spread (for zero beam emittance) and transverse beam emittance (for zero beam energy spread) for Example 1 lattice. We can see that both larger energy spread and transverse beam emittance result in more Landau damping, and the optimum wavelength drifts toward longer wavelengths. It is also found that, from Figs. 6.14 (b) and 6.15 (b), the optimum wavelengths $\lambda_{\rm opt}$ scale linearly and radically against beam energy spread and transverse beam emittance, respectively. The solid lines in Figs. 6.14 (b) and 6.15 (b) are obtained from linear and radical scaling relations [see Eqs. (6.11) and (6.12) below], respectively. Furthermore, we find in Figs. 6.14 (c) and 6.15 (c), the maximal gains $G_{f,\rm max}$ behave largely proportional to $\sigma_\delta^{-24/3}$ and $\epsilon_{\rm nx}^{-12/3}$. Again, the solid lines in the figures are drawn based on the scaling relations [see Eqs. (6.13) and (6.14)]. Here we note that, for cases with vanishingly small energy spread or beam emittance, the maximal gain is extremely high due to lack of Landau damping (e.g. $\sim 10^{10}$ for $\sigma_\delta = 10^{-5}$ with $\epsilon_n = 0$) and the results could be suspicious for practical considerations; since our formulation assumes the gain evolves in linear regime. At the ultrahigh gain the assumption of linear amplification may no longer be valid. Note also that there are small but sharp spectral peaks seen at very small modulation wavelengths in Fig. 6.14 (a), where the 1-D CSR model may not be valid and not of our current interest. Here we only consider those spectral peaks occurred at moderate modulation wavelength ranges.

Similarly, Figs. 6.16 and 6.17 show the parametric dependencies of maximal gains $G_{f,\rm max}$ and optimum wavelengths $\lambda_{\rm opt}$ as functions of energy spread (for zero transverse beam emittance) and transverse beam emittance (for zero beam energy spread) for Example 2 lattice. The larger the energy spread or transverse beam emittance, the more the Landau damping is induced, with a shift of optimum wavelength $\lambda_{\rm opt}$ toward longer wavelength. It is found that, from Figs. 6.16 (b) and 6.17 (b), the optimum wavelengths $\lambda_{\rm opt}$ largely scale as linear and radical functions of beam energy spread and transverse beam emittance, respectively. For relatively small beam energy spread (i.e. $\sigma_\delta < 3.5 \times 10^{-4}$) in Fig. 6.16 (a), the maximal CSR gain becomes huge (up to about 10^6) and, interestingly, features a relatively broad (flat-top) spectrum, e.g. the red curve in Fig. 6.16 (a). The identification of the corresponding optimum wavelength $\lambda_{\rm opt}$ is not clear. This fact is reflected in Fig. 6.16 (b) that, for smaller energy spread, the optimum wavelength is a bit deviated from

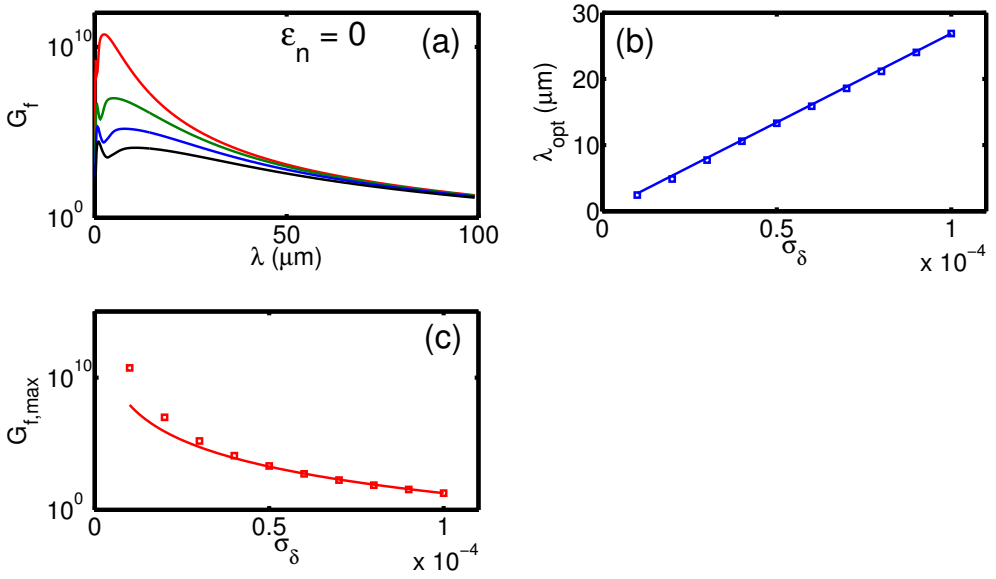

Figure 6.14: (a) Gain spectra $G_f(\lambda)$ for different energy spreads in the case of zero beam emittance for Example 1 lattice; (red) $\sigma_\delta = 1.0 \times 10^{-5}$ (green) $\sigma_\delta = 2.0 \times 10^{-5}$ (blue) $\sigma_\delta = 3.0 \times 10^{-5}$ (black) $\sigma_\delta = 1.0 \times 10^{-4}$; (b) Optimum wavelengths $\lambda_{\rm opt}$ as a function of beam energy spread; (c) Maximal CSR gain $G_{f,\rm max}$ as a function of energy spread. For (b) and (c) the solid lines are obtained from scaling relations [Eqs. (6.11) and (6.13) for $M = 6$].

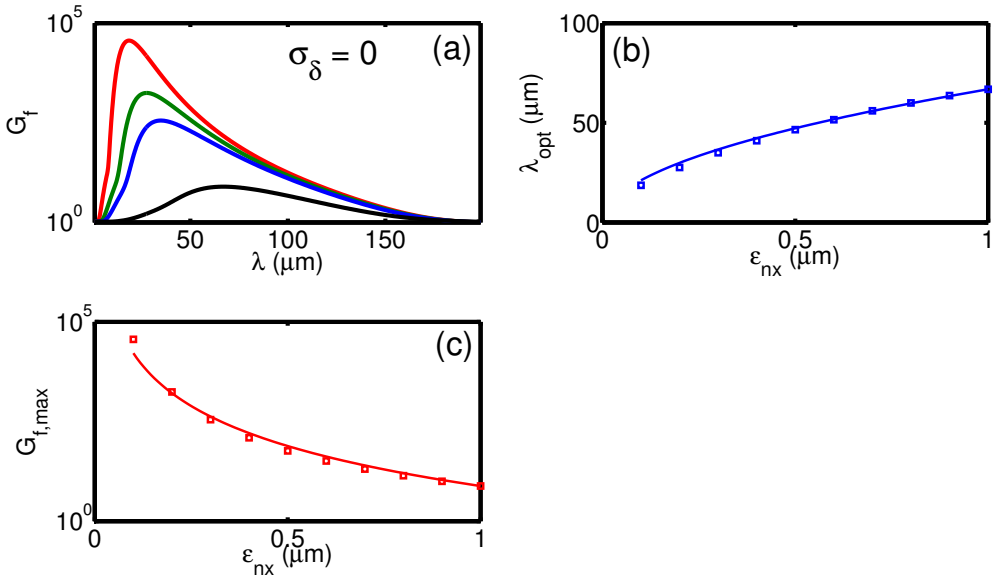

Figure 6.15: (a) Gain spectra $G_f(\lambda)$ for different transverse beam emittances in the case of zero beam energy spread for Example 1 lattice; (red) $\epsilon_{\rm nx} = 0.1$ μm (green) $\epsilon_{\rm nx} = 0.2$ μm (blue) $\epsilon_{\rm nx} = 0.3$ μm (black) $\epsilon_{\rm nx} = 1.0$ μm; (b) Optimum wavelength $\lambda_{\rm opt}$ as a function of transverse beam emittance; (c) Maximal CSR gain $G_{f,\rm max}$ as a function of transverse beam emittance. For (b) and (c) the solid lines are obtained from scaling relations [Eqs. (6.12) and (6.14) for $M = 6$].

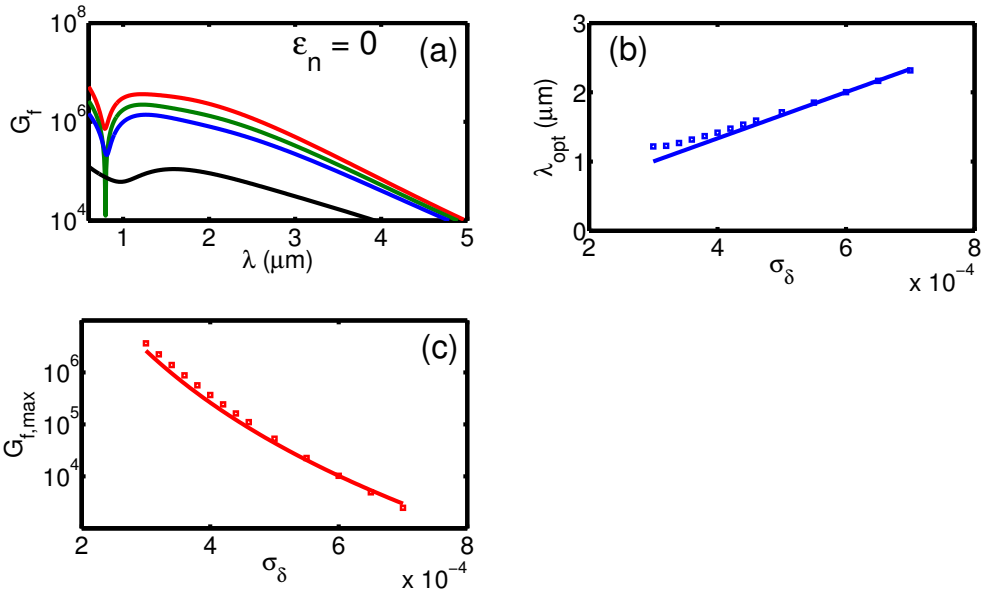

Figure 6.16: (a) Gain spectra $G_f(\lambda)$ for different beam energy spreads in the case of zero beam emittance for Example 2 lattice; (red) $\sigma_\delta = 3.0 \times 10^{-4}$ (green) $\sigma_\delta = 3.2 \times 10^{-4}$ (blue) $\sigma_\delta = 3.4 \times 10^{-4}$ (black) $\sigma_\delta = 4.6 \times 10^{-4}$; (b) Optimum wavelength $\lambda_{\rm opt}$ as a function of beam energy spread; (c) Maximal CSR gain $G_{f,\rm max}$ as a function of energy spread. For (b) and (c) the solid lines are obtained from scaling relations [Eqs. (6.11) and (6.13) for $M = 6$].

the scaling relation, though the deviation is ≤ 0.2 μm. Further, in Figs. 6.16 (c) and 6.17 (c), the maximal gains $G_{f,\rm max}$ behave largely proportional to and [see below Eqs. (6.13) and (6.14)]. Because the Example 2 lattice was originally free from CSR microbunching instability, as shown in Fig. 6.7. In order to study the parametric dependencies for Example 2 lattice in the case of zero beam energy spread (Fig. 6.17), we have deliberately increased the beam current up to 400 A so as to clearly identify the peaked gains.

Having carefully examined the parametric dependencies for Example 1 and 2 lattices, we find that, for vanishing emittances, the behaviour of optimum wavelength $\lambda_{\rm opt}$ features a linear relationship with the beam energy spread σ_δ as

$$\lambda_{\rm opt} \propto \sigma_\delta \tag{6.11}$$

The solid lines in Figs. 6.14 (b) and 6.16 (b) are obtained by Eq. (6.11). Again we note that in Fig. 6.16 (b) this linear scaling relation is not perfectly followed for smaller energy spread. We have attributed such deviation to the difficulty of clearly identifying the optimum wavelength due to the flattop feature of the gain spectra.

Here we note that Ref. [152] gives a linear expression on how the optimum wavelength $\lambda_{\rm opt}$ relates to beam energy spread σ_δ assuming two-stage amplification in a typical bunch compressor chicane for zero-

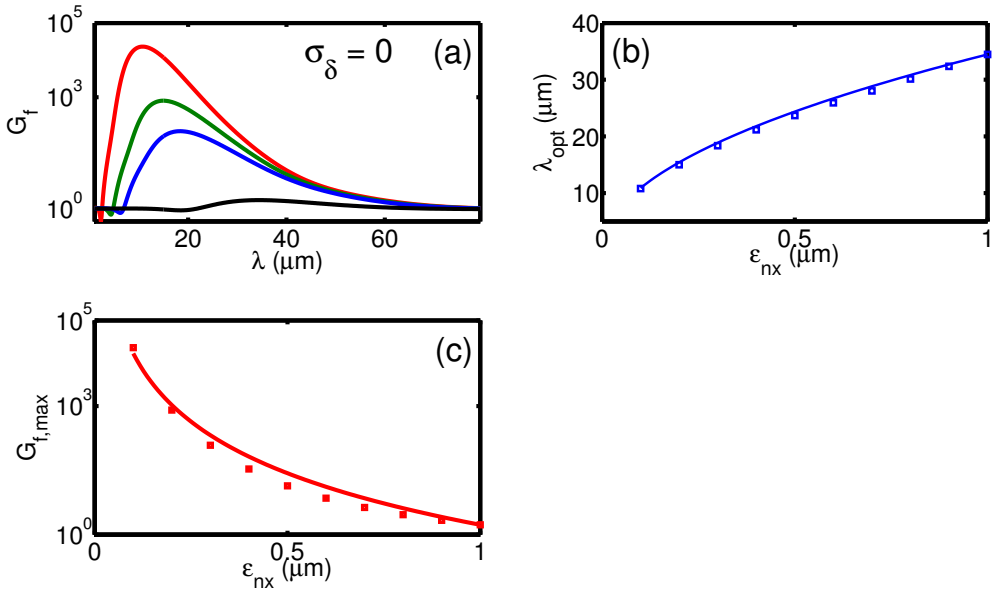

Figure 6.17: (a) Gain spectra $G_f(\lambda)$ for different transverse beam emittances in the case of zero beam energy spread for Example 2 lattice; (red) $\epsilon_{\rm nx} = 0.1$ μm (green) $\epsilon_{\rm nx} = 0.2$ μm (blue) $\epsilon_{\rm nx} = 0.3$ μm (black) $\epsilon_{\rm nx} = 1.0$ μm; (b) Optimum wavelength $\lambda_{\rm opt}$ as a function of beam emittance; (c) Maximal CSR gain $G_{f,\rm max}$ as a function of beam emittance. Note here the beam current is set 400 A. For (b) and (c) the solid lines are obtained from scaling relations [Eqs. (6.12) and (6.14) for $M = 6$].

emittance beam[117]. Although our example lattices (e.g. Example 1 and 2) feature six-stage amplification, the optimum wavelength is still characteristic of linear relation to beam energy spread [Eq. (6.11)]. Whether such observations reflect the general behavior for multistage amplification, for arbitrary range of different beam parameters and/or for an arbitrary lattice is still a question for further investigation. Similarly, for vanishing beam energy spread, we obtain a relation for the dependence of the optimum wavelength $\lambda_{\rm opt}$ on transverse beam emittance as [also see solid lines in Figs. 6.16 (b) and 6-17 (b)],

$$\lambda_{\rm opt} \propto \sqrt{\epsilon_{\rm nx}} \tag{6.12}$$

Again, we reserve our comment about the generalization of Eq. (6.12) to a general case.

Furthermore, we find the maximal gain can also be scaled in the case of vanishing beam emittance at M-th stage as, [also see solid lines in Figs. 6.14 (c) and 6.16 (c)]

$$G_{f,\rm max} \propto \frac{1}{\sigma_\delta^{(4/3)M}} \tag{6.13}$$

and in the case of vanishing beam energy spread at M-th stage as, [also see solid lines in Figs. 6.15 (c) and

[117]Equation (9) or the one above Eq. (27) in Ref. [152]

6.17 (c)]

$$G_{f,\max} \propto \frac{1}{\epsilon_{\mathrm{nx}}^{(2/3)M}} \tag{6.14}$$

For the above two Example lattices, we found Eqs. (6.13) and (6.14) for $M = 6$ can match well, though not exactly, with those maximal values obtained by Eq. (6.2). This observation can be considered to be qualitatively consistent to the results presented in Sec. 6.5.1 (see Figs. 6.7), based on the mathematical iterative approach. Such semi-analytically derived scaling properties [Eqs. (6.11) to (6.14)] also correspond well to the gain behavior in a typical bunch compressor chicane featuring two-stage amplification ($M = 2$), as shown in Ref. [81]. These relations can serve as quick estimate of (maximal) CSR microbunching gains when the energy spread or transverse emittance scales.

6.6 Summary

In this chapter, we have outlined two approaches to the governing equation of microbunching gains, which can be obtained self-consistently (i.e., direct solution) or derived through numerical iterations (i.e., iterative solution). The stage gain concept can be used to physically and quantitatively connect the individual iterative solutions by using the lattice optics pattern [i.e., $R_{56}(s' \to s)$]. The developed method can be used to characterize the multistage behavior of CSR gain amplification along a beamline and to compare the impact of lattice optics on microbunching development. Moreover, the stage gain coefficient [defined in Eq. (6.9)], which is independent of the beam current and beam energy, can be used as quick estimate of the maximal CSR gain, provided $d_m^{(\lambda)}$ of a lattice is given (Fig. 6.11). Detailed analysis including Landau damping has been systematically investigated in Sec. 6.5.2, where we also semi-analytically derived the scaling relations for maximal CSR gains and optimum wavelengths.

CHAPTER 7
Control of CSR Effects in Multibend Transport or Recirculation Arcs

The coherent synchrotron radiation (CSR) of a high-brightness electron beam traversing a series of dipoles, such as transport or recirculation arcs, may result in beam phase space degradation. On one hand, CSR can perturb electron transverse motion in dispersive regions along the beamline and possibly cause emittance growth. On the other hand, the CSR effect on the longitudinal beam dynamics could result in microbunching instability. For transport arcs, several schemes have been proposed to suppress the CSR-induced emittance growth. Correspondingly, a few scenarios have been introduced to suppress CSR-induced microbunching instability, which however mostly aim for linac-based machines. In this Chapter we study the conditions for control or suppression of CSR-induced emittance growth and microbunching gains along multi-bend transport or recirculation arcs. Examples are presented with the relevant microbunching analyses carried out by our developed semi-analytical Vlasov solver [177]. The example lattices include low-energy (∼100 MeV) and high-energy (∼1 GeV) recirculation arcs, and medium-energy compressor arcs. Our studies show that lattices satisfying the proposed conditions indeed have the desired beam emittance preserved and microbunching gain suppressed. Bunch charge/current dependences of beam emittance and maximal CSR microbunching gains are also demonstrated, which should help outline a beamline design for different scales of nominal currents. The analysis in this Chapter should shed light on lattice design approach that aims to control the CSR-induced effects.

In Sec. 7.1, we will give an overview of existing mitigation schemes including compensation of the CSR-induced emittance growth and suppression of longitudinal microbunching gains. In Sec. 7.2, we would discuss the strategies for transverse emittance preservation by formulating the expression for CSR-induced emittance growth along a beamline. Then in Sec. 7.3 the previously derived integral equation that governs CSR microbunching instability was applied. Then we outline the option of making small relative momentum compaction $R_{56}^{s_1\rightarrow s_2}$, and discuss the conditions for CSR microbunching suppression in four situations: achromatic, dispersive, isochronous, and non-isochronous modules. Through the analysis, it is found the kernel function plays a key role for microbunching gain development. In Sec. 7.4, we examine these conditions by illustrating three sets of comparative examples, including low-energy (∼100 MeV) and high-energy (∼1 GeV) recirculation arcs, and medium-energy compressor arcs. Beam current dependences of maximal CSR microbunching gains are also demonstrated, which should help outline a beamline design for different current scales and give guidance of the level how small/large the relative momentum compaction should be retained. Finally, we conclude in Sec. 7.5 our findings and comment the difference of conditions between the transverse CSR emittance compensation and the longitudinal CSR microbunching suppression.

Part of the work in this Chapter, especially Sec. 7.3 to 7.5, has been published with the title *Conditions for coherent-synchrotron-radiation-induced microbunching suppression in multibend beam transport or*

recirculation arcs, in Physical Review Accelerator and Beams 20, 024401 (2017). They were also presented in 7th International Particle Accelerator Conference (IPAC), May 8-13, 2016, Busan, Korea.

7.1 Overview of existing mitigation schemes

Coherent synchrotron radiation (CSR) has been recognized as one of the most challenging issues for high-brightness beam transport line and recirculation machine designs, in which the beam phase-space quality is always aimed to preserve as well as possible before the beam fulfills its scientific mission or is transported to subsequent beamline complex. As introduced in the preceding chapters, CSR can be generated from electron coherent radiation emission inside a bend at a wavelength range comparable to the bunch length scale or to the order of the ripple density fluctuations atop. The radiation reaction can have effects on both transverse and longitudinal planes. In the transverse plane, because of the dispersive nature of a bending system, the energy change due to CSR can be correlated to the transverse coordinates (x or x') through the dispersion functions R_{16} or R_{26}. Since the energy change varies for different slices of particles, such energy variation within a beam bunch can potentially dilute the projected transverse emittance. In the longitudinal plane, initial small density modulations can be converted into energy modulations due to the tail-head collective interaction. Then the energy modulations can be transformed back to density counterparts downstream in dispersive regions via momentum compaction. The density-energy conversion, if forming a positive feedback in a multi-dipole system, can result in the enhancement of modulation amplitudes. This has been known as the CSR-induced microbunching instability [152, 79, 81]. Below we give a brief overview of existing mitigation schemes for CSR-induced emittance growth and microbunching gain suppression.

7.1.1 Overview of CSR-induced emittance growth in a transport line

There have been many approaches proposed to minimize or cancel the CSR-induced emittance growth. For example, Hajima [74] used the beam envelope matching method by characterizing the transverse phase-space ellipse tilt due to CSR. This method concludes that with proper arrangement of lattice optics in a unit cell along the major axis of the transverse beam phase space ellipse, the beam emittance growth due to steady-state CSR can be minimized. Figure 7.1 illustrates the concepts. Jing *et al.* [89] studied a similar concept for ERL-based FEL in eRHIC. Douglas [58, 59, 60, 61] and Di Mitri *et al.* [50] employed cell-to-cell phase matching to compensate or cancel the CSR kicks. The strategy is schematically illustrated in Fig. 7.2. With dedicated beamline design, this approach can achieve the cancellation of CSR-induced emittance growth. Jiao *et al.* [88] extended the above two methods to give generic conditions for suppression of the CSR-induced emittance growth in a two-dipole achromat unit. Di Mitri and Cornacchia [53] also extended their previous analysis to the case of compressor arcs.

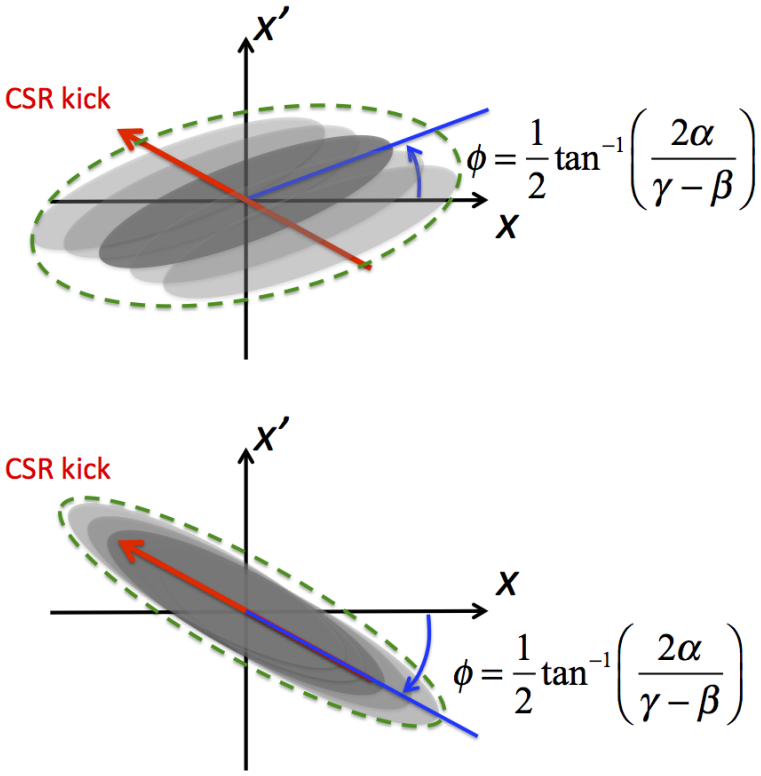

Figure 7.1: Illustration of CSR-induced (sliced) transverse phase space dilution. In the top figure the emittance growth due to CSR-kick is larger than the bottom figure because of the difference of phase space orientation (or tilt angle ϕ).

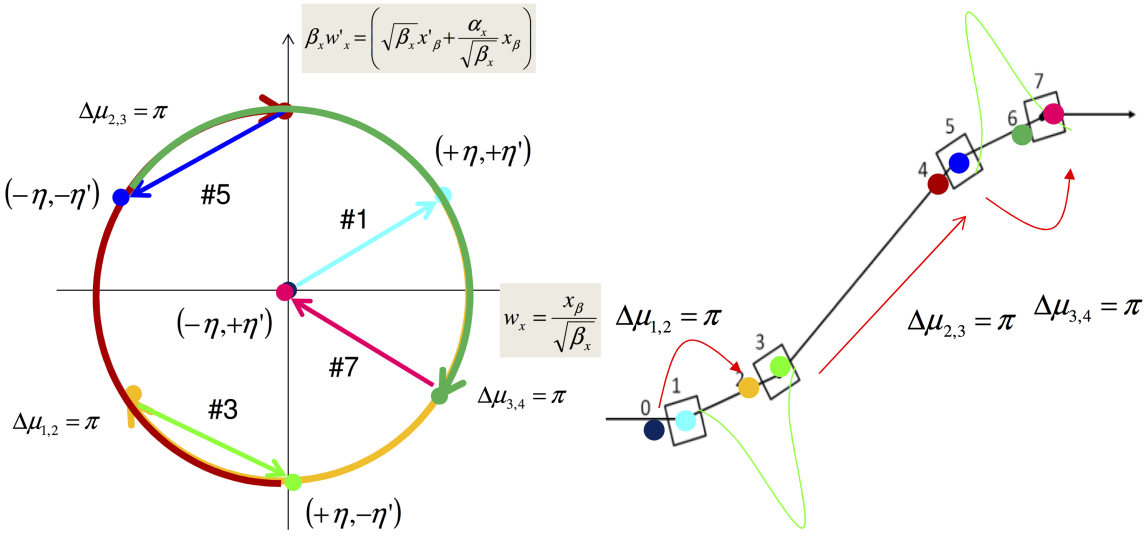

Figure 7.2: Illustration of cell-to-cell phase matching to cancel the CSR kick (left) and a four-dipole transport line (right). η and $\eta\prime$ are dispersion and its derivative due to CSR kick. The CSR kick causes a shift (of reference particle) in the (normalized) transverse phase space. The normalized phase space here is a circle, instead of an ellipse in the (un-normalized) phase space [Fig. 7.1]. The design optics gives a betatron phase advance of π in the bending plane between two consecutive dipoles. It corresponds to a clockwise π rotation. Picture from Ref. [54].

7.1.2 Overview of microbunching gain suppression

In this subsection we give an overview of MBI suppression schemes. Here we assume MBI is quantified by the microbunching gain, defined in Eq. (3.66), i.e. $b(k; s_f) = G \cdot b(k; s_0)$. The cure of MBI can be undertaken from either keeping the beam conditions as smooth as possible (i.e. keep $b(k; s_0)$ small) or the suppression of amplification mechanism (i.e. keep G small). The former depends on the manipulation of bunch current distribution at some particular locations, e.g. at the upstream electron gun system. As for the latter, it can usually be related to dedicated beamline designs and is of our primary interest. The strategy of the beamline designs can be further categorized into two types:

(i) make the relative momentum compaction function as small as possible throughout the beamline [see Eq. (3.43)];

(ii) enhance the Landau damping through the exponent term [see Eq. (3.40)].

Regarding to (ii), laser heating [153, 83] has been commonly employed in linac-based FEL facilities to effectively suppress MBI. The basic idea is to use a laser beam to interact with electrons in a short undulator to induce an additional uncorrelated energy spread in order to enhance the Landau damping. In addition to the laser heating technique, the electron-magnetic-phase mixing was also proposed [51]. The magnetically mixing chicane is utilized to smoothen the bunch current and energy distribution by forcing the electrons smear (or, slip) in the longitudinal phase space. It has been experimentally demonstrated that MBI using this technique can be reduced by an order of magnitude [51]. Other specialized beamline designs to mitigate the MBI have also been proposed. For example, by adding a set of transverse deflecting RF cavities upstream and downstream of a bunch compressor can increase an additional Landau damping and thus effectively suppress the MBI [13]. The additional energy spread is introduced in the first RF cavity, which is used to suppress the microbunching instability, and then the induced energy spread is eliminated in the second RF cavity. In Ref. [142], Qiang *et al.* proposed an inexpensive scheme to suppress MBI in a linac-based XFEL light source by inserting a pair of bending magnets in the accelerator transport system. This setup can induce the longitudinal mixing associated with the transverse spread of the beam, i.e. increasing the Landau damping term via Eq. (3.40).

Pursuing the other path, we have recently demonstrated a set of recirculation arc lattices specifically for control of CSR and microbunching effects during transport of high brightness electron beams [59, 61]. The basic idea behind the design strategy is based on (i) to make the recirculation arc as achromatic and locally isochronous. The local isochronicity insures that the bunch length be kept the same at phase homologous CSR emission sites. The local isochronicity can result in small relative momentum compaction function throughout the beamline. The detailed discussion can be found in Sec. 7.3.

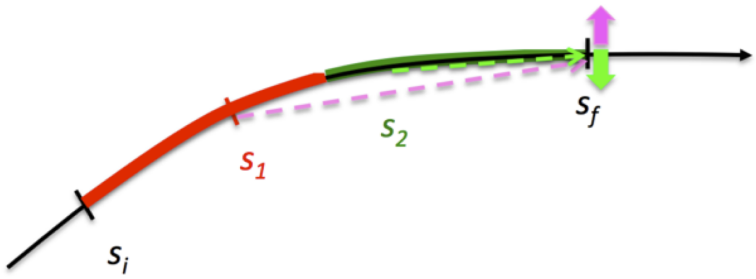

Figure 7.3: Conceptual illustration of CSR-induced energy kicks generated from s_1 and s_2 and eventually cancelled at s_f. Here $s_1 \in S_1, s_2 \in S_2,\ s_1 < s_2$, and $S_1 \cup S_2 = [s_i, s_f]$.

7.2 Strategy for transverse emittance preservation due to CSR

In this section we follow the general discussion by Emma, Brinkmann [27] and Venturini [197]. Consider a beamline starting from s_i to s_f, as shown in Fig. 7.3. The single-particle transverse coordinates at the end of the beamline can be expressed as

$$x(s_f) = x_\beta(s_f) + \int_{s_i}^{s_f} R_{16}^{s\to s_f}(s)\frac{d\delta(z)}{ds}ds \equiv x_\beta(s_f) + \hat{x}(z) \tag{7.1}$$

where x_β denotes the particle's beatron oscillation, which is not of our interest. The remaining contribution to the final transverse particle displacement comes from the dispersion function R_{16} with finite energy deviation $\Delta\delta(z) = \Delta s d\delta(z)/ds$. In what follows, we are interested in the energy deviation by CSR. In addition to the transverse displacement, the transverse angular divergence can be formulated as

$$x'(s_f) = x'_\beta(s_f) + \int_{s_i}^{s_f} R_{26}^{s\to s_f}(s)\frac{d\delta(z)}{ds}ds \equiv x'_\beta(s_f) + \hat{x}'(z) \tag{7.2}$$

with R_{26} the derivative of dispersion function.

For simplicity, assume $\langle x_\beta \rangle = 0$ and $\langle x_\beta \Delta\hat{x} \rangle = 0$ for 1-D CSR. Formulating by using the beam sigma matrix, Eq. (3.80), and expressing the longitudinal bunch distribution $\lambda(z)$, the perturbed beam emittance can be expressed as

$$\epsilon_x^2 = \epsilon_{x0}^2 + \epsilon_{x0}\left(\beta_x \left\langle \Delta x'^2 \right\rangle + 2\alpha_x \langle \Delta x \Delta x' \rangle + \gamma_x \left\langle \Delta x^2 \right\rangle\right) \tag{7.3}$$

where ϵ_{x0} is the unperturbed beam emittance, the pure-optics Twiss parameters $\alpha_x = -\langle xx' \rangle/\epsilon_{x0}$, $\beta_x =$

$\langle x^2 \rangle / \epsilon_{x0}$, $\gamma_x = (1+\alpha_x^2)/\beta_x$, and

$$\left\langle (\Delta x)^2 \right\rangle = \left[\int_{s_i}^{s_f} g(s) R_{16}^{s \to s_f} ds \right]^2 \left\langle \left(\Delta \hat{\delta}' \right)^2 \right\rangle \tag{7.4}$$

$$\left\langle (\Delta x')^2 \right\rangle = \left[\int_{s_i}^{s_f} g(s) R_{26}^{s \to s_f} ds \right]^2 \left\langle \left(\Delta \hat{\delta} \right)^2 \right\rangle \tag{7.5}$$

$$\langle (\Delta x \Delta x') \rangle = \left[\int_{s_i}^{s_f} g(s) R_{16}^{s \to s_f} ds \right] \left[\int_{s_i}^{s_f} g(s) R_{26}^{s \to s_f} ds \right] \left\langle \left(\Delta \hat{\delta} \right)^2 \right\rangle \tag{7.6}$$

where

$$g(s) \equiv \begin{cases} \left(\dfrac{\kappa}{\rho(s)} \right)^{2/3}, \text{ inside a dipole} \\ 0, \text{ outside a dipole} \end{cases} \tag{7.7}$$

and

$$\hat{\delta}'(z) = \frac{2mc^2}{3^{1/3} \kappa^{2/3}} \int_z^{\infty} \frac{1}{(\zeta - z)^{1/3}} \frac{d\lambda(\zeta)}{d\zeta} d\zeta \tag{7.8}$$

In Eq. (7.3), we have assumed $\Delta \epsilon_x^2 = \left\langle (\Delta x)^2 (\Delta x')^2 \right\rangle - \langle (\Delta x)(\Delta x') \rangle^2 = 0$. From Eq. (7.3), there are two possible strategies for controlling emittance growth along a beamline:

(i) choose Twiss parameters appropriately;

(ii) manipulate the beam second moments.

For the former strategy, it involves the preparation of matched transverse Twiss parameters for the beam and the transport line. In the following we focus on the latter case. The condition of minimizing (or vanishing) the beam emittance can be formulated to be

$$\int_{s_i}^{s_f} g(s) R_{16}^{s \to s_f}(s) ds = 0 \text{ and } \int_{s_i}^{s_f} g(s) R_{26}^{s \to s_f}(s) ds = 0 \tag{7.9}$$

Assuming the same dipole radius in a specific cell unit, Eq. (7.9) can be re-written as

$$\begin{cases} R_{16}^{s_1 \to s_f} = -R_{16}^{s_2 \to s_f} \\ R_{26}^{s_1 \to s_f} = -R_{26}^{s_2 \to s_f} \end{cases} \tag{7.10}$$

where s_1 and s_2 are assigned as shown in Fig. 7.3.

It turns out that the above conditions lead to the two sub-cases below:

$$\mathbf{R}_{2\times 2}^{s_1\to s_2} = -\mathbf{I} \text{ or } \mu_{1\to 2} = \pi \tag{7.11}$$

$$\mathbf{R}_{2\times 2}^{s_1\to s_2} = \mathbf{I} \text{ or } \mu_{1\to 2} = 2\pi \tag{7.12}$$

between the dipoles in the cell, where $\mathbf{R}_{2\times 2}$ is the standard two-by-two (x, x') transfer matrix. The two explicit conditions can explain why many low-emittance beamline lattices employ π or 2π phase difference between neighboring cell units or superperiods.

7.3 Strategy for longitudinal microbunching gain suppression

In this section we provide a set of *sufficient* conditions for suppression of CSR-induced microbunching in arcs. We are particularly interested in the transport arcs of recirculation machines, which usually consist of several to tens of bending magnets. Our findings are also suitable for multi-dipole transport lines in single-pass facilities. It deserves here to further clarify the target of the beamlime design. By recirculation here we mean a beam only passes through the arcs a few times. This is in contrast with storage-ring arcs, in which the assumption of an infinite number of beam passages is made. In addition, throughout the analysis we only consider the steady-state CSR effect and for the moment exclude other effects such as transient CSR and space charge effects. The exit transient CSR (or CSR drift) in fact plays an equal (or even more) important role as it can further enhance the CSR microbunching gains (see, for example, Ref. [177]) in multi-bend transport arcs. The reason we assume only steady-state CSR interaction in this study is because of its simplicity; similar to discussion of suppression (or cancellation) of CSR-induced emittance growth introduced in Sec. 7.2, we always start from a simple consideration and later deal with transient effects. In the following discussion, for clarity we may repeat the equations derived in the preceding chapters.

Theoretical formulation of the CSR-induced microbunching instability based on the linearized Vlasov equation has been developed in Sec. 3.3 for a single-pass beam transport system. The formulation assumes that initial modulation wavelength is small compared with the whole bunch duration (i.e. coasting-beam approximation), consistent with most practical situations. In the linearized Vlasov treatment, the CSR effect is treated as a small perturbation to the beam phase space distribution. By the method of characteristics, the equation that governs the evolution of the complex bunching factor along a beamline can be written in the following integral equation

$$b(k;s) = b_0(k;s) + i\int_0^s ds'\Lambda\mathcal{K}(s,s')b(k;s') \tag{7.13}$$

where s' denotes the location where CSR emission may occur and s denotes the location where the beam bunch receives the energy kick. The bunching factors $b(k;s)$ and $b_0(k;s)$ are defined as the Fourier transformation of the longitudinal z coordinate for perturbed and unperturbed (i.e. pure optics, in the absence of collective effect) phase space distributions, respectively. The coefficient Λ characterizes the beam current and energy dependence

$$\Lambda = \frac{I_b}{\gamma I_A} \tag{7.14}$$

where γ is the relativistic factor, I_b is the instantaneous beam current (depends on path length when bunch length varies), and I_A is the Alfven current. The kernel function is particularly expressed as

$$\mathcal{K}(s,s') = k(s) R_{56}^{s'\to s} Z_{CSR}^{ss}(k;s')\,\{L.D.;s,s'\} \tag{7.15}$$

where, of our primary interest, only the one-dimensional steady-state free-space CSR impedance (per unit length) is considered

$$Z_{\mathrm{CSR}}^{\mathrm{ss}}\left(k(s);s\right) = (1.63 + 0.94i)\,\frac{k(s)^{1/3}}{|\rho(s)|^{2/3}} \tag{7.16}$$

where $k = 2\pi/\lambda$ is the spatial wavenumber (with λ the modulation wavelength), ρ is the bending radius of a dipole, the transport matrix elements

$$R_{56}^{s'\to s} = \left[\mathbf{R}^{s'\to s}\right]_{56} = \left[\mathbf{R}^{0\to s}\left(\mathbf{R}^{0\to s'}\right)^{-1}\right]_{56} \tag{7.17}$$

and the Landau damping term

$$\{L.D.;s,s'\} = \exp\left\{-\frac{k_0^2\epsilon_{x0}\beta_{x0}}{2}\left[\left(R_{51}(s,s') - \frac{\alpha_{x0}}{\beta_{x0}}R_{52}(s,s')\right)\right]^2 - \frac{k_0^2\epsilon_{x0}}{2}R_{52}^2(s,s') - \sigma_{\delta 0}^2 R_{56}^2(s,s')\right\} \tag{7.18}$$

with $k_0 = k(s=0)$. Here we note that the above expressions are applicable to combined-function dipoles. ϵ_{x0} is the horizontal geometric emittance, α_{x0} and β_{x0} are the initial Twiss parameters, and $\sigma_{\delta 0}$ is the rms uncorrelated relative energy spread assuming Gaussian energy distribution. $R_{5i}(s,s') = C(s)R_{5i}(s) - C(s')R_{5i}(s')$, where $i = 1,2,6$, and $C(s) = [1 - hR_{56}(s)]^{-1}$ is the bunch compression factor, and h is the initial chirp of the beam (assuming $z > 0$ for the bunch head). To quantify the microbunching, we define the amplification gain as modular ratio of bunching factors

$$G_f \equiv \left|\frac{b(k;s_f)}{b_0(k;0)}\right| \tag{7.19}$$

where s_f is denoted the exit location of a beamline. When the gain due to CSR is much larger than unity in a beamline, the lattice is said to be susceptible to CSR microbunching instability. From Eq. (7.15), the cure of CSR-induced microbunching can be undertaken by either enhancing Landau damping or making

the relative momentum compaction function as small as possible throughout the beamline. Here we take the latter. To proceed, let us introduce a parameter, which we will use to characterize the CSR effect in a beamline lattice [see also Eq. (7.15)]

$$\xi = \left| \max\left\{ R_{56}^{s'\to s} \right\} \frac{k^{1/3}}{\rho^{2/3}} \Delta L \right| \tag{7.20}$$

where ΔL is the effective distance of CSR interaction. It is evaluated to be the length between repetitive patterns of largest $\left|R_{56}^{s'\to s}\right|$ in a beamline design (as we will demonstrate later), because they usually characterize the most contributed CSR microbunching gain development (see Chapter 6). In case there is not a clear repetitive structure in $\left|R_{56}^{s'\to s}\right|$, usually in arc compressors, the effective distance can be estimated as the width of the largest $\left|R_{56}^{s'\to s}\right|$ block.

It has been found that ξ, together with the concept of multistage CSR amplification, can be used to quantify the lattice impact of CSR microbunching. Note that ξ is independent of beam properties. The dependence of beam parameters goes in Λ and Landau damping term through Eq. (7.18). In the subsequent discussion of this section regarding conditions of suppression of CSR-induced microbunching gain, we have excluded the effect of Landau damping; we only aim to reach small $\left|R_{56}^{s'\to s}\right|$ of beamline optics, thus small ξ, in order to eventually have small kernel function $\mathcal{K}$. However, when demonstrating example lattices in Sec. 7.4, we include all relevant beam dynamics in the calculation of CSR microbunching for thorough consideration.

In Chapter 6 we had indicated the important role of the relative momentum compaction $R_{56}^{s'\to s}$ for CSR microbunching development. Local isochronicity associated to smallness of the dispersion function (hence small ξ) can result in effective CSR microbunching suppression. Here we try to relate this important quantity to lattice Twiss parameters using standard linear matrix analysis [29]. Our goals are to find explicit conditions for CSR microbunching suppression and to further evaluate the design performance of a beamline lattice for the particular issue. Below we consider a general beamline as shown in Fig. 7.4. We want to formulate in terms of typical Twiss parameters the relative momentum compaction function $R_{56}^{s_1\to s_2}$, where, inside the two dipoles, s_1 and s_2 are measured from entrances of their corresponding dipoles. Assume the bend-plane of the beamline lattice lies in (x, z). The four-by-four linear transport matrix from the CSR emission site (s_1) to receiving site (s_2) can be obtained by $\mathbf{R}^{total} = \mathbf{R}^{s_2\to L_b}\mathbf{R}^{s_1\to s_2}\mathbf{R}^{0\to s_1}$, i.e.

$$\mathbf{R}^{s_1\to s_2} = \mathbf{R}^{dipole}\left(\theta = -\frac{L_b - s_2}{\rho_2}\right)\mathbf{R}^{total}\mathbf{R}^{dipole}\left(\theta = \frac{-s_1}{\rho_1}\right) \tag{7.21}$$

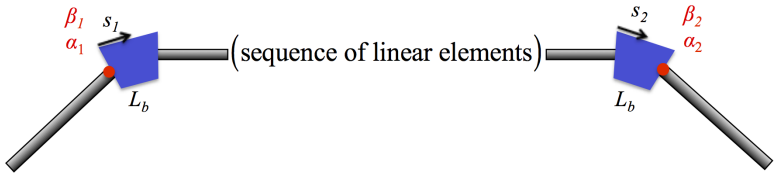

Figure 7.4: Illustration of a two-dipole system. The in-between section can be a general transport section. (see context for definition of notations).

where the transfer matrix for a sector dipole $\mathbf{R}^{dipole}$ can be expressed as [29]

$$\mathbf{R}^{dipole}(\theta) = \begin{bmatrix} \cos\theta & \rho\sin\theta & 0 & \rho\left(1-\cos\theta\right) \\ -\frac{1}{\rho}\sin\theta & \cos\theta & 0 & \sin\theta \\ -\sin\theta & -\rho\left(1-\cos\theta\right) & 1 & -\rho\left(\theta-\sin\theta\right) \\ 0 & 0 & 0 & 1 \end{bmatrix} \tag{7.22}$$

and the transfer matrix $\mathbf{R}^{total}$ in the two-dipole system can be in general parameterized by Twiss parameters [102]

$$\mathbf{R}^{total} = \begin{bmatrix} \sqrt{\frac{\beta_2}{\beta_1}}\left(\cos\psi_{21}+\alpha_1\sin\psi_{21}\right) & \sqrt{\beta_2\beta_1}\sin\psi_{21} & 0 & R_{16} \\ -\frac{1+\alpha_2\alpha_1}{\sqrt{\beta_2\beta_1}}\sin\psi_{21}+\frac{\alpha_1-\alpha_2}{\sqrt{\beta_2\beta_1}}\cos\psi_{21} & \sqrt{\frac{\beta_1}{\beta_2}}\left(\cos\psi_{21}-\alpha_2\sin\psi_{21}\right) & 0 & R_{26} \\ R_{51} & R_{52} & 1 & R_{56} \\ 0 & 0 & 0 & 1 \end{bmatrix} \tag{7.23}$$

where $\alpha_1, \alpha_2, \beta_1,$ and β_2 are assigned at locations illustrated in Fig. 7.4. Note that the in-between section can consist of any sequence of linear elements, e.g. drifts, dipoles, quadrupoles and etc.

The symplecticity condition imposes the following constraints to the transport matrix Eq. (7.23) [see also Eqs. (2.60) and (2.61)]:

$$\begin{aligned} R_{51} &= R_{16}R_{21} - R_{26}R_{11} \\ R_{52} &= R_{16}R_{22} - R_{26}R_{12} \end{aligned} \tag{7.24}$$

Note that R_{56} in Eq. (7.23) is considered a free parameter and independent of R_{51} and R_{52} (thus R_{16} and R_{26}).

After some algebraic manipulation, the relative momentum compaction function $R_{56}^{s_1\to s_2}$ can be ana-

lytically obtained:

$$
\begin{aligned}
R_{56}^{s_1\to s_2} = {} & R_{56} + L_b \pm s_1 - s_2 + R_{26}\rho_2\left(\cos\frac{s_2-L_b}{\rho_2} - 1\right) \\
& \mp \rho_1 \sin\frac{s_1}{\rho_1} - R_{16}\sin\frac{s_2-L_b}{\rho_2} + \rho_2\sin\frac{s_2-L_b}{\rho_2} \mp \sin\frac{s_1}{\rho_1} \\
& \times \left\{ \begin{array}{l} -R_{26}\sqrt{\beta_1\beta_2}\sin\psi_{21} - \sqrt{\beta_1\beta_2}\sin\dfrac{s_2-L_b}{\rho_2}\sin\psi_{21} \\ +\sqrt{\dfrac{\beta_1}{\beta_2}}\left(\cos\psi_{21} - \alpha_2\sin\psi_{21}\right)\left[R_{16} + \rho_2\left(\cos\dfrac{s_2-L_b}{\rho_2} - 1\right)\right] \end{array} \right\} \\
& + \rho_1\left(1 - \cos\frac{s_1}{\rho_1}\right) \\
& \times \left\{ \begin{array}{l} -\sqrt{\dfrac{\beta_2}{\beta_1}}\left(\cos\psi_{21} + \alpha_1\sin\psi_{21}\right)\left(R_{26} + \sin\dfrac{s_2-L_b}{\rho_2}\right) \\ -\dfrac{R_{16} + \rho_2\left(\cos\frac{s_2-L_b}{\rho_2} - 1\right)}{\sqrt{\beta_1\beta_2}}\left[(\alpha_2-\alpha_1)\cos\psi_{21} + (1+\alpha_1\alpha_2)\sin\psi_{21}\right] \end{array} \right\}
\end{aligned}
\tag{7.25}
$$

where the upper (lower) sign is for forward (reverse) bending.

As mentioned, to have effective suppression of CSR microbunching gain, one option we take is to pursue small ξ (hence small $\mathcal{K}$) by manipulating $R_{56}^{s_1\to s_2}$. We remind that $R_{56} = 0$ does not imply $R_{56}^{s_1\to s_2} = 0$ and, if considering the transverse degrees of freedom, in general $R_{56}^{s_1\to s_2} \neq R_{56}(s_2) - R_{56}(s_1)$. To get feeling of how $R_{56}^{s_1\to s_2}$ behaves in Eq. (7.25), in the following subsections we would numerically illustrate the parametric dependencies of $R_{56}^{s_1\to s_2}$ for some specific cases.

7.3.1 For achromatic and isochronous modules

We start from the simplest case with $R_{16} = R_{26} = R_{56} = 0$ (m). For simplicity, we assume $\rho_1 = \rho_2 = 10$ m, $L_b = 1$ m, $\beta_1 = \beta_2 = \beta$, $\alpha_1 = \alpha_2 = \alpha$, and s_1 and s_2 locate in the middle of dipoles. Given R_{16}, R_{26}, and R_{56} for the two-dipole module (see Fig. 7.4), $R_{56}^{s_1\to s_2}$ depends only on lattice Twiss parameters α, β and phase difference ψ_{21}, i.e. $R_{56}^{s_1\to s_2} = f(\alpha, \beta, \psi_{21})$. Figure 7.5 shows the typical $|R_{56}^{s_1\to s_2}|$ pattern for an achromatic ($R_{16} = R_{26} = 0$) and isochronous ($R_{56} = 0$) module. Note that in general $R_{56}^{s_1\to s_2}$ does not vanish even for an isochronous module. From the figure, it is obviously seen that small β function is preferred. The choice of α function does not affect the resultant $|R_{56}^{s_1\to s_2}|$ too much in this specific parameter regime. The featured fact that $\psi_{21} \approx \pi$ (or its integer multiples) can lead to minimal $R_{56}^{s_1\to s_2}$ is also observed for all α's and β's in Fig. 7.5.

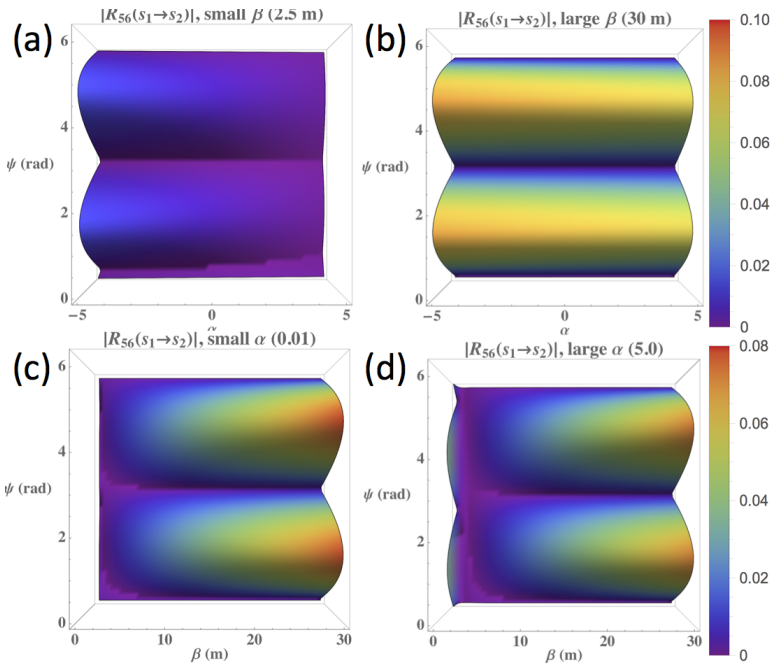

Figure 7.5: $|R_{56}^{s_1\to s_2}|$ pattern for an achromatic and isochronous unit, $R_{16} = R_{26} = R_{56} = 0$ m. (Top) $R_{56}^{s_1\to s_2}(\alpha, \psi)$ for (a) small and (b) large β functions; (bottom) $R_{56}^{s_1\to s_2}(\beta, \psi)$ for (c) small and (d) large α functions. The color bar is measured in meter.

7.3.2 For dispersive and/or non-isochronous modules

When the two-dipole module is dispersive (i.e. $R_{16} \neq 0$, while assuming $R_{26} = R_{56} = 0$), the typical $|R_{56}^{s_1\to s_2}|$ patterns become distorted, as shown in Fig. 7.6. Our investigation finds that the *action* of nonzero R_{16} can create low-lying areas in some regions, see Fig. 7.6(a,b). Small $|R_{56}^{s_1\to s_2}|$ however can still occur around $\psi_{21} \approx \pi$ except at $\alpha \approx 0$. The action of nonzero R_{56} is to have either upper or lower ($\psi_{21} > \pi$ or $\psi_{21} < \pi$) portion shrink asymmetrically, depending on the sign of R_{56}, as illustrated in Fig. 7.7 with positive R_{56}. Figure 7.8 demonstrates the action of R_{26}, in which it tends to restore the shape to that as Fig. 7.5 shows (see also Fig. 7.7); if R_{26} continues to increase, Fig. 7.8 would reduce to Fig. 7.5. From observation of top left figures of Figs. 7.6 to 7.8, small β function is found to be a preferred choice to generate small relative momentum compaction. Furthermore, the choice of $\psi_{21} \approx \pi$ (or its multiple integers) usually result in minimal $|R_{56}^{s_1\to s_2}|$, e.g. Fig. 7.6 (a) and (b).

For a more general case of both dispersive and non-isochronous module, $R_{16}, R_{26}, R_{56} \neq 0$, the pattern of relative momentum compaction becomes more complicated, as shown in Figs. 7.9 and 7.10. Small β function usually serves as a guideline to give small $|R_{56}^{s_1\to s_2}|$ [see Figs. 7.9(a) and 7.10(a)]. In addition, the choice of small β function provides more flexible parametric space of $|R_{56}^{s_1\to s_2}|$ than that of larger β function, although larger β function may still result in small $|R_{56}^{s_1\to s_2}|$ provided the betatron phase difference is properly chosen. As shown in Fig. 7.9 (c) and (d), dependence of $|R_{56}^{s_1\to s_2}|$ on α function can be weak. For larger dispersion, Fig. 7.10 (c) and (d) indicate moderate α function can be preferred.

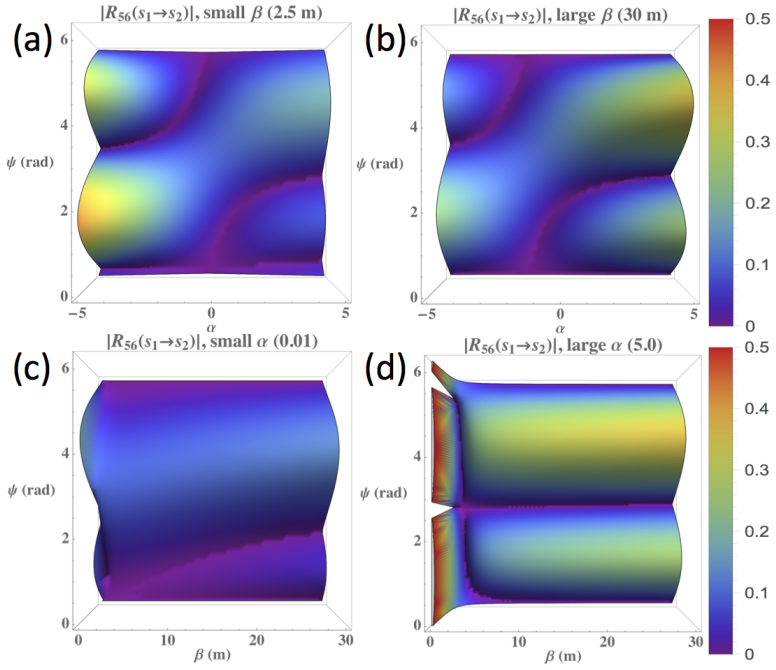

Figure 7.6: $|R_{56}^{s_1 \to s_2}|$ pattern for a dispersive but isochronous unit, $R_{16} = 1$ m, $R_{26} = 0, R_{56} = 0$ m. (Top) $R_{56}^{s_1 \to s_2}(\alpha, \psi)$ for (a) small and (b) large β functions; (bottom) $R_{56}^{s_1 \to s_2}(\beta, \psi)$ for (c) small and (d) large α functions.

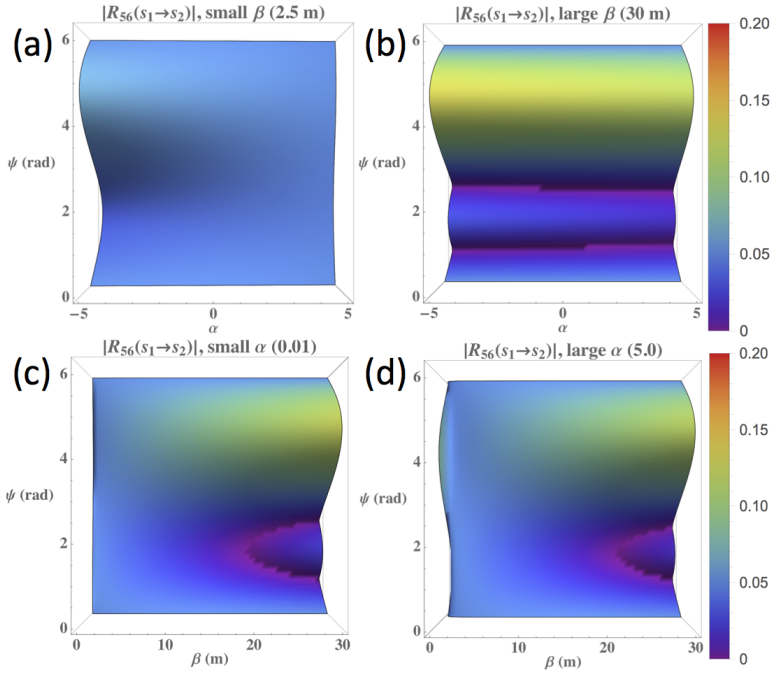

Figure 7.7: $|R_{56}^{s_1 \to s_2}|$ pattern for an achromatic and isochronous unit, $R_{16} = R_{26} = 0$, $R_{56} = 0.05$ m. (Top) $R_{56}^{s_1 \to s_2}(\alpha, \psi)$ for (a) small and (b) large β functions; (bottom) $R_{56}^{s_1 \to s_2}(\beta, \psi)$ for (c) small and (d) large α functions. The color bar is measured in meter.

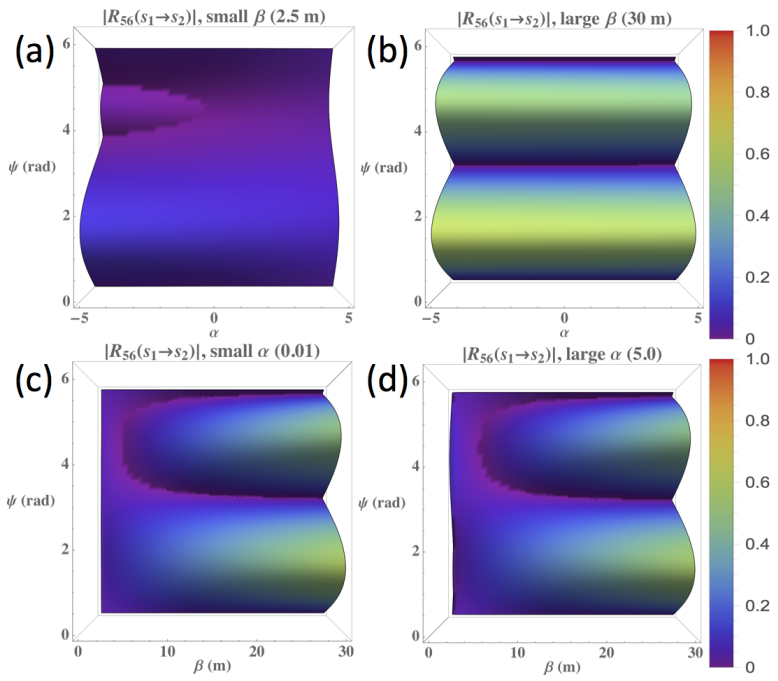

Figure 7.8: $|R_{56}^{s_1\to s_2}|$ pattern for an achromatic and isochronous unit, $R_{16} = 0$, $R_{26} = 0.4$, $R_{56} = 0.05$ m. (Top) $R_{56}^{s_1\to s_2}(\alpha, \psi)$ for (a) small and (b) large β functions; (bottom) $R_{56}^{s_1\to s_2}(\beta, \psi)$ for (c) small and (d) large α functions. The color bar is measured in meter.

7.3.3 Short summary

In Sec. 7.3.1 and 7.3.2 we have already seen the parametric dependencies of $|R_{56}^{s_1\to s_2}|$ for a total of four typical cases:

(i) achromatic and isochronous module $R_{16} = R_{26} = R_{56} = 0$ (Fig. 7.5);

(ii) dispersive but isochronous module $R_{16} \neq 0, R_{26} = 0, R_{56} = 0$ (Figs. 7.6);

(iii) achromatic but non-isochronous module (Fig. 7.7), and

(iv) dispersive and non-isochronous module $R_{16}, R_{26}, R_{56} \neq 0$ of a beamline (Figs. 7.8 to 7.10).

From the investigation of the $|R_{56}^{s_1\to s_2}|$ behavior, we conclude that:

(1) small β functions (at entrances and exits of dipoles),

(2) moderate α functions (at entrances and exits of dipoles), and

(3) $\psi_{21} \approx \pi$ (or its integer multiples) between two relevant dipoles

can in general lead to small relative momentum compaction function in a general transport line. In a preliminary beamline design, Eq. (7.25) can serve as a way to check whether notional Twiss parameters (at

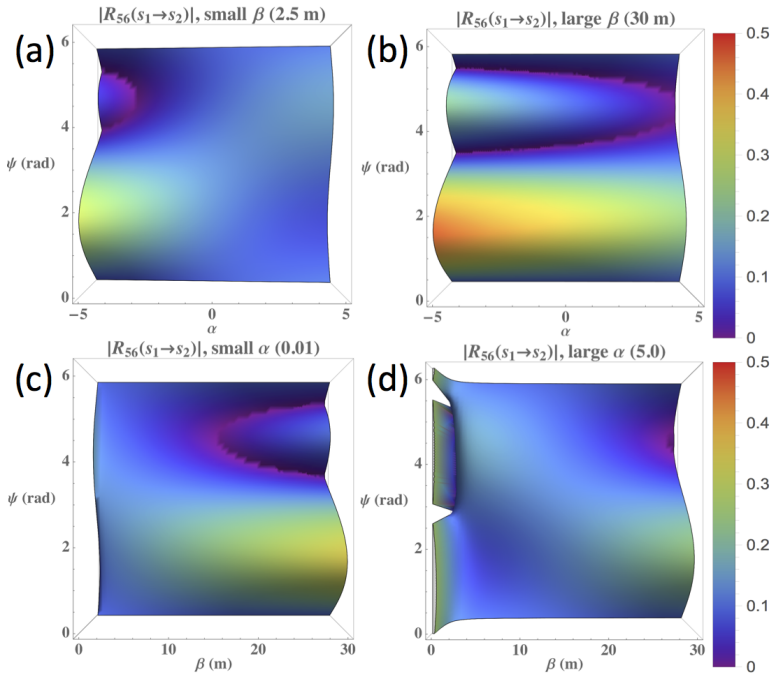

Figure 7.9: $|R_{56}^{s_1\to s_2}|$ pattern for an achromatic and isochronous unit, $R_{16} = 0.4$ m, $R_{26} = 0.2$, $R_{56} = 0.1$ m. (Top) $R_{56}^{s_1\to s_2}(\alpha, \psi)$ for (a) small and (b) large β functions; (bottom) $R_{56}^{s_1\to s_2}(\beta, \psi)$ for (c) small and (d) large α functions. The color bar is measured in meter.

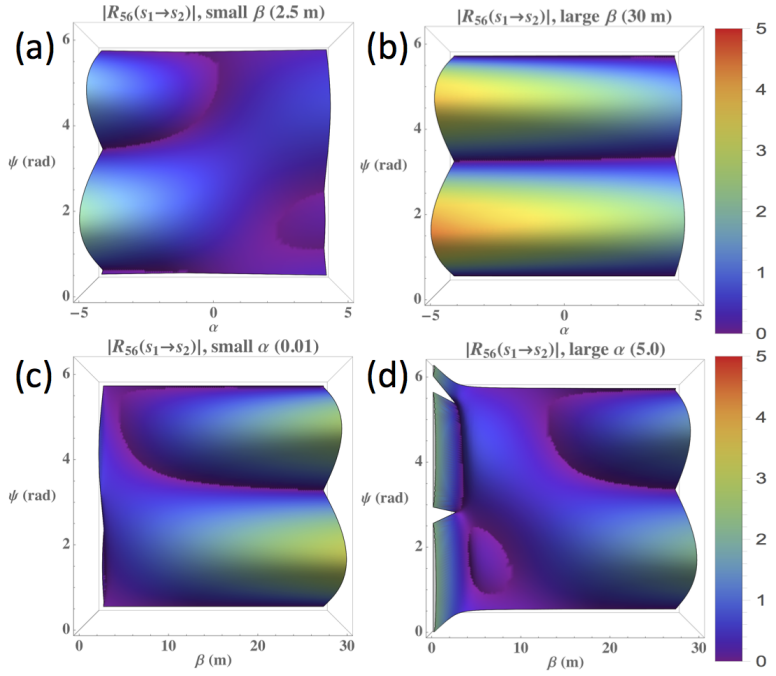

Figure 7.10: $|R_{56}^{s_1\to s_2}|$ pattern for an achromatic and isochronous unit, $R_{16} = 4$ m, $R_{26} = 2$, $R_{56} = 0.1$ m. (Top) $R_{56}^{s_1\to s_2}(\alpha, \psi)$ for (a) small and (b) large β functions; (bottom) $R_{56}^{s_1\to s_2}(\beta, \psi)$ for (c) small and (d) large α functions. The color bar is measured in meter.

entrances and exits of dipoles) are properly chosen to avoid being located at large $|R_{56}^{s_1\to s_2}|$. Whenever an optimal design is considered, one can in principle use Eq. (7.25) for more dedicated choice of Twiss functions and betatron phase advance. The small $|R_{56}^{s_1\to s_2}|$ (and hence small $\mathcal{K}$) will eventually bring about effective CSR microbunching suppression. Here we note that, although there is not a stability margin for $|R_{56}^{s_1\to s_2}|$ (or $\mathcal{K}$) in an absolute sense to have effective CSR gain suppression, since the collective interaction is intensity dependent (through Λ), our proposed optics conditions shall minimize the CSR-induced microbunching gain for any given beam current level. We also emphasize that these conditions are sufficient; other schemes of making small $\mathcal{K}$ are not excluded, e.g. Refs. [13, 142, 51] through enhancing Landau damping [see Eq. (7.15)].

7.4 Lattice examples

7.4.1 High-energy recirculation arcs

The first set of comparative examples involves two 1.3 GeV High-Energy Recirculation Arcs (hereafter named HERA v1 and v2 lattices), as were applied in Chapter 6. Here we give more detailed introduction regarding the design strategies of the two arcs [58].

HERA v2 is similar to the CEBAF arc transport line, by which nearly all requirements for CSR suppression are met. Figure 7.11 presents a conceptual representation of one of the four superperiods of a CEBAF arc. It is simply a pair of betatron phase 90-deg FODO dispersion suppressors; it is nominally linearly achromatic, imaging in both transverse planes (i.e. $\mathbf{R}_{4\times4} = \mathbf{I}$), but nonisochronous $R_{56} \neq 0$. By increasing the strength of the highlighted quadrupole pair (which are separated by 180-deg in betatron phase), the dispersion is driven down in the inner pair of dipoles (also reducing the momentum compaction), and the horizontal and vertical tunes split (horizontal upward, vertical downward). Fitting on all quad families then allows a precise trim of matched beam envelope, achromaticity, momentum compaction, and tune. A choice of quarter integer tunes (5/4 horizontal, 3/4 vertical) then leads to the desired second order achromatic configuration when four superperiods are used to generate a complete arc. However, this configuration is disadvantageous in that the bend-plane beam envelopes are not forced to small values in the dipoles. This would increase betatron response to radiation events (aggravating both incoherent and coherent synchrotron radiations, ISR and CSR) and decrease beam divergence in the dipoles, magnifying the relative impact of a radiative shift in dispersive angle. In addition, control of T566 and other nonlinear compaction terms is not entirely transparent. In order to reduce the in-bend bend-plane envelopes and provide a knob for T566, we have in this study used a slightly different focusing structure, shown in Figs. 7.12 and 7.13. We begin by generating a single 90-deg theoretical-minimum-emittance (TME) focusing structure [9] as shown in Figure 7-12. When four such cells are put together, an achromatic (to second order) but nonisochronous superperiod results (Figure 7.13). By increasing the strength of the highlighted quadrupoles (again, which have 180-deg betatron phase separation), the dispersion can be driven down in the inner dipoles, the tunes split, and a linearly achromatic, isochronous superperiod obtained. As with CEBAF, optimization using

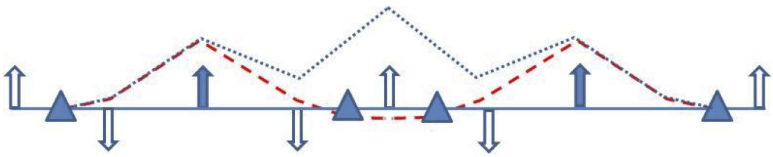

Figure 7.11: CEBAF superperiod, with notional dispersion pattern for initial tuning as paired 90-deg FODO dispersion suppressors (blue dotted) and, after increase in strength of highlighted quads, for quarter-integer isochronous achromat (red dashed). Picture from Ref. [58].

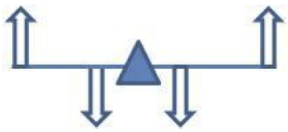

Figure 7.12: Single period building block of modified transport line. Picture from Ref. [58].

all quad families then allows choice of tune, matched envelopes, enforced achromaticity, and selection of momentum compaction. After simulation trials of solutions using different superperiod tunes, we find that sixth-integer tunes (7/6 horizontal, 5/6 vertical) provide good chromatic behavior and admits a particularly simple means of control of T_{566} (and in principle W_{5666}). Six superperiods then form a second-order achromatic arc; the higher periodicity also reduces the individual bend angle below that used in CEBAF, providing further mitigation of radiation effects. Figure 7.14 (b) shows beam envelope functions for a full arc. As noted, horizontal beam envelopes are small within the bends. As there are a total of 24 bends in the arc, each dipole provides 7.5-deg deflection, yielding small R_{16} and R_{26} in the bends, and together with the relatively large beam divergence at the same location helping reduce the impact of both ISR and CSR effects. Table 7.1 provides a list of relevant beam and lattice parameters.

Most importantly, the betatron phasing associated with the second order achromatic architecture also introduces emittance compensation in the manner discussed above: each dipole has a partner with $\psi \approx \pi$ or a half-betatron-wavelength away, at which the bunch length and all beam envelope functions are the same, so that emittance-degrading effects cancel. This is particularly strongly enforced by use of a periodically isochronous structure, which insures that the bunch length is the same at phase-homologous CSR emission sites. The small dispersion and dispersive slope result not only in a small (zero) momentum compaction in

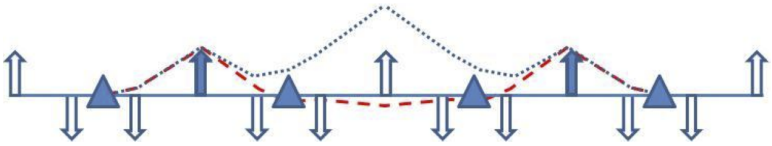

Figure 7.13: Modified superperiod, with notional dispersion pattern for initial tuning as four 90-deg theoretical-minimum-emittance (TME) cells in second order achromat (blue dotted) and, after increase in strength of highlighted quads, for quarter-integer isochronous linear achromat (red dashed). Picture from Ref. [58].

each superperiod, but the modulation of the momentum compaction through the system is extremely small, potentially providing some limitation on microbunching gain. Figure 7.14 (d) shows the evolution of R_{56} through the arc; maximum and minimum values are at the millimeter level.

To explore the effectiveness of the periodically isochronous and second-order achromat-based CSR MBI suppression scheme, we have generated the example design HERA v1. It is based on HERA v2, and is also a second-order achromat. Rather than individually isochronous superperiods, it is rendered globally isochronous by dispersion modulation across the entire arc. This allows an assessment of the impact of large compaction oscillations, large dispersion, and the absence of multiply periodic isochronicity. Starting with the same basic TME cell and four-cell superperiod structure employed in HERA v2, a process similar to that used in early CEBAF design studies [64] is used. We tune each TME cell to fractional tunes of 5/24 horizontally and vertically (instead of splitting tunes). Four TME cells then form a superperiod with tunes of 5/6 in both planes; quads in each superperiod are fit to hold this tune while forcing R_{56} to zero at the end. Individual superperiods are, however, not achromatic, by virtue of the weaker horizontal focusing or lower horizontal tune. Though the constraint that $R_{56} = 0$ locally eliminates the linear dependence of path length on energy, superperiods are thus not strictly isochronous. When six such superperiods are combined to form a complete 180-deg arc, the resulting second-order achromat then displays an oscillatory dispersion pattern that in turn drives the arc to be achromatic from end to end and then suppresses the overall momentum compaction. A final fit of the arc as a whole renders it six-fold periodic, sets the tunes to 5 wavelengths in both planes, holds achromaticity, and forces the whole beamline to be isochronous from end to end. Individual superperiods remain at 5/6 integer tunes, but have nonzero matched dispersion and small but nonzero (positive) R_{56}. Matched Twiss parameters are modest; the large dispersion oscillation reaches a peak of $\sim$4 m amplitude. Beam envelopes, dispersion, and the strongly oscillatory evolution of R_{56} are shown in Figure 7.14 (a,c). For the detailed description of the design for the two example lattices, we refer the interested reader to Ref. [58].

Table 7.1 provides a list of beam and lattice parameters. For both examples, the (peak) beam current is chosen to be 65 A, the transverse normalized emittances are assumed 0.3 μm, and the uncorrelated energy spread is assumed 1.23×10^{-5}. These beam parameters are typical for next-generation light source facilities based on recirculation or energy recovery linacs (ERL) machines. Other relevant initial beam and lattice parameters are summarized in Table 7.1. For microbunching development, we are more interested in $R_{56}^{s' \to s}$ than merely R_{56}. Figure 7.15 shows the nominal relative momentum compaction functions $R_{56}^{s' \to s}$ for the two arc lattices. We remind the difference between the pattern $R_{56}^{s' \to s}$ in Fig. 7.15 and the variations of $R_{56}^{s_1 \to s_2}$ in a range of Twiss parameters, shown in Figs. 7.5 to 7.10. The former indicates how the CSR emission (s') and receiving (s) relate, and the latter demonstrates how behaves as a function of varying Twiss parameters. Note that $R_{56}^{s' \to s}$ plays the more essential role in determining the resultant microbunching gain than $R_{56}(s)$ does [see Eq. (7.15)]. This is because the energy modulation, induced by CSR within dipoles, will be transformed back to density modulation downstream a beamline through the relative momentum

Table 7.1: Selected beam and lattice parameters used in HERA arcs.

Name	HERA v1	HERA v2	Unit
Beam energy	1.3	1.3	GeV
Peak current	65	65	A
Slice rms energy spread	1.23×10^{-5}	1.23×10^{-5}	
Normalized transverse emittance	0.3	0.3	μm
Chirp	0	0	m^{-1}
Compression factor	1	1	
Superperiod length	40	40	m
Superperiod dispersions, R_{16}, R_{26}	-1.601, 0	0, 0	m, rad
Superperiod compactions, R_{56}, T_{566}	0.062, 0.24	0, 0.878	m, m
Superperiod chromaticity, ξ_x, ξ_y	0, 0	0, 0	
Superperiod tunes, ν_x, ν_y	5/6, 5/6	7/6, 5/6	
Dipole radius, ρ	3.614	3.614	m
ΔL	40	20	m
max. $R_{56}(s\prime \to s)$	0.52	0.13	m
$G_{\mathrm{f,max}}$	300	1	
λ_{opt}	40	20	μm
ξ	477.8	75.2	m

compaction $R_{56}^{s'\to s}$, instead of $R_{56}(s) = R_{56}^{0\to s}$. The deep red blocks, considered as dangerous areas shown in Fig. 7.15 with larger $\left|R_{56}^{s'\to s}\right|$, indeed result in enhancement of energy-to-density conversion and cause CSR microbunching instability. The quantity ΔL, defined as the effective length of CSR interaction, can be evaluated from Fig. 7.15 as the edge-to-edge distance between adjacent large-amplitude (deep-red) blocks. For HERA v1, ΔL is roughly twice larger than that of HERA v2 (see Table 7.1). To make ΔL small, it is preferred to design a beamline with more repetitive cell units, as the case of HERA v2.

As Eq. (7.17) shows, the momentum compaction function is indeed a continuous function, albeit Fig. 7.15 appears to feature a step-like diagram. This impression can be due to mere visualization effect. As R_{56} only varies within dipoles, it is not easy to observe the transition for the length of a beamline relatively larger than individual dipole lengths. For example, in Fig. 7.15 the dipole length for HERA v1 and v2 is 4.7 cm and the total length of the beamlines is 240 m. While the momentum compaction (or the slippage) factor is often to characterize one-turn R_{56} effect in a storage-ring accelerator, in the single-pass system (e.g. in linear or recirculation accelerators) it was usually treated as a function of path length, as was dealt with in Fig. 1 of Ref. [79] for study of CSR microbunching in the bunch compressor chicane of Linac Coherent Light Source (LCLS).

Figure 7.16 shows the CSR-induced microbunching gain spectra for HERA v1 and v2 arcs, respectively. They were calculated with our developed semi-analytical Vlasov solver. A major difference between the two examples is observed that HERA v1 is vulnerable to the CSR microbunching instability whereas the microbunching gain in HERA v2 remains around unity (i.e. there is no microbunching amplification). To validate our linear Vlasov results, we benchmark the two example lattices by using `elegant`, with which

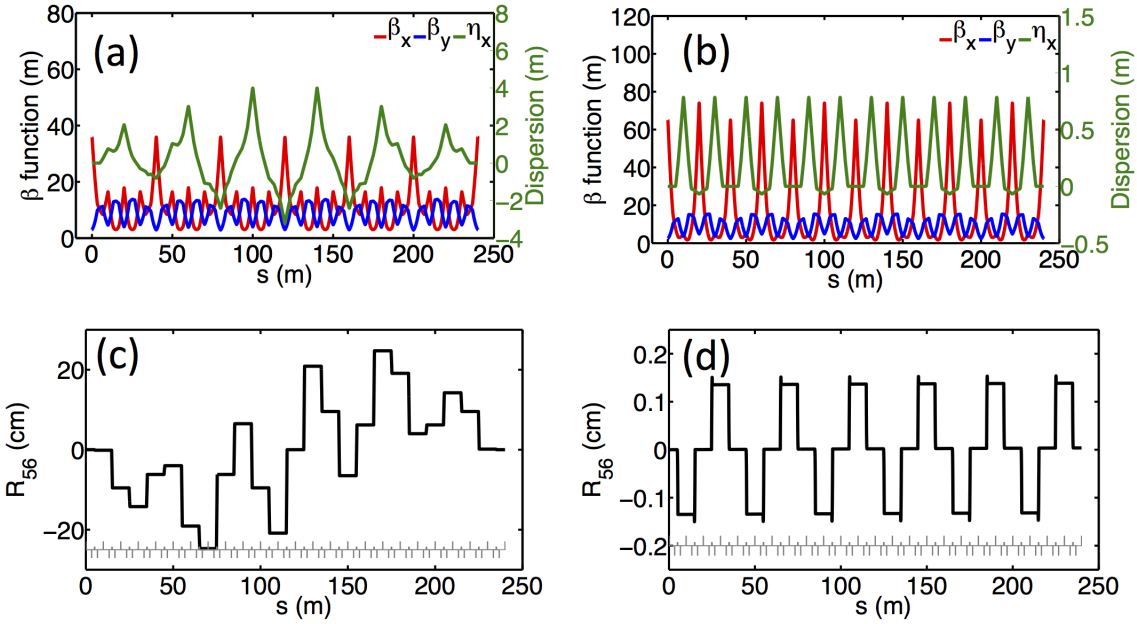

Figure 7.14: Twiss functions and $R_{56}(s)$ for HERA v1 (a, c) and v2 (b, d).

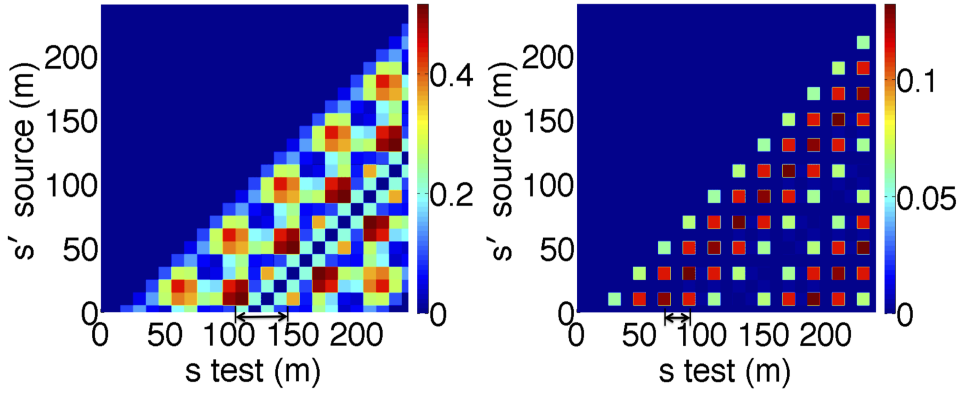

Figure 7.15: Relative momentum compaction function $\left|R_{56}^{s'\to s}\right|$ for HERA v1 (left) and v2 (right). Note that s' is denoted as the source position and s the observation or test position. The function is evaluated by Eq. (7.17). We quantify ΔL as 40 m and 20 m for HERA v1 and v2.

extensive convergence studies were performed (see Ref. [173] or Chapter 5). The numerical procedures were introduced in Chapter 5. Both our semi-analytical solutions and `elegant` tracking results show good agreement in microbunching gain estimation (see Fig. 7.16).

From Fig. 7.16, we find that the microbunching gain including both steady-state and entrance transient CSR effects is slightly lowered from the case of steady-state CSR alone. This is because the CSR impedances including entrance transient effect become a bit reduced near the dipole entrance when the beam traverses across the bend. We also observe that with the inclusion of all relevant CSR effects, the microbunching gain increases about 400% compared with that of steady-state case. This indicates that without

optical compensation the CSR exit transient effect can make a significant contribution on microbunching gain development. Yet with optical compensation, even with the same dipole configuration over the beamline, HERA v2 is not subject to CSR-induced MBI (the overall gain is still around unity). This highlights the impact of optical lattice design for recirculation arcs on microbunching gain development. Here we note that, because of extremely high gain of HERA v1 lattice when we include all relevant CSR impedances, `elegant` tracking results were averaged over a range of initial modulation amplitudes 0.01-0.04% and 70-million macroparticles were used in the tracking simulation. In postprocessing of `elegant` tracking results, we determine the modulation amplitude at a specific location by the procedures outlined in Chapter 5. We notice that with the large gain shown in Fig. 7.16 the microbunching mechanism may reach nonlinear regime where linearized Vlasov solutions are no longer valid from a practical point of view. For the validity of linear microbunching gain analysis using particle tracking, it is required that the initial perturbation be sufficiently small (although in some practical cases it may not be so small) that the magnitude of the bunching factor along the beamline should not exceed a certain value. Here we suggest a merit to our semi-analytical Vlasov approach: since the microbunching gain obtained from particle tracking depends sensitively on the numerical parameters used for tracking (e.g. macroparticle numbers, meshes, bins, and etc), benchmarking the semi-analytical gain results with the tracking results could also help us to establish the suitable numerical parameters for particle tracking that would give convergent physical results.

Next, we examine our proposed conditions in Sec. 7.3 for the two examples. Figure 7.17 (a) and (b) compares Twiss α functions at dipole locations and betatron phase differences ψ_{21} between near-neighbor dipoles. As mentioned, moderate α function [Fig. 7.17(b)] is usually not a bad choice to produce small relative momentum compaction. The phase differences between near-neighbor dipoles for the two examples are illustrated in Fig. 7.17 (c) and (d), respectively. HERA v2 with $\sim$0 or $\sim \pi$ phase difference between adjacent dipoles indeed satisfies our proposed condition that smaller relative momentum compaction can be achieved when $\psi_{21} \approx \pi$ (or its integer multiples). In contrast, HERA v1 with scattering from 0 to $\pi/2$ does not meet our proposed condition of phase difference. At dipoles, $\beta_x \leq 10$ m for the two examples are comparable. The maximal magnitude of $R_{56}^{s'\rightarrow s}$ for HERA v1 is four times larger than that of HERA v2. It is this difference in $R_{56}^{s'\rightarrow s}$ that makes the distinct CSR microbunching development. To further evaluate the performance of the lattice designs, for each dipole pair as a two-dipole module, we vary the nominal values of Twiss functions in a range and see where the design value of the momentum compaction $R_{56}^{s'\rightarrow s}(\alpha_{x0}, \beta_{x0}, \psi_{21})$ locates in the parameter space $(\alpha, \beta, \psi_{21})$, where $\alpha \in (0.1\alpha_{x0}, 10\alpha_{x0})$, $\beta \in (0.1\beta_{x0}, 10\beta_{x0})$, and $\psi_{21} \in (0, 2\pi)$. Then we consider a pair to be dangerous once the nominal $R_{56}^{s_1\rightarrow s_2}(\alpha_{x0}, \beta_{x0}, \psi_{21})$ is larger than 80% of maximum value in the parameter space $\max\{R_{56}^{s_1\rightarrow s_2}(\alpha, \beta, \psi_{21})\}$. Having examined *all* possible pairs of the two-dipole modules for HERA v1, we found 27 pairs (among a total of 276 combinations) are indicated as *dangerous* pairs and 12 of them are from near-neighbor dipoles. For HERA v2, all the near-neighbor pairs are evaluated to be *safe*.

The parameters Λ and ξ can be used to scale the maximal gain for comparative lattices. ξ for HERA v1 is about 6.4 times larger than that of HERA v2. We see in Fig. 7.18 that indeed this multiplicative factor

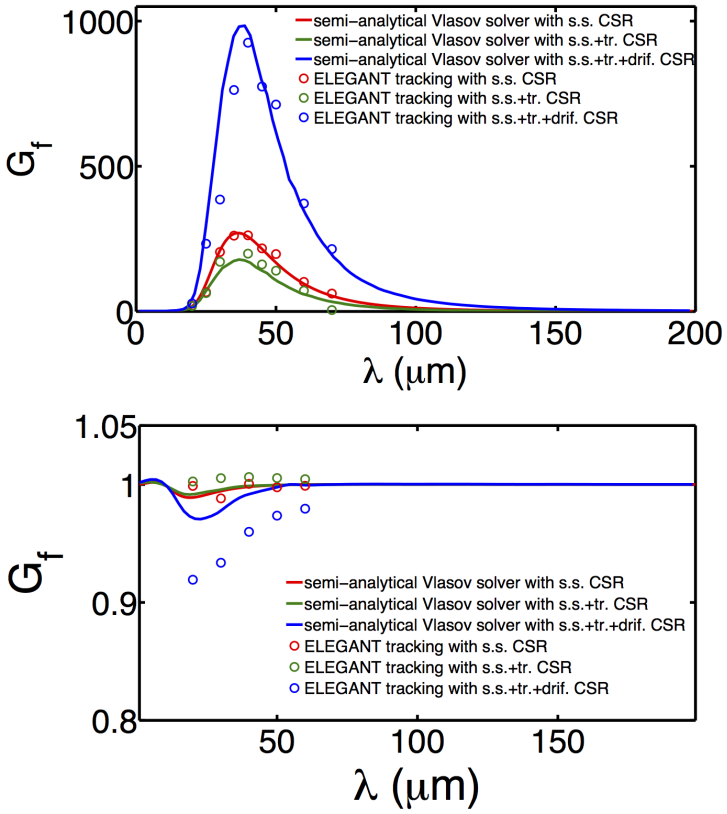

Figure 7.16: CSR microbunching gain spectrum for HERA v1 (left) and v2 (right). The dots are taken from particle tracking simulation by `elegant`. For HERA v1, the initial density modulation is set 0.05% for steady-state case; 0.06% for steady-state and entrance-transient case; 0.01-0.04% for all relevant CSR effects including entrance, exit transients and steady-state CSR. With larger gain, to keep the microbunching process remaining in the linear regime, it is required the initial modulation amplitude be smaller (see also comments in the context). For HERA v2, the initial modulation amplitude is set 0.8% and the same number of macroparticles as HERA v1 is used. For HERA v2, the apparent difference between Vlasov solutions and `elegant` tracking is actually small; note the vertical scale in small numerics.

can reflect the scaling of bunch current for the maximal gains. This scaling can be used as a guideline of setting the order of magnitude of the maximal relative momentum compaction function $R_{56}^{s'\to s}$ (via $\mathcal{K}$) for specified design goals. Assume we have already known the performance of HERA v2 and had no a priori detailed study of CSR microbunching about HERA v1. Now we want to estimate under what level of beam current can the beam be transported through HERA v1 with little CSR microbunching effect. Provided HERA v1 lattice is given, ξ can be determined and compared with that of HREA v2. We then expect that a circulating beam with peak current six times smaller than that of nominal one of HERA v2, i.e. $\sim$10A or six-times smaller Λ, should not be subject to CSR microbunching instability. This is immediately confirmed in the figure.

As described, HERA v2 satisfies all requirements of CSR suppression, and is therefore expected to

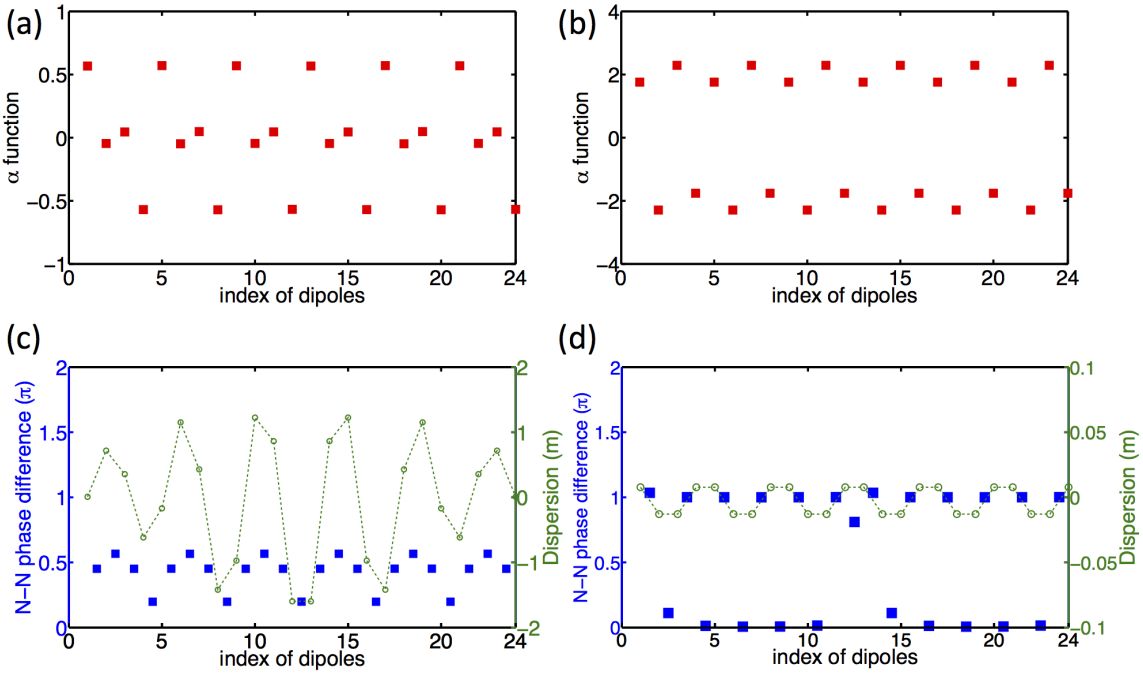

Figure 7.17: Twiss α functions at dipoles and betatron phase differences ψ_{21} (in unit of π) for HERA v1 (a, c) and v2 (b, d). The dashed lines in (c) and (d) only help visualize the dispersion within dipoles.

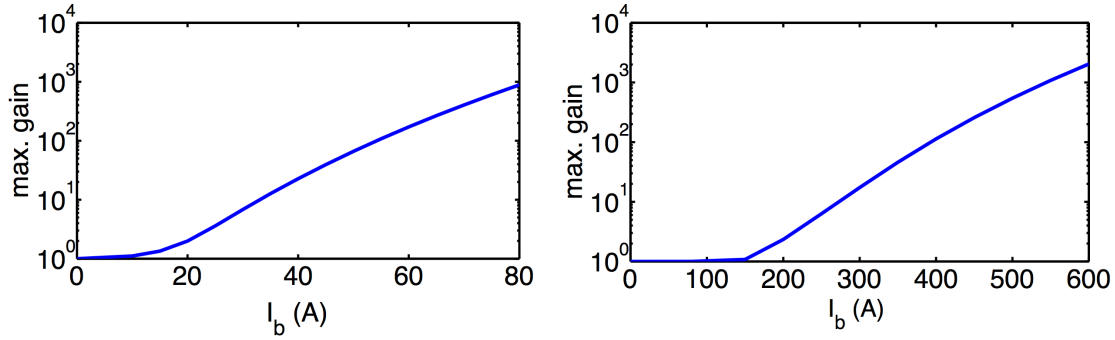

Figure 7.18: Dependence of maximal CSR gains of HERA v1 (left) and v2 (right) on initial (peak) bunch current.

preserve the beam phase space qualities. The resultant CSR-induced emittance growths and microbunching gains for the two Examples are shown in Fig. 7.19. From this figure one can see the transverse beam emittance at the exit of the arc is well preserved in HERA v2 while features four times increase for 500 pC in HERA v1.

To end this subsection, it may deserve here to comment on the relation between the study in Chapter 6 and the present analysis to suppress CSR-induced MBI. Here we quantified the lattice performance to CSR microbunching effect by the dimensionless parameter ξ. From Eq. (6.9), it can be seen that $\left|\tilde{G}_f^{(M)}\right| \sim \sum_{m=0}^{M} \left[\Lambda\xi A\left\{L.D.; s, s'\right\}\right]^m$. For the presented examples, $\Delta L \approx 40$ m for HERA v1 and $\Delta L \approx 20$ m

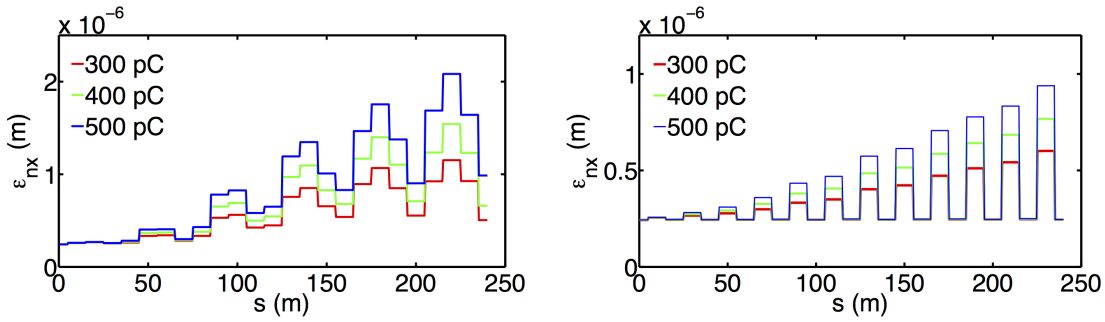

Figure 7.19: Evolution of the transverse normalized emittances for HERA v1 (left) and HERA v2 (right) lattices.

for HERA v2 arcs. Here the proposed conditions aim to make ξ as small as possible, lead to smallness of kernel function $\mathcal{K}$, and thus small microbunching gain in general. The two differences, however, should be highlighted here: (i) the quantity ξ does not take Landau damping into account. That is the proposed conditions are sufficient; another schemes for suppression of MBI was proposed of utilizing Landau damping effect, as mentioned before, and (ii) the present analysis only accounts for $m = 1$ case in Eq. (6.9). It should be straightforward that a first-iterative beamline design, as well as the first-stage CSR microbunching amplification, may start from the lowest order and later deal with higher order effects.

Table 7.2: Selected beam parameters used in LERA arcs.

Name	LERA v1	LERA v2	Unit
Beam energy	150	100	MeV
Peak current	70	70	A
Slice rms energy spread	2×10^{-5}	2×10^{-5}	
Normalized transverse emittance	0.25	0.25	μm
Chirp	0	0	m^{-1}
Compression factor	1	1	
Dipole radius, ρ	0.5	0.5	m
ΔL	4	2	m
max. $R_{56}(s\prime \to s)$	0.3	0.3	m
$G_{\mathrm{f,max}}$	34	1.2	
λ_{opt}	68	104	μm
ξ	86.1	37.4	m

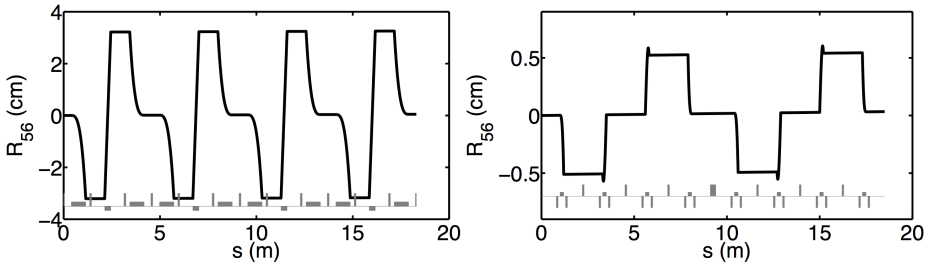

Figure 7.20: $R_{56}(s)$ for LERA v1 (left) and v2 (right).

7.4.2 Low-energy recirculation arcs

The second set of examples consists of two Low-Energy Recirculation Arcs (LERA v1 and v2). LERA v1 is based on the design of an example arc outlined in Ref. [58] and proposed to serve as the return arc for a recirculating intra-beam scattering (RIBS) beamline [52]. LERA v2 is designed for similar purpose to LERA v1 but more intended for mitigation of CSR microbunching instability. The design of LERA v2 follows the guideline described in HERA v2 in the previous subsection. Both arcs are achromatic and (quasi-)isochronous. Suppression of CSR-induced emittance growth has been taken care for both examples (not shown here) [52]. Table 7.2 summarizes the relevant beam and lattice parameters and the featured parameters for the subsequent analysis.

Figure 7.20 illustrates the momentum compaction functions along the beamline $R_{56}(s)$, in which the momentum compactions for the two lattices can be different by an order of magnitude. Figure 7.21 shows the quilt plots for LERA v1 and v2. As reasoned in the previous examples, the deep red blocks, with larger $R_{56}^{s' \to s}$, indeed result in enhancement of energy-to-density conversion and can potentially cause CSR microbunching instability.

Figure 7.22 shows the CSR microbunching gain spectra for LERA v1 and v2, respectively, where we can see the steady-state gain for LERA v1 can be up to 35 at $\lambda = 68\mu$m while LERA v2 has nearly no gain

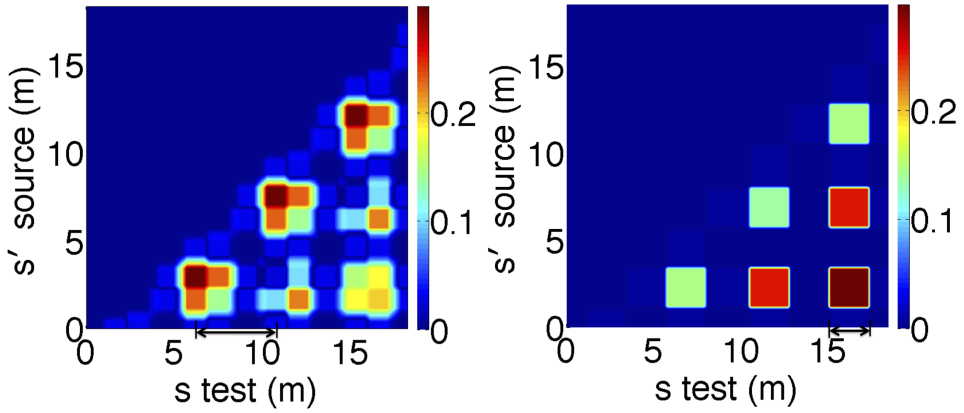

Figure 7.21: Relative momentum compaction function $\left|R_{56}^{s'\to s}\right|$ for LERA v1 (left) and v2 (right). Note that s' is denoted as the source position and s the observation or test position. We quantify ΔL as 4 m and 2 m for LERA v1 and v2.

(≈ 1.2 at $\lambda = 104\mu$m). Our simulation results also indicate that, for all relevant CSR effects included, the gain can be up to 60 for LERA v1 and 1.4 for LERA v2. This again confirms the importance of optical compensation scheme employed in the beamline design. It is interesting to find that such LERA v1 design, which preserves the transverse beam emittance (when including CSR), does not necessarily ensure immunity from CSR microbunching instability. Filamentation of the longitudinal beam phase space distribution has been numerically observed and confirmed due to the CSR instability (not shown here) [52].

Now we examine our proposed conditions in Sec. 7.3 for the two lattices. Figure 7.23 (a) and (b) compares Twiss α functions at dipole locations and betatron phase differences ψ_{21} between near-neighbor dipoles. One can see from the top row of Fig. 7.23 that α's for LERA v2 are in general larger than for LERA v1. The phase differences between near-neighbor dipoles for the two examples are illustrated in Fig. 7.23 (c) and (d), respectively. LERA v1 with $\psi_{21} \approx 0.5\pi$ does not meet our proposed condition of phase difference with π. In contrast, LERA v2 with $\sim$0 or $\sim \pi$ phase difference between adjacent dipoles is favored based on our previous analysis. Although the maximum values of $R_{56}^{s'\to s}$ are comparable for LERA v1 and v2, the deep-red blocks in LERA v1 can accumulate up to three times (of energy-density conversion) while it is only effective at one time for LERA v2. For the two examples, their averaged β functions at dipoles ($\beta_x \leq 2$) are comparable (not shown here). From Fig. 7.23, we conclude that LERA v2 lattice meets our proposed conditions and thus has CSR gain suppressed. Moreover, for LERA v1, we found 6 pairs (among a total of 66 combinations) are indicated as dangerous pairs. For LERA v2, all the pairs are considered to be safe.

Similar to HERA examples, the scaling of Λ is still followed for LERA arcs. For LERA v1, ξ is about 3.5 times larger than that of LERA v2 when beam energy is scaled to the same for both examples. We see in Fig. 7.24 that indeed the maximal gains follow the scaling of Λ. In view of the beam current scaling (together with Fig. 7.18), we can think of HERA v2 (LERA v2) as 6.4 (3.5) times effective suppression of

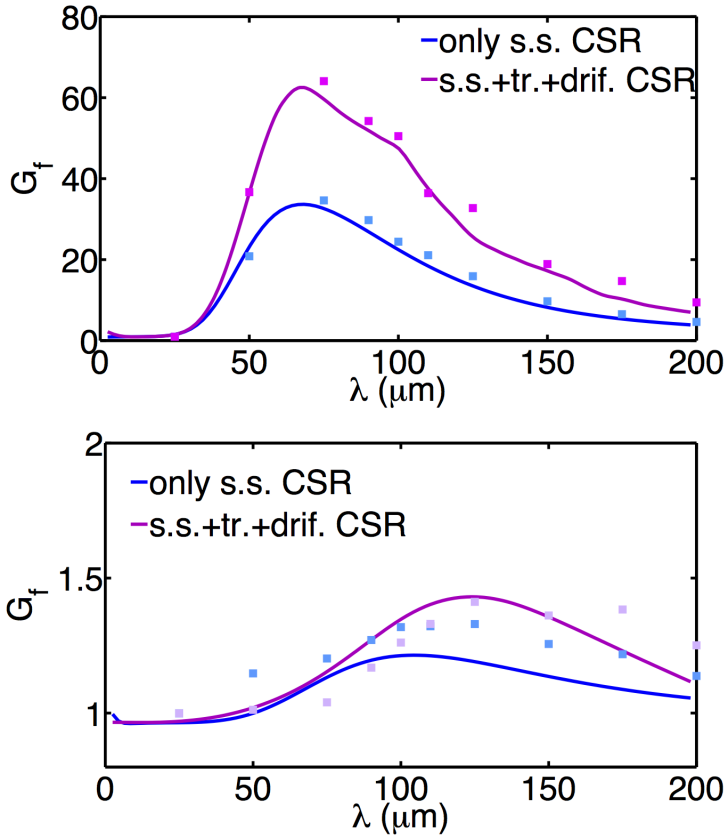

Figure 7.22: CSR microbunching gain spectrum for LERA v1 (left) and v2 (right). The dots are taken from particle tracking simulation by `elegant`, with total of 40-million (with 0.1% initial modulation amplitude) and 10-million (with 0.5% initial modulation amplitude) macroparticles are used for LERA v1 and v2, respectively.

CSR microbunching than HERA v1 (LERA v1).

Figure 7.25 shows the CSR-induced emittance growths for LERA v1 and v2. In this figure, the beam emittances for both LERA v1 and v2 are largely preserved below 400 pC.

7.4.3 Medium-energy compressor arcs

As the third set of examples, we consider two arcs that compress a high-brightness electron beam with nearly no beam quality degradation: the FODO compressor arc and the modulated compressor arc [61]. The FODO compressor arc, considered as a conventional beamline design, consists of eight $\pi/2$ FODO cells. All the bending radii are 2 m and form a 180-deg arc. After careful examination and optimization of phase-space distortion subject to CSR, the CSR-induced emittance growth, though difficult to exactly cancel, can be minimized [61]. The modulated compressor arc, a novel beamline design, is made up of total 9 combined-function dipoles. Those dipoles are no longer constant-angle dipoles but wittingly designed with gradually reduced bending angles in order to avoid the increasingly detrimental CSR effects among the downstream

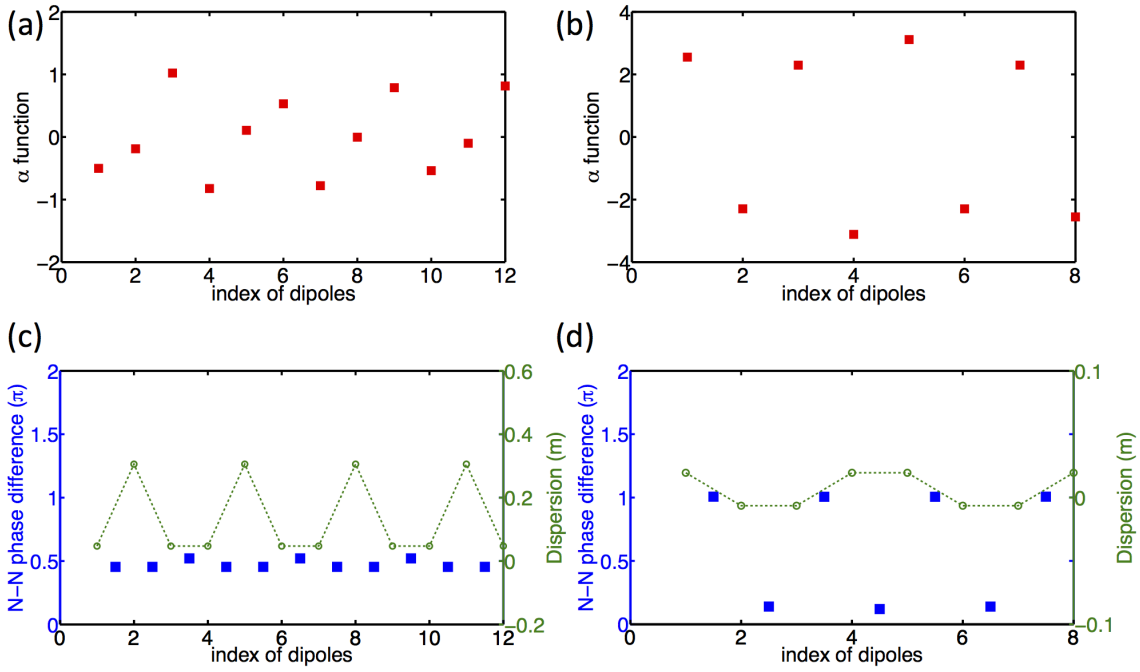

Figure 7.23: Twiss α functions at dipoles and betatron phase differences ψ_{21} (in unit of π) for LERA v1 (a, c) and v2 (b, d). The dashed lines in (c) and (d) only help visualize the dispersion within dipoles.

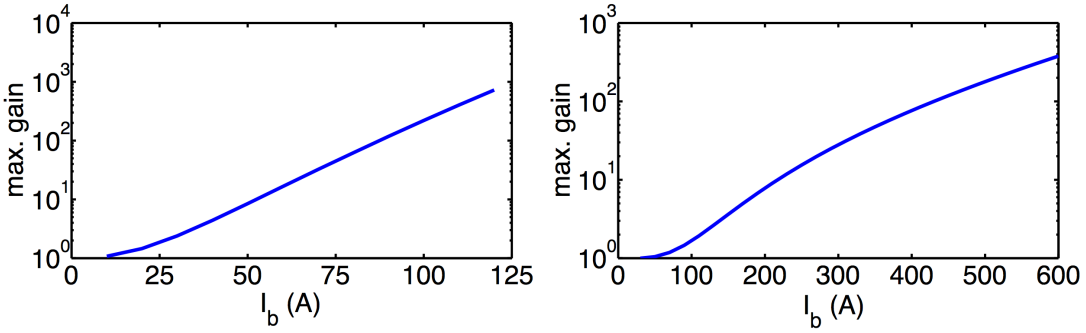

Figure 7.24: Dependence of maximal CSR gains on (peak) bunch current for LERA v1 (left) and v2 (right).

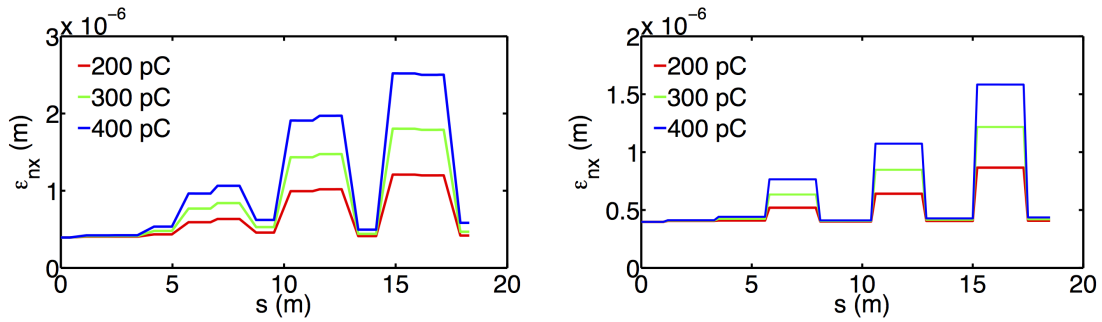

Figure 7.25: Evolution of the transverse normalized emittances for LERA v1 (left) and LERA v2 (right) lattices.

Table 7.3: Selected beam parameters used in compressor arcs.

Name	FODO compressor arc	Modulated compressor arc	Unit
Beam energy	0.71	0.75	GeV
Peak current (before, after)	7.9, 405	7.9, 405	A
Slice rms energy spread	1.13×10^{-5}	1.13×10^{-5}	
Normalized transverse emittance	0.75	0.75	μm
Chirp	-1.577	-0.6344	m^{-1}
Compression factor	51.26	51.26	
Dipole radius, ρ	2	2	m
ΔL	2.71	2.36	m
max. $R_{56}(s\prime \to s)$	0.62	1.6	m
$G_{\mathrm{f,max}}$	2.8	2.2	
λ_{opt}	1800	4400	μm
ξ	16.1	26.8	m

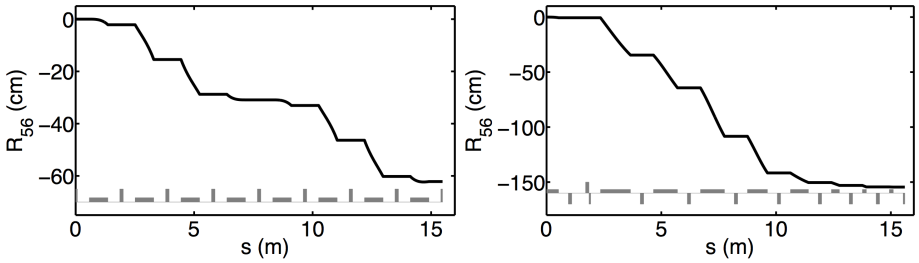

Figure 7.26: $R_{56}(s)$ for FODO compressor arc (left) and modulated compressor arc (right).

bending magnets. The design strategy is based on the following physical intuitions. First, the energy change due to CSR effect is proportional to the CSR force (in steady state) F^{CSR} multiplied by the length of the dipole Δs. Decreasing Δs may reduce the CSR effect, though the gradually compressed electron bunch will result in the increase of Λ and enhance CSR microbunching. Second, when the dipole length becomes shorter than the overtaking distance [42, 153], the transient effect appears and tends to make CSR not be formed timely. We find that such design strategy effectively alleviates the CSR-induced microbunching instability. The initial beam and lattice parameters for the two compressor arcs are tabulated in Table 7.3. Figure 7.26 shows the momentum compaction functions $R_{56}(s)$ of the two arc compressors. To compare, the initial beam parameters of the two arcs, except for bunch chirp, are assumed the same, and the output beams are compressed by the same ratio.

In Table 7.3, the parameter ξ is found to be comparable for the two arc designs; we expect the effect of steady-state CSR microbunching will be comparable as well (Λ is the same). To examine the energy-density conversion, Fig. 7.27 shows the $R_{56}^{s' \to s}$ quilt plots for the two arcs. The two quilt patterns are found to be similar, although FODO compressor arc features smaller relative momentum compaction. The average β functions are about 1 and 2.5 m respectively for FODO and modulated compressor arcs, both of which are within preferred range. Figure 7.28 shows Twiss α functions and betatron phase differences ψ_{21} of near-neighbor dipoles. Except the first pair, although $\psi_{21} \approx 0.5\pi$ for the modulated arc compressor, considered

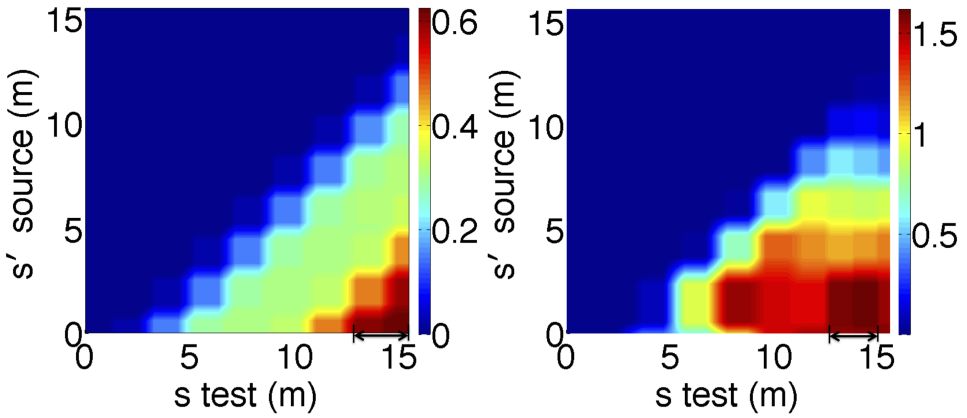

Figure 7.27: Relative momentum compaction function $\left|R_{56}^{s'\to s}\right|$ for FODO compressor arc (left) and modulated compressor arc (right). Note that s' is denoted as the source position and s the observation or test position. ΔL is approximately quantified to be 2.7 m and 2.4 m for FODO and modulated arcs.

not favored, it does not hit the dangerous region much. Our analysis shows that there are two near-neighbor dipole pairs in which $R_{56}^{s'\to s}$ locate within dangerous areas for both compressor arcs.

Steady-state CSR microbunching gain spectra for the two arc compressors are presented in Fig. 7.29. The steady-state gains smaller than 3 indicate that the steady-state CSR does not have significant effect on the two arcs. In Fig. 7.29, our Vlasov calculation further indicates the maximum CSR gain ∼15 for FODO compressor arc and ∼3 for modulated arc when including transient CSR effects[118]. The CSR gain is commonly considered to be small below 10, so the modulated compressor arc becomes a better design from this point of view. Note that the arc compressors presented here can be different from those specified as four-dipole compressor chicanes in that the arcs can have much larger total R_{56} so that the typical microbunched structure (∼1 mm) is usually much larger than that of typical bunch compressor chicanes (∼50 μm).

7.5 Summary and Conclusion

In this chapter we have applied our developed semi-analytical Vlasov solver to study CSR-induced microbunching instability in various recirculation arc designs, including low-energy and high-energy recirculation arcs and medium-energy compressor arcs. We proposed and verified the validity of sufficient conditions for effective suppression of CSR-induced microbunching gains in recirculation arcs. The conditions of preferring small β functions at dipoles and of keeping $\psi_{21} \approx m\pi$, with m to be an integer, in consecutive two-dipole

[118]When the modulation wavelength becomes longer, we notice that the free-space CSR impedance models may be invalid when the wall shielding effect becomes important. In that case the radiation shielding should be taken into account when the distance from the beam orbit to the walls $h/2$ satisfies $h \leq (\rho\lambda^2)^{1/3}$. In addition, when the modulation wavelength is comparable to the bunch length, the coasting beam model is no longer valid and finite bunched beam model shall be employed in the microbunching analysis of the long wavelength regime.

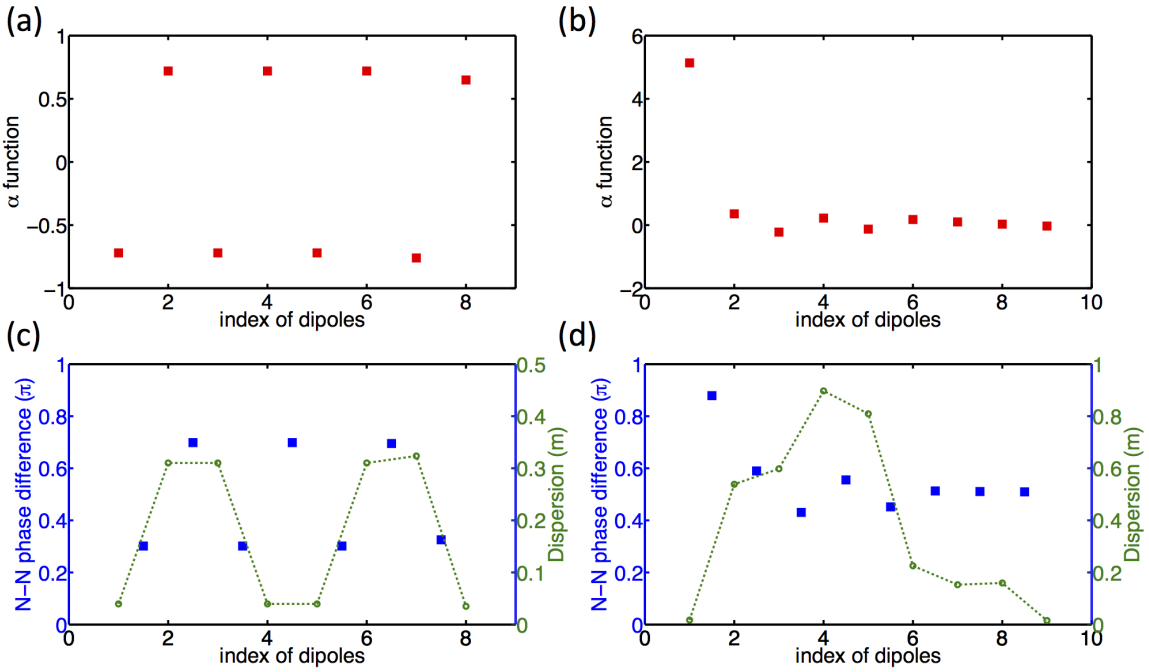

Figure 7.28: Twiss α functions at dipole locations and betatron phase differences ψ_{21} (in unit of π) for FODO compressor arc (a, c) and modulated compressor arc (b, d). The dashed lines in (c) and (d) only help visualize the dispersion within dipoles.

modules, aim for minimizing ξ (hence the kernel function $\mathcal{K}$) through the *relative* momentum compaction function $R_{56}^{s'\to s}$ in a beamline design. Those conditions apply to both periodic and non-periodic magnetic lattices, from low to high energy regimes, and for constant as well as varying bunch length along a beamline. In the most general case of non-achromatic and non-isochronous beamline, the constraint of betatron phase difference can be weakened (other values slightly different from $m\pi$ may be preferred, e.g. see Figs. 7.8 to 7.10), depending on the specific lattice design. In that case, Eq. (7.25) can be used to examine or optimize a beamline design when CSR microbunching becomes a concern.

Since the CSR-induced instability is intensity dependent, our proposed conditions can minimize the CSR-induced microbunching for any given electron bunch peak current. The three sets of example lattices can prove useful for beamline designs at difference energies or bunch currents through the scaling parameter . We have thus investigated the scaling of beam current for maximum CSR gains, and it can serve as a guideline of setting the maximal magnitude of the relative momentum compaction to be designed for similar purposes at different level of bunch currents or beam energies.

We found that, in general, our proposed conditions can be different from the conditions for cancellation or minimization of CSR-induced emittance. For example, compensation of CSR-induced emittance growth usually features some symmetry and can be achieved by separating dipoles (where CSR kicks occur) by π *cell by cell*, but not necessarily needs to be for *every dipole pairs*, as intended in our situation. In this

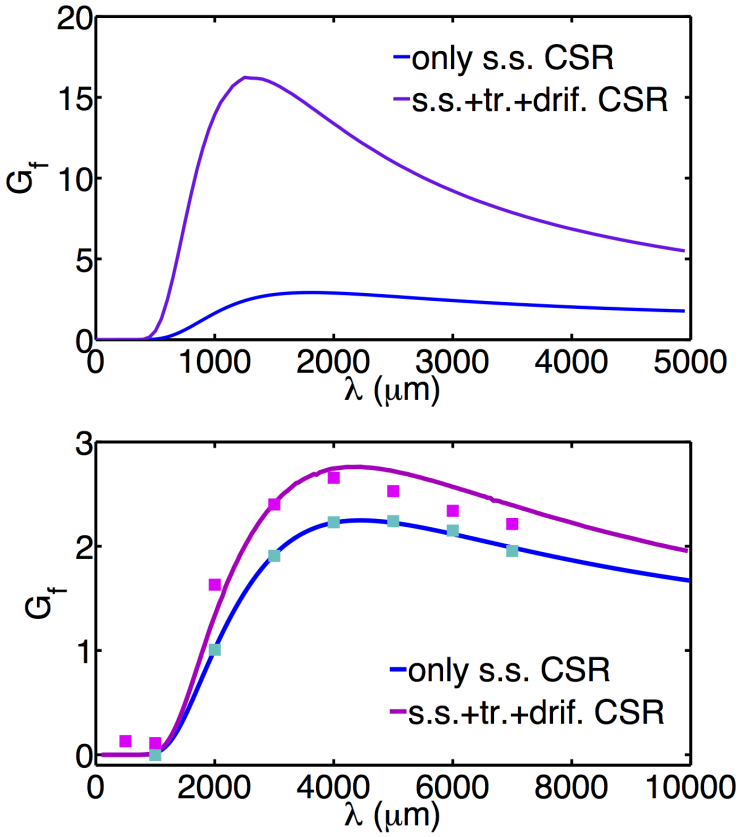

Figure 7.29: CSR microbunching gain spectrum for FODO compressor arc (left) and modulated compressor arc (right). The dots in the right figure are taken from `elegant` by tracking a total of 60-million macroparticles with the initial modulation amplitude set 1%.

sense, our proposed conditions appear stronger, and, in principle, would result in emittance preservation under CSR effect. In addition, CSR-induced microbunching features multistage amplification, as introduced in Chapter 6 (see also Figs. 7.15 and 7.21). To avoid accumulation of effects from those deep-red blocks (i.e. strong energy-density conversion), a lattice with more repetitive cell units (i.e. local isochronicity) can lead to smaller momentum compaction and is therefore preferred. We also note that this study is to some extent empirical and qualitative. In fact, since the CSR-induced microbunching instability is intensity dependent and behaves as an amplifier [152] in a single-pass system, there is not a clear threshold for a lattice design to be immune from the effect.

Last but not least, in the beamlines of interest here, we know the longitudinal space charge (LSC) induced microbunching can be as (or more) important as that induced by CSR, and possibly dominating the overall microbunching gain. We believe the proposed optics conditions for suppression of CSR microbunching can work to the suppression of LSC microbunching as well because we intend to minimize the kernel function $\mathcal{K}$ via $R_{56}^{s'\to s}$ and do not fully exclude the impedance term other than CSR. Although our previous studies support this statement, further investigation is certainly needed. At least, the proposed conditions

Table 7.4: Summary of various mitigation schemes for CSR-induced transverse emittance growth and longitudinal microbunching gains.

Mitigation of CSR or microbunching effects on beam dynamics		
Dimension	Mitigation schemes	Note
Transverse	Cell-to-cell phase matching (Douglas, Di Mitri *et al.*)	optics adjustment
	Beam envelope matching (Hajima)	
	Combination of the above concepts, application to DBA/TBA (Jiao *et al.*) or bunch compressor system (Jing *et al.*)	
	Longitudinal bunch shaping (Mitchell *et al.*)	tailoring initial condition
Longitudinal	Laser heating (Saldin *et al.*, Huang *et al.*)	Landau damping enhancement via σ_δ
	Magnetic mixing chicane (Di Mitri *et al.*)	
	Reversible electron beam heating (Behrens *et al.*)	
	Insertion of dipole pair in an accelerator system (Qiang *et al.*)	Landau damping enhancement of ϵ_x via R_{51} and/or R_{52}
	Optical balance satisfying the proposed conditions	small momentum compactionand local isochronisity (Douglas *et al.*)

here have to be included in the first-iterative beamline designs, similar to the situation of the conditions for suppression or cancellation of CSR-induced emittance growth. However, we notice that a potentially new mechanism, other than what Eq. (7.15) depicts, can drive microbunching instability as well, which is beyond the scope of our current study. Such mechanism, recently identified in Ref. [199], is due to projection of space charge force on transverse-longitudinal dimension (x, z) and is numerically observed to result in longitudinal microbunching amplification in LCLS-II dogleg design. How this transverse space-charge (TSC) induced microbunching can impact recirculating beamlines and whether our proposed conditions for suppression of CSR still work for this TSC microbunching deserve further investigation and would be in our plan.

Finally we note that, being the proposed conditions sufficient, they do not exclude other possible mitigation schemes. To end this chapter, Table 7.4 below summarizes several proposed schemes to mitigate CSR/microbunching effects.

CHAPTER 8
Analysis of Microbunching Structures in Transverse and Longitudinal Phase Spaces

Microbunching instability (MBI) has been a challenging issue in high-brightness electron beam transport for modern accelerators. Our Vlasov analysis of MBI is based on single-pass configuration [79, 81], and the concept of MBI has been understood as a klystron-like amplifier [152]. It has been known that for a cascaded amplifier in circuit electronics, the total amplification gain can be estimated as the product of individual gains. For multi-pass recirculation or a long beamline in an accelerator facility, the intuitive argument of quantifying MBI, by successive multiplication of microbunching density gains of sub-beamline sections, was however found to underestimate the overall effect [175, 185]. While this indication does not imply the existing theory is incorrect, we wish to find an improved way to retain the concept of successive multiplication, or to obtain an extended formulation from which we can still *factor out* the MBI analyses of individual sub-beamline sections.

As will be elaborated later, the concept of microbunching gain as a *scalar* quantity will be extended to the concept of microbunching *gain matrix*. The analyses based on concatenation of gain matrices initially aimed to combine both density and energy modulations for a general beamline [175]. Yet, quantification still focuses on characterizing the longitudinal phase space; microbunching structures residing in (x, z) and (x', z) [or (y, z) and (y', z)] was observed in particle tracking simulation. Inclusion of such cross-plane microbunching structures in Vlasov analysis shall be a crucial step to systematically characterize MBI for a beamline complex in terms of concatenating individual beamline segments. From this viewpoint, the previously developed theoretical formulation is incomplete because only initial density modulation is considered (although its evolution along a beamline is self-consistently formulated). To be specific, if we only care about the resultant microbunching density modulation from initial density modulation in an intact beamline, the previous analysis has taken care of it and works with no problem. In the previous theory the intermediate conversions, including the density-energy conversion, as well as the longitudinal-transverse phase space correlation, have all been taken into account during beam transport. Now, when a (long) beamline is cut into pieces and is no longer intact, at the ends of each pieces the MBI gains can be underestimated if only density modulation (of the previous piece) is taken into account for calculation of microbunching gains. In this regard, i.e. if we want to complete the MBI analysis while retain the concept of concatenating MBI gains from sub-beamline sections, it becomes necessary to extend the previously developed theoretical formulation to include more aspects of MBI.

In this chapter we would derive explicit formulas to include the microbunching structures occurring in longitudinal and transverse phase spaces. Using these generalized formulas, we studied an example recirculation ring lattice [52] and found the microbunching gains calculated from multiplication of concatenated

gain matrices can be considered as upper limit to the start-to-end gains.

All of the work in this Chapter has been separately presented in 7th International Particle Accelerator Conference (IPAC), May 8-13, 2016, Busan, Korea, with the title *Combination of density and energy modulation in microbunching analysis* (TUPOR020), and in 2016 North American Particle Accelerator Conference (NAPAC), October 9 - 14, 2016, Chicago, Illinois, with the title *Analysis of microbunching structures in transverse and longitudinal phase spaces* (THPOA35).

8.1 Introduction and Motivation

Theoretical formulation of MBI has been developed both in single-pass [152, 79, 81] and in storage-ring [164, 32] systems. Hetfeis, Stupakov, and Krinsky [79] had derived a linear integral equation in terms of the density modulation (or, the bunching factor). Huang and Kim [81] obtained the integral equation in a more concise way and outlined the microbunching due to initial energy modulation. Those have been re-derived and extended in Chapter 3 and become the building block for the subsequent studies.

To quantify MBI in a beam transport system, we estimate the microbunching amplification factor (or, gain) along the beamline. For a long transport line of a recirculation machine, people tend to treat the microbunching problem as a single-pass system. More commonly, concatenations of sub-beamline sections were studied and the overall microbunching gain is speculated as the multiplication of gains from individual subsections. Though this concatenation approach seems intuitive, we need a more rigorous and detailed justification of its validity. Our previous work, which takes both density (z) and energy (z, δ) modulations in the longitudinal beam phase-space distribution, had shown that a mere product of microbunching gains from individual subsections could underestimate the overall effect (i.e. smaller than the start-to-end gain). This means that the previously developed theoretical formulation can be incomplete. If we only care about the resultant microbunching density gain from initial density modulation, i.e. density-to-density modulation, the previous analysis has taken care of it. In the previous theory the density-energy conversion, as well as the longitudinal-transverse phase space correlation, has been taken care during/within excursion of beam transport. However, when a (long) beamline is cut into pieces, at the end of each piece MBI gains can be underestimated if only density modulation (of the previous piece) is taken into account for calculation of microbunching gains. In this regard, i.e. if we would like to concatenate individual microbunching analyses from sub-beamline sections, it becomes necessary to extend the previously developed theoretical formulation to include more aspects of MBI. This motivates development of the concept of gain matrix, as detailed in Sec. 8.2. In what follows we take a further step. We consider the situation where microbunching structures residing in transverse-longitudinal dimension (x, z) and (x', z) [or (y, z) and (y', z)] can be quantified, and derive a set of governing equations for the microbunching evolution in terms of density, energy, transverse-longitudinal modulations along a general beamline lattice. Then we study an example of recirculating beamline [52] in Sec. 8.4. From the numerical results, we have some interesting observations and have found such combined

analysis can give more information than the previous treatment. Although the formulations seem to require further extension, the microbunching modulations calculated from multiplication of concatenated gain matrices can be considered as upper limit to the start-to-end gains. Comparison of the results with `elegant` tracking has given qualitative agreement. Extension of this study to include more aspects of microbunching can be possible future work.

8.2 Concept of gain matrix

As outlined in the previous section and in Chapter 3, it is found that the way people tend to estimate the overall/total microbunching (density) gain by direct multiplication of individual gains from sub-beamline sections can result in underestimation [Eq. (8.1)]. The reason is the microbunching structure residing in the beam may not be only the density modulation in the longitudinal z coordinate at the end of a sub-beamline section. The previous developed theoretical formulation takes care of all possible energy-density conversions, as well as the longitudinal-transverse correlation, in the presence of (only) longitudinal collective interactions. However the consideration is only valid during beam transport within a beamline. The derivation does not ensure the validity if we estimate total microbunching gain for a long beamline by directly multiplying the calculated microbunching gains from individual sub-beamline sections. We have already known that the resultant microbunching effects on beam phase space distribution lead to not only the modulation in z, i.e. density modulation, but also in other subspace(s) of beam 6-D phase space dimension, e.g. in (z, δ), (x, z), (x', z) and etc.

$$G_{\text{total}} = \prod_{q=1}^{N} G_q = G_1 G_2 G_3 ... G_N \tag{8.1}$$

The top row of Fig. 8.1 illustrates the concept of direct multiplication, where each sub-beamline section is characteristic of one number, the amplification ratio (or the gain)[119]. Now that we have known the microbunching can occur in other aspects of beam phase space modulations, it is natural that we are tempted to develop the aforementioned concept of estimating overall microbunching effects. Instead of using a number, we now assign a state vector $\mathbf{V}$ to each sub-beamline section. Each element in the vector $\mathbf{V}$ represents a type of phase space modulation. The "transport" of amplification ratio or the gain now evolves from a number to a matrix. The total gain matrix of a (long) beamline can be evaluated as

$$\mathcal{G}_{\text{total}} = \mathcal{G}_N ... \mathcal{G}_3 \mathcal{G}_2 \mathcal{G}_1 \tag{8.2}$$

where $\mathcal{G}_i$ represents the gain matrix for i-th sub-beamline section[120]. The bottom row of Fig. 8.1 illustrates this extended concept. It is trivial that when $\mathbf{V} \to b$, $\mathcal{G} \to G$; Eq. (8.2) is reduced to Eq. (8.1).

[119] It is a number/scalar, depending on the initial modulation wavelength, because we have made the coasting beam approximation.

[120] Not to be confused with the individual stage gain, as defined in Eq. (6.10).

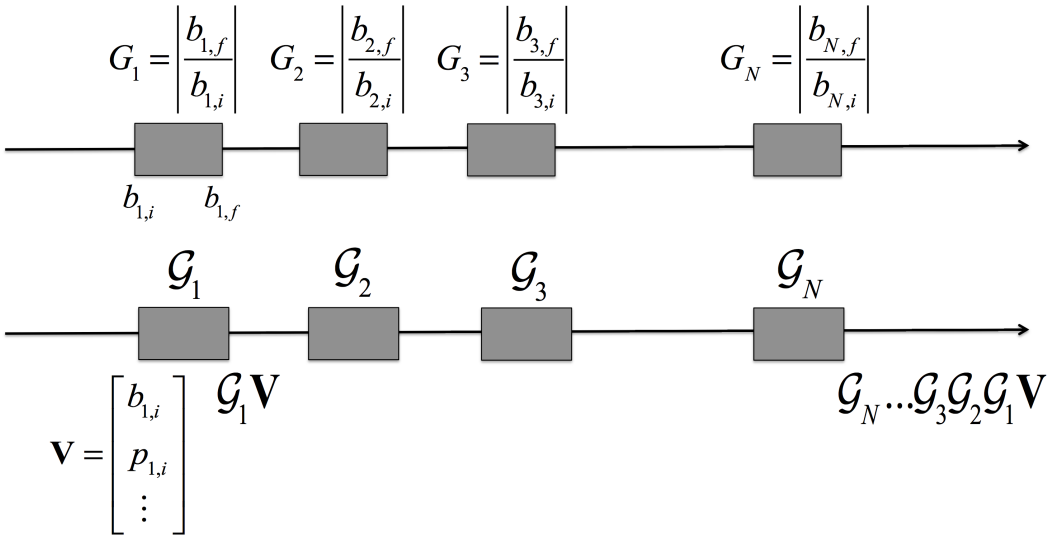

Figure 8.1: Illustration of concepts of scalar gain multiplication (top) and gain matrix (bottom).

In what follows we try to consolidate this extended concept by constructing the state vector $\mathbf{V}$. We note that the number of elements of $\mathbf{V}$ can vary; it depends on how many type(s) of the beam phase space modulations we care about. Below we try to include the modulations in z coordinate [density modulation], (z, δ) [the longitudinal phase space modulation], (x, z) [the transverse-longitudinal configuration space], (x', z) and/or (y, z), and (y', z), as we have observed the microbunched structures in these subspaces of 6-D beam phase space. These observations do not exclude possibilities in other subspaces. In fact, what we consider in this dissertation only involves the longitudinal collective interaction. This may limit the microbunched structures residing in a few numbers of subspaces.

Having identified four possible types of microbunching structures, they can be summarized by Eqs. (8.3) to (8.6). The superscripts on the right hand sides (RHS) of the equations indicate the source of modulation. Notice that the resultant modulations of each type can be transformed by and contribute to other aspects of modulations. For simplicity, we assume the accelerator system is planar in horizontal x and longitudinal z degrees of freedom. Inclusion of y dimension can be straightforward.

$$b(k_z; s) = b^{(z)}(k_z; s) + b^{(\delta,z)}(k_z; s) + b^{(x,z)}(k_z; s) + b^{(x',z)}(k_z; s) \tag{8.3}$$

$$p(k_z; s) = p^{(z)}(k_z; s) + p^{(\delta,z)}(k_z; s) + p^{(x,z)}(k_z; s) + p^{(x',z)}(k_z; s) \tag{8.4}$$

$$a_x(k_z; s) = a_x^{(z)}(k_z; s) + a_x^{(\delta,z)}(k_z; s) + a_x^{(x,z)}(k_z; s) + a_x^{(x',z)}(k_z; s) \tag{8.5}$$

$$a_{x'}(k_z; s) = a_{x'}^{(z)}(k_z; s) + a_{x'}^{(\delta,z)}(k_z; s) + a_{x'}^{(x,z)}(k_z; s) + a_{x'}^{(x',z)}(k_z; s) \tag{8.6}$$

Before proceeding to the next section, let us estimate the total number of equations/expressions we need for this extension. As elaborated in Chapter 3, for each type of modulation, we require one integral

equation that governs the collective interactions, i.e. Eqs. (3.27) to (3.30). Therefore, four integration equations are required. We also need an analytical expression for each type of modulation resulting from one specific modulation. Note that we would have a total of $4 \times 4 = 16$ expressions, because the evolution of each type of modulation can originate from four different types of modulations and we have a total of four equations of motion (i.e. four different types of evolutions), i.e. Eq. (3.53)[121].

For convenience, let us repeat the following definitions of various aspects of phase space modulations for subsequent discussion:

$$b(k_z;s) = \frac{1}{N}\int d\mathbf{X}\ f(\mathbf{X};s)e^{-ik_z(s)z_s} \tag{8.7}$$

$$p(k_z;s) = \frac{1}{N}\int d\mathbf{X}\ \left(\delta_s - hz_s\right) f(\mathbf{X};s)e^{-ik_z(s)z_s} \tag{8.8}$$

where h characterizes the correlation between $z-\delta$,

$$a_x(k_z;s) = \frac{1}{N}\int d\mathbf{X}\ \left(x_s\right) f(\mathbf{X};s)e^{-ik_z(s)z_s} \tag{8.9}$$

$$a_{x'}(k_z;s) = \frac{1}{N}\int d\mathbf{X}\ \left(x_s{}'\right) f(\mathbf{X};s)e^{-ik_z(s)z_s} \tag{8.10}$$

The four types of initial modulations are quantified as

$$b_0(k_0;0) \equiv \frac{n_0}{N}\int dz_0 \left(\frac{\Delta n(z_0)}{n_0}\right) e^{-ik_0z_0} \tag{8.11}$$

$$p_0(k_0;0) \equiv \frac{n_0}{N}\int dz_0\ \Delta\delta(z_0)e^{-ik_0z_0} \tag{8.12}$$

$$a_{x0}(k_0;0) \equiv \frac{n_0}{N}\int dz_0\ \Delta x_0(z_0)e^{-ik_0z_0} \tag{8.13}$$

$$a_{x'0}(k_0;0) \equiv \frac{n_0}{N}\int dz_0\ \Delta x_0'(z_0)e^{-ik_0z_0} \tag{8.14}$$

Figure 8.2 gives a conceptual illustration to the modulations described by Eqs. (8.7) to (8.10) [or Eqs. (8.11) to (8.14)].

Below we would consider how these different phase-space modulations evolve in the presence of collective effects. The detailed derivation for density modulation has been shown in Sec. 3.3. For the remaining cases they are similar and not shown here but only the resultant formulas are summarized. The four integral

[121] There will be a total of $6 \times 6 = 36$ expressions and 6 integral equations if we include y and y'.

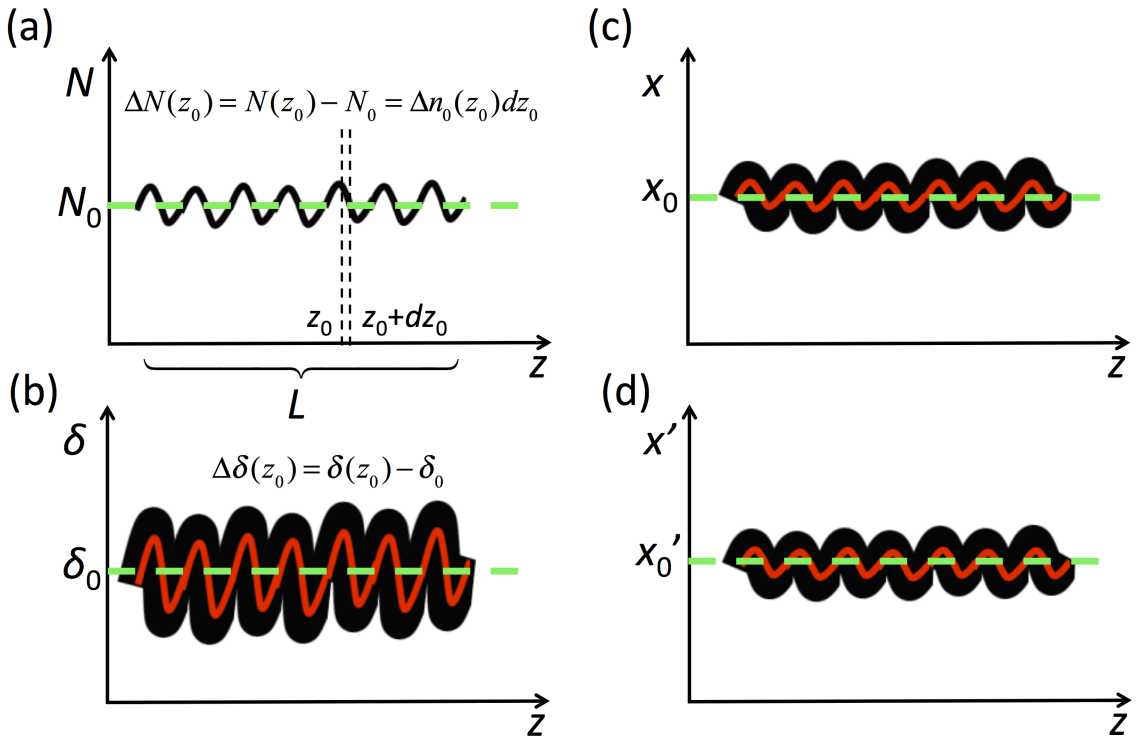

Figure 8.2: Illustration of various microbunched modulations. (a) density modulation; (b) energy modulation; (c) transverse-longitudinal (x, z) modulation, and (d) transverse-longitudinal (x', z) modulation. The green dashed line represents the (averaged) constant offset and the red solid line indicates the (averaged) sinusoidal modulation.

equations governing $b(k_z; s)$, $p(k_z; s)$, $a_x(k_z; s)$, and $a_{x'}(k_z; s)$ are, respectively,

$$b\left(k_z; s\right) = b_0\left(k_z; s\right) + \int_0^s d\tau K\left(\tau, s\right) b\left(k_z; \tau\right) \tag{8.15}$$

$$p(k_z; s) = p_0(k_z; s) + \int_0^s d\tau M(\tau, s) b(k_z; \tau) - \int_0^s d\tau L(\tau, s) b(k_z; \tau) \tag{8.16}$$

$$a_x(k_z; s) = a_{x0}(k_z; s) + \int_0^s d\tau A(\tau, s) b(k_z; \tau) \tag{8.17}$$

$$a_{x'}(k_z; s) = a_{x'0}(k_z; s) + \int_0^s d\tau B(\tau, s) b(k_z; \tau) \tag{8.18}$$

where the kernel functions are expressed as

$$K(\tau, s) = ik_z(s) \frac{I_b(\tau)}{\gamma_0 I_A} R_{56}(\tau \to s) Z_0^{\parallel}(k_z; \tau) \left\{\text{L.D.}; \tau, s\right\} \tag{8.19}$$

$$M(\tau,s)=\frac{I_b(\tau)}{\gamma_0 I_A}\left\{ik_z^2(s)\sigma_\delta^2 R_{56}(\tau\to s)U(s,\tau)\right\}Z_0^{\parallel}(k_z(\tau);\tau)\left\{\text{L.D.};\tau,s\right\} \tag{8.20}$$

$$L(\tau,s)=\frac{I_b(\tau)}{\gamma_0 I_A}Z_0^{\parallel}(k_z(\tau);\tau)\left\{\text{L.D.};\tau,s\right\} \tag{8.21}$$

$$\begin{aligned}A(\tau,s)=&\frac{I_b(\tau)}{\gamma_0 I_A}Z_0^{\parallel}(k_z(\tau);\tau)\\&\times\left\{\begin{array}{l}i\hat{R}_{16}(\tau\to s)-k_z^2(s)\hat{R}_{56}(\tau\to s)\times\\ \left[\begin{array}{ll}\hat{R}_{11}(\tau\to s) & \left[\begin{array}{l}\hat{R}_{11}(\tau)\epsilon_{x0}\left(W\alpha_{x0}-V\beta_{x0}\right)+\\ \hat{R}_{12}(\tau)\epsilon_{x0}\left(W\gamma_{x0}-V\alpha_{x0}\right)-\\ \hat{R}_{16}(\tau)\sigma_{\delta0}^2U\end{array}\right]+\\ \hat{R}_{12}(\tau\to s) & \left[\begin{array}{l}\hat{R}_{21}(\tau)\epsilon_{x0}\left(W\alpha_{x0}-V\beta_{x0}\right)+\\ \hat{R}_{22}(\tau)\epsilon_{x0}\left(W\gamma_{x0}-V\alpha_{x0}\right)-\\ \hat{R}_{26}(\tau)\sigma_{\delta0}^2U\end{array}\right]-\hat{R}_{16}(\tau\to s)\sigma_{\delta0}^2U\end{array}\right]\end{array}\right\}\left\{L.D.;s,\tau\right\}\end{aligned} \tag{8.22}$$

$$\begin{aligned}B(\tau,s)=&\frac{I_b(\tau)}{\gamma_0 I_A}Z_0^{\parallel}(k_z(\tau);\tau)\\&\times\left\{\begin{array}{l}i\hat{R}_{26}(\tau\to s)-k_z^2(s)\hat{R}_{56}(\tau\to s)\times\\ \left[\begin{array}{ll}\hat{R}_{21}(\tau\to s) & \left[\begin{array}{l}\hat{R}_{11}(\tau)\epsilon_{x0}\left(W\alpha_{x0}-V\beta_{x0}\right)+\\ \hat{R}_{12}(\tau)\epsilon_{x0}\left(W\gamma_{x0}-V\alpha_{x0}\right)-\\ \hat{R}_{16}(\tau)\sigma_{\delta0}^2U\end{array}\right]+\\ \hat{R}_{22}(\tau\to s) & \left[\begin{array}{l}\hat{R}_{21}(\tau)\epsilon_{x0}\left(W\alpha_{x0}-V\beta_{x0}\right)+\\ \hat{R}_{22}(\tau)\epsilon_{x0}\left(W\gamma_{x0}-V\alpha_{x0}\right)-\\ \hat{R}_{26}(\tau)\sigma_{\delta0}^2U\end{array}\right]-\hat{R}_{26}(\tau\to s)\sigma_{\delta0}^2U\end{array}\right]\end{array}\right\}\left\{L.D.;s,\tau\right\}\end{aligned} \tag{8.23}$$

$$\left\{\text{L.D.};\tau,s\right\}\equiv e^{-\frac{k_0^2\epsilon_{x0}\beta_{x0}}{2}\left(V(s,\tau)-\frac{\alpha_{x0}}{\beta_{x0}}W(s,\tau)\right)^2-\frac{k_0^2\epsilon_{x0}}{2\beta_{x0}}W^2(s,\tau)-\frac{k_0^2\sigma_{\delta0}^2}{2}U^2(s,\tau)} \tag{8.24}$$

and

$$\begin{aligned} V(s,\tau) &\equiv C(s)\hat{R}_{51}(s) - C(\tau)\hat{R}_{51}(\tau) \\ W(s,\tau) &\equiv C(s)\hat{R}_{52}(s) - C(\tau)\hat{R}_{52}(\tau) \\ U(s,\tau) &\equiv C(s)\hat{R}_{56}(s) - C(\tau)\hat{R}_{56}(\tau) \end{aligned} \tag{8.25}$$

In the above expressions, the relative transport matrix elements can be evaluated by the matrix multiplication,

$$\mathbf{R}(\tau \to s) = \mathbf{R}(s)\mathbf{R}^{-1}(\tau) \tag{8.26}$$

The explicit expressions of Eq. (8.26) can be found in Appendix A (Sec. A.3). Here we remind that the beam phase-space distribution is assumed to uniform in z (with sinusoidal modulation atop) and Gaussian over the remaining phase space coordinates. The perturbed distribution function is assumed to have the following form,

$$f_0(\mathbf{X}_0) = \frac{n_0 + \Delta n_0(z_0)}{(2\pi)\,\epsilon_{x0}\sqrt{2\pi}\sigma_{\delta 0}} e^{-\frac{(x_0+\Delta x_0(z_0))^2+(\beta_{x0}(x_0{}'+\Delta x_0'(z_0))+\alpha_{x0}(x_0+\Delta x_0(z_0)))^2}{2\epsilon_{x0}\beta_{x0}} - \frac{(\delta_0 - hz_0+\Delta\delta(z_0))^2}{2\sigma_{\delta 0}^2}} \tag{8.27}$$

where the individual perturbations are assumed to be small compared with the unperturbed one. The pure-optics terms $b_0(k_z;s)$, $p_0(k_z;s)$, $a_{x0}(k_z;s)$, and$a_{x\prime 0}(k_z;s)$, contributed from separate phase space modulations [see also Eq. (3.53)], can be analytically evaluated and summarized in Appendix A [Eqs. (A.18) to (A.33), see also Eqs. (8.3) to (8.6)].

At each location, the modulations can be recorded as a *state vector*, defined as

$$\mathbf{V}(s) \equiv \left[b(k_z;s)\ p(k_z;s)\ a_x(k_z;s)\ a_{x'}(k_z;s)\right]^T \tag{8.28}$$

where each element is evaluated by Eqs. (8.3) to (8.6). The aforementioned formulas can be expressed in terms of Eq. (8.28) in a vector-matrix form

$$\mathbf{V}(s) = \mathcal{G}_k \mathbf{V}^{(0)}(s) \tag{8.29}$$

where the gain matrix is

$$\mathcal{G}_k = \begin{pmatrix} (\mathbf{1}-\mathbf{K})^{-1} & \mathbf{0} & \mathbf{0} & \mathbf{0} \\ (\mathbf{M}-\mathbf{L})\,(\mathbf{1}-\mathbf{K})^{-1} & \mathbf{1} & \mathbf{0} & \mathbf{0} \\ \mathbf{A}(\mathbf{1}-\mathbf{K})^{-1} & \mathbf{0} & \mathbf{1} & \mathbf{0} \\ \mathbf{B}(\mathbf{1}-\mathbf{K})^{-1} & \mathbf{0} & \mathbf{0} & \mathbf{1} \end{pmatrix} \tag{8.30}$$

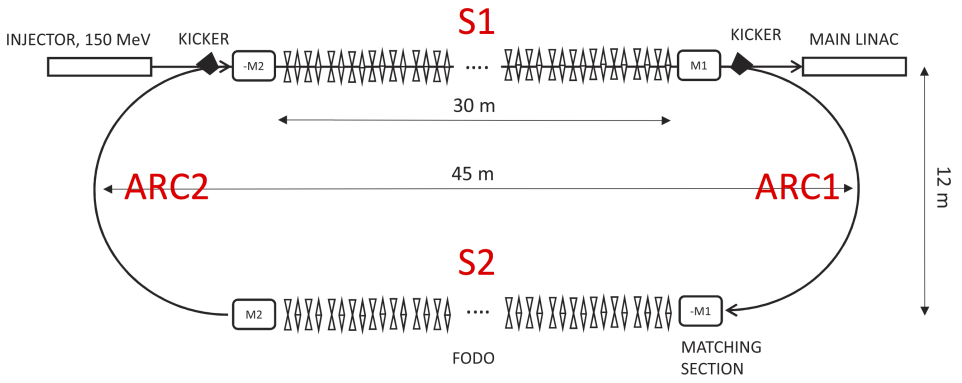

Figure 8.3: Schematic layout of the recirculating beamline (not to scale), from Ref. [52].

Here the subscript k denotes the whole matrix is evaluated in a specific modulation wavelength. We also remind that the superscript (0) in Eq. (8.30) stands for the state vector in the absence of collective effect, instead of initial state vector.

8.3 A recirculation ring as example lattice

In this section, we would apply the generalized formulation, Eq. (8.29), to an example of recirculating machine [52]. This recirculating beamline consists of two 180-deg arcs and the design is based on that outlined in Ref. [58] (also see Sec. 7.4). One of the two identical arcs is composed of four triple-bend-achromatic (TBA) units. The arcs are achromatic and quasi-isochronous. Let us separate this machine into four pieces: S1, ARC1, S2, and ARC2 (see Fig. 8.3). In this example, the beam is assumed 150 MeV in energy, peak bunch current ~60 A, with normalized emittance 0.4 μm and relative energy spread 1.33×10^{-5}. Figure 8.4 shows Twiss and momentum compaction functions along the beamline. For simplicity only steady-state CSR effect is included.

First, let us examine the difference depicted in Fig. 8.1. In the discussion we would estimate only the density modulations at the end of the beamline (ARC2) but begin from different sub-beamline sections. Then we compare the obtained results from the above different concatenations. Let us illustrate the difference/underestimation of direct multiplication from start-to-end calculation, as shown in Fig. 8.5. Again in this figure only initial density modulation is included. The red and dashed green curves represent the CSR microbunching (density) gain spectra, which are identical because the two arcs are the same. The blue curve, evaluated as the product of the red and dashed green curves, should be the resultant gain spectral curve if we apply the intuitive argument for microbunching gain estimation. It is found that the blue curve is smaller than the resultant gains evaluated from start to end (black curve). Later we would investigate the information missed in the intuitive way of gain estimation.

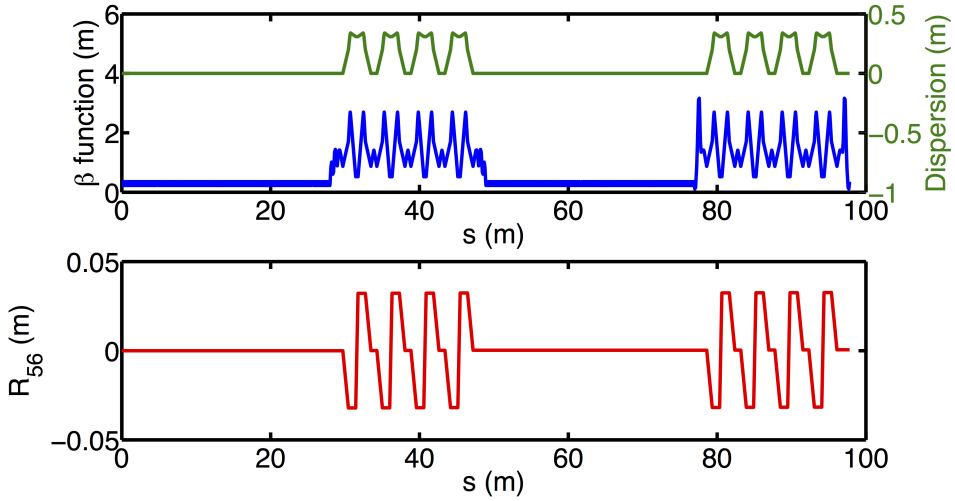

Figure 8.4: Twiss and momentum compaction functions along the beamline.

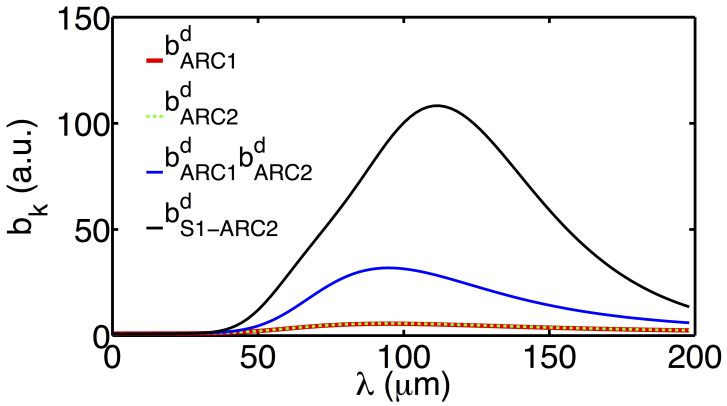

Figure 8.5: Comparison of density modulation spectra via start-to-end (black curve) and direct-multiplication (blue) consideration. Only initial density modulation is included.

Let us now consider both energy and density modulations in the calculation. Consider the simplest case shown in Fig. 8.6, where the modulations evolve in the absence of collective effects (i.e. pure optics). The various concatenations of the matrices $\mathcal{G}$ from sub-beamline sections match well with that of the start-to-end case. This appears in our intuitive expectation, though there is minuscular deviation among them. Now we include steady-state CSR, which only occurs in ARC1 and ARC2. Figure 8.7 shows the resultant density and energy modulation spectra at the end of the beamline, assuming only initial density modulation exists. From the figure, we can see differences between the start-to-end (black) and S2-ARC (light green and blue) curves. From Figs. 8.7, it is found that even though both the density and energy modulations are included, the resultant modulations (either density or energy) are underestimated compared with start-to-end calculations. We claim that the differences originate from correlation between ARC1 and ARC2. That is to say, for S2-ARC2 case, the initial conditions used in our analysis $[\mathbf{b}\ \mathbf{p}]^T$, given at the exit of ARC1, are

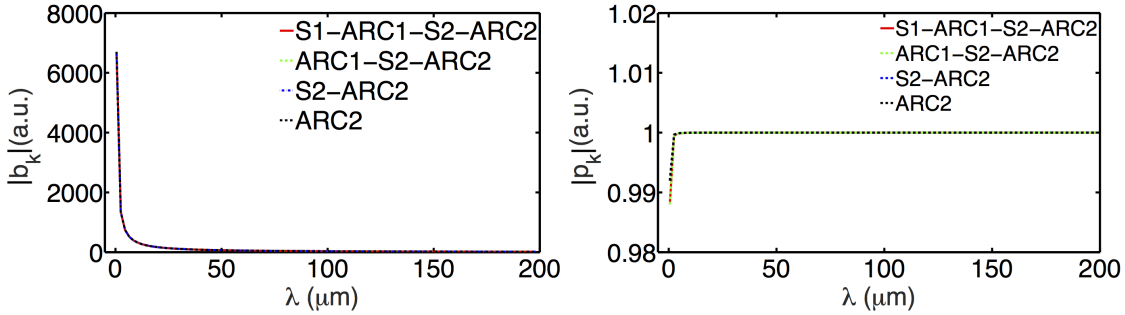

Figure 8.6: Density (left) and energy (right) modulation spectra for pure optics. Both initial density and energy modulations are included at the beginning.

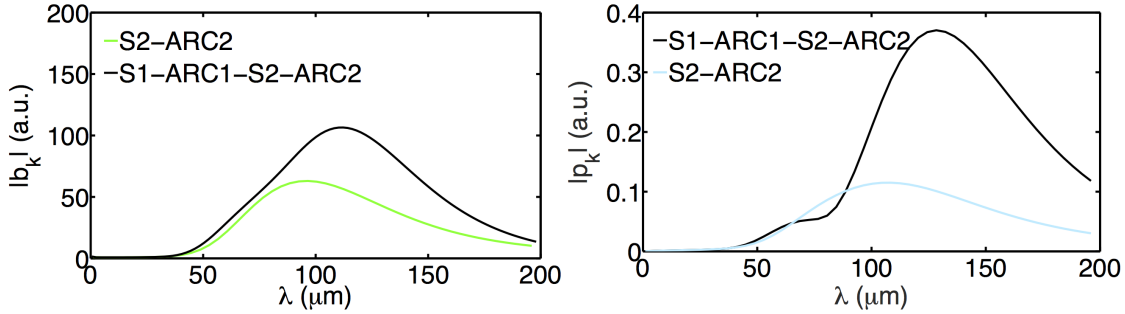

Figure 8.7: Density (left) and energy (right) modulation spectra including CSR effect. Only initial density modulation is included.

insufficient to fully describe the CSR interaction occurred upstream in ARC1.

To confirm this claim, we run a particle tracking simulation using `elegant`. In the tracking simulation, it is observed that such correlation information resides in the 4-D/6-D beam phase-space distributions at the exits of every subsections of the beamline. For qualitative comparison, let us consider the two cases in particle tracking:

(i) start-to-end tracking (S1-ARC1-S2-ARC2);

(ii) S2-ARC2 with initial longitudinal phase-space conditions deduced from those of (i) at the exit of ARC1 while the initial transverse phase-space distribution is set as that of pure optics at the exit of ARC1.

Note that Case (ii) would be different from Case (i) in that the transverse-longitudinal correlation has been neglected. To be consistent, only steady-state CSR is included in the tracking simulation. For Case (i), we assume 5% initial density modulation at 100 μm in the particle tracking. For Case (ii), to obtain the initial conditions (at the entrance of S2), we need to identify Twiss functions at the exit of ARC1 to characterize the transverse phase-space distribution but retain the longitudinal phase-space distribution of Case (i) as input at this particular position. Figure 8.8 compares the current density distributions for both

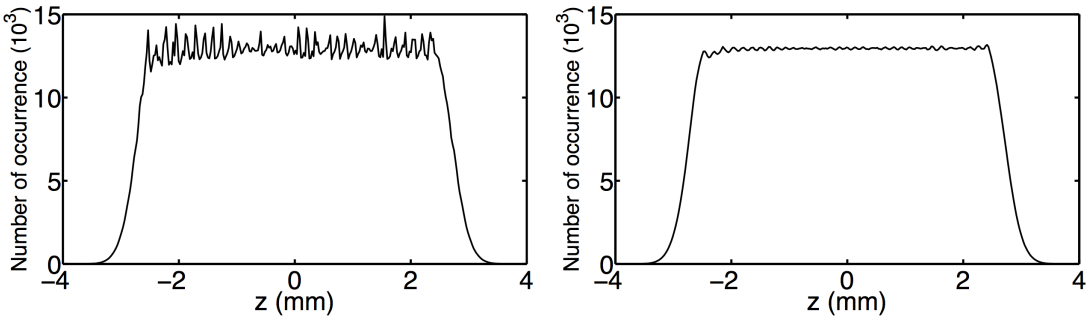

Figure 8.8: The bunch current profile for case (i) (left) and (ii) (right) at the end of beamline.

cases at the end of the beamline. The obvious difference has qualitatively confirmed our Vlasov results; the start-to-end (S1-ARC1-S2-ARC2) calculations are larger (and make more sense) than those starting from midway (S2-ARC).

Further investigation of where the difference originates, it was found a microbunching structure resides in (x, z) and (x', z) at the exits of ARC1 and of the beamline, as shown in Fig. 8.11 to 8.13 below, when we include transverse-longitudinal modulations into the analysis.

Below we would estimate both the density and energy modulations at the end of the beamline but now incorporate the transverse-longitudinal correlations. Let us still begin from two different scenarios; one is start-to-end case [S1-ARC1-S2-ARC2] and the other is mid-to-end case [S2-ARC2]. Consider the following combinations:

(i) start-to-end case, with initial density modulation, $\mathbf{V}(0) \equiv [1\ 0\ 0\ 0]^T$;

(ii) start-to-end case, with initial energy modulation, $\mathbf{V}(0) \equiv [0\ 1\ 0\ 0]^T$;

(iii) mid-to-end case, the initial condition to S2 takes the value at the exit of ARC1, $\mathbf{V}(s2) \equiv [b(k_z; s_2)\ p(k_z; s_2)\ a_x(k_z; s_2)\ a_{x'}($ for case (i) and (ii), based on the present 4-D theory; (iv) mid-to-end case, the initial condition to S2 takes the value at the exit of ARC1, $\mathbf{V}(s2) \equiv [b(k_z; s_2)\ p(k_z; s_2)]^T$ for case (i) and (ii), based on 2-D theory.

Note that the output state vectors are in general complex quantities. For example, for the resultant density modulation in Eq. (8.3), each *individual* contribution can have different phases. Taking absolute values for all individual contributions, the interference is then ignored and the resultant modulation can be considered as the upper limit. This case is denoted as $G_\chi^{\rm sup} = \sum \left|\chi^{(\omega)}\right|$, where $\omega = (z), (\delta, z), (x, z), (x', z)$, and $\chi = b, p, a_x, a_{x'}$. For comparison, the other case with account of phase information is denoted as $G_\chi = \left|\sum \chi^{(\omega)}\right|$.

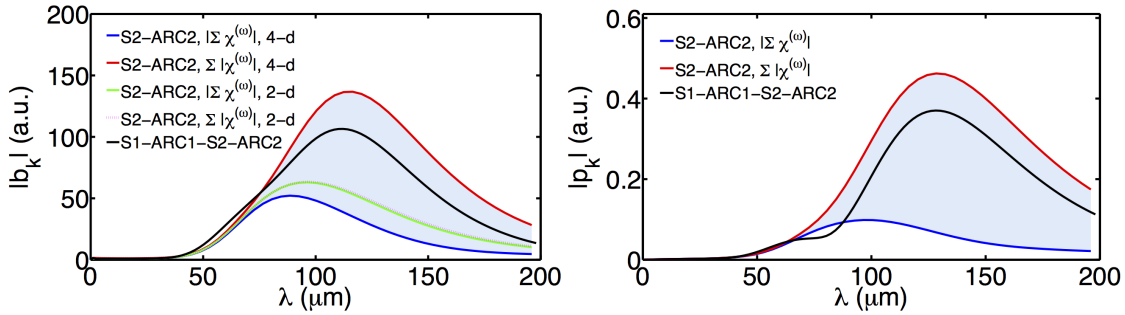

Figure 8.9: Density (left) and energy (right) modulation spectra with initial density modulation.

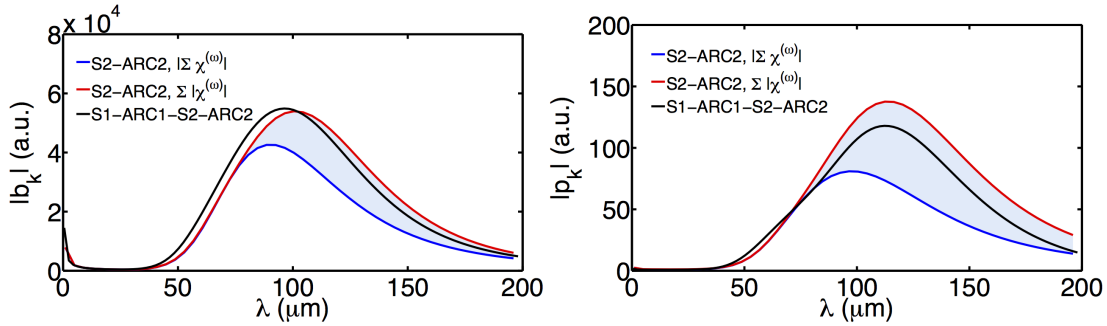

Figure 8.10: Density (left) and energy (right) modulation spectra with initial energy modulation.

For the case of initial density modulation, Fig. 8.9 shows the density and energy modulation spectra at the end of ARC2. From the figure, we can see differences between red and blue curves, both of which are evaluated based on 4-D theory. The red curves, with *output* by taking absolute values for individual contributions, largely give the upper limit. The black curves can be considered as start-to-end gains for the beamline. The blue curves are found to underestimate the overall modulation. Similar results can be observed for the case of initial energy modulation, shown in Fig. 8.10.

In Fig. 8.7, we claimed that the underestimation of the 2-D $[b(k_z; s_2)\ p(k_z; s_2)]^T$ description originates from lack of inclusion of transverse-longitudinal correlations, e.g. (x, z) and/or (x', z) modulations. Now we can estimate the modulation spectra residing in (x, z) and (x', z), shown in Fig. 8.11. To confirm, we used `elegant` to track a beam of particles and indeed observed the microbunching structures in (x, z) and (x, z), shown in Fig. 8.12 and 8.13. By demonstrating the two distinct modulation wavelengths, $\lambda = 50$ and 125 μm, we qualitatively confirm the our Vlasov results.

We make an additional comment in the left panel of Fig. 8.9. In that figure we compared the microbunching (density) gains calculated from three different ways: the start-to-end approach (black curve), the 4-D approach (red and blue curves, from S2 to ARC2) and the 2-D approach (green curve and red dots, from S2 to ARC2). With inclusion of transverse-longitudinal microbunching structures, the calculated (concatenated) gains from sub-beamline section span a range, which largely covers the start-to-end gains.

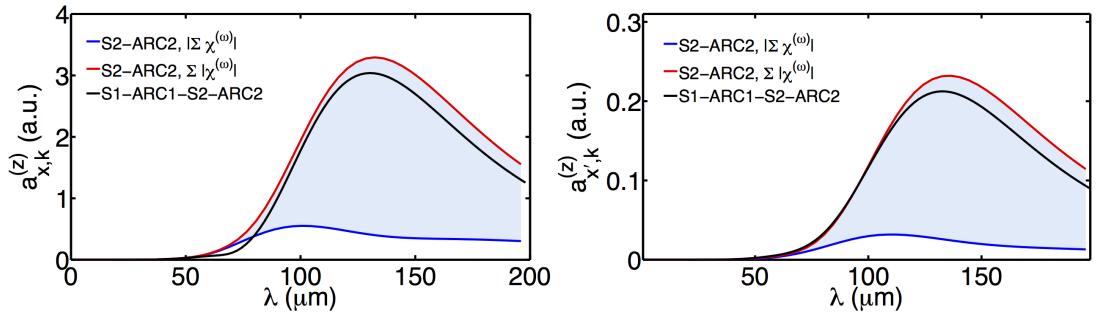

Figure 8.11: $x - z$ (left) and $x' - z$ (right) modulation spectra with initial density modulation.

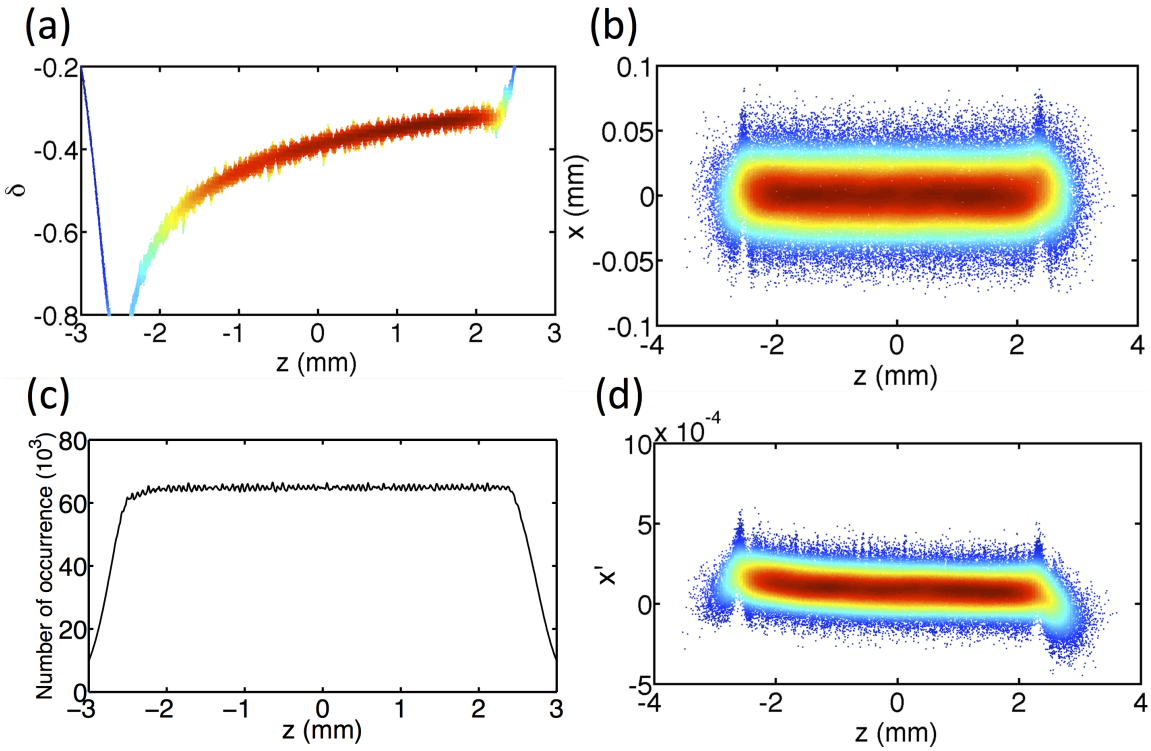

Figure 8.12: Qualitative confirmation of transverse-longitudinal microbunching for $\lambda = 50\mu$m with initial density modulation. The results are recorded at the end of the beamline. The initial density modulation is set 0.005% and 50-million of macroparticles are used.

So far we have investigated the microbunching gain spectra from start-to-end and concatenation methods. Before ending this section, we take a look at the spatial evolution of phase space modulations. A specific modulation wavelength of $\lambda = 120\mu$m is assigned (c.f. Fig. 8.9). Figure 8.14 shows the phase space modulation as a function of s. It becomes clear that the red curve (with 4-D theory, $\mathbf{V} = [b, p, a_x, a_{x'}]^T$) make more consistent estimations to start-to-end results (black curves) than the green curves (with 2-D theory, $\mathbf{V} = [b, p]^T$). Figures 8.15 and 8.16 take a closer look at the modulation evolution in the first and the second arcs.

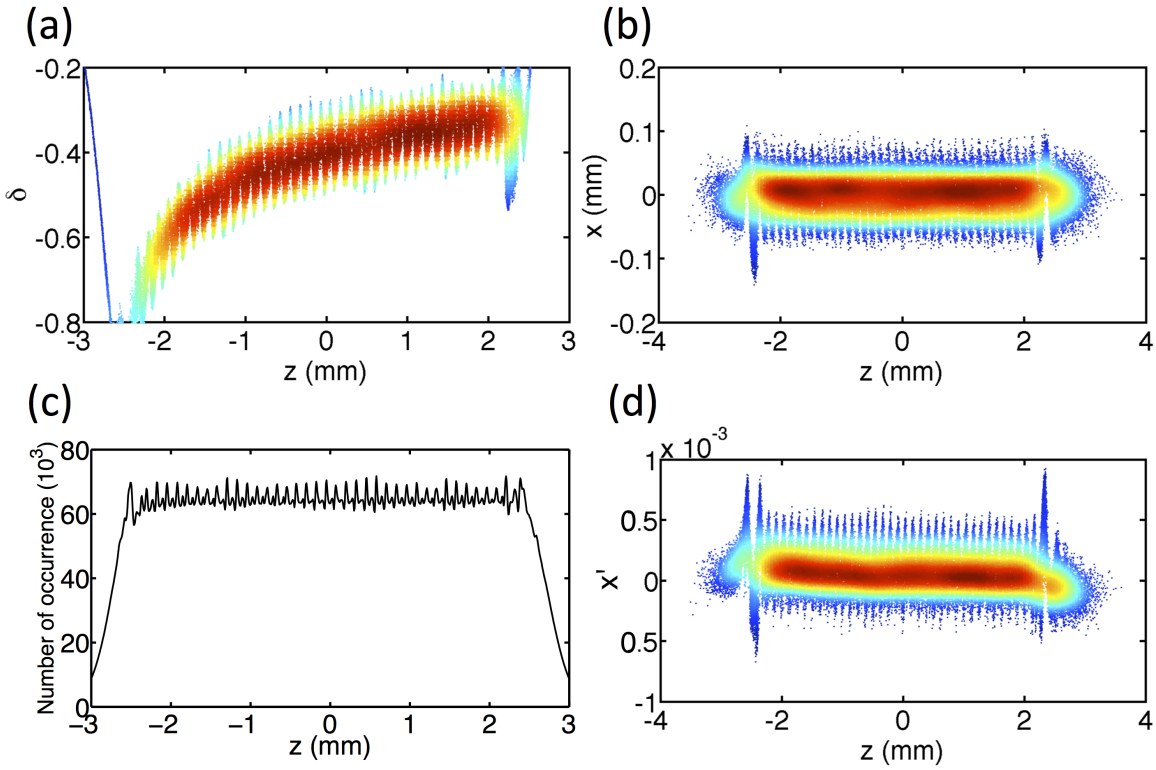

Figure 8.13: Qualitative confirmation of transverse-longitudinal microbunching for $\lambda = 125\mu$m with initial density modulation. The results are recorded at the end of the beamline. The initial density modulation is set 0.005% and 50-million of macroparticles are used.

8.4 Summary and Discussion

In this chapter we summarized a set of governing equations for microbunching modulations in different dimensions, including density, energy, and transverse-longitudinal modulations, and apply to an example of recirculating machine. The semi-analytical Vlasov solutions and tracking simulations agree qualitatively with each other. Although the Vlasov results from concatenated sub-beamline sections do not match well with those obtained directly from the start-to-end Vlasov solution, $G^{\text{sup}} = \sum \left|\chi^{(\omega)}\right|$ gives upper limit for both density, energy, and transverse-longitudinal modulations. In addition, the extended formulations can give us further insights on how upstream beamline sections can accumulate density, energy, and/or transverse-longitudinal microbunching, when the full-ring lattice is not provided. The study in this chapter should also help investigate microbunching dynamics in multi-pass recirculating systems.

Finally, we comment that the aforementioned energy modulation, i.e. microbunched structure in Fig. 8.2 (b), may differ from the energy modulation often cited in the literature. The energy modulation associated with FEL community, especially when it comes to the concepts of HGHG (High Gain Harmonic

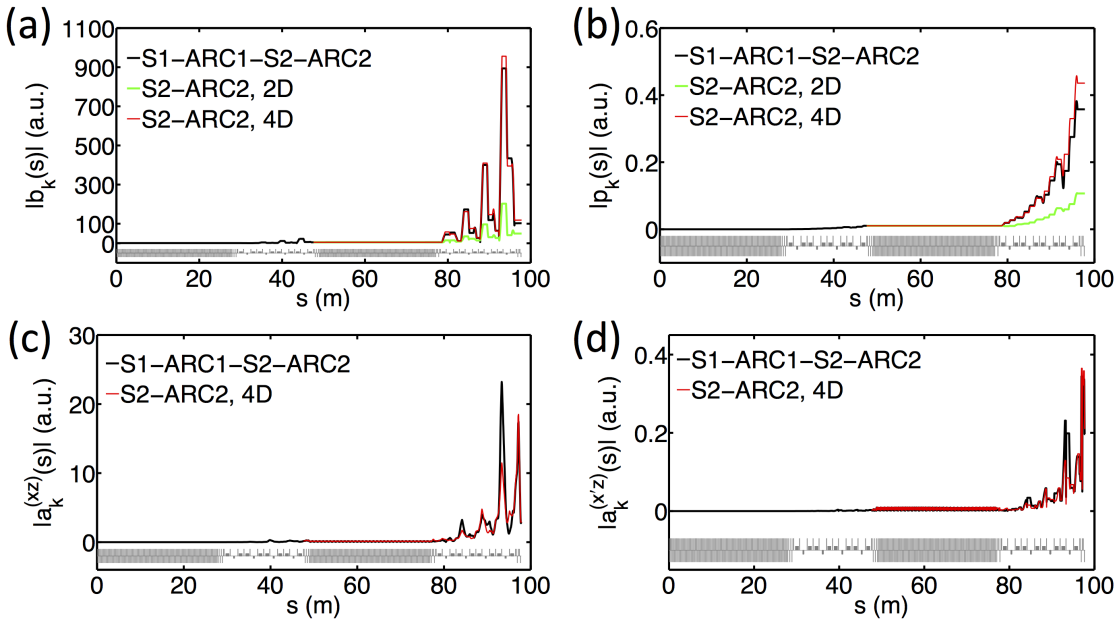

Figure 8.14: Spatial evolution of various phase space modulations: (a) density modulation; (b) energy modulation; (c) transverse-longitudinal (x, z) modulation; (d) transverse-longitudinal (x', z) modulation. In the numerical calculation we have assumed only initial density modulation with $\lambda = 120\mu$m.

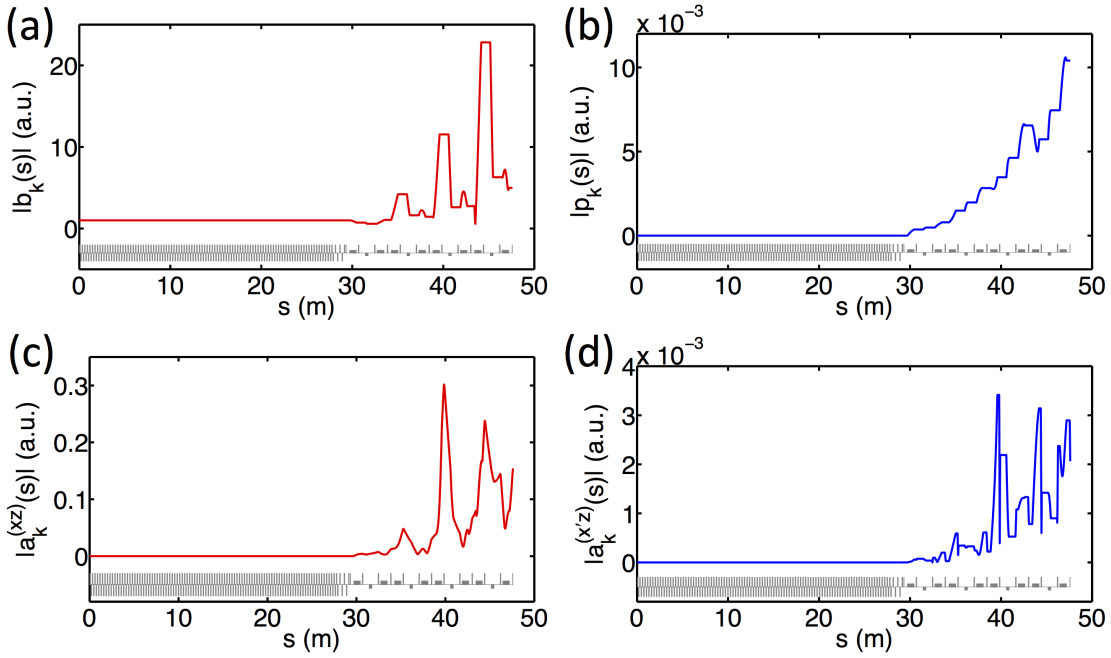

Figure 8.15: Zoom in of Fig. 8.14 for the first half of the ring.

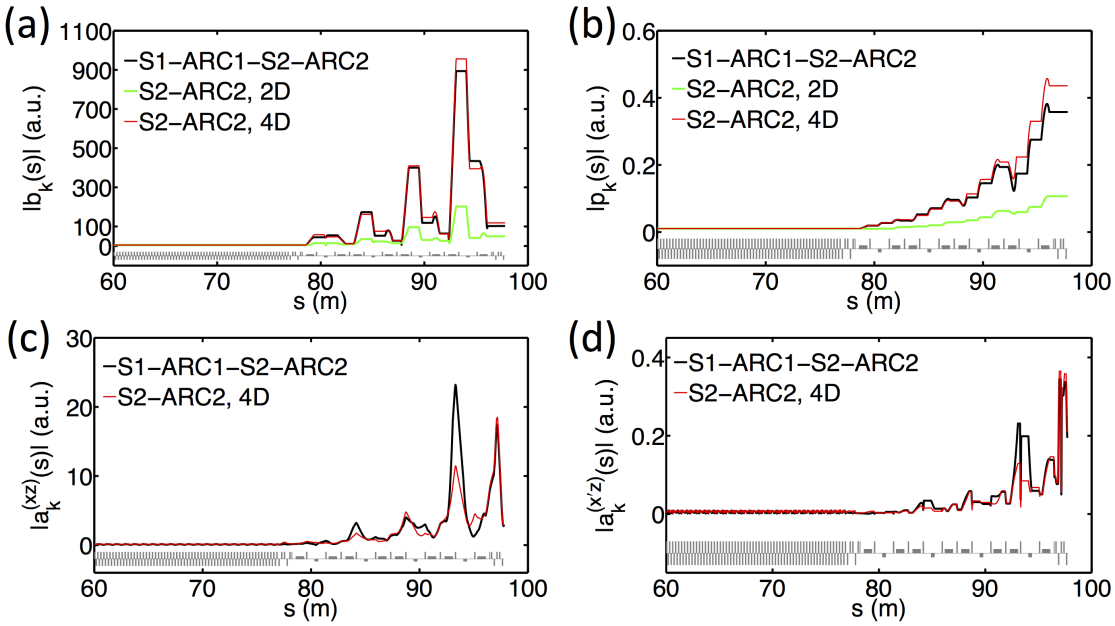

Figure 8.16: Zoom in of Fig. 8.14 for the second half of the ring.

Generation) [216] and EEHG (Echo-Enabled Harmonic Generation) [166], should be characterized as [Note the difference from Eq. (8.8)]

$$p(k_z; s) = \int d\mathbf{X} f(\mathbf{X}; s) e^{-ik_z \delta} \tag{8.31}$$

Such microbunched structure is not included in our analysis.

CHAPTER 9
Vlasov Analysis of Microbunching Instability for Magnetized Beams

For a high-brightness electron beam with high bunch charge traversing a recirculation beamline, coherent synchrotron radiation (CSR) and space charge, particularly the longitudinal space charge (LSC), effects may result in the microbunching instability (MBI) [134, 169, 180]. Both tracking simulation and Vlasov analysis for an early design of Circulator Cooler Ring (CCR) [43] for the Jefferson Lab Electron Ion Collider (JLEIC) reveal significant MBI. It is envisioned that the MBI could be substantially suppressed by using a magnetized beam [46]. By the magnetized beam it means in general the beam has non-zero canonical angular momentum, and is therefore considered to be a transversely coupled beam. In this chapter we intend to generalize the existing Vlasov analysis, originally developed for a non-magnetized beam (or transversely uncoupled beam), to the description of transport of a magnetized beam including relevant collective effects. The new formulation is then employed to confirm prediction of microbunching suppression for a magnetized beam transport in the recirculation arc of a recent JLEIC energy recovery linac (ERL) based cooler design for electron cooling. It is found that the smearing effect in the longitudinal beam phase space originates from the large transverse beam size as a nature of the magnetized beams and becomes effective through the $x - z$ correlation when the correlated distance is larger than the microbunched scale.

In the remainder of this chapter, Sec.9.1 briefly describes the motivation of utilizing magnetized beam transport. In Sec. 9.2 we then introduce single-particle magnetized beam (or transversely coupled) dynamics based on the concepts of transport matrix and beam sigma matrix introduced in Sec. 2.3. To characterize the general feature of a magnetized (or transversely coupled) beam, we use the beam sigma matrix, although a set of generalized Twiss (or Courant-Snyder) parameters can do the same thing in another way, e.g. Ref. [101]. In Sec. 9.3 we derive the integral equations, which govern microbunching for a general transverse coupled beam in a single-pass system. In many situations, the coasting beam model serves as an excellent approximation to further simplify the subsequent semi-analytical calculations. Similar to the traditional treatment (see Chapter 3), we quantify the microbunching phenomena by calculating both the density and energy modulations of a beam along a transport line. For a transversely uncoupled beam and linear optics transport, the governing equation for density modulation is reduced to that derived by Heifets, Stupakov, and Krinsky [79] and Huang and Kim [81]. In Sec. 9.4, we apply the resultant formulas derived in the previous sections to a specialized recirculation arc for magnetized beam transport in a recent ERL cooler design for JLEIC [14]. In the same section, as a comparison, MBI analysis of the early design of JLEIC CCR is also presented. In spite of the different beamline designs and distinct natures of the circulating beams for CCR and ERL cooler ring, it still serves informative comparison in view of microbunching studies. The underlying physics of effective suppression of MBI in a magnetized beam transport is discussed. We also benchmark our semi-analytical Vlasov solutions against particle tracking by `elegant`. Both approaches are in good agreement. Finally Sec. 9.5 summarizes our findings.

Part of the work in this Chapter, especially Sec. 9.3 to Sec. 9.5, will be soon published with the title *Vlasov analysis of microbunching instability for magnetized beams*, in Physical Review Accelerator and Beams. This work was also presented in 2016 North American Particle Accelerator Conference (NAPAC), October 9 - 14, Chicago, Illinois, with a similar title *Vlasov Analysis for Microbunching Gain for Magnetized Beams* (WEA2CO04).

9.1 Introduction and Motivation

The motivation of this work originates from the early design of the Circulator Cooler Ring (CCR) [43] for the Jefferson Lab Electron Ion Collider (JLEIC) [1]. Utilizing the conventional electron cooling scheme, the goal of JLEIC cooler design is to achieve a significant reduction of the six-dimensional ion beam emittance and to deliver the beam with small spot size at the interaction point for high luminosities. The cooler design thus serves as a critical technology element in delivering high luminosities over a broad center-of-mass energy range in JLEIC. In addition to the same longitudinal velocity (or Lorentz relativistic factor) of the electron beam as that of ion beam and satisfying the optics matching condition in cooling solenoid section, general requirements of electron beams for efficient electron cooling are:

(1) high bunch charge;

(2) low beam temperature (or small electron beam emittance and energy spread); and

(3) large enough transverse beam size in order to cool the traversing ion beams.

The cooling electron beam then features high peak bunch current and low energy (usually ∼55 MeV to cool proton beam at ∼100 GeV). These usually set stringent requirements on electron beam brightness because the high peak bunch current and low energy would enhance the collective interaction, and small beam emittance or energy spread would weaken Landau damping or phase-space smearing effect. Both tracking simulations [169, 134] and Vlasov analysis [179, 180, 181] have shown that MBI is a serious concern for the early CCR design. The one-turn steady-state CSR microbunching gain is found to be up to 4000 at the modulation wavelength of 360 μm and is even higher when additional collective effects, such as CSR transient or LSC effects, are included. To be specific, this is mainly due to the high bunch charge (∼2 nC) and relatively low energy (∼55 MeV) of the cooling beam circulating in the CCR and because of ineffective Landau damping due to small beam emittance (∼ 3μm, normalized) and small relative energy spread (∼10-4). Mitigation of MBI thus becomes an issue for a high-brightness beam transport in recirculating machines.

Several mitigation schemes have been proposed in the literature for different machine configurations (see Chapter 7) and can be in general divided into two categories: those addressing the transport lattice optics, and those directed at the transported beam. For the former aspect, the optics impact of beamline

lattice designs on MBI has been recently investigated. In those beamline designs, the beam is assumed transversely uncoupled, i.e. non-magnetized. For the latter aspect, Derbenev (see, for example, Ref. [44, 45]) had proposed using magnetized beam to improve electron cooling performance and to mitigate collective effects [47]. A magnetized beam in general features non-zero canonical angular momentum, thus considered to be a transversely coupled beam. Concerning why JLEIC cooler design considers using magnetized beam for cooling, the track of thought may be clarified as follows: the last two items of the aforementioned requirements (small beam emittance and large enough beam size) for efficient electron cooling seem to contradict, at least for non-magnetized beams. For a magnetized beam, it can be however admitted: the key to efficient electron cooling lies in the requirement of different descriptions of beam emittance for magnetized beam from that for non-magnetized beam. Through a coordinate transformation from Cartesian coordinate frame to beam rotating frame, the transverse intrinsic beam spread can be characterized by Larmor and drift emittances, ϵ_L and ϵ_d, respectively[122]. The transverse 4-D emittance is evaluated as the geometric mean $\epsilon_{4D} = \sqrt{\epsilon_L \epsilon_d}$. In Refs. [70, 136, 137, 217], the electron cooling efficiency can be greatly improved by employing a magnetized beam. The reason is that, in a strong magnetic field, the transverse degree of freedom of electron beam motion does not take part in the energy exchange, because collisions are adiabatically slow relative to the cyclotron oscillations. That is to say, the electron beam temperature is indeed determined by the (smaller) Larmor emittance ϵ_L, instead of the emittance $\epsilon_{x,y}$ or ϵ_{4D}. The transverse beam size during transport is then related to the drift emittance ϵ_d. In this regard, the low temperature and large transverse size of the beam may not conflict for a magnetized beam. The (larger) drift emittance results in larger transverse beam size and, together with low electron temperature, can effectively enhance the cooling efficiency. This clarifies the advantage of using magnetized beam for electron cooling considered in JLEIC. Magnetized beam cooling was found to be an extremely useful technique in obtaining high-brightness hadron beams with low longitudinal momentum spread [70]. Another advantage of using magnetized beams has also been suggested, because it was believed to mitigate some collective effects such as space charge [47] and MBI (our primary focus in this chapter) because of its relatively larger transverse beam size. A magnetized beam can be generated by immersing the cathode in an axial solenoid magnetic field and thus features a nonzero angular momentum. In general, the magnetized beam is a transversely coupled beam.

Now that the magnetized beam has a promising yet qualitative feature of mitigating collective effects, for our purpose we want to confirm its effectiveness on MBI using a more quantitative model. There are many challenges in the theoretical study of MBI for a magnetized beam. In theory, to the best of our knowledge, there is not yet a linear Vlasov formalism addressing the microbunching instability for the transversely coupled beam transport through a beamline including relevant collective effects. In numerical simulation, e.g. particle tracking simulation (see, for example, [21]) with inclusion of relevant collective effects can be valuable for beam dynamics studies. It allows realistic particle beam distribution and general beamline

[122]For the $x-y$ uncoupled beam, the beam emittances in the horizontal and vertical dimensions, ϵ_x and ϵ_y, can be considered as eigen-emittances. For the magnetized beam, the non-vanishing angular momentum, or non-vanishing $\langle xy' \rangle$ and $\langle x'y \rangle$, makes the beam rotate in the $x-y$ coordinate. ϵ_x and ϵ_y are no longer constant and not good numbers to quantify the beam. By converting the $x-y$ frame to the beam rotating frame, we obtain the Larmor and drift emittances, ϵ_L and ϵ_d, which define the beam rotation and beam size, respectively. The detailed discussion can be found in Sec. 9.2.

lattice, but also requires careful treatment of various numerical parameters to ensure numerical convergence before the reliable results are obtained, in particular for the microbunched phase space dynamics. The time-domain treatment turns out to be considerably challenging when MBI becomes severe, e.g. for the early design of JLEIC CCR (see Sec. 9.4). Usually a large number of simulation particles and long computation time are required for reaching convergent results of microbunching gains, and strenuous efforts are needed to do parametric studies for machine designs or optimization in order to minimize MBI. In addition to microbunching dynamics, the numerical setup needs to take care of transverse angular momentum of the beam from its origination to preservation during beam transport. In practice, many other issues remain to be solved regarding how a magnetized beam can be generated with both high bunch charge and low temperature and how it can be transported while preserving outstanding beam phase space quality with its magnetization until cooling section and so on. In this Chapter we are interested in the aforementioned theory and simulation parts, where we have generalized the existing linear Vlasov analysis, originally developed for a non-magnetized beam (or transversely uncoupled beam) [79, 81], to the description of transport of a magnetized beam including relevant collective effects and also developed a new semi- analytical Vlasov solver for this particular feature of the beam.

9.2 Basics of phase-space dynamics for a magnetized beam

In this section we would introduce the basics of phase space dynamics for a magnetized beam. A magnetized beam is a special case of the transversely coupled beam. To describe the beam and its optical transport, we use beam sigma matrix, as introduced in Chapter 2, although a set of generalized Twiss (or Courant-Snyder) parameters can do the same thing in another way, e.g. Ref. [101]. The discussion in this section largely follows Kim's formulation [94]. For convenience of the subsequent discussion, we define the two-component vectors,

$$X = [x \ p_x]^T \tag{9.1}$$

and

$$Y = [y \ p_y]^T \tag{9.2}$$

where

$$p_x = p_s \, (x') \tag{9.3}$$

is the particle momentum in the axial direction. As introduced in Sec. 2.3, the beam can be in general characterized by the beam sigma matrix. For the transverse 4-D case, we have

$$\Sigma_{4D} = \begin{pmatrix} \langle XX^T \rangle & \langle XY^T \rangle \\ \langle YX^T \rangle & \langle YY^T \rangle \end{pmatrix} \tag{9.4}$$

where $\langle X \rangle = \mathbf{0}$ and $\langle Y \rangle = \mathbf{0}$ are assumed.

Note that transport of the beam sigma matrix follows Eq. (2.52) and the symplecticity condition Eq. (2.11), which are expressed below,

$$\Sigma_{4D}(s) = \mathbf{R}_{4D}\Sigma_{4D}(0)\mathbf{R}_{4D}^T \tag{9.5}$$

and

$$\mathbf{R}_{4D}^T\mathbf{S}\mathbf{R}_{4D} = \mathbf{S} \tag{9.6}$$

The following two quantities are found to be invariants under the transformation [145],

$$\epsilon_{4D} = \sqrt[4]{\det(\Sigma)} = \epsilon_{\text{thermal}} \tag{9.7}$$

and

$$I_2(\Sigma) = -\frac{1}{2}\text{tr}(J\Sigma_{4D}J\Sigma_{4D}) \tag{9.8}$$

where tr takes the trace of a matrix.

Now we consider the transversely round beam transport in a cylindrically symmetric environment. From Eq. (9.5) with the fact $\mathbf{R}_{4D}^T = \mathbf{R}_{4D}^{-1}$ for a rotating matrix,

$$\Sigma_{4D}(s) = \mathbf{R}_{4D}(\theta)\Sigma_{4D}(0)\mathbf{R}_{4D}^{-1}(\theta) \tag{9.9}$$

where $\mathbf{R}_{4D}(\theta)$ can be parameterized by

$$\mathbf{R}_{4D}(\theta) = \begin{pmatrix} \mathbf{I}\cos\theta & \mathbf{I}\sin\theta \\ -\mathbf{I}\sin\theta & \mathbf{I}\cos\theta \end{pmatrix} \tag{9.10}$$

where $\mathbf{I}$ is the identity matrix. By demanding that θ in Eq. (9.9) be arbitrary, we find that $\langle XX^T \rangle = \langle YY^T \rangle$ and $\langle XY^T \rangle^T = -\langle XY^T \rangle$. Then we can further represent the two-by-two block matrices in Eq. (9.4) as

$$\langle XY^T \rangle = \mathcal{L}\mathbf{s} \tag{9.11}$$

with the (one-half of) canonical angular momentum in the lab frame $\left\langle XY^T \right\rangle = \mathcal{L}\mathbf{s}$, where $\mathcal{L} = \frac{1}{2}\left\langle xp_y - yp_x \right\rangle \equiv \frac{eB_{s=0}\sigma_c^2}{2mc}$ the magnetic field $B_{s=0}$ and the transverse beam size σ_c are measured at cathode surface ($s = 0$), and

$$\left\langle XX^T \right\rangle = \epsilon_{\text{eff}} T_d \tag{9.12}$$

where ϵ_{eff} is the effective emittance, which will be clarified soon,

$$T_d = D(d) T_0 D^T(d) \tag{9.13}$$

and

$$D(d) = \begin{pmatrix} 1 & d \\ 0 & 1 \end{pmatrix} \tag{9.14}$$

and

$$T_0 = \begin{pmatrix} \beta & 0 \\ 0 & \beta^{-1} \end{pmatrix} \tag{9.15}$$

For a transverse round beam, we have $\beta_x = \beta_y = \beta$. From Eqs. (9.11) and (9.12), Eq. (9.4) can be re-written as

$$\Sigma_{4D} = \begin{pmatrix} \epsilon_{\text{eff}} T_d & \mathcal{L}\mathbf{s} \\ -\mathcal{L}\mathbf{s} & \epsilon_{\text{eff}} T_d \end{pmatrix} \tag{9.16}$$

From Eq. (9.16) it can be found that with cylindrically symmetric beam, the beam sigma matrix can be characterized by the four parameters, ϵ_{eff}, β, $\mathcal{L}$, and d. Thus far we have reduced the general form of Eq. (9.4) to the cylindrical symmetric case of Eq. (9.16), in which a magnetized beam usually features. Now we want to utilize Eqs. (9.7) and (9.8) to derive invariant quantities. From Eqs. (9.7), (9.16) and the identity $\mathbf{s}T_0\mathbf{s} = -T_0^{-1}$, we have

$$\epsilon_{\text{eff}} = \sqrt{\epsilon_{\text{th}}^2 + \mathcal{L}^2} \tag{9.17}$$

From Eq. (9.8) and (9.16), we can obtain

$$I_2 = 2\left(\epsilon_{\text{eff}}^2 + \mathcal{L}^2\right) = \text{invariant} \tag{9.18}$$

With the above invariants, we can now introduce the eigen-emittances for the magnetized beams. Since the beam sigma matrix is real and symmetric, it is always diagonalizable. For simplicity, assume $d = 0$

(i.e. the beam at waist), Eq. (9.16) can be diagonalized

$$\Sigma_{4D} \to \begin{pmatrix} \epsilon_+ T_+ & \mathbf{0} \\ \mathbf{0} & \epsilon_- T_- \end{pmatrix} \tag{9.19}$$

where

$$T_\pm = \begin{pmatrix} \beta_\pm & 0 \\ 0 & \beta_\pm^{-1} \end{pmatrix} \tag{9.20}$$

Now the subscript $\pm$ denotes the two eigen-axes where the quantities are measured. Taking the determinant of Eq. (9.19) and the trace of $\mathbf{s}\Sigma_{4D}\mathbf{s}\Sigma_{4D}$, we have

$$\epsilon_{\rm th}^2 = (\epsilon_{\rm eff}^2 - \mathcal{L}^2) = \epsilon_+ \epsilon_- \tag{9.21}$$

and

$$I_2 = 2(\epsilon_{\rm eff}^2 + \mathcal{L}^2) = \epsilon_+^2 + \epsilon_-^2 \tag{9.22}$$

Solving the above two equations, we have

$$\epsilon_\pm = \epsilon_{\rm eff} \pm \mathcal{L} \tag{9.23}$$

With vanishing angular momentum, $\epsilon_{\rm eff} = \epsilon_{\rm thermal} = \epsilon_+ = \epsilon_-$. When a beam is said to be angular momentum dominated, $\mathcal{L} \gg \epsilon_{\rm th}$ and $\epsilon_+/\epsilon_- \approx (2\mathcal{L}/\epsilon_{\rm th})^2$. We have introduced the thermal emittance $\epsilon_{\rm th}$, which is also the 4-D emittance ϵ_{4D} by our definition, the effective emittance $\epsilon_{\rm eff}$, and the eigen-emittances $\epsilon_\pm$. All of them are related to each other. Figure 9.1 below illustrates the relations among them [112]. In Sec. 9.1 we mentioned the important role of beam emittances for electron cooling efficiency, which involves the (smaller) Larmor and (larger) drift emittances. Those emittances are measured in a rotating frame in the cooling solenoid section. Note that different configurations of beam emittances can play different roles in different physical processes.

In the next section, we would discuss the application of (round) magnetized beam transport in an arc with collective effects included. Here let us take a quick example for another application of the magnetized beam to round-to-flat (RTF) beam transformation. A flat beam is characteristic of high transverse emittance ratio, e.g. $\epsilon_x/\epsilon_y \gg 1$. Physically it may look like $\sigma_x/\sigma_y \gg 1$. The RTF transform has been applied in linear colliders and accelerator-based light source facilities [167]. For the former, the flat beam can help mitigate the beamstrahlung effect [213] while keeping the luminosity as desired. For the latter, the flat beam can be used to produce ultrashort x-ray radiation pulses [161] or employed to enhace beam-wave interaction in Smith-Purcell radiation light sources [161]. Figure 9.2 below demonstrates the transformation before and

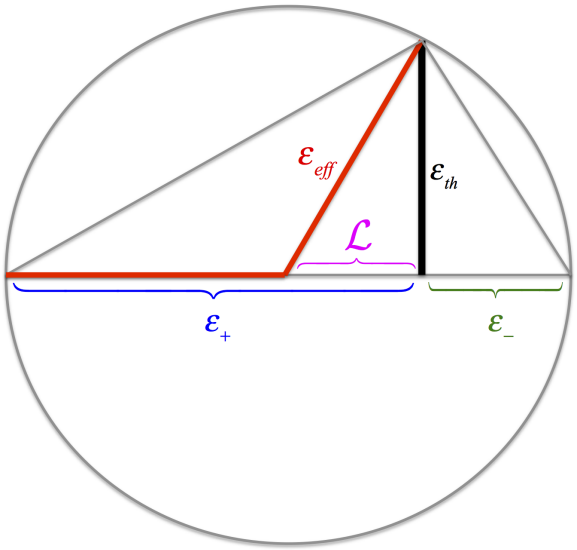

Figure 9.1: Conceptual illustration of various emittances introduced in this section.

after the RTF, which can be implemented by a set of (at least) three skew-quadrupoles [28].

The beam sigma matrix for a round magnetized beam can be formulated in Eq. (9.16) or (9.19). We can also write the sigma matrix in terms of beam size σ_c (or β), angular momentum $\mathcal{L}$, and effective emittance ϵ_{eff}, and the virtual drift distance d. Assume all the beam correlations vanish at the cathode location except $\langle x_c^2 \rangle = \langle y_c^2 \rangle = \sigma_c^2$ and $\langle p_{xc}^2 \rangle = \langle p_{yc}^2 \rangle = \sigma_{pc}^2$. Then the general expression for the magnetized beam can be described to be

$$
\begin{aligned}
\Sigma &= M_d \Sigma_0 M_d^T \\
&= \begin{pmatrix} 1 & d & 0 & 0 \\ 0 & 1 & 0 & 0 \\ 0 & 0 & 1 & d \\ 0 & 0 & 0 & 1 \end{pmatrix} \begin{pmatrix} \sigma_c^2 & 0 & 0 & \mathcal{L} \\ 0 & \left(\frac{\epsilon_{\text{eff}}}{\sigma_c}\right)^2 & -\mathcal{L} & 0 \\ 0 & -\mathcal{L} & \sigma_c^2 & 0 \\ \mathcal{L} & 0 & 0 & \left(\frac{\epsilon_{\text{eff}}}{\sigma_c}\right)^2 \end{pmatrix} \begin{pmatrix} 1 & 0 & 0 & 0 \\ d & 1 & 0 & 0 \\ 0 & 0 & 1 & 0 \\ 0 & 0 & d & 1 \end{pmatrix} \\
&= \begin{pmatrix} \Sigma_{11} & \Sigma_{12} & \Sigma_{13} & \Sigma_{14} \\ \Sigma_{21} & \Sigma_{22} & \Sigma_{23} & \Sigma_{24} \\ \Sigma_{31} & \Sigma_{32} & \Sigma_{33} & \Sigma_{34} \\ \Sigma_{41} & \Sigma_{42} & \Sigma_{43} & \Sigma_{44} \end{pmatrix}
\end{aligned}
\tag{9.24}
$$

with $\mathcal{L} = \kappa_0 \sigma_c^2$, $\kappa_0 = \frac{eB_{s=0}}{2mc}$, $\epsilon_{\text{eff}} = \sqrt{\epsilon_{\text{th}}^2 + \mathcal{L}^2}$, $\epsilon_{\text{th}} = \sigma_c \sigma_{pc}$, and $\beta = \frac{\sigma_c^2}{\epsilon_{\text{eff}}} = \frac{\sigma_c^2}{\sqrt{\epsilon_{\text{th}}^2 + \mathcal{L}^2}}$.

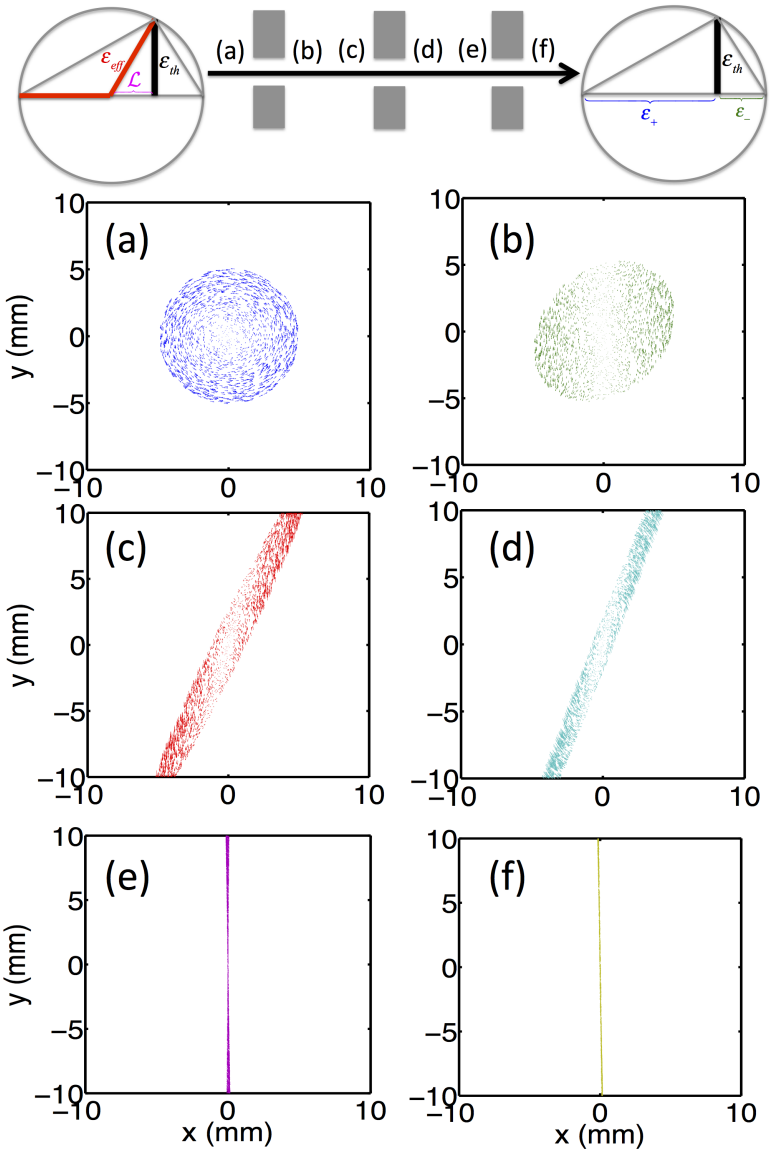

Figure 9.2: Illustration of beam round-to-flat (RTF) transformation using a set of three skew quadrupoles. The quantification of beam emittances are denoted using Fig. 9.1 in the upper left and right corners of this figure.

Writing Eq. (9.24) explicitly, we have

$$\Sigma = \begin{pmatrix} \sigma_c^2 + \frac{d^2\epsilon_{\text{eff}}^2}{\sigma_c^2} & \frac{d^2\epsilon_{\text{eff}}^2}{\sigma_c^2} & 0 & \mathcal{L} \\ \frac{d^2\epsilon_{\text{eff}}^2}{\sigma_c^2} & \left(\frac{\epsilon_{\text{eff}}}{\sigma_c}\right)^2 & -\mathcal{L} & 0 \\ 0 & -\mathcal{L} & \sigma_c^2 + \frac{d^2\epsilon_{\text{eff}}^2}{\sigma_c^2} & \frac{d^2\epsilon_{\text{eff}}^2}{\sigma_c^2} \\ \mathcal{L} & 0 & \frac{d^2\epsilon_{\text{eff}}^2}{\sigma_c^2} & \left(\frac{\epsilon_{\text{eff}}}{\sigma_c}\right)^2 \end{pmatrix} \tag{9.25}$$

In Sec. 9.4 we would use Eq. (9.25) to parameterize the input beam distribution to study the effect

of beam magnetization.

9.3 Governing equation for magnetized beam in the presence of collective effects

In Chapter 3, we have derived the linearized Vlasov equation in Eq. (3.14). By integrating Eq. (3.14) over s along the unperturbed phase space trajectory and taking advantage of the total derivative, we obtain the relation between the phase space distribution functions *before* and *after* the collective-effect energy kick,

$$f_1(\mathbf{X}_s) \simeq f_1^{(0)}(\mathbf{X}_0) - \int_0^s d\tau \frac{\partial \bar{f}(\mathbf{X}_\tau)}{\partial \delta} \frac{d\delta}{d\tau} \tag{9.26}$$

where $f_1^{(0)}(\mathbf{X}_0)$, being the small perturbed distribution function, is evaluated *before* the energy kick. This expression, considered as a form of the linearized Vlasov equation, would be used below and referred as a fundamental relation. To proceed, we first need to specify the initial unperturbed electron phase space distribution. We assume the Gaussian distribution in the six-dimensional phase space coordinate,

$$\bar{f}_0(\mathbf{X}_0) = \frac{N}{(2\pi)^3 \sqrt{\det \Sigma_0}} \exp\left\{ \frac{-1}{2} \mathbf{X}_0^T \Sigma_0^{-1} \mathbf{X}_0 \right\} \tag{9.27}$$

where we remind that the overline atop f_0 is used to denote the unperturbed distribution, the subscript "0" stands for the quantity evaluated at $s = 0$. For an uncoupled beam, the beam distribution can be parameterized by Twiss (or Courant-Snyder) parameters, as introduced in Eq. (3.17). The invariant for (x, x'),

$$\mathbf{X}_{2D,0}^T \Sigma_{2D}^{-1} \mathbf{X}_{2D,0} = \frac{x_0^2 + (\beta_{x0} x_0{}' + \alpha_{x0} x_0)^2}{\epsilon_{x0} \beta_{x0}} \tag{9.28}$$

with $\det(\Sigma_{2D}) = \epsilon_{x0}^2$. The invariant for (y, y') is similar and thus not shown here. For a transversely coupled beam or magnetized beam, Eq. (9.28) is no longer valid to describe the beam. Therefore Eq. (9.27) is retained as the final form of the beam phase space distribution.

Since we are interested in the microbunching development along a beamline; microbunching can still be quantified by the Fourier transformation of z coordinate of the perturbed phase space distribution function as the density modulation (or, bunching factor), which we repeat here

$$b(k_z; s) = \frac{1}{N} \int d\hat{\mathbf{X}} e^{-ik_z z_s} f_1(\hat{\mathbf{X}}; s) \tag{9.29}$$

In addition, microbunching can arise from or result in energy modulation, which is quantified by the

Fourier transformation of the energy-modulated phase space distribution,

$$p(k_z;s) = \frac{1}{N}\int d\mathbf{X} e^{-ik_z z_s}\,(\delta - hz)\, f_1(\mathbf{X};s) \tag{9.30}$$

Note that, in Eqs. (9.29) and (9.30), the phase space variables are evaluated at s. For $s = 0$, we quantify the initial density and energy modulations as follows,

$$b_0(k_0) = b(k_z;0) = \frac{n_0}{N}\int dz_0 \left(\frac{\Delta n(z_0)}{n_0}\right) e^{-ik_0 z_0} \tag{9.31}$$

and

$$p_0(k_0) = p(k_z;0) = \frac{n_0}{N}\int dz_0 \Delta\delta(z_0) e^{-ik_0 z_0} \tag{9.32}$$

where

$$\Delta\delta(z_0) = \delta_0 - hz_0 \tag{9.33}$$

Our goal is to derive the governing equations for $b(k_z;s)$ and $p(k_z;s)$ valid for magnetized beams. By multiplying on both sides of Eq. (9.26) with $\exp\left[-ik_z(s)z_s\right]$, and integrating over the six-dimensional phase space $\mathbf{X}$, we have

$$\begin{aligned} b(k_z;s) &= b^{(0)}(k_z;s) \\ &\quad - \frac{1}{N}\int_0^s d\tau ik_z(s)\frac{I_b(\tau)}{\gamma I_A} R_{56}(\tau\to s)\int \frac{d\kappa}{2\pi} Z_0^{\parallel}(\kappa;\tau) b(\kappa;\tau)\int d\mathbf{X}_\tau \bar{f}(\mathbf{X}_\tau) e^{-ik_z z_s(\mathbf{X}_\tau)+i\kappa z_\tau} \end{aligned} \tag{9.34}$$

where $I_b(\tau)$ is the instantaneous bunch current at $s = \tau$, and I_A is the Alfven current ($\approx$ 17045 A). $R_{56}(\tau\to s) = \left[\mathbf{R}(s)\mathbf{R}^{-1}(\tau)\right]_{56}$ is the relative momentum compaction function from τ to s. The first term on the right side (RHS) of Eq. (9.34) is evaluated by Eq. (9.29) using $f_1(\mathbf{X};s) = f_1^{(0)}(\mathbf{X}_s)$. The explicit form of $f_1^{(0)}(\mathbf{X}_s)$ can be in Eq. (3.45) or (3.46). This term corresponds to the bunching evolution in the absence of collective effects. We want to work out the second term on RHS of Eq. (9.34) by tracing the relevant phase space coordinates at $s = \tau$ back to the initial location ($s = 0$) with the help of Eqs. (3.3) and (3.6). z_s in the exponent of the second term on RHS of Eq. (9.34) can be expressed as

$$z_s = \sum_{j=1}^{6} R_{5j}(\tau\to s) X_\tau^j = \sum_{j=1}^{6} R_{5j}(s) X_0^j \tag{9.35}$$

where the superscript j indicates the j-th component of the phase space coordinate vector $\mathbf{X}$. Similarly, for z_τ, we have $z_\tau = \sum_{j=1}^{6} R_{5j}(\tau) X_0^j$.

Now, in the second term of RHS of Eq. (9.34), the integration over $\mathbf{X}_0$ (originally over $\mathbf{X}_\tau$) involves

the term in the exponent,

$$-\frac{1}{2}\mathbf{X}_0^T\Sigma_0^{-1}\mathbf{X}_0 - ik_z z_s(\mathbf{X}_0) + i\kappa z_\tau(\mathbf{X}_0) = -\frac{1}{2}\mathbf{X}_0^T\Sigma_0^{-1}\mathbf{X}_0 - i\sum_{j=1}^{6}\Re_{5j}(s,\tau)X_0^j \tag{9.36}$$

where we have defined

$$\Re_{5j}(s,\tau) = k_z(s)R_{5j}(s) - \kappa(\tau)R_{5j}(\tau), j = 1,2,...,6 \tag{9.37}$$

For a coupled beam, the term $\mathbf{X}_0^T\Sigma_0^{-1}\mathbf{X}_0$ in Eq. (9.36) usually consists of the mixed terms, such as x_0x_0', x_0y_0, x_0y_0', and etc. These mixed terms can very much complicate the integration. As discussed in Sec. 9.2, since the beam sigma matrix is real and symmetric, it can be always diagonalized. That is to say, there always exists a real $\mathbf{V}$ such that

$$\mathbf{V}\Sigma\mathbf{V}^T = \mathbf{D} \tag{9.38}$$

with $\det(\mathbf{V}) = 1$. In Eq. (9.38), the matrix $\mathbf{V}$ embodies the eigenvectors and the diagonal matrix $\mathbf{D}$ accommodates the corresponding eigenvalues. After the diagonalization, the basis coordinate $\mathbf{X}$ experiences a coordinate transformation to $\mathbf{U}$ with $\mathbf{U} = \mathbf{V}\mathbf{X}$. It is obvious that this transformation preserves the invariant (physically, the beam emittance is unchanged through the transformation). And we have

$$\mathbf{X}^T\Sigma^{-1}\mathbf{X} = \mathbf{U}^T\mathbf{D}^{-1}\mathbf{U} \tag{9.39}$$

The above mathematical treatment is in fact equivalent to finding a normal form from a set of coordinates. For example, for two-dimensional subspace (x, x'), throughout the coordinate transformation of Eq. (9.40) below,

$$\mathbf{V}_{2D} = \begin{pmatrix} \frac{1}{\sqrt{\beta_x}} & 0 \\ \frac{\alpha_x}{\sqrt{\beta_x}} & \sqrt{\beta_x} \end{pmatrix} \tag{9.40}$$

the invariant $\mathbf{X}_{2D}^T\Sigma_{2D}^{-1}\mathbf{X}_{2D} = \epsilon_x^{-1}\left(\gamma_x x^2 + 2\alpha_x xx' + \beta_x x'^2\right)$ can be re-written as $\epsilon_x^{-1}\left(\bar{x}^2 + \bar{x}'^2\right)$ with $\bar{x} = x/\sqrt{\beta_x}$ and $\bar{x}' = (\alpha_x x + \beta_x x')/\sqrt{\beta_x}$. Here β_x and α_x are Twiss [191] (or Courant-Snyder [41]) parameters and the 2-D beam sigma matrix is parameterized by

$$\Sigma_{2D} = \epsilon_x \begin{pmatrix} \beta_x & -\alpha_x \\ -\alpha_x & \gamma_x \end{pmatrix} \tag{9.41}$$

where ϵ_x is the (rms) horizontal geometric emittance of the beam and $\gamma_x = \left(1 + \alpha_x^2\right)/\beta_x$.

When the subspace is extended to 4-D (x, x', z, δ), we have similarly the transformation of Eq. (9.42)

[38],

$$\mathbf{V}_{4D} = \begin{pmatrix} \frac{1}{\sqrt{\beta_x}} & 0 & 0 & -\frac{\eta_x}{\sqrt{\beta_x}} \\ \frac{\alpha_x}{\sqrt{\beta_x}} & \sqrt{\beta_x} & 0 & -\frac{\alpha_x\eta_x+\beta_x\eta_x{}'}{\sqrt{\beta_x}} \\ \eta_x{}' & -\eta_x & 1 & 0 \\ 0 & 0 & 0 & 1 \end{pmatrix} \tag{9.42}$$

where η_x and η_x' are the dispersion function and its derivative, or R_{16} and R_{26}. In Eqs. (9.40) and (9.42), the Twiss (or Courant-Snyder) parameters are assumed to be of the beam's. If a beam is said *matched* to a beamline, these parameters are equal to the Twiss functions at the entrance of the beamline.

We are particularly interested in the case of transversely coupled beams, i.e. $\mathbf{X}_0^T\Sigma_0^{-1}\mathbf{X}_0 = \mathbf{X}_{4D,0}^T\Sigma_{4D,0}^{-1}\mathbf{X}_{4D,0} + \frac{(\delta_0-hz_0)^2}{\sigma_{\delta 0}^2}$, where $\mathbf{X}_{4D,0} = (x_0, x_0{}', y_0, y_0{}')^T$. Following Eqs. (9.38) and (9.39), the integration over $\mathbf{X}_{4D,0}$ now becomes the integration over $\mathbf{U}_{4D} = (u_1, u_2, u_3, u_4)^T$, and we have

$$\begin{aligned} &\int d\mathbf{X}_{4D,0} \exp\left\{-\frac{1}{2}\mathbf{X}_{4D,0}^T\Sigma_{4D,0}^{-1}\mathbf{X}_{4D,0} - i\sum_{j=1}^{4}\Re_{5j}(s,\tau)X_{j,0}\right\} \\ &= \prod_{m=1}^{4}\int du_m \exp\left\{-\frac{1}{2}D_{mm}^{-1}u_m^2 - i\sum_{j=1}^{4}\Re_{5j}(s,\tau)\mathbf{V}_{jm}^{-1}u_m\right\} \\ &= \prod_{m=1}^{4}\sqrt{\frac{2\pi}{D_{mm}^{-1}}}\exp\left\{-\frac{1}{2D_{mm}^{-1}}\left[\sum_{j=1}^{4}\Re_{5j}(s,\tau)\mathbf{V}_{jm}^{-1}\right]^2\right\} \end{aligned} \tag{9.43}$$

where D_{mm}^{-1} for $m = 1$ to 4 are diagonal terms of $\mathbf{D}^{-1}$. The positive definiteness of $\mathbf{X}_{4D,0}^T\Sigma_{4D,0}^{-1}\mathbf{X}_{4D,0}$ assures that of $\mathbf{U}_{4D}^T\mathbf{D}^{-1}\mathbf{U}_{4D}$, and thus $D_{mm}^{-1} > 0$. From Eqs. (9.34) and (9.43), we have

$$\int \frac{d\kappa}{2\pi}Z_0^{\parallel}(\kappa;\tau)b(\kappa;\tau)\int d\mathbf{X}_0\bar{f}_0(\mathbf{X}_0)e^{-ik_zz_s(\mathbf{X}_0)+i\kappa z_\tau(\mathbf{X}_0)} = Z_0^{\parallel}(k_z(\tau);\tau)b(k_z(\tau);\tau)\{L.D.;s,\tau\} \tag{9.44}$$

where the term $\{L.D.;s,\tau\}$ characterizes the smearing effect or Landau damping,

$$\{L.D.;s,\tau\} = \exp\left\{-\frac{1}{2}\sum_{m=1}^{4}\frac{1}{D_{mm}^{-1}}\left(\sum_{j=1}^{4}\Re_{5j}(s,\tau)V_{jm}^{-1}\right)^2 - \frac{1}{2}\sigma_{\delta 0}^2\Re_{56}(s,\tau)\right\} \tag{9.45}$$

and

$$\Re_{5j}(s,\tau) = k_z(s)R_{5j}(s) - k_z(\tau)R_{5j}(\tau) = k_0\left[C(s)R_{5j}(s) - C(\tau)R_{5j}(\tau)\right] \tag{9.46}$$

$j = 1, 2, 3, 4$, and 6. where use has been made of the coasting beam approximation;

$$\int \frac{d\kappa}{2\pi} \int dz_0 \exp\left\{-i\left[k_z(s)/C(s) - \kappa(\tau)/C(\tau)\right] z_0\right\} = 1 \text{ when } \kappa(\tau) = k_z(s)C(\tau)/C(s)$$

and $C(\tau) \equiv \left[1 - hR_{56}(\tau)\right]^{-1}$ is the bunch compression factor at $s = \tau$.

Note that the matrix $\mathbf{V}$ in Eq. (9.45) has been obtained when we numerically diagonalize Σ_0 (or Σ_0^{-1}) [see Eq. (9.38)]. For the case of an uncoupled beam, Eq. (9.45) is reduced to Eq. (3.40)

$$\{L.D.; s, \tau\} = \exp\left\{\frac{-1}{2}\begin{bmatrix} \epsilon_{x0}\beta_{x0}\left(\Re_{51}(s,\tau) - \dfrac{\alpha_{x0}}{\beta_{x0}}\Re_{52}(s,\tau)\right)^2 + \dfrac{\epsilon_{x0}}{\beta_{x0}}\Re_{52}^2(s,\tau) + \\ \epsilon_{y0}\beta_{y0}\left(\Re_{53}(s,\tau) - \dfrac{\alpha_{y0}}{\beta_{y0}}\Re_{54}(s,\tau)\right)^2 + \dfrac{\epsilon_{y0}}{\beta_{y0}}\Re_{54}^2(s,\tau) + \sigma_{\delta 0}^2\Re_{56}^2(s,\tau) \end{bmatrix}\right\} \tag{9.47}$$

Putting all together, we arrive at the governing equation, Eq. (9.34), for density modulation (or bunching factor) as a compact integral equation,

$$b\left(k_z; s\right) = b^{(0)}\left(k_z; s\right) + \int_0^s d\tau K\left(\tau, s\right) b\left(k_z; \tau\right) \tag{9.48}$$

where the kernel function has the same form as that for uncoupled beams,

$$K\left(\tau, s\right) = ik_z(s)\frac{I_b(\tau)}{\gamma I_A} R_{56}(\tau \to s) Z_0^{\parallel}(k_z; \tau)\left\{L.D.; s, \tau\right\} \tag{9.49}$$

Similar to the case of density modulation, we can also obtain the equation for energy modulation from the fundamental relation, Eq. (9.26). Multiplying on both sides of Eq. (9.26) with $(\delta_s - hz_s)\times\exp\left[-ik_z(s)z_s\right]$ and integrating over the six-dimensional phase space $\mathbf{X}$, the resultant governing equation can be expressed in terms of Eqs. (9.29) and (9.30),

$$p\left(k_z; s\right) = p^{(0)}\left(k_z; s\right) + \int_0^s d\tau\left[M\left(\tau, s\right) - L\left(\tau, s\right)\right] b\left(k_z; \tau\right) \tag{9.50}$$

where the kernel functions are

$$M\left(\tau, s\right) = ik_z(s)\frac{I_b(\tau)}{\gamma I_A}\sigma_{\delta 0}^2 R_{56}(\tau \to s)\Re_{56}(s,\tau) Z_0^{\parallel}(k_z; \tau) = \sigma_{\delta 0}^2\Re_{56}(s,\tau) K\left(\tau, s\right) \tag{9.51}$$

and

$$L\left(\tau, s\right) = \frac{I_b(\tau)}{\gamma I_A} Z_0^{\parallel}(k_z; \tau) \tag{9.52}$$

Now we have derived two integral equations that govern the evolution of both density and energy

modulations along a beamline. However we have not yet obtained $b^{(0)}(k_z;s)$ and $p^{(0)}(k_z;s)$. This requires the explicit expressions of the initial density- and energy-perturbed phase-space distribution functions. They can be respectively formulated as [see also Eqs. (3.45) and (3.46)]

$$f_1^{(0,d)}(\mathbf{X}_0) = \frac{\Delta n(z_0)}{n_0}\bar{f}_0(\mathbf{X}_0) \tag{9.53}$$

and

$$f_1^{(0,e)}(\mathbf{X}_0) = \frac{(\delta_0 - hz_0)\Delta\delta(z_0)}{\sigma_{\delta 0}^2}\bar{f}_0(\mathbf{X}_0) \tag{9.54}$$

where a second superscript, (d) or (e), is used to denote either the density or energy modulation.

Substituting Eqs. (9.53) and (9.54) into Eqs. (9.29) and (9.30), we have a total of four combinations,

$$b^{(0,d)}(k_z;s) = b_0(k_0)\{L.D.;s,0\} \tag{9.55}$$

$$b^{(0,e)}(k_z;s) = -ik_z(s)R_{56}(s)p_0(k_0)\{L.D.;s,0\} \tag{9.56}$$

$$p^{(0,d)}(k_z;s) = -ik_z(s)R_{56}(s)\sigma_{\delta 0}^2 b_0(k_0)\{L.D.;s,0\} \tag{9.57}$$

$$p^{(0,e)}(k_z;s) = \left(1 - k_z^2(s)R_{56}^2(s)\sigma_{\delta 0}^2\right)p_0(k_0)\{L.D.;s,0\} \tag{9.58}$$

which are, respectively, the density modulations due to initial density [Eq. (9.55)] and energy [Eq. (9.56)] modulations, and energy modulations due to initial density [Eq. (9.57)] and energy [Eq. (9.58)] modulations. Note that Eqs. (9.55) to (9.58) determine the pure-optics evolution of density and energy modulations. One can see, in the absence of collective effects, a (downstream) resultant density modulation can be either inherent, i.e. from Eq. (9.55), or transformed from energy modulation via the momentum compaction function R_{56} upstream a beamline, i.e. Eq. (9.56). Similarly, for a (downstream) energy modulation, it can be either inherent, Eq. (9.58), or resulted from finite energy spread in a density-modulated beam, Eq. (9.57). In the presence of collective effects, such as CSR and LSC, they will complicate the conversion between density and energy modulations. In total, we have four different combinations, each of which corresponds to an integral equation derived in Eqs. (9.48) to (9.52). By dividing a beamline into grids, these four integral equations can be cast into vector/matrix form as,

$$\begin{bmatrix} \mathbf{b}^{(d)} \\ \mathbf{b}^{(e)} \\ \mathbf{p}^{(d)} \\ \mathbf{p}^{(e)} \end{bmatrix} = \begin{pmatrix} (\mathbf{1}-\mathbf{K})^{-1} & \mathbf{0} & \mathbf{0} & \mathbf{0} \\ \mathbf{0} & (\mathbf{1}-\mathbf{K})^{-1} & \mathbf{0} & \mathbf{0} \\ (\mathbf{M}-\mathbf{L})(\mathbf{1}-\mathbf{K})^{-1} & \mathbf{0} & \mathbf{1} & \mathbf{0} \\ \mathbf{0} & (\mathbf{M}-\mathbf{L})(\mathbf{1}-\mathbf{K})^{-1} & \mathbf{0} & \mathbf{1} \end{pmatrix}_{4M\times 4M} \begin{bmatrix} \mathbf{b}^{(0,d)} \\ \mathbf{b}_0^{(0,e)} \\ \mathbf{p}_0^{(0,d)} \\ \mathbf{p}_0^{(0,e)} \end{bmatrix} \tag{9.59}$$

where $\mathbf{b} \equiv [b(s_1), b(s_2), ..., b(s_M)]^T$ and $\mathbf{p} \equiv [p(s_1), p(s_2), ..., p(s_M)]^T$, and $s_i (i = 1, 2, ..., M)$ represents the grid along a beamline ($s_1 = 0$ and $s_M = s_f$ denote the entrance and the exit of a beamline). $\mathbf{1}$ is the

M-by-M identity matrix, $\mathbf{0}$ is the zero matrix, and $\mathbf{K}$, $\mathbf{L}$, and $\mathbf{M}$ are the matrix representations of Eqs. (9.49), (9.51), and (9.52). By virtue of the matrix language, Eq. (9.48) has been expressed as $\mathbf{b} = \mathbf{b}^{(0)} + \mathbf{K}\mathbf{b}$ and Eq. (9.50) as $\mathbf{p} = \mathbf{p}^{(0)} + (\mathbf{M} - \mathbf{L})\,\mathbf{b}$. The existence of the inverse matrix is assumed. Equation (9.59) can be expressed in a more compact form as

$$\begin{bmatrix} \mathbf{b} \\ \mathbf{p} \end{bmatrix} = \begin{pmatrix} (\mathbf{1} - \mathbf{K})^{-1} & \mathbf{0} \\ (\mathbf{M} - \mathbf{L})\,(\mathbf{1} - \mathbf{K})^{-1} & \mathbf{1} \end{pmatrix} \begin{bmatrix} \mathbf{b}^{(0)} \\ \mathbf{p}^{(0)} \end{bmatrix} \tag{9.60}$$

where $\mathbf{b} \equiv \mathbf{b}^{(d)} + \mathbf{b}^{(e)}$ and $\mathbf{p} \equiv \mathbf{p}^{(d)} + \mathbf{p}^{(e)}$. In writing Eq. (9.60) we have assumed the modulation wavelengths in density and energy modulations are the same.

The quantity of particular interest is the microbunching gain, defined as the modular ratio of density modulations at a certain location s to the initial location $s = 0$,

$$G(s) \equiv \left| \frac{b(k_z; s)}{b^{(0)}(k_0; 0)} \right| \tag{9.61}$$

Similar to the situation in Chapter 8, when it comes to different types of modulations, e.g. the density-to-energy or energy-to-density microbunching, we directly refer to values of $b(k_z; s)$ and $p(k_z; s)$, evaluated in unit of $b^{(0)}(k_0; 0)$ or $p^{(0)}(k_0; 0)$.

To facilitate the discussion, in what follows we call $G(s)$, the gain function, which is a function of s for a given modulation wavenumber, and refer to $G_f(\lambda) = G(s = s_f; \lambda = 2\pi/k_z)$ as the gain spectrum, a function of modulation wavelength at the exit (the subscript f indicates the exit of a beamline).

9.4 Examples

In this section we apply the results obtained in the previous sections to two example lattices. The first example is the early design of MEIC CCR [1], and the second one is a recent ERL cooler ring design for electron cooling at JLEIC [14]. The two examples have different beamline designs and distinct natures of the circulating electron beams. For CCR, the beam is non-magnetized and MBI was not much taken care of in the early design. For ERL cooler ring, the beam is magnetized and the steering magnets are designed according to Ref. [30]. Presenting the first example here serves two informative purposes.

In view of microbunching dynamics, the CCR features an ultrahigh gain, with maximum steady-state CSR gain up to 4000 at $\lambda \approx 360\mu$m and even higher when LSC is included [179], as well as significant longitudinal phase space fragmentation [169, 134]. In contrast, the arc design of ERL cooler ring is free from MBI, with maximum gain around unity.

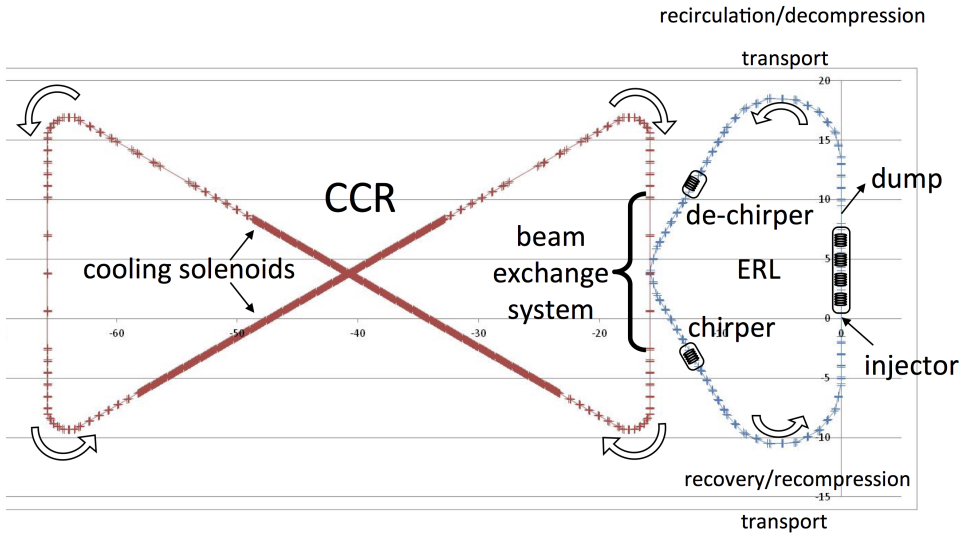

Figure 9.3: Schematic layout of the early CCR design for JLEIC [1].

From the viewpoint of sanity test in the modified semi-analytical Vlasov solver, we use this CCR lattice to confirm that the developed solver based on Eq. (9.59) indeed gives identical results to those obtained by our previous one, specialized for non-magnetized beam transport. The underlying physics of effective suppression of MBI in a magnetized beam transport would be discussed. We also carefully benchmark our semi-analytical Vlasov solutions against particle tracking by `elegant`. Both approaches are found in good agreement.

9.4.1 JLEIC CCR: an early design for non-magnetized cooling

The linear optics design was completed as the circulating cooler ring (CCR) for electron cooling in the ion collider ring at Medium-energy Electron-Ion Collider (MEIC) project [1] at JLab (now JLEIC [2]). It has been known that maintaining excellent phase space quality for the electron beam is crucial to the electron cooling efficiency. This preliminary design is based upon the topological structure of figure-8 collider ring, as illustrated in Fig. 9.3 [1]. Such design of an electron cooler ring is characteristic of two 30-m cooling solenoids cross the center of the electron collider ring (not shown here) and composed of horizontal dipoles around the four corners and vertical bending dipoles around the two diagonal corners to meet the requirement of vertically stacked figure-8 rings [1]. The circulating electron beam was initially assumed uncoupled in transverse planes. Note that the transverse beam dynamics of horizontal and vertical planes are coupled inside and decoupled outside the cooling solenoids. In the case with mere CSR effect, which only occurs within bending dipoles, we can artificially vanish the solenoid sections in the simulations without affecting the microbunching dynamics. If LSC is to be considered, the two 30-m cooling solenoids should be included.

Table 9.1 lists the initial beam and Twiss parameters for the CCR beamline design. The steady-state

Table 9.1: Initial beam parameters for CCR used in the simulation.

Name	Value	Unit
Beam energy	54	MeV
Bunch charge	2	nC
Initial peak bunch current	60	A
Transverse normalized emittance	3	μm
Compression factor	1	
Chirp	0	m^{-1}
Uncorrelated rms energy spread	1×10^{-4}	

CSR gain functions $G(s)$ for three different modulation wavelengths are demonstrated in Fig. 9.4 where we found the microbunching gain with $\lambda = 360\mu$m is much larger compared with the other two cases $\lambda = 100$ and 1000 μm, particularly at the last several bends. Because of frequency dependence of the impedances, more thorough consideration is to scan a spectral range of modulation wavelengths. Figure 9.5 shows the steady-state CSR gain spectrum $G_f\lambda$ as a function of initial modulation wavelengths at the exit of the lattice. In this figure, the same result with two different theoretical formulations is obtained; the red curve, obtained by the formulation derived in Sec. 9.3, and the blue curve, from our developed semi-analytical Vlasov solver for non-magnetized beams (see Sec. 3.3). This numerically verifies the equivalence of the generalized formulation to the existing one for the special case of transversely uncoupled beams. One can see in Figs. 9.4 and 9.5 that the shorter wavelengths enhance the Landau damping or smearing in phase space [through Eq. (9.45) or (9.47)] while the longer wavelengths feature negligible CSR effect. Though not shown here, our Vlasov analysis indicates that, with inclusion of CSR transient effects, the maximum gain can be at least two orders of magnitude larger than the steady-state CSR gain. We notice that with the huge gain shown in Figs. 9.4 and 9.5 the microbunching mechanism may enter nonlinear regime where the linearized Vlasov solutions are no longer valid from a practical point of view. That situation is however beyond the scope of our analysis. Here we note that, due to the ultrahigh gain for JLEIC CCR, particle tracking simulation by `elegant` imposes a significant challenge to obtain the converged results.

To compare with the linear theory (or at the onset of MBI), the numerically imposed density modulation needs to be small enough to remain in the linear regime while such modulation requires to be large enough to rise above the numerical noises originated from the limited number of simulation particles. This implies that a large number of simulation particles and long computation time are required for reaching convergent results of microbunching gain. Thus, to validate our semi-analytical results against `elegant`, and to ease the numerical difficulties with `elegant` tracking, we intentionally increase the transverse beam emittances ten times larger than the nominal values shown in Table 9.1 (i.e. $\epsilon_{nx} = \epsilon_{ny} = 30$ μm) because larger emittance is known to induce more Landau damping, resulting in lower microbunching gain. Lower gain can thus release the stringent requirement of imposing small initial density modulation as well as large number of simulation particles; thus relax numerical difficulties. The benchmark results of CCR for the case with $\epsilon_{nx} = \epsilon_{ny} = 30$ μm are shown in Figs. 9.6 and 9.7. With the increased transverse emittances while

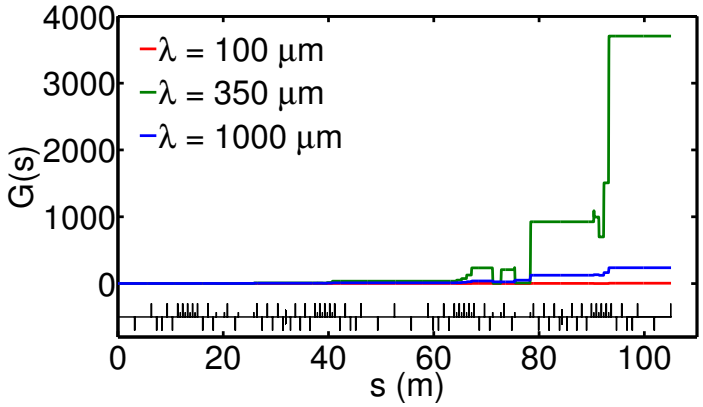

Figure 9.4: CSR gain functions $G(s)$ for MEIC CCR lattice: (red) $\lambda = 100\mu$m, (green) $\lambda = 360\mu$m, (blue) $\lambda = 1000\mu$m.

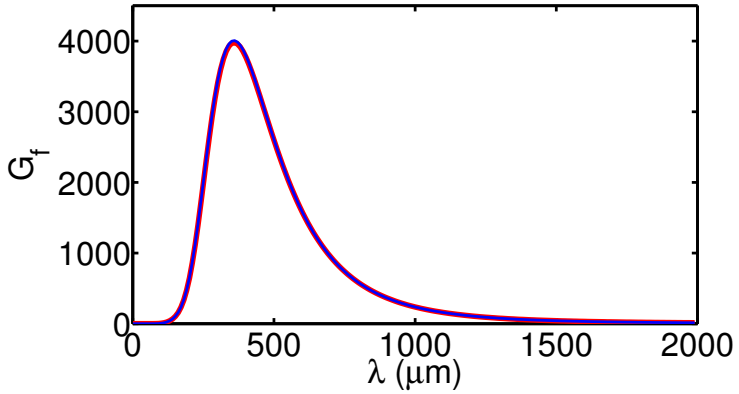

Figure 9.5: CSR gain spectra as a function of initial modulation wavelengths for JLEIC CCR lattice. G_f is evaluated as one-turn microbunching gain. The red curve is obtained by the formulation developed in this paper, while the blue curve from our previously developed semi-analytical Vlasov solver for non-magnetized beams.

keeping other beam and lattice parameters the same, we plot the steady-state CSR gain function $G(s)$ and spectrum $G_f(\lambda)$ together with `elegant` tracking results shown in Figs. 9.6 and 9.7. In `elegant`, 50-million macroparticles were used and 10000 bins employed in simulating CSR effect within dipoles. Both our semi-analytical Vlasov results and `elegant` tracking are in excellent agreement. This validates our semi-analytical Vlasov calculation.

Here we have an interesting observation that, in almost-no-gain regions, the bunching factors (or, microbunching gains) extracted from particle tracking simulation exhibit some fluctuations. These regions happen to locate at larger dispersive locations; thus transverse coordinates (e.g. x and x') can be coupled to the longitudinal coordinate z by non-zero energy displacement (via R_{16} and R_{26}, or R_{51} and R_{52}). In general, $z_s = R_{51}x_0 + R_{52}x'_0 + R_{53}y_0 + R_{54}y'_0 + z_0 + R_{56}\delta_0$, the non-zero dispersion thus smears out z coordinate and causes the (projected) bunch distribution not as smooth as those at other locations.

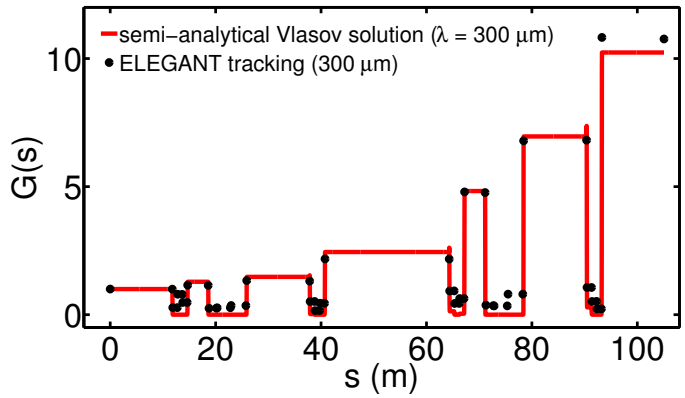

Figure 9.6: Steady-state CSR gain functions $G(s)$ for JLEIC CCR lattice. Note here that $\lambda = 300\mu$m for both the semi-analytical solution and `elegant` tracking. In `elegant` tracking we impose an initial density modulation amplitude 0.2% on a flattop density distribution.

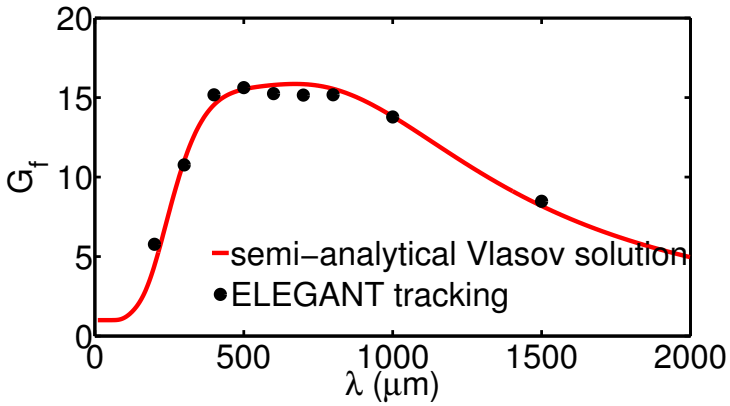

Figure 9.7: Steady-state CSR gain spectrum as a function of the initial modulation wavelength for JLEIC CCR lattice. Here we fix the initial density modulation amplitudes to be 0.2% for various modulation wavelengths to obtain the final gain spectrum.

We remind that, in both our semi-analytical Vlasov analysis and `elegant` tracking, we only consider the CSR microbunching instability in a single turn for the CCR. Our study indicates that the preliminary design of CCR for high-energy electron cooling is at risk of microbunching instability; an improved design is required to suppress such instability and/or alternative beam transport scheme would be considered in order to compensate and to circulate the electron beam as many turns as possible while maintaining high phase space quality of the electron beam required by electron cooling efficiency.

It is investigated that, for JLEIC CCR, due to the high bunch charge ($\sim$ 2 nC) and small beam emittance as well as low energy spread ($\sim 10^{-4}$), the CSR-induced microbunching quickly accumulates and reaches to a maximum gain $\sim$4000 at $\lambda \approx 360\mu$m in the design. Figure 9.8 illustrates the longitudinal phase space fragmentation due to CSR using `elegant`. In the `elegant` tracking simulation, we use 3-million

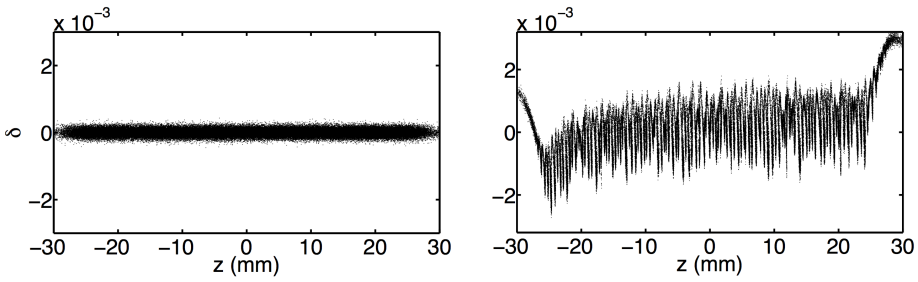

Figure 9.8: Longitudinal phase space distributions for JLEIC CCR: (left) initial quiet beam; (right) when the beam circulates one turn. Note that $z > 0$ is for bunch head.

macroparticles with quiet start. The numerical setting to properly simulate CSR effect within bending dipoles follows that described in Ref [22]. The number of macroparticles employed here is far from enough to meet the quantitatively converged results. Nevertheless, Fig. 9.8 serves an informative purpose to qualitatively demonstrate the phase space modulation due to severe CSR effects.

9.4.2 ERL Cooler Design for Magnetized Cooling

In this subsection we perform the microbunching analyses by considering a recent arc design of JLEIC ERL cooler ring for magnetized electron cooling. Figure 9.9 shows the schematic layout of the recent ERL cooler ring design for JLEIC [14]. This design is different from the previous CCR design [1, 43], in which the beam was non-magnetized and that electron beam ($\sim$2 nC with peak current 60 A) was targeted for strong cooling. This current ERL cooler ring design is however to transport magnetized beam and so far designed for weak cooling [217]. A beam with magnetization is generated in the magnetized gun, immersed in a solenoid. Then the beam is injected in the energy-recovered linac and accelerated to about 55 MeV. The choice of the energy is for the purpose of downstream electron cooling of ion beams. The two arcs, presumed identical, are designed to transport and decompress/compress the beam bunch before/after the cooling section. Table 9.2 summarizes the beam parameters at the entrance of the first arc for our simulation. This achromatic arc is composed of eight cells, and each cell is constructed by two inward and one outward bends. The total bending angle is 180 degrees. Each bending dipole is designed as a half-indexed [30] and combined-function dipole. The arc lattice serves to transport the beam, to match toward the downstream solenoid entrance, as well as to preserve the axial symmetry [30].

Figure 9.10 shows the simulation results for this example arc. An initial nonzero chirp is imposed to the beam so that the bunch is de-compressed while it traverses through the arc. The evolution of bunch current is shown in Fig. 9.10(a). The microbunching gain function, defined in Eq. (9.61), is illustrated in Fig. 9.10(b) for $\lambda = 300\mu$m. In this figure, the dots are obtained from `elegant` tracking with inclusion of 1-D steady-state CSR effect. In `elegant`, a total of 16-million simulation particles are used and 700 bins are set to ensure the convergence of the results and the minimum resolved modulation wavelength down to 50 μm. The input beam phase-space distribution for particle tracking is prepared according to Sec. 5.3.2 (or

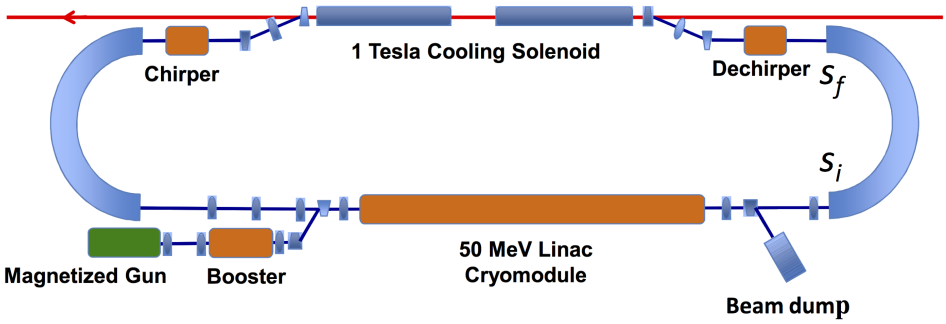

Figure 9.9: Schematic layout of JLEIC ERL cooler design [14].

Table 9.2: Initial beam parameters for JLEIC ERL magnetized beam transport

Name	Value	Unit
Beam energy	55	MeV
Bunch charge	420	pC
Initial peak bunch current	22.5	A
4-D geometric emittance	0.11	μm
Compression factor	0.28	
Chirp	4.465	m^{-1}
Uncorrelated rms energy spread	1.15×10^{-4}	

see Ref. [63]). The data postprocessing follows that described in Sec. 5.3.3. The overall amplification ratio smaller or around unity indicates that the beam during transport is free from MBI. Figure 9.10(c) shows the microbunching gain spectra at the exit of the arc as a function of initial modulation wavelength. This figure shows nearly absence of microbunching in the beam transport even with inclusion of both CSR and LSC. From Figs. 9.10(b) and 9.10(c), we find both the newly developed semi-analytical Vlasov solutions and particle tracking simulations agree with each other. The analysis shows that there is basically no gain growth along the arc. That is, the phase space quality of the beam is well preserved in the transport arc. As a reference, Fig. 9.10(d) indicates the validity of 1-D CSR model [42] used in the simulation, where the so-called Derbenev ratio is defined as $\kappa = \sigma_x/\lambda^{2/3}\rho^{1/3}$ [not to confuse with the dummy variable used in Eq. (9.24)]. This ratio is assumed to be small when 1-D model is valid. When the ratio is no longer small, the transverse variation of the CSR field needs to be taken into account, and a 2-D CSR model would be required [48, 105].

Compared to a non-magnetized beam, for example the beam in JLEIC CCR, a general feature of a magnetized beam is the (much) larger transverse beam size because of its intrinsic angular momentum. This larger beam size can have an effective smearing effect at locations where $R_{51}(s)\sigma_x(s) > \lambda(s)$. In this magnetized beam transport arc example, the maximum correlated length $R_{51}\sigma_x \approx 2$ mm, much longer than the modulation wavelength of interest. The smearing mechanism is similar to that due to finite energy spread, which becomes effective when $R_{56}(s)\sigma_\delta(s) > \lambda(s)$. In the example of the magnetized ERL cooler arc design,

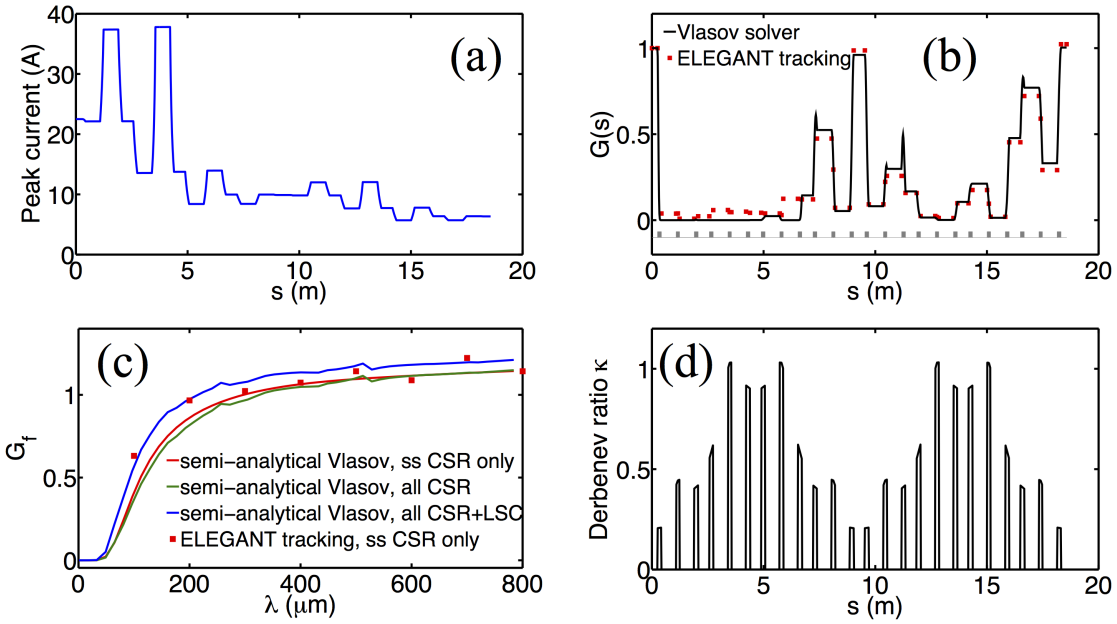

Figure 9.10: (a) bunch decompression along the arc; (b) microbunching gain function $G(s)$ for $\lambda = 300\mu$m; (c) gain spectrum; (d) Derbenev ratio as a function of s.

it is found the effect of smearing in the longitudinal plane, $R_{56}\sigma_\delta \approx 80\mu$m is negligible, compared with sub-millimeter [Fig. 9.10(c)]. Therefore, it is the larger transverse beam size that helps mitigate the MBI in this arc. Compared with the first example of CCR, the smearing distances $R_{51}\sigma_x \approx 10\mu$m and $R_{56}\sigma_\delta \approx 30\mu$m are found to be much shorter than the typical microbunched structure at $\lambda \approx 360\mu$m, where the maximal gain of CCR occurs. Thus, the absence of effective Landau damping or smearing may be expected and can lead to MBI.

As discussed in Sec. 9.3, the microbunching can be seeded by either initial density or energy modulation. The resultant microbunched structure can reside in the forms of density and energy modulations. Thus the full consideration should be given to the total four types of conversion mechanisms. Shown in Fig. 9.11, we found the spectral behaviour of the modulations is largely from pure optics of beam transport. The seemingly large number shown in Fig. 9.11(c) as energy-to-density ratio may not really cause significant microbunching because the initial energy modulation can be small. Let us presume the energy modulation is of the same order as uncorrelated energy spread 10^{-4} at 150 μm, the resultant density modulation due to energy-to-density conversion at the exit of arc is 0.4, which is considered negligible. The preliminary particle tracking simulation with inclusion of space charge and relevant collective effects shows no evidence of energy modulation in the beam phase space. This better situation, however, requires further start-to-end investigation once a full ring lattice is available.

Having investigated the microbunching spectra in various aspects, we now evaluate the beam current

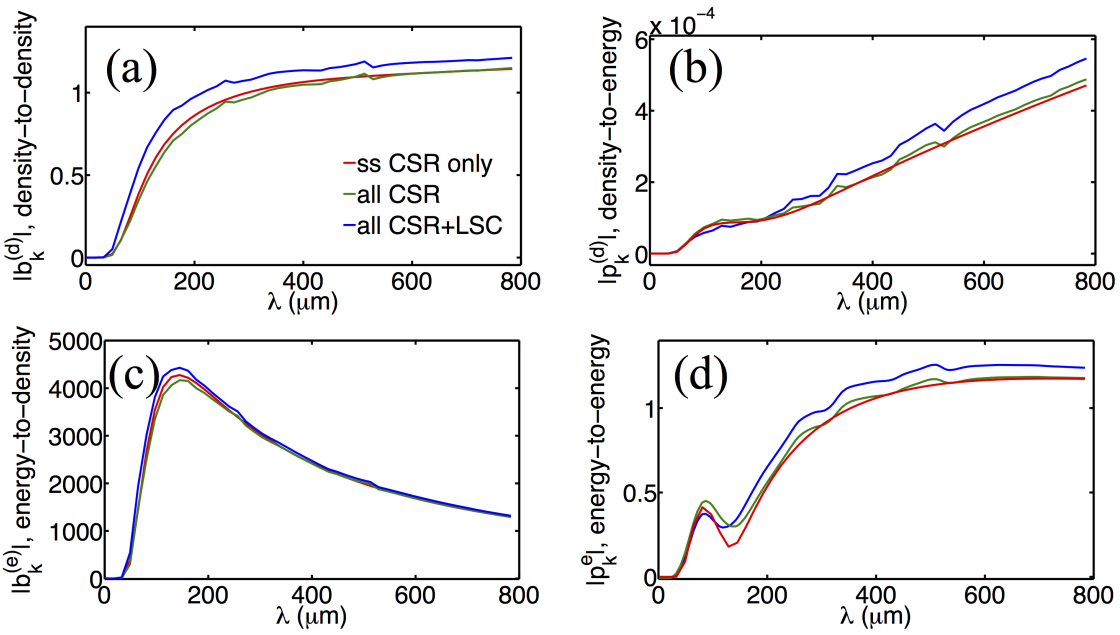

Figure 9.11: Microbunching gain spectra for (a) density-to-density; (b) density-to-energy; (c) energy-to-density; (d) energy-to-energy modulation. Note that in the figures the resultant modulations are evaluated in units of initial modulations.

dependence of the maximal microbunching (density) gain for the magnetized beam transport arc. For the moment, let us neglect the state-of-art technology that thus far can be achieved in the upstream magnetized gun system and ignore other types of collective effects but only focus on MBI due to CSR and LSC. Figure 9.12 shows the current dependence of maximum microbunching gain, in which we find the overall gain smaller than two can be retained up to the (peak) bunch current ∼100 A, five times higher than the nominal value summarized in Table 9.2. This, to some extent, demonstrates the effectiveness of utilizing the magnetized beam for mitigation of MBI. The advantage of using beam magnetization on microbunching suppression can be seen much more prominently for the strong cooling in next-iterative cooler ring design when the bunch charge is increased.

To end this section, let us make an attempt to compare the performance of the above two beamline designs. Note that the comparison may not be fair because the two beamline designs have distinct optical behaviors and different beam properties, as summarized in Tables 9.1 and 9.2. In what follows we only consider steady-state CSR effect. To compare, we first ask ourselves the question: if we gradually remove the beam magnetization, how does the microbunching gain grow? To be specific, instead of using the initial beam parameters as listed in Table 9.2, we make some modification for fairer comparison. Let us presume strong cooling would occur in the ERL cooler design. The (peak) bunch current is set 60 A, the same as that for CCR beam. For simplicity we do not impose a chirp on the circulating beam so that there is no bunch compression. The way we parameterize the beam sigma matrix is as follows. For the moment the full ERL cooler design is not yet available, we extrapolate the beam parameters according to Eq. (9.25).

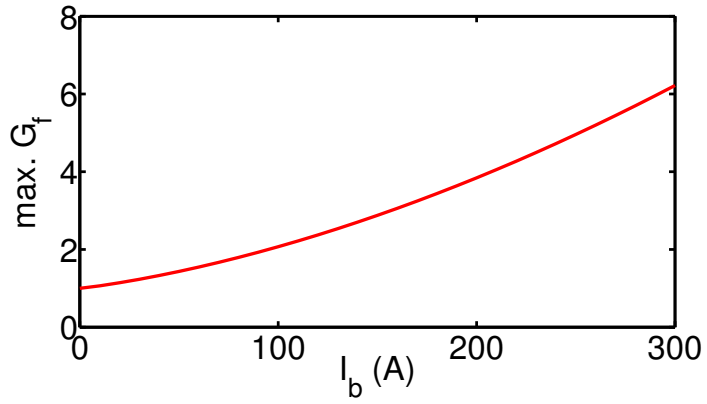

Figure 9.12: Initial current dependence of the maximal microbunching gains for the cooler arc. In the simulation we have included CSR and LSC effects.

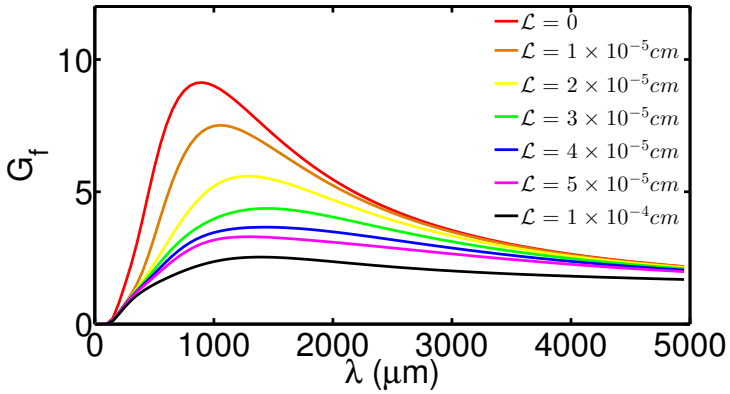

Figure 9.13: Dependence of beam magnetization in terms of $\mathcal{L}$ introduced in this chapter.

From Σ_{14}, we can identify the (half) canonical angular momentum $\mathcal{L}$. Using the fact that the 4-D beam emittance is invariant, the effective emittance can be obtained by Eq. (9.17). Then from Σ_{22}, the beam size σ_c at the reference location, e.g. $s = 0$, can be evaluated. Finally, via Σ_{11}, the virtual distance d can be estimated according to $d = \sigma_c \sqrt{|\Sigma_{11} - \sigma_c^2|} \Big/ \epsilon_{\text{eff}}$. Having obtained the above information, we vary the beam magnetization $\mathcal{L}$ while keeping σ_c and d fixed. In Fig. 9.13, the dependence of beam magnetization on the CSR gain spectra is illustrated. Here the extrapolated beam size at the reference location is $\sigma_c \approx 0.72$ mm, $d \approx 1.77$ cm, and $\mathcal{L} \approx 3.2 \times 10^{-5}$ cm. From Fig. 9.13, we can see that the gain decreases as the beam magnetization increases (beam size thus increases), as expected. Comparing the nominal case (the green curve) with the case without beam magnetization (the red curve), the maximal CSR gains differ by a factor of 2.

For further comparison, one might wonder that the demonstrated CSR gain spectra for CCR in Fig. 9.5 is one-turn gain but the gain for ERL cooler in Fig. 9.10(c) is only for one arc or half turn. Figure 9.14 below illustrates the half-turn microbunching gain spectra for CCR based on the same initial beam

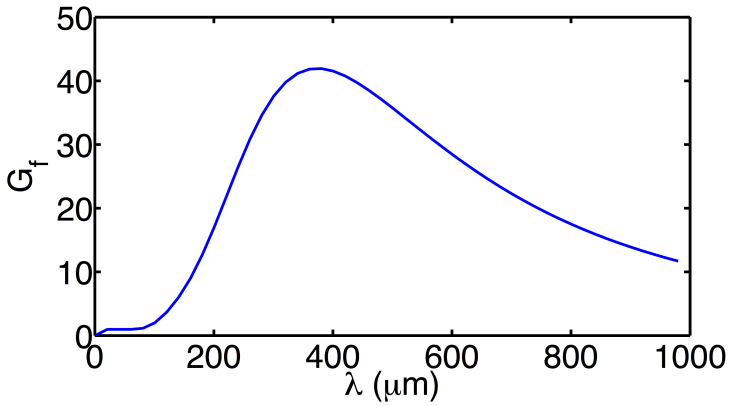

Figure 9.14: Steady-state CSR microbunching gain spectrum of CCR for half a recirculation only.

parameters in Table 9.1. From Figs. 9.13 and 9.14 we may estimate the performance of the two designs that the ERL cooler arc design can result in a factor of 4 reduction of (maximal) CSR microbunching gains reached in CCR, and the beam magnetization leads to a factor of 2 gain reduction for the ERL arc.

9.5 Summary and Conclusion

In this chapter we have reviewed the single-particle magnetized beam dynamics and applied the concept of beam sigma matrix to characterize a beam with correlation between transverse dimensions. Dodging the usage of Twiss (or Courant-Snyder) parameterization in a coupled beam, we take advantage of diagonalizing beam sigma matrix and find it can greatly simplify the formulation for Vlasov analysis of microbunching for a magnetized beam. A set of governing equations for microbunching analysis of general coupled beams has been derived. The theoretical treatment we followed is still largely in the spirit of that we derived in Chapter 3. Solutions to the integral equations have been found to reduce to the existing well-known formulas for non-magnetized beams and have been benchmarked against particle tracking simulation. The results all show good agreement. An arc lattice, designed to transport a magnetized beam for downstream ERL electron cooling of JLEIC, is shown to have nearly no MBI. As a comparison, MBI analysis of the early CCR design is also presented. Suppression of microbunching is found due to effective smearing of relatively large transverse beam size via the transverse-longitudinal correlation R_{51} along the beamline. This smearing takes advantage of a typical feature of beam magnetization. Then a more thorough consideration is taken for both density and energy modulations. Although not fully fair comparison, we did an evaluation to the two beamline designs, where we conclude that the ERL cooler ring can have better performance due to different design strategies of the arc and the magnetization of the beam. More complete analysis will be carried out when a full-ring lattice is available.

CHAPTER 10
Summary and Outlook

In the preceding chapters we have already investigated many aspects of microbunching instability (MBI) in single-pass accelerator systems from theoretical formulation to practical applications. The findings or conclusions were individually summarized in the end of each of chapters. In this final chapter we make general remarks of the work of this dissertation and propose potential further extensions as advanced studies of MBI-related phenomena.

10.1 General remarks

The importance of collective interaction of the high-intensity or high-brightness beam and its self-fields has been addressed, in that it poses significant challenges to the machine design and operation. A recently explored outstanding instability mechanism, MBI, has then become the main topic of this dissertation. The theoretical formulation (a simple model, from current points of view) had been developed in the past decade and a half for linac-based and storage-ring machine configurations. Recently the theory of MBI has been improved in storage-ring accelerators to give more accurate predictions. For recirculating or energy-recovery-linac (ERL) accelerators, in which both the beam properties and lattice design strategy tend to be single-pass configuration (i.e. initial-value problem), the beamline complexity does hardly allow analytical solution to the problem of MBI. In addition, many numerical (particle tracking) challenges that limit the MBI analysis also motivate the work of this dissertation. With the increasing demands of novel recirculating or ERL machines, it is pressing that the existing theory (for linac-based configuration) be extended and an efficient while accurate enough computation tool for MBI analysis be developed. In this dissertation we therefore resort to a semi-analytical route for development of a Vlasov solver in order to fill the gap between linac and storage-ring configurations.

The theoretical formulation is based on the linearized Vlasov equation. In the research work we have extended the previous formulation in the following four aspects:

(1) It allows both transverse horizontal and vertical bending/steering elements in an arbitrary linear beamline lattice. In many recirculation or ERL machines, the beamline consists of spreaders and recombiners and features a three-dimensional machine configuration;

(2) It includes the beam acceleration or deceleration along a beamline, as is typical in such a sort of recirculating or ERL machines. Furthermore it is important to include the LSC effect into account for the downstram MBI amplification;

(3) In addition to the density-to-density microbunched modulations, more complete analysis should include the energy modulation and transverse-longitudinal correlated modulations and have these analyses implemented in a Vlasov solver; and

(4) It permits the calculation of MBI for transversely coupled beams, and the coupled beam transport lattices are also included in our formulation.

Work on **(1)** and **(2)** has been recently published in [177] or presented [174, 179, 183]. Detailed numerical algorithm and benchmarking with `elegant` have been documented in JLab internal technote [173, 176] with `elegant` pre- and post-processing scripts [186]. Work on **(3)** has been presented in recent accelerator conferences [175, 185]. For **(4)**, the most recent work, which is detailed in Chapter 9, is also presented in [187] and will appear in press soon. All the above extensions shall provide and have proven to be an effective tool for microbunching analyses in recirculation or ERL based accelerator studies.

Development and implementation of the theoretical formulation and Vlasov solver in this dissertation have also explored the following angles and applications:

(1) Exploration of multistage amplification behavior of CSR microbunching development. Unlike the two-stage amplification of four-dipole bunch compressor chicanes employed in linacs, the recirculation arcs, which are usually constituted by several tens of bending magnets, show a distinguishing feature of up to six-stage microbunching amplification for our example lattices. That is to say, the maximal CSR amplification can be proportional to the peak bunch current up to sixth power. A method to compare lattice performance was developed in terms of gain coefficients, which nearly only depend on the lattice properties. This method was also proven to be an effective way to quantify the current dependence of the maximal CSR gains. This work has been presented in 36th and 37th Free Electron Laser Conference.

(2) Control of CSR MBI in transport or recirculation arcs. The existing mitigation schemes of MBI mostly aim to linac-based accelerators and may not be practical to the recirculation or ERL facilities. A set of sufficient conditions for suppression of CSR MBI was proposed: i) small β function and ii) large α function within dipoles, and iii) the betatron phase difference $\sim \pi$ or its integer multiples between dipoles. These conditions have been examined and confirmed effectiveness of CSR MBI suppression for low ($\sim$100 MeV), medium ($\sim$750 MeV), and high ($\sim$1 GeV) energy example lattices. This work has been presented in 2016 International Particle Accelerator Conference (IPAC) and the manuscript has been published in [188].

(3) Study of more aspects of microbunched structures in beam phase spaces. The scalar gain multiplication was examined and found to underestimate the overall microbunching amplification. The concept of gain matrix was developed, which includes the density, energy and transverse-longitudinal modulations, and used to analyze MBI for a recirculating machine design [52]. Utilizing the gain matrix approach, it reasonably gives the upper limit of spectral MBI gain curves. As a future work, it can be employed to study multi-pass recirculation. Part of this work has been presented in IPAC and 2016 North American Particle Accelerator Conference (NAPAC16) [175, 185].

(4) Study of MBI for magnetized beams. Driven by a recent ERL cooler design for electron cooling at Jefferson Lab Electron-Ion Collider (JLEIC) Project, the generalized theoretical formulation to a transversely coupled beam, the item (4) above, was applied to this study. A novel idea of utilizing magnetized beam transport was proposed for improvement of cooling efficiency. A magnetized beam, which in general possesses nonzero (transverse) angular momentum, can be produced by a source/gun immersed within a longitudinal (solenoidal) magnetic field, or so-called magnetized gun. Preserving the beam magnetization from collective effects is of a critical issue during beam transport. A concern of MBI regarding this design was studied and excluded. The large beam size associated with the beam magnetization is found to help suppress MBI via the transverse-longitudinal correlation. Part of this work in this dissertation has been presented in [187] and a manuscript has been submitted for publication in a journal [189].

In sum, we have generalized the existing theoretical formulation of MBI in many aspects including the beam itself, the beamline transport optics, and the driving sources (e.g. CSR). We have also developed a numerical tool as a semi-analytical Vlasov solver for the aforementioned exploration and application of MBI studies. In addition, the Vlasov solver has been proven a useful tool for MBI analysis in a wide range of recirculation machine designs, for example, the linear IOTA (Intregable Optics Test Accelerator) ring lattice at Fermilab [138] for optical stochastic cooling experiment, the FFAG (Fixed-Field Alternating Gradient) arc design[123] in the ERL-based machine CBETA at Cornell [122, 190], JLEIC CCR, recirculating IBS ring [52], and potential industrial applications [158].

10.2 Future directions

The scope is divided into the following four aspects, including beam dynamics, field dynamics, numerical code implementation, and more potential applications.

10.2.1 Beam dynamics aspect

The extended theoretical formulation of MBI for a single-pass accelerator system is still based on the following assumptions. These have guided to a path of potential extensions.

Coasting-beam model: MBI is quantified by the amplification of a modulation on top of the (unperturbed) beam phase space distribution, in which the modulation wavelength is assumed small compared with the entire bunch length. This approximation is no longer valid when a bunch experiences the critical or roll-over (parasitic) compression, as may occur at times.

[123] At the moment the MBI analysis serves as a rough estimation since FFAG-type beamline optics is essentially different from what was introduced in Chapter 2.

Linear lattice: The use of linear beam optics greatly simplifies the theory and matches many practical situations. However, in long transport lines of recirculating or ERL-based accelerator systems, nonlinear elements, e.g. sextupoles, are routinely used for longitudinal beam phase space matching and other design considerations. The nonlinear curvature effect[124], from which the local charge can concentrate, may result in more beam emittance growth and increase of energy spread than expected from usual analytical model [111]. Looking at the bunch internal structure, the microbunching appears to reduce based on a few experiences from particle tracking simulation, shown in Fig. 10.1. Such nonlinear effect and dependence on the nonlinearity can be studied in more detail by using our Vlasov solver once the the approximation is relieved. To include the nonlinearity, both the pure optics transport Eq. (2.54) and beam sigma matrix Eq. (2.68) should be extended (see for example Ref. [68]).

Bunched-beam model and nonlinear lattice: Preliminary studies indicate that the above two items can be treated with the help of differential algebra (DA) in a unified way while including transversely coupled beam and coupled lattice (the approach we adopted in Chapter 9, Sec. 9.3). However, the static effect was neglected, i.e. the potential-well distortion of such a bunch, which satisfies Haissinski equation [35] or Eq. (3.67), was not included in the analysis. Analysis of microwave instability in storage rings has been successfully extended from coasting beam model [164] to finite-bunch model [32]. The proposed item will investigate such extension for the Vlasov solver based on single-pass accelerator configuration. Study of dependence of MBI on finite-bunch length using tracking code should also yield important understanding and can serve as benchmark for the analysis.

More aspects of MBI: Motivated by Ref. [211], we found a more complete or elegant description of MBI may follow the definition below as a state in 6-D Fourier spectral domain (or **k**-space)

$$\mathbf{b}(\mathbf{k};s)=\int d\zeta f(\zeta;s)e^{-i\mathbf{k}^T\zeta} \tag{10.1}$$

where f is the phase space distribution, ζ and $\mathbf{k}$ are the corresponding phase space coordinate and its Fourier conjugate.

The traditional characterization of MBI usually refers to a subset of Eq. (10.1): $\mathbf{k}\rightarrow k_z$. The author has extended a few more subsets of Eq. (10.1) from practical interests, e.g. the energy modulation $p(k_z;s)=i\Big[\hat{\delta}\partial\mathbf{b}(\mathbf{k};s)/\partial\mathbf{k}\Big]_{\mathbf{k}=k_z}$. However many experiments suggest that a more complete description of MBI

[124]It can originate from the nonlinearity imprinted on the beam, i.e. nonlinear chirp, T_{655}. For example, due to RF curvature, a traversing bunch will have

$$R_{65}=\frac{eV_{\rm RF}}{E_0}k_{\rm RF}\sin\phi$$

and

$$T_{655}=-\frac{eV_{\rm RF}}{2E_0}k_{\rm RF}^2\cos\phi$$

where the cosine convention ($\phi=0$ on peak voltage) is used in the above formulas. It can also come from the nonlinearity of the beamline, i.e. T_{566}. By adjusting a beamline design, to some extent, T_{566} can be used to correct T_{655}.

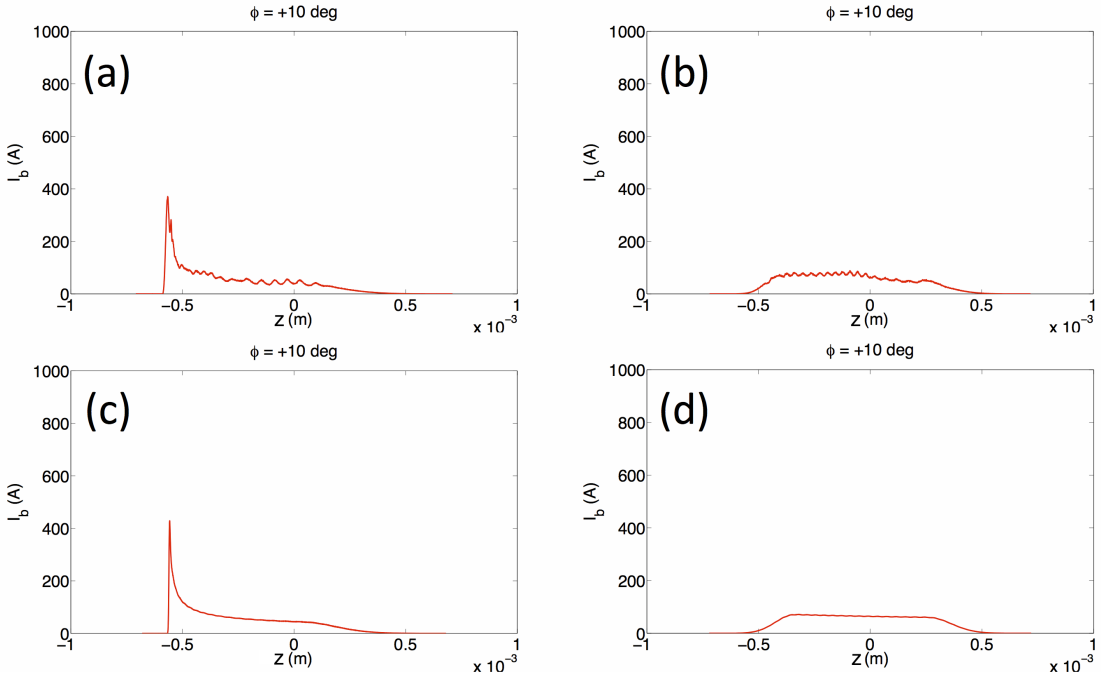

Figure 10.1: Bunch current profiles with T_{655} and/or T_{566} ($z < 0$ for bunch head). (a,c) Only T_{655}, without T_{566} sextupole field correction; (b,d) Only T_{655}, with T_{566} sextupole field correction. The top two figures are with steady-state CSR and the bottom two figures are without CSR. The nonlinear chirp T_{655} assumes $f_{\rm RF} = 1497$MHz, $k_{\rm RF} = 2\pi f_{\rm RF}/c = 31.353$ m^{-1}, $E_0 = 1.3$GeV, $V_{\rm RF} = 1.2$GV. HERA v1 (see Sec. 7.4.1) is used in the tracking simulation. The initial beam parameters follow Table 7.1.

requires more aspects of phase-space modulation characterization with relevant collective effects included. To the author's knowledge, the theoretical analysis has not yet been fully explored and the extension may rely on practical interests of experimental measurements.

First-order (linear) perturbation: Most theoretical/classical treatment of collective instabilities is based on linearization of Vlasov equation, as presented in the preceding chapters. This approach can be valid only at the onset of MBI. However, MBI indeed plays a special role from the viewpoint of beam-wave interaction: before an undulator, MBI is intentionally suppressed, while within the FEL undulator, it is deliberately enhanced by all means. The linear analysis is no longer valid at the intermediate stage including near saturation regime.

Quasi-linear formulation: The extension requires development of a quasi-linear theory suitable for MBI and FEL processes. Despite excellent work [201] had been done on FEL themes, the extension and generalization deserve further investigation. Constructing a hybrid code between the two regimes is an exciting project and may not yet be fully explored.

Transition from single-pass to storage-ring systems: At present, the microbunching analysis for single-

pass system solves initial value problem for 4-D/6-D phase space transport, and the Landau damping from emittance and uncorrelated energy spread depends on details of local optics. The every detail of local optics (and collective effects) have been considered. On the other hand, most microwave instability (MWI) studies solve eigenvalue problems for only 2-D longitudinal phase space transport and the Landau damping depends only on energy spread and *globally smoothed* optics of a storage-ring system. Possible local effects might have been overlooked. In storage rings the energy spread is much larger than that for single-pass accelerators and causes the dominant Landau damping effects, yet this is not true if a machine is operated for a few turns of circulation prior to reaching synchrotron radiation equilibrium. Studying how the two distinct analyses transit should help bridge the understanding of the above two scenarios and for recirculating based machines. The results shall be compared with the existing formulations based on 4-D dispersion relation and eigenvalue approach [32, 164], benchmarked against massive particle tracking simulations and with possible experiments.

Inclusion of laser heating and intrabeam scattering (IBS) into the solver: The heating effects from external laser system and/or IBS in a single-pass accelerator system were analytically estimated. By reformulating the theory in a modified Vlasov equation [165], they might be semi-analytically implemented into the solver. The extension was driven by a potential application of utilizing IBS in a recirculating machine for downstream linac-driven x-ray FELs [52].

Development of Vlasov solver into graphical user interface (GUI): Because of the strengths of the semi-analytical Vlasov solver (fast, free from numerical noise, reasonably accurate and capable of adopting general beamline lattice), it shall be suitable to study MBI-related beam dynamics phenomena in machine beamline studies or to serve as quick design estimation/iteration when MBI can be a concern in a high-brightness transport line. The developed solver can be further employed to perform more systematic studies in more general single-bunch instabilities, and help explore underlying physics. This solver was originally supporting preliminary beamline designs for ERL-based EUV FELs for industrial applications and has been proved a useful tool due to its graphical user interface and incorporation with `elegant` inputs/outputs.

10.2.2 Field dynamics aspect

Longitudinal force: The collective effects considered in the existing (single-pass) MBI theory assumes in the longitudinal direction only. Recently Venturini and Qiang [199] explored a new mechanism, which involves the transverse-longitudinal projection of space charge force and can potentially lead to MBI. Their work motivates this proposed research toward more general aspects of MBI.

Transverse force: The above analysis by Venturini and Qiang in Ref. [199] may be extended, re-formulated and incorporated into the Vlasov solver and then can be applied to perform more thorough MBI analyses, e.g. LCLS-II design studies.

Analytical or numerical impedance models: The developed Vlasov solver has so far only adopted

analytically available impedance models. The analytical formulas may not reflect a satisfactory situation in practice. A set of simplified yet with satisfactorily accurate solvers can be incorporated/integrated, e.g. a parabolic solver for CSR impedances calculation (see, for example, Ref. [7]). It has been known that there are several codes for CSR or general impedance calculation developed in this community for the purpose of estimating MBI more accurately along a beamline. They employ different approaches, including mesh in frequency domain [7], mode expansion [163, 113], finite-element method [203] and etc. The power of the developed semi-analytical Vlasov solver may be enhanced once it can properly incorporate the dedicated impedance solvers.

Two-dimensional CSR studies: Thus far the CSR wakefield or impedance models employed in most MBI analysis are one-dimensional (longitudinal). When a bunch experiences the critical (or parasitic) compression, the (longitudinal) CSR force can have sensitive dependence on the transverse position of the test particle in the bunch in some parameter regimes [105]. In another viewpoint, when a bunch has relative large transverse dimensions, the dependence of CSR force on transverse coordinates needs to be taken into account. The studies of MBI for magnetized beam transport (see Chapter 9) had indicated that 1-D CSR model may not be valid in some parameter regimes.

10.2.3 Numerical code development

It can be expected that when a beamline is longer and longer, as will be encountered when studying the transition to storage-ring case, and the inclusion of collective effects becomes more comprehensive, they require more the computing time. To improve the computational efficiency, the solver can be implemented by parallelizing some of the codes. It is straightforward that the parallelization can be done under coasting beam approximation because the modulation wavelengths are independent to each other.

The ultimate application of the solver can be the combination of it with machine optimization. In contrast to start-to-end tracking simulations, this solver is much more efficient in characterizing the single-bunch phenomena for an arbitrary beamline lattice. It is straightforward to combine machine optimization algorithms such as the genetic algorithm (GA) with the solver and make it a powerful tool for design optimization.

10.2.4 Potential applications

Because of the strengths of the semi-analytical Vlasov solver (fast, free from numerical noise, reasonably accurate and capable of adopting general beamline lattice), it shall be suitable to study MBI in an existing beamline, e.g. LCLS, or to serve as quick design estimation/iteration when MBI can be a concern, e.g. LCLS-II. The developed solver can be further employed to perform more systematic studies in more aspects of MBI (or single-bunch instabilities), and help explore underlying physics. This solver was originally supporting preliminary beamline designs for ERL-based EUV FELs for industrial applications and has been

proved a useful tool due to its graphical user interface and incorporation with `elegant` inputs/outputs [114].

Recently Ratner and Chao [148] proposed a mechanism utilizing MBI to produce high-repetition-rate (or continuous-wave) and high-brilliance coherent radiations. The steady-state microbunched (SSMB) electron beam circulates in a storage ring that promises the output performance before beam phase space quality degradation. The SSMB design shall serve as good examples for the study of the aforementioned items and as mutual benefit the developed solver shall help improve/evaluate the design.

APPENDIX A
Explicit expressions of some integrals

In this appendix, we complete the integrals of Eq. (3.53) for the pure optics case. In Sec. A.1, we make a list to summarize the integration formulas that will be used in the expression of phase space modulation integrals. In Sec. A.2, the resultant expressions of Eq. (3.53) are evaluated.

A.1 List of integration formulas

$$\frac{1}{N}\int d\mathbf{X}_0\ f_1^{(z)} e^{-ik_z(s)z_s(\mathbf{X}_0)} = b_0(k_0;0)\,\{L.D.;s,0\} \tag{A.1}$$

$$\frac{1}{N}\int d\mathbf{X}_0\ f_1^{(\delta,z)} e^{-ik_z(s)z_s(\mathbf{X}_0)} = -ik_z(s)R_{56}(s)p_0(k_0;0)\,\{L.D.;s,0\} \tag{A.2}$$

$$\begin{aligned}&\frac{1}{N}\int d\mathbf{X}_0 f_1^{(x,z)}(\mathbf{X}_0) e^{-ik_z(s)z_s(\mathbf{X}_0)} = ik_z(s)\times\\ &\left[2\alpha_{x0}\gamma_{x0}R_{52}(s) - \left(\beta_{x0}\gamma_{x0}+\alpha_{x0}^2\right)R_{51}(s)\right] a_{x0}\,(k_0;0)\,\{L.D.;s,0\}\end{aligned} \tag{A.3}$$

$$\begin{aligned}&\frac{1}{N}\int d\mathbf{X}_0 f_1^{(x',z)}(\mathbf{X}_0) e^{-ik_z(s)z_s(\mathbf{X}_0)} = -ik_z(s)\times\\ &\left[2\alpha_{x0}\beta_{x0}R_{51}(s) - \left(\beta_{x0}\gamma_{x0}+\alpha_{x0}^2\right)R_{52}(s)\right] a_{x'0}\,(k_0;0)\,\{L.D.;s,0\}\end{aligned} \tag{A.4}$$

$$\frac{1}{N}\int d\mathbf{X}_0\ \left(\delta_0 - hz_0\right) f_1^{(z)} e^{-ik_z(s)z_s(\mathbf{X}_0)} = -ik_z(s)R_{56}(s)\sigma_{\delta0}^2 b_0(k_0;0)\,\{L.D.;s,0\} \tag{A.5}$$

$$\frac{1}{N}\int d\mathbf{X}_0\ \left(\delta_0 - hz_0\right) f_1^{(\delta,z)} e^{-ik_z(s)z_s(\mathbf{X}_0)} = \left(1 - k_z^2(s)R_{56}^2(s)\sigma_{\delta0}^2\right) p_0(k_0;0)\,\{L.D.;s,0\} \tag{A.6}$$

$$\begin{aligned}&\frac{1}{N}\int d\mathbf{X}_0\,(\delta_0 - hz_0)\, f_1^{(x,z)}(\mathbf{X}_0) e^{-ik_z(s)z_s(\mathbf{X}_0)}\\ &= k_z^2(s)R_{56}(s)\sigma_{\delta0}^2\left[2\alpha_{x0}\gamma_{x0}R_{52}(s) - \left(\beta_{x0}\gamma_{x0}+\alpha_{x0}^2\right)R_{51}(s)\right] a_{x0}\,(k_0;0)\,\{L.D.;s,0\}\\ &= -ik_z(s)R_{56}(s)\sigma_{\delta0}^2 b_0^{(x,z)}\end{aligned} \tag{A.7}$$

$$\frac{1}{N}\int d\mathbf{X}_0\,(\delta_0 - hz_0)\,f_1^{(x',z)}(\mathbf{X}_0)e^{-ik_z(s)z_s(\mathbf{X}_0)}$$
$$= -k_z^2(s)R_{56}(s)\sigma_{\delta 0}^2\left[2\alpha_{x0}\beta_{x0}R_{51}(s) - \left(\beta_{x0}\gamma_{x0} + \alpha_{x0}^2\right)R_{52}(s)\right]a_{x'0}\,(k_0;0)\,\{L.D.;s,0\}$$
$$= ik_z(s)R_{56}(s)\sigma_{\delta 0}^2 b_0^{(x',z)} \tag{A.8}$$

$$\frac{1}{N}\int d\mathbf{X}_0\ \ (x_0)\,f_1^{(z)}e^{-ik_z(s)z_s(\mathbf{X}_0)} = ik_z(s)\epsilon_{x0}\left(R_{52}(s)\alpha_{x0} - R_{51}(s)\beta_{x0}\right)b_0(k_0;0)\,\{L.D.;s,0\} \tag{A.9}$$

$$\frac{1}{N}\int d\mathbf{X}_0\ \ (x_0)\,f_1^{(\delta,z)}e^{-ik_z(s)z_s(\mathbf{X}_0)} = k_z^2(s)\epsilon_{x0}R_{56}(s)\left(R_{52}(s)\alpha_{x0} - R_{51}(s)\beta_{x0}\right)p_0(k_0;0)\,\{L.D.;s,0\} \tag{A.10}$$

$$\frac{1}{N}\int d\mathbf{X}_0\ \ (x_0')\,f_1^{(z)}e^{-ik_z(s)z_s(\mathbf{X}_0)} = ik_z(s)\epsilon_{x0}\left(R_{52}(s)\gamma_{x0} - R_{51}(s)\alpha_{x0}\right)b_0(k_0;0)\,\{L.D.;s,0\} \tag{A.11}$$

$$\frac{1}{N}\int d\mathbf{X}_0\ \ (x_0')\,f_1^{(\delta,z)}e^{-ik_z(s)z_s(\mathbf{X}_0)} = k_z^2(s)\epsilon_{x0}R_{56}(s)\left(R_{52}(s)\gamma_{x0} - R_{51}(s)\alpha_{x0}\right)p_0(k_0;0)\,\{L.D.;s,0\} \tag{A.12}$$

$$[\![x_0x_0]\!] \equiv \int dx_0dx_0'd\delta_0\,(x_0x_0)\,\bar{f}_0(\mathbf{X}_0)e^{-ik_z(s)z_s(\mathbf{X}_0)}$$
$$= \left[\epsilon_{x0}\beta_{x0} - k_z^2(s)\epsilon_{x0}^2\left(R_{52}(s)\alpha_{x0} - R_{51}(s)\beta_{x0}\right)^2\right]\{L.D.;s,0\} \tag{A.13}$$

$$[\![x_0x_0']\!] \equiv \int dx_0dx_0'd\delta_0\,(x_0x_0')\,\bar{f}_0(\mathbf{X}_0)e^{-ik_z(s)z_s(\mathbf{X}_0)}$$
$$= \left[\epsilon_{x0}\alpha_{x0} - k_z^2(s)\epsilon_{x0}^2\left(R_{52}(s)\alpha_{x0} - R_{51}(s)\beta_{x0}\right)\left(R_{52}(s)\gamma_{x0} - R_{51}(s)\alpha_{x0}\right)\right]\{L.D.;s,0\} \tag{A.14}$$

$$[\![x_0'x_0']\!] \equiv \int dx_0dx_0'd\delta_0\,(x_0'x_0')\,\bar{f}_0(\mathbf{X}_0)e^{-ik_z(s)z_s(\mathbf{X}_0)}$$
$$= \left[\epsilon_{x0}\gamma_{x0} - k_z^2(s)\epsilon_{x0}^2\left(R_{52}(s)\gamma_{x0} - R_{51}(s)\alpha_{x0}\right)^2\right]\{L.D.;s,0\} \tag{A.15}$$

$$[\![x_0\delta_0]\!] \equiv \int dx_0dx_0'd\delta_0\,(x_0\delta_0)\,\bar{f}_0(\mathbf{X}_0)e^{-ik_z(s)z_s(\mathbf{X}_0)}$$
$$= k_z^2(s)R_{56}(s)\sigma_{\delta 0}^2\epsilon_{x0}\left(R_{52}(s)\alpha_{x0} - R_{51}(s)\beta_{x0}\right)\{L.D.;s,0\} \tag{A.16}$$

$$[\![x_0'\delta_0]\!] \equiv \int dx_0 dx_0' d\delta_0 \, (x_0'\delta_0) \, \bar{f}_0(\mathbf{X}_0) e^{-ik_z(s)z_s(\mathbf{X}_0)}$$
$$= k_z^2(s) R_{56}(s) \sigma_{\delta 0}^2 \epsilon_{x0} \left(R_{52}(s)\gamma_{x0} - R_{51}(s)\alpha_{x0} \right) \{L.D.; s, 0\} \tag{A.17}$$

A.2 Expressions of Eq. (3.53)

$$b_0^{(z)}(k_z; s) = \frac{1}{N} \int d\mathbf{X}_0 f_1^{(z)} e^{-ik_z(s)z_s(\mathbf{X}_0)} = b_0(k_0; 0) \{L.D.; s, 0\} \tag{A.18}$$

$$b_0^{(\delta,z)}(k_z; s) = \frac{1}{N} \int d\mathbf{X}_0 \; f_1^{(\delta,z)} e^{-ik_z(s)z_s(\mathbf{X}_0)} = -ik_z(s) R_{56}(s) p_0(k_0; 0) \{L.D.; s, 0\} \tag{A.19}$$

$$b_0^{(x,z)}(k_z; s) = \frac{1}{N} \int d\mathbf{X}_0 \; f_1^{(x,z)} e^{-ik_z(s)z_s(\mathbf{X}_0)}$$
$$= ik_z(s) \left[2\alpha_{x0}\gamma_{x0} R_{52}(s) - \left(\beta_{x0}\gamma_{x0} + \alpha_{x0}^2 \right) R_{51}(s) \right] a_{x0}(k_0; 0) \{L.D.; s, 0\} \tag{A.20}$$

$$b_0^{(x',z)}(k_z; s) = \frac{1}{N} \int d\mathbf{X}_0 \; f_1^{(x',z)} e^{-ik_z(s)z_s(\mathbf{X}_0)}$$
$$= -ik_z(s) \left[2\alpha_{x0}\beta_{x0} R_{51}(s) - \left(\beta_{x0}\gamma_{x0} + \alpha_{x0}^2 \right) R_{52}(s) \right] a_{x'0}(k_0; 0) \{L.D.; s, 0\} \tag{A.21}$$

$$p_0^{(z)}(k_z; s) = \frac{1}{N} \int d\mathbf{X}_0 \, (\delta_0 - hz_0) \, f_1^{(z)} e^{-ik_z(s)z_s(\mathbf{X}_0)} = -ik_z(s) R_{56}(s) \sigma_{\delta 0}^2 b_0(k_0; 0) \{L.D.; s, 0\} \tag{A.22}$$

$$p_0^{(\delta,z)}(k_z; s) = \frac{1}{N} \int d\mathbf{X}_0 \; (\delta_0 - hz_0) \, f_1^{(\delta,z)} e^{-ik_z(s)z_s(\mathbf{X}_0)}$$
$$= \left(1 - k_z^2(s) R_{56}^2(s) \sigma_{\delta 0}^2 \right) p_0(k_0; 0) \{L.D.; s, 0\} \tag{A.23}$$

$$p_0^{(x,z)}(k_z; s) = \frac{1}{N} \int d\mathbf{X}_0 \; (\delta_0 - hz_0) \, f_1^{(x,z)} e^{-ik_z(s)z_s(\mathbf{X}_0)}$$
$$= k_z^2(s) R_{56}(s) \sigma_{\delta 0}^2 \left[2\alpha_{x0}\gamma_{x0} R_{52}(s) - \left(\beta_{x0}\gamma_{x0} + \alpha_{x0}^2 \right) R_{51}(s) \right] a_{x0}(k_0; 0) \{L.D.; s, 0\}$$
$$= -ik_z(s) R_{56}(s) \sigma_{\delta 0}^2 b_0^{(x,z)} \tag{A.24}$$

$$
\begin{aligned}
p_0^{(x',z)}(k_z;s) &= \frac{1}{N}\int d\mathbf{X}_0\ \left(\delta_0 - hz_0\right) f_1^{(x',z)} e^{-ik_z(s)z_s(\mathbf{X}_0)} \\
&= -k_z^2(s)R_{56}(s)\sigma_{\delta 0}^2\left[2\alpha_{x0}\beta_{x0}R_{51}(s) - \left(\beta_{x0}\gamma_{x0}+\alpha_{x0}^2\right)R_{52}(s)\right] a_{x'0}\left(k_0;0\right)\left\{L.D.;s,0\right\} \\
&= ik_z(s)R_{56}(s)\sigma_{\delta 0}^2 b_0^{(x',z)}
\end{aligned} \tag{A.25}
$$

$$
\begin{aligned}
a_{x0}^{(z)}(k_z;s) &= \frac{1}{N}\int d\mathbf{X}_s\left(x_s\right) f_1^{(z)}(\mathbf{X}_s) e^{-ik_z(s)z_s(\mathbf{X}_s)} \\
&= \frac{R_{11}(s)}{N}\int d\mathbf{X}_0\left(x_0\right) f_1^{(z)}(\mathbf{X}_0) e^{-ik_z(s)z_s(\mathbf{X}_0)} \\
&+ \frac{R_{12}(s)}{N}\int d\mathbf{X}_0\left(x_0{}'\right) f_1^{(z)}(\mathbf{X}_0) e^{-ik_z(s)z_s(\mathbf{X}_0)} \\
&+ \frac{R_{16}(s)}{N}\int d\mathbf{X}_0\left(\delta_0\right) f_1^{(z)}(\mathbf{X}_0) e^{-ik_z(s)z_s(\mathbf{X}_0)}
\end{aligned} \tag{A.26}
$$

$$
\begin{aligned}
a_{x0}^{(\delta,z)}(k_z;s) &= \frac{1}{N}\int d\mathbf{X}_s\left(x_s\right) f_1^{(\delta,z)}(X;s) e^{-ik_z(s)z_s(\mathbf{X}_s)} \\
&= \frac{R_{11}(s)}{N}\int d\mathbf{X}_0\ \left(x_0\right) f_1^{(\delta,z)}(\mathbf{X}_0) e^{-ik_z(s)z_s(\mathbf{X}_0)} \\
&+ \frac{R_{12}(s)}{N}\int d\mathbf{X}_0\ \left(x_0{}'\right) f_1^{(\delta,z)}(\mathbf{X}_0) e^{-ik_z(s)z_s(\mathbf{X}_0)} \\
&+ \frac{R_{16}(s)}{N}\int d\mathbf{X}_0\ \left(\delta_0\right) f_1^{(\delta,z)}(\mathbf{X}_0) e^{-ik_z(s)z_s(\mathbf{X}_0)}
\end{aligned} \tag{A.27}
$$

$$
\begin{aligned}
a_{x0}^{(x,z)}(k_z;s) &= \frac{1}{N}\int d\mathbf{X}_s(x_s) f_1^{(x,z)} e^{-ik_z(s)z_s(\mathbf{X}_s)} \\
&= \frac{1}{N}\int d\mathbf{X}_0\left(R_{11}(s)x_0 + R_{12}(s)x_0' + R_{16}(s)\delta_0\right)\left(1+\frac{\gamma_{x0}x_0+\alpha_{x0}x_0'}{\epsilon_{x0}}\Delta x_0(z_0)\right)\bar{f}_0(\mathbf{X}_0) e^{-ik_z(s)z_s(\mathbf{X}_0)} \\
&= a_{x0}(k_0;0)\left\{\begin{array}{l}
R_{11}(s)\dfrac{\gamma_{x0}}{\epsilon_{x0}}\left[\!\left[x_0x_0\right]\!\right] + R_{11}(s)\dfrac{\alpha_{x0}}{\epsilon_{x0}}\left[\!\left[x_0x_0'\right]\!\right] \\
+R_{12}(s)\dfrac{\gamma_{x0}}{\epsilon_{x0}}\left[\!\left[x_0'x_0\right]\!\right] + R_{12}(s)\dfrac{\alpha_{x0}}{\epsilon_{x0}}\left[\!\left[x_0'x_0'\right]\!\right] \\
+R_{16}(s)\dfrac{\gamma_{x0}}{\epsilon_{x0}}\left[\!\left[\delta_0x_0\right]\!\right] + R_{16}(s)\dfrac{\alpha_{x0}}{\epsilon_{x0}}\left[\!\left[\delta_0x_0'\right]\!\right]
\end{array}\right\}
\end{aligned} \tag{A.28}
$$

$$
\begin{aligned}
a_{x0}^{(x',z)}(k_z;s) &= \frac{1}{N}\int d\mathbf{X}_s(x_s) f_1^{(x',z)} e^{-ik_z(s)z_s(\mathbf{X}_s)} \\
&= \frac{1}{N}\int d\mathbf{X}_0 \left(R_{11}(s)x_0 + R_{12}(s)x_0' + R_{16}(s)\delta_0\right)\left(1+\frac{\beta_{x0}x_0'+\alpha_{x0}x_0}{\epsilon_{x0}}\Delta x_0'(z_0)\right)\bar{f}_0(\mathbf{X}_0)e^{-ik_z(s)z_s(\mathbf{X}_0)} \\
&= a_{x'0}(k_0;0)\left\{\begin{array}{l} R_{11}(s)\dfrac{\beta_{x0}}{\epsilon_{x0}}[\![x_0x_0']\!] + R_{11}(s)\dfrac{\alpha_{x0}}{\epsilon_{x0}}[\![x_0x_0]\!] \\ +R_{12}(s)\dfrac{\beta_{x0}}{\epsilon_{x0}}[\![x_0'x_0']\!] + R_{12}(s)\dfrac{\alpha_{x0}}{\epsilon_{x0}}[\![x_0'x_0]\!] \\ +R_{16}(s)\dfrac{\beta_{x0}}{\epsilon_{x0}}[\![\delta_0x_0']\!] + R_{16}(s)\dfrac{\alpha_{x0}}{\epsilon_{x0}}[\![\delta_0x_0]\!] \end{array}\right\}
\end{aligned} \tag{A.29}
$$

$$
\begin{aligned}
a_{x'0}^{(z)}(k_z;s) &= \frac{1}{N}\int d\mathbf{X}_s\,({x_s}')\, f_1^{(z)}(\mathbf{X}_s)e^{-ik_z(s)z_s(\mathbf{X}_s)} \\
&= \frac{R_{21}(s)}{N}\int d\mathbf{X}_0\,(x_0)\, f_1^{(z)}(\mathbf{X}_0)e^{-ik_z(s)z_s(\mathbf{X}_0)} \\
&+ \frac{R_{22}(s)}{N}\int d\mathbf{X}_0\,({x_0}')\, f_1^{(z)}(\mathbf{X}_0)e^{-ik_z(s)z_s(\mathbf{X}_0)} \\
&+ \frac{R_{26}(s)}{N}\int d\mathbf{X}_0\,(\delta_0)\, f_1^{(z)}(\mathbf{X}_0)e^{-ik_z(s)z_s(\mathbf{X}_0)}
\end{aligned} \tag{A.30}
$$

$$
\begin{aligned}
a_{x'0}^{(\delta,z)}(k_z;s) &= \frac{1}{N}\int d\mathbf{X}_s\,({x_s}')\, f_1^{(\delta,z)}(\mathbf{X}_s)e^{-ik_z(s)z_s(\mathbf{X}_s)} \\
&= \frac{R_{21}(s)}{N}\int d\mathbf{X}_0\,(x_0)\, f_1^{(\delta,z)}(\mathbf{X}_0)e^{-ik_z(s)z_s(\mathbf{X}_0)} \\
&+ \frac{R_{22}(s)}{N}\int d\mathbf{X}_0\,({x_0}')\, f_1^{(\delta,z)}(\mathbf{X}_0)e^{-ik_z(s)z_s(\mathbf{X}_0)} \\
&+ \frac{R_{26}(s)}{N}\int d\mathbf{X}_0\,(\delta_0)\, f_1^{(\delta,z)}(\mathbf{X}_0)e^{-ik_z(s)z_s(\mathbf{X}_0)}
\end{aligned} \tag{A.31}
$$

$$
\begin{aligned}
a_{x'0}^{(x,z)}(k_z;s) &= \frac{1}{N}\int d\mathbf{X}_s(x_s') f_1^{(x,z)} e^{-ik_z(s)z_s(\mathbf{X}_s)} \\
&= \frac{1}{N}\int d\mathbf{X}_0 \left(R_{21}(s)x_0 + R_{22}(s)x_0' + R_{26}(s)\delta_0\right)\left(1+\frac{\gamma_{x0}x_0+\alpha_{x0}x_0'}{\epsilon_{x0}}\Delta x_0(z_0)\right)\bar{f}_0(\mathbf{X}_0)e^{-ik_z(s)z_s(\mathbf{X}_0)} \\
&= a_{x0}(k_0;0)\left\{\begin{array}{l} R_{21}(s)\dfrac{\gamma_{x0}}{\epsilon_{x0}}[\![x_0x_0]\!] + R_{21}(s)\dfrac{\alpha_{x0}}{\epsilon_{x0}}[\![x_0x_0']\!] \\ +R_{22}(s)\dfrac{\gamma_{x0}}{\epsilon_{x0}}[\![x_0'x_0]\!] + R_{22}(s)\dfrac{\alpha_{x0}}{\epsilon_{x0}}[\![x_0'x_0']\!] \\ +R_{26}(s)\dfrac{\gamma_{x0}}{\epsilon_{x0}}[\![\delta_0x_0]\!] + R_{26}(s)\dfrac{\alpha_{x0}}{\epsilon_{x0}}[\![\delta_0x_0']\!] \end{array}\right\}
\end{aligned} \tag{A.32}
$$

$$
\begin{aligned}
a_{x'0}^{(x',z)}(k_z;s) &= \frac{1}{N}\int d\mathbf{X}_s(x'_s) f_1^{(x',z)} e^{-ik_z(s)z_s(\mathbf{X}_s)} \\
&= \frac{1}{N}\int d\mathbf{X}_0 \left(R_{21}(s)x_0 + R_{22}(s)x'_0 + R_{26}(s)\delta_0\right)\left(1+\frac{\beta_{x0}x'_0+\alpha_{x0}x_0}{\epsilon_{x0}}\Delta x'_0(z_0)\right)\bar{f}_0(\mathbf{X}_0)e^{-ik_z(s)z_s(\mathbf{X}_0)} \\
&= a_{x'0}(k_0;0)\left\{\begin{array}{l} R_{21}(s)\dfrac{\beta_{x0}}{\epsilon_{x0}}[\![x_0x'_0]\!] + R_{21}(s)\dfrac{\alpha_{x0}}{\epsilon_{x0}}[\![x_0x_0]\!] \\ +R_{22}(s)\dfrac{\beta_{x0}}{\epsilon_{x0}}[\![x'_0x'_0]\!] + R_{22}(s)\dfrac{\alpha_{x0}}{\epsilon_{x0}}[\![x'_0x_0]\!] \\ +R_{26}(s)\dfrac{\beta_{x0}}{\epsilon_{x0}}[\![\delta_0x'_0]\!] + R_{26}(s)\dfrac{\alpha_{x0}}{\epsilon_{x0}}[\![\delta_0x_0]\!] \end{array}\right\}
\end{aligned} \tag{A.33}
$$

For the above quantities with double bracket, see Eqs. (A.13) to (A.17). Relevant equations involving the above expressions can be found in Eqs. (3.20) to (3.25), Eqs. (3.45) to (3.50), Eq. (3.53), Eqs. (3.52), (3.54) to (3.65), or Eqs. (8.11) to (8.26).

A.3 Explicit expressions of $\mathbf{R}(\tau \to s)$ elements

In Eqs. (3.59) to (3.64) [or Eqs. (8.19) to (8.23)], the relative transport matrix elements $\mathbf{R}(\tau \to s)$ can be evaluated by the matrix multiplication, i.e. $\mathbf{R}(\tau \to s) = \mathbf{R}(s)\mathbf{R}^{-1}(\tau)$. Their explicit expressions are summarized below:

$$R_{11}(\tau \to s) = R_{11}(s)R_{22}(\tau) - R_{12}(s)R_{21}(\tau) \tag{A.34}$$

$$R_{12}(\tau \to s) = R_{12}(s)R_{11}(\tau) - R_{11}(s)R_{12}(\tau) \tag{A.35}$$

$$R_{21}(\tau \to s) = R_{21}(s)R_{22}(\tau) - R_{22}(s)R_{21}(\tau) \tag{A.36}$$

$$R_{22}(\tau \to s) = R_{22}(s)R_{11}(\tau) - R_{21}(s)R_{12}(\tau) \tag{A.37}$$

$$R_{16}(\tau \to s) = R_{16}(s) + R_{12}(s)R_{51}(\tau) - R_{11}(s)R_{52}(\tau) \tag{A.38}$$

$$R_{26}(\tau \to s) = R_{26}(s) + R_{22}(s)R_{51}(\tau) - R_{21}(s)R_{52}(\tau) \tag{A.39}$$

$$R_{33}(\tau \to s) = R_{33}(s)R_{44}(\tau) - R_{34}(s)R_{43}(\tau) \tag{A.40}$$

$$R_{34}(\tau \to s) = R_{34}(s)R_{33}(\tau) - R_{33}(s)R_{34}(\tau) \tag{A.41}$$

$$R_{43}(\tau \to s) = R_{43}(s)R_{44}(\tau) - R_{44}(s)R_{43}(\tau) \tag{A.42}$$

$$R_{44}(\tau \to s) = R_{44}(s)R_{33}(\tau) - R_{43}(s)R_{34}(\tau) \tag{A.43}$$

$$R_{36}(\tau \to s) = R_{36}(s) + R_{34}(s)R_{53}(\tau) - R_{33}(s)R_{54}(\tau) \tag{A.44}$$

$$R_{46}(\tau \to s) = R_{46}(s) + R_{44}(s)R_{53}(\tau) - R_{43}(s)R_{54}(\tau) \tag{A.45}$$

$$R_{56}(\tau \to s) = R_{56}(s) - R_{56}(\tau) + R_{51}(\tau)R_{52}(s) - R_{51}(s)R_{52}(\tau) + R_{53}(\tau)R_{54}(s) - R_{53}(s)R_{54}(\tau) \tag{A.46}$$

APPENDIX B
List of acronyms

- APS, Advanced Photon Source, at Argonne National Laboratory
- BC1, first bunch compressor
- BC2, second bunch compressor
- CCR, circulating cooler ring
- COTR, coherent optical transition radiation
- CSR, coherent synchrotron radiation
- `elegant`, ELEctron Generation ANd Tracking
- ERL, energy recovery linac
- EUV, extreme ultraviolet
- FEL, free electron laser
- FFT, fast Fourier transform
- FODO, focusing-drift-defocusing-drift
- HERA, high energy recirculation arc
- HK, Huang and Kim, used to refer Ref. [81]
- HSK, Heifets, Stupakov, and Krinsky, used to refer Ref. [79]
- JLEIC, Jefferson Lab Electron Ion Collider project (former MEIC)
- LCLS, Linac Coherent Light Source, at SLAC National Laboratory
- L.D., Landau damping
- LERA, low energy recirculation arc
- LERF, Low Energy Recirculation Facility, at Jefferson Lab
- LSC, longitudinal space charge
- MAD, Methodical Accelerator Design
- MBI, microbunching instability

- MEIC, Medium-energy Electron Ion Collider project
- MWI, microwave instability
- N-D, N-dimensional
- NAFF, Numerical Analysis of Fundamental Frequencies
- NSLS, National Synchrotron Light Source, at Brookhaven National Laboratory
- PIC, particle in cell
- PSD, power spectral density
- PWD, potential well distortion
- RF, radio frequency
- RTF, round-to-flat transformation
- SDDS, self-describing data sets
- SDL, Source Development Laboratory, at Brookhaven National Laboratory
- SR, synchrotron radiation
- SSY, Saldin, Schneidmiller, and Yurkov, used to refer Refs. [152] and [153]
- XTCAV, X-band transverse deflecting cavity

Bibliography

[1] S. Abeyratne, A. Accardi, S. Ahmed, D. Barber, J. Bisognano, A. Bogacz, A. Castilla, P. Chevtsov, S. Corneliussen, W. Deconinck, P. Degtiarenko, J. Delayen, Ya. Derbenev, S. DeSilva, D. Douglas, V. Dudnikov, R. Ent, B. Erdelyi, P. Evtushenko, Yu. Filatov, D. Gaskell, R. Geng, V. Guzey, T. Horn, A. Hutton, C. Hyde, R. Johnson, Y. Kim, F. Klein, A. Kondratenko, M. Kondratenko, G. Krafft, R. Li, F. Lin, S. Manikonda, F. Marhauser, R. McKeown, V. Morozov, P. Nadel-Turonski, E. Nissen, P. Ostroumov, M. Pivi, F. Pilat, M. Poelker, A. Prokudin, R. Rimmer, T. Satogata, H. Sayed, M. Spata, M. Sullivan, C. Tennant, B. Terzic, M. Tiefenback, H. Wang, S. Wang, C. Weiss, B. Yunn, and Y. Zhang, Science Requirements and Conceptual Design for a Polarized Medium Energy Electron-Ion Collider at Jefferson Lab, available at https://arxiv.org/abs/1209.0757 (2012)

[2] S. Abeyratne, D. Barber, A. Bogacz, P. Brindza, Y. Cai, A. Camsonne, A. Castilla, P. Chevtsov, E. Daly, Y. S. Derbenev, D. Douglas, V. Dudnikov, R. Ent, B. Erdelyi, Y. Filatov, D. Gaskell, J. Grames, J. Guo, L. Harwood, A. Hutton, C. Hyde, K. Jordan, A. Kimber, G. A. Krafft, A. Kondratenko, M. Kondratenko, R. Li, F. Lin, T. Mann, P. McIntyre, T. Michalski, V.S. Morozov, P. Nadel-Turonski, Y.M. Nosochkov, P. N. Ostroumov, K. Park, F. Pilat, M. Poelker, N. J. Pogue, R. Rimmer, Y. Roblin, T. Satogata, A. Sattarov, M. Spata, R. Suleiman, M. Sullivan, A. Sy, C. Tennant, H. Wang, M-H Wang, S. Wang, U. Wienands, H. Zhang, Y. Zhang, and Z. Zhao, MEIC Design Summary, https://arxiv.org/abs/1504.07961

[3] M. Abo-Bakr, J. Feikes, K. Holldack, P. Kuske, and G. Wustefeld, Coherent emission of synchrotron radiation and longitudinal instabilities, in Proceedings of the 2003 Particle Accelerator Conference, Portland, OR (IEEE, New York, 2003), p. 3023

[4] M. Abo-Bakr, J. Feikes, K. Holldack, G. Wstefeld, and H.-W. Hubers, Steady-State Far-Infrared Coherent Synchrotron Radiation detected at BESSY II, Phys. Rev. Lett. 88, 254801 (2002)

[5] M. Abramowitz and I. A. Stegun, Handbook of Mathematical Functions, Dover, New York, 1965

[6] E. B. Abubakirov and V. L. Bratman, Principles of High-Power Microwave Generation and Their Application to R&D of Relativistic BWOs (2007)

[7] T. Agoh and K. Yoloya, Calculation of coherent synchrotron radiation using mesh, Phys. Rev. ST Accel. Beams 7, 054403 (2004)

[8] T. Agoh, Dynamics of Coherent Synchrotron Radiation by Paraxial Approximation, Ph.D. dissertation, University of Tokyo (2004)

[9] G. B. Arfken and H. J. Weber, Mathematical Methods for Physicists, sixth edition, Elsevier Science (2006)

[10] K. L. F. Bane, F.-J. Decker, Y. Ding, D. Dowell, P. Emma, J. Frisch, Z. Huang, R. Iverson, C. Limborg-Deprey, H. Loos, H.-D. Nuhn, D. Ratner, G. Stupakov, J. Turner, J. Welch, and J. Wu, Measurements and modeling of coherent synchrotron radiation and its impact on the Linac Coherent Light Source electron beam, Phys. Rev. ST Accel. Beams 12, 030704 (2009)

[11] G. Bassi, J. Ellison, K. Heinemann, and R. Warnock, Microbunching instability in a chicane: two-dimensional mean field treatment, Phys. Rev. ST Accel. Beams 12, 080704 (2009)

[12] C. Behrens, F.-J. Decker, Y. Ding, V. A. Dolgashev, J. Frisch, Z. Huang, P. Krejcik, H. Loos, A. Lutman, T. J. Maxwell, J. Turner, J. Wang, M.-H. Wang, J. Welch, and J. Wu, Few-femtosecond time-resolved measurements of X-ray free-electron lasers, Nature Commun. 5, 3762 (2014)

[13] C. Behrens, Z. Huang, and D. Xiang, Reversible electron beam heating for suppression of microbunching instabilities at free-electron lasers, Phys. Rev. ST Accel. Beams 15, 022802 (2012)

[14] S. Benson, Requirements and Status of Bunched Beam ERL Cooler Design, JLEIC Collaboration Meeting, Spring 2016

[15] M. Berz, H.G. Blosser, K. Gelbke, R. York, J. Bisognano, R. Davidson, S. Gruner, M. Tigner, C. Joshi, C. Pellegrini, J. Kirz, J. Rush, Enhancing Accelerator Science and its Impact on Other Sciences: the Role of Universities, 2003. http://www.cap.bnl.gov/mumu/info/white-paper.doc

[16] M. Berz, K. Makino, and W. Wan, An Introduction to Beam Physics, Series in High Energy Physics, Cosmology, and Gravitation, CRC Press (2014)

[17] B. E. Billinghurst, J. C. Bergstrom, C. Baribeau, T. Batten, T. E. May, J. M. Vogt, and W. A. Wurtz, Longitudinal bunch dynamics study with coherent synchrotron radiation, Phys. Rev. Accel. Beams 19, 020704 (2016)

[18] B. E. Billinghurst, J. C. Bergstrom, C. Baribeau, T. Batten, L. Dallin, T. E. May, J. M. Vogt, W. A. Wurtz, R. Warnock, D. A. Bizzozero, and S. Kramer, Observation of Wakefields and Resonances in Coherent Synchrotron Radiation, Phys. Rev. Lett. 114, 204801 (2015)

[19] M. Borland, Y.-C. Chae, S.V. Milton, R. Soliday, V.K. Bharadwaj, P. Emma, P. Krejcik, C. Limborg, H.-D. Nuhn, M. Woodley, Start-to-End Jitter Simulations of the Linac Coherent Light Source, Proceedings of the 2001 Particle Accelerator Conference, pp. 2707-2709 (2001) (WPPH103)

[20] M. Borland, Y.-C. Chae, P. Emma, J.W. Lewellen, V. Bharadwaj, W.M. Fawley, P. Krejcik, C. Limborg, S.V. Milton, H.-D. Nuhn, R. Soliday, M. Woodley, Start-to-end simulation of self-amplified spontaneous emission free electron lasers from the gun through the undulator, Nucl. Instrum. Methods Phys. Res., Sect. A 483, 268 (2002).

[21] M. Borland, `elegant`: A Flexible SDDS-Compliant Code for Accelerator Simulation, APS Light Source Note LS-287 (2000) and Modeling of microbunching instability, Phys. Rev. ST Accel. Beams 11, 030701 (2008)

[22] M. Borland, Controlling noise and choosing binning parameters for reliable CSR and LSC simulation in `elegant`, OAG-TN-2005-027

[23] M. Borland, Growth of density modulation in an energy recovery linac light source due to coherent synchrotron radiation and longitudinal space charge, LINAC08 (TUP024)

[24] M. Borland, Modeling the microbunching instability, Phys. Rev. ST Accel. Beams 11, 030701 (2008)

[25] M. Borland, Simple method for particle tracking with coherent synchrotron radiation, Phys. Rev. ST Accel. Beams 4, 070701 (2001)

[26] R. A. Bosch, Longitudinal wake of a bunch of suddenly accelerated electrons within the radiation formation zone, Phys. Rev. ST Accel. Beams 10, 050701 (2007)

[27] R. Brinkmann, Application of Flat-to-Round Beam Transformation for Radiation Sources, Proceedings of EPAC 2002, Paris, France (2002), TUPRI044

[28] R. Brinkmann, Y. Derbenev and K. Floettmann, A low emittance, flat-beam electron source for linear colliders, Phys. Rev. ST Accel. Beams 4, 053501 (2001).

[29] K. L. Brown, A First and Second Order Matrix Theory for the Design of Beam Transport Systems and Charged Particle Spectrometers, Adv. Part. Phys. 1, 71-134 (1968) and SLAC-75 Rev.4 (1982)

[30] A. Burov, S. Nagaitsev, A. Shemyakin, and Ya. Derbenev, Optical principles of beam transport for relativistic electron cooling, Phys. Rev. ST Accel. Beams 3, 094002 (2000)

[31] J. M. Byrd, W. P. Leemans, A. Loftsdottir, B. Marcelis, M. C. Martin, W. R. McKinney, F. Sannibale, T. Scarvie, and C. Steier, Observation of Broadband Self-Amplified Spontaneous Coherent Terahertz Synchrotron Radiation in a Storage Ring, Phys. Rev. Lett. 89, 224801 (2002).

[32] Y. Cai, Linear theory of microwave instability in electron storage rings, Phys. Rev. ST Accel. Beams 14, 061002 (2011)

[33] G.L. Carr, S. Kramer, J. Murphy, J. LaVeign, R. Lobo, D. Reitze, and D. Tanner, Investigation of coherent emission from the NSLS VUV ring, in Proceedings of the 18th Particle Accelerator Conference, New York, 1999 (IEEE, New York, 1999), p. 134

[34] G.L. Carr, L.F. DiMauro, W.S. Graves, E.D. Johnson, J.B. Murphy, J. Rudati, B. Sheehy, C.P. Neuman, L. Mihaly, D. Talbayev, Coherent Radiation Measurements at the NSLS Source Development Lab, Proc. PAC 2001, Chicago (WPPH069)

[35] A. W. Chao, Physics of Collective Beam Instabilities in High Energy Accelerators, John Wiley and Sons, Inc. (1993).

[36] A. W. Chao, Collective Instability in Accelerators, Lecture Note presented in OCPA School, 2010.

[37] A. W. Chao, K. H. Mess, M. Tigner, and F. Zimmermann, Handbook of Accelerator Physics and Engineering, second edition, World Scientific (2013).

[38] A. W. Chao, Lecture Notes on Special Topics in Accelerator Physics, Report No. SLAC-PUB-9574 (2002), available at http://www.slac.stanford.edu/ achao/lecturenotes.html

[39] A. W. Chao, SLIM – an early work revisited, Proceedings of EPAC08, Genoa, Italy, 2008 (THPPGM04)

[40] M. Conte and W. MacKay, An Introduction to the Physics of Particle Accelerators, second edition, World Scientific (2008)

[41] E. D. Courant and H. S. Snyder, Theory of the Alternating-Gradient Synchrotron, Annals Phys. 3 (1958) 1-48

[42] Ya. S. Derbenev, J. Rossbach, E. L. Saldin, and V. D. Shiltsev, Microbunch radiative tailhead interaction, TESLA-FEL-Report 1995-05

[43] Ya. S. Derbenev and Y. Zhang, Electron cooling for electron ion collider at JLab, Proceedings of Workshop on Beam Cooling and Related Topics, COOL09, Lanzhou, China, 2009, FRM2MCCO01

[44] Ya. S. Derbenev and I. Meshkov, Studies on electron cooling of heavy particle beams made by the VAPP-NAP group at the Nuclear Physics Institute of the Siberian Branch of the USSR Academy of Science at Novosibirsk, CERN 77-08 (1977)

[45] Ya. S. Derbenev and A. N. Skrinsky, The effect of an accompanying magnetic field on electron cooling, Particle Accelerators, Vol. 8, 1978, pp. 235-243

[46] Ya. S. Derbenev, Cooling with Magnetized Electron Beam, MEIC Spring Collaboration meeting, March 30, 2015

[47] Ya. S. Derbenev, A Method to Overcome Space Charge at Injection, AIP Conf. Proc., 773, 335 (2005)

[48] Ya. S. Derbenev and V. Shiltsev, Transverse Effects of Microbunch Radiative Interaction, Report No. SLAC-PUB-7181 (1996)

[49] Ya. S. Derbenev, Advanced Concepts for Electron-Ion Collider, Proceedings of EPAC 2002, Paris, (2002) (MOPLE046)

[50] S. Di Mitri, M. Cornacchia, and S. Spampinati, Cancellation of Coherent Synchrotron Radiation Kicks with Optics Balance, Phys. Rev. Lett. 110, 014801 (2013)

[51] S. Di Mitri and S. Spampinati, Microbunching instability suppression via electron-magnetic-phase mixing, Phys. Rev. Lett. 112, 134802 (2014)

[52] S. Di Mitri, Intrabeam scattering in high brightness electron linacs, Phys. Rev. ST Accel. Beams 17, 074401 (2014)

[53] S. Di Mitri and M. Cornacchia, Transverse emittance-preserving arc compressor for high-brightness electron beam-based light sources and colliders, EPL, 109 (2015) 62002

[54] S. Di Mitri, CSR-Induced Emittance Growth and Related Design Strategies, USPAS Lecture Note of Linear Accelerator Design for Free Electron Lasers (2015)

[55] M. Dohlus, T. Limberg, and P. Emma, Bunch Compression for Linac-based FELs, ICFA Beam Dynamics Newsletter No. 38, 2005

[56] M. Dohlus and T. Limberg, `CSRtrack`: Faster calculation 3-D CSR effects, Proceedings of the 2004 FEL Conference, 18-21 (MOCOS05)

[57] M. Dohlus, A. Kabel, and T. Limberg, Efficient field calculation of 3D bunches on general trajectories, Nucl. Instrum. Methods Phys. Res. Sect. A 445 338 (2000)

[58] D. Douglas, S.V. Benson, A. Hutton, G.A. Krafft, R. Li, G.R. Neil, Y. Roblin, C.D. Tennant, C. -Y. Tsai, Control of coherent synchrotron radiation and microbunching effects during transport of high brightness electron beams, arXiv: 1403.2318v1 [physics.acc-ph]

[59] D. Douglas, S.V. Benson, A. Hofler, R. Kazimi, R. Li, Y. Roblin, C.D. Tennant, G.A. Krafft, B. Terzic, and C. -Y. Tsai, Control of synchrotron radiation effects during recirculation, IPAC15 (TUPMA038)

[60] D. Douglas, Suppression and enhancement of CSR-driven emittance degradation in the IR-FEL Driver, JLAB-TN-98-012, 1998

[61] D.R. Douglas, S.V. Benson, R. Li, Y. Roblin, C.D. Tennant, G.A. Krafft, B. Terzic, and C. -Y. Tsai, Control of synchrotron radiation effects during recirculation with bunch compression, IPAC15 (TUPMA037)

[62] D. Douglas and C. Tennant, Betatron matching magnetized beams, Report No. JLAB-TN-15-026

[63] D. Douglas, Twiss parameterization of flat beam transforms including beam divergence, Report No. JLAB-TN-15-022

[64] D. Douglas, Second Order Achromatic High Dispersion Configuration for Low Energy Beam Lines, CEBAF-TN-90-197, (1990)

[65] A. J. Dragt, R. L. Gluckstern, F. Neri, and G. Rangarajan, Theory of emittance invariants, Frontiers of Particle Beams; Observation, Diagnosis and Correction, Vol. 343, Lecture Notes in Physics, pp. 94-121

[66] The user's manual for `elegant`, available at http://www.aps.anl.gov/Accelerator_Systems _Division/Accelerator_Operations_Physics/manuals/elegant_latest/elegant.html

[67] P. Emma and G.V. Stupakov, CSR Wake for a Short Magnet in Ultrarelativistic Limit, in Proc. of 8th European Accel. Conf. (2002) 1479

[68] R. J. England, Longitudinal Shaping of Relativistic Bunches of Electrons Generated by an RF Photoinjector, UCLA Ph.D. dissertation (2007)

[69] C. Evain, J. Barros, A. Loulergue, M. A. Tordeux, R. Nagaoka, M. Labat, L. Cassinari, G. Creff, L. Manceron, J. B. Brubach, P. Roy, and M. E. Couprie, Spatio-temporal dynamics of relativistic electron bunches during the microbunching instability in storage rings, Europhys. Lett. 98, 40006 (2012).

[70] A. V. Fedotov, I. Ben-Zvi, D. L. Bruhwiler, V. N. Litvinenko, and A. O. Sidorin, High-energy electron cooling in a collider, New Journal of Physics 8 (2006) 283

[71] R. L. Gluckstern, Longitudinal impedance of a periodic structure at high frequency, Phys. Rev. D 39, 2780 (1989)

[72] R. L. Gluckstern, High-frequency behavior of the longitudinal impedance for a cavity of general shape, Phys. Rev. D 39, 2773 (1989)

[73] H. Goldstein, C. P. Poole, and J. L. Safko, Classical Mechanics, third edition, Addison Wesley (2001)

[74] R. Hajima, A First-Order Matrix Approach to the Analysis of Electron Beam Emittance Growth Caused by Coherent Synchrotron Radiation, Japanese Journal of Applied Physics, 42 (2003)

[75] A. Halavanau and P. Piot, Simulation of a cascaded longitudinal space charge amplifier for coherent radiation generation, available at https://arxiv.org/pdf/1510.00679.pdf

[76] C. C. Hall, S. G. Biedron, A. L. Edelen, S. V. Milton, S. Benson, D. Douglas, R. Li, C. D. Tennant, and B. E. Carlsten, Measurement and simulation of the impact of coherent synchrotron radiation on the Jefferson Laboratory energy recovery linac electron beam, Phys. Rev. ST Accel. Beams 18, 030706 (2015)

[77] J. Halton, Algorithm 247: Radical-inverse quasi-random point sequence, ACM, p. 701, (1964)

[78] A. He, F. Willeke, L. -H. Yu, L. Yang, T. Shaftan, G. Wang, Y. Li, Y. Hidaka, and J. Qiang, Design of low energy bunch compressors with space charge effects, Phys. Rev. ST Accel. Beams 18, 014201 (2015)

[79] S. Heifets, G. Stupakov, and S. Krinsky, Coherent synchrotron radiation instability in a bunch compressor, Phys. Rev. ST Accel. Beams 5, 064401 (2002)

[80] G. Hoffstaetter, V. Litvinenko, and H. Owen, Optics and beam transport in energy recovery linacs, Nucl. Instru. Methods in Phys. Res. Sec. A 557, 2006, pp. 345-353

[81] Z. Huang and K. -J. Kim, Formulas for coherent synchrotron radiation microbunching in a bunch compressor chicane, Phys. Rev. ST Accel. Beams 5, 074401 (2002)

[82] Z. Huang, M. Borland, P. Emma, J. Wu, C. Limborg, G. Stupakov, and J. Welch, Suppression of microbunching instability in the linac coherent light source, Phys. Rev. ST Accel. Beams 7 074401 (2004)

[83] Z. Huang, P. Emma, M. Borland, and K. -J. Kim, Effect of linac wakefield on CSR microbunching in the Linac Coherent Light Source, in Proceedings of the 2003 Particle Accelerator Conference, Portland, OR (IEEE, New York, 2003)

[84] Z. Huang, J. Wu and T. Shaftan, Microbunching Instability due to Bunch Compression, ICFA Beam Dynamics Newsletters 38 (2005)

[85] C. Huang, T. J. T. Kwan, and B. E. Carlsten, Two dimensional model for coherent synchrotron radiation, Phys. Rev. ST Accel. Beams 16, 010701 (2013)

[86] S. Ichimaru, Basic Principles of Plasma Physics: A Statistical Approach, Frontiers in Physics, W. A. Benjamin Inc. (1973)

[87] J. D. Jackson, Classical Electrodynamics, third edition, John Wiley and Sons, Inc. (1998).

[88] Y. Jiao, X. Cui, X. Huang, and G. Xu, Generic conditions for suppressing the coherent synchrotron radiation induced emittance growth in a two-dipole achromat, Phys. Rev. ST Accel. Beams 17, 060701 (2014)

[89] Y. Jing, Y. Hao, and V. N. Litvinenko, Compensating effect of the coherent synchrotron radiation in bunch compressors, Phys. Rev. ST Accel. Beams 16, 060704 (2013)

[90] V. Judin, N. Hiller, A. Hofmann, E. Huttel, B. Kehrer, M. Klein, S. Marsching, C. Meuter, A.-S. Mueller, M. J. Nasse, M. Schuh, M. S. N. Smale, and M. I. Streichertin, Spectral and Temporal Observations of CSR at ANKA, in Proceedings of the International Particle Accelerator Conference, New Orleans, USA, (IPAC'12 OC/IEEE, and the Joint Accelerator Conferences Website (JACoW), CERN, Geneva, 2012), TUPPP010, p. 1623

[91] E. Karantzoulis, G. Penco, A. Perucchi, and S. Lupi, Characterization of coherent THz radiation bursting regime at Elettra, Infrared Phys. 53 300 (2010)

[92] S. Khan, Collective Phenomena in Synchrotron Radiation Sources – Particle Acceleration and Detection, Springer Berlin Heidelberg (2007)

[93] K. -J. Kim, An Oscillator Configuration of an X-Ray Free-Electron Laser for Exceptional Spectral Purity and Stability, Proceedings of ERL2011, Tsukuba, Japan (2011) (PLT005)

[94] K. -J. Kim, Round-to-flat transformation of angular-momentum-dominated beams, Phys. Rev. ST Accel. Beams 6, 104002 (2003)

[95] M. Klein, T. Bckle, M. Fitterer, A. Hofmann, A.-S. Mller, K.G. Sonnad, I. Birkel, E. Huttel, and Y.-L. Mathis, Studies of Bunch Distortion and Bursting Threshold in the Generation of Coherent THz-Radiation at the ANKA Storage Ring, Proceedings of PAC09, Vancouver, BC, Canada (FR5RFP095)

[96] B. Koltenbah, C. G. Parazzoli, R. B. Greegor, and D. H. Dowell, `PARMELA_B`: a new version of `PARMELA` with coherent synchrotron radiation effects and a finite difference space charge routine, 487, 249-267 (2002)

[97] G. A. Krafft, Energy Recovery Linacs, Proceedings of LINAC08, Victoria, BC, Canada (WE101).

[98] S. Kramer, Direct observation of beam impedance above cutoff, Phys. Rev. ST Accel. Beams 5, 112001 (2002)

[99] J. Laskar, C. Froeschle, and A. Celletti, The measure of chaos by the numerical analysis of the fundamental frequencies. Application to the standard mapping, Physica D 56 (1992) 253-269

[100] Conceptual Design Report (CDR) for the Linac Coherent Light Source (LCLS), SLAC-R-593 or UC-414, available at http://www-ssrl.slac.stanford.edu/lcls/cdr/

[101] V. A. Lebedev and S. A. Bogacz, Betatron motion with coupling of horizontal and vertical degrees of freedom, Journal of Instrumentation, Vol. 5 (2010)

[102] S. Y. Lee, Accelerator Physics, second edition, World Sci. Pub. Co. Pte. Ltd. (2004)

[103] R. Li and C. -Y. Tsai, CSR impedance for non-ultrarelativistic beams, IPAC15 (MOPMN004)

[104] R. Li and C. -Y. Tsai, Entrance and Exit CSR Impedance for Non-ultrarelativistic Beams, (in preparation)

[105] R. Li, Curvature-induced bunch self-interaction for an energy-chirped bunch in magnetic bends, Phys. Rev. ST Accel. Beams 11, 024401 (2008)

[106] R. Li, Sensitivity of the CSR self-interaction to the local longitudinal charge concentration of an electron bunch, Nucl. Instrum. Methods Phys. Res. Sect. A 475, 498-503 (2001)

[107] R. Li and Ya. S. Derbenev, Canonical Formulations and Cancellation Effect in. Electrodynamics of Relativistic Beams on a Curved Trajectory, JLAB-TN-02-054, 2002

[108] R. Li and Ya. S. Derbenev, Discussions on the Cancellation Effect on a Circular Orbit, Proc. 2005 PAC, p. 1631 (2005) TPAT019

[109] R. Li, Progress on the study of CSR effects, Proceedings of the 2nd ICFA Advanced Accelerator Workshop, p.369 (1999)

[110] R. Li, Self-consistent simulation of the CSR effect on beam emittance, Nuclear Instrum. Methods Phys. Res., Sect. A 429, 310 (1998)

[111] R. Li, Analysis and simulation of the enhancement of the CSR effects, XX International Linac Conference, Monterey, California, 2000 (MOE01)

[112] R. Li, A Discussion on Phase Space and Beam Emittance, NAPAC16 (TUB1TU01)

[113] R. Li, Radial Eigenmodes for a Toroidal Waveguide with Rectangular Cross Section, Proceedings of IPAC2012, New Orleans, Louisiana, USA (WEPPR095)

[114] R. Li and C. -Y. Tsai, Studies of CSR-Induced Microbunching Gain for Beam Transport in Project E (2015) (unpublished)

[115] Y. Li, Studies of microwave instability in the small isochronous ring, Ph.D. dissertation, Michigan State University (2014)

[116] V.N. Litvinenko, I. Ben-Zvi, L. Ahrens, M. Bai, J. Beebe-Wang, M. Blaskiewicz, J.M. Brennan, R. Calaga, X. Chang, A.V. Fedotov, W. Fischer, D. Kayran, J. Kewisch, W.W. MacKay, C. Montag, B. Parker, S. Peggs, V. Ptitsyn, T. Roser, A. Ruggiero, T. Satogata, B. Surrow, S. Tepikian, D. Trbojevic, V. Yakimenko, S.Y. Zhang, M.Farkhondeh, and A. Deshpande, ERL Based Electron-Ion Collider eRHIC, Proceedings of 2005 PAC, Knoxville (2005) (TPPP043)

[117] V. N. Litvinenko and G. Wang, Relativistic Effects in Micro-bunching, Proceedings of FEL2014, Basel, Switzerland, 2014 (THP035)

[118] A. H. Lumpkin, Overview and Issues of Experimental Observation of Microbunching Instabilities, Fifth Microbunching Instability Workshop (2013), FERMILAB-CONF-14-105-AD

[119] W. Magnus, On the exponential solution of differential equations for a linear operator. Comm. Pure and Appl. Math. VII (4): 649-673 (1954)

[120] `MATLAB` 8.1.0, R2013a, The MathWorks, Inc., Natick, Massachusetts, United States.

[121] C. Mayes and G. Hoffstaetter, Exact 1D model for coherent synchrotron radiation with shielding and bunch compression, Phys. Rev. ST Accel. Beams 12, 024401 (2009)

[122] C. Mayes, private communication

[123] L. Merminga, D. R. Douglas, and G. A. Krafft, High-current Energy-Recovery Electron Linacs, Annu. Rev. Nucl. Part. Sci., 53, 387 (2003).

[124] M. G. Minty and F. Zimmermann, Measurement and Control of Charged Particle Beams, Springer (2003)

[125] C. Mitchell and J. Qiang, Effects of transient CSR wakefields on microbunching in a bunch compressor, IPAC13 (TUPWA057)

[126] C. Mitchell, J. Qiang, and P. Emma, Longitudinal pulse shaping for the suppression of coherent synchrotron radiation induced emittance growth, Phys. Rev. ST Accel. Beams 16, 060703 (2013)

[127] A.-S. Muller, Accelerator-based sources of infrared and terahertz radiation, Rev. Accel. Sci. Techol. 03, 165 (2010)

[128] J. B. Murphy, S. Krinsky, and R. L. Gluckstern, Longitudinal wakefield for an electron moving on a circular orbit, Part. Accel. 1997, Vol. 57, pp. 9-64

[129] J. B. Murphy, Coherent Synchrotron Radiation in Storage Rings, ICFA Beam Dynamics Newsletter No. 35, 2004

[130] N. Nakamura, Review of ERL Projects at KEK and Around the World, Proceedings of IPAC 2012, New Orleans, Louisiana, USA (TUXB02)

[131] G. R. Neil, C. L. Bohn, S. V. Benson, G. Biallas, D. Douglas, H. F. Dylla, R. Evans, J. Fugitt, A. Grippo, J. Gubeli, R. Hill, K. Jordan, R. Li, L. Merminga, P. Piot, J. Preble, M. Shinn, T. Siggins, R. Walker, and B. Yunn, Sustained Kilowatt Lasing in a Free-Electron Laser with Same-Cell Energy Recovery, Phys. Rev. Lett. 84, 662 (2000)

[132] G. R. Neil and L. Merminga, Technical approaches for high-average-power free-electron lasers, Rev. Mod. Phys. 74, 685 (2002)

[133] K. Y. Ng, Physics of Intensity Dependent Beam Instabilities, World Scientific (2005)

[134] E. Nissen, Y. Zhang, R. Li, D. Douglas and C. Tennant, Microbunching Effects Induced by CSR in the MEIC Circulator Cooler Ring, Proceedings of EIC14 Workshop, Newport New, Virginia, USA (2014)

[135] NLC Zeroth-Order Design Report, available at http://www.slac.stanford.edu/accel/nlc/zdr/

[136] V. V. Parkhomchuk and A. N. Skrinsky, Electron cooling: physics and prospective applications, Rep. Prog. Phys. 54, 919 (1991)

[137] V. Parkhomchuk and I. Ben-Zvi, Electron Cooling for RHIC, Report No. C-A/AP/47 (2001)

[138] P. Piot and A. Halavanau, private communication

[139] W. Press, S. Teukolsky, W. Vetterling, and B. Flannery, Numerical Recipes in C, Cambridge University Press, New York, 1998

[140] J. Qiang, Y. Ding, P. Emma, Z. Huang, D.F. Ratner, and T.O. Raubenheimer, Simulation of the Shot-Noise Driven Microbunching Instability Experiment at the LCLS, Proceedings of NA-PAC2016, Chicago, IL, USA (WEPOB30)

[141] J. Qiang, R. Ryne, S. Habib, and V. Decyk, An object-oriented parallel particle-in-cell code for beam dynamics simulation in linear accelerators, J. Comp. Phys. 163, 434-451 (2000)

[142] J. Qiang, C. Mitchell, and M. Venturini, Suppression of Microbunching Instability Using Bending Magnets in Free-Electron-Laser Linacs, Phys. Rev. Lett. 111, 054801 (2013)

[143] J. Qiang, S. Lidia, R. D. Ryne, and C. Limborg-Deprey, Three-dimensional quasistatic model for high brightness beam dynamics simulation, Phys. Rev. ST Accel. Beams 9, 044204 (2006)

[144] J. Qiang, R. D. Ryne, M. Venturini, and A. A. Zholents, Billion Particle Linac Simulations for Future Light Sources, Proceedings of LINAC08, Victoria, BC, Canada (FR105)

[145] G. Rangarajan, F. Neri, and A. Dragt, Generalized Emittance Invariants, in Proceedings of the 1989 Particle Accelerator Conference, Chicago, IL (IEEE, Piscataway, NJ, 1989), p. 1280

[146] D. Ratner, C. Behrens, Y. Ding, Z. Huang, A. Marinelli, T. Maxwell, and F. Zhou, Time-resolved imaging of the microbunching instability and energy spread at the Linac Coherent Light Source, Phys. Rev. ST Accel. Beams 18, 030704 (2015)

[147] D. Ratner, A. Chao, and Z. Huang, Three-Dimensional Analysis of Longitudinal Space Charge Microbunching Starting From Shot Noise, Proceedings of 30th International Free Electron Laser Conference (FEL 2008) and SLAC-PUB-13392

[148] D. Ratner and A. Chao, Steady-State Microbunching in a Storage Ring for Generating Coherent Radiation, Phys. Rev. Lett. 105, 154801 (2010)

[149] J. R. Rees, Symplecticity in Beam Dynamics: An Introduction, SLAC-PUB-9939 (2003)

[150] M. Reiser, Theory and Design of Charged Particle Beams, WILEY-VCH Verlag (2004)

[151] R. D. Ryne, C.E. Mitchell, J. Qiang, B.E. Carlsten, N.A. Yampolsky, Large-scale Simulation of Synchrotron Radiation using a Lienard-Wiechert Approach, Proceedings of IPAC2012, New Orleans, Louisiana, USA (TUPPP036)

[152] E. L. Saldin, E. A. Schneidmiller, and M. V. Yurkov, Klystron instability of a relativistic electron beam in a bunch compressor, Nucl. Instrum. Methods Phys. Res. Sect. A 490, 1 (2002)

[153] E. L. Saldin, E. A. Schneidmiller, and M. V. Yurkov, On the coherent radiation of an electron bunch moving in an arc of a circle, NIMA 398, 373 (1997)

[154] E. L. Saldin, E. A. Schneidmiller, and M. V. Yurkov, Longitudinal space charge-driven microbunching instability in the TESLA Test Facility linac, NIM A 528 (2004), pp. 355-359

[155] E.L Saldin, E.A Schneidmiller, and M.V Yurkov, An analytical description of longitudinal phase space distortions in magnetic bunch compressors, Nucl. Instrum. Methods Phys. Res. Sect. A 483, 516(2002)

[156] J. Schwinger, On the Classical Radiation of Accelerated Electrons, Phys. Rev. 75, 1912 (1949)

[157] S. Seletskiy, B. Podobedov, Y. Shen, and X. Yang, Seeding, Controlling, and Benefiting from the Microbunching Instability, Phys. Rev. Lett. 111, 034803 (2013)

[158] I. Setija, private communication

[159] W. Shields, R. Bartolini, G. Boorman, P. Karataev, A. Lyapin, J. Puntree, and G. Rehm, Microbunch instability observations from a THz detector at diamond light source, J. Phys. Conf. Ser. 357, 012037 (2012)

[160] T.I. Smith, H.A. Schwettman, R. Rohatgi, Y. Lapierre, and J. Edighoffer, Development of the SCA/FEL for use in biomedical and materials science experiments, Nucl. Instrum. Methods A 259, 1-7 (1987)

[161] S. J. Smith and E. M. Purcell, Visible Light from Localized Surface Charges Moving across a Grating, Phys. Rev. 92, 1069 (1953)

[162] G. Stupakov, Lecture notes on Classical Mechanics and Electromagnetism in Accelerator Physics, The US Particle Accelerator School, June 13-24, 2011

[163] G. Stupakov and I. Kotelnikov, Shielding and synchrotron radiation in toroidal waveguide, Phys. Rev. ST Accel. Beams 6, 034401 (2003)

[164] G. Stupakov and S. Heifets, Beam instability and microbunching due to coherent synchrotron radiation, Phys. Rev. ST Accel. Beams 5, 054402 (2002)

[165] G. Stupakov, Effect of Coulomb Collisions on Echo-enabled Harmonic Generation, FEL2013 (WEPSO68)

[166] G. Stupakov, Using the Beam-Echo Effect for Generation of Short-Wavelength Radiation, Phys. Rev. Lett. 102, 074801 (2009)

[167] Y. Sun, Angular-momentum-dominated electron beams and flat-beam generation, Ph.D. dissertation, University of Chicago (2005) FERMILAB-THESIS-2005-17

[168] Y. Takashima, M. Katoh, M. Hosaka, A. Mochihashi, S. -I. Kimura, and T. Takahashi, Observation of Intense Bursts of Terahertz Synchrotron Radiation at UVSOR-II, Jpn. J. Appl. Phys. 44, L1131 (2005)

[169] C. Tennant and D. Douglas, Coherent synchrotron radiation induced beam degradation in the MEIC Circulator Cooler Ring, Report No. JLAB-TN-12-027 (2012)

[170] B. Terzic and R. Li, New Particle-in-cell Code for Numerical Simulation of Coherent Synchrotron Radiation, Proceedings of IPAC2010, Kyoto, Japan (2010) TUPEC084

[171] A. M. Tigner, Possible apparatus for electron-clashing experiments, Nuovo Cimento 37 (1965).

[172] K. Togawa, T. Hara, H. Maesaka, S. Matsubara, S. Inoue, Y. Otake, and H. Tanaka, COTR Phenomena Observed in SCSS Test Accelerator and SACLA, 4th Microbunching Instability Workshop, Univ. of Maryland April 11-13, 2012

[173] C. -Y. Tsai and R. Li, Simulation of coherent synchrotron radiation induced microbunching gain using `elegant`, JLAB-TN-14-016

[174] C. -Y. Tsai, D. Douglas, R. Li, and C. Tennant, Linear Vlasov Solver for Microbunching Gain Estimation with Inclusion of CSR, LSC and Linac Geometric Impedances, FEL15 (MOP052)

[175] C. -Y. Tsai and R. Li, Combination of density and energy modulation in microbunching analysis, IPAC16 (TUPOR020)

[176] C. -Y. Tsai and R. Li, Step-by-step guide to using `volterra_mat` and some notes on the code, JLAB-TN-15-019

[177] C. -Y. Tsai, D. Douglas, R. Li, and C. Tennant, Linear microbunching analysis for recirculation machines, Phys. Rev. Accel. Beams 19, 114401 (2016)

[178] C. -Y. Tsai, D. Douglas, R. Li, and C. Tennant, Multistage CSR microbunching gain development in transport or recirculation arcs, FEL15 (MOP087)

[179] C. -Y. Tsai, D. Douglas, R. Li, and C. Tennant, Linear microbunching gain estimation including CSR and LSC impedances in recirculation machines, Proceedings of The 56th ICFA Advanced Beam Dynamics Workshop on Energy Recovery Linacs (ERL2015) (TUICLH2034)

[180] C. -Y. Tsai, D. Douglas, R. Li, and C. Tennant, Growth of density modulation in MEIC CCR due to coherent synchrotron radiation, EIC14 The International Workshop on Accelerator Science and Technology for Electron-Ion Collider (poster)

[181] C. -Y. Tsai, D. Douglas, R. Li, and C. Tennant, Theoretical Investigation of Coherent Synchrotron Radiation Induced Micro-bunching Instability for High-Energy Recirculation Arcs, MEIC Circulator Cooling Ring, and a Novel Compressor Arc: Benchmarking, Stage Gain Analysis, and Parametric Studies, Report No. JLAB-TN-16-030 (2016)

[182] C. -Y. Tsai, D. Douglas, R. Li, and C. Tennant, Theoretical investigation of coherent synchrotron radiation induced microbunching instability in transport and recirculation arcs, FEL14 (THP022)

[183] C. -Y. Tsai, D. Douglas, R. Li, and C. Tennant, CSR induced microbunching gain estimation including transient effects in transport and recirculation arcs, IPAC15 (MOPMA025)

[184] C. -Y. Tsai, S. Di Mitri, D. Douglas, R. Li, and C. Tennant, Conditions for CSR microbunching gain suppression, IPAC16 (TUOAB02)

[185] C. -Y. Tsai and R. Li, Analysis of microbunching structures in transverse and longitudinal phase spaces, NA-PAC16 (THPOA35)

[186] C. -Y. Tsai, Simple scripts for microbunching gain analyses, JLAB-TN-16-022

[187] C. -Y. Tsai, Ya. Derbenev, D. Douglas, R. Li, and C. Tennant, Vlasov Analysis of Microbunching Gain for Magnetized Beams, NA-PAC 2016 (WEA2CO04)

[188] C. -Y. Tsai, S. Di Mitri, D. Douglas, R. Li, and C. Tennant, Conditions for coherent-synchrotron-radiation-induced microbunching suppression in multibend beam transport or recirculation arcs, Phys. Rev. Accel. Beams 20, 024401 (2017)

[189] C. -Y. Tsai, Ya. Derbenev, D. Douglas, R. Li, and C. Tennant, Vlasov analysis of microbunching instability for magnetized beams (submitted to Phys. Rev. Accel. Beams)

[190] C. -Y. Tsai and R. Li, Preliminary study of microbunching for CBETA arc, JLAB-TN-16-028

[191] R. Q. Twiss and N. H. Frank, Orbital Stability in a Proton Synchrotron, Rev. Sci. Instr. 20 (1949), 1

[192] M. Venturini, R. Warnock, R. Ruth, and J. A. Ellison, Coherent synchrotron radiation and bunch stability in a compact storage ring, Phys. Rev. ST Accel. Beams 8, 014202

[193] M. Venturini, Microbunching instability in a single-pass systems using a direct two-dimensional Vlasov solver, Phys. Rev. ST Accel. Beams 10, 104401 (2007)

[194] M. Venturini, Models for longitudinal space charge impedance for microbunching instability, Phys. Rev. ST Accel. Beams 11, 034401 (2008)

[195] M. Venturini, M. Migliorati, C. Ronsivalle, M. Ferrario, and C. Vaccarezza, Dynamics of longitudinal phase-space modulation in an RF compressor for electron beams, Phys. Rev. ST Accel. Beams 13, 080703 (2010)

[196] M. Venturini, R. Warnock, and A. Zholents, Vlasov solver for longitudinal dynamics in beam delivery systems for x-ray free electron lasers, Phys. Rev. ST Accel. Beams 10, 054403 (2007)

[197] M. Venturini, CSR-induced emittance growth in achromats: Linear formalism revisited, NIM A 794 (2015), pp. 109-112

[198] M. Venturini, Design of a triple-bend isochronous achromat with minimum coherent-synchrotron-radiation-induced emittance growth, Phys. Rev. Accel. Beams 19, 064401 (2016)

[199] M. Venturini and J. Qiang, Transverse space-charge induced microbunching instability in high-brightness electron bunches, Phys. Rev. ST Accel. Beams 18, 054401 (2015)

[200] M. Venturini, Shot-noise seeded microbunching instability: Second-order correction to the gain function, NIM A 599, pp. 140-145 (2009)

[201] N. A. Vinokurov, Z. Huang, O. A. Shevchenko, and K. -J. Kim, Quasilinear theory of high-gain FEL saturation, NIM A 475, Issue 1-3, pp. 74-78 (2001)

[202] A. A. Vlasov, On Vibration Properties of Electron Gas, J. Exp. Theor. Phys. 8, 291 (1938)

[203] L. Wang, Three-dimensional Robust Solver for Parabolic Equation, Proposal in LCLS effort meeting (2011), slides available

[204] R. Warnock, Shielded coherent synchrotron radiation and its effects on very short bunches, SLAC-PUB-5375, 1990

[205] R. Warnock and P. Morton, Fields excited by a beam in a smooth toroidal chamber. Part I: Longitudinal coupling impedance, Part.Accel. 25 (1990) 113 and SLAC-PUB-4562

[206] R. Warnock and J. Bergstrom, Coherent radiation in whispering gallery modes, SLAC-PUB-16667

[207] S. D. Webb, A Hamiltonian perturbation theory for the nonlinear Vlasov equation, Journal of Math. Physics, 57 (2016)

[208] A. Wolski, Beam Dynamics in High Energy Particle Accelerators, Imperial College Press (2014)

[209] J. Wu, Z. Huang, and P. Emma, Analytical analysis of longitudinal space charge effects for a bunched beam with radial dependence, Phys. Rev. ST Accel. Beams 11, 040701 (2008)

[210] G. Wustefeld, J. Feikes, M. Hartrott, M. Ries, A. Hoehl, R. Klein, R. Muller, A. Serdyukov, and G. Ulm, Coherent THz Measurements at the Metrology Light Source, in Proceedings of the International Particle Accelerator Conference, Kyoto, Japan, 2010 (ICR, Kyoto, 2010), p. 2508

[211] N. A. Yampolsky, Description of modulated beam dynamics, available at https://arxiv.org/abs/1112.0553v1 (2011)

[212] K. Yokoya and K. Bane, The longitudinal high-frequency impedance of a periodic accelerating structure, PAC 1999

[213] K. Yokoya and P. Chen, Electron Energy Spectrum and Maximum Disruption Angle Under Multi-Photon Beamstrahlung, in Proceedings of the 1989 Particle Accelerator Conference, Chicago, IL (IEEE, New York, NY, 1989), pp. 1438-1440

[214] L. M. Young, TStep, more information at http://tstep.lmytechnology.com/TSTEP.html

[215] R. C. York, 5 upgradable to 25 keV free electron laser facility, Phys. Rev. ST Accel. Beams 17, 010705 (2014)

[216] L. H. Yu, Generation of intense UV radiation by subharmonically seeded single-pass free-electron lasers, Phys. Rev. A, 44, 8 (1991)

[217] H. Zhang, D. Douglas, Ya Derbenev, and Y. Zhang, Electron cooling study for MEIC, Proceedings of the 6th International Particle Accelerator Conference (2015), TUPWI037

[218] D. Zhou, An alternative 1D model for CSR with chamber shielding, IPAC12 (MOOBB03)